# Discontinuous Carbon Fibre Composites for Automotive Applications

*by*

Lee Thomas Harper

MEng. (Hons.)

Thesis submitted to the University of Nottingham for the degree of

Doctor of Philosophy

August 2006

# Abstract

Increasingly stringent emissions targets are encouraging vehicle manufacturers to prioritise reduction of vehicle mass. The falling cost of carbon fibre is increasing the viability of lightweight carbon-based body panel systems across a broad range of production volumes. In the present work an automated process has been developed for the manufacture of random fibre preforms at medium volume production levels (30-50,000ppa).

This thesis seeks to understand the influence of key microstructural parameters on the mechanical and physical properties of carbon fibre laminates produced by directed fibre preforming. The principal parameters studied are fibre length, tow filament count and laminate thickness. A statistical process simulation has been developed to predict preform density variation and the results are compared with experimental tensile properties.

Experimental studies have shown that there is a notable reduction in areal density variation and consequently an increase in tensile properties with shorter fibres (115mm to 6mm) and thicker laminates (1.5mm to 4mm for a constant volume fraction). Shorter lengths improved preform coverage and gave higher tensile strength, whilst thicker laminates reduced the presence of unreinforced areas which cause stress concentrations. Tow filamentisation has been induced by pneumatic means to reduce the mean filament count and maximise the mechanical performance when using inexpensive, 24K bundles. By maximising the level of filamentisation both stiffness and strength can be increased by 20% and 45% respectively.

An analytical stiffness model is presented to predict the effect of tow filament count on the in-plane elastic constants. Filament count and out-of-plane fibre orientation distributions are determined from optical microscopy and are incorporated into a multi-level Mori-Tanaka based model. Predictions are within 8% of the experimental data for laminates containing large fibre bundles and 10% for laminates with highly filamentised bundles. An expression for critical bundle length has been developed for more accurate strength prediction, based on the number of filaments within the bundle.

Experimental results confirm that the critical tow length is proportional to the tow filament count.

Directed fibre preforming has been benchmarked against other competing processes in respect of mechanical properties, weight saving potential and cost. A full-scale demonstrator component has been manufactured using a variety of carbon composite solutions, which can all provide 40 to 50% weight saving for an equivalent bending stiffness to steel and greatly improved dent resistance. Directed fibre preforming has shown great promise for both semi-structural and structural components for medium volume applications, particularly when aligned fibres are introduced. The results from this work can be directly scaled for industrial application to provide a cost effective, lightweight alternative to steel.

# Acknowledgements

The author wishes to acknowledge the advice and support of his academic supervisors, Dr Nicholas Warrior and Professor Christopher Rudd.

Special thanks go to Dr Thomas Turner for his invaluable help and for developing both the DCFP machine (Chapter 2) and the technical cost model (Chapter 6). Thanks also go to Roger Smith, Paul Johns and Geoffrey Tomlinson for their technical assistance during the practical aspects of this work.

The author gratefully acknowledges the financial support of the DTI / DfT under the Foresight Vehicle Programme and the collaborative support of the Ford Motor Company, Aston Martin Lagonda, QinetiQ, Hexcel and Toho Tenax Europe GmbH.

Most importantly, I am eternally indebted to my fiancée, Debbie, who has offered me love, support and encouragement at all times.

# Contents

Abstract ..... 1
Acknowledgements ..... 4
Contents ..... 5
Chapter 1. Introduction ..... 9
1.1. Drivers of affordable lightweight automotive materials ..... 9
1.1.1. Weight ..... 9
1.1.2. Cost ..... 10
1.1.3. Recycling ..... 12
1.2. Candidate automotive systems – current state of the art ..... 13
1.2.1. Steel ..... 13
1.2.2. Aluminium ..... 14
1.2.3. Magnesium ..... 15
1.2.4. Fibre reinforced plastics ..... 15
1.3. Applications of composites within the automotive industry ..... 16
1.3.1. High volume (50,000-200,000ppa) ..... 17
1.3.2. Medium volume (1000 – 50,000ppa) ..... 19
1.3.3. Low volume (<1000ppa) ..... 19
1.4. Composite preforming techniques ..... 21
1.5. Directed fibre preforming ..... 24
1.6. Theme of work ..... 26
Chapter 2. DCFP process development ..... 28
2.1. Objectives ..... 28
2.2. University of Nottingham DCFP facility ..... 28
2.2.1. Introduction to the process ..... 28
2.2.2. Issues with current DFP installations ..... 29
2.2.3. DCFP developments ..... 32
2.2.4. Nottingham DCFP preforming cycle ..... 36
2.2.5. Fibre alignment ..... 40
2.3. DCFP process optimisation ..... 45
2.3.1. The effect of DCFP machine parameters ..... 45
2.3.1.1. Coverage optimisation ..... 46
2.3.1.2. Effect of lay-down strategy ..... 52
2.3.1.3. DCFP optimisation conclusions ..... 54
2.3.2. Binder study ..... 55
2.4. DCFP process simulation ..... 59
2.5. Conclusions ..... 63
Chapter 3. The effect of microstructural parameters on the in-plane properties of DCFP laminates ..... 64
3.1. Introduction ..... 64
3.2. Size and scale effects ..... 65
3.2.1. Background ..... 65
3.2.2. DCFP mesostructure ..... 66
3.2.3. Stiffness – Effect of RVE size ..... 66
3.2.4. Weibull theory ..... 68
3.2.5. Size effects – Filament level (microscopic) ..... 70
3.2.6. Size effects – Bundle level (mesoscopic) ..... 71
3.2.7. Size effects – Laminate level (macroscopic) ..... 72

3.2.8. Analytical investigation into the effect of specimen size ..... 74
3.2.8.1. Homogeneity of fibre orientation distribution ..... 74
3.2.8.2. Homogeneity of areal density ..... 76
3.2.9. Experimental investigation into the effect of specimen size ..... 78
3.2.10. Conclusions ..... 80
3.3. Effect of areal density variation (Fibre coverage) ..... 82
3.3.1. Background ..... 82
3.3.2. Independent variables ..... 83
3.3.3. Experimental methodology ..... 84
3.3.4. Results ..... 85
3.3.4.1. Areal density variation ..... 85
3.3.4.2. Mechanical Properties ..... 88
3.3.5. Discussion ..... 91
3.3.6. Conclusions ..... 94
3.4. Effect of fibre length ..... 95
3.4.1. Background ..... 95
3.4.2. Results and discussion ..... 96
3.4.3. Conclusions ..... 98
3.5. Effect of tow filamentisation ..... 102
3.5.1. Background ..... 102
3.5.2. Filamentisation techniques ..... 104
3.5.3. Experimental methodology ..... 105
3.5.4. Results and discussion ..... 106
3.5.4.1. Effect of filamentisation on mechanical properties ..... 106
3.5.4.2. Effect of filamentisation on preform loft ..... 107
3.5.5. Conclusions ..... 112
3.6. In-plane material characterisation ..... 112
3.6.1. Background ..... 112
3.6.2. Independent variables ..... 113
3.6.3. Results and Discussion ..... 114
3.6.4. Conclusions ..... 118
3.7. Chapter conclusions ..... 119
Chapter 4. Analytical tensile stiffness prediction ..... 121
4.1. Objectives ..... 121
4.2. Literature review ..... 121
4.2.1. Fibre orientation mechanisms ..... 121
4.2.1.1. Comparison with experimental data ..... 125
4.2.2. The effect of fibre length ..... 127
4.2.3. Micromechanics (Anisotropy) ..... 129
4.2.4. The effect of fibre bundling ..... 132
4.2.4.1. Filament count quantification ..... 134
4.2.5. Current modelling limitations ..... 134
4.3. DCFP stiffness model ..... 135
4.3.1. Introduction ..... 135
4.3.2. Level 1 - Elastic constants of a transversely isotropic bundle ..... 138
4.3.3. Level 2 - Elastic constants of a UD ply containing tows ..... 140
4.3.4. Level 3 - Orientation averaging ..... 142
4.3.5. Level 4 - Aggregate averaging ..... 143
4.3.6. Image analysis methodology ..... 144
4.3.6.1. Filament count distribution ..... 145

4.3.6.2. Orientation distributions ..... 150
4.4. Results and discussion ..... 153
4.4.1. Sensitivity study ..... 153
4.4.2. Constant filament count ..... 159
4.4.3. Variable filament counts ..... 162
4.4.4. Effect of fibre length ..... 165
4.4.5. Full material characterisation ..... 167
4.5. Conclusions ..... 171
Chapter 5. Analytical tensile strength prediction ..... 173
5.1. Objectives ..... 173
5.2. Literature review ..... 173
5.3. Current modelling limitations ..... 175
5.4. Critical bundle length model ..... 176
5.4.1. Introduction ..... 176
5.4.2. Methodology ..... 177
5.4.3. Results and discussion ..... 180
5.5. Analytical strength model ..... 183
5.5.1. Introduction ..... 183
5.5.2. Level 1 – Single UD fibre strength ..... 183
5.5.3. Level 2 – UD bundle strength ..... 185
5.5.4. Level 3 – UD ply strength ..... 186
5.5.5. Level 4 – Orientation averaging ..... 189
5.5.6. Results and discussion ..... 190
5.6. Stochastic strength model ..... 193
5.6.1. Introduction ..... 193
5.6.2. Methodology ..... 194
5.6.3. Results and discussion ..... 197
5.7. Conclusions ..... 200
Chapter 6. Comparison of DCFP with commercial body panel systems ..... 201
6.1. Objectives ..... 201
6.2. Introduction ..... 201
6.3. Material characterisation for semi-structural applications ..... 202
6.3.1. Material selection ..... 202
6.3.2. Flexural properties ..... 205
6.3.3. Fabric formability ..... 207
6.3.4. Dent resistance ..... 211
6.3.5. In-plane mechanical performance ..... 214
6.3.6. Notch sensitivity ..... 219
6.3.6.1. Introduction ..... 219
6.3.6.2. Methodology ..... 220
6.3.6.3. Results and discussion ..... 220
6.3.7. Material characterisation conclusions ..... 223
6.4. Semi-structural DCFP demonstrator component ..... 225
6.5. Cost analysis ..... 229
6.5.1. Introduction ..... 229
6.5.2. Results ..... 230
6.6. Conclusions ..... 234
Chapter 7. Conclusions ..... 236
7.1. Thesis conclusions ..... 236
7.1.1. Process development ..... 236

7.1.2. Areal density effects ..... 237
7.1.3. Filamentisation effects ..... 237
7.1.4. Length effects ..... 238
7.1.5. In-plane study ..... 239
7.1.6. Stiffness modelling ..... 239
7.1.7. Strength modelling ..... 240
7.1.8. DCFP comparison with commercial systems ..... 240
Appendix.A. Publications ..... 242
Appendix.B. Materials investigated ..... 244
Appendix.C. Manufacture ..... 263
Appendix.D. Experimental methods ..... 268
Appendix.E. Characterisation methods ..... 287
Appendix.F. DCFP process simulation methodology ..... 294
Appendix.G. Experimental Results ..... 299
Appendix.H. Multi-level analytical stiffness model ..... 307
Appendix.I. Contracted tensor notation ..... 333
Appendix.J. Tensor transformations ..... 334
References ..... 335

# Chapter 1. Introduction

With the volume of traffic increasing on today's roads there is a global pressure on vehicle manufacturers to produce cleaner and more efficient vehicles. Consumers are now demanding cleaner vehicles due to increasing fuel prices and emissions regulated tax. One of the major challenges facing automotive manufacturers is the balance between more environmentally friendly cars and the level of comfort, safety and price expected by the consumer. Manufacturers are attempting to maintain this balance by investing in the technology to exploit lightweight materials for lean weight designs.

## *1.1. Drivers of affordable lightweight automotive materials*

### 1.1.1. Weight

The Kyoto Protocol (1997) aims to combat global climate change through reducing or reversing greenhouse gas emissions. The Protocol intends to reduce the green house gas emission levels of 1990 by 5.2%, during the period 2008-2012 [1]. With 75% of a vehicles' fuel consumption being directly linked to factors associated with vehicle mass [2, 3], manufacturers are attempting to adopt a lean weight policy for new vehicles. Additionally, the location of weight reduction will have an influence on the safety, comfort, and manoeuvrability of the vehicle. By reducing the weight away from the centre of gravity, the handling of the vehicle can be significantly improved.

'Body in white' (BIW) is a term used in automotive design to describe the parts of a car made from sheet metal. These parts are commonly welded or glued together before the remaining components of the vehicle are added (e.g. suspension, interior and engine). Figure 1-1 shows that the BIW accounts for approximately a quarter of its mass and this offers the greatest scope for making a substantial overall weight saving. Significant weight savings are achievable by replacing steel parts with aluminium, magnesium or fibre reinforced composites. Manufacturers such as Jaguar have realised the weight saving potential of aluminium for body panels and structural parts, and currently

produce an all-aluminium BIW XJ model. Jaguar reports an overall weight saving of 40% and a stiffness increase of 60% in comparison to the previous steel version [4].

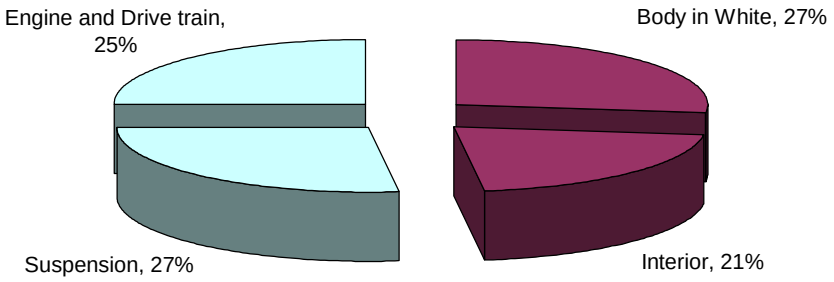


**Figure 1-1 Weight distribution of compact executive vehicle (Mercedes Benz C180) [2]**

To advance beyond the 40% weight saving threshold of aluminium there will be an inevitable requirement for advanced composite materials. Carbon fibre reinforced composites are common in aerospace applications but are currently of low significance for the drive towards lightweight automotives because of the high associated costs. It is believed that weight savings approaching 50-70% are achievable over steel, when replacing steel components with comparable carbon fibre components [5]. The development of affordable carbon fibre reinforced composites for the automotive industry is therefore a way of improving vehicle efficiency through weight reduction.

Weight reduction is not only achievable through the development of high specific strength materials, but also through efficient, lean weight designs. These are not achieved by simply replacing metallics with lightweight alternatives, components must be optimised for the expected load and produced from an appropriate material [2]. Designers must consider issues such as production costs, mechanical performance, durability and recycling when attempting to use lightweight alternatives to steel.

### 1.1.2. Cost

The successful substitution of alternative lightweight materials into any industry is largely dependant on cost. Final component cost is influenced by many factors, including raw materials, processing, finishing, transportation, assembly and recycling. Lighter, mechanically efficient materials often come with high material cost penalties

compared to their predecessors. However, high raw material costs should not necessarily restrict their use. Manufacturers can potentially overcome the inflated price of unconventional lightweight materials by selecting or developing a more cost effective manufacturing route. The high raw material costs of aluminium relative to steel can be balanced by lower manufacturing and assembly costs. Manufacturing aluminium extrusions requires lower capital investment than producing steel stampings and innovative aluminium joining techniques, such as bonding and riveting, are cost effective because they require less energy than traditional spot-welding [6].

For these reasons, high raw material costs are not deterring manufacturers from increasing the use of magnesium in mainstream production. For applications such as the mechanical hardtop for the Mercedes SLK (45,000 units pa), magnesium can be an economical alternative to aluminium due to faster and cheaper processing and its competitive cost per unit volume. Although raw material costs per unit weight of magnesium are 50-100% more than that of aluminium the density is only two thirds, therefore the cost per unit volume can be almost identical to aluminium [7].

Metallic processing and joining techniques are unsuitable for fibre reinforced plastics (FRP) and therefore investment in new tooling and experienced labour is required. Manufacturers often shy away from using FRPs because of the investment required and the lack of knowledge compared with metallics. Unlike steel, FRPs have multiple processing options consisting of many variables, making it considerably more challenging to select the most cost effective. However, FRPs generally require lower tooling investment over metallics, provide more design flexibility and the ability to integrate parts. This presents manufacturers with a potential lightweight, cost effective solution. Although raw material costs are generally 20 times higher for carbon/epoxy composites than steel, the final part cost for a carbon fibre composite monocoque BIW has been estimated to be only 76% higher than a steel unibody for an annual production volume of 250,000 parts [8]. In order for composite materials to compete with metallic systems, higher value must be added in terms of functionality and cost reductions must be made in manufacturing cycles to balance the higher raw material cost. Månson *et al.* [9] show an example of how fibre reinforced composites can be both cost effective and provide additional performance over a steel counterpart. An SMC cross-brace for under the dashboard of a pick-up truck improves the resistance to sagging and enhances the

noise, vibration and harshness (NVH) characteristics within the cabin. The two-piece bonded structure replaces 25 steel parts with a cycle time of only 1 minute, to enable 940,000 parts to be produced per annum.

### 1.1.3. Recycling

The End of Life Vehicle (ELV) Directive came into force in October 2000 and aims to reduce impact of the nine million tonnes of ELVs which arise each year in Europe. The directive sets new standards for the scrapping of ELVs and operators must meet a recovery target of 95% by weight of all ELVs by January 2015 [10]. The vehicle manufacturer is responsible for the costs incurred during the recovery process. The increasing use of exotic lightweight materials is posing a financial problem for manufacturers trying to meet these future weight recovery targets. It is no longer environmentally feasible to salvage only ferrous materials and send the remaining scrap to landfill, as the consumption of ferrous materials in automotive applications is in decline.

Recycling costs are directly proportional to the degree of separation required. The intended use of the recyclate must therefore be established prior to the recovery stage to avoid incurring unnecessary costs. If the recyclate is to be used as a bulking filler then there is no incentive to separate the scrap ahead of the milling stage. However, if the reclaimed material remains within the industry to replace virgin material, care must be taken to separate the different components to avoid contamination and to preserve purity. In the case of aluminium, if steel joining rivets and different alloys are not separated prior to recycling, the reclaimed aluminium is only suitable for low purity castings rather than extruded sections. However, the increase in use of extrusions makes it easier to recover aluminium in a purer form [6]. If the industry were able to condense the number of different alloys used in vehicles it would reduce the cost of recycling and furthermore reduce the cost of raw materials.

The future of FRPs within the automotive industry largely depends on the ability to successfully recycle them [10]. Manufacturers may have to sacrifice low weight composites and re-embrace metallics if suitable recycling processes and infrastructures are not installed. Research is in progress to address the composite recycling problem.

Existing composite recovery systems can be divided into mechanical, thermal or chemical processes. Mechanical processes include milling or grinding composite waste to produce fillers to be used in new FRP parts. However, fillers can only account for a limited percentage of any given part, resulting in excess supply over demand. In order to incorporate recycled fibres in new composite production the matrix must be separated from the high-value fibres using either a thermal process or a chemical process.

A thermal separation technique has been studied at The University of Nottingham to recover fibres for use in sheet moulding compounds (SMC) and long-fibred injection moulding applications. A fluidised bed is used to thermally separate fibres and fillers from thermoset resins and contaminates such as paints. The fibres and filler materials are suspended in the fluidising air before separation by a rotating sieve. Results show that no significant loss of mechanical properties occur when up to 50% recycled fibres are substituted into dome moulding compounds (DMC). Fluidised bed separation looks promising for composite recycling since the cost effective break even point would be only 9000 tonnes per year, 0.1% of the total weight of ELVs generated in Europe each year [11].

## *1.2. Candidate automotive systems – current state of the art*

### 1.2.1. Steel

Steel remains the primary material in the automotive industry, but its use has seen a small decline over recent years in favour of aluminium and polymer composites (Figure 1-2). The Ultra Light Steel Auto Body (ULSAB) project was a multi-phase study initially started in the 1990's by a consortium of 35 worldwide steel companies, to raise the profile of steel in lightweight automotive applications. Weight reduction and increased performance of automotive steel formings was achieved by developing the use of 'tailored welded blanks' [12]. The outcome of the ULSAB project showed that the main attributes of steel, such as low cost, high strength and its ability to be formed into complex shapes, still make it highly suitable for the mass production of lightweight vehicles.

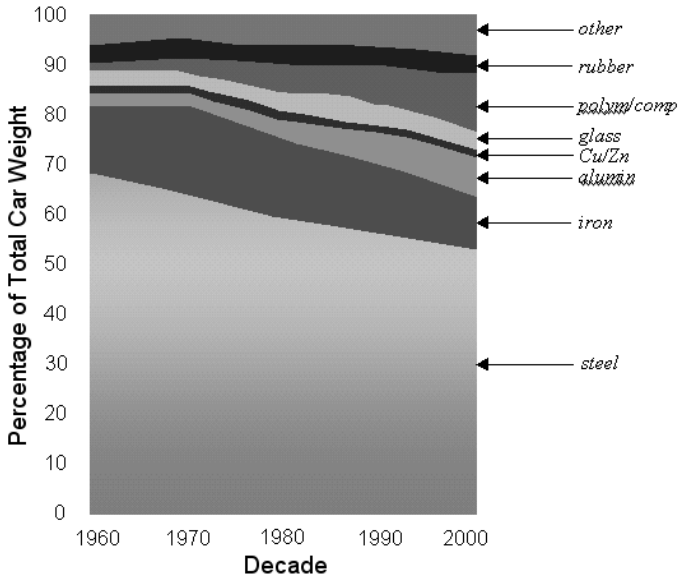


**Figure 1-2 The change in material composition of the average passenger vehicle over the last forty years [13]**

### 1.2.2. Aluminium

The use of aluminium in automotive applications has increased by 80% since 1995 and is expected to increase by a further 70% by 2015 [13]. Aluminium castings have been used in the automotive industry for some time but the increase in aluminium consumption is mainly due to the introduction of wrought aluminium, in the form of sheet panels and extruded sections. The space frame technique is a successful concept that has enabled manufacturers such as Audi, Honda and more recently Jaguar to produce all aluminium car bodies. The space frame consists of closed-sectioned aluminium extrusions to construct a structural unit that exhibits high torsional rigidity and stiffness due to the elimination of spot welded seams. A combination of riveting, adhesive bonding and clinching (press-joining) are the most popular methods for fixing the stamped aluminium panels to the space frame, replacing traditional spot welding techniques used for sheet steel production [6]. In addition to the problems of forming and joining, low scratch resistance and the formation of oxide layers makes aluminium more difficult to paint than steel [14].

### 1.2.3. Magnesium

Magnesium, the lightest metallic available to the automotive industry, was widely used in the early 1930's for applications such as steering wheels, steering column support brackets and seat base structures. Its popularity declined when raw material costs increased, but the automotive industry has seen a recent revival in the use of magnesium because of its weight saving potential. Magnesium is typically die-cast due to the elevated forming temperatures required and is therefore, at present, not cost effective in wrought sheet form. However, Volkswagen predict that they will have doubled the mass of magnesium used in the drive-train and interior of their mainstream cars between 2001 and 2006, and have the first uses for magnesium in body components by the end of 2006 [15]. In common with aluminium, the main problems associated with magnesium are the poor surface finish of outer skins and galvanic corrosion that occurs when in contact with steel [2, 15].

### 1.2.4. Fibre reinforced plastics

Fibre reinforced plastics (FRP) are amongst the other lightweight materials competing for market share in the automotive industry. FRPs were initially introduced into the market in the early 1950's; one of the earliest examples being the fibreglass bodied 1953 Chevrolet Corvette [16]. Fifty years on, more intense efforts have been spent on developing FRPs for mainstream automotive applications to exploit their high strength to weight ratios, stiffness and energy absorbing properties [17]. Arguably, FRPs have high production costs, long cycle times and a poor surface finish. However, recent advancements in processing technology have enabled manufacturers to use materials that were once only considered for the high performance, low volume end of the market. The composite pick-up truck cargo box [18] was a major breakthrough in high volume composite production in the year 2000. The use of robots to automate preform production has enabled General Motors to produce structural parts with a weight advantage over steel for up to 80,000 units per annum [18, 19]. Directed fibre preforming is currently only suitable for glass fibres and offers weight savings in the region of 30% over steel, but savings of 50-70% have been predicted if the process is adaptable for carbon fibres [20]. Studies forecast an annual growth of carbon fibre

consumption within the American automotive industry of 8.9% per annum over the next five years, due to global reductions in price [21].

## *1.3. Applications of composites within the automotive industry*

Fibre reinforced composites are typically used within the automotive industry for applications such as body panels, suspension, steering, brakes, and other accessories. FRPs are still predominantly used in non-structural and cosmetic elements, but over the last decade there has been significant progress for structural applications, with the first production car to incorporate a carbon-fibre crash structure being launched in 2003 [22]. Whilst FRPs offer design and manufacturing flexibility, wider applicability is prevented by high raw material costs and long cycle times. Figure 1-3 demonstrates that mechanical performance can be considered to be a function of production volume. High performance composites are typically reserved for low volume, structural applications, such as racing or super cars. They are designed to transmit primary loads and have a reinforcement volume fraction ($V_f$) generally greater than 35%. Intermediate performance materials are often used for semi-structural applications where both cycle time and mechanical performance are of precedence. Semi-structural components are designed to transmit secondary loads and are often under body parts rather than exterior panels ($V_f$<35%). Low performance FRPs are commonly used for cosmetic applications in high volumes such as commercial vehicles. Cosmetic panels are not designed to transmit any load and typically have a $V_f$ of less than 20%. This section discusses the use of FRPs for various automotive applications, in terms of production volume, performance expectation and manufacturing process.

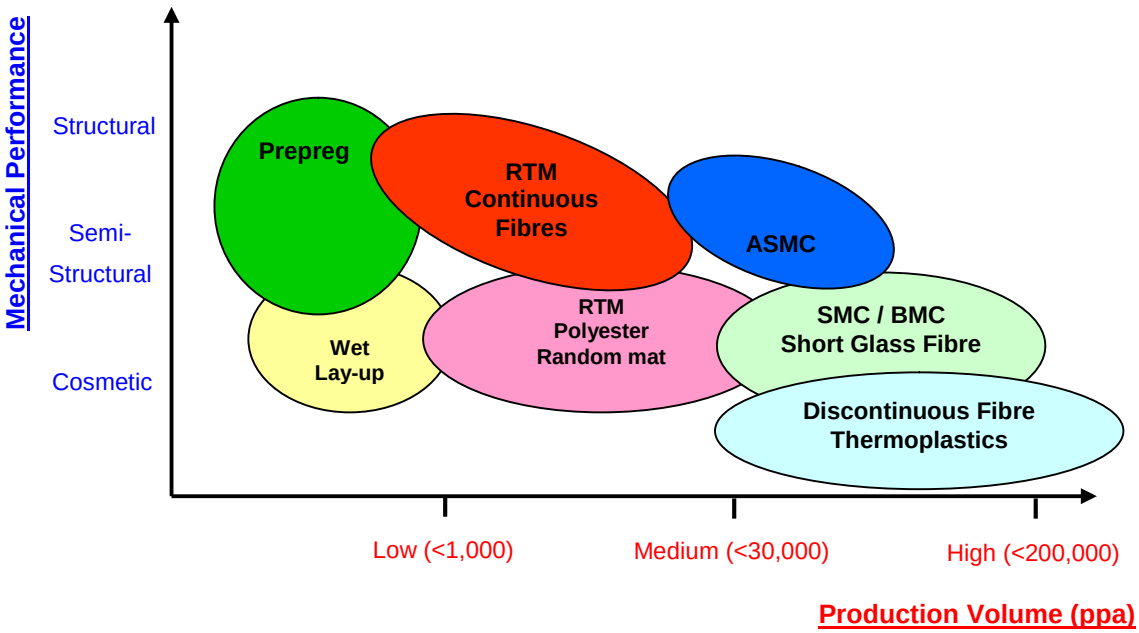


**Figure 1-3 Mechanical performance vs. production volume vs. manufacturing process. Modified from [23] and internal report supplied by Hexcel, Duxford.**

### 1.3.1. High volume (50,000-200,000ppa)

The most commonly used fibre reinforced materials in automotive components are thermoplastics, providing high production rates via injection moulding and its derived processes. Applications for which thermoplastic materials are routinely employed include engine inlet manifolds, door trims, interior components and light housings, all of which can be manufactured with high dimensional precision. Structural long fibre reinforced thermoplastic components are also now starting to emerge, experiencing a 30% increase in North America and Europe in the last decade [21]. One such example is a support lid on the 2001 Volvo V70 XC AWD [16]. This component, manufactured from glass reinforced polypropylene, replaces an existing cast aluminium frame. It supports the rear differential and is bolted directly to the vehicle's rear axle. The part weighs 2 kg, 27% less than its aluminium counterpart. Furthermore, the manufacturing cycle time is less than 4 minutes. Another recent example of a structural thermoplastic component is the bumper beam of the 2001 BMW M3 (50,000ppa). The E-glass/nylon6 Towflex® material provides enhanced levels of energy absorption from a single design, meeting worldwide legislative requirements as well as generating a 60% weight reduction [24].

The most widely used thermoset composites in the automotive industry consist of chopped, glass fibres, in the form of sheet moulding compounds (SMC). SMCs account for 65% of the total automotive thermoset composites market [25], approximately 95,000 tonnes in Europe in 2005 [26], since they are highly competitive for bolt-on exterior panels such as bonnets (hoods), boots (deck lids) and wings (fenders). This is largely because of styling flexibility and weight/cost savings, which make SMCs an attractive alternative to steel or aluminium for low performance applications. A charge, consisting of random fibres and a partially cured resin, partly covers one half of a matched mould set. The charge is rapidly compressed and the fibres and resin flow in order to fill the mould cavity. High tool closure pressures (50-200bar [27]) make this process uneconomical for short production runs, because of the tooling investment required compared with alternative composite processes. Conversely, Ford used glass SMCs for 60% of the body panels on the 2002 Thunderbird because the tooling costs were reported to be 50% lower than for steel [16]. Whilst the random nature of the fibres limits the mechanical properties to 20-40% of an aligned material, cycle times are typically only 100-200 seconds. High production volumes are therefore feasible (approaching 200,000ppa) for large components such as panels for commercial vehicles [28].

Historically, discontinuous carbon fibre formats were unavailable commercially, given the high fibre manufacturing costs and the fact that the fibres are most efficient in continuous form. Recently material manufacturers such as Hexcel [29], Quantum Composites [30] and Menzolit-Fibron GmbH [31] have introduced carbon SMCs to their product ranges due to the changing demands from the automotive industry. Advanced SMCs (ASMC) are stiffer and therefore have better potential for structural applications, such as the windshield surround on the 2003 Dodge Viper [30] and the rear scuttle panel on the 2005 Mercedes-McLaren SLR [31]. Cycle times for ASMCs (5 to 45 minutes) are commonly longer than for SMCs because an epoxy matrix is used rather than polyester, restricting production volumes to less than 80,000ppa.

### 1.3.2. Medium volume (1000 – 50,000ppa)

For semi-structural and structural applications the mechanical performance of discontinuous materials, such as SMCs and ASMCs, is often inadequate. The strength of random fibre materials rarely exceeds 300MPa [29]. Continuous fibres enable the full potential of the reinforcement phase to be exploited and failure strengths in excess of 2500MPa are achievable (at 60% $V_f$) with perfectly aligned carbon filaments. For complex components it is difficult to ensure that the fibres remain at the prescribed orientation during processing and therefore the fibres are often pre-shaped before being impregnated by a low-viscosity resin. Intermediate fibre preforming inevitably increases cycle time and cost, which limits annual production levels to less than 30,000ppa [32]. (Preforming options are discussed in Section 1.4). Liquid moulding is proven to be cost effective at this level, with Resin Transfer Moulding (RTM) being the most commonly used for automotive applications [27], the first being the 1974 Lotus Elite [33]. A matched sided tool enables complex 3D parts to be fabricated with dimensional stability, with the opportunity for parts integration and moulded-in features such as bolt anchors etc. Part finish mirrors the surface of the tool for 'Class A' applications and components are near net shape to minimise post-moulding operations. Moulding pressures are considerably lower than for SMC, therefore capital costs have been reported to be approximately 10% compared with compression moulding [34]. However, the process is potentially uneconomical for short production runs of less than 100ppa [27]. RTM has been used extensively for automotive applications, for example by Aston Martin (2001 Vanquish 'A-pillar' [600ppa] and Vanquish transmission tunnel [300ppa]), Ford (1999 Hi-Cube Transit roof [18,000ppa], 1996 Escort Cosworth under shield and rear spoiler [2500ppa]) and Renault (1996 Espace tail gate [30,000ppa]) [33].

### 1.3.3. Low volume (<1000ppa)

Changing consumer demands mean the vehicle life cycle is decreasing and models are being revised every 6 to 10 months. Composites can be attractive for niche vehicles or prototypes where only a small number are ever produced (<1000ppa). They offer greater design freedom and low moulding pressures enable the use of lightweight

tooling, which is produced at a fraction of the cost of metal forming sets. Single sided tools are commonly used for low volume production to further reduce tooling costs. A flexible bag is used to enclose the entire mould and the laminate is cured under a vacuum. Vacuum infusion of liquid resins is commonly reserved for the marine industry where poor dimensional stability (compared with RTM) can be tolerated. Low volume automotive applications are more likely to use pre-impregnated fibres to produce high quality, high $V_f$ (~60%) laminates. Pre-impregnating the fibres with resin increases the raw material costs by approximately 50%, but this additional cost is recoverable within the low volume sector due to the high retail prices of niche vehicles. Current vehicles that use extensive carbon prepreg include the Ferrari Enzo, Porsche Carrera GT and the McLaren SLR, all of which cost in excess of £200,000.

Prepregs often require higher compaction pressures than is possible with vacuum bagging, in order to minimise surface porosity and interlaminar voids. This is achieved by applying a compressed gas (up to 15MPa [23]) to the laminated stack, whilst covered by a vacuum bag, inside a pressure vessel (an autoclave). Autoclave curing has historically restricted the use of prepregs to a few hundred components per annum due to lengthy 8 hour cure cycles, but recent developments in resin chemistry have seen the introduction of semi-impregnated fibres using resin films (see Chapter 6), which permit the use of high performance woven textiles without the need for an autoclave. Dedicated body panel systems coupled with resin surfacing films, such as SP System's SPRINT®, are enabling manufacturers to achieve a 'class A' surface finish using vacuum only curing. TVR report cost savings of up to 60% against conventional prepregs using this film technology and Porsche report weight savings of 75% over steel [16]. Out-of-autoclave processing is now possible for pre-impregnated materials, reducing both capital expenditure and cycle time, enabling production volumes to exceed 1000ppa.

Liquid moulding techniques currently bridge the wide gap between high volume compression moulding (50-200,000ppa) and low volume prepreg (~1000ppa). Whilst 50,000ppa is not unrealistic, intermediate preforming increases cycle time and consequently restricts the productivity of processes such as RTM to 30,000ppa. The following section will review conventional preforming methods for liquid moulded composites and Section 1.5 will look at the state-of-the-art.

## *1.4. Composite preforming techniques*

Preforms are fibre forms produced prior to the moulding stage, for manufacturing 3D shapes via liquid impregnation routes. Preforming enables the fibres to be handled and improves the dimensional control and fibre alignment of the final cured component [35]. Considerable cost savings are also achieved by shaping the fibres before they enter the mould. Cycle times are reduced and there is the opportunity to improve the net shape of the moulded component, thus reducing the number of post-moulding operations required [36]. Furthermore, moulding issues, such as fibre washing and race tracking, are prevented by net-shape manufacturing and higher volume fractions can be achieved due to the compacted fibre form.

One-dimensional preforms are simply linear assemblies of filaments, known as yarns or rovings. The inherent flexibility of yarns enables them to be subsequently processed into 2D textile preforms such as random mats, weaves, braids, and knits. Fibres can also be introduced in the third dimension, with processes such as weaving, braiding and knitting, in order to create 3D preforms with increased interlaminar properties. As Figure 1-4 shows, engineered fabrics and textiles form a large proportion of the preforming methodologies available. This section will concentrate on random fibre preforms only since they are the most widely used in composite material applications, particularly within the automotive industry where cost is the primary driver rather than mechanical performance.

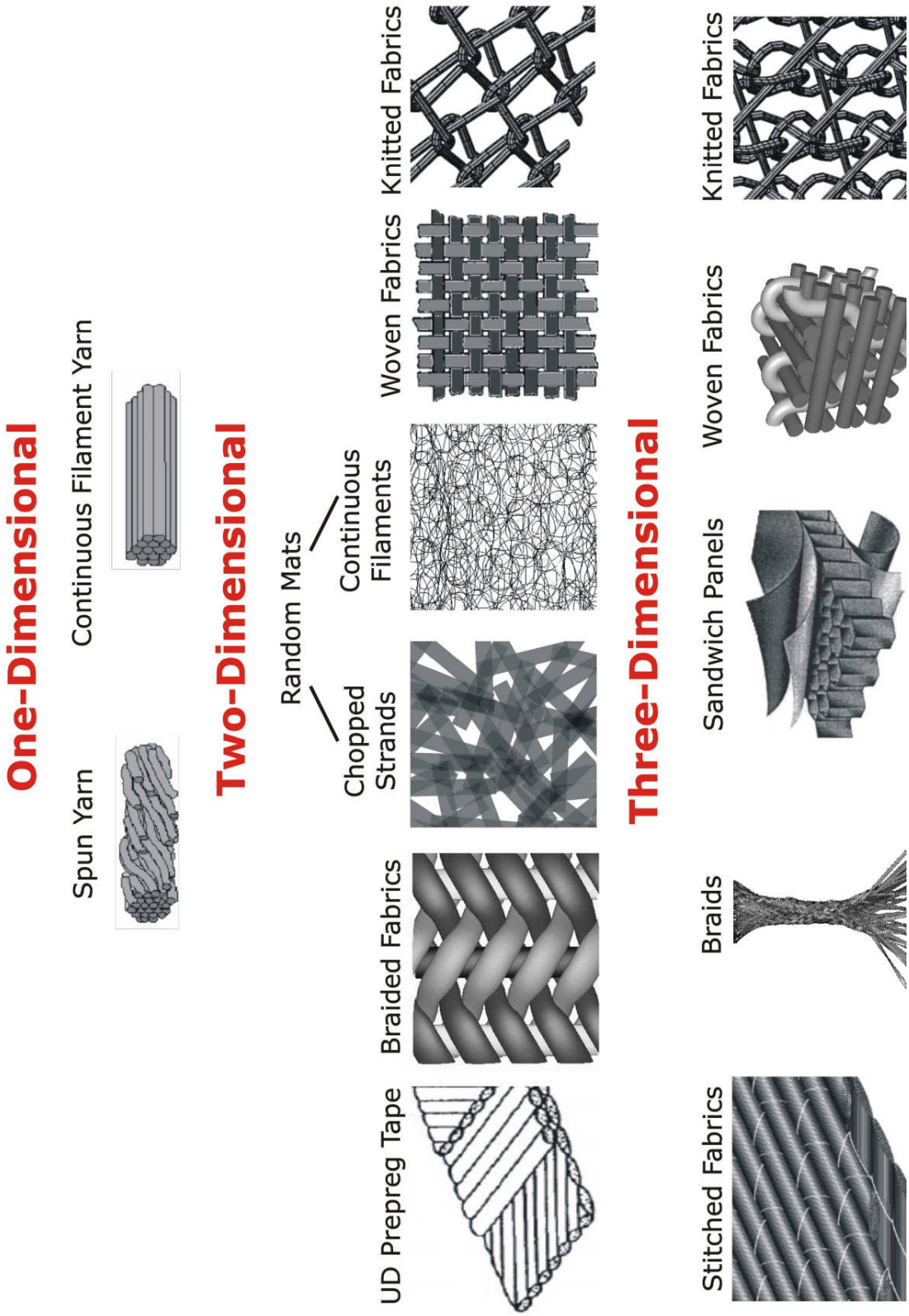


**Figure 1-4** **Preforming routes categorised according to dimensional hierarchy**

Random fibre preforms are characterised by the orientation of the fibres, which are generally arbitrary within the 1-2 plane. Consequently the stiffness and strength is much lower than for aligned fibres and inefficient fibre packing results in a much lower ultimate volume fraction (a function of the fibre aspect ratio) [37, 38]. Glass fibres are therefore commonly used for random preforms, because of the carbon fibre cost penalty, particularly for non structural, cosmetic applications such as automotive body panels. Random fibre preforms can be further characterised according to fibre length (discontinuous or continuous), binder method (mechanical or chemical), areal mass (veil or mat) and the presence of matrix (dry or pre-impregnated) [35].

The conventional method for producing random fibre preforms is to use an un-catalysed resin, which is either sprinkled as a powder and set by heat, or sprayed as a molten liquid to rigidise the fibres. Typically, between 1wt% and 9wt% of binder is applied to provide sufficient fibre-fibre adhesion [39], but excessive amounts of binder (~6%) can result in lower mechanical performance due to poor interfacial properties between the fibre and the matrix [40].

Chopped strand mats (250-1000gsm) are produced by mechanically chopping glass roving into 25-50mm lengths over a moving conveyor belt. The fibres are chemically bonded by uniformly spraying a thermoset or thermoplastic binder over the surface. If preform strength is required in the dry state only then polyester or polystyrene binder is used, which is subsequently dissolved in the resin to improve the impregnation process [35]. However, if there is insufficient clamping pressure from the mould tool then fibres may wash. Low solubility binders are available, but these tend to have a negative effect on the mechanical properties. Alternatively, continuous filaments can be deposited onto the conveyor, using a swirling motion to create Continuous Filament Random Mats (CoFRM). The absence of fibre ends improves mechanical properties and reduces the risk of fibre washing, enabling lower volumes of binder to be used. A certain degree of directionality can also be introduced by controlling the speed of the conveyor belt relative to the fibre deposition rate.

Random fibre preforms are usually thermoformed into 3D shapes using a preforming press. The thermoplastic or B-staged thermoset binders soften upon heating, enabling the random fibres to conform to the tool. The binder is consolidated and the preform is

extracted and transferred to a moulding station for the injection of liquid resin. Thermoforming can result in preform thinning and even tearing of the random mats at deep draw angles. However, random fibre preforms are more tolerant of fibre misalignment and breakage and therefore offer considerable scope for process automation [41].

Development work has focused on automating preform manufacture to improve consistency in order to produce low cost, high quality components and structures. The following section will discuss a process which has been developed to automate the production of random fibre preforms for RTM/SRIM moulding.

## *1.5. Directed fibre preforming*

Directed fibre preforming (DFP) is an established process [42] in which chopped glass fibre and an emulsified binder are manually sprayed directly onto a tool face. The elimination of intermediate fibre conversion reduces costs compared with engineered fabrics, but historically, DFP laminates suffer low fibre volume fractions and poor part consistency compared with competing preforming processes. Automated variants now exist for the production of net shape preforms of higher volume fraction, which address some of the historical limitations. The process is automated to dispense low cost fibre in roving form. It has the potential for low cycle times (~5mins) and allows the production of complex shapes with reported mass variations of only 2% between preforms [20]. Mechanical properties are reported to be comparable with chopped strand mat at similar fibre volume fractions [43], but raw material costs are less than 50% and wastage levels are down from 30wt% to 3wt% [44].

The technology has been further developed within the automotive industry for low volume applications using glass fibre [45] (see Figure 1-5). Chevrolet also introduced a DFP/SRIM moulded truck bed into its mainstream production of the Silverado, without a cost penalty to the consumer [46]. The glass fibre box was corrosion resistant and was reported to have improved dent resistance and scratch resistance compared with its steel predecessor. Adding coloured pigments at the moulding stage eliminated the painting process and reduced the overall cost of the DFP box to 3% below the steel

counterpart. In addition, the 30% weight saving translated into a 6-8 gallon fuel saving per truck per annum.

Mass reduction potential for DCFP however, is limited to 20-30% over steel pressings for typical automotive applications. The substitution of carbon fibre potentially offers 40-60% weight reduction, with significant cost savings over alternative carbon fibre processing technologies [47]. The introduction of low-cost, large tows (>24K) offers further cost reductions. The potential of directed carbon fibre preforming (DCFP) for structural applications has been investigated within the aerospace industry [48, 49] and in large wind turbine applications [50, 51]. Various mechanisms have been explored to orientate the chopped tows to improve the mechanical properties and to increase fibre volume fractions. However, most result in substantially longer cycle times [52], rendering the methods unsuitable for high throughput applications. Industrial development of this technique continues [53-57], driven by cost predictions which show that DFP and DCFP are cost effective at annual volumes of up to 50,000 parts per annum [58, 59].

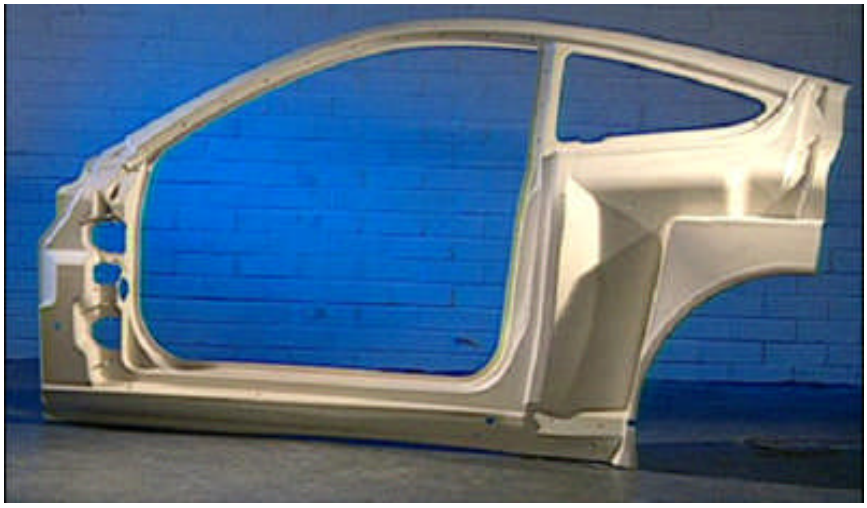

**Figure 1-5 Vehicle body side made from glass fibre DFP/RTM for the 2001 Aston Martin Vanquish**

## *1.6. Theme of work*

In order to meet projected vehicle emissions targets it is increasingly clear that vehicle construction must shift from steel at high volume and sheet moulding compounds at intermediate volume to aluminium and carbon composites respectively. Global reductions in the pricing of carbon fibre now mean that this shift may be made without pushing unit costs to unacceptable levels, but carbon composites still remain at a cost disadvantage to aluminium, for all but low volumes. Intermediate processes such as textile conversion and pre-impregnation are partly responsible, accounting for around 50% of materials costs, which are unacceptable for volume manufacture.

This work seeks to reduce or eliminate intermediate costs by delivering a solution that provides the mass reduction potential that carbon fibre offers, together with cost parity with aluminium. Potential application areas for this work are seen primarily as cosmetic body panels for the automotive industry, but with potential for semi-structural or structural applications within the automotive and aerospace industries.

The transition from glass to carbon is a major challenge and modifications to the existing DFP process are required. Following an extensive DCFP optimisation study investigating the causes of areal mass variation in Chapter 2, a comprehensive programme of mechanical testing and material characterisation is presented in Chapter 3. In particular, tow filament count is of interest. Higher filament count tows present significant cost savings, but are expected to have a negative effect on the mechanical performance of the laminate. Fibre length effects are also studied to determine if a critical bundle length exists for the tow reinforcement, whilst laminate thickness is varied to establish if DCFP is suitable for producing thin (~2mm) cosmetic panels with a Class A surface finish. Although outer panels are not primary load bearing structures they are subjected to in-service impacts in car parks and from road debris etc. and must therefore exhibit sufficient stiffness and strength. Tensile testing is initially conducted for screening purposes during the optimisation study, followed by a full range of in-plane characterisation tests. In addition, notch sensitivity and out-of-plane dent resistance tests are performed on the DCFP material and the results are compared against conventional body panel materials in Chapter 6. A front fender demonstrator

component has been chosen to study the in-service bending performance of a selection of the candidate systems. The 4-point loading results in a combination of local membrane and bending loads, and therefore the performance of the part is represented by a combination of the properties mentioned above. A cosmetic variant of the DCFP material is compared against a carbon/epoxy semi-preg and the steel counterpart. A costing analysis is also presented to establish the economic operating volumes for each material.

Initial calculations suggest that carbon DFP could potentially be used for structural applications, such as secondary aircraft components. Methods for orientating the fibres are explored to improve the efficiency of the reinforcement in the loading direction, but also to increase fibre volume fraction by improving the fibre packing characteristics. A novel test method is developed to determine the level of fibre directionality and the material properties are compared with a commercial non-crimp fabric, commonly used for structural applications.

Mechanical property prediction is vital to the uptake of the technology into the motor industry. A basic requirement for all new materials and processes is that they can be modelled and their performance predicted within reasonable limits. A process simulation has been developed to model fibre deposition in order to optimise the lay down strategy. Conventional stiffness and strength models for discontinuous fibre composites are reviewed and new multi-level analytical models have been developed to capture the complex fibre architecture associated with the DCFP material (Chapter 4 – Stiffness, Chapter 5 – Strength). Predictions are compared against the experimental results from Chapter 3 and values reported in the literature.

This work was conducted under a DTi/DfT industrial project, ‘Affordable Lightweight BOdy Structures’, part of the Foresight Vehicle Programme. The resulting publications are presented in Appendix.A.

# Chapter 2. DCFP process development

## *2.1. Objectives*

The use of carbon rather than glass fibre presents a challenge both from a processing perspective and in terms of the mechanical performance of DCFP laminates. This chapter seeks to improve the quality of directed fibre preforms by minimising the areal mass variation caused by poor control at the fibre deposition stage. Process developments have been made through the use of a research-scale machine, which can be readily scaled for use in a production environment. An extensive optimisation programme is undertaken to establish the influence of a number of machine-related parameters on the degree of areal mass variation. The results from this study are subsequently used to develop a DCFP process simulation to model the fibre deposition stage, in order to reduce inter- and intra-preform variation.

## *2.2. University of Nottingham DCFP facility*

### 2.2.1. Introduction to the process

Industrial directed fibre preforming facilities [42, 60, 61] commonly consists of four main stages; deposition, consolidation, stabilisation and extraction (see Figure 2-1). A robot–mounted mechanical chopper head sprays fibres and a polymeric, powdered binder onto a perforated tool. (The use of a powdered rather than emulsified binder reduces cycle time by eliminating the need to dry the preform prior to moulding.) Air is evacuated from the underside of the tool and the resulting pressure differential holds the deposited fibres in place. When material deposition is complete, a matched perforated tool is lowered to compress the preform to control the preform thickness. Hot air is cycled through the perforations to melt the binder and subsequently ambient air is cycled to stabilise the preform. Finally, the preform is extracted from the

preforming station and transferred to a separate moulding station for the injection of liquid resin via conventional means.

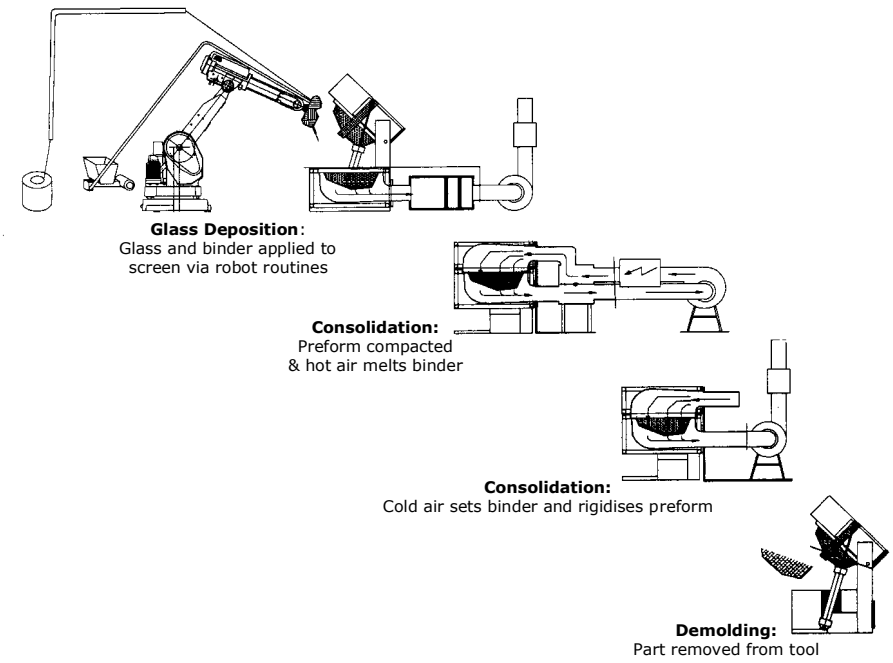


**Figure 2-1 The four DFP process steps for preform production. Schematic taken from [20].**

### 2.2.2. Issues with current DFP installations

Glass fibre is available in a number of material forms, one of which is 'gun roving', which is specifically manufactured for processing through chopping apparatus. No analogous material exists in carbon form which makes carbon tows difficult to process [20]. A number of observations were made whilst operating DFP machines at Sotira, Saint Meloir des Ondes, France and the National Composites Center, Ohio, USA. The higher strength and lower failure strain of carbon relative to glass fibre increases problems with fibre handling and cutting. Carbon tows experience damage prior to chopping from the fibre delivery system due to the aggressive movement of the robot arm. This can lead to either fibre blockages upstream in the chopping apparatus (location (1) in Figure 2-2) or complete yarn breakage, both of which increase machine down-time and material wastage. Processing shorter fibres (<25mm) is also a challenge because they tend to adhere to the pressure roller at location (2) once chopped, rather

than exiting the gun at location (3). Short fibres are thus cycled over the knife roller, degrading the fibre length and potentially causing further blockages at (2).

The low density of carbon fibre relative to E-glass creates difficulties in placement, as the transporting air stream at the exhaust of the chopping apparatus (see location (3) tends to disrupt previously deposited fibres, particularly from vertical tool faces. The final position of the carbon tow on the preforming screen is also not as controllable as with glass fibres. This causes much greater variation in local areal density and in turn, variation in mechanical properties.

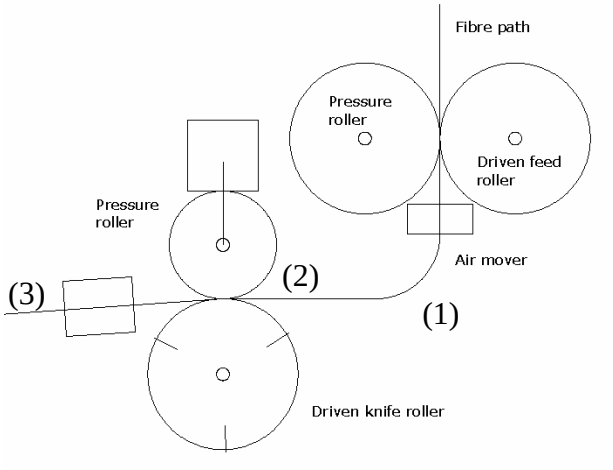


**Figure 2-2 Conventional fibre chopping apparatus commonly used on industrial DFP machines. Manufactured by Aplicator System AB, Sweden [62].**

Once the fibre preform has been manufactured it is transferred to a separate moulding station for the injection of liquid resin. Carbon preforms are notably more difficult to handle than glass fibre preforms. The bending stiffness of a carbon filament is typically three times lower than for glass because of a smaller second moment of area (filament diameter is 8μm for the carbon filament as opposed to 14μm for glass). This makes carbon fibre preform extraction and transportation difficult to automate and further increases the risk of sustaining damage to the preform.

Preliminary tensile testing (see Appendix C.1.1 and D.1.2 for manufacture and test methods respectively) showed that the mechanical performance of DCFP laminates was much lower than anticipated (Figure 2-3). The tensile stiffness of a carbon laminate was only 100% higher than an equivalent glass laminate; despite the constituent fibre

stiffness being more than 200% higher. The tensile strength was actually 17% lower for the carbon plaque when compared to the glass DFP. Both discrepancies can be attributed to the use of high filament count (24K) carbon tows, which are used for their cost effectiveness. The cross-sectional aspect ratio of larger tows makes it increasingly difficult to achieve uniform coverage for thin laminates, as shown by Figure 2-4.

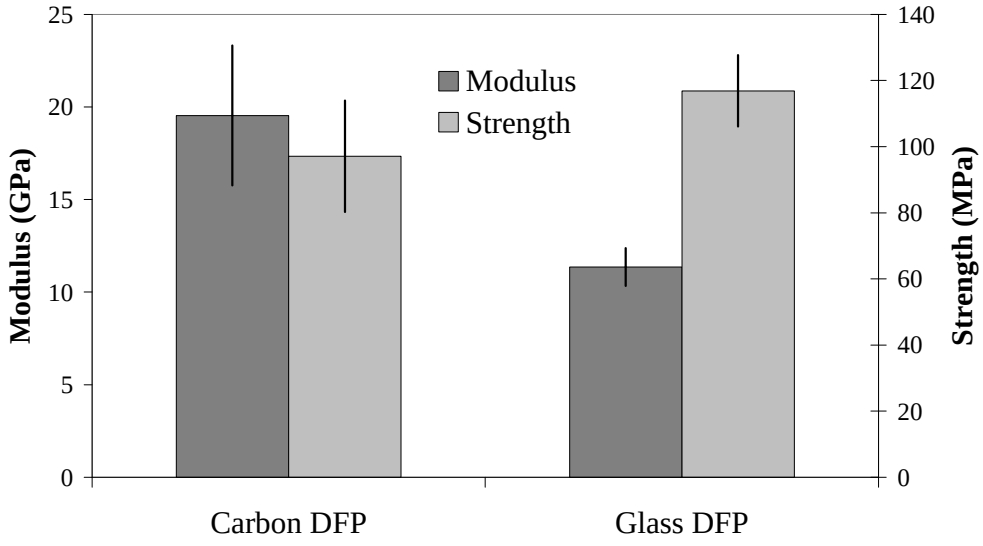


**Figure 2-3 Comparison of tensile properties of carbon and glass DFP plaques. A fibre length of 23mm and a fibre volume fraction of 30% were used in both instances. Preforms were moulded via RTM using DLS1678, a development epoxy resin supplied by Hexcel. (Standard deviation bars shown).**

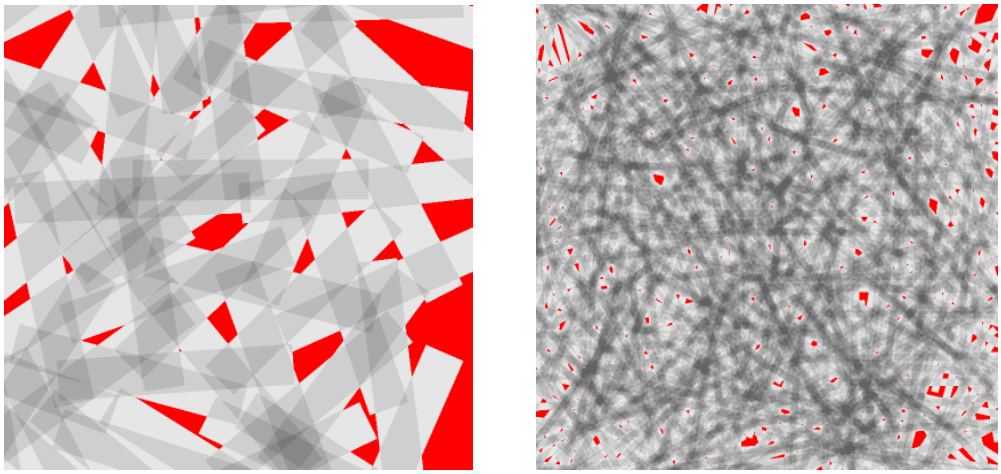

**Figure 2-4 The effect of using high filament count tows on preform areal coverage. Images were simulated using the DCFP process model outlined in Section 2.4. (Left) A preform consisting of 24K tows, showing large unreinforced areas. (Right) A preform with the same areal mass of fibre (750gsm) but in a 3K tow format. The average area of each unreinforced region (shown in red) is 14 times smaller for the 3K fibre than the 24K.**

Large unreinforced areas proliferate as the tow filament count increases, causing areas of local weakness. Glass fibre tows of a similar filament count are typically constructed by gathering a number of smaller bundles (e.g. 24 × 1K), creating a large multi-ended tow. This type of bundle readily splits into the individual bundles upon chopping, reducing the nominal tow filament count within the laminate. This type of fibre format does not currently exist for carbon fibres, in which case this method would prove to be extremely costly.

It is clear that the principal goals for optimising the DCFP process involve improving the current fibre delivery and chopping systems to enable reliable processing, but also to minimise the errors associated with uniformity of carbon coverage and preform consistency in order to improve the mechanical performance.

### 2.2.3. DCFP developments

This section details the advancements made in order to address the processing related issues outlined in Section 2.2.1. A laboratory-scale DFP preformer was constructed at the University of Nottingham for directed carbon fibre preform (DCFP) development. The concept was based on the installation at Sotira, Saint Meloir des Ondes, France, which is currently used for producing glass fibre preforms for Aston Martin Lagonda [45, 57]. Fundamental changes were made to the design to enable carbon fibre processing. The maximum preform capability is 1m×1m×0.25m within a system biased towards research rather than production (see Figure 2-10). The system is unable to match the low cycle times of existing industrial installations because of the inefficient preform heating procedure, but developments produced using this machine can be readily transferred.

A fibre delivery system was developed to reduce the level of damage caused when transporting the tows from the bobbins to the chopping apparatus (Figure 2-5). A series of air movers were used to minimise the level of friction through the eyelets when guiding the tows to the end of the robot arm. The system was based on the F3P design disclosed in United States patents 6,527,533 & 6,540,495. The use of trailing arms to provide a fibre reserve were not included because the robot reach is much lower than

for the F3P system and there is no seventh axis (robot does not move between multiple stations), reducing the risk of fibre breakage caused by the acceleration of the robot arm. The system was designed to handle 4 tows through 2 independent feed systems for hybrid fibre processing e.g. glass/carbon.

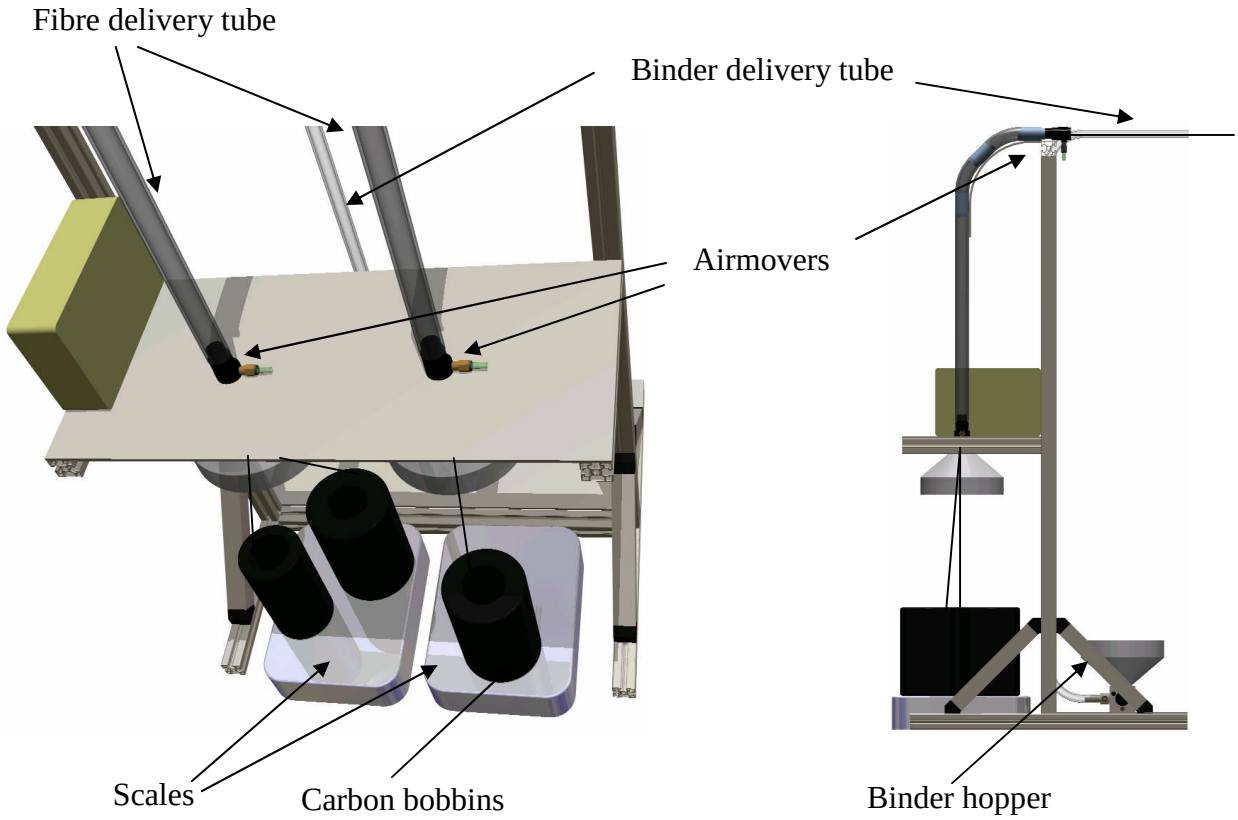


**Figure 2-5 Fibre delivery system for the Nottingham DCFP facility. The use of air movers reduces the amount of damage in the tow prior to chopping.**

The original P4 chopper design (conceived by Aplicator System AB, Sweden – U.S Patent 5,779,793 [62]) is still in use today on the few DFP machines in existence. A new chopping apparatus was designed as part of this work to alleviate some of the problems associated with cutting carbon tows. Figure 2-6 shows the complexity of the Aplicator design in comparison to the replacement gun used on the Nottingham DCFP machine. Trials at Sotira, Saint Meloir des Ondes, France showed that carbon fibres are more likely to block the Aplicator chopping apparatus than glass fibres. The fibre path has been modified on the revised gun to make it more direct, by removing the 90º bend where the majority of blockages previously occurred. In addition, high velocity air is used to prevent the chopping apparatus from clogging as shown in Figure 2-7. Jets of

air are directed at the bottom of both the knife and pressure rollers to strip the fibres and prevent them from sticking.

Existing fibre chopping systems typically employ an air amplifier to collectively eject the fibres from the gun, provide filamentisation (tow splitting) and prevent clogging. A degree of filamentisation is unavoidable using this approach due to the turbulent, high velocity air stream. This air also tends to disrupt previously laid-down fibres when working with low density carbon filaments. In the present chopping system these functions have been separated to allow independent control. As the fibres exit the rotating knife section of the gun they are carried by the air stream to a cylindrical air mover (see Figure 2-7). High velocity air is introduced at the base of the airmover through four Ø0.3mm holes. Turbulence causes the filaments within the bundles to separate (filamentise) to effectively reduce the filament count within the tow, improving the mechanical performance of the laminate. It is therefore possible to eject fibres from the gun with a wide range of controlled filamentisation levels by changing the air pressure within the airmover. This also alleviates the need for a separate veil and reinforcement choppers, which are commonly used in industrial preforming for surface critical applications [20, 63].

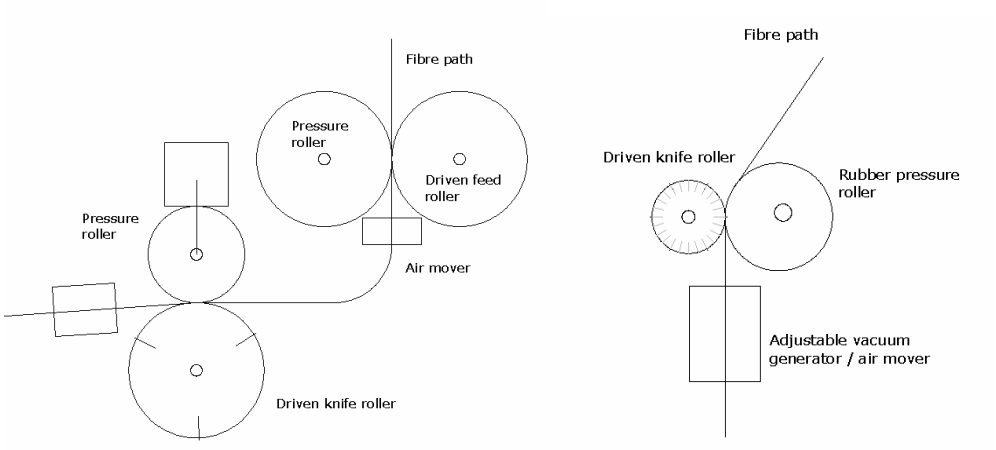


**Figure 2-6 Schematics of two chopper guns. (Left) Aplicator SMART chopping system used on industrial machines at Sotira, Saint Meloir des Ondes, France and the National Composites Centre, Ohio, USA. (Right) Simplified chopper design used on the Nottingham DCFP facility.**

Whilst the revised chopping apparatus does not clog and the tows are successfully split, the additional air flow from the air curtains and the filamentisation chamber cause further problems with fibre placement. A diffuser was designed using COSMOS

FloWorks (a computational fluid dynamics package compatible with Solidworks) to minimise the air velocity at the fibre outlet (see Figure 2-7), significantly reducing the disruption of the existing placed fibres. The increase in diameter from the airmover to the diffuser increases the air pressure and consequently reduces the air velocity and the unwanted high pressure is subsequently vented through the top of the diffuser. The air velocity is reduced by 62% at a distance of 0.25m from the point of chopping (shown in Figure 2-8), when a diffuser is connected to the end of the airmover. Fibre placement is now more controllable and preform disruption is minimised, enabling more consistent processing and resulting in inter preform variations of only ±3%.

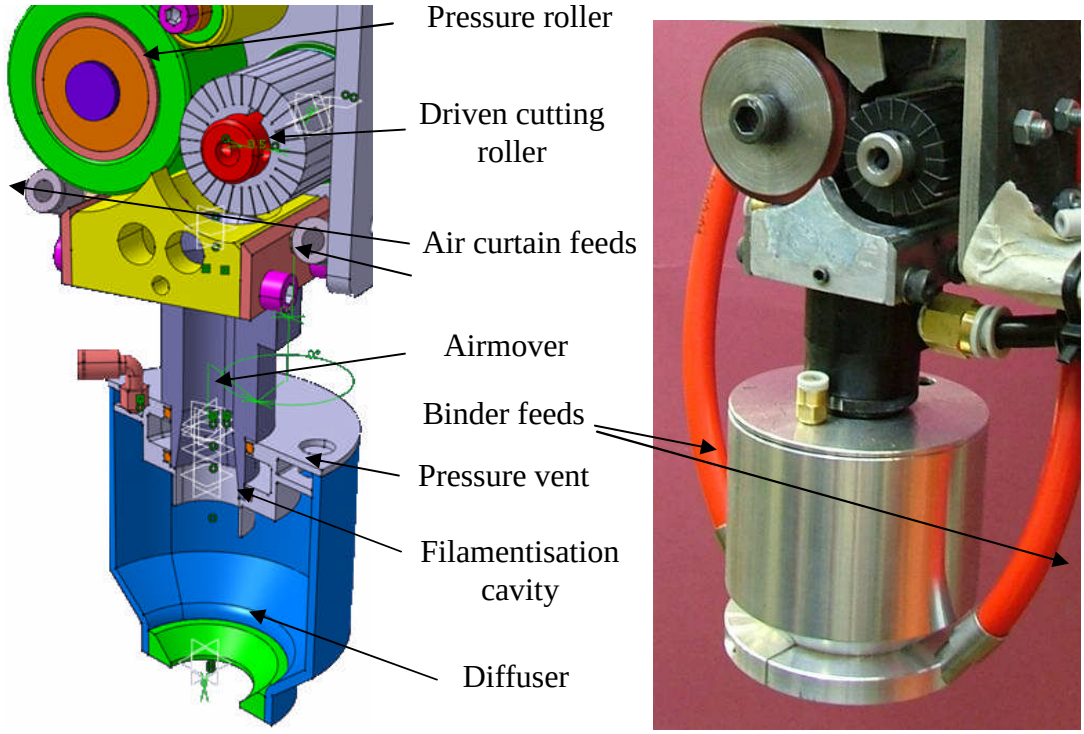


**Figure 2-7 CAD drawing and photograph of current chopper gun design**

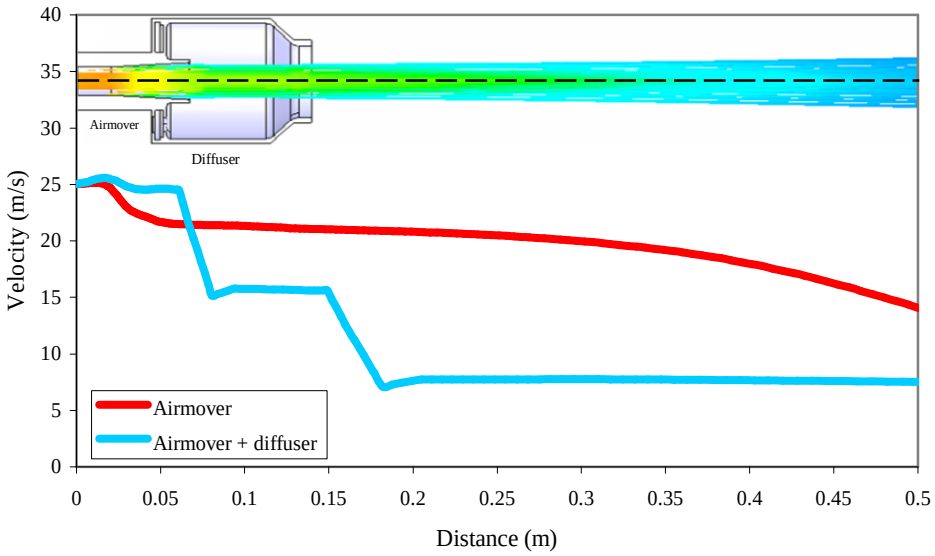


**Figure 2-8 Velocity profiles for the modified chopper gun design generated using COSMOS FloWorks CFD. Lines shown represent the air velocity with and without the diffuser along the dotted centre line. The origin is the point at which the fibres fall from the knife roller. This study was completed as part of the chopper gun design by Dr T Turner, University of Nottingham.**

### 2.2.4. Nottingham DCFP preforming cycle

A schematic diagram of the process is shown in Figure 2-9, which illustrates the four main preforming stages. During step 1 a robot-mounted mechanical chopper head sprays fibres and a polymeric, powdered binder onto the lower perforated tool. As the fibres are being sprayed, air is evacuated from the underside of the perforated tool and the resulting pressure differential holds the deposited fibres in place. A 37kW motor drives a centrifugal fan to create sufficient holding force for the fibres. A powdered binder material (see Appendix B.4.2) is held in a hopper and metered to the chopper head by a high volume, low pressure air system from a screw conveyor. The required percentage of binder is input to a programmable logic controller and the necessary speed is fed to a servo drive. The binder delivery system was designed to handle powdered binders at 0-10%wt of the fibre output. Fibre deposition rate is monitored by closed-loop control on a servo-driven chopper gun. The system is able to process 48K of carbon tows (2×24K, 4×12K etc.) at a maximum deposition rate of 4kg/minute. Fibre length is changed manually by adding additional blades to the knife roller, where the lengths available are equal divisions of the circumference of the roller (115mm).

When material deposition is complete, a matched perforated tool is lowered to compress the preform in order to control the preform thickness at stage 2. Four double-acting pneumatic cylinders are used to lower/raise the upper preform tool, but also to apply up to 5kN of compaction force to the preform. Banks of heaters within the lower plenum are used to raise the air temperature to 150ºC, which cycles through the perforations in the tools to consolidate the powdered binder. At stage 3 the hot air is followed by ambient air, which is cycled through the preform to stabilise the binder. Stages 2 and 3 typically take 20 minutes, compared with 3 minutes for production optimised machines, due to restricted floor space. The heaters are initially at room temperature and are ramped up to 150ºC and back to ambient for each individual preform, rather than having a reservoir of hot air. A typical heating/cooling cycle is shown in Figure 2-11. The heater fins reach 450ºC as the air in the plenum is heated to 150°C. The temperature is held constant for 300 seconds once the tool temperature has reached 140°C. Preforms are subsequently de-moulded when the lower platen temperature has fallen to 50°C. Finally at stage 4, the preform is extracted manually from the preforming station and transferred to a separate moulding station for the injection of liquid resin via resin transfer moulding (see Appendix C.1.1). A typical 1m×1m preform takes 25 minutes to produce on the laboratory system, compared with approximately 8 minutes for a production-optimised machine.

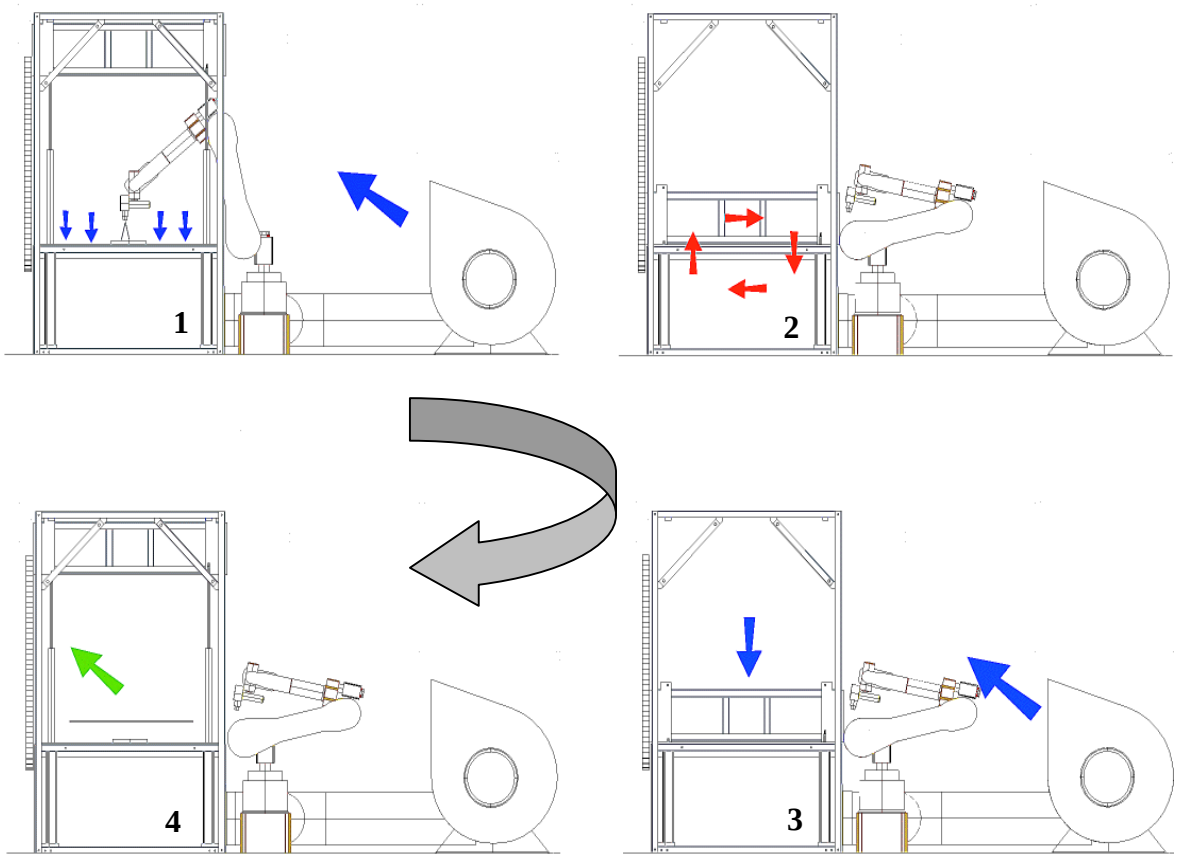


**Figure 2-9 DCFP process schematic illustrating the four main production steps: (1) Fibre and binder deposition. (2) Binder heating. (3) Binder stabilisation. (4) Preform extraction.**

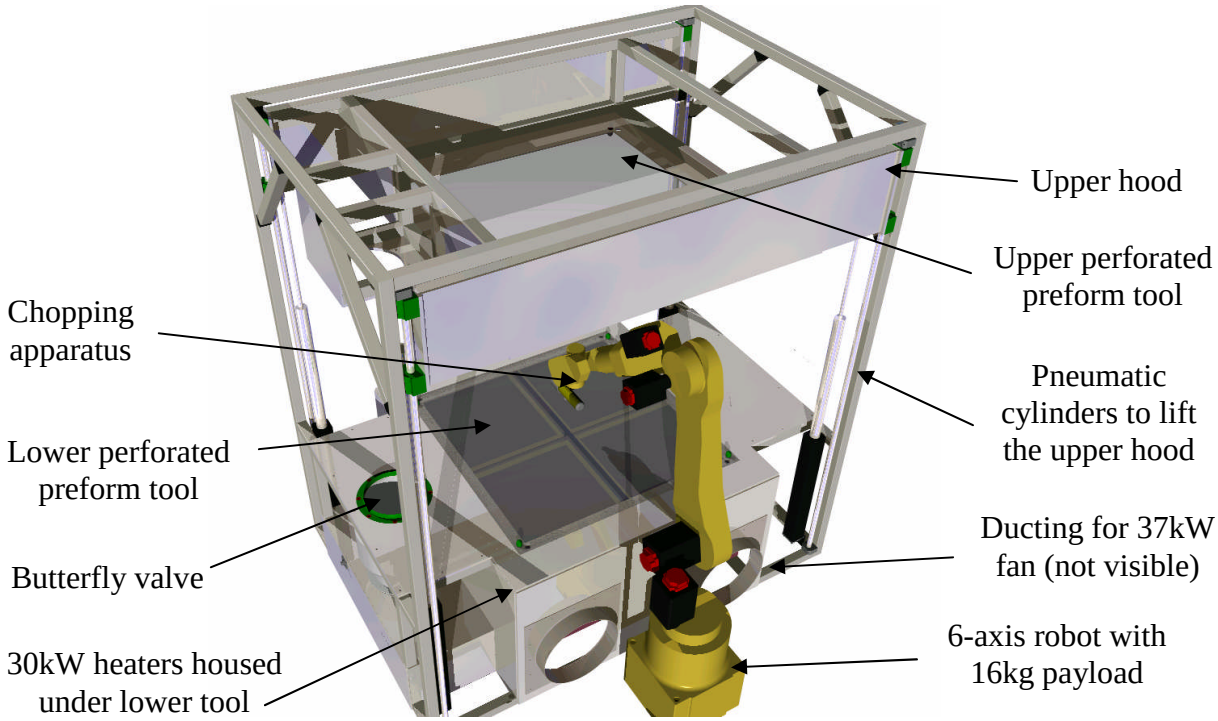


**Figure 2-10 University of Nottingham laboratory-scale DCFP facility. The cover of the upper hood is removed to visualise the upper perforated preform tool. A 1m×1m preform tool for producing 2D preforms is shown but there is the capability to produce parts up to 0.25m deep.**

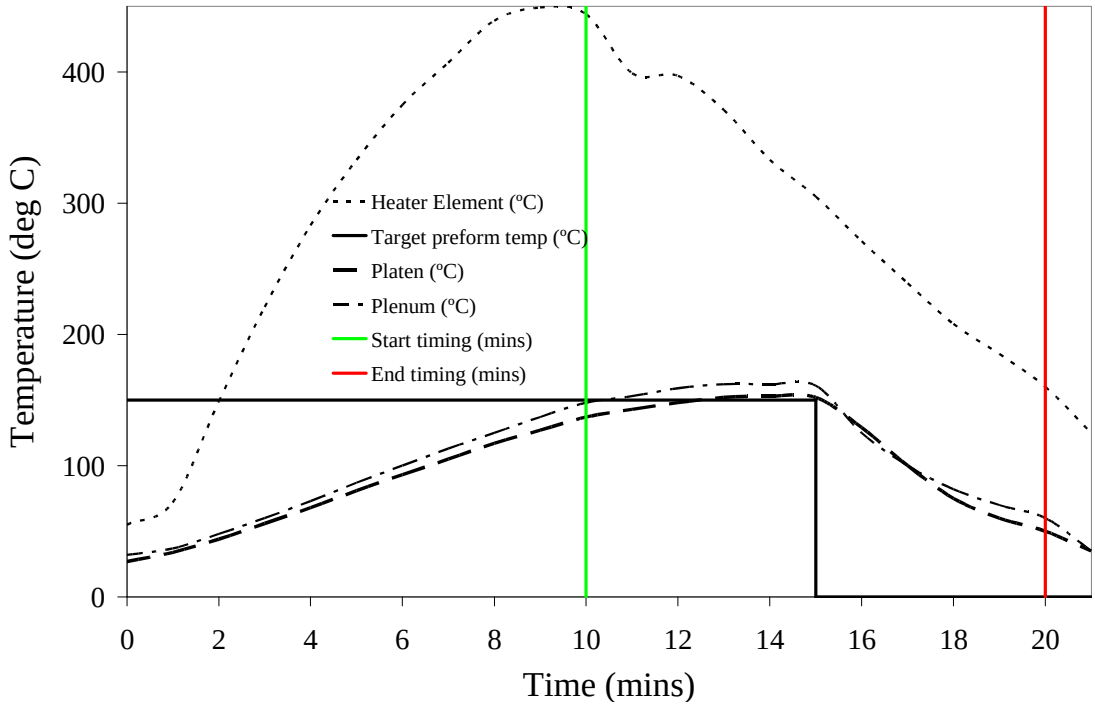


**Figure 2-11 Typical heating / cooling cycle for the University of Nottingham's DCFP facility. The preform was de-moulded once the platen (tool) temperature had fallen to 50ºC.**

### 2.2.5. Fibre alignment

Previous industrial DCFP developments include fibre alignment mechanisms for producing structural aerospace components [48, 49, 52]. Orientating the chopped tows can enhance mechanical performance and improve the fibre packing characteristics to enable higher mouldable fibre volume fractions. However, most result in substantially longer cycle times [52], rendering the methods unsuitable for high volume applications. This section demonstrates the advantage of producing a biased fibre orientation distribution in order to balance the degree of fibre alignment and deposition rate. A progressive failure model using laminate theory and the maximum stress criterion [64] illustrates how only a small degree of fibre bias can lead to dramatic increases in both tensile stiffness and strength. Both the stiffness and strength increase by approximately 100% for the SMC-R50 material modelled in Figure 2-12 when the fibres are distributed according to a biased trigonometric function rather than being isotropic. Only 2% of the total fibre content is orientated a 0º for the trigonometric function and the remaining fibres are orientated between 1º and 75º according to a cosine function.

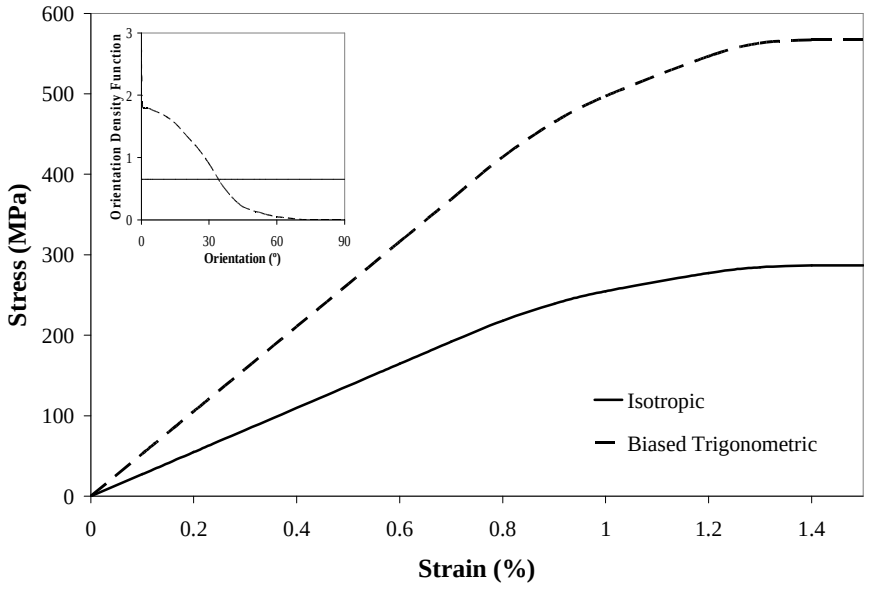


**Figure 2-12 Predicted stress-strain profiles for a glass SMC-R50 material (50% fibre weight fraction), using the analytical model of Giurgiutiu and Reifsnider reproduced from [64]. Inset are the two orientation distributions modelled; the solid line is for a perfectly isotropic case and the dashed line is a biased trigonometric distribution.**

Early fibre directionality developments using the Nottingham installation concentrated on longer fibres (~100mm). The chopping apparatus was positioned within 50mm of

the tool surface and the fibres were aligned as they were dropped from the gun by the robot displacement ("quasi tow lay-down"). Tool coverage was poor and the fibre deposition rate was around a sixth of that used for the current random fibre strategy. The present work has investigated the possibility of partially orientating shorter fibres to improve mechanical performance whilst maintaining processing speed. A concentrator system with a rectangular orifice has been developed to integrate with the existing chopping device (Figure 2-13). Greater levels of directionality can be achieved by reducing the opening in the concentrator, but this consequently increases the risk of blockages. A narrower slot also reduces the width of the effective spray path, requiring more robot passes per fibre layer to achieve the same level of fibre coverage. The slot width also limits the operating speed of the chopping gun because of the increased risk if fibre blockages. The maximum achievable fibre deposition rates before blockages occur are quoted in subsequent figures. Plaques have been produced from 24K carbon tows with various fibre lengths (14, 28, 57mm) to compare against the quasi tow lay-down method and the conventional random fibre deposition. Tensile testing was used to assess the degree of directionality by comparing properties in the 0º (direction of alignment) and 90º directions. Three-point bend tests were also performed at intermediate orientations to determine stiffness, using Ø200mm discs to reduce the number of specimens required (see Appendix D.1.8 for methodology). Discs were water-jet cut from 3mm plaques with an average fibre volume fraction of 30%. Each disc was supported on a pair of Ø10mm rollers spaced 150mm apart and loaded to 200N within the elastic region, using a Ø10mm circular bar. The load was removed; the disc was rotated and then tested again. Three discs were used for each scenario and standard deviation bars are presented in Figure 2-14. Each disc was tested at 18º intervals, between 0º and 180º inclusive and bending results were all normalised with respect to the flexural stiffness at 0º.

The 3 point bend disc test served as an effective method for rapid determination of the level of orthotropy. Increasing fibre length improved the level of fibre alignment when using a concentrator as shown by Figure 2-14. The degree of directional bias for this approach falls between the random fibre case and the fully aligned case (calculated from rule of mixtures). The fibre deposition rate and the longitudinal stiffness $E_1$ from conventional tensile tests are plotted against the degree of directionality ($E_1/E_2$ normalised with respect to the aligned case) in Figure 2-15. A 14% increase in stiffness

is achieved over the random case, using the concentrator to partially align 14mm fibres, although a 50% reduction in deposition rate is experienced. Deposition rates are based on the current DCFP installation and are limited by the concentrator design. When the fibre length is increased to 115mm the composite stiffness is 77% of a fully aligned, continuous fibre laminate.

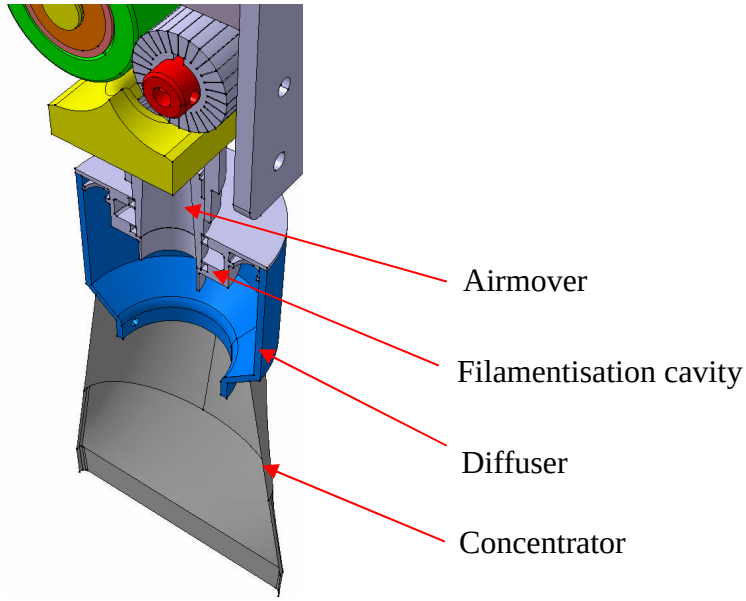


**Figure 2-13 DCFP chopping apparatus; including sectioned view of filamentisation cavity and directionality concentrator. The rectangular opening at the end of the concentrator is 80mm×8mm.**

Figure 2-16 demonstrates that an increase in tensile strength can also be expected for increasing fibre length because of increasing levels of fibre alignment. There is an initial strength increase of 39% from the isotropic 6mm fibre case to the partially aligned 14mm fibres. However, as fibre length increases the rate of increase in strength reduces. The tensile strength is only within 25% of the theoretical aligned case for the partially aligned 115mm fibres. This is much lower than the stiffness retention reported above and also the 51% strength retention reported for the P4A project [49]. Tensile strength is strongly influenced by the presence of fibre ends in the discontinuous material. Unlike stiffness, the strength of a discontinuous laminate will never attain that of a continuous laminate, because of the stress concentrations present at the fibre ends. Higher strength retentions reported in [49] can be attributed to lower filament count tows (3K rather than 24K) and therefore smaller stress concentrations, due to fewer synchronised filament ends. Another possibility is that the fibre lengths are below the critical fibre length (discussed in detail in Chapter 5), which is reported as up to 10

times longer for strength than for stiffness [65]. Therefore the bundles pull-out from the matrix material and the full mechanical potential of the fibre is not realised.

In summary, adopting a partial fibre alignment approach can provide worthy gains in mechanical performance. Tensile stiffness and strength of a partially aligned laminate are 77% and 25% respectively of a unidirectional, continuous laminate. However, the degree of alignment for the methods used in Figure 2-15 and Figure 2-16 is inversely proportional to deposition rate. Selection of the orientation method (random, concentrator, quasi tow lay-down or dedicated tow lay-down) is therefore dependent on the level of directionality required and the desired cycle time. The introduction of directional fibres for high volume applications is only intended for local improvements in fibre reinforcement in critical areas. Aligned fibres are unlikely to be used globally and therefore the relatively low cycle times for random fibres can still be exploited.

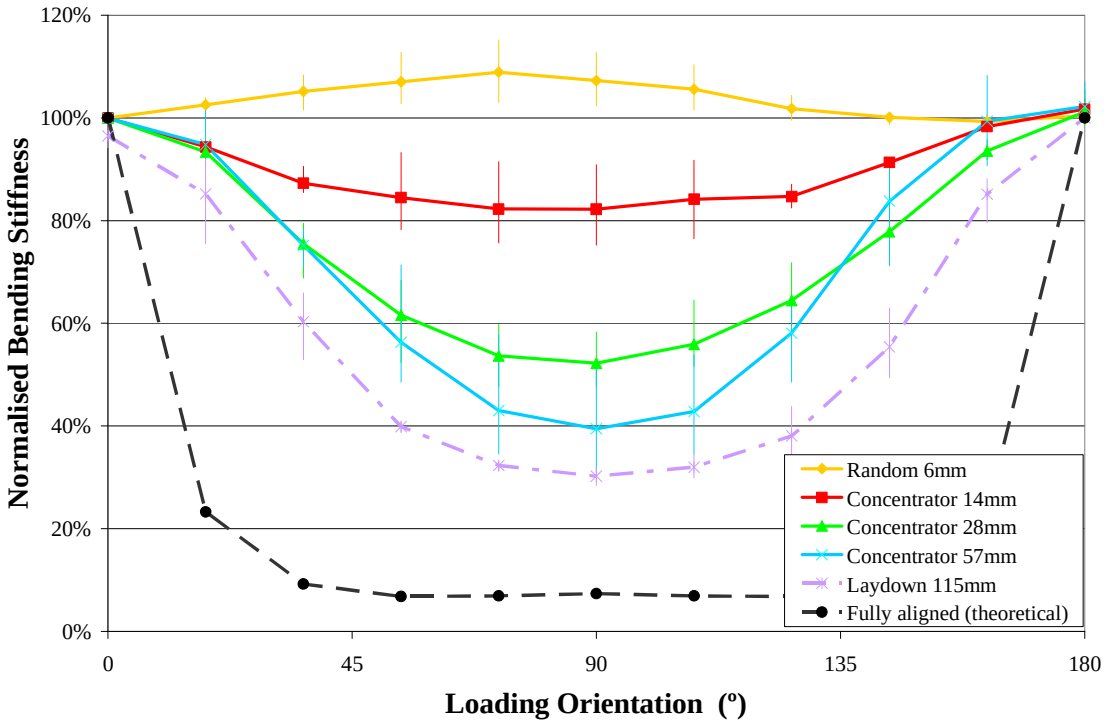


**Figure 2-14 Flexural disc testing shows the relative degree of fibre alignment for increasing fibre length. All values are normalised with respect to the 0º orientation. Three repeat plaques were tested for each fibre length and standard deviation bars are shown. The theoretical line was determined using a classical laminate approach.**

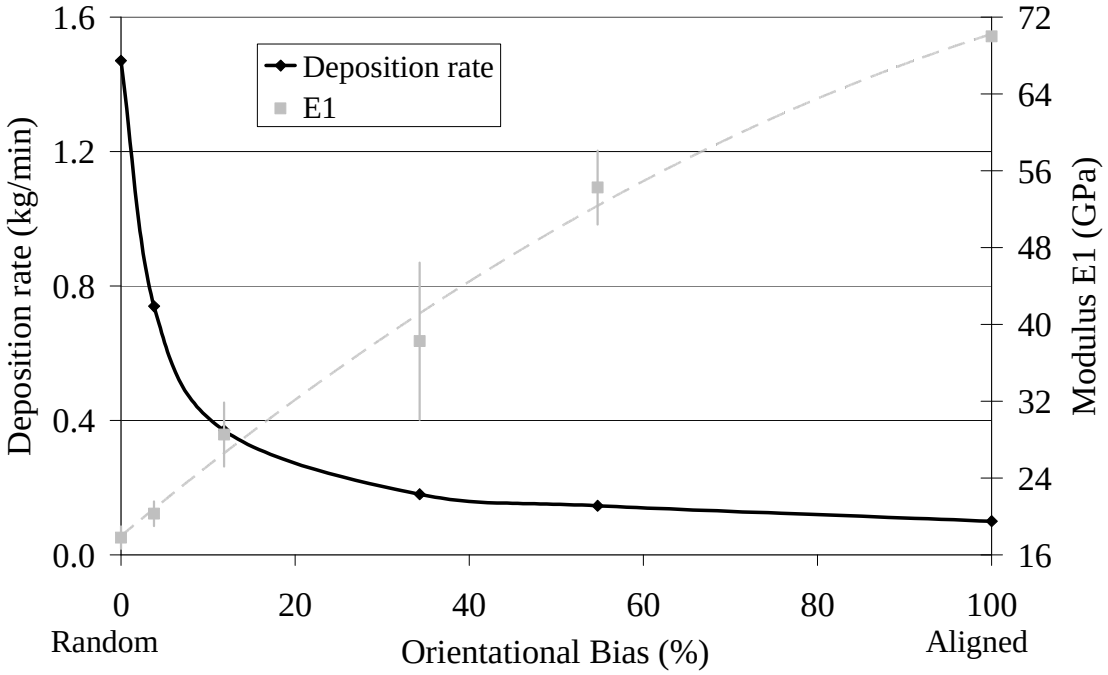


**Figure 2-15 Comparison of the longitudinal tensile stiffness against maximum achievable fibre deposition rate. From left to right: Random 6mm fibres, concentrator (14, 28, 57mm), quasi tow lay-down (115mm) and the fully aligned case is calculated using a classical laminate theory model to simulate a dedicated tow lay-down system. All laminates have a 30% fibre volume fraction.**

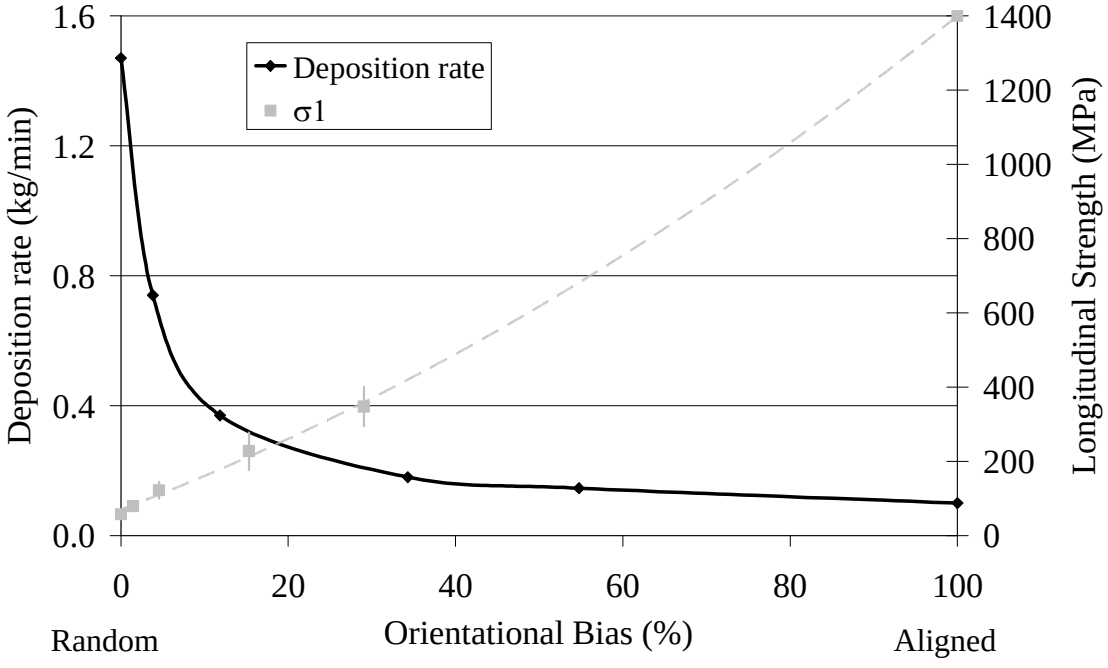


**Figure 2-16 Comparison of the longitudinal tensile strength against maximum achievable fibre deposition rate. From left to right: Random 6mm fibres, concentrator (14, 28, 57mm), quasi tow lay-down (115mm) and the fully aligned case is calculated using a classical laminate theory model to simulate a dedicated tow lay-down system. All laminates have a 30% fibre volume fraction.**

## *2.3. DCFP process optimisation*

### 2.3.1. The effect of DCFP machine parameters

The mechanical properties of DCFP components are directly influenced by the quality of the preforms. This study aims to determine the significance of a number of machine parameters in order to improve the quality of preforms produced on the Nottingham DCFP facility. This will eliminate some of the systematic error associated with the process and will provide higher levels of confidence in future experimental results.

Four main factors control the quality of DCFP preforms, which are all associated with the uniformity of fibre coverage when measured by image analysis techniques:

- Areal density consistency – inter and intra plaque
- Fibre orientation distribution
- Fibre length distribution
- Induced filamentisation level (average tow filament count)

During the development stage of the Nottingham DCFP machine the following parameters were found to affect the uniformity of fibre coverage:

- Airmover flow
- Robot speed
- Chopper gun speed
- Fibre type
- Tool centre-point height (height of chopper gun above preform tool)
- Lay-down strategy / sweep offset
- Number of tows processed simultaneously

The main airmover serves to prevent fibre blockages by ejecting the fibres from the gun. High airmover flow means fewer fibre blockages but also tends to blast existing

fibres off the tool surface and filamentise the fibre tows. These three functions have been separated on the revised chopper gun design (discussed in Section 2.2.3) to give greater levels of control. High velocity air within the filamentisation chamber (see Figure 2-7) separates the filaments to provide smaller bundles and therefore greater macroscopic homogeneity because there are more bundle segments for a given volume of carbon fibre. The effects of filamentisation can be seen in Figure 2-17. The plaques shown were produced with the same fibre type and all other machine settings were the same. Filamentisation is discussed in more detail in Section 3.5.

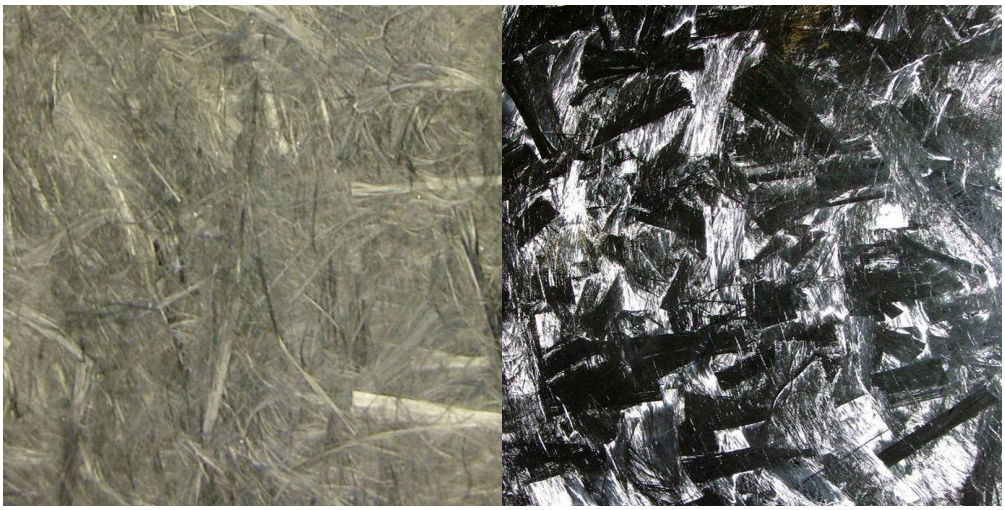

**Figure 2-17 (Left) High pressure in filamentisation cavity (7 Bar) produces fluffy fibre preforms consisting of smaller filament counts (Right) No pressure produces 'log' shaped tows**

Of the remaining machine parameters, the following were selected for further investigation: Robot speed, TCP height and lay-down strategy. These factors are discussed in the following two studies: Coverage optimisation and effect of lay-down strategy.

#### *2.3.1.1. Coverage optimisation*

Coverage optimisation is to ensure that uniform layers of random fibres are deposited onto the preform screen. Chopped fibres leave the gun in a cone formation, such that the spray diameter is determined by chopper gun height and the linear robot speed. Preforms with artificially low areal densities (0.25kg/m$^2$) were manufactured to study the influence of the tool-centre-point height (distance between the chopping apparatus

and the preform tool) and robot speed on the fibre placement characteristics. TCP height is of particular interest because it is often dictated by part geometry or features, which limits the line of sight of the chopping apparatus. The following independent variables were studied during this investigation:

- Robot speed (200mm/s, 400mm/s & 800mm/s)
- Tool centre-point (TCP) (100mm, 200mm & 300mm above bed)

The following variables remained constant:

- Areal density constant ($0.25kg/m^2$) – chopper speed adjusted to compensate
- Fibre length at 23mm
- Path offset at 50mm

Whilst the path offset significantly affects the degree of preform coverage, it is clear that smaller path offsets yield more uniform fibre coverage. The path offset is infinitely variable and can be fully controlled within the robot program. However, the optimum path offset is a function of the fibre length, robot speed and the TCP, which are not infinitely variable. Fibre lengths range from 3mm to 115mm and the practical upper limit for the robot speed is 1m/s. The TCP height may be restricted for complex 3D shapes, preventing the chopper head from getting close to the tool surface. Therefore, this study focuses on the effects of robot speed and TCP height rather than the path offset, which can be fully adjusted to compensate for the poor fibre coverage resulting from these two variables.

Preforms for this study were manufactured in the conventional way (see Section 2.2.4) and were analysed on a glass box, back lit by a fluorescent tube. The low areal mass ($0.25kg/m^2$) of the preform provided sufficient dark-to-light contrast in order to establish a measure of fibre coverage and degree of uniformity. The resulting digital images were converted to black and white at a preset threshold of 156 on the greyscale as shown in Figure 2-18.

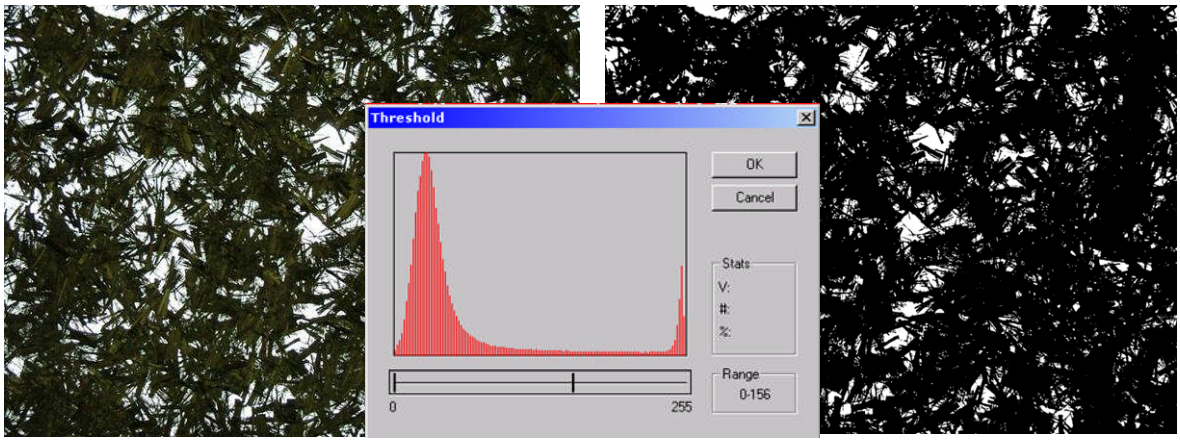


**Figure 2-18 Image processing for coverage optimisation study was performed using UTHSCSA ImageTool v3. Images were converted to black and white using a manual threshold value of 156 on the greyscale.**

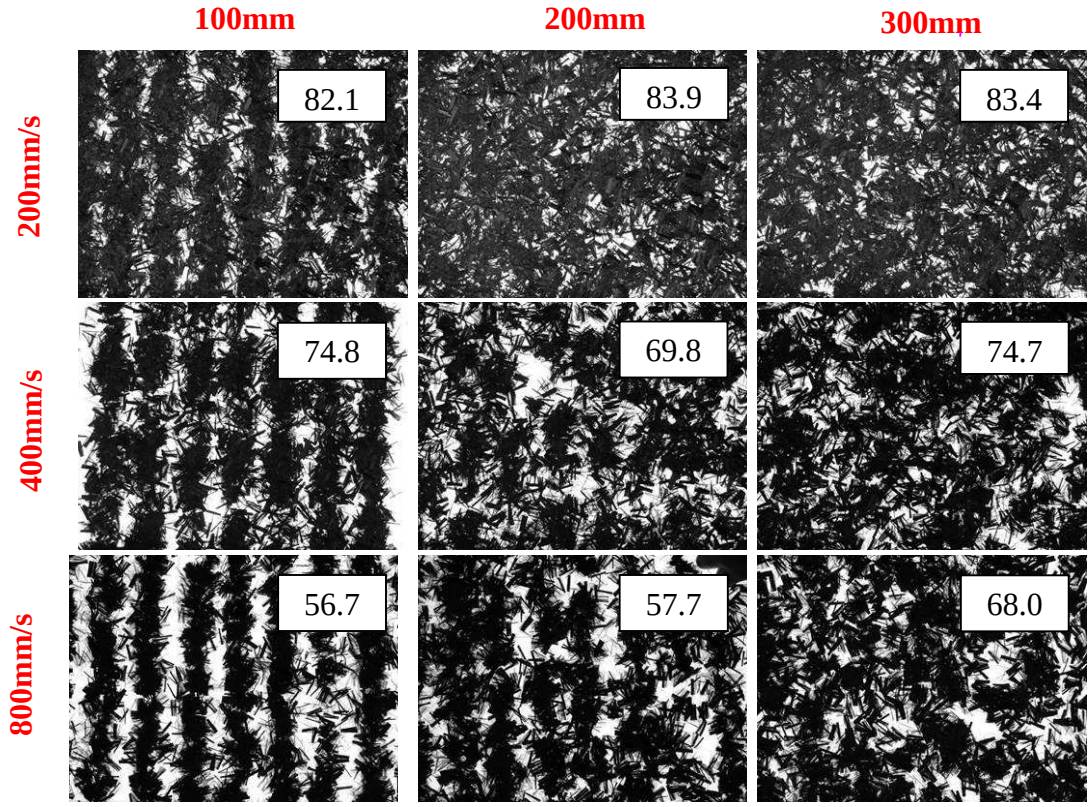


**Figure 2-19 Matrix of images from uniformity study. (Left to right) Increasing tool-centre-point height (Top to bottom) Increasing robot speed. (Percentage coverage values displayed)**

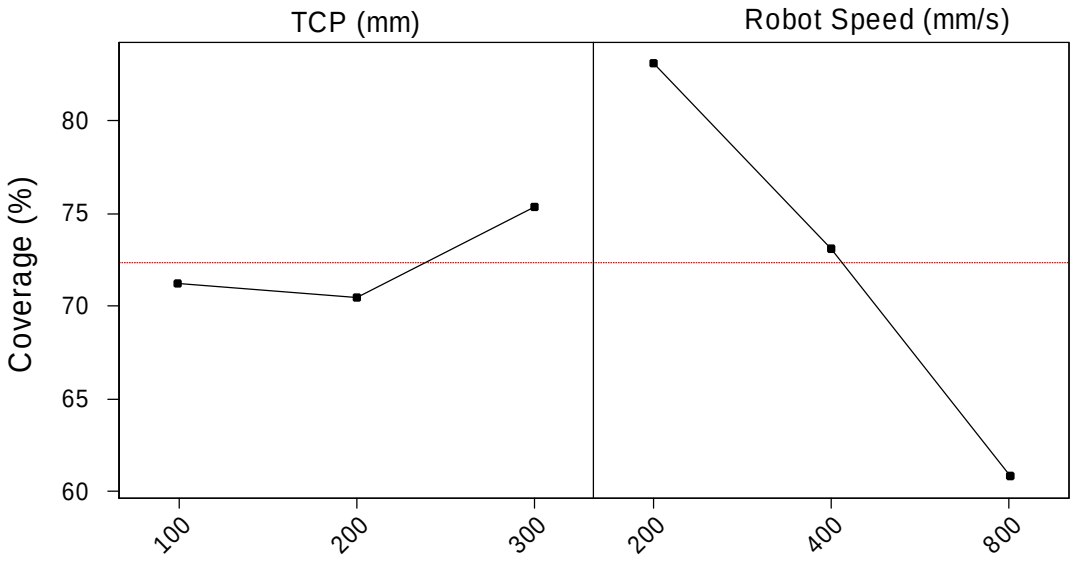


**Figure 2-20 Mean effects plot for fibre coverage study – Effect of TCP and robot speed**

The black and white images were assessed for coverage by counting the total number of black and white pixels and thus generating a 'black fraction'. The nine permutations, consisting of three robot speeds and three TCPs, are shown in Figure 2-19. The percentage coverage values were analysed in Minitab® v14 to determine the mean effects of each independent variable (Figure 2-20). The dominant variable in determining fibre coverage is robot speed. Increasing the linear speed of the robot from 200mm/s to 800mm/s decreases the percentage fibre coverage linearly from 83% to 61%, a reduction of 26%. As the robot speed increases, the chopper gun speed is also increased to maintain a constant areal density of fibre. The effective spray cone tends to tighten due to faster chopper gun speeds as the fibres exit the gun with greater inertia, causing the number of unreinforced stripes to increase (see bottom left of Figure 2-19).

The effect of changing the TCP has a less dramatic effect on the percentage coverage value. A decrease in TCP height from 300mm to 100mm decreases the percentage coverage value by only 5%. However visually, Figure 2-19 shows that the TCP height affects the uniformity of the preform. The TCP affects the spray pattern in a predictable manner as shown by Figure 2-21. The effect of decreasing the TCP from 300mm to 200mm and 100mm decreases the diameter of the spray cone, hence the width of the spray path, from 71mm to 64mm and 37mm respectively (determined from digital images using ImageTool). This causes stripes to occur, but this is not reflected by the percentage coverage values (going from left to right) in the matrix in Figure 2-19.

**Figure 2-21 The effect of increasing the TCP height from (left) 100mm, (centre) 200mm to (right) 300mm. As the TCP height increases the diameter of the virtual spray cone projected from the end of the chopping apparatus also increases. (The holes in the perforated plate are Ø3mm)**

Preform uniformity is a more intuitive measure of the quality of DCFP preforms. This can be determined by analysing the number of light to dark transitions across the plaque to account for the striped effect. The same images were processed by drawing a line across the centre of the image and plotting the greyscale value (from 0 to 255) for each pixel along the line. A constant grey level indicates a uniform distribution of fibres rather than many sharp, dark to light transitions. The methodology is shown in Figure 2-22.

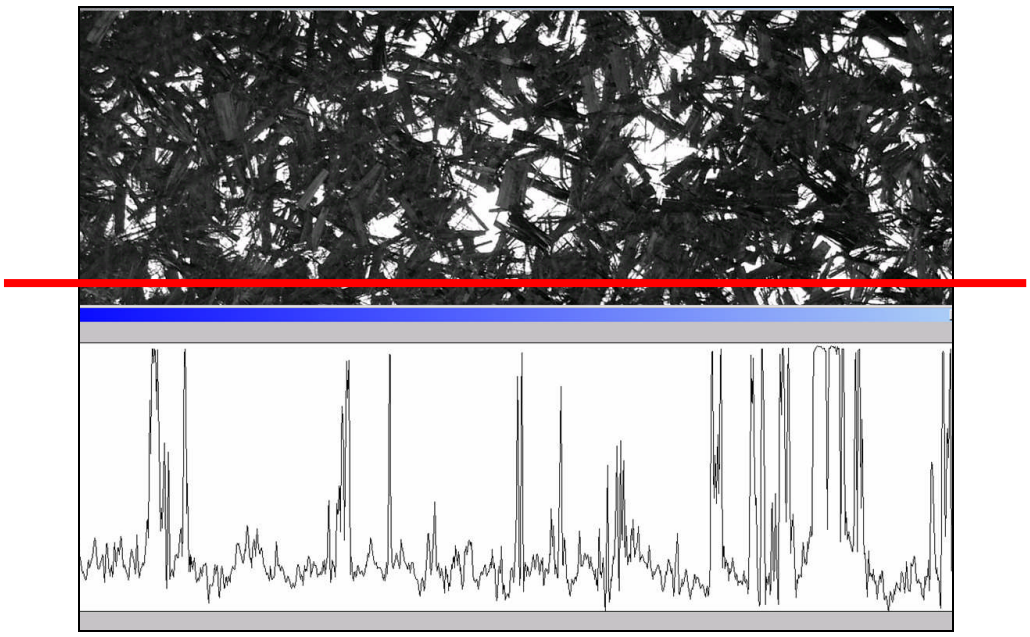

**Figure 2-22 Image processing for uniformity study. A line is drawn across the centre of the image (shown in red) and the greyscale value of the pixels along that line are plotted on a scale from 0 (black) to 255 (white)**

Figure 2-23 and Figure 2-24 show the differences between best and worst case images. It proved difficult to quantify the differences in plaques so a subjective analysis is presented. The conclusions from this work were that low robot speed and high TCP were critical in giving good preform uniformity and fibre coverage.

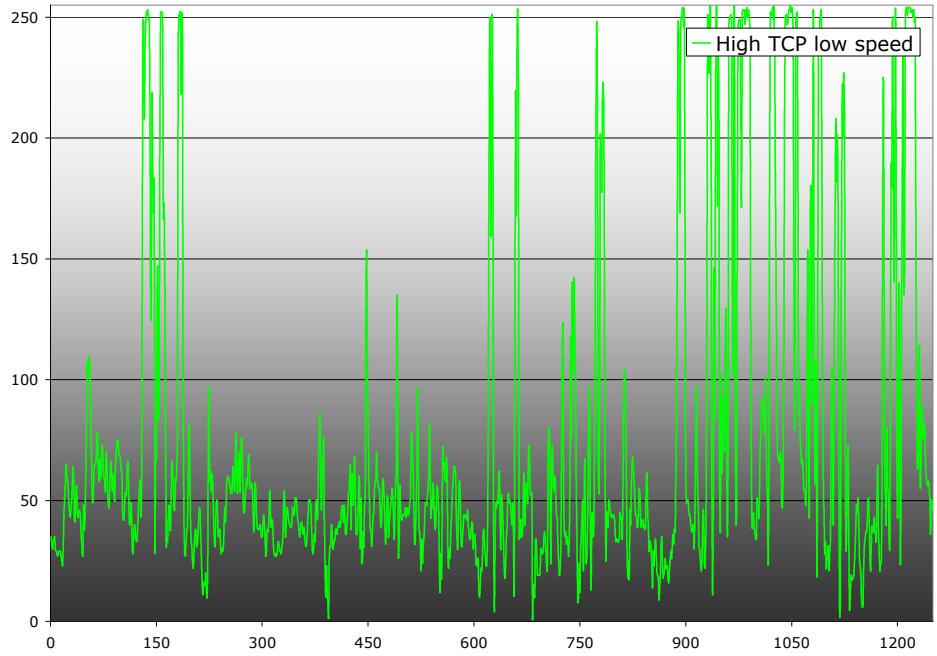


**Figure 2-23 High TCP low robot speed (see top-right image of Figure 2-19)**

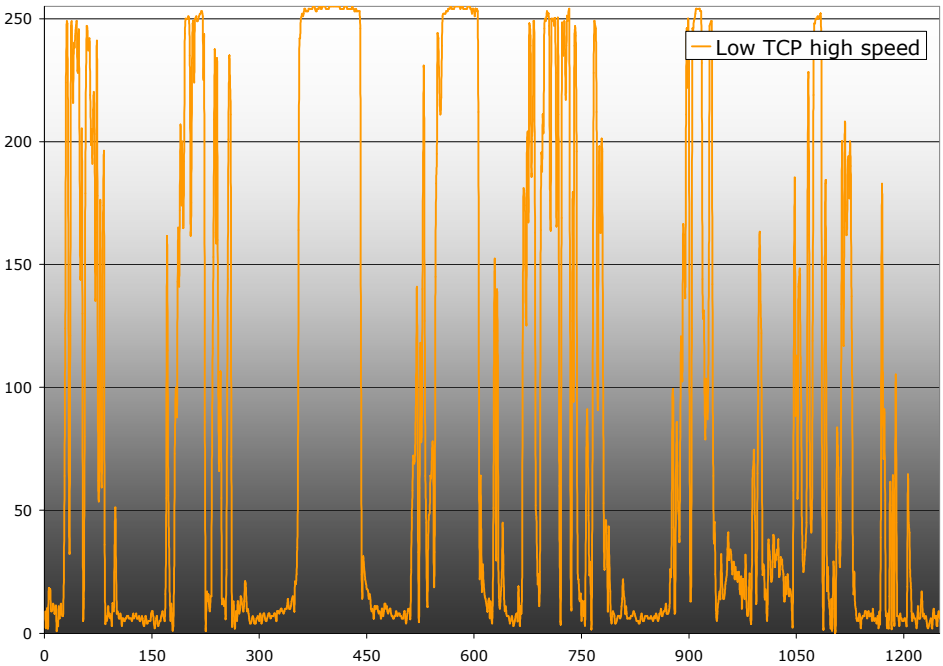


**Figure 2-24 Low TCP high robot speed (see bottom-left image of Figure 2-19)**

### *2.3.1.2. Effect of lay-down strategy*

The fibre lay-down strategy was investigated as a potential means of improving preform quality. The lay-down strategy describes both the movement of the robot, the number of sprayed layers and the number of tows processed simultaneously. Four different scenarios were tested to determine their effect on the areal mass variation across 2D preforms. The four lay-down strategies are summarised in Table 2-1.

| | 2 Sprayed Layers<br>1× 24K Tow | 1 Sprayed Layer<br>2× 24K Tows |
|---|---|---|
| East/West Pass<br>East/West Pass | ✓ | ✓ |
| East/West Pass<br>North/South Pass | ✓ | ✓ |

**Table 2-1 Permutations for lay-down strategy investigation**

Each single sprayed layer (1000gsm) consists of two passes of 500gsm each. A pass can either be in the east/west direction or in the north/south direction as indicated by Figure 2-25. Each sweep of the robot is offset by 50mm, but the second pass is offset from the first by 25mm when both passes are in the east/west direction to give an effective sweep offset of 25mm. Each preform consists of 2000gsm which is sprayed in a single layer using two 24K tows or as two layers with just one tow. The overall effect of using each lay-down strategy was measured by weighing stamped coupons from each preform. Coupons were 50×50mm square with contiguous boundaries and were used to create an areal density map for each preform. Specimens were weighed to an accuracy of ±10µg and the standard deviation between coupons was used to measure the consistency of each preform. The results can be used to accurately quantify the variation in mass across the plaques. A typical plot is shown in Figure 2-26.

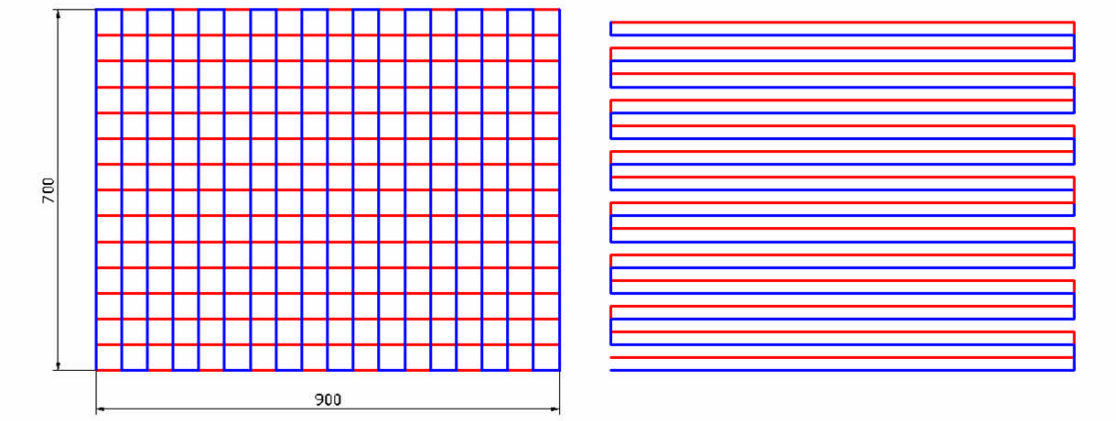


**Figure 2-25 Two lay-down strategies. (Left) An east/west pass is followed by a north/south pass. (Right) The first east/west pass is followed by a second east/west pass, offset from the first by 25mm. Two fibre passes (500gsm) constitute one single layer of 1000gsm. (Dimensions in mm)**

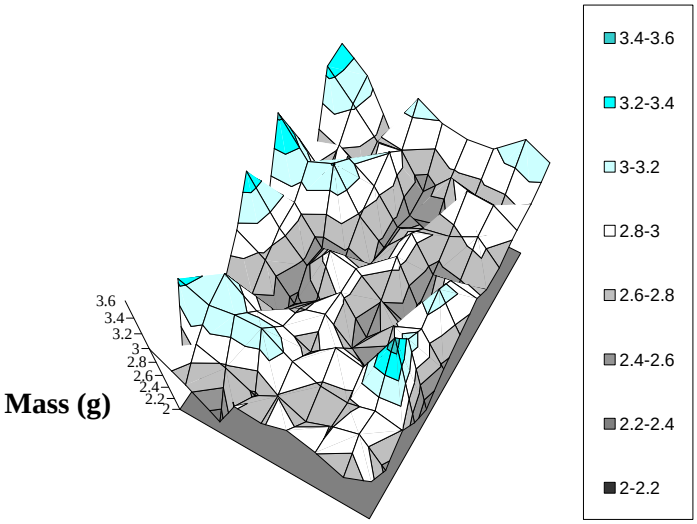


**Figure 2-26 Typical areal mass variation plot for a 2D preform, using 50×50mm contiguous square coupons.**

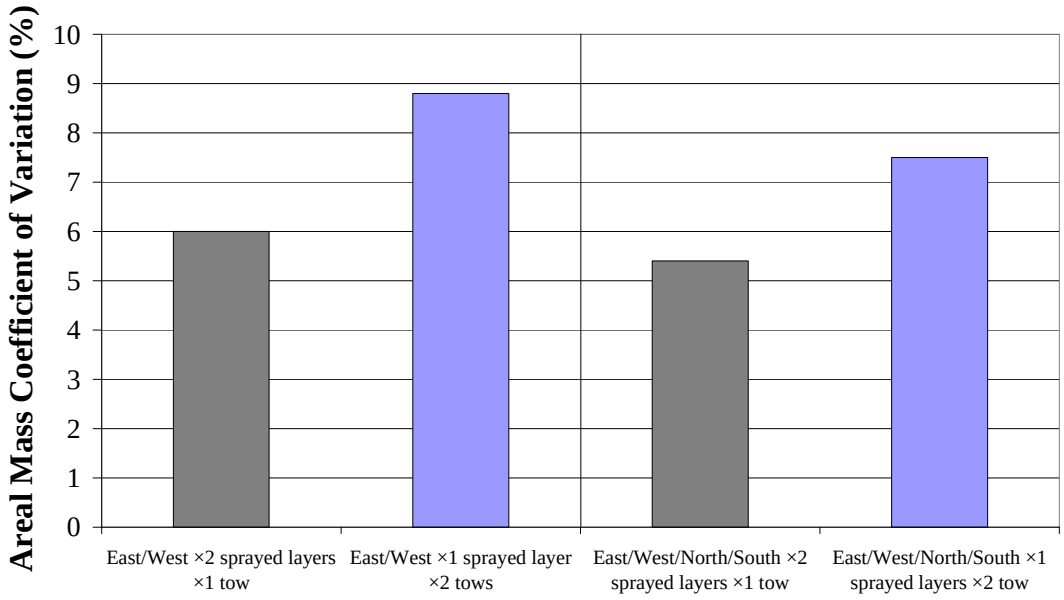


**Figure 2-27 Results of areal mass / lay-down strategy study**

The results of the lay-down strategy investigation can be seen in Figure 2-27. The number of layers versus the number of tows has more impact on the areal mass variation than the direction of the sprayed passes (east/west versus east/west/north/south). Adopting a double layer approach with 1 tow, rather than a single layer with two tows decreases the areal mass variation by approximately 30%. Whereas, adopting an east/west/north/south lay-down rather than an east/west only strategy decreases the areal mass variation by only 10-14%. This is an important discovery for industrial applications. It is not always feasible to vary the spray direction, particularly for complex 3D components; therefore it would be more beneficial to process only a single tow over two layers to achieve critical areal mass requirements. However, this effectively doubles the cycle time, which may also be unfeasible for medium volume applications.

#### *2.3.1.3. DCFP optimisation conclusions*

The effects of tool centre point height, robot speed and spray pattern on preform quality have been investigated. This work has shown that a high TCP (300mm) and low robot speed (200mm/s) produce preforms with the highest level of fibre coverage uniformity. Areal mass plots have shown that the mass variation across the surface of a preform can

be reduced to around 5% when a single tow is processed over two individual layers whilst adopting an east/west/north/south spray pattern. These parameters will be used to improve part integrity and repeatability, to provide more confidence in future experimental trends. However, it is not suggested that this strategy for preform production is indicative of industrial practice. Firstly, the direction of fibre lay-down is dictated by the geometry of the component, which may make an east/west/north/south strategy unfeasible. Secondly, a high TCP prevents the chopper gun from accessing complex part geometry and also increases the degree of fibre overspray.

### 2.3.2. Binder study

Binder material is an essential part of the DCFP process, providing cohesion between the fibres to enable mechanical handling between the preformer and the moulding station. Binder also enhances the level of compaction during the consolidation stage to increase the moulded laminate volume fraction. However, a review of literature indicates that an excessive level of binder material can reduce the mechanical performance of the composite. Double cantilever beam (DCB) tests have been used to show that a small amount (2%wt) of thermoplastic binder can increase the toughness of unsaturated polyester by 13%, giving higher Mode-I interlaminar fracture toughness values for the composite [66]. However, adding more binder between 2 and 5%wt begins to detrimentally affect resin properties, with a 33% reduction in Mode-I fracture toughness. Tanoğlu and Seyhan [67] found that the highest level of preform compaction (hence laminate $V_f$) was obtained with 3%wt thermoplastic binder, whilst further increases in binder level reduced preform compaction. The in-plane compressive stiffness and strength of the moulded composite were also at a maximum with 3%wt binder, however increasing binder levels (up to 6%wt) reduced the compressive properties because of lower interlaminar properties.

Clearly a balance is required to achieve the maximum mechanical performance of the laminate whilst maintaining sufficient rigidity to handle the preform. This study investigates both percentage binder level and binder type in order to establish the optimum parameters for future preform production in this work. Three powdered binders have been used on the DCFP machine;

• Reichhold Pretex 110 – A catalysed epoxy with heat activated curing agent
• Wacker Vinnex M81 – Cross-linking styrene acrylic copolymer
• DSM Neoxil 940 – Thermoplastic polyester

The aim of the following testing was to observe both dry preform strength and also the effect on the in-plane tensile modulus and strength of the moulded DCFP laminates. Three levels of binder addition were used as representative of the full range: 3%, 6% and 9% by preform mass were deposited on the preforms. Tenax 24K STS fibre was chopped into 23mm lengths to create preforms with an areal density of 1.5kg/m$^2$, generated by using 3 successive layers with a 50mm offset between robot passes. All preforms were consolidated according to the cycle outlined in Figure 2-11. Two preforms were made for each binder level; one for dry testing and the other for moulding. Ten samples for dry tensile testing were cut 115mm by 280mm. A distance between the grips of 200mm was used and the test speed was 10mm/min, in accordance to [68]. Preforms were moulded using DLS1648 (see Appendix B.2) in a 3mm cavity to yield an approximate volume fraction of 30%. Twenty tensile specimens (25mm x 250mm) were cut from each plaque using an abrasive waterjet at 50mm/min.

Due to the difference in bulk density of the three binders the percentage weights were adjusted to avoid the need to recalibrate the binder delivery system. The revised values are normalised with respect to the Pretex material, for which the binder delivery system was designed (see Table 2-2).

| Pretex (%wt) | Neoxil (%wt) | Vinnex (%wt) |
|---|---|---|
| 3 | 3.3 | 2.9 |
| 6 | 6.6 | 5.8 |
| 9 | 9.9 | 8.7 |

**Table 2-2 Values for the percentage binder by weight, adjusted according to the bulk density of the binder and normalised with respect to the Pretex system**

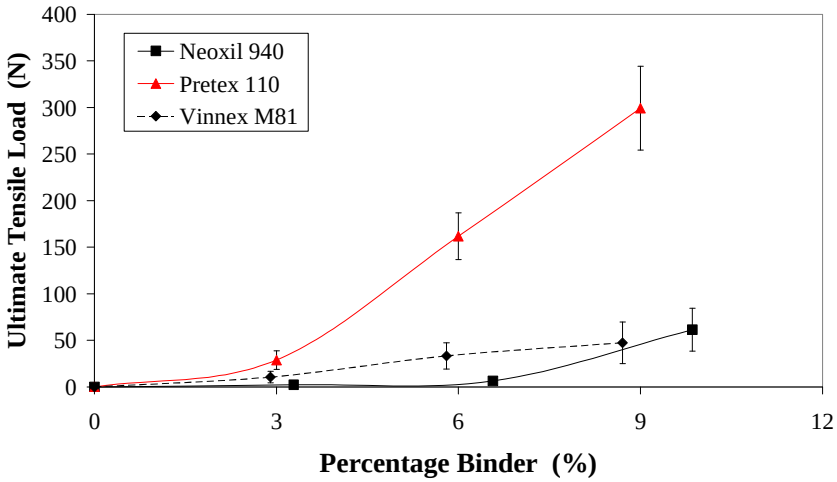


**Figure 2-28 Dry preform tensile results for varying levels and types of powdered binder**

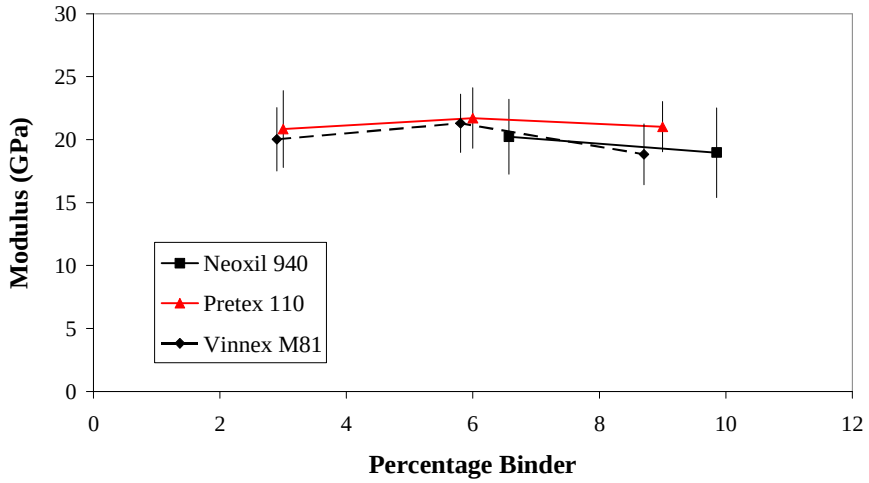


**Figure 2-29 Modulus comparison for three powdered binder types at three binder percentages by weight**

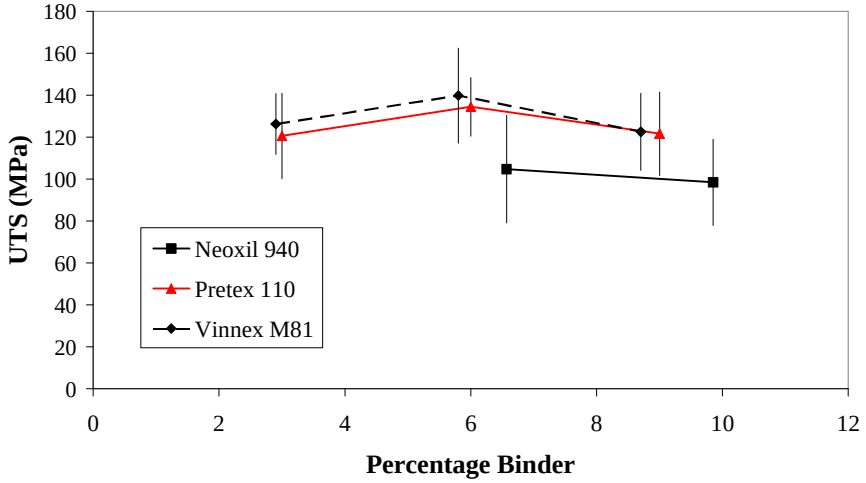


**Figure 2-30 Ultimate tensile strengths for laminates produced with varying binder types and percentage levels by weight**

Figure 2-28 shows the average peak load in each case for the dry preform tensile tests. There is an unsurprising increase in peak load with increasing percentage binder content for the three binder types tested. Pretex is the best performing binder in this test. For 9%wt binder levels the peak load attained with the Pretex system is approximately 5 to 6 times higher than the other two systems, given the variation in bulk density. This can be attributed to binder loss through the perforated tool. Manufacturer's data on particle size suggests that 30% of Pretex particles pass through a #100 mesh, whereas almost 60% passes through the same mesh size for the Vinnex and Neoxil systems. Further difficulty was experienced in processing the Vinnex material with the existing binder delivery system, as the material did not flow in the feed hopper. The particle size for the Vinnex and Neoxil systems is also too small to adequately bond the large carbon tows together in a very high loft preform.

Figure 2-29 and Figure 2-30 show the influence of binder type and level on the tensile stiffness and strength of the moulded laminates. No data is available for the 3%wt Neoxil point because of moulding difficulties due to insufficient binder strength. There is little difference in modulus for the three binder types, considering the level of experimental variation (~13% denoted by standard deviation bars in Figure 2-29). The tensile strength appears to be dominated more by the binder parameters than the stiffness. Figure 2-30 shows a maximum at 6%wt for the three binder levels tested for each system. However, the two cross-linking binders (Vinnex and Pretex) out-perform the Neoxil system by approximately 25-35%. The Neoxil system was specifically formulated for use with polyester matrices and therefore the bond strength between the binder particles and the matrix is lower than for the epoxy binder systems.

The two cross-linking binders provide comparable in-plane tensile properties. Both systems increase the tensile performance of the laminate when the binder level is increased from 3%wt to 6%wt, but further additions up to 9%wt tend to reduce the properties. The binder is believed to have a toughening effect at relatively low additions but acts as a pollutant at higher levels, which interferes with the cohesive strength of the matrix.

The reviewed literature is supportive of these results. This study has shown that 6%wt of powdered binder is the optimum level for in-plane mechanical performance for DCFP laminates. The two cross-linked systems showed insignificant differences in tensile properties for the moulded laminates, but the dry preform testing indicated that the ultimate tensile load of preforms manufactured using the Pretex system was 5-6 times higher. All subsequent preforms will be manufactured using 6%wt of Pretex 110 powdered binder.

## *2.4. DCFP process simulation*

Local variation in areal density yields inconsistent volume fractions across the laminate and, in turn, variation in mechanical properties. Clearly a principal goal in optimisation of the DCFP process involves minimising errors associated with uniformity of carbon coverage and improving preform consistency. However, the aspect ratio of larger tows makes it increasingly difficult to achieve uniform coverage for thin laminates. Areal density variation has been studied above by manually cutting and weighing contiguous coupons from each preform, or by measuring light transmission through the preform using image analysis software [69]. In this section of the work a process simulation has been developed to provide an effective method for rapidly predicting the effects of material and process parameters on local areal density variation.

Kinematic mapping is utilised here to investigate the stochastic effects associated with parameters such as fibre length, filament count and areal density etc. on the local density variation across 2D preforms. A robot spray path is defined from the specified tool geometry and spray path offset. Figure 2-31 shows the virtual circle, depicting the base of the spray cone projected onto the tool surface at each time step. The diameter of the circle is determined by the height of the chopping apparatus relative to the tool surface. The shape of the spray cone is assumed to remain symmetrical; therefore the effects of robot speed are overlooked. The polar coordinates of the centroid of each deposited tow are determined by the generation of two random numbers. $\theta_{ij}$ is a random angle between 0 and $2\pi$ radians and the radius $R_{ij}$ is based on a random number returned from a normal distribution, with mean 0 and standard deviation 0.5. A standard deviation higher than zero enables fibres to fall outside the virtual circle, as

fibres bounce off the tool surface. This value was determined experimentally using digital images such as those presented in Figure 2-21. Finally, the tow orientation $\phi_{ij}$ about its geometric centre is determined by a third random number between 0 and $\pi$ radians. The number of tows deposited within each circle represents the number of tows being processed simultaneously through the chopping apparatus. However, the time step is very small (typically 0.01s) and a large degree of overlap (~95% for a robot speed of 200mm/s) is experienced between neighbouring circles; the overall effect is shown in Figure 2-32. Any fibre orientation distribution can be generated over the spray circle in the simulation code, but in the present work a uniform random distribution of fibres is assumed. The methodology behind the process simulation is discussed in more detail in Appendix.F

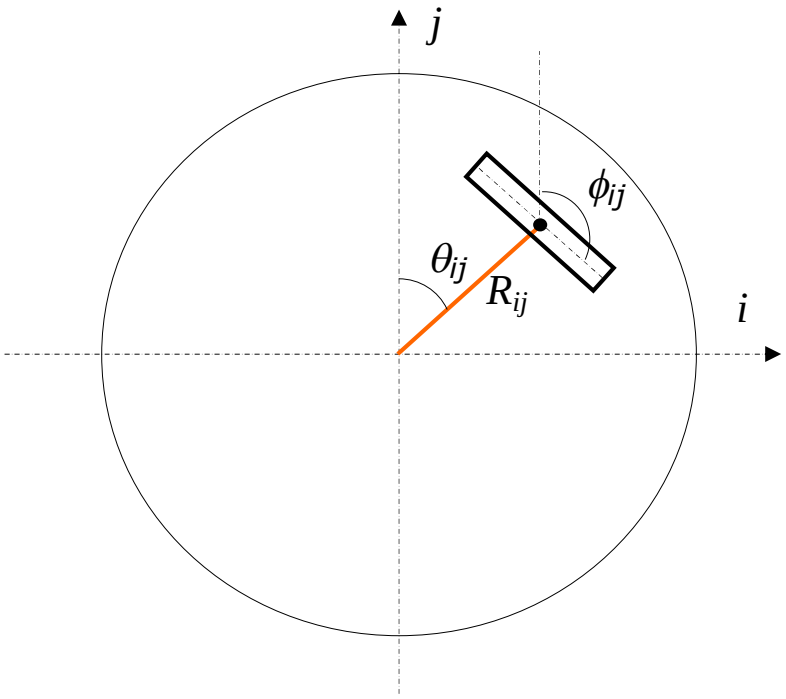


**Figure 2-31 Virtual circular base of the spray cone used in DFP process simulation, where the centre point is determined by the robot time step along the robot path. $\theta_{ij}$, $\Phi_{ij}$ and $R_{ij}$ define the centre of mass for $tow_{ij}$.**

A quantitative prediction of local density variation is obtained from the simulation. An analysis grid is defined and at each of the analysis points the number of tows is computed to produce an 'x-ray' image. The output from the process simulation is visually compared with an equivalent preform in Figure 2-33. An artificially low areal

density (0.25kg/m$^2$) is shown in order to increase contrast. Subsequent validation has been conducted at higher areal densities.

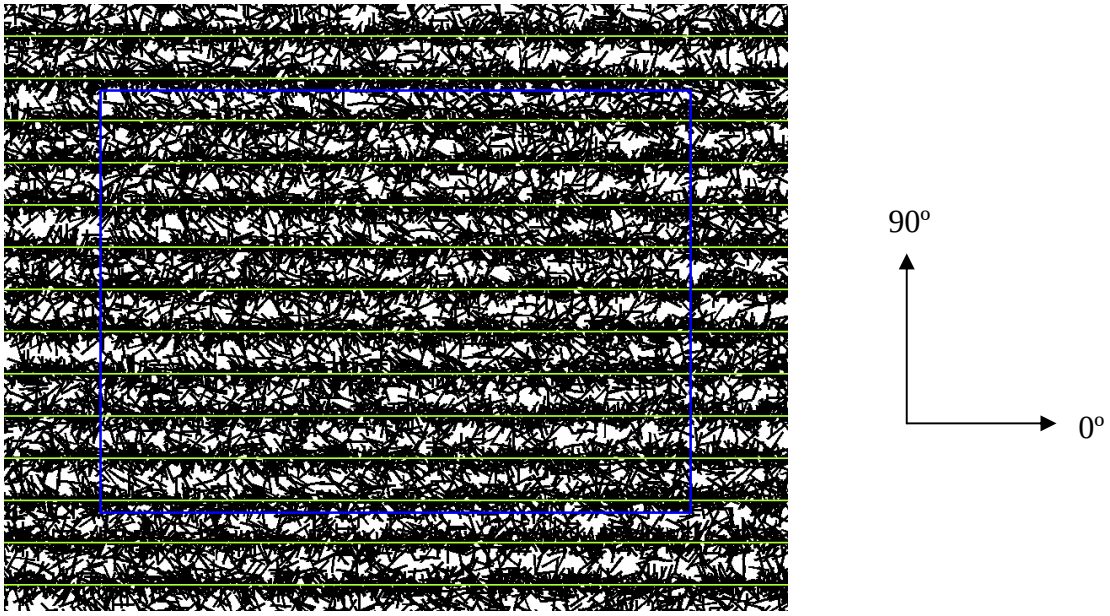


**Figure 2-32 Output from DFP process simulation for a low areal density of fibre (0.5kg/m$^2$). The horizontal lines represent the spray path centre line and the rectangle represents the 700×500mm preform area typically moulded via RTM.**

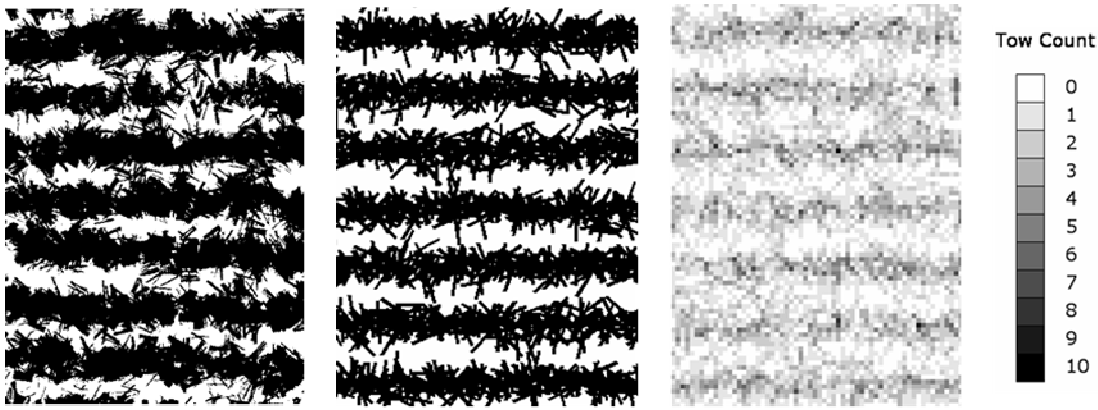


**Figure 2-33 (Left) Black and white photo of deposited fibres. (Centre) Black and white pixel representation of simulated tow deposition. (Right) 'X-ray' of deposited fibres showing how many tows are present in the third dimension**

The DCFP process simulation has been used to predict the effect of tow filament count and fibre length on the areal mass variation of 2D preforms. Figure 2-34 and Figure 2-35 demonstrate that both variables have a significant impact on the areal mass variation and consequently this can be expected to influence the variation in mechanical properties. High filament count tows are attractive from a cost perspective,

but Figure 2-34 demonstrates that a 100% increase (4% to 8%) in areal mass variation can be expected when the tow size increases from 6K to 48K. This physical effect was previously seen in Figure 2-4, where the sizes of the resin rich regions surrounding the tows tend to increase with increasing filament count. However, Figure 2-35 indicates that shorter fibres can be used as a partial solution to maintaining a low areal mass variation when processing higher filament counts, since greater levels of homogeneity can be achieved with shorter fibres. Further predictions from the process model are used in Chapter 3 to rationalise the experimental results for a study investigating the effect of key microstructural parameters on the mechanical performance of DCFP. Currently, no experimental tests have been conducted to validate these results.

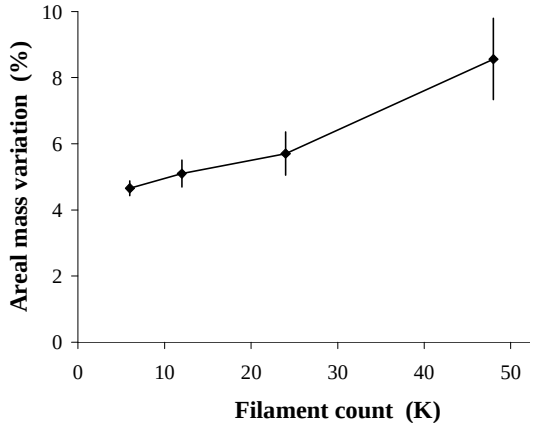


**Figure 2-34 The effect of increasing filament count on the areal mass variation across 2D preforms with 50mm long fibres. Five preforms were simulated by the process model for each filament count. The areal mass variation was calculated for each preform using the methodology outlined in Appendix.F.**

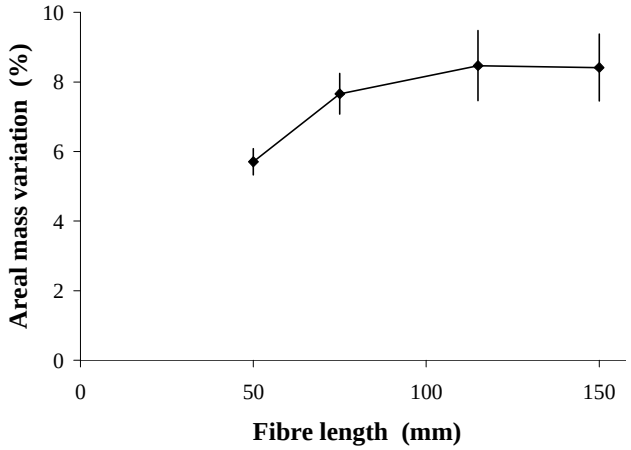


**Figure 2-35 The effect of increasing fibre length on the areal mass variation across 2D preforms with 24K tows. Five preforms were simulated by the process model for each fibre length. The areal mass variation was calculated for each preform using the methodology outlined in Appendix.F.**

## 2.5. Conclusions

The objective of this chapter was to overcome the current problems associated with the industrial DCFP process, in order to produce higher quality preforms by reducing the areal mass variation across the part. A number of problems were highlighted and a research-scale DCFP machine was commissioned at the University of Nottingham. The most significant development was a new chopping apparatus, which splits the original airmover functionality into three separate tasks. The new device permits independent control of filamentisation level, exhaust pressure and blockage prevention to minimise the disruption of previously deposited fibres.

An optimisation study was undertaken to establish the influence of a selection of machine parameters. Preform coverage and uniformity were studied by analysing greyscale images of low areal density preforms. The results indicated that a high tool-centre-point (300mm) and low robot speed (200mm/s) produced a more even coverage of fibre, (83% fibre coverage, compared with only 53% for a low TCP (100mm) and a higher robot speed (800mm/s)). A second study investigating the effect of fibre lay-down strategy has shown that spraying two orthogonal layers only marginally (~10%) improves the areal density variation across the plaque. However, processing a single 24K tow over two separate layers, rather than two tows over a single layer, improves the areal density variation by up to 30%.

A DCFP process model has been developed to predict the effects of material and process parameters on local areal density variation. The computational program provides quick and reliable simulations of 2D preforms and can be used to minimise the areal mass variation across the plaque. Initial results show that shorter fibre lengths can be used to compensate for the high areal mass variation encountered when processing high filament count tows. The areal mass variation can theoretically be reduced to approximately 5% when using 50mm long, 24K tows.

# Chapter 3. The effect of microstructural parameters on the in-plane properties of DCFP laminates

## *3.1. Introduction*

The fundamental objective of this chapter is to understand the influence of key microstructural parameters on the mechanical and physical properties of structural DCFP laminates. Results are presented for five key areas of research:

- Size and scale effects
- Effect of areal density variation
- Effect of fibre length
- Effect of tow filamentisation
- In-plane material characterisation

A review of size and scale literature is conducted in order to establish a representative coupon geometry for characterising the unconventional DCFP material. The process simulation (developed in Chapter 2) is used to establish the effects of fibre length and tow filament count on the homogeneity of the fibre orientation distribution and the homogeneity of local areal mass.

The process simulation tool is also used to improve local areal density variation caused by the nature of the fibre deposition process. Three important microstructural parameters are studied: filament count, fibre length and laminate thickness. Simulations are compared against tensile data to establish whether a correlation exists between areal density variation and mechanical performance.

Results from separate experimental studies are presented for the effect of filament count and fibre length, since these parameters are not mutually exclusive. The effect of reducing preform areal density is also investigated for applications that require thinner laminates, such as automotive ‘closures’ [45].

High repeatability, low cost and short cycle times are what make directed fibre preforming attractive for medium volume applications. It is essential that these attributes are retained during the transition from glass fibre to carbon fibre materials. The most significant study investigates the feasibility of using inexpensive, 24K carbon tows without detriment to the mechanical and physical properties. Filamentisation techniques developed in Chapter 2 are used to reduce the filament count, in order to overcome the associated difficulties of using large tows.

Finally, a full range of in-plane tests are conducted to characterise laminates with the optimum microstructural design. This data provides validation for analytical models presented in Chapter 4.

## *3.2. Size and scale effects*

### 3.2.1. Background

There is concern over the use of coupon test data for large component design because of fears that the failure strength of a small coupon bears little resemblance to component behaviour, due to the presence of size and scale effects [70, 71]. This section of the work aims to establish if these effects are applicable to DCFP, by investigating the effects of increasing specimen volume on the in-plane tensile properties.

The terms ‘size effect’ and ‘scale effect’ are often misconceived to be the same, but a clear distinction between the two terms is provided in a review by Sutherland [72]. A size effect is a discrepancy in properties which occurs when scaling from a model to a full size structure. This is thought to be due to the increased probability that larger structures contain more critical flaws, large enough to lead to failure. However, the observed effect for composites is often confounded by a scale effect, which occurs due to the scale of production [70, 73]. It is likely that a comparable specimen cut from a large structure will have been subjected to different manufacturing conditions. For example, larger structures may not experience the same level of compaction as a scaled model and hence inter-lamina voids form [71], or bundles may become damaged in

larger mouldings due to elevated injection pressures. This review is concerned with the effects of specimen size only, since subsequent analyses are for coupons manufactured under identical processing conditions.

### 3.2.2. DCFP mesostructure

It is commonly acknowledged that composites containing bundles possess a meso-type structure [74-79]. Filaments tend to remain in bundle form when tows or roving are chopped. The filaments are aligned within the bundle with coplanar ends and this synchronisation causes large stress concentrations to develop, which results in a loss in strength [76]. Bundled filaments therefore behave completely different in comparison to the same volume of evenly dispersed fibres. Many studies have shown that bundled filaments are analogous to large single fibres, whereby if the length is below the critical threshold the bundle will pull out from the matrix material as a single unit [80, 81], or will fracture at longer lengths. The structure of the material is therefore categorised somewhere between the individual filament scale (microscopic) and the laminate level (macroscopic) [78]. A meso-scale reinforcement can cause increased variation in local volume fraction [74], particularly when the fibres are discontinuous and randomly orientated. This causes high scatter in the mechanical properties and increases the heterogeneity of the material, making it increasingly difficult to determine representative values for volume-averaged properties such as stiffness. There is concern therefore, that coupon data from DCFP laminates will provide a conservative estimate for the mechanical properties of a full scale structure.

### 3.2.3. Stiffness – Effect of RVE size

Stiffness is commonly perceived to be independent of any potential size effects since it is a volume averaged property. In order to determine the magnitude of stiffness size effects, it is important to ensure that specimen dimensions encompass the representative volume element (RVE). Determining the RVE for aligned fibres or woven fabrics is relatively straightforward because there is an obvious repeating pattern, but the task is more involved for random fibre composites, particularly those with a mesoscale architecture. The RVE is well defined when stiffness converges with

respect to increasing specimen volume. Therefore, strength related size effects can only be studied with confidence for volumes larger than the RVE, to ensure complete macroscopic homogeneity.

Some authors [82, 83] have developed mathematical models for determining suitable RVE sizes for random composite materials. A spring network model for needle inclusions is solved in [82] under both constant displacement and constant stress boundary conditions. The RVE is well defined when the Dirichlet (uniform displacement) response is the same as the Neumann (uniform stress) response [84]. The model is applied only to a dilute suspension (<2% $V_f$) of soft inclusions ($E_f<E_m$) and shows that the RVE size increases with increasing fibre length and decreasing fibre stiffness. No experimental validation is presented, but values from the spring network model are within ±5% of a finite element (FE) calculation.

Kanit *et al.* [85] demonstrate that the RVE size is specific to the physical property in question, for example thermal properties are shown to have a different RVE to elastic properties. They propose that specimen volumes smaller than the RVE can be used to determine representative properties, providing sufficient test repeats are executed. The relative error (absolute error/mean) on the mean value obtained with $n$ realisations of volume $V$ can be calculated as follows:

$$\varepsilon_{rela} = \frac{\varepsilon_{abs}}{Z} = \frac{2D_Z(V)}{Z\sqrt{n}} \qquad \textbf{Equation 3-1}$$

where $Z$ is the apparent mean value of the physical property and $D_Z(V)$ is the standard deviation of the property for a specimen volume of $V$. Equation 3-1 can be rearranged to predict the minimum number of realisations that must be considered for a given volume size, in order to estimate the effective property for a given precision:

$$n = \frac{4{D_Z}^2(V)}{Z^2{\varepsilon_{rela}}^2} \qquad \textbf{Equation 3-2}$$

The authors also provide a quantitative definition of RVE size, expressed as a function of five parameters, namely; the physical property in question, fibre volume fraction, contrast of properties (e.g. $E_f/E_m$), the number of realisations (number of test repeats or model simulations) and the relative precision required. More recently Ionita and Weitsman [86, 87] have determined the RVE size for DCFP laminates using a moving window technique in order to calculate the departure from isotropy and homogeneity. Fibre bundles were assumed to be uniformly distributed at random orientations and therefore processing influences such as the robot path offset were overlooked. For laminates made with 25mm and 50mm long carbon fibre bundles the RVE was predicted to be 127mm and 152mm respectively, which is considered to be of structural size. For a fibre length of 50.8mm, the mean stiffness appears to be only 1.3% lower for a gauge width of 25mm compared with a width of 152mm. However, the scatter is 3 times higher at 25mm than at 152mm. This supports the statement by Kanit *et al.* [85], that narrow specimens are representative fro stiffness, providing sufficient samples are tested to improve confidence. The rate of convergence (i.e. RVE size) and the degree of scatter in the results is strongly dependent on the laminate thickness, where thicker specimens have a smaller RVE. The same trend is anticipated for fibre volume fraction because the RVE size appears to be dependent on the number of fibre-fibre contacts or fibre crossovers per unit area (as shown in Section 3.2.8). If the fibre orientation is purely random, an increase in fibre crossovers increases homogeneity and therefore stiffness tends towards being independent of any size effects.

### 3.2.4. Weibull theory

The most well-known statistical consideration of strength is the weakest link theory proposed by Weibull [88]. Weibull showed that this model could be applied to many brittle materials, based on the analogy that the structure of the material is constructed from small elements linked in series. Failure of the material occurs when any one of these links fails when subjected to a stress $\sigma$. Hence, the probability of failure of $n$ elements can be expressed as a two parameter distribution:

$$F_n(\sigma) = 1 - \exp\left[ -n\left( \frac{\sigma}{\sigma_0} \right)^m \right]$$ **Equation 3-3**

$\sigma_o$ and $m$ are the Weibull scale parameter and shape parameter (Weibull modulus) respectively. The scale parameter is a reference value for a unit volume of material and the shape parameter is a measure of material variability, where low values of $m$ correspond to high variability. ($m$ is typically 5-20 for ceramics, 5-30 for composites and >30 for metals.)

Equation 3-3 is often expressed in terms of specimen volume, $V$ in order to determine if the material does follow a Weibull distribution:

$$F_V(\sigma) = 1 - \exp\left[ -V\left( \frac{\sigma}{\sigma_0} \right)^m \right]$$ **Equation 3-4**

It is convenient to rearrange Equation 3-4 in order to describe experimental data. Rearranging and taking logarithms twice gives;

$$\ln\left[ \ln\left( \frac{1}{1 - F_V(\sigma)} \right) \right] = m\ln(\sigma) - m\ln(\sigma_0) + \ln(V)$$ **Equation 3-5**

If the experimental data does follow a Weibull distribution then a logarithmic plot of $\ln(\sigma)$ versus the left hand side of Equation 3-5 will yield a linear relationship. The Weibull modulus ($m$) and the scale parameter ($\sigma_0$) can be determined from the gradient of the line and the y-axis intercept respectively. It is then possible to correlate the strengths of specimens of different sizes based on the Weibull modulus alone. For two specimen volumes, $V_1$ and $V_2$, subjected to constant stresses, $\sigma_1$ and $\sigma_2$, the magnitude of the size effect can be determined by assuming an equal probability of survival in each:

$$\frac{\sigma_2}{\sigma_1} = \left( \frac{V_1}{V_2} \right)^{\frac{1}{m}}$$ **Equation 3-6**

Equation 3-6 directly links strength to specimen size. It is important to note that the Weibull modulus and failure mechanism must remain constant over the entire volume range for the theory to be valid. Harlow and Phoenix [89] have shown that this is true, even when the volume varies by orders of magnitude.

Weibull theory is well established for isotropic, brittle materials such as ceramics [70], but it is questionable whether the theory holds for fibre reinforced composites. There is evidence [73] to suggest that size effects are present in composites and at multiple levels. Here the filament, bundle and laminate levels are considered in turn.

### 3.2.5. Size effects – Filament level (microscopic)

A composite has defects according to its microstructure which can cause local weakness. Heterogeneities result from fibre packing, fibre clustering, resin rich regions, voids, broken fibres and misalignment. The microstructure of the composite governs the magnitude of the defect which can lead to component failure [71]. Two of the most common microstructural defects result from flaws in the matrix and fibres. A 53% reduction in strength was reported in [90] when the gauge volume of epoxy resin specimens was increased, because of a 50% increase in defect size (determined by SEM). Many studies have also shown that strength decreases with increasing length for brittle fibres [72, 73, 91-93]. This reported size effect is well documented for carbon fibres since they are almost completely brittle and show 100% elastic recovery below the fracture strength [94]. Moreton [95] showed the strength of a range of carbon fibres to be 30% higher for 5mm fibre lengths than for 50mm lengths. The various strengths of the 5mm fibres were used to predict the strengths at 50mm and 100mm using a Weibull distribution. Predicted values were 6-17% lower than the experimental values because the strength of the 5mm reference sample was considered to be lower than the true value because of potential misalignment in the test fixture and stress concentrations at the grips. Authors [92, 96] have subsequently modified the basic theory to improve strength predictions. A common extension is used in [97] to predict the strength of discontinuous fibre composites and in [91, 93] to investigate the effect

of tensile gauge length for continuous fabrics. Originally formulated by Coleman [96], the mean fibre strength, $\bar{\sigma}_f$ for a length, $l_f$ is given by the following gamma function:

$$\bar{\sigma}_f = \left(l_f \sigma_0\right)^{-\frac{1}{m}} \Gamma\left(1+\frac{1}{m}\right) \qquad \textbf{Equation 3-7}$$

Van Hattum [97] used Equation 3-7 to predict the strengths of fibres ranging from 5mm to 80mm. Experimental validation was within a 95% confidence limit of the predicted strengths. The strength of 80mm carbon fibres was shown to be 40% lower than the strength of 5mm fibres. Typical values of the Weibull modulus, *m*, are reported to be approximately 20 for carbon filaments [98, 99].

### 3.2.6. Size effects – Bundle level (mesoscopic)

Bader and Priest [100] reported that the mean strength of 1K carbon tows was reduced by 10% when the gauge length was increased from 20mm to 300mm. Weibull theory can equally be applied at the bundle level, based on the assumption that fibre failure strength reduces with increasing length, following a similar gamma function to Equation 3-7. Coleman [96] showed that theoretically the strength of a bundle (containing *N* filaments) is of the same order of magnitude, but is 50-65% less than the mean strength of the constituent filaments of the same length due to size effects. Some authors have developed a more comprehensive model to account for the increase in filament count. Weibull theory assumes that failure is sudden and therefore component failure coincides with failure of the weakest link. Although most composite failures occur at low strains, final failure usually occurs after some damage accumulation. Zweben and Rosen [101] developed the *modified weakest link* theory to model the progressive failure of fibre reinforced composites, where individual fibres in the bundle represent the links in the chain. Load is redistributed to adjacent fibres when a single fibre fails, by shear transfer through the matrix, therefore the bundle as a whole does not fail. Bundle strength is therefore a function of both length and filament count.

According to a review by Sutherland [72], the improved accuracy of the modified model [101] over the original weakest link theory [88] is insignificant, compared to the

inherent errors associated with estimating parameters such as the fibre ineffective length (the length at the fibre ends where a lower tensile stress is maintained [102], see Chapter 5). Harlow and Phoenix [89] derived the *chain-of-bundles model* based on the modified weakest link and in more recent work [103], have developed a more comprehensive network failure model to account for statistical variation in bundle strength. A major drawback with this model is that some of the parameters have no clear connection to the material microstructure. Element strengths are expressed in terms of failure probability on a scale of $\alpha=0$ (high strength) to $\alpha=1$ (low strength). No experimental validation is presented, but simulations show that the strength of the bundle can increase with increasing filament count if the strength of the fibres is low ($\alpha=0.99$). For higher fibre strengths the relationship follows the characteristic Weibull curve.

### 3.2.7. Size effects – Laminate level (macroscopic)

Zweben [73] presents sufficient evidence to suggest that size effects do exist at the laminate level, reporting the strength of a 100 ply unidirectional (UD) laminate to be 15% lower than a 25 ply laminate in both tension and compression [73]. Crowther and Starkey [104] demonstrate that increasing specimen volume reduces the fatigue life of composite laminates and that this size effect can be predicted by fitting a Weibull distribution. Hwang *et al.* [98] has shown that size effects exist at the fibre level, laminate level and component level for large scale pressure vessels. The investigation of size effects at the laminate level are probably the most significant because experimental data is often directly scaled for large component design. However, it is at this level where the most uncertainty lies. Hitchon and Philips [70] demonstrated that Weibull theory is adequate for predicting differences in strength when volume varies due to changes in length in the reinforcement direction, but not when volume varies due to changes in cross sectional area.

Potential size effects at the laminate level can often be confounded by experimental and statistical error. Marissen and Linsen [105] investigated the variability of the flexural strength of SMCs and found that wider specimens exhibited higher strength and lower variability. This positive effect may be attributable to the size of the specimen relative

to the size of potential defects, since the tested volume is smaller than the RVE. Pan *et al.* [93] examined the existence of size effects at different structural levels (filament, bundle, fabric) and found that both the filament and bundle levels follow Weibull strength distributions, but not the fabric level. An initial increase in fabric strengths between specimen lengths of 10mm and 20mm suggests that the gauge length is smaller than the RVE at the fabric level, especially since the tensile stiffness is also inconsistent at these tested lengths. The shorter specimens may have also been influenced by the stress concentrations due to the gripping arrangement. The geometry of test coupons should therefore be designed with the size of critical defects and the repeated unit cell in mind [71]. For materials such as DCFP this may result in specimens much larger than conventional test geometry to account for characteristic dimensions. However, in some instances the RVE size of the material may be larger than the structural features of the component. This would result in higher levels of variation between finished parts and therefore less confidence in the material.

It is widely acknowledged that the magnitude of the observed size effect depends on the test type. Flexural tests are commonly used for screening purposes and to approximate tensile data because of their relative efficiency. Whilst flexural and tensile moduli are usually similar, flexural strengths are often higher than tensile strengths because of the associated size effects. Flexural tests subject a smaller volume of material to the maximum stress (three-point-bend testing being worse than four-point), resulting in over optimistic strength values compared with pure tension. Theoretically, this can be explained using Weibull theory, since the failure strength is inversely proportional to the stressed volume [99]:

$$\frac{\sigma_{3PB}}{\sigma_T} = \left[ 2(m+1)^2 \frac{V_T}{V_{3PB}} \right]^{1/m} \qquad \textbf{Equation 3-8}$$

Subscripts *3PB* and *T* refer to 3-point-bending and tension respectively. Bullock [99] was able to predict the tensile strength for two carbon/epoxy laminates using experimental three-point-bend data and Equation 3-8 to within ±5% of the true values. However, the stress field through the thickness of flexural specimens is non constant and it is questionable whether the observed effects are size related or in fact, due to the

stress gradient. By investigating the effect of different processing routes, Hitchon and Philips [70] found evidence to suggest that the bend specimens failed prematurely in compression or shear rather than in pure tension, hence lower strength values were predicted for the tensile failure when using Weibull theory.

Holmberg [106] developed the Weibull model to predict the strength of random composites subjected to biaxial loads. The laminate is modelled as UD, quasi-isotropic plies in order to predict material properties. These properties are subsequently used in an FE calculation to determine the stress field in a biaxial bending test. The basis for the model is the observation that fibre bundles dominate the tensile failure and the strength of the bundles can be determined by Weibull theory. Predictions are within ±10% of the experimental values and are considered 'reasonable' for predicting random composite strength. But the assumption that there is no local load sharing because bundles are too far apart is only valid for low volume fractions and therefore the accuracy of the model is expected to reduce as $V_f$ increases.

## 3.2.8. Analytical investigation into the effect of specimen size

### *3.2.8.1. Homogeneity of fibre orientation distribution*

The DCFP process simulation (developed in Chapter 2) is utilised here to investigate scatter and size effects for laminates containing random bundles. The number of tows $N$ in a volume of composite $abc$ can be evaluated as;

$$N = \frac{abcV_f}{A_{tow} l_f} \qquad \textbf{Equation 3-9}$$

where $V_f$ is the volume fraction of tows within the prescribed volume $abc$, $A_{tow}$ is the tow cross sectional area (calculated in Section 5.4.2) and $l_f$ is the tow length.

According to Equation 3-9, shorter bundles (decreasing $l_f$) or thicker laminates (increasing $c$) give higher numbers of tows per specimen and hence an improved homogeneity for a given filament count. The extent of the orientation inhomogeneity has been evaluated by the DCFP process simulation. Tows are deposited at constant

time steps along a robot tool path and fibre orientations are determined by computing random numbers between 0 and π radians. The orientation of *N* tows (calculated by Equation 3-9) containing 24K filaments were analysed within a constant volume to create a discrete frequency distribution (i.e. 180 classes of 1° width) shown in Figure 3-1. The coefficient of variation (COV) (standard deviation of frequencies over the average frequency) was used as a measure of randomness, where COV→0 denotes a uniform random distribution. The chop length varied from 3mm to 115mm to encompass the current DCFP processing capability and the analysis volume was equivalent to the tensile specimen geometry between the fixture jaws (200×25×3mm). Each of the *N* bundles was positioned randomly to ensure that at least one of the bundle ends was contained within the specified volume.

The COV for 100 random runs is presented in Table 3-1 for each fibre length. The trend follows a power law relationship where shorter fibres tend to have smaller variations across the orientation distribution and hence improved homogeneity. This implies that shorter lengths are more likely to exhibit a uniform, random orientation distribution than longer fibres for this particular volume of material. The COV is reduced by 83% when the fibre length is reduced from 115mm to 3mm. Significant variation in mechanical properties can be expected for longer fibres, purely on the basis of angle inhomogeneity.

| **Fibre length (mm)** | **3** | **6** | **14** | **23** | **29** | **38** | **58** | **115** |
|---|---|---|---|---|---|---|---|---|
| Number of bundles | 3248 | 1624 | 696 | 423 | 336 | 256 | 168 | 84 |
| Average angular COV (%) | 23.5 | 32.2 | 50.7 | 64.8 | 73.3 | 84.3 | 102.7 | 146.5 |

**Table 3-1 The effect of fibre length on the coefficient of variation (COV) for fibre orientation. The COV was determined from 100 runs of a DCFP process simulation. The number of 24K bundles expected in a tensile specimen (200×25×3mm) was calculated using Equation 3-9.**

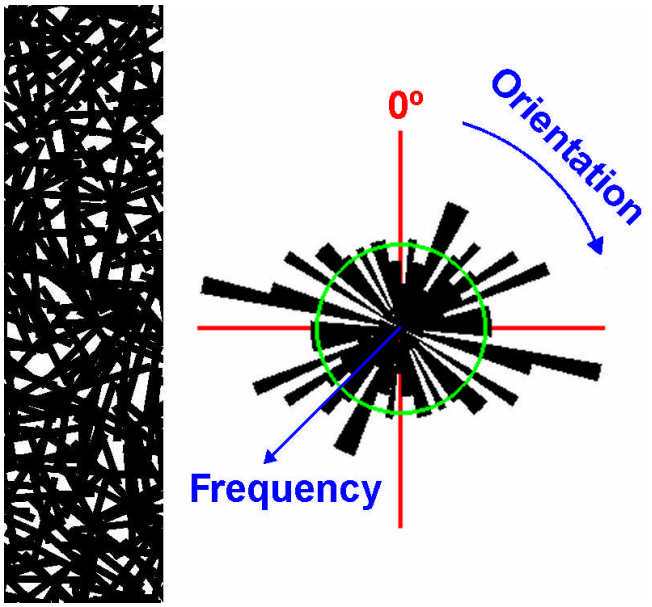


**Figure 3-1 (Left) Screen shot from DCFP process simulation used to study fibre orientation homogeneity. Image shows only a third of the required deposited fibres used in the study, in order to provide sufficient contrast. Analysis area was 200×25mm for an areal density of 1.5kg/m$^2$. (Right) Radial histogram plotted to assess fibre orientation. The DCFP simulation generates random orientations between 0 and π radians and therefore the histogram has rotational symmetry (order 2). The circle represents the average frequency of all classes and is used in the COV calculation.**

### *3.2.8.2. Homogeneity of areal density*

The number of fibre-fibre crossovers per unit length is indicative of the coverage or areal density variation within a preform [107], which consequently influences the ultimate failure strength. Fibre contact areas are potential sites for inter-fibre bonding, and the degree of bonding influences the load distribution along the fibres [108]. A photo-elastic study [109] confirms that load sharing occurs at fibre crossover points, such that the probability of fracture is reduced through localised strengthening [107]. Pan [110] presents a modified analysis of the Komori and Makishima [111] model to estimate the number of fibre to fibre crossovers. This method has recently been used to estimate the RVE size for a 3D random material [112]. The model is applied here to a random 2D network of fibres (with a thickness equal to two bundle diameters). The mean number of crossovers per unit fibre length is given by;

$$X = \frac{16\pi V_f}{\emptyset_{tow}\left(\pi^3 + 16AV_f\right)} \qquad \textbf{Equation 3-10}$$

Where $V_f$ is the volume fraction of the composite and $A$ is a geometric constant based on the fibre dimensions as follows;

$$A = \ln\left[\cot\left(\frac{\arcsin\left(\frac{\varnothing_{tow}}{l_f}\right)}{2}\right)\right]$$

**Equation 3-11**

$\varnothing_{tow}$ denotes the equivalent tow diameter assuming a circular profile, calculated using the tow perimeter method outlined in Section 5.4.2.

Table 3-2 shows the number of fibre-fibre crossovers for estimated mean bundle sizes for given fibre lengths. The results indicate that coverage (number of fibre-to-fibre crossovers per unit length) is significantly affected by filamentisation and by fibre length. Coverage is approximately three times better for highly filamentised fibres than for non-filamentised fibres, based on the number of fibre-fibre crossovers, at fibre lengths up to 29mm. Results from Sections 3.2.8.1 and 3.2.8.2 suggest that laminate thickness will be a critical factor in determining final part properties. The number of bundles within a laminate increases as the laminate thickness increases for a constant fibre volume fraction. This results in more fibre-fibre contacts and an increase in local reinforcement at the crossover point through load sharing. Thicker laminates will therefore tend to give full realisation of properties and thinner parts will have lower strength and greater variability.

| Fibre length (mm) | Induced Filamentisation | Mean bundle size (number of filaments) | Bundles per cm$^3$ | COV angle (%) | Fibre-fibre crossovers per unit length |
|---|---|---|---|---|---|
| 3 | Yes | 24 | 203356 | 7.4 | 8078 |
| 6 | Yes | 109 | 22387 | 8.9 | 3791 |
| 14 | Yes | 551 | 1968 | 30.4 | 1686 |
| 23 | Yes | 1411 | 480 | 59.2 | 1053 |
| 29 | Yes | 2205 | 245 | 87.0 | 843 |
| 58 | Yes | 8820 | 30 | 246.1 | 421 |
| 115 | Yes | 24000 | 5 | 615.6 | 250 |
| 3 | No | 338 | 14439 | 10.8 | 2534 |
| 6 | No | 1527 | 1598 | 33.3 | 1192 |
| 14 | No | 7752 | 139 | 113.8 | 529 |
| 23 | No | 19845 | 34 | 228.9 | 331 |
| 29 | No | 24000 | 22 | 292.5 | 296 |
| 115 | No | 24000 | 5 | 615.6 | 250 |

**Table 3-2 Mean bundle sizes and angle variation for varying chop lengths and levels of filamentisation. The level of filamentisation is reflected in the mean filament count, estimated using the method outlined in Appendix H.6. A composite volume fraction of 30% and a tow volume fraction of 60% are assumed.**

### 3.2.9. Experimental investigation into the effect of specimen size

The effect of specimen geometry has been investigated using a series of tensile tests for specimens of increasing width. Whilst thickness is a potential parameter, it is directly influenced by the areal density of fibre (for a constant volume fraction) and this will be the subject of further discussion in Section 3.3.

Three DCFP plaques were produced consecutively under identical conditions to minimise inter-plaque variation. Preforms were produced using 6K HTA fibre to ensure a consistent bundle size when chopped. A fibre length of 25mm and an areal density of 2.25kg/m$^2$ were chosen. Plaques were subsequently moulded using DLS1648 epoxy resin in a 4mm cavity ($V_f$=30%) and specimens were water-jet cut at random positions and orientations over the plaque to minimise systematic errors. Specimen widths ($w$) were chosen to be 10, 15, 20, 25, 30 and 40mm (Table 3-3) in order to bridge the fibre length. Figure 3-2 demonstrates that the UTS appears to be independent of the

specimen width at this fibre length. There is only 5% variation between the maximum ($w$=30mm) and minimum ($w$=20mm) mean strengths and the regression analysis shows that the gradient of the best fit line is approaching zero. The relative error has been calculated using Equation 3-1 and is presented in the form of vertical bars in Figure 3-2. Table 3-3 shows that the maximum relative error is 9% and the magnitude of the error is approximately uniform at each width (Figure 3-2). This level of confidence suggests that sufficient specimens were tested and that the trend is representative.

Figure 3-3 shows the effect of increasing specimen width on tensile modulus. There is an initial reduction in modulus between 10 and 20mm, after which there appears to be a plateau for increasing widths. This trend can be attributed to the RVE size for this material. The plateau begins at a gauge width close to the fibre length, which suggests the RVE is of the same order of magnitude as the fibre length. The relative error is higher in most cases for the stiffness compared with the strength. Table 3-3 shows that the 15mm and 30mm wide specimens have two of the highest relative errors. These widths were not initially included in the experimental design and therefore only 4-5 repeats were possible. Equation 3-2 indicates that up to 16 specimens are required in order to reduce the relative error to 10%.

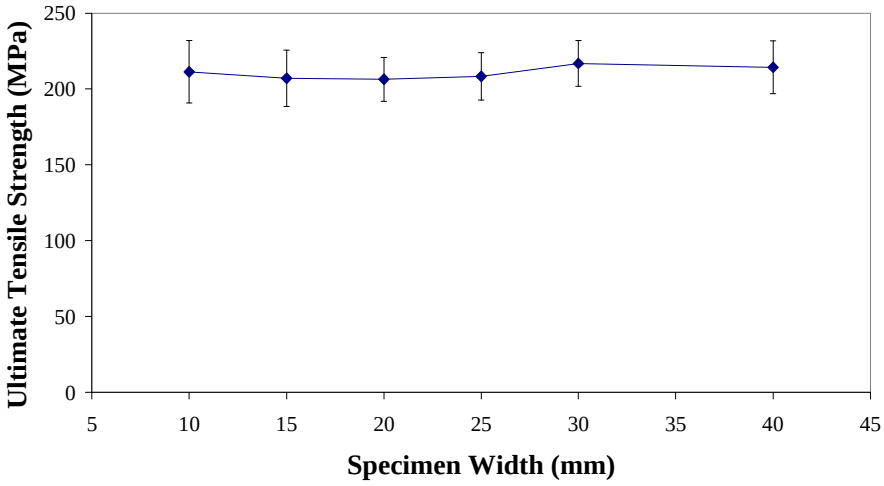


**Figure 3-2 Effect of increasing specimen width on the UTS for a DCFP laminate. Equation shown is the result of a linear regression analysis. Vertical bars represent the relative error from Equation 3-1.**

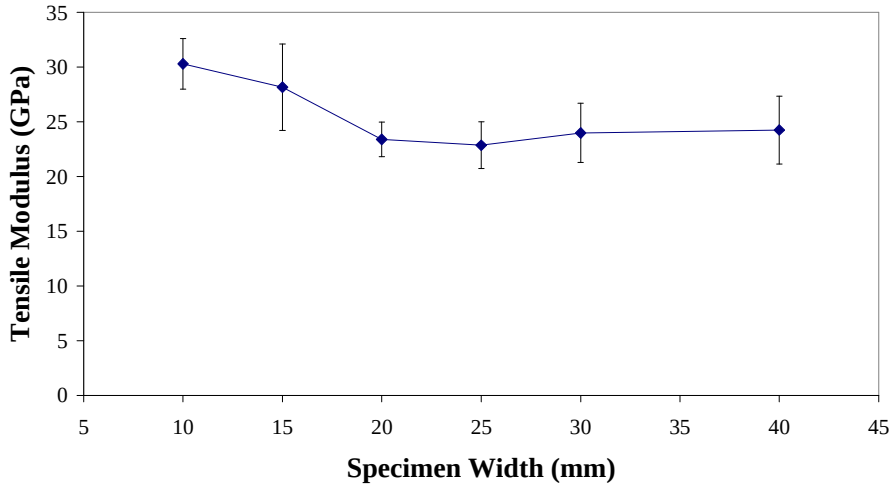


**Figure 3-3 Effect of increasing specimen width on the tensile modulus of DCFP laminates. Vertical bars represent the relative error calculated from Equation 3-1.**

| Width (mm) | # Specimens | Modulus (GPa) | St Dev (GPa) | Rel Error (%) | n | UTS (MPa) | St Dev (MPa) | Rel Error (%) | n |
|---|---|---|---|---|---|---|---|---|---|
| 10 | 12 | 30.3 | 4.02 | 7.7 | 7 | 211.3 | 35.57 | 9.719 | 11 |
| 15 | 4 | 28.2 | 3.96 | 14.1 | 8 | 207.0 | 18.57 | 8.970 | 3 |
| 20 | 10 | 23.4 | 2.49 | 6.7 | 5 | 206.3 | 22.75 | 6.973 | 5 |
| 25 | 10 | 22.9 | 3.37 | 9.3 | 9 | 208.3 | 24.63 | 7.481 | 6 |
| 30 | 5 | 24.0 | 3.01 | 11.2 | 6 | 216.9 | 16.92 | 6.977 | 2 |
| 40 | 10 | 24.2 | 4.92 | 12.8 | 16 | 214.3 | 27.59 | 8.141 | 7 |

**Table 3-3 Experimental results for unit width study. Number of specimens tested is indicated for each respective width. The relative error shown is calculated from Equation 3-1 and the value n indicates the number of specimens required to achieve a relative error of 5%, calculated from Equation 3-2.**

### 3.2.10. Conclusions

There is sufficient evidence to suggest that size effects are present at the microscopic, mesoscopic and macroscopic levels for fibre reinforced composites. Statistical Weibull theory is the most widely used model to determine the effects of increasing specimen volume on the failure strength of the system. Weibull provides reasonable predictions at the micro to meso scales but limited accuracy is shown at the macro level due to complex failure modes and idealistic assumptions relating to fibre arrangement, load sharing and geometrical parameters. Extensions to Weibull theory have been made to account for more progressive failures, but the increased complexity yields minor

improvement in accuracy. There are also errors inherent in determining parameters such as the filament ineffective length after fracture. These theories are less than clear for fibre reinforced composites and the results are often contradictory.

In this work, an experimental study has shown that specimen width has an insignificant effect on the tensile strength of DCFP laminates. The tensile modulus is constant when the gauge width is greater than the fibre length, but is seen to increase for gauge widths less than the fibre length. This suggests that the RVE should encompass at least one fibre length, in order to determine representative values for design purposes. With fibre lengths ranging from 3-115mm, it is neither practical nor feasible to test large DCFP specimens, since current test equipment is restricted to a specimen width of 50mm.

The RVE size is also strongly dependent on the specimen thickness relative to the dimensions of the fibre reinforcement. Analytical calculations have been used to investigate the effect of reinforcement geometry on the consistency of areal density and fibre orientation distribution. Increasing the number of fibre-fibre contacts per unit volume prevents unreinforced areas from occurring and increases homogeneity. The RVE size is therefore much smaller if the laminate contains single filaments rather than the equivalent volume of bundles, the $V_f$ is high or the laminate is much thicker than the reinforcement phase.

A recent model applied to DCFP shows that the RVE is proportional to the fibre length, but is inversely proportional to specimen thickness. Representative properties can be determined by using a conventional testing geometry, providing specimens are thick relative to the mesoscale dimensions and sufficient test repeats are conducted. The number of coupons required to give a specified level of confidence can be calculated analytically. Standard tensile geometry has been adopted for all subsequent testing using a thickness of 3mm and a fibre volume fraction of 30%. Up to 60 specimen repeats were performed for each scenario, which is significantly more than the 3-5 recommended by the testing standard. In each case, statistical significance is provided to support the observed trends.

## *3.3. Effect of areal density variation (Fibre coverage)*

### 3.3.1. Background

This section aims to quantify the influence of microstructural parameters on the mechanical and physical properties of DCFP composites in order to establish whether a correlation exists between local areal density variation and mechanical performance.

The principal goal for process optimisation involves minimising errors associated with uniformity of carbon coverage and improving preform consistency. Local variation in areal density yields inconsistent volume fractions across the laminate and in turn, variation in mechanical properties. The aspect ratio of larger tows makes it increasingly difficult to achieve uniform coverage for thin laminates, because of the highly concentrated filament regions and contrasting resin rich areas (illustrated by Figure 3-4).

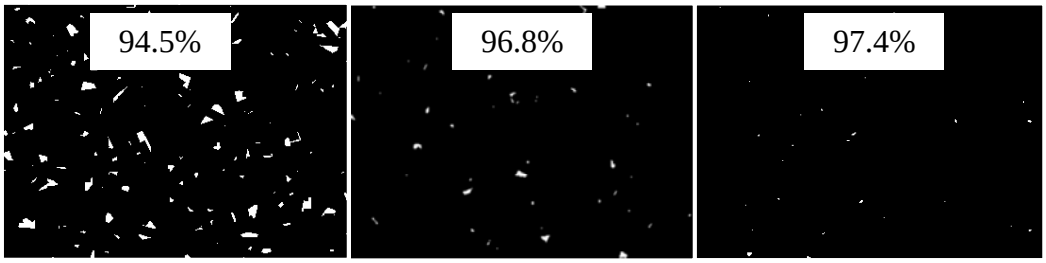


**Figure 3-4 Three plan view images show the coverage issues associated with using larger tow sizes for thin components. Each image represents a 350mm×250mm section from a simulated 2D preform. Tow length is a constant 50mm in each image but tow size decreases from left to right (48K, 24K & 12K). The same mass of fibre is sprayed in each image but clearly smaller bundles give a more uniform coverage (percentage coverage values displayed).**

Areal density variation is generally mapped by manually cutting and weighing contiguous coupons from the preform, or, as in [69], by measuring light transmission through the preform using image analysis software. In the present work, the process simulation outlined in Chapter 2 is used to predict the effects of material and process parameters on local areal density variation. The predicted areal mass variation values are validated against limited experimental data and the results are then compared against tensile properties to establish whether a trend exists.

### 3.3.2. Independent variables

A Taguchi orthogonal array was adopted to investigate the effect of fibre length; filament count and global areal density (laminate thickness) on the local density variation using a statistical process model. Five repeat preforms were simulated for each scenario outlined in Table 3-4. Minitab® v.14 was used to analyse the Taguchi array by performing a general linear analysis of variance (ANOVA) to determine the significance of each variable.

| Permutation | Fibre Length (mm) | Target Areal Density ($kg/m^2$) | Filament Count (K) | Areal Density Variation (%) | COV (%) |
|---|---|---|---|---|---|
| 1 | 25 | 0.75 | 6 | 9.14 | 4.40 |
| 2 | 25 | 1.5 | 12 | 9.57 | 7.39 |
| 3 | 25 | 2.25 | 24 | 11.65 | 3.29 |
| 4 | 50 | 0.75 | 12 | 14.59 | 13.06 |
| 5 | 50 | 1.5 | 24 | 13.40 | 6.14 |
| 6 | 50 | 2.25 | 6 | 7.02 | 9.38 |
| 7 | 75 | 0.75 | 24 | 20.07 | 3.76 |
| 8 | 75 | 1.5 | 6 | 7.15 | 15.65 |
| 9 | 75 | 2.25 | 12 | 8.56 | 8.89 |

**Table 3-4 Permutations used in a Taguchi design to model the effect of three parameters on the local areal density variation using a process simulation**

A full factorial experimental design was subsequently adopted to investigate the same three independent variables to determine tensile modulus and tensile strength. Fibre lengths of 25mm, 50mm and 75mm were chosen to span the practical operating range for the chopping apparatus. Tows with filament counts of 6K, 12K and 24K were used. The global areal density was tested at $0.75kg/m^2$, $1.5\ kg/m^2$ and $2.25\ kg/m^2$, representing part thicknesses of 1.5mm, 3mm and 4mm respectively at a nominal fibre volume fraction of 30%. Three fibre grades and two surface treatments were considered (see Table 3-5, values taken from Appendix B.2).

| Filament Count (K) | Grade | Surface treatment |
|---|---|---|
| 6 | HTA | Epoxy |
| 12 | HTS | Polyurethane |
| 24 | STS | Polyurethane |

**Table 3-5 Tow selection for fibre coverage study. The lowest cost option was chosen from the Toho Tenax GmbH range for each filament count.**

### 3.3.3. Experimental methodology

Carbon fibre preforms were manufactured at the National Composites Center (NCC), USA on a bespoke DFP machine optimised for glass roving [53-56]. Fibres were processed using an Aplicator Systems AB chopper gun mounted on a six axis robot. During deposition, a total filament count of 48K was processed simultaneously (i.e. 2×24K, 4×12K or 8×6K). The preform tool was flat and measured 700mm × 700mm. The linear speed of the chopper gun was 100mm/s and the linear distance between passes was 60mm. The second layer was offset from the first by 30mm to create an effective sweep offset of 30mm. 5 wt% epoxy powder binder (Reichhold Pretex 110) was used in each case. The preforms were trimmed to 700mm × 500mm for moulding. Circular samples of Ø25mm were stamped at 25mm centres from the trimmed surplus of some preforms and weighed to an accuracy of ±10μg, in order to establish areal density variation.

All plaques were processed by resin transfer moulding (RTM) using DLS1648 (see Appendix.B and Appendix.C for details of materials and processing methods used). Picture frames were used to vary cavity depths (1.5mm, 3mm and 4mm) and thereby areal density (0.75, 1.5, 2.25 kg/m$^2$), while holding fibre volume fractions reasonably uniform at around 30% (27.6%, 27.6% and 31.1% respectively). Twenty seven plaques were produced for the designed experiments and a further eight were produced to study inter-plaque variability. Tensile specimens were cut at both 0º and 90º orientations to study levels of orthotropy, following the method outlined in Appendix D.1.2. All results were normalised linearly with respect to fibre volume fraction prior to analysis at a level of 27.6%. The difference due to scaling was small. The properties of nine

plaques were reduced by 11%, which was within the average of their coefficient of variations (11% and 15% for stiffness and strength respectively).

### 3.3.4. Results

#### *3.3.4.1. Areal density variation*

Each simulation was discretised into 25mm×25mm squares over the entire 700mm×500mm preform area, and the areal density variation was calculated by averaging the number of tow intersections at the grid points within each square (see Appendix.F). The standard deviation of all the squares gives the global areal density variation. This was compared to the variation seen in contiguous coupons cut from experimental preforms. For a 50mm long, 24K tow and areal density of 1.5kg/m$^2$, the predicted 5.6% is in good agreement with the experimental value of 6.0%.

The main effects plot from the simulation is shown in Figure 3-5. Each of the three variables is shown in isolation – increasing fibre length from 25mm to 75mm will increase areal density variation from 10% to 12%; increasing filament count from 6K to 24K increases areal density variation from 8% to 15%, and increasing the target areal density from 0.75kg/m$^2$ to 2.25 kg/m$^2$ decreases density variation from 15% to 9%. Probability-value (P-value) tests demonstrate that filament count is the most significant variable, closely followed by areal density for a significance level (alpha) of 0.05. On this basis, fibre length is insignificant but an interaction plot of all three variables in Figure 3-6 implies that fibre length is more statistically significant for thin preforms (0.75kg/m$^2$) (Cell C), particularly for high filament counts (24K) (Cell E). There is a distinct reduction in density variation when processing shorter fibres for low areal density preforms (0.75kg/m$^2$). There is also a noticeable reduction in density variation when shorter fibres and high filament count tows are processed. In summary, high areal density variation associated with thin preforms can be compensated for by using a combination of short fibres and low filament counts. Observed trends for some of the remaining squares (A and B for example) are less clear, which can be attributed to the relatively small number of repeat simulations.

The areal density variation was also investigated experimentally by weighing samples cut from preforms manufactured with a range of tow sizes. Figure 3-7 shows that on average, the areal density variation across the three preforms varies by 15%, supporting the simulation data in Figure 3-5 and Figure 3-6.

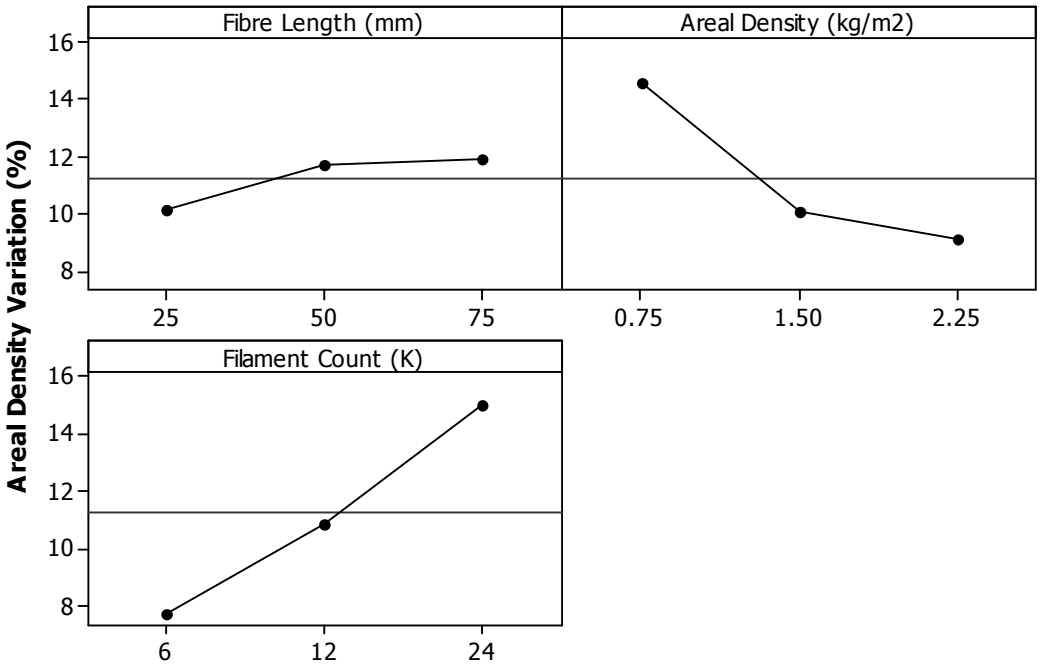


**Figure 3-5 Main effects plot for a Taguchi design to investigate the effect of three variables on the percentage areal density variation of simulated 2D flat laminates**

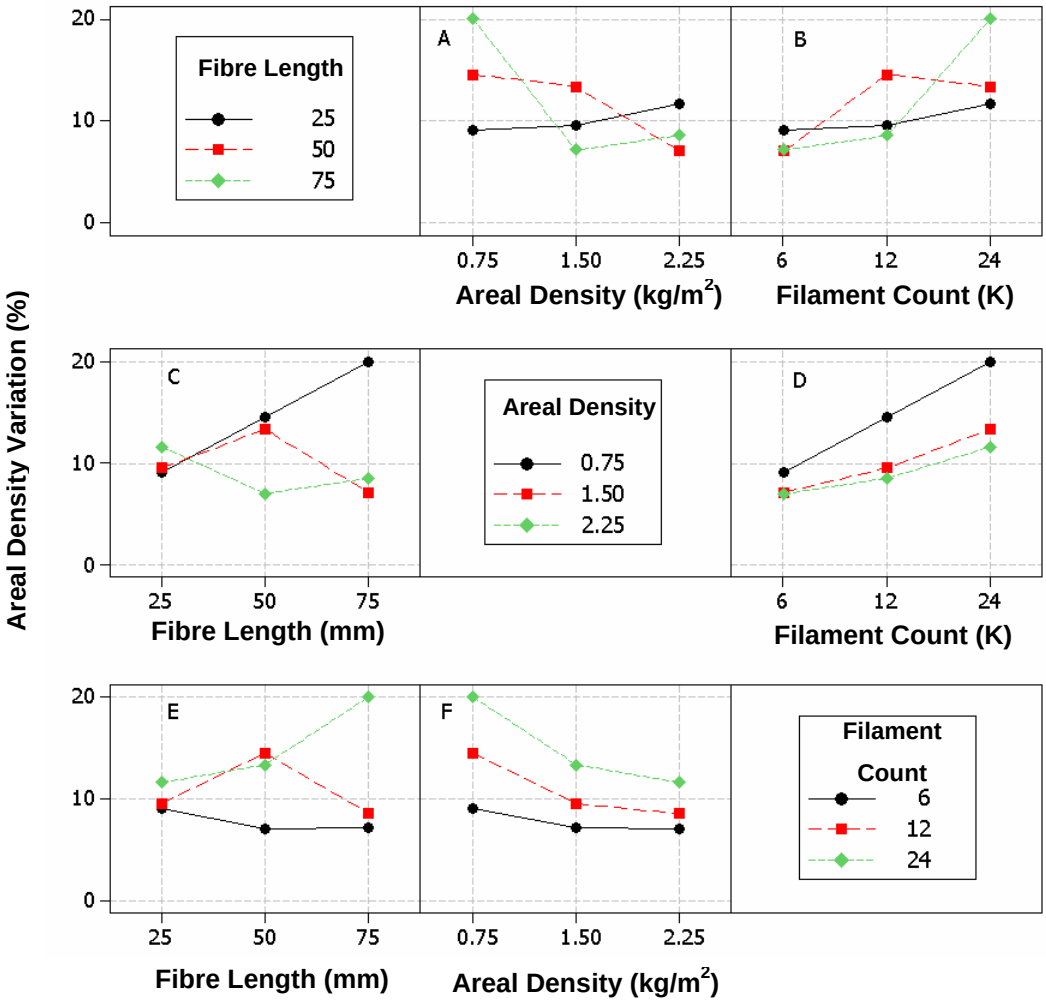


**Figure 3-6** **An interaction plot for a Taguchi design to investigate the synergistic effect of three variables on the areal density variation of 2D laminates. Results were generated from a process simulation to replicate the areal density variations expected from weighing contiguous, 50mm × 50mm coupons from preforms. The solid line in Cell C shows a clear reduction in areal density variation when processing shorter fibres for low areal density preforms. The green dotted line in Cell E demonstrates that shorter fibres improve the density variation for large filament counts.**

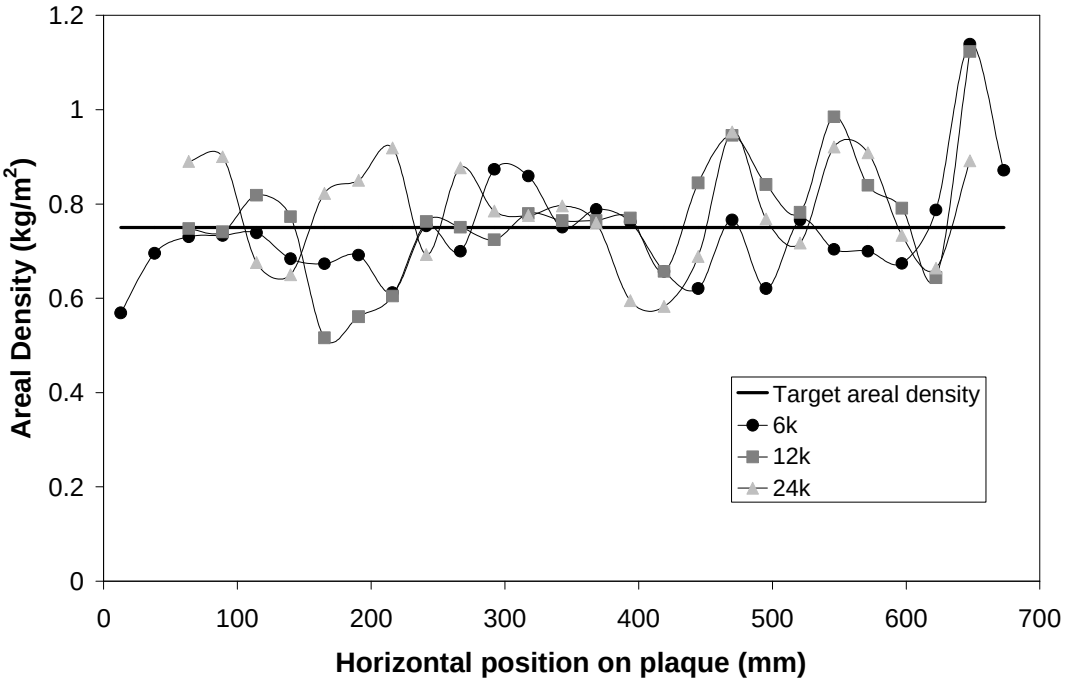


**Figure 3-7 Local areal density variation measured at discrete locations from three preforms with 75mm long tows of various filament counts.**

### *3.3.4.2. Mechanical Properties*

Experimental results are tabulated in Appendix.G for the tensile tests performed, including a selection of stress/strain curves. A summary of the experimental data is presented in Table 7-6, Appendix.G. These results are summarised in Figure 3-8 and Figure 3-9 in the form of main effects plots for modulus and UTS. The P-value from significance testing indicates that filament count is insignificant at a confidence level of 95%. This is confirmed by the main effects plots presented in Figure 3-8 and Figure 3-9 where the variation in modulus and UTS across filament counts was within ±3% of the mean. Comparing the polyurethane sized 12K and 24K fibres, stiffness decreased by 3.3% and strength decreased by only 1.3% as filament count increased. The tensile stiffness and strength both decrease linearly as fibre length is increased from 25mm to 75mm. A 7% decrease in stiffness and a 16.8% decrease in strength were observed when the tow length was increased from 25mm to 75mm. The tensile stiffness and strength both decreased with decreasing areal density, although the effect was non-linear. Reducing the areal density by one third caused an insignificant reduction in stiffness and strength, whilst a reduction by two thirds became significant at a 7.5% reduction in stiffness and an 18.8% reduction in strength. In summary, the target areal

density was the most influential variable, closely followed by fibre length, whilst filament count was insignificant at the levels studied.

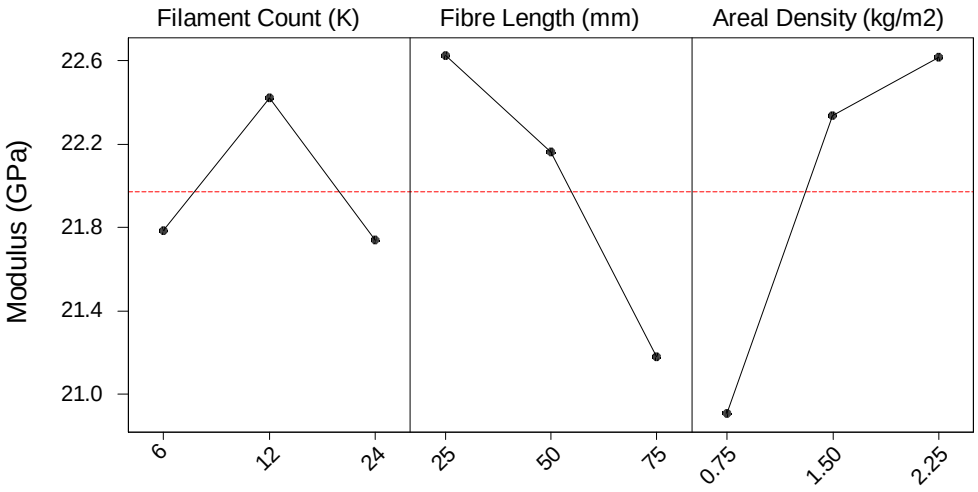


**Figure 3-8 Main effects plot for modulus. Each point represents the mean modulus for each factor level. The dotted line shows the overall mean for all 350 tensile specimens.**

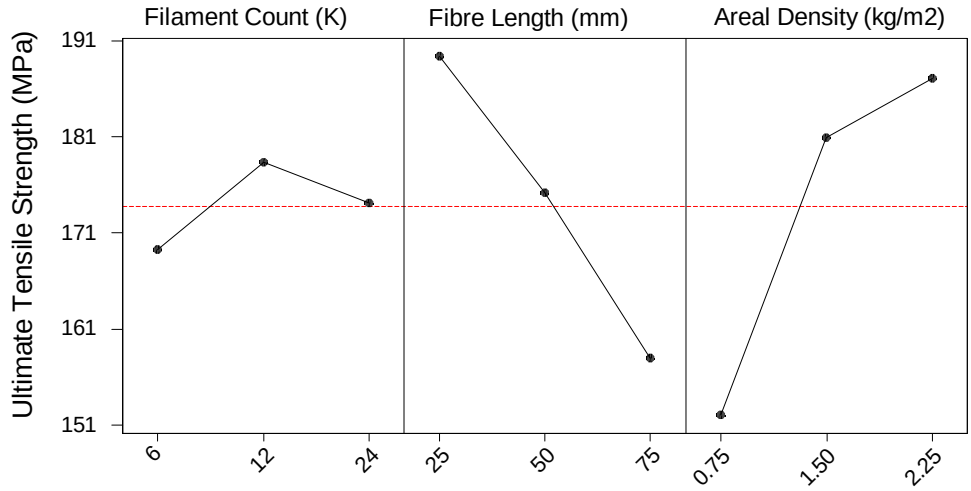


**Figure 3-9 Main effects plot for ultimate tensile strength. Each point represents the mean UTS for each factor level. The dotted line shows the overall mean for all 350 tensile specimens.**

It was clear when processing the three tows that the bundle integrity was dependent on the fibre surface treatment. The epoxy surface treatment used for the 6K HTA fibres maintained the filament count within each bundle, however, the polyurethane surface treatment used for both 12K and 24K STS caused tow splitting, or filamentisation, under identical processing conditions.

The inter-plaque variation was calculated from five plaques comprising similar 6K, 50mm long tows with a target areal density of 2.25kg/m$^2$. The inter-plaque variation (standard deviation/mean) for tensile stiffness and strength was 4.7% and 8.8% respectively, shown in Figure 3-10. The effect of systematic variation of material properties within the plaque is considered in Figure 3-11, by comparing modulus and UTS for specimens at different locations and orientations. The main effects plots presented in Figure 3-11 show that 90º specimens on average exhibit 5.6% higher stiffness and 9.1% higher strength than 0º specimens (where 0º is the direction of robot travel).

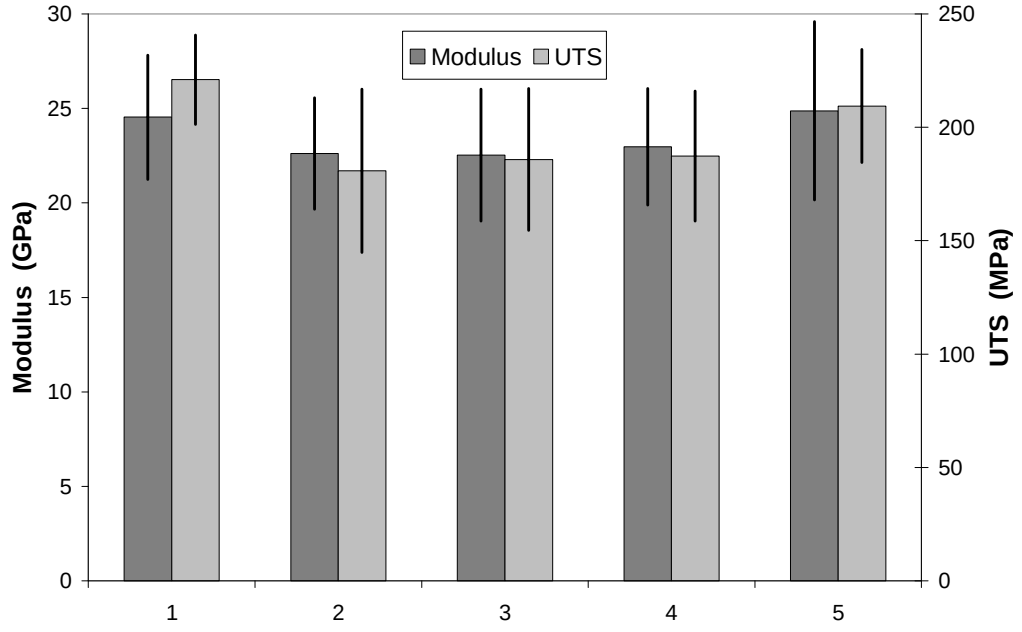


**Figure 3-10 Inter-plaque variability of stiffness and strength for five similar plaques manufactured with 6K, 50mm long tows at an areal density of 2.25kg/m$^2$.**

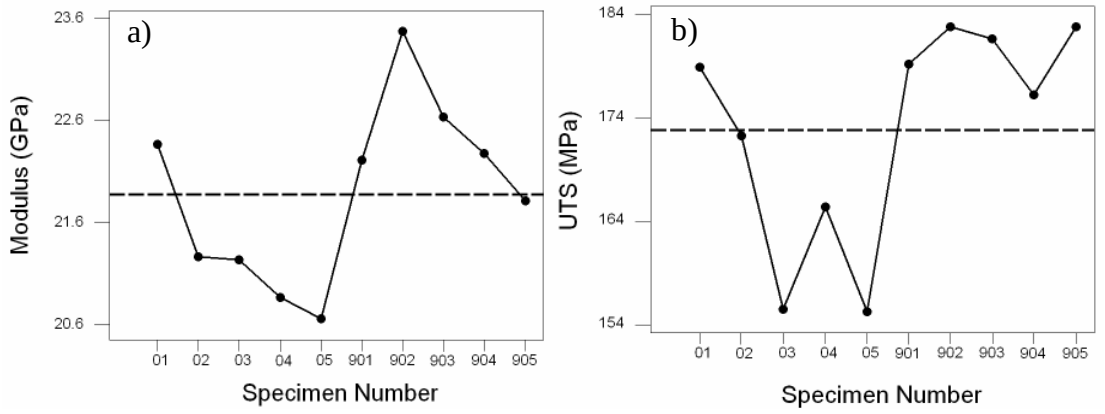


**Figure 3-11 Main effect plot for specimen number against (a) tensile modulus and (b) tensile strength, for all 35 random fibre plaques tested. Specimens were water-jet cut to ensure they were taken from the same location on each plaque. Specimen numbers 01 to 05 were cut at 0º, which corresponds to the direction of travel of the robot. Specimen numbers 901 to 905 were cut at 90º. Each point represents the mean of the response variable for each factor level. The dotted line shows the mean value for all points.**

### 3.3.5. Discussion

The aim of this work was to quantify the effect of three microstructural parameters on the mechanical performance of random carbon fibre laminates. The fundamental goal was to establish whether a correlation exists between local areal density variation and tensile properties. Of the three microstructural parameters considered, a strong correlation exists for fibre length and laminate thickness (target areal density), but the effect of filament count is less clear.

A reduction in the target areal density from 2.25kg/m$^2$ to 0.75kg/m$^2$ results in a 61% increase in the areal density variation (Figure 3-5). The 0.75kg/m$^2$ preforms clearly contained unreinforced areas, and consequently the 7.5% reduction in stiffness and 18.8% reduction in strength can be attributed to stochastic coverage effects.

The process simulation (Figure 3-5) suggested a general increase in local density variation with increasing fibre length. The tensile stiffness and strength both decrease linearly as fibre length is increased from 25mm to 75mm. Figure 3-8 and Figure 3-9 show that a 7% decrease in stiffness and a 16.8% decrease in strength were seen over the tow length range. This phenomenon is also observed beyond the critical length by Katayama *et al*. [113] and is predicted by Trapeznikov *et al*. [114]. In the present work the decrease in mechanical properties can also be attributed to stochastic coverage effects - shorter fibres inherently improve the coverage for thin laminates when processing large tows as demonstrated by the process model. In addition, as the tow segments become shorter the bundle integrity is reduced and the filaments become separated. Figure 3-12 demonstrates the change in fibre architecture as the bundle length decreases. The bundle splits into smaller sub-units and single filaments providing a more homogenous distribution of filaments throughout the thickness of the laminate.

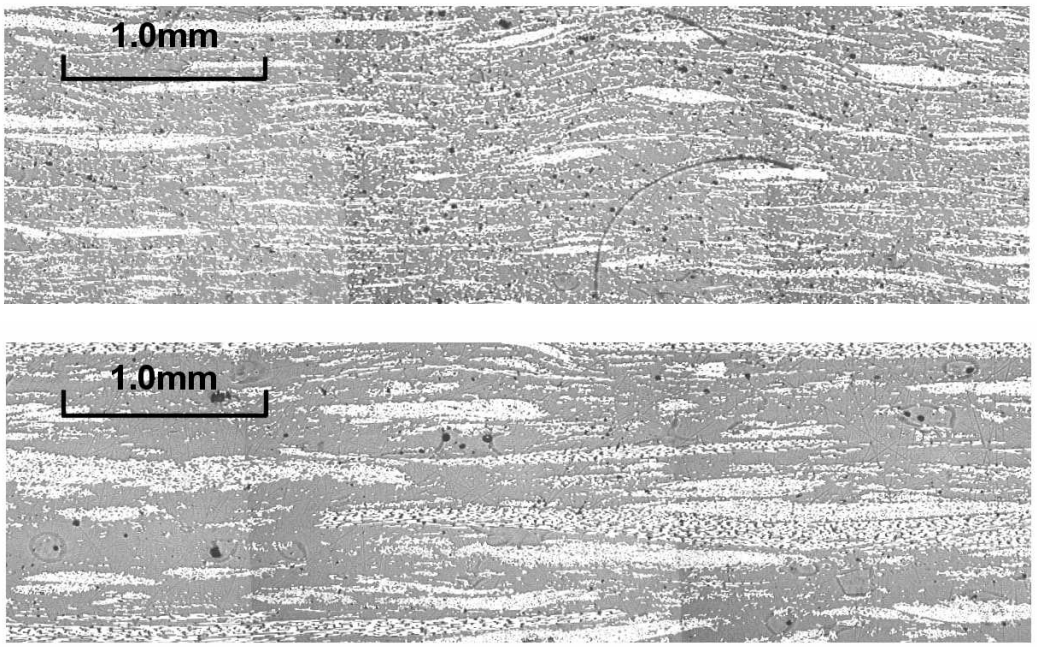


**Figure 3-12 Micrographs from two samples with bundle lengths of 7mm (top) and 23 mm (bottom). More single filaments and smaller clusters of filaments are present with the shorter length. (The virgin tow size was 24K).**

Areal density predictions from the process model imply that filament count is the most significant variable investigated, yet mechanical properties were relatively insensitive to this parameter for the three fibre types processed. However, an important secondary effect was noted in the fibre architecture produced for the different sizing agents; the degree of filamentisation was greater with the polyurethane sizing (i.e. for the 12K and 24K tows), see Figure 3-13. This effect may account for the dependence on filament count noted in Figure 3-8 and Figure 3-9, where maxima were seen for 12K tow. Filamentised 6K tows would be expected to produce higher properties because of the associated improvement in fibre coverage over higher filament counts. A trend of reducing properties with decreasing filament count would then support the areal density predictions. By considering the trends in Figure 3-8 and Figure 3-9, the effect of filamentisation may increase the UTS by 11% and the modulus by 5%, an effect noted by Dockum and Schell [42] who reported a 21% increase in strength of DFP glass coupons for a 50% reduction in filament count.

The filamentisation level is of particular importance for thinner panels. Unreinforced areas are likely to proliferate as larger tows and longer fibres are employed for lower areal densities. However, filamentisation does increase the preform loft due to the

packing characteristics of single filaments. Permeability is also reduced as bundle diameters become smaller and intra tow pore sizes are reduced [115, 116]. These factors increase cycle time and complicate the moulding process.

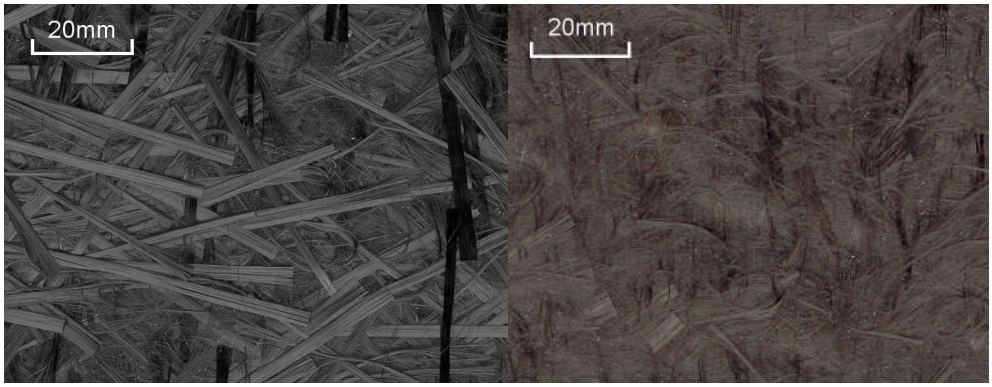


**Figure 3-13 Photographs taken prior to moulding of two carbon preforms. The difference in fibre architecture is visible between the non-filamentised epoxy sized tows (left) and the filamentised polyurethane sized tows (right).**

Characterisation of the laminates has demonstrated a significant variation in mechanical properties across each plaque (see COV in Table 7-6) which can be attributed to local variations in areal density as a result of the fibre deposition strategy. All three experimental areal density curves are periodic (see Figure 3-7), with the wavelength coinciding with the 60mm offset of the chopper spray pattern. Additional simulations indicate that a significant reduction in areal density variation is experienced when the spray passes are mutually orthogonal. Figure 3-14 shows that on average the absolute areal density variation for a parallel layered strategy is reduced by 30% when an orthogonal layered approach is used. In addition, from Figure 3-11, the employed robot trajectory induces fibre directionality and orthotropy. Orthogonal layers would also minimise this effect to yield more consistent mechanical properties across the laminate

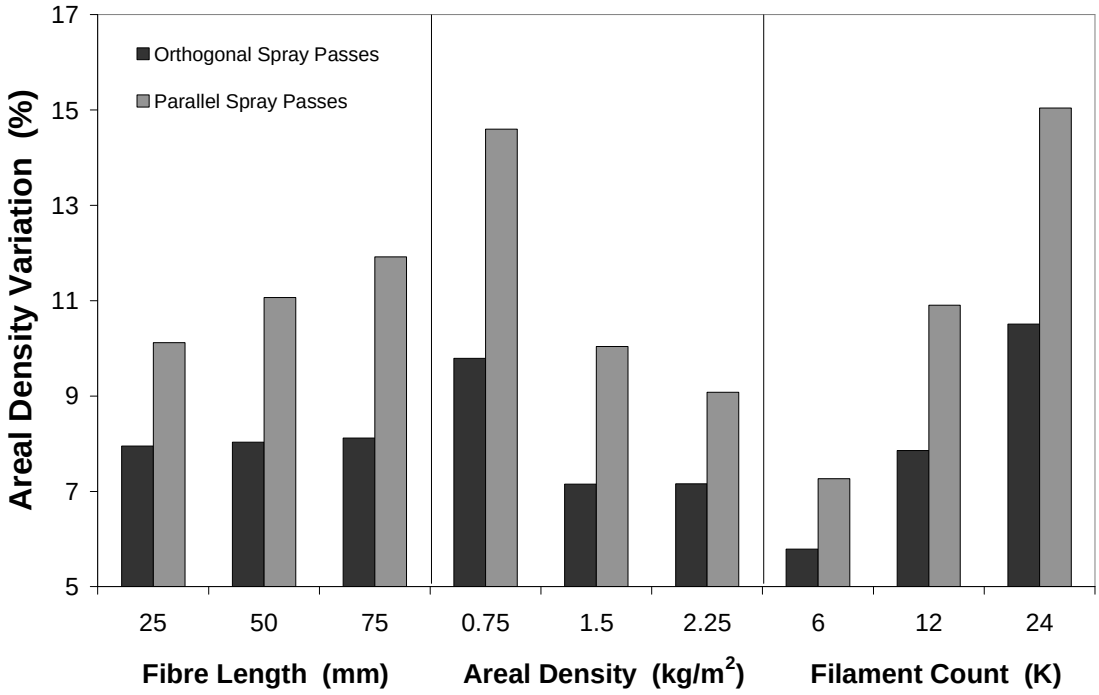


**Figure 3-14 The effect of different spray strategies on the areal density variation. Results were generated using a DFP process simulation.**

### 3.3.6. Conclusions

An industrial DFP machine processing large, carbon tows has been used to produce thin, structural laminates. Low inter-plaque variability demonstrates that the process is highly repeatable, but further gains can be made by optimising the fibre deposition strategy. (The inter-plaque variability for the tensile stiffness and strength was 4.7% and 8.8% respectively).

A correlation exists between local areal density variation and the mechanical performance of DCFP laminates. Both fibre length and global areal density significantly influence the local density variation, but the effect of filament count is less clear.

Global areal density (laminate thickness) is the most significant variable of the three independent variables considered. Mechanical properties are reduced in thin parts as a consequence of poor fibre coverage leading to unreinforced areas. Stiffness was reduced by 7.5% and strength by 18.8% when the areal density was reduced from 2.25kg/m$^2$ to 0.75kg/m$^2$.

Both tensile stiffness and strength decrease as fibre length is increased. This can be attributed to stochastic coverage effects as shown by modelling the fibre deposition process. Whilst shorter fibres improve coverage, it is important to establish the critical bundle length to ensure that the full mechanical potential of the fibres is exploited. The effects of fibre length will be studied in more detail in Section 3.4.

Tensile testing shows that filament count has an insignificant effect on mechanical performance, relative to the cost savings that are attainable from using high filament count tows. However, process simulation indicates that filament count is an important parameter, but it is clear that a secondary effect of sizing agent has been observed experimentally. Tows with polyurethane surface treatment filamentised to a higher degree than with epoxy, creating more uniform coverage with higher material properties. The effect of tow filamentisation will be studied in more detail in Section 3.5, whilst endeavouring to isolate the effects of filament count from the chop length.

## *3.4. Effect of fibre length*

### 3.4.1. Background

Mechanical properties of random carbon composites produced by directed fibre preforming (DFP) are heavily influenced by size and scale effects as shown in Sections 3.2 and 3.3. Large filament counts (24K+) create high variations in local properties (particularly for thin laminates) and filament end synchronisation causes local weak points. Uniform fibre coverage and smaller bundle sizes are therefore desirable. There is an increased tendency for the tow to filamentise into smaller bundles of filaments for shorter chop lengths. This intrinsic splitting is influenced by the fibre surface treatment and processing conditions, and inherently reduces the areal density variation associated with high filament count tows.

This section investigates the effect of fibre length on the tensile properties of directed carbon fibre preforms. Section 3.3 demonstrated that shorter fibres give improved mechanical properties as a result of improved coverage. The aim of the present work

was to extend the existing study of fibre lengths (limited to 25, 50 and 75mm) to encompass the entire range of the chopping apparatus, with a focus on shorter lengths. Lengths (3mm, 6mm, 14mm, 23mm, 29mm, 58mm and 115mm) were integer divisions of the cutting roller circumference (115mm).

Two sets of data are presented; one for unfilamentised tows (no induced filamentisation) and the other for highly filamentised material (maximum induced filamentisation using full airline pressure). For this reason the filamentised and unfilamentised properties are considered as practical upper and lower bounds respectively for the current machine. Initial optimisation showed that cycle time had to be increased in order to achieve extremely high filamentisation and that this practice could not necessarily be supported in a production process.

Carbon preforms were manufactured using 24K Toho Tenax STS fibres and were moulded via RTM in a 3mm cavity to produce laminates with a fibre volume fraction of 30% using DLS1678.

### 3.4.2. Results and discussion

The tensile properties are primarily affected by stochastic effects; shorter fibres and smaller bundles provide a more even coverage. There are additional processing benefits to shorter fibres; lower preform loft, better surface finish, greater fibre placement precision and improved definition of radii and other part features. However, short fibres are prone to washing during the moulding process and also reduce preform rigidity.

Tensile testing results are presented in Table 7-7, Appendix.G. Since the RVE size is proportional to the fibre length, there were concerns that standard coupon properties would not be representative for laminates containing longer fibres. Sixty tensile specimens were tested and the relative error for both modulus and UTS was under 10% for every scenario (see Table 7-7). This level of error does not have any significant impact on the observed trends presented in Figure 3-15 and Figure 3-16. Therefore, 60 realisations were considered to provide sufficient confidence at all of the tested fibre lengths.

In general, the effect of filamentisation increases the tensile properties over the range of fibre lengths tested by reducing the overall bundle size, exposing more of the filament surface area to the matrix material [42, 60]. The tensile stiffness increases by 18.9% and the tensile strength by 44.1% when the level of filamentisation is maximised over the length range (excluding the 3mm fibres).

Previous studies [42, 60] investigating the effect of fibre length for glass preforms were inconclusive due to process variation. Current tensile testing reveals that the average tensile modulus remains constant with increasing fibre length. However, the standard deviation bars in Figure 3-15 indicate that the level of scatter in the results increases with increasing fibre length. The error bars for the tensile strength (Figure 3-16) also increase with increasing length, but the mean strength values generally decrease with increasing length.

According to Figure 3-15 and Figure 3-16 there is an initial increase in tensile properties between 3mm and 6mm for the non-filamentised case, implying that the critical length is somewhere between these lengths. The critical tow length is undetermined for the filamentised bundles, which supports the assumption that it is proportional to the filament count. Scanning electron micrographs (SEM) in Figure 3-17 show the failure mechanisms for the two plaques produced with 3mm fibres. Images (a) and (b) show clear signs of fibre pull-out for the low filamentisation plaque. The tow end in image (b) appears to be encased in resin and there is no sign of fibre breakage. The fibre architecture of the highly filamentised laminate is much finer than the contrasting low filamentisation case, with the bundles in image (c) being orders of magnitude smaller than those in image (a). Image (d) confirms that the highly filamentised bundles fractured as the ends are visible and are synchronised with the fracture plane. These images support the assumption that a high filament count tow is analogous to a large single fibre.

Beyond the 6mm fibre length, at both filamentisation levels, the length-strength relationship obeys a decaying power law. Similar trends are experienced with injection moulded materials [113, 117], as longer fibres tend to curl and therefore the load transfer to the matrix is less efficient. Fibre curvature was observed for this material as

lengths increased and filament counts were reduced. There are known stochastic coverage effects that exist with this random material. Within the paper making industry, long fibres cause poor sheet formation and reduce strength as a result of stress concentrations generated by non-uniform mass distributions [118]. Shorter fibres provide lower areal density variations and a more homogenous coverage, but also naturally filamentise further to reduce the net filament count within each bundle, which has already proved to be a successful method for increasing tensile strength.

### 3.4.3. Conclusions

This section of work quantifies the effect of fibre length on the mechanical properties of random carbon composites. The nature of the directed fibre preforming process produces varying degrees of filamentisation over the range of tow lengths considered, and consequently length effects are not seen in isolation. However, the net effect of reducing fibre length is clear; shorter fibres significantly improve composite performance down to the critical length. Strength is enhanced due to fewer critical flaws (Weibull effects), improved preform coverage and lower filament counts through natural filamentisation.

Composite stiffness is seen to be independent of fibre length beyond the critical value. However, stiffness does increase with increasing levels of filamentisation (an average of 23.7GPa vs. 19.4GPa). Strength obeys a characteristic Weibull-shaped relationship (decreasing power law) with increasing length, except with the non-filamentised bundles at lengths around 3mm – where a critical length effect is seen. This work has shown that stochastic variation is very important in a material of this nature.

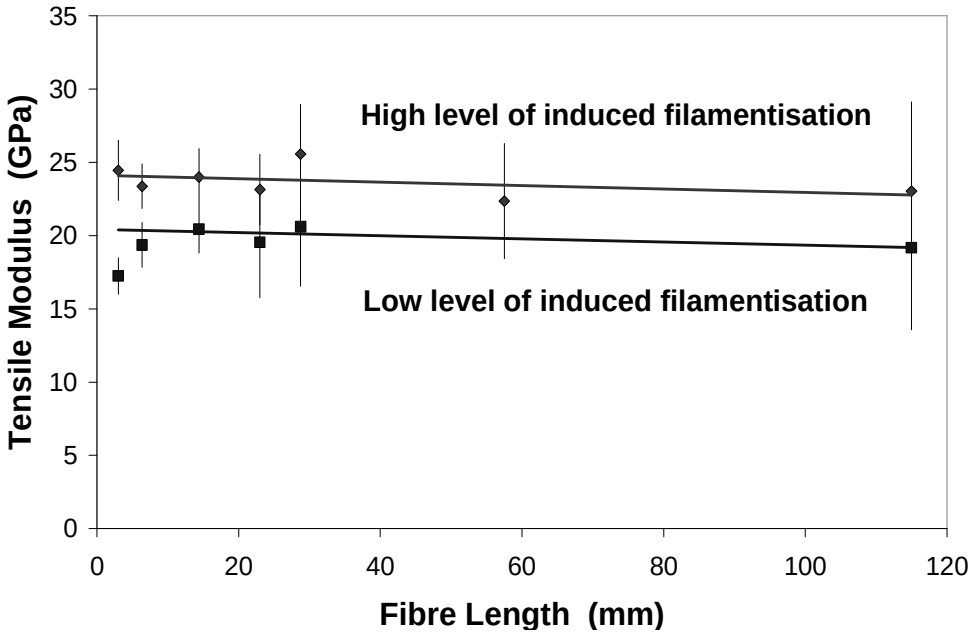


**Figure 3-15 Experimental modulus results as a function of fibre length and degree of induced filamentisation (Note: experimental points are the average of 60 tests, with standard deviation bars shown)**

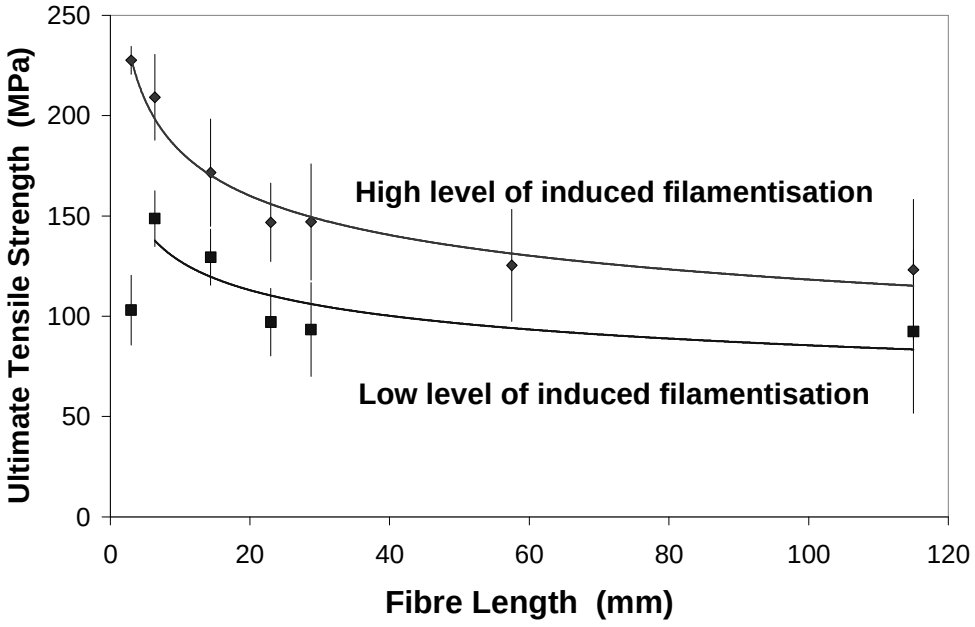


**Figure 3-16 Ultimate tensile strength as a function of fibre length and level of induced filamentisation. The level of natural filamentisation is a function of fibre length, which increases with shorter fibres. (Note: experimental points are the average of 60 tests, with standard deviation bars shown)**

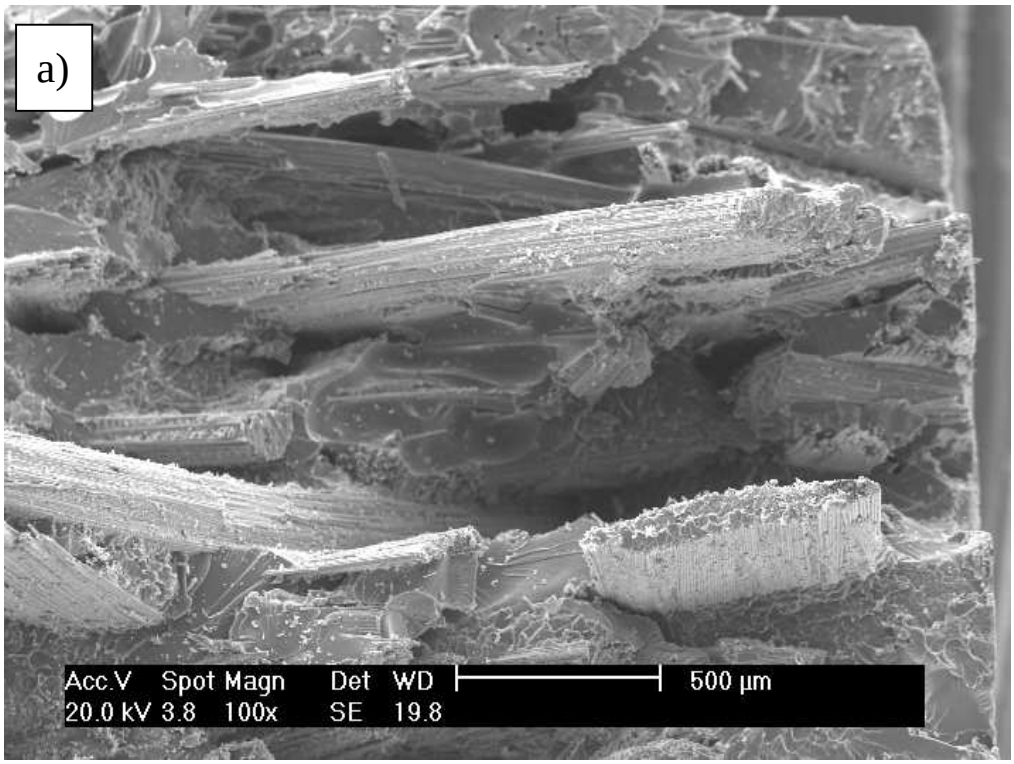
a)
Acc.V Spot Magn Det WD 500 µm
20.0 kV 3.8 100x SE 19.8

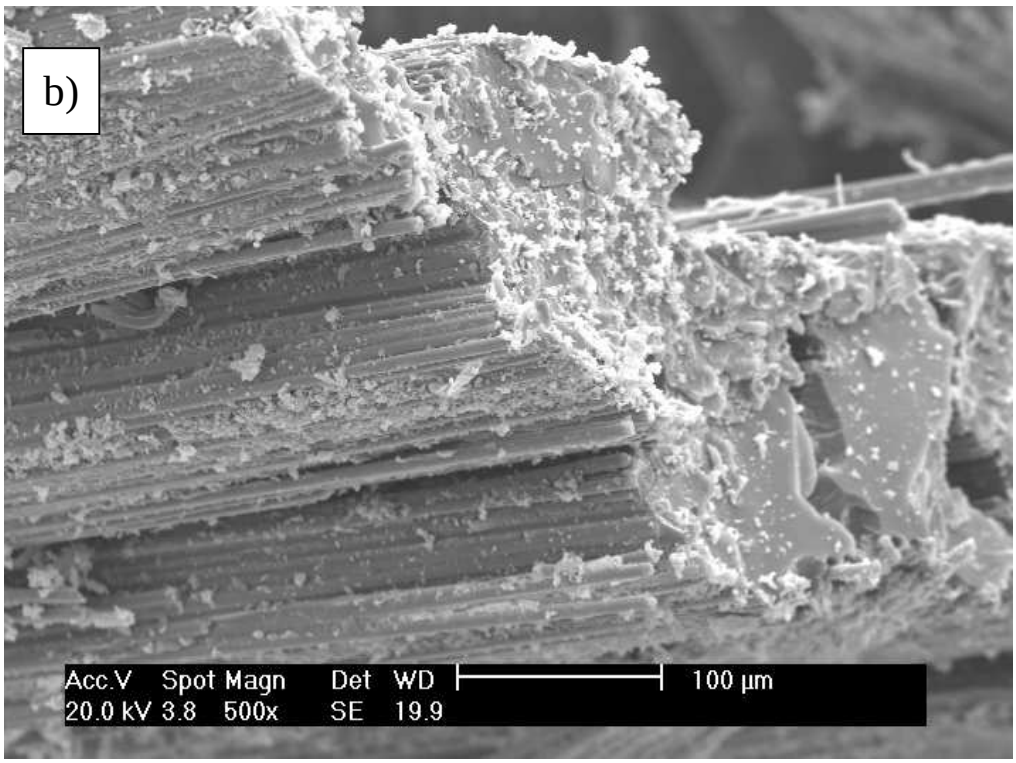
b)
Acc.V Spot Magn Det WD 100 µm
20.0 kV 3.8 500x SE 19.9

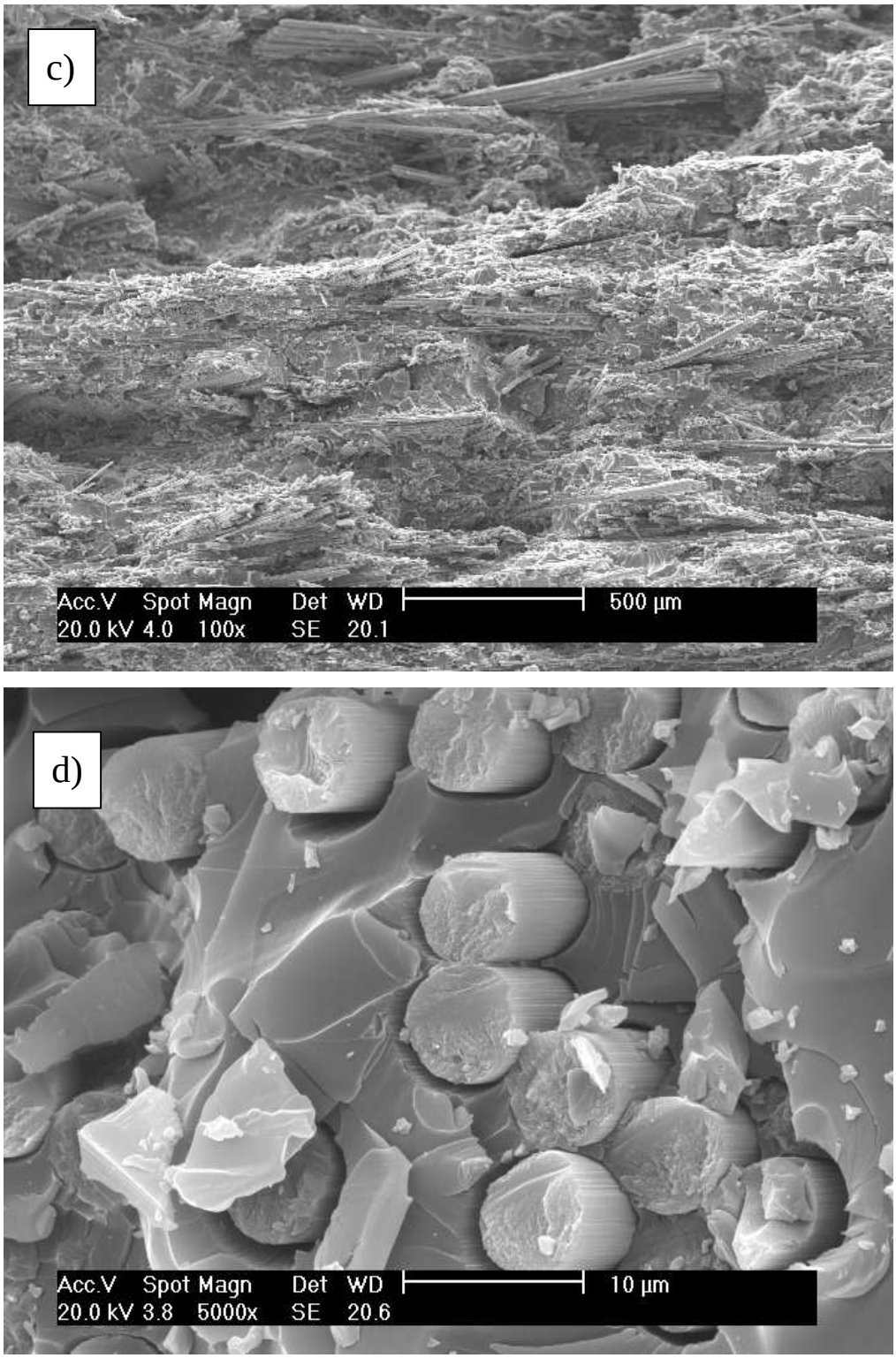


**Figure 3-17 SEM images taken from the fracture sites of two different DCFP laminates. Both plaques had 3mm long, 24K tows but images a) and b) were taken from a plaque with a low level of induced filamentisation and images c) and d) were taken from a plaque with high levels of filamentisation. Magnification levels are indicated at the bottom of each image.**

## *3.5. Effect of tow filamentisation*

This section presents a method for fragmenting large tows into smaller bundles in order to achieve uniform preform coverage whilst exploiting the financial benefits of using high filament counts. Varying levels of tow filamentisation are induced within the limits of the present installation, to fabricate laminates of different microstructures, in order to study the effect of filament count distribution on the mechanical and physical properties.

### 3.5.1. Background

During DCFP processing, carbon fibres tend to cohere in a tow due to the fibre surface treatment. There is an increased natural tendency for the tow to fragment when cut shorter, hence filament count is proportional to fibre length. This intrinsic splitting is dependent on the level and type of sizing agent applied to the fibre, where higher levels of sizing limit the amount of splitting. It is possible to impose a degree of filamentisation on the tow by mechanical means or, as in the present work, by using high velocity air perpendicular to the direction of fibre travel. Two distinct types of filamentisation clearly exist and in this work are termed “natural” and “induced”.

Filamentisation is essential for attaining uniform fibre coverage for thin laminates, in terms of areal mass variation and fibre angle variation (Section 3.2.8), potentially enabling inexpensive, high filament count tows to be used. However, depending on fibre type and method of induced filamentisation, there are disadvantages to high levels of filamentisation. Preform loft can increase by up to 650% (see Section 3.5), which is problematic for handling and cutting. Smaller tows also reduce preform permeability, which lengthens injection time. Filamentisation must therefore be controlled to ensure that the virgin tow is split in a regular manner to avoid the occurrence of single filaments, which improves fibre packing efficiency and thereby reduces preform loft.

Laminates produced from random tows via directed-fibre preforming have been shown to possess a meso-structure (see Section 3.2.2). Highly concentrated bundles of fibre are embedded in matrix-only regions, which cause large variations in local fibre

volume fraction. Filaments are aligned within each tow such that ends are coplanar, causing stress concentrations [75, 76] and consequently a loss in strength of up to 80% [78, 119]. Mechanical properties are therefore dominated by the heterogeneity of the mesostructure [120]. In Section 3.4 homogeneity improved with shorter fibre lengths as the reduction in bundle integrity caused higher levels of natural filamentisation. This is particularly important when the composite laminate is thin (~3mm) and the tow is large (24K-80K), as the stochastic effects become more significant and the likelihood of low fibre content regions increases.

The inability to accurately control filament count during preform manufacture makes the determination of the effects of filamentisation difficult. Historically, attempts have been made to prevent large bundles from splitting because properties such as fracture toughness and energy absorption are proportional to the effective bundle diameter [121]. This type of mesostructure is termed *secondary disordered* [76] because undesired tow splitting occurs in an otherwise ordered structure. To prevent filamentisation, Meraghni and Benzeggagh [119] over-injected random, pre-impregnated bundles with a liquid resin. Both stiffness and strength were reduced with increasing filament count (although the additional interface at the tow boundary would affect the mechanical response compared with a conventionally moulded laminate). Others [74, 78] have used inert wax to preserve bundles, which is removed by heat once the preform has been produced. However, both these methods only vary the volume fraction ratio of bundles to single filaments within the laminate [78], rather than generating filament count distributions as with DCFP.

Worrall and Wells [77] manufactured non-filamentised laminates by scattering tows into static resin to avoid fragmentation, rather than infusing under pressure. For comparison they produced filamentised laminates by removing the binder from the surface of the tows and then vigorously mixing in resin. A similar approach is used in the paper making industry to create mechanical pulps and within the composites industry to produce veil materials [122, 123]. The effects of fibre length and fibre coarseness on the strength of paper are reported in [118] and [124]. Longer, coarser fibres produce uneven mass distribution during paper formation, resulting in poorer strength properties due to local stress concentrations. This is an example of a *secondary ordered* mesostructure [76] because the unintentional clustering of fibre at the filament

level creates local order in the laminate. This undesirable agglomeration commonly occurs in injection moulded materials [125] and is reported to reduce the stiffness of SMC by up to 17% [126].

### 3.5.2. Filamentisation techniques

Mechanical filamentisation methods are described in [61] and [60] for inducing fragmentation during directed-fibre spray processes. The tow is passed over and under a series of breaker bars to spread the filaments prior to cutting. Tow spreading has also been accomplished using pneumatic techniques prior to chopping [127]. This allows high velocity air to separate the filaments as the chopped tows are transported to the preform tool. Highly filamentised fibres are commonly used as veil to improve the surface quality of laminates [32, 57] by promoting a resin rich surface.

Existing fibre chopping systems typically employ an air amplifier to collectively eject the fibres from the gun, provide filamentisation and prevent clogging. A degree of filamentisation is unavoidable using this approach due to the turbulent, high velocity air stream. This air also tends to disrupt previously laid-down fibres when working with the smaller, lighter carbon filaments compared with glass. In the present chopping system these functions have been separated to allow independent control. Consequently it is possible to eject the fibres from the gun with a wide range of controlled filamentisation levels.

The degree of fibre dispersion during processing can generally be controlled through material selection. The characteristics of the sizing agent and surface treatment can strongly affect bundle integrity. The solubility of the fibre sizing agent will control the dispersion in shear-flow processes such as compression and injection moulding [74]. The percentage of sizing agent and its chemical composition were seen to affect filamentisation potential in [53]. Finally, tow architecture is an important factor. Large, single-ended glass tows are more economical than multi-ended variants and have no detrimental effect on laminate properties according to [60]. However, other studies [20, 69] show that grouped bundles of small tows (0.5-1K) are required to achieve optimum

fibre coverage for carbon preforms, since they are one of the only commercial formats available at present that generate sufficient filamentisation.

### 3.5.3. Experimental methodology

In the present work induced levels of filamentisation are imposed in order to maximise mechanical properties without undesired permeability or lofting issues. A controlled balance of natural and induced filamentisation will be used to limit the number of single filaments. In practice this is the situation with glass fibre reinforcement, where commercial product forms readily split into bundles of e.g. 100 filaments but not into single filaments. This is because they consist of multiple, gathered bundles, which are coated with a surface treatment to form a larger bundle. The current study employs two different 24K STS carbon tows with identical fibre type, sizing level and surface chemistry. The two fibres are subjected to different manufacturing conditions, resulting in different cross-sectional profiles. In the present application Fibre I is elliptical and has a high natural tendency to fragment compared with Fibre II. The profile of Fibre II is much flatter and is the same fibre as used previously in Section 3.4, where filament count was seen to be proportional to fibre length. The low natural filamentisation of Fibre II eliminates an independent variable and limits the number of single filaments in order to reduce preform loft. Induced filamentisation is then imposed to both fibres by high velocity air at five levels, between 0% (no air pressure in filamentisation chamber) and 100% (7 bar applied to filamentisation apparatus). A fibre length of 14mm was chosen for this study to provide a contrast in natural filamentisation between Fibres I and II. Preforms were moulded using DLS1692 in a 3mm cavity to yield a 30% fibre volume fraction. Twenty repeat specimens were tested in tension according to the method outlined in Appendix D.1.2.

## 3.5.4. Results and discussion

### *3.5.4.1. Effect of filamentisation on mechanical properties*

Representative photomicrographs of the extreme filamentisation levels are shown in Figure 3-18. The images show the difference in microstructure between the two fibre types, with Fibre II typically having much larger bundles but more significantly, fewer single filaments.

Figure 3-19 and Figure 3-20 show the effect of increasing the level of induced filamentisation on the tensile modulus and strength for Fibres I and II. Trends for Fibre I are clear, with increased filamentisation improving mechanical properties. As the level of induced filamentisation increases from 0% to 100%, modulus increases by 3% and strength by 50%. The improvement at all levels of filamentisation for Fibre I with respect to Fibre II is also apparent; the average increase in modulus is 10% and in strength 60%.

Whilst filamentisation has a clear benefit for Fibre I the evidence is less pronounced for Fibre II. Fibre II is less susceptible to natural filamentisation and the level of induced filamentisation is less controllable during preform production. Tow ends tend to fan outwards when high air pressures are applied, which may reduce the stress concentration at the bundle ends without necessarily breaking up the tow along its entire length. For Fibre II, modulus generally increases by 15% for filamentisation levels between 0% and 100%. However, strength shows no clear trend with induced filamentisation since the highest strength occurs at a level of 60% (low to high strength being 0, 40, 80, 20, 100, 60%). The strength increases by 63% between 0% and 60% induced filamentisation (see Table 7-8).

In general, filamentisation improves the mechanical performance of DCFP laminates since fragmenting the tow is analogous to processing smaller filament counts. As reported by Meraghni and Benzeggagh [119], materials with fewer fibres per bundle were found to have higher stiffness and strength. Ericson and Berglund [120] propose

that the mechanical properties, particularly strength, are dominated by the inhomogeneity of the material. For the present material the number of unreinforced zones or areas of low fibre volume fraction clearly decrease with decreasing tow filament count (for a constant volume of material).

### *3.5.4.2. Effect of filamentisation on preform loft*

Preform thickness was measured using a rule to provide a quantitative estimate of fibre loft. Figure 3-21 shows that Fibre I can have up to 120mm of loft prior to compaction (before stage 2 of the DCFP process), which may be a limiting factor for complex 3D geometries. At high filamentisation levels the bundles are broken-down and the loft increases, but after compaction the preforms are between 3mm and 5mm thick for Fibre II. Greater binder content may reduce these values further; particularly for the filamentised Fibre I preforms, which currently have around 15mm of post-compacted loft.

Figure 3-22 shows the results of the compaction testing (see Appendix D.1.9 for methodology). The platen separation has been expressed in terms of volume fraction and the force required to compress the preform section has been expressed as pressure. It is conventional to fit experimental data to a power law relationship of the form:

$$V_f = K + AP^B$$ **Equation 3-12**

Equation 3-12 was established using a combination of the models presented in [128] and [129]. The fibre volume fraction $V_f$ is determined at a given compaction pressure, $P$ using the fitting parameters $A$ and $B$ (the compaction stiffening index, where B<1) [128]. The inclusion of the volume fraction offset, $K$, is indicative of the uncompressed volume fraction of the laminate [129], which is used to model the horizontal portion of each curve in Figure 3-22.

Comparison of the correlation coefficients from a non-linear regression analysis confirm that Equation 3-12 is a more reliable method for fitting the experimental data within the range of compaction pressures shown, compared with the methods presented

in [128, 129]. Table 3-6 shows the curve fitting parameters for the upper and lower bounds for both fibre types within the 0-100% filamentisation range. Also shown is the representative preform rigidity parameter *M*, which is the gradient of a straight line from $0.2P_{max}$ to $P_{max}$ (where $P_{max}$=0.1MPa, see [128]).

Fibre I-0% has an uncompressed volume fraction of only 19.5% compared with 26.1% for Fibre II-0% (See *K* values in Table 3-6). Utilising Fibre II yields a more compact preform and enables much higher ultimate volume fractions to be achieved, since the filaments are packed more efficiently within the preform when in bundle form. Fibre II also has a low representative rigidity (*M* = 5.93MPa), which indicates that a lower compaction pressure is required to achieve the target volume fraction compared with the highly filamentised Fibre I-100% and Vetrotex U101 materials. This behaviour is also thought to result from the high tow filament count and the resulting compact structure: The number of fibre crossovers is reduced per unit area as filament count is increased and therefore the compression of a non-filamentised material is dominated by the tow volume fraction, whereas the compaction of a highly filamentised material is predominantly influenced by the number of fibre-fibre crossovers.

| Material | K | A | B | M (MPa) | $R^2$ |
|---|---|---|---|---|---|
| Fibre I-0% | 0.195 | 0.00454 | 0.34634 | 6.67 | 0.996 |
| Fibre I-100% | 0.061 | 0.00097 | 0.47615 | 8.60 | 0.993 |
| Fibre II-0% | 0.261 | 0.00313 | 0.39832 | 5.93 | 0.991 |
| Fibre II-100% | 0.087 | 0.02104 | 0.24647 | 5.93 | 0.999 |
| Vetrotex U101 [128] | - | 0.0177 | 0.2340 | 9.92 | - |

**Table 3-6 Compaction parameters for the extreme levels of filamentisation for fibre types I and II. Vetrotex U101 values are for three layers (1350gsm). $R^2$ shows Pearson's correlation coefficient against the experimental data ($R^2$=1 indicates perfect correlation).**

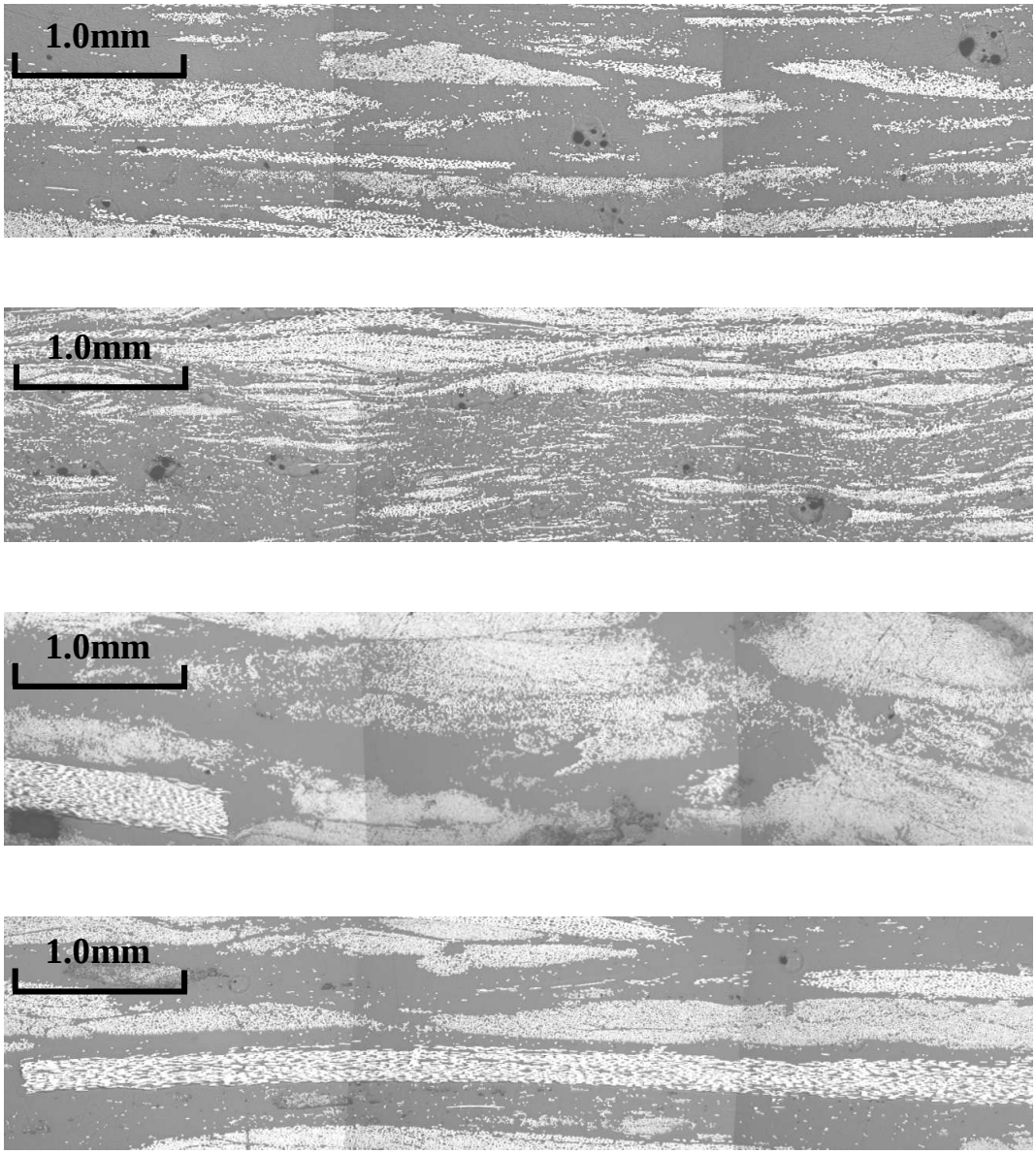


**Figure 3-18 Photo micrographs of sample cross-sections; from top; Fibre I-0%, Fibre I-100%, Fibre II-0%, Fibre II-100%.**

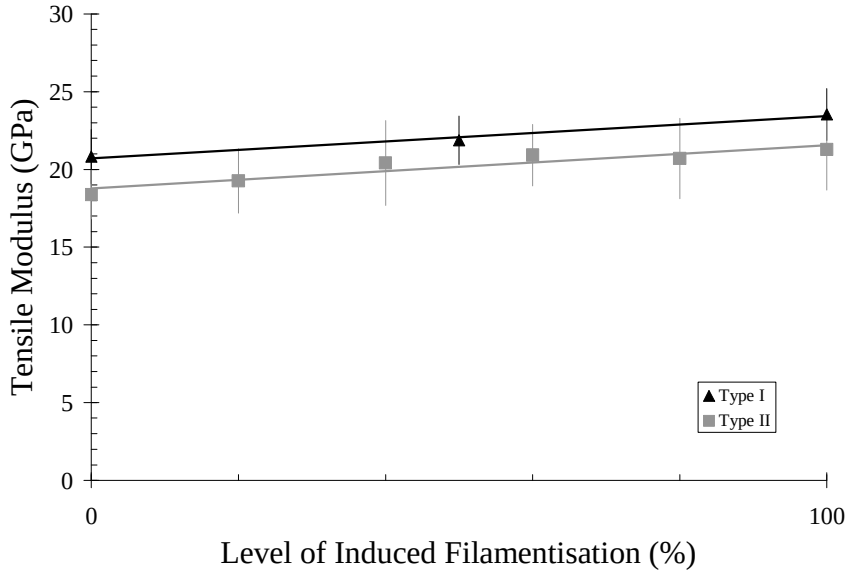


**Figure 3-19 Tensile modulus for fibre types I (high natural filamentisation) and II (low natural filamentisation) for increasing levels of induced filamentisation. Standard deviation bars are displayed.**

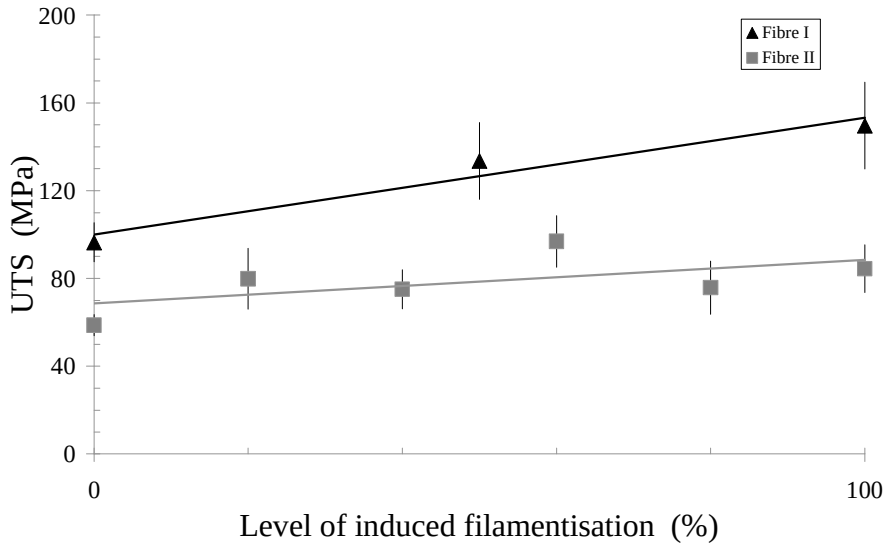


**Figure 3-20 UTS for fibre types I (high natural filamentisation) and II (low natural filamentisation) for increasing levels of induced filamentisation. Standard deviation bars are displayed.**

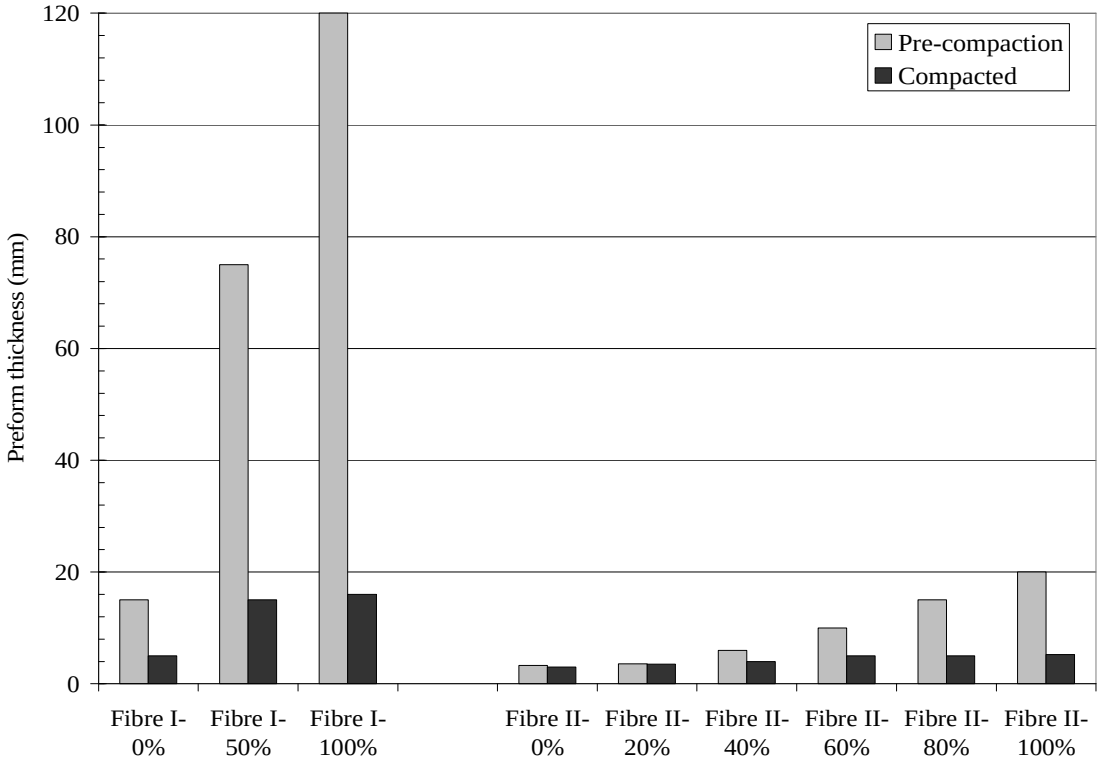


**Figure 3-21 Preform thickness before and after the heating cycle for both fibre types at various induced filamentisation levels. A tool clamping pressure of 5.4kPa is applied during heating.**

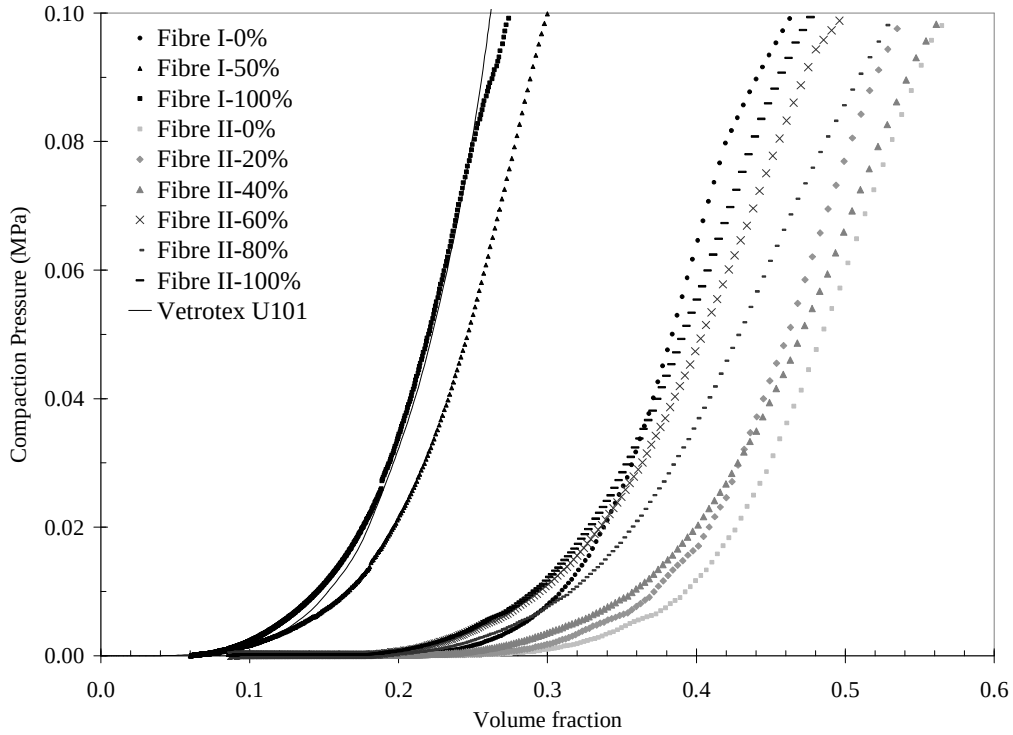


**Figure 3-22 Compaction pressure vs. laminate volume fraction**

### 3.5.5. Conclusions

Maximising tow filamentisation reduces the average tow filament count to provide a more homogeneous distribution of fibres within directed fibre preforms. Filamentisation not only minimises the occurrence of unreinforced areas with the laminate, but also reduces the magnitude of the stress concentrations experienced at the bundle ends. Increases in both stiffness (13%) and strength (55%) were recorded when the level of induced filamentisation was maximised for a 24K tow (Fibre I). The average filament count was only 425 filaments and the preform compaction study showed that an unacceptable level of loft is created with this material. Preforms of highly filamentised Fibre I are up to 120mm thick prior to compaction and 16mm thick after being heated under a pressure of 5.4kPa in the preform tool. This high level of loft limits the maximum volume fraction to under 30% when moulded by vacuum infusion (compaction pressure of 100kPa) and presents a real challenge for exploiting the full potential of the process for producing 3D shapes.

Preforms produced from Fibre II exhibit much lower levels of loft (under 5mm thick after compaction) and consequently volume fractions of around 50% are achievable. Tensile properties are shown to be much lower than for Fibre I, even for high levels of induced filamentisation. Clearly a balance is required between low preform loft and in-plane properties.

## *3.6. In-plane material characterisation*

### 3.6.1. Background

So far in this chapter the effects of key microstructural parameters have been studied to determine their influence on mechanical and physical properties of structural DCFP laminates. Tensile testing has been used for screening purposes during process optimisation, because of the relative efficiency compared with other in-plane tests. A full range of in-plane tests are therefore conducted in this section of the work to establish if the current trends for increasing fibre length can be universally applied to

all other material properties. The results from this section provide validation for the analytical stiffness model developed in Chapter 4.

### 3.6.2. Independent variables

The knowledge gained from Sections 3.2 to 3.5 has been used to formulate an optimum DCFP mesostructure for industrial trials. Fibre II has been used in a 24K format to produce all preforms, since it was shown to exhibit low levels of natural filamentisation in Section 3.5. Whilst Fibre II generally had lower mechanical properties than Fibre I, it produced lower loft and therefore volume fractions approaching 50% are achievable. However, maximum levels of induced filamentisation have been imposed on Fibre II during deposition to reduce the filament count, in order to provide a balance between loft and mechanical performance. In-plane tensile, compressive and shear tests are performed at a range of practical fibre volume fractions (10, 20, 30 & 40%) to study the mechanical response (see Appendices D.1.2 & D.1.3 for test methods). Ten specimens were tested for each material and for each test method.

Two fibre lengths of 6mm and 23mm were chosen. Results from Section 3.4 showed that maximum tensile properties were attained using shorter fibre lengths. The shortest, practical length is 6mm because shorter fibres are pulled through the Ø5mm perforations in the preform tool. Preforms manufactured with fibres shorter than 6mm also have poor rigidity, making it difficult to transfer the preform to the mould tool. Longer, 23mm fibres were also tested because it was anticipated that the trend established for tensile performance and increasing fibre length may not be replicated in compression or shear. All DCFP preforms were manufactured using the same practice as in Section 3.5. Preforms were moulded using DW2, a non-commercial epoxy with mechanical performance similar to an RTM120 system (see Appendix B.2). A constant mould cavity of 3mm was used and volume fraction was controlled by varying preform areal density.

Many authors [130-135] assert that a random fibre composite is analogous to a continuous fibre laminate stacked in a quasi-isotropic arrangement $(0^o/\pm45^o/90^o)_s$. A commercial non-crimp fabric (NCF) is tested here to compare against DCFP. The NCF

preform was manufactured by stamping four layers of ±45º CBX440 carbon fabric (supplied by Saint-Gobain BTI) with a die-cutter and interleaving each layer with binder (5wt%). The fibre volume fraction was approximately 35% and preforms were impregnated with DW2 in the same 3mm tool.

### 3.6.3. Results and Discussion

Test results are presented in Figure 3-24 and Figure 3-25 for the in-plane characterisation study. All moduli exhibit a strong linear relationship with fibre volume fraction, as the correlation coefficient ($R^2$) is 0.97 or above in each case (Figure 3-24). The average tensile moduli at each fibre volume fraction appear to be independent of fibre length as previously seen in Section 3.4. However, the scatter in the experimental data is generally lower for shorter fibre lengths. This is also true in compression and shear. The compressive modulus is approximately 20% lower than the tensile modulus at 10% $V_f$ but only 2% lower at 40% $V_f$. The shear modulus is approximately a third of the tensile stiffness, which can be expected for an isotropic material ($G = E/(2(1+\upsilon))$, where Poisson's ratio, $\upsilon$ is approximately a third).

Strength results also follow linear trends for increasing volume fractions, although the correlation coefficients range from 0.94 to 0.99 (Figure 3-25). Shear strength is seen to be independent of fibre length but laminates with 6mm fibres have 15% higher tensile strength and 24% higher compressive strengths than those with 23mm fibres. Stress concentrations caused by fibre ends and unreinforced areas dominate the tensile strength. Specimens tend to fail at the weakest link caused by critical flaws, which are more evenly distributed when shorter fibres are used. The impact of a critical flaw will be reduced because of greater levels of homogenisation, where the load of the failed fibre will be shared amongst a greater number of neighbouring fibres. Longer fibres loaded in compression are more likely to fail due to Euler buckling because of increased fibre waviness and consequently exhibit lower compressive strengths. The two different failure modes observed are shown in Figure 3-23. The compression specimen on the left shows a representative failure for the 6mm laminates. Following fracture, the upper half of the specimen forms a wedge and re-enters the lower part of the specimen. The photo on the right shows that the 23mm specimens failed due to

bending. A crack formed through the thickness of the specimen at 45º, as the left hand surface of the specimen was in tension and the right hand surface was in compression. This was also confirmed by the strain gauge readings from opposite faces of the specimen.

Shear strengths are approximately the same as the tensile strengths, but compressive strengths are up to 250% higher at 10%$V_f$ and up to 55% higher at 40% $V_f$. This was previously reported in [136] for DCFP materials. Brittle materials often have superior compressive strengths because in compression they are less susceptible to flaws. Voids present in the material close during compression to prevent microcracks from propagating, enabling higher loads to be attained.

**Figure 3-23 (Left) Typical compression failure for 6mm fibre DCFP laminate. (Right) Typical compression failure for 23mm DCFP laminate.**

According to Figure 3-24, the matrix tensile modulus is between 3.0GPa and 3.2GPa for the 6mm and 23mm fibre lengths respectively, when the linear regression lines are extrapolated to $V_f$ = 0%. This is in close agreement with the experimentally determined matrix modulus of 3.2 GPa (±13%). However, the tensile strengths of both the 6mm (60MPa) and 23mm (40MPa) laminates are lower for a fibre volume fraction of 10% than the experimental matrix strength of 76MPa (±4%). Low volumes of fibre appear to act as a pollutant to the matrix material, significantly reducing the tensile strength. This is expected for composites containing tightly packed fibre bundles. Large variations in

local fibre volume fraction cause local weaknesses and large stress concentrations form at the bundle ends because of the synchronised filament ends. Damage is initiated at these highly stressed areas or at transversely orientated fibre bundles [137]. Regular cracks form, which propagate along transverse fibres or through resin rich regions, joining the highly stressed regions together. The damage zone is therefore large in comparison to a single filament material of the same fibre volume fraction because the cracks tend to circumvent bundles. The failure is therefore matrix dominated.

Values for the 6mm fibre case have been taken from Figure 3-24 and Figure 3-25 and compared with a quasi-isotropic laminate at a volume fraction of 35%. DCFP compression and shear moduli are considered to be the same as for the NCF, given the magnitude of error (Figure 3-27). DCFP tensile stiffness retention is 82% compared with the continuous fibre NCF. Compression and shear strengths are comparable between the two materials but the tensile strength of DCFP is only 48% of the NCF tensile strength due to the discontinuous nature of the material. This finding is supported by the work of Rondeau *et al.* [48] and Reeve *et al.* [49] who find that the tensile stiffness of discontinuous fibres can approach 90% of the tensile stiffness of an aligned system, but the tensile strength rarely exceeds 50% even when the fibre length is beyond the critical length.

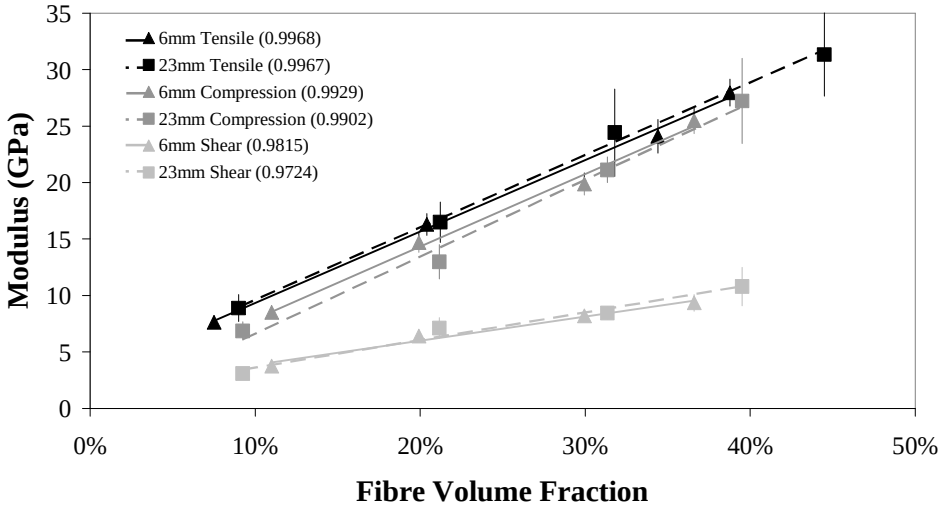


**Figure 3-24 Stiffness for DCFP laminates with two fibre lengths at a range of fibre volume fractions. Mean and standard deviation were calculated from 20 specimen repeats for each test condition. Values in brackets are the Pearson correlation coefficients for the linear regression fit.**

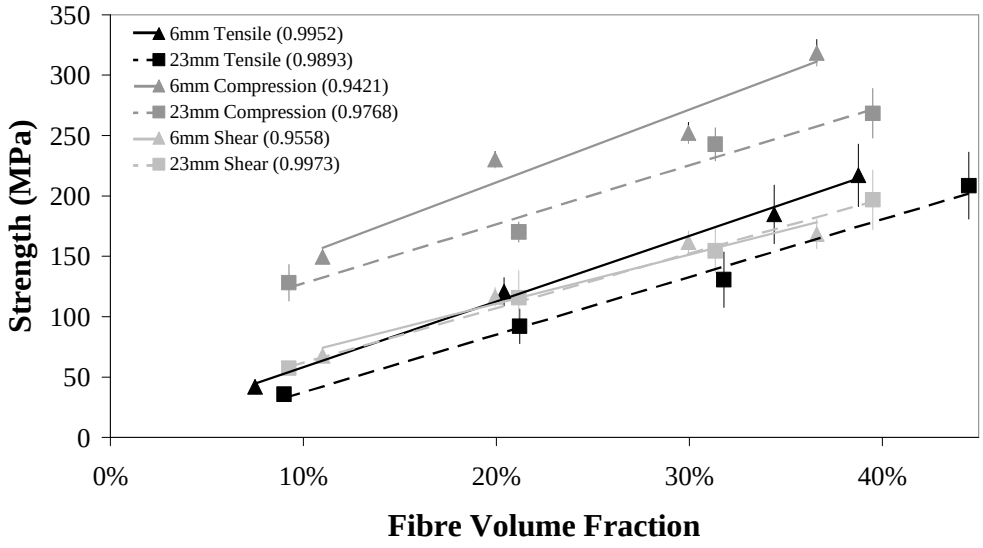


**Figure 3-25 DCFP laminates strengths for two fibre lengths at a range of fibre volume fractions. Mean and standard deviation were calculated from 20 specimen repeats for each test condition. Values in brackets are the Pearson correlation coefficients for the linear regression fit.**

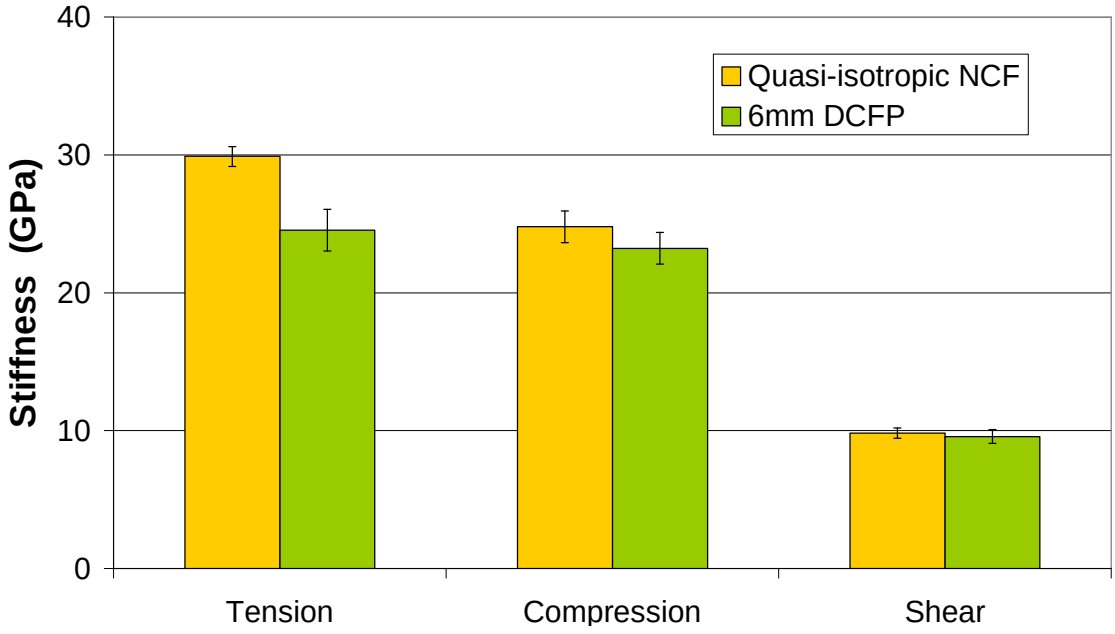


**Figure 3-26 Comparison of stiffness for two carbon fibre preforming methods. A continuous fibre, quasi-isotropic, NCF is compared against a DCFP random preform with 6mm fibres. $V_f$ is 35% in both cases. DCFP stiffness values at 35% $V_f$ are directly scaled from Figure 3-24 since there is such a strong linear relationship.**

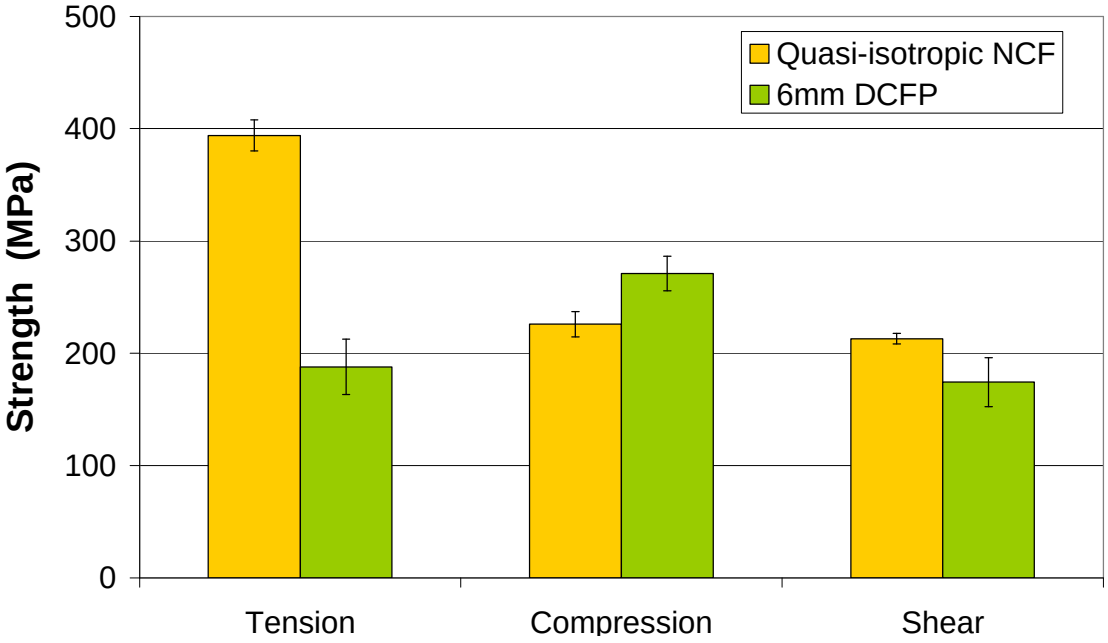


**Figure 3-27 Comparison of strength for two carbon fibre preforming methods. A continuous fibre, quasi-isotropic, NCF is compared against a DCFP random preform with 6mm fibres. $V_f$ is 35% in both cases. DCFP stiffness values at 35% $V_f$ are directly scaled from Figure 3-24 since there is such a strong linear relationship.**

### 3.6.4. Conclusions

This study has shown that the in-plane properties of DCFP follow a strong, linear relationship with increasing fibre volume fraction. Tensile, compressive and shear moduli are independent of fibre length. Whilst shear strength also appears to be independent of fibre length, both tensile and compressive strengths are lower for longer fibre lengths over the range tested. In tension, the fibre strength at the microscopic level is lower for longer fibres and longer bundles are also less susceptible to natural filamentisation. In compression, longer fibres are more likely to fail due to Euler buckling because of increased levels of waviness, and consequently exhibit lower compressive strengths.

This study has also shown that the shear strengths are the same magnitude as the tensile strengths, but the compressive strengths are up to 3.5 times higher. This is common for brittle materials because voids tend to close under compressive loading to prevent microcracks from propagating, enabling higher loads to be attained.

Comparison with a quasi-isotropic NCF has shown that the moduli of random DCFP are within 16% of the continuous fibre material. Compression and shear strengths are also comparable but the tensile strength is only 48% of that of the NCF because of the presence of fibre ends. Improvements can be made but smaller bundle sizes are required without the occurrence of high preform loft.

## *3.7. Chapter conclusions*

The objective of this chapter was to understand the influence of microstructural parameters on the mechanical and physical properties of DCFP laminates. DCFP laminates have an unconventional fibre architecture and weaknesses are generated in the laminate because of variations in local volume fraction and large stress concentrations at bundle ends. It was anticipated that these inhomogeneities would influence the consistency of the material and consequently size effects may exist. An essential part of this work was to establish if inexpensive, 24K carbon tows are suitable for producing thin components (<3mm), in order for DCFP to maintain an advantage over competing carbon fibre processing routes.

Bundle filamentisation has proven to be an effective means for reducing the net filament count of rovings, producing a more homogeneous distribution of filaments within directed fibre preforms. Increases in both stiffness (13%) and strength (55%) were reported when the mean filament count was reduced from 24,000 to just 425. Comparison with a quasi-isotropic NCF has shown that the moduli of random DCFP are within 16% of a comparable continuous fibre material. Compression and shear strengths are also similar but the tensile strength is only 48% of that of the NCF because of the stress concentrations caused by poor fibre coverage and the presence of fibre ends. Improvements can be made, but smaller bundle sizes result in an increase in preform thickness of over 200% for highly filamentised fibres. This limits the maximum volume fraction to below 30% when using vacuum infusion (100kPa compaction pressure) and restricts part complexity.

Additional gains in mechanical performance can be achieved by optimising fibre length. The nature of the DCFP process produces varying degrees of filamentisation

over the possible range of tow lengths, and consequently length effects are not seen in isolation. However, the net effect of reducing fibre length is clear; shorter fibres improve composite performance by up to 85% (for a length reduction from 115mm to 6mm). Strength is enhanced due to fewer critical flaws, improved preform coverage and lower filament counts through natural filamentisation. Strength obeys a characteristic Weibull-shaped relationship (decreasing power law) with increasing length, except below the critical bundle length. Whilst shorter fibres improve coverage, it is important to establish the critical bundle length to ensure that the full mechanical potential of the fibres is exploited.

A strong correlation exists between local areal density variation and the mechanical performance of DCFP laminates. Fibre length, filament count and laminate thickness significantly influence the local density variation. Global areal density (laminate thickness) is the most significant variable of the three independent variables considered. Mechanical properties are reduced in thin parts as a consequence of poor fibre coverage leading to unreinforced areas. Stiffness was reduced by 7.5% and strength by 18.8% when the areal density was reduced from 2.25kg/m$^2$ to 0.75kg/m$^2$.

In order for high filament count (+24K) tows to be suitable for thin laminates (<3mm) a balance is required between the degree of preform loft and in-plane mechanical performance. This can be achieved by controlling fibre length and level of induced filamentisation.

# Chapter 4. Analytical tensile stiffness prediction

## *4.1. Objectives*

An analytical model is developed in this chapter to predict the tensile stiffness of DCFP laminates. A review of literature builds on the discussions from Chapter 3 in order to establish an accurate model. Discontinuous fibres and random orientations both increase the scatter in experimental data and therefore complicate property prediction. Discontinuous reinforcement effects are considered, in addition to fibre bundling effects that are inherent with this type of process. A multi-level approach is adopted, which is validated using the experimental data from Chapter 3.

## *4.2. Literature review*

### 4.2.1. Fibre orientation mechanisms

Cox [138] was the first to consider the orientation effects of continuous fibres in a random composite, using statistical density functions to determine the influence of fibre angle on the elastic modulus. The in-plane tensile modulus for a 2D random array of fibres was given as:

$$E_{2D} = \frac{E_f V_f}{3} \qquad \textbf{Equation 4-1}$$

This approach is well known as under-predicting the tensile modulus because of the neglected matrix and transverse fibre contributions [139-142].

Nielsen and Chen [143] used elasticity theory to determine the orientation dependence (efficiency factor) of unidirectional lamina subjected to off-axis loadings. The efficiency factor varies moderately with volume fraction but dramatically with the ratio of the constituents' moduli.

A common approach is to use an efficiency factor in conjunction with the rule of mixtures. Possibly the most well-known orientation efficiency factor was derived by Krenchel [144]. It was assumed that the fibres could be grouped by orientation and a weighted summation made:

$$\eta_o = \sum_{n=1}^{\infty} a_n Cos^4\theta_n$$

$a_n$ – proportion of fibres

$\theta_n$ – the inclined angle

**Equation 4-2**

For a completely random material the summation is replaced by an integration over the orientation range for the entire proportion of fibres. The efficiency factor is equal to 0.375 for a perfectly planar random distribution. Pan [139, 145] highlights one possible limitation of the rule of mixtures (ROM) for predicting the properties of random fibre materials. The local fibre area fraction is a function of fibre direction, and is hence different to the global volume fraction, since a random number of fibre ends can exist at any given point within the composite. A simple statistical approach has been derived to modify the ROM to account for this. The tensile modulus for a perfectly planar random array of fibres is:

$$E_{2D} = E_f \frac{V_f}{\pi} + E_m\left(1 - \frac{V_f}{\pi}\right)$$

**Equation 4-3**

Classical laminate theory (CLT) is often used in conjunction with a micro-mechanical model to simulate random fibre composites [131, 133]. First proposed by Halpin and Pagano [135], the concept assumes that discontinuous fibres, orientated in unidirectional (UD) plies within a quasi-isotropic configuration, are mathematically equivalent to a homogeneous random fibre material. The accuracy of this approach is essentially dependent on the micromechanical model used to predict the properties of the fictitious UD plies. Many models currently exist, but for simplicity, often the empirical Halpin-Tsai [132] set of equations are used. The UD plies are subsequently arranged in a 0º/+45º/-45º/90º configuration and the modulus is calculated at each of the off-axis orientations. The transformation equation between the components of the stiffness matrix in the on-axis system to that of the off-axis system is calculated as follows:

$$\begin{Bmatrix} C'_{11} \\ C'_{22} \\ C'_{12} \\ C'_{66} \\ C'_{16} \\ C'_{26} \end{Bmatrix} = \begin{Bmatrix} m^4 & n^4 & 2m^2n^2 & 4m^2n^2 \\ n^4 & m^4 & 2m^2n^2 & 4m^2n^2 \\ m^2n^2 & m^2n^2 & m^4+n^4 & -4m^2n^2 \\ m^2n^2 & m^2n^2 & -2m^2n^2 & \left(m^2-n^2\right)^2 \\ m^3n & -m^3n & mn^3-m^3n & 2\left(mn^3-m^3n\right) \\ m^3n & -m^3n & m^3n-mn^3 & 2\left(mn^3-m^3n\right) \end{Bmatrix} \times \begin{Bmatrix} C_{11} \\ C_{22} \\ C_{12} \\ C_{66} \end{Bmatrix} \qquad \textbf{Equation 4-4}$$

where $m = \cos\theta$ and $n = \sin\theta$

A weighted volume-average is performed to determine the random composite stiffness matrix, $\overline{A}_{ij}$:

$$\overline{A}_{ij} = \sum_{k=1}^{M} C'_{ij}\, h_k \qquad \textbf{Equation 4-5}$$

where $M$ is the total number of plies in the laminate and $h_k$ is the thickness of the $k^{th}$ ply.

Unlike Halpin-Tsai, the concentric cylinders assemblage (CCA) [146] physically represents the fibre microstructure by considering a unidirectional, continuous fibre composite to be a group of concentric cylinders. Each cylinder comprises a fibre core encased in a matrix annulus with the size of the cylinder varying to fill the entire volume, whilst maintaining a constant fibre volume fraction in all the cylinders. Such a material is transversely isotropic and represents the filaments within the roving/tow with a high degree of accuracy [147].

Christensen and Waals [142] adopted a statistical averaging process rather than CLT to enable the CCA to be used for random fibre predictions. For low volume fractions (<20%), a simplified approximation of the random CCA model becomes equivalent to the Cox model plus a matrix contribution term:

$$E_{2D} = \frac{V_f E_f}{3} + \left(1 + V_f\right) E_m \qquad \textbf{Equation 4-6}$$

Discontinuous laminates rarely contain perfectly aligned or uniformly random fibre orientations because of processing influences, such as flow induced alignment in moulding compounds or injection moulding. Authors have studied the effects of partially aligned fibres on both stiffness [148, 149] and strength [150-153] by employing fibre orientation distributions to describe the orientation state. For 3D orientations the following normalisation condition must hold true:

$$\int_0^{2\pi} \int_0^{\pi} \psi(\theta, \phi) \sin\theta \, d\theta \, d\phi = 1 \qquad \textbf{Equation 4-7}$$

$\psi(\theta,\phi)$ is a 3D probability density function, where $\theta$ is the in-plane fibre orientation and $\phi$ represents the out-of-plane. This type of distribution is typically used to perform a weighted average of properties using a CLT-based approach, or to determine a more realistic efficiency factor than that of Krenchel for a ROM calculation. However, it is only commonly applied to 2D fibre distributions [150, 152] because it is cumbersome to use for 3D orientation states. Advani and Tucker [154] demonstrate that orientation tensors are a much more concise way of representing 3D fibre orientation distributions because only 5 (second order) or 12 (fourth order) independent constants are sufficient to fully describe the orientation state. The tensor components are used to average the sub-unit properties over the relevant directions, by calculating the orientation average of the stiffness tensor (similar to using the CLT method):

$$\begin{aligned} \left\langle C_{ijkl} \right\rangle = {} & B_1 a_{ijkl} + B_2 \left(a_{ij}\delta_{ij} + a_{kl}\delta_{ij}\right) \\ & + B_3 \left(a_{ik}\delta_{jl} + a_{il}\delta_{jk} + a_{ji}\delta_{ik} + a_{jk}\delta_{il}\right) \\ & + B_4 \left(\delta_{ij}\delta_{kl}\right) + B_5 \left(\delta_{ik}\delta_{jl} + \delta_{il}\delta_{jk}\right) \end{aligned} \qquad \textbf{Equation 4-8}$$

Where $\langle\ \rangle$ signifies the orientation average of the stiffness tensor, $C_{ijkl}$, $a_{ij}$ and $a_{ijkl}$ are second and fourth order tensor components and $\delta_{ij}$ is the Kronecker delta function. The $B$ constants are invariants of the $C_{ijkl}$ and are provided in Appendix H.3.2. Orientation tensors are often used in conjunction with micromechanical models such Eshelby [155]

or Mori-Tanaka [156] based methods to describe the 3D orientation state of spherical inclusions. Orientation tensors have been chosen as the foundation for DCFP stiffness prediction because of their flexibility and concise nature. The concept is discussed in more detail in Section 4.3.4.

#### *4.2.1.1. Comparison with experimental data*

The literature has shown that existing analytical models for random composite stiffness prediction can be broadly classified into three groups: Statistical approaches including ROM; Classical Laminate Theory; and inclusion approaches utilising orientation tensors [154]. In the present section, a selection of ROM and CLT methods are compared with experimental data from Section 3.3. The inclusion-based methods are reviewed in Sections 4.2.2 and 4.2.3 along with other suitable micromechanical models.

The ROM and CLT are widely used for their simplicity to obtain approximate stiffness values for design purposes. They are commonly applied in the literature to materials containing very short (<10mm), random single filaments. This section applies the simple models reviewed above to bundled DCFP laminates, to investigate their validity for meso-structured materials. The models studied are:

1. Cox (Equation 4-1) [138]
2. Nielsen and Chen [143]
3. Pan (Equation 4-3) [145]
4. Christiensen and Waals (exact) [142]
5. Krenchel (Equation 4-2) [144] / ROM
6. Concentric cylinder assemblage [146] / CLT [135]

The tensile fibre modulus is taken to be 238GPa (see
Table 7-1, Appendix B.1) and the tensile modulus of the matrix is taken to be 3GPa (see Table 7-3, Appendix B.2). A comparison of in-plane modulus versus volume fraction is presented in Figure 4-1 for the six analytical methods. Experimental results from Table 7-6 and Table 7-9 are plotted for each plaque for volume fractions ranging

from 9.9% to 37.8%, giving a range of 7GPa to 36GPa for tensile stiffness, illustrating the full range of variability seen in the experimental programme.

In the ROM models the stiffness predictions are based on simple considerations of volume fraction, the ratio of the constituents' moduli and a statistical approximation of the effects of fibre direction. The rigour of the ROM models is therefore limited since they do not consider the effect of key parameters such as fibre anisotropy or fibre bundle size for the DCFP process.

For the ROM methods at a volume fraction of 30%, the range of predicted stiffness is 15-29GPa (Figure 4-1). The Cox model is within 2% of the mean experimental moduli for the two fibre volume fractions presented. This method neglects all matrix effects and is generally accepted as a lower bound solution. Nielsen and Chen significantly under-predicts the tensile modulus by 34% as shown in Figure 4-1. A constant stress field is assumed (Reuss average) which ignores the complicated interactions such as shear coupling between the fibres and matrix, resulting in lower values than for a constant strain approach (Voigt average), particularly when the ratio of the constituents' moduli is as large as for carbon/epoxy.

Krenchel is 20% higher than the mean and falls outside of the experimental data range. The Pan model provides a reasonable upper bound to the experimental data and can include the effects of biased fibre distribution to model anisotropic laminates.

In general, both CLT based methods are seen to over-predict the experimental data, falling within the range of 28-29GPa at 30% $V_{f.}$ Figure 4-1 shows that the CCA/CLT and Christensen & Waals methods yield very similar results, confirming that a quasi-isotropic arrangement is a reasonable assumption for the CLT method. The laminate approach is relatively involved compared with the statistical approaches and some authors [157, 158] have attempted to give approximations. Rigour is lost as the accuracy of these approximations is limited by volume fraction and the ratio of the constituents' moduli. A comparison by Fu and Lauke [150] shows that the laminate approaches are generally more accurate than the modified ROM since they account for the transverse fibre contributions.

Reinforcement length has been ignored in Figure 4-1 but some of the models have previously been extended to account for this. Commonly, an additional efficiency factor is introduced to the ROM to model the length effects of short fibre composites. Either the Cox [138] or the simpler Kelly-Tyson [102] factor is used to reduce the effective properties of the fibres due to the reinforcement discontinuity. Advanced micro-mechanical models exist to account for reinforcement aspect ratio and can be incorporated into the CLT approach [155, 156]. Length effects will be studied in more detail in Sections 4.2.2 and 4.2.3.

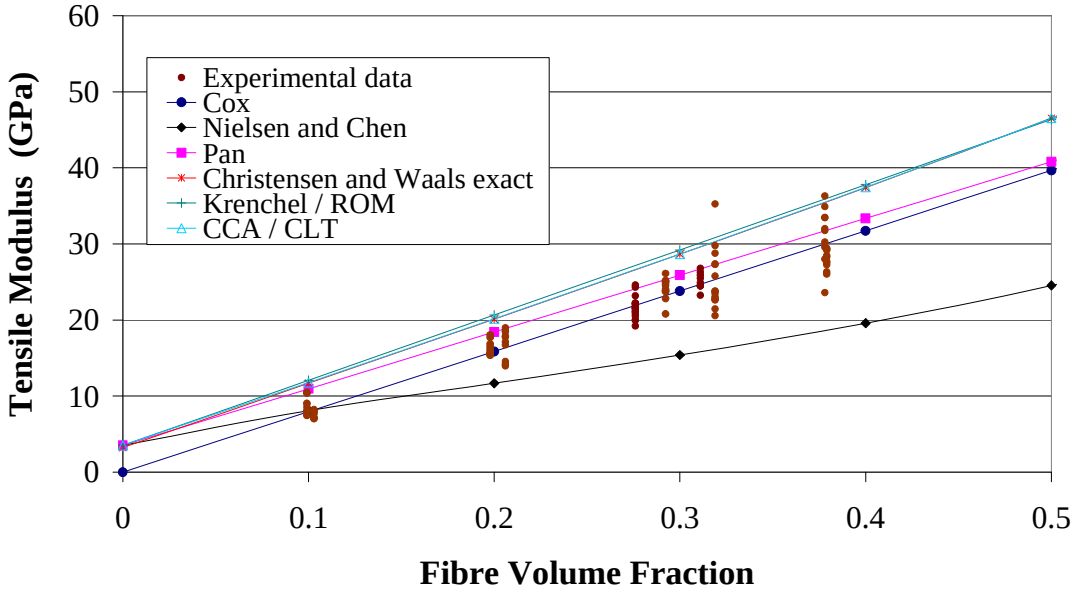


**Figure 4-1 Comparison of common models used to predict the tensile modulus for random fibre composites over a sensible range of volume fractions. Experimental data values shown are taken from Table 7-6 and Table 7-9 (Appendix.G).**

### 4.2.2. The effect of fibre length

Random orientations and finite fibre lengths complicate the prediction of discontinuous fibre composite properties. Section 4.2.1 considered the simplest of random fibre architectures as a platform for the development of more comprehensive physical models. This section aims to establish fibre length influences on the mechanical properties.

Fibre length effects are anticipated in two areas; critical fibre length effects and coverage effects. The first category is a universal consideration of discontinuous

composites and has been widely discussed. Maximum utilisation of the fibre properties only occurs beyond a critical length, at the transition from fibre pull-out to fibre breakage. The second is stochastic, where shorter fibres give greater macroscopic homogeneity of both areal density and fibre orientation distribution for a finite area. Both effects must be considered at the tow level rather than the filament level, as the tow cross-section is on the same scale as the thickness of the laminate.

Cox [138] pioneered the prediction of fibre length effects on modulus by realising the significance of the fibre-matrix interface for stress transfer in discontinuous fibre composites. *Shear-lag analysis* assumes that the fibre ends do not carry any load and therefore the reinforcing efficiency of the fibre increases as fibre length increases, since a greater proportion of the fibre length is loaded. This analytical solution is often incorporated as an efficiency factor in a modified Rule of Mixtures (ROM) equation. A critical fibre aspect ratio (length/diameter) of 600 typically exists for a carbon/epoxy system according to [94], below which the modulus of the composite is reduced. Thus, a critical tow length also exists [94, 159, 160] since synchronised filaments within tows are analogous to large, single fibres [80, 81].

A limitation of the shear-lag model is the assumption that the tensile stress at the fibre ends is zero. Previous studies suggest strains of up to 0.5% are present at the fibre ends when $E_f/E_m = 16$ [161]. However, it was evident that these end effects were negligible as $E_f/E_m$ tends to 100 (as is the case for carbon/epoxy) [162].

The effect of fibre aspect ratio has been investigated using micro-mechanical approaches in conjunction with classical laminate theory (CLT) [131, 133, 135, 163]. The concentric cylinders assemblage (CCA) [146] was discussed in Section 4.2.1 to predict theoretical, unidirectional (UD) ply properties. Although exact [147], the CCA is only applicable to discontinuous fibre materials with high aspect ratios, (i.e. at the filament level). Variants of the Halpin-Tsai [164-166] and Mori-Tanaka [156] methods are the most common micro-mechanical approaches for discontinuous fibre composites. Based on the dilute particulate method of Eshelby [155], the Mori-Tanaka [156] model not only considers the stress and strain fields around and within each inclusion, but more importantly accounts for changes in these fields due to fibre interactions at higher volume fractions (>5%). Closed-form equations have been

derived for the elastic constants of discontinuous UD composites [167, 168]. The model is accurate at low ($V_f$<0.3) and at extremely high volume fractions ($V_f \rightarrow 1$), but the values at intermediate $V_f$ are the result of a mathematical fit and are physically unrealistic. This is confirmed by comparisons of the shear modulus for continuous fibres [169], which show that the model diverges from the physical result beyond the dilute case. Despite this, the simple closed form of the Mori-Tanaka method is still applicable to discontinuous fibre composites [147] and comparisons with finite element models [170, 171] show that the Mori-Tanaka method is superior to the shear-lag theory and Halpin-Tsai for aligned short fibres. The closed-form expressions have been reformulated by Qiu and Weng [172, 173] to include the effects of anisotropic constituents, such as carbon fibre. A comparison is made in Section 4.2.3 to show the influence of fibre anisotropy and fibre aspect ratio on the mechanical properties for aligned, discontinuous fibre materials.

Variations in fibre length are encountered not only due to processing inconsistencies but also due to a length-dependent critical fibre volume fraction [114]. Increasing fibre-to-fibre contact beyond a critical point causes fibre breakage and consequently a reduction in mechanical properties. Established analytical models have been developed further [133, 174] to study the effect of fibre length distributions (FLD) on the tensile stiffness. Comparisons with experimental data and finite element models [171] show that the mean fibre length is sufficient to model length effects, providing the modal length is close to the mean value [150]. The chop length variability for the studied DCFP process follows a normal distribution and hence, the number-average length is representative. (Fibre lengths were measured to accuracy of 0.01mm using a vernier calliper. For a mean length of 38.3mm the coefficient of variation (COV) was 0.6%).

### 4.2.3. Micromechanics (Anisotropy)

Figure 4-2 shows the effect of fibre aspect ratio on the elastic properties ($E_1$ and $E_2$ only) over a range of volume fractions, using a selection of the micro-mechanical models reviewed in Section 4.2.2. It is assumed that the fibres are aligned, transversely isotropic and are therefore representative of filaments within a carbon tow. The input data for the various models used in this section is taken from Table 7-12, Appendix.H.

Although the CCA method is restricted to continuous fibres, it is included here as a benchmark against other micro-mechanical approaches applied at the filament level, since all filament lengths (3mm to 115mm) are over the critical length.

Figure 4-2 also shows the sensitivity of the longitudinal and transverse moduli to fibre aspect ratio of an aligned carbon/epoxy material. Increasing aspect ratio has a significant effect on the longitudinal modulus ($E_1$). All of the models agree for $E_1$ when the filament aspect ratio is sufficiently large (the continuous case). Analysis shows that carbon fibres are considered to be continuous ($E_1$ within 99% of continuous case) when the aspect ratio is approximately 200. This critical aspect ratio is lower than the value of 600 outlined by Hull [94] using the Cox methodology [138], but is in agreement with the work of Brady and Kardos [65] who show that the critical aspect ratio is approximately 200 as $E_f/E_m$ tends towards 100 (carbon/epoxy).

A maximum fibre packing term is included in the Halpin-Tsai equations [165, 166] to improve predictions for short fibres, by accounting for a limiting volume fraction due to irregular packing. The maximum packing fraction is incorporated into the Halpin-Tsai equations using the analytical expression of McGee and McCullough [166]. This is an appropriate method since the modulus of the fibres is much greater than the modulus of the matrix [175]. The accuracy of the modified Halpin-Tsai model is very sensitive to the maximum packing value and is studied here between 0.785 (square packed fibres) and 0.5. A reduction from 0.785 to 0.5 reduces $E_1$ by 24% at a volume fraction of 40%. Qiu-Weng and Mori-Tanaka yield identical results at all aspect ratios for $E_1$. The modified Halpin-Tsai predictions for $E_1$ are generally in good agreement with the these predictions at low volume fractions (<30%). However, very large longitudinal moduli are experienced at higher volume fractions as the aspect ratio and packing fraction decrease. This is not physically representative since a mathematical fit is used to force the maximum moduli through the maximum packing fraction point.

The transverse modulus ($E_2$), is insensitive to aspect ratio since lines (vi) to (x) are unchanged (except for an aspect ratio <1, not shown). This is also true for the other three elastic constants obtained from the inclusion methods, $G_{12}$, $G_{23}$ and $K_{23}$. It is acknowledged that the remaining elastic constants can be calculated from continuous fibre models [171], since only $E_1$ is sensitive to aspect ratio.

The effect of fibre anisotropy has a significant influence on the transverse stiffness when comparing the isotropic Mori-Tanaka case and the anisotropic Qiu-Weng case. $E_2$ is 20% lower for anisotropic fibres at volume fractions of 50%, but 33% lower when the volume fraction increases to 70%. This represents the range of volume fractions that are expected within the tow. $E_2$ is over estimated if the constituents are assumed to be isotropic, leading to over predicted values for the random composite stiffness. The maximum value of $E_2$ does not coincide with the fibre modulus at a $V_f$ of unity when adopting the Qiu-Weng methodology, (the transverse modulus of the tow is 10 times lower than the longitudinal modulus according to this model). It is also important to note that the Mori-Tanaka and Qiu-Weng methods yield very similar values to the continuous CCA method for the transverse modulus. This supports the use of these methods for long fibres but also implies that the modified Halpin-Tsai model is inaccurate at the filament level.

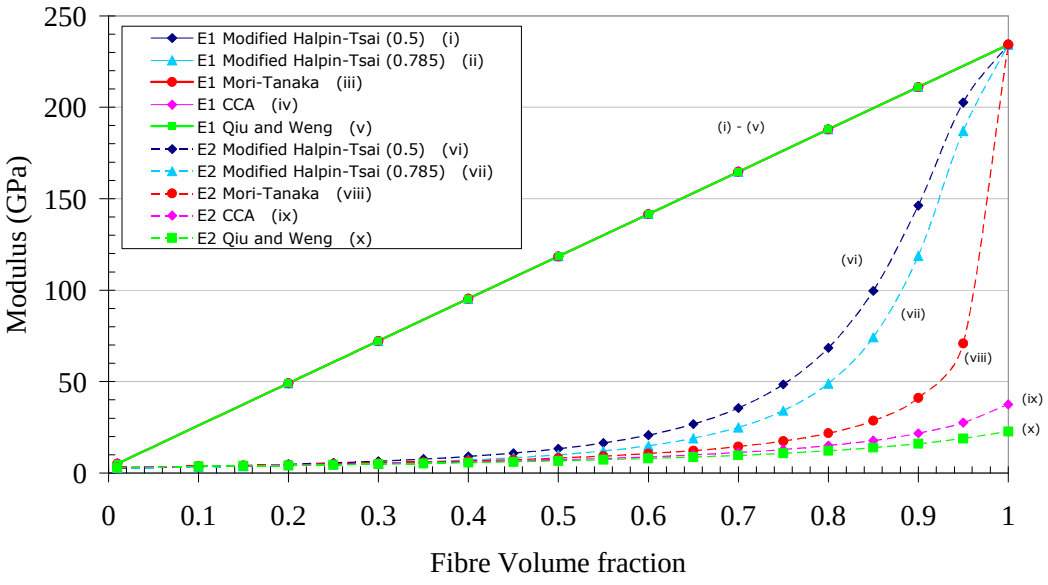


Continuous fibre (Aspect ratio = ∞)

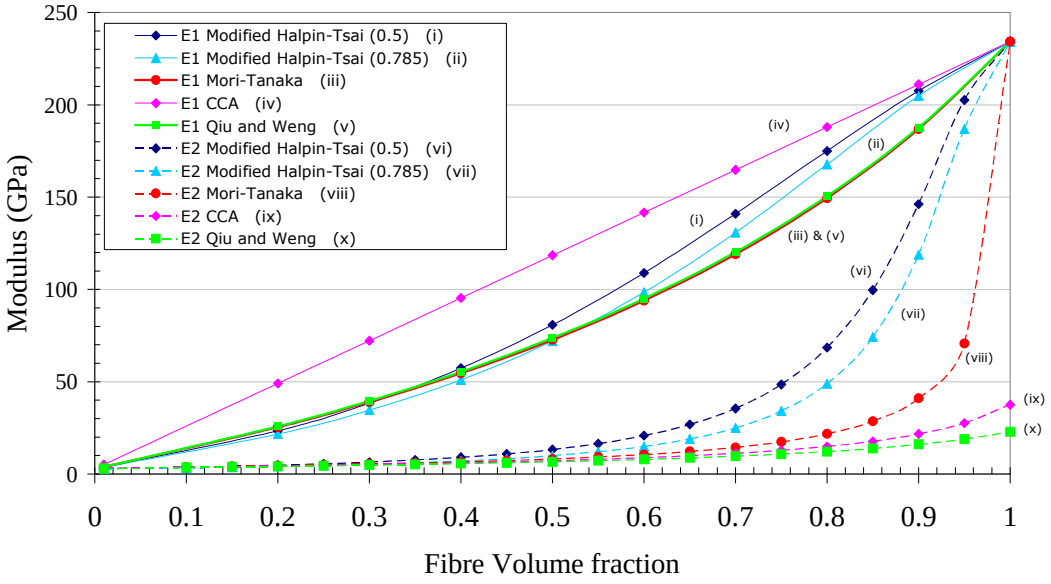


Aspect ratio = 20

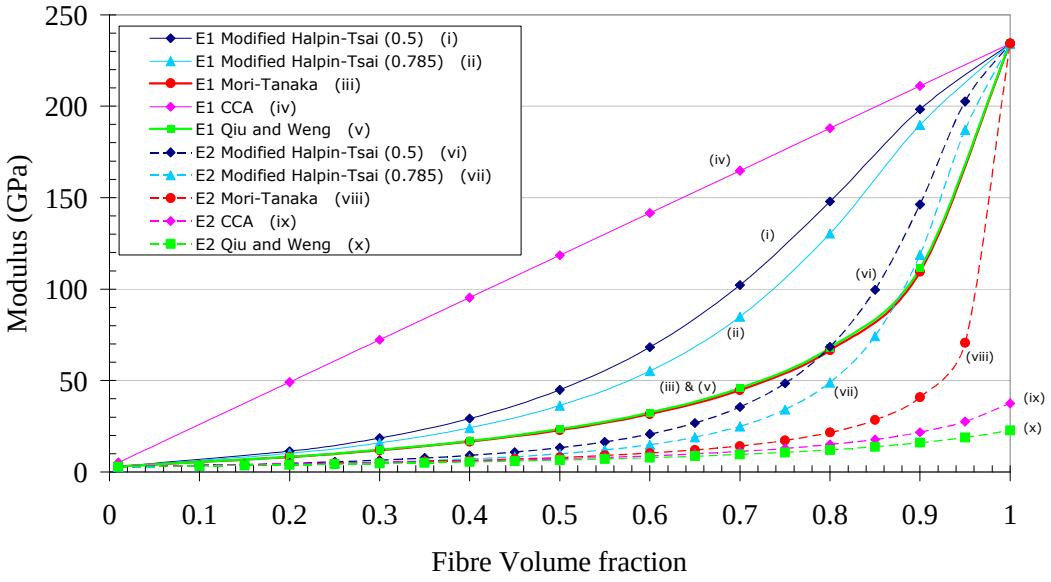


Aspect ratio = 5

**Figure 4-2 Predicted aspect ratio dependence of the effective moduli of aligned carbon/epoxy filaments within a single tow.**

### 4.2.4. The effect of fibre bundling

The architecture of spray-processed carbon fibre preforms has a number of significant differences to conventional materials. The tow filament count distribution is highly

non-uniform (e.g. Figure 3-12) and the mean filament count is not sufficiently accurate for property prediction. Modelling approaches for tow materials generally idealise the bundle of filaments as equivalent large fibres, with properties generated from the local volume fraction. Accurate predictions therefore depend on the bundle properties, which are determined from the knowledge of the tow filament count. Classical analytical methods can also be inaccurate for bundled materials because the unit cell is large with respect to the specimen dimensions and therefore the material is inhomogeneous and stochastic effects dominate. The basic assumptions used with many models can be invalidated by the size of large equivalent "fibres" (bundles) with respect to the laminate thickness and also by considerable fibre-to-fibre contact.

SEM micrographs showing tow pull-out [80, 81] confirm that fibre bundles are analogous to large, single fibres when the ratio $E_f/E_m$ is large. The Cox length efficiency factor [138] is used in [80] to verify that the variation in stiffness at different levels of filamentisation can be attributed to bundle aspect ratio. A similar method is adopted in [78] to develop a weighted rule of mixtures (ROM) average to predict the stiffness for laminates containing various proportions of bundles and single filaments. Good agreement is shown for the two extreme filamentisation cases (100% filaments and 100% bundles), however the experimental data is over-predicted by up to 50% at the intermediate levels. Again, this method only considers a single mean filament count and not the range of bundle sizes encountered in laminates manufactured by DCFP.

Other stiffness models are based on modifications to the inclusion-based methods [156]. Kataoka *et al.* [176] show that a 10% reduction in stiffness can be expected when the volume fraction of clusters (agglomerations) increases from 0% (fully filamentised) to 30%. This model however, considers the effect of unintentional clustering during injection moulding and therefore the filament ends are not synchronised. Other inclusion methods [119, 126] also confirm that dispersed fibres are more efficient as reinforcement than bundles. Meraghni and Benzeggagh [119] use a modified Mori-Tanaka model at both the filament and bundle levels and incorporate matrix micro-cracking to predict the stiffness of a random fibre composite. Tensile stiffness is reduced by 12% when the glass filament count is increased from 800 filaments to 2000 filaments. The model accounts for both matrix micro-cracking and

bundle mechanisms, however acoustic emissions testing is required to determine an empirical damage parameter.

#### *4.2.4.1. Filament count quantification*

The spatial distribution of filaments in aligned composites has been assessed using a variety of image analysis techniques. Voronoi tessellation and fractal dimensions have been used [177] to quantify the size of resin regions around filaments to ascertain the degree of bundling in woven fabrics. The potential for extension of these techniques to study short, randomly orientated tows is limited because of the range in aspect ratios experienced from off-axis, contacting bundles.

Katayama et al. [178] used fractal variance analysis to study the degree of filamentisation using a decreasing grid technique over an optical micrograph. The ratio of black to white pixels was recorded for each grid cell. A Richardson plot consisting of the log of cell variance against the inverse of cell size was plotted, where the slope denotes the degree of filamentisation. The bundling parameter is utilised in a simplified critical zone model (see Section 5.6) to determine the effects of incidental clustering on strength.

Worrall and Wells [77] developed a fractal variance technique to size clusters from micrographs. An abrupt change in slope on the Richardson plot identifies the presence of a change in scale and also sizes the bundle according to the position of the local minima on the plot. Acceptable results are achieved for low levels of filamentisation when applying this method to directed-fibre preforms, but fractal variance is only valid when the inclusion/bundle is small relative to the image size. Spurious results were also obtained when the images contained bundles with varying filament counts; therefore this technique cannot accommodate multiple changes in scale.

### 4.2.5. Current modelling limitations

A review of common analytical models has been conducted (see Figure 4-1) and the results indicate that a simplistic approximation yields over estimated values for the in-

plane tensile properties because of the idealised assumptions (isotropic fibres, reinforcement scale, bundling etc.). A unique attribute of the DCFP material is the variation in bundle size encountered as a result of the tow selection and processing conditions, and clearly a more thorough modelling approach is required to account for these effects. The inherent fibre mesostructure exhibits large variations in local volume fraction, with local alignment of fibres and filament end synchronisation as shown by (Figure 3-13). Potentially a multi-scaled (microscopic, mesoscopic and macroscopic) approach is required to account for the unusual fibre architecture.

The analytical models in their present form are unable to account for large variations in areal mass. It is assumed that the fibres, although randomly dispersed, are distributed uniformly and hence zero fibre areas are overlooked. An analytical solution that can account for irregularities in the mesostructure would be favourable, similar to the work of Pan [91, 93], since fibre coverage is such a dominant factor.

It is clear that most of these developments require prior knowledge of the bundle size distribution and this is a major barrier for accurate property prediction. It is difficult to capture the bundle size with existing methods, because image analysis techniques rely on a constant aspect ratio in order to determine and compensate for off-axis orientations. The bundles have irregular shapes due to fibre-fibre interaction and conformity. Under certain conditions a wide range of bundle sizes are expected and this will significantly affect the mechanical performance of the composite.

## *4.3. DCFP stiffness model*

### 4.3.1. Introduction

From the discussion in Section 4.2 it has been established that a multi-scale modelling approach is required to account for the meso-scale DCFP architecture. Methodology similar to [119, 179, 180] will be adopted, utilising micro-mechanical models at the first two levels to consider the effects of the constituent materials. Level 1 determines the effective properties of UD, impregnated tows, whilst Level 2 determines the properties of UD sub-units consisting of UD tows embedded in matrix (Figure 4-3).

Finally, Level 3 randomises the sub-units using an orientation averaging process to simulate a random fibre composite. The model is extended to a fourth level to account for filament count distributions, utilising an aggregate averaging process. A concise overview of the model is given in the following sections, but a full derivation is provided in Appendix.H.

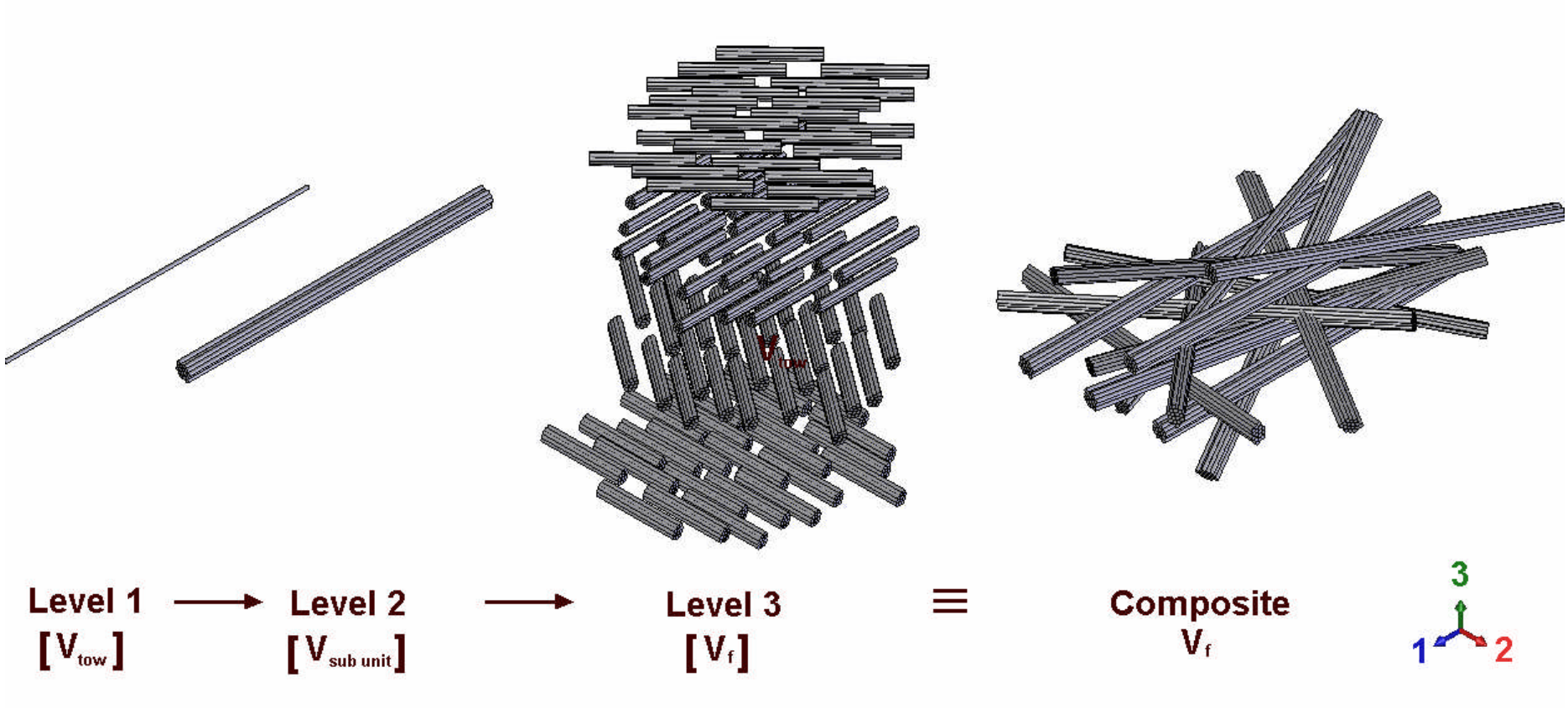


**Figure 4-3 Three level modelling strategy for random composite property prediction (not to scale). The constituent properties of the carbon filaments and the epoxy matrix are used at level 1 to determine tow data. At level 2 tows are arranged into UD plies and are orientationally averaged at level 3. The relationship between the relative input volume fractions at each level can be calculated from Equation 4-20.**

### 4.3.2. Level 1 - Elastic constants of a transversely isotropic bundle

A carbon fibre tow is assumed to be a transversely isotropic unit containing multiple filaments of a constant diameter (filaments are randomly distributed through the tow cross section in the 2-3 plane as shown by Figure 4-4). The elastic constants of the tow have been calculated using the Qiu and Weng model [173] previously reviewed in Section 4.2.3.

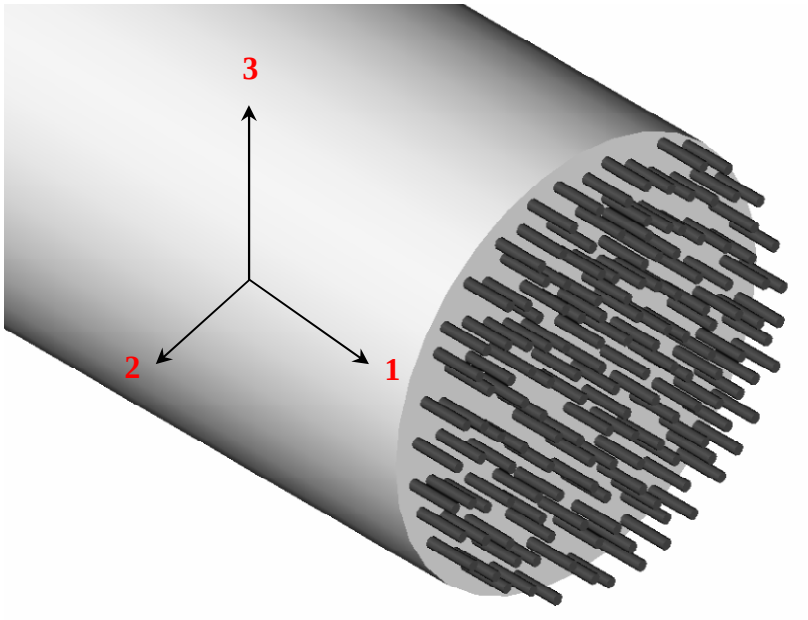


**Figure 4-4 Transversely isotropic carbon tow**

Following the notation used by Hill [181], the stress-strain relationship for a transversely isotropic arrangement of fibres is as follows:

$$\sigma = L_{tow}\varepsilon \qquad \textbf{Equation 4-9}$$

where $L_{tow}$ is the effective stiffness tensor of the tow.

Weng's [172] reformulation of the Mori-Tanaka theory is thus used to calculate the effective moduli for the composite under a prescribed displacement:

$$L_{tow} = \left( \sum_{r=0}^{1} c_r L_r A_r \right) \left( \sum_{r=0}^{1} c_r A_r \right)^{-1}$$ **Equation 4-10**

Subscript $r$ refers to the phase, where 0 is the matrix phase and 1 the reinforcement phase. $L_r$ and $c_r$ are the elastic moduli tensor and the volume fraction of the $r^{th}$ phase respectively. Therefore $c_1$ is equivalent to the assumed tow volume fraction, $V_{tow}$ (volume of carbon filaments within the tow). $A_r$ is the average strain-concentration tensor, which relates the average strain in the $r^{th}$ phase inclusion to the far field boundary strain in the infinite matrix. This can be calculated as follows:

$$A_r = \left[ I + S_0 L_0^{-1} \left( L_r - L_0 \right) \right]^{-1}$$ **Equation 4-11**

where $I$ is the fourth order unit tensor, $I = [1,0,0,1,1,1]$. $S_0$ is the Eshelby $S$-tensor for the matrix phase [155] and this is a function of inclusion aspect ratio and matrix Poisson's ratio (see Appendix.H for details). According to Hill [181], if the effective stiffness tensors of the $r^{th}$ phases ($L_r$) possess diagonal symmetry they can be expressed as only five components:

$$L_r = (2k, l, n, 2m, 2p)$$ **Equation 4-12**

$k$, $l$, $n$, $m$, $p$ are therefore the plane-strain bulk modulus, cross modulus, axial modulus under axial strain, and the transverse and axial shear moduli respectively. These are the main inputs for the model and are determined experimentally for each of the respective phases. The effective stiffness tensor components for carbon and epoxy are summarised in Table 4-1. The output for this level of the model is in the form of Equation 4-10. The components of the stiffness tensor of the tow, $L_{tow}$ can be used directly to calculate the conventional engineering constants of the carbon/epoxy tow:

$$E_{11} = n - \frac{l^2}{k}$$ **Equation 4-13**

$$\nu_{12} = \frac{l}{2k}$$ **Equation 4-14**

$$\mu_{23} = m \qquad \textbf{Equation 4-15}$$

$$\mu_{12} = p \qquad \textbf{Equation 4-16}$$

$$k_{23} = k \qquad \textbf{Equation 4-17}$$

$$E_{22} = \frac{4\left(kn - l^2\right)m}{n\left(m + k\right) - l^2} \qquad \textbf{Equation 4-18}$$

Figure 7-51 (Appendix.H) shows the effect of increasing tow volume fraction on the six elastic constants calculated from Equation 4-13 through to Equation 4-18. The longitudinal modulus $E_1$ is identical to the continuous fibre case in Figure 4-2, which implies that a fibre length of 23mm is beyond the critical length.

| Property | | Phase | | Bundle |
|---|---|---|---|---|
| | | r =1 | r =0 | |
| Plane strain bulk modulus (GPa) | $k_r$ | 20.19 | 4.53 | 8.97 |
| Cross modulus (GPa) | $l_r$ | 12.14 | 3.44 | 5.90 |
| Axial modulus under axial strain (GPa) | $n_r$ | 234.23 | 5.62 | 141.25 |
| Transverse shear modulus (GPa) | $m_r$ | 8.06 | 1.09 | 2.74 |
| Axial shear modulus (GPa) | $p_r$ | 10.00 | 1.09 | 3.11 |

**Table 4-1 Effective stiffness tensor components for carbon (phase 1) and epoxy (phase 0). Values for carbon are taken directly from [173] and represent the Tenax STS fibre. Values for epoxy are experimental but are expressed in the present form using Equation 7-45 through to Equation 7-48 (see Appendix H.1). The final column shows typical values for a carbon/epoxy bundle at a constant tow volume fraction of 60%.**

### 4.3.3. Level 2 - Elastic constants of a UD ply containing tows

The discontinuous carbon bundles generated at Level 1 are subsequently arranged in UD ply formation to create a theoretical sub-unit. Carbon bundles are assumed to be the reinforcement phase at Level 2, with an effective diameter ($Ø_{tow}$) proportional to the filament count and filament diameter, but inversely proportional to the tow volume fraction:

$$Ø_{tow} = \sqrt{\frac{N Ø^2_{fil}}{V_{tow}}} \qquad \textbf{Equation 4-19}$$

Level 2 seeks to determine the elastic stiffness tensor of the sub-units ($L_{sub}$) by substituting $L_{tow}$ back into the model and repeating Level 1. Although the filaments at Level 1 were discontinuous, a sensitivity analysis showed that the aspect ratio was beyond the critical value for the practical range of DCFP chop lengths and is considered to be continuous for fibre lengths between 3mm and 115mm. The length efficiency of the reinforcement is therefore determined at the bundle level since Figure 3-17 confirms that bundles behave as single reinforcement units. The volume fraction at Level 2 ($V_{sub\ unit}$) is a function of the tow volume fraction at Level 1 and the overall composite volume fraction ($V_f$) at Level 3. $V_{sub\ unit}$ is a volume fraction adjustment to account for the volume of resin contained within the tow at Level 1:

$$V_{sub\,unit} = \frac{V_f}{V_{tow}}$$ **Equation 4-20**

The effective stiffness tensor from Level 2 is summarised in Table 4-2 for a UD ply containing 3K carbon bundles. The effective stiffness tensor of the UD ply, $L_{sub}$ can be expressed in tensor form using Hill's [181] notation:

$$C_{ij} = \begin{pmatrix} n & l & l & 0 & 0 & 0 \\ l & m+k & k-m & 0 & 0 & 0 \\ l & k-m & m+k & 0 & 0 & 0 \\ 0 & 0 & 0 & m & 0 & 0 \\ 0 & 0 & 0 & 0 & p & 0 \\ 0 & 0 & 0 & 0 & 0 & p \end{pmatrix}$$ **Equation 4-21**

| Property | | UD Ply |
|---|---|---|
| Plane strain bulk modulus (GPa) | $k$ | 6.12 |
| Cross modulus (GPa) | $l$ | 4.36 |
| Axial modulus under axial strain (GPa) | $n$ | 67.75 |
| Transverse shear modulus (GPa) | $m$ | 1.66 |
| Axial shear modulus (GPa) | $p$ | 1.78 |

**Table 4-2 Components of the effective stiffness tensor for a UD ply containing 3K carbon bundles. A tow volume fraction and final laminate volume fraction of 60% and 30% are assumed respectively.**

### 4.3.4. Level 3 - Orientation averaging

The spatial orientation of a single fibre can be described by the Cartesian components ($p_1$, $p_2$, $p_3$) of a unit vector ***p***, as shown in Figure 7-53 [154]. A representative element of the present random material contains many fibres of a constant length but different orientations, which can be generally described by a probability density function $\psi(\theta,\phi)$. Although the probability density function is a complete description, orientation tensors are more compact and are formed by calculating the dyadic product of the vector ***p*** and integrating with the distribution function over all possible directions. Only the even order tensors are of interest, since the odd orders are all zero. The second and fourth order orientation tensors are evaluated as:

$$a_{ij} = \left\langle p_i p_j \right\rangle \equiv \int_0^{2\pi}\int_0^{\pi} p_i p_j \psi(\theta,\phi) \sin\theta \, d\theta \, d\phi \qquad \textbf{Equation 4-22}$$

$$a_{ijkl} = \left\langle p_i p_j p_k p_l \right\rangle \equiv \int_0^{2\pi}\int_0^{\pi} p_i p_j p_k p_l \psi(\theta,\phi) \sin\theta \, d\theta \, d\phi \qquad \textbf{Equation 4-23}$$

where $\langle\ \rangle$ denotes the orientational average.

The primary advantage of a tensorial approach over CLT is the ability to incorporate 3D fibre distributions. All of the orientation components can be derived experimentally by measuring the in-plane ($\phi$) and out-of-plane ($\theta$) fibre orientations from optical micrographs. This is discussed in detail in Section 4.3.6. A closure approximation is then used to represent the data set, which governs the precision of predictions when using tensors rather than a complete probability density function [154]. This stage of the model determines the off-axis properties for the UD ply generated in Section 4.3.3. Invariants of the effective stiffness tensor in Equation 4-21 are multiplied by second and fourth order orientation tensors in order to describe a distribution of fibre angles.

The orientation averages are calculated directly from the orientation tensors and the fourth order stiffness matrix $C_{ijkl}$ [182]. The invariants of $C_{ijkl}$ can be expressed in contracted form using Equation 4-21:

$$B_1 = C_{11} + C_{22} - 2C_{12} - 4C_{66} \quad \textbf{Equation 4-24}$$

$$B_2 = C_{12} - C_{23} \quad \textbf{Equation 4-25}$$

$$B_3 = C_{66} + \tfrac{1}{2}\left(C_{23} - C_{22}\right) \quad \textbf{Equation 4-26}$$

$$B_4 = C_{23} \quad \textbf{Equation 4-27}$$

$$B_5 = \tfrac{1}{2}\left(C_{22} - C_{23}\right) \quad \textbf{Equation 4-28}$$

The final orientation average of the stiffness tensor $C_{ijkl}$ is calculated using the invariants ($B$) and the second ($a_{ij}$) and fourth ($a_{ijkl}$) order orientation tensor components from Equation 4-22 and Equation 4-23 as follows:

$$\begin{aligned}\left\langle C_{ijkl} \right\rangle = {} & B_1 a_{ijkl} + B_2\left(a_{ij}\delta_{ij} + a_{kl}\delta_{ij}\right) \\ & + B_3\left(a_{ik}\delta_{jl} + a_{il}\delta_{jk} + a_{ji}\delta_{ik} + a_{jk}\delta_{il}\right) \\ & + B_4\left(\delta_{ij}\delta_{kl}\right) + B_5\left(\delta_{ik}\delta_{jl} + \delta_{il}\delta_{jk}\right)\end{aligned} \quad \textbf{Equation 4-29}$$

where $\delta_{ij}$ is the Kronecker delta function. The compliance matrix $\left\langle S_{ijkl} \right\rangle$ of the random composite is therefore calculated from the inverse of the stiffness matrix $\left\langle C_{ijkl} \right\rangle$ in order to determine the engineering constants of a laminate containing random bundles of a fixed filament count.

### 4.3.5. Level 4 - Aggregate averaging

Finally, the multi-level modelling approach is extended further here to accommodate a distribution of filament counts. Following the model of Camacho and Tucker [182], the laminate is assumed to be a hybrid, containing multiple, two-phase composites. Each two-phase composite has a different mean filament count and each corresponding stiffness matrix $\langle C_{ijkl} \rangle$ is determined using the multi-level approach outlined in Sections 4.3.2 to 4.3.4. The effective diameter of the constituent tows in each composite is a function of the number of filaments. The stiffness matrix of the overall

random laminate is determined by averaging the stiffness matrices of all the two-phase composites, assuming a constant strain is applied to each.

$$\{C\} = \sum_{i=1}^{N} \alpha_i \langle C^i \rangle \qquad \textbf{Equation 4-30}$$

where $<C^i>$ is the stiffness tensor of the $i^{th}$ two-phase composite (post orientation averaging), $N$ is the total number of discrete bundle sizes and $\alpha_i$ is the proportion of tows of a specific filament count. This aggregate averaging procedure takes the same form as the orientational averaging of Advani and Tucker [154] however, in the present work the weighting fraction ($\alpha_i$) refers to the volume of material assigned to each two-phase composite, rather than the volume assigned to the orientation.

It is possible to introduce a range of filament counts into the model at Level 2, prior to the orientation averaging stage. This route would have eliminated the need for aggregate averaging, since each reinforcement phase (each filament count) would be weighted according to volume fraction within the ply. However, separate orientation and aggregate averaging is preferred, since Benveniste *et al.* [183] show that for a linear elastic multiphase composite, diagonal symmetry of the overall stiffness tensor is guaranteed only when the dispersed inclusions have the same shape, aspect ratio and alignment. Asymmetry would be lost for this material, especially for short bundle lengths, since a large range in aspect ratios can be expected between single filaments and non-filamentised tows.

### 4.3.6. Image analysis methodology

The presented model for DCFP stiffness prediction relies on empirical parameters to accurately describe the fibre architecture because of processing variability. Optical photomicrographs have been taken to determine tow volume fraction, filament count distribution and out-of-plane orientation distribution, using the methodology outlined in Appendix H.5.

Sections from tensile test specimens were cast using high clarity polyester resin. Once cured, specimens were ground parallel using a ceramic wheel and then polished using a succession of abrasive papers (see Appendix E.1). Micrographs were captured using Aphelion image analysis software via a monochrome CCD on a Zeiss microscope. Images of 512 x 512 pixels were taken using both ×5 and ×50 magnification lenses to determine bundle and filament properties respectively. Image acquisition was automated using to capture large fields of interest using an in-house macro [184].

#### *4.3.6.1. Filament count distribution*

Ten contiguous images were taken for each sample at the bundle level (×5 magnification) using a Multicontrol® 2000 stage to ensure image alignment. This procedure was repeated 3 times per material permutation, taking sections from different specimens in each case. Micrographs were compiled into 5120x512 montages and a 4000x400 region was selected from the centre. A 'white-top-hat' transformation was performed to homogenise the pixel intensity of the matrix background, in order to differentiate it from the fibres. The images were subsequently segmented according to a threshold value (see Appendix H.5), which was used to convert the micrograph into a binary image of fibre and non-fibre regions. The selection of an appropriate pixel threshold intensity was apparent by a sharp peak in the intensity histogram in each case (see Figure 7-60, Appendix H.5).

UTHSCSA ImageTool v3 (developed by the University of Texas Health Science Centre at San Antonio) was used to find objects in the image and to characterise them with respect to the area of a single pixel, following the methodology outlined by Turner [185]. A graticule was used to establish a conversion factor of 242 pixels per linear millimetre for the images taken at ×5 magnification. This was used to convert number of pixels into number of filaments, assuming a constant tow volume fraction of 60%. An average tow volume fraction was established by taking micrographs from random locations inside large tows at a magnification of ×50. A sensitivity analysis in Section 4.4.1 indicates that the stiffness predictions are insensitive to tow volume fraction for laminates containing low (~10) filament count bundles. However, an increase in tow

volume fraction from 60% to 70% for a tow filament count of 12,000 results in a 5% reduction in the overall composite stiffness.

The resolution of the micrographs at the ×5 magnification level is 4μm/pixel, which is of the same order of magnitude as the radius of a single monofilament. The accuracy of this method is therefore limited for determining bundle sizes of low filament counts (<10 filaments per bundle), but the methodology is effective for capturing the wide range in scale experienced with the DCFP material. However, the sensitivity analysis in Section 4.4.1 shows that the stiffness prediction is insensitive to the tow filament count below a value of 100 filaments for this fibre length.

The frequency of each respective filament count was expressed as a percentage of the total image area. A reduction factor of 0.6366 was determined to compensate for non-perpendicular tows in the micrograph plane, resulting from the random in-plane fibre orientation distribution. The average increase in cross sectional area was calculated for a cylindrical filament rotated between 0º and 90º, based on the error estimation technique for 3D fibre orientations presented in [186]. The number of filaments observed in each bundle was multiplied by the reduction factor and the data was subsequently filtered into discrete classes, based on the number of filaments contained within each bundle of constant volume fraction. A convergence study was performed on the two extreme data sets from the filament count study in Chapter 3 (Fibre II-0% and Fibre I-100%), to determine the number of class intervals required to accurately summarise the data. One hundred class intervals gave sufficient resolution when compared with the exact solution (within a 99% confidence limit of using 24,000 individual classes for each filament count) and the rate of convergence was maximised by adopting a logarithmic relationship to increment the upper bound of each class $\beta_i$. The class intervals were increased by a factor of $10^{0.0445}$ to provide 100 bins from 1 to 24,000:

$$\beta_i = \beta_{i-1} \times 10^{0.0445} \qquad \text{for } i=1 \text{ to } 100 \qquad \text{where } \beta_0=1 \qquad \textbf{Equation 4-31}$$

Equation 4-31 is therefore used to calculate $\alpha_i$ in Equation 4-30 (the proportion of tows of size $\beta_{i-1} \times 10^{0.0445}$ for classes $\beta_1$ to $\beta_{100}$) and the tow diameter.

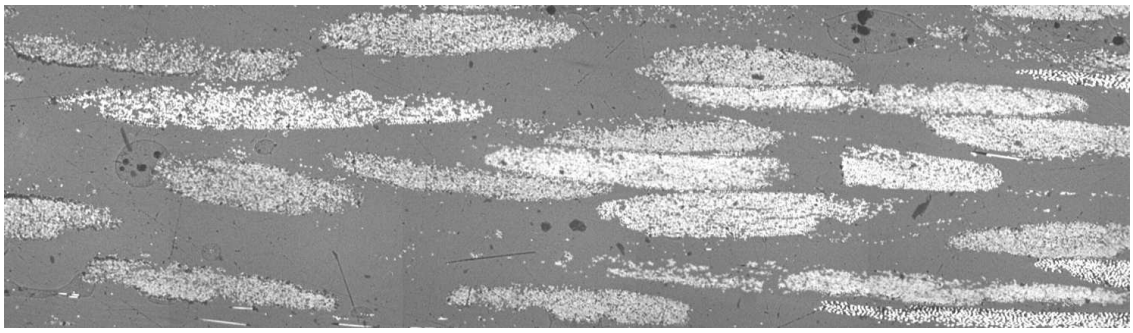

**Figure 4-5 One optical micrograph of a section through a laminate containing constant 3K carbon bundles which was used to validate the image analysis method. The bundles resist fragmentation and consequently very few single filaments exist. Images were taken at ×5 magnification.**

The image analysis methodology has been validated by comparing stiffness predictions with experimental data, to ensure that the filament count distributions are representative. A 3K carbon tow that resists fragmentation was used as a suitable benchmark to provide a laminate with tows of a constant filament count (see Figure 4-5). Stiffness predictions were initially made using the first three levels of the model, assuming a mean filament count of 3000. Predictions were subsequently repeated using the four-level model, incorporating a filament count distribution determined by image analysis (Figure 4-6). A comparison with the experimental data is presented in Figure 4-7. Firstly, the constant filament count prediction is in excellent agreement with the experimental data and an error of only 5% suggests that the micromechanical model is accurate in this instance. Secondly, the prediction utilising the filament count distribution is within 3% of the constant filament count prediction, which implies that the image analysis technique is representative.

A selection of distributions is presented in Figure 4-8 for the extreme filamentisation cases of Fibres I and II studied in Chapter 3. Mean filament counts range from 425 to 983 (Fibre I) and 3378 to 5572 (Fibre II) depending on the level of induced filamentisation imposed on the 24K STS tow.

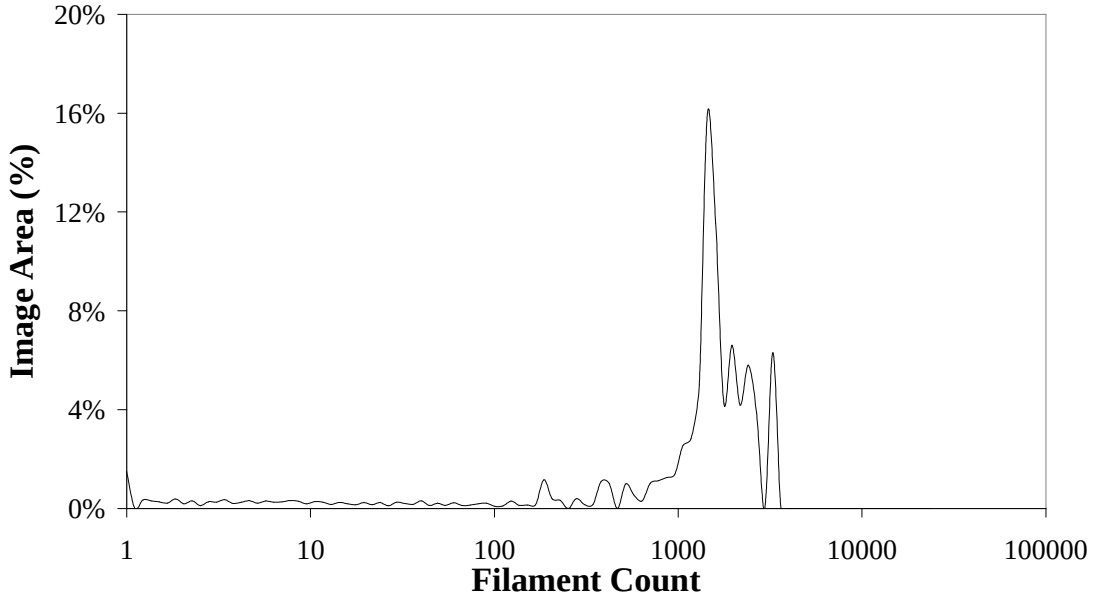


**Figure 4-6 Filament count distribution for a 3K AS4 carbon tow.**

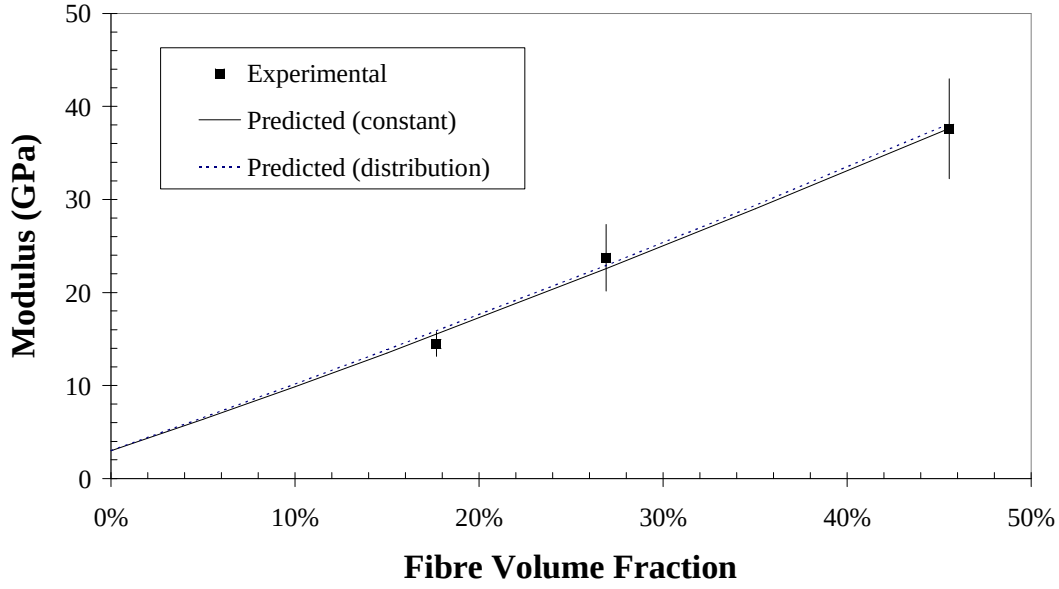


**Figure 4-7 Validation of the image analysis technique used for determining tow filament count distributions. A comparison is presented between experimental data and predictions from the multi-level stiffness model. The experimental laminate was manufactured using 3K AS4 carbon tows, which exhibit low levels of natural filamentisation. The solid line assumes a constant mean filament count of 3K and the dotted line is determined using the filament count distribution presented in Figure 4-6.**

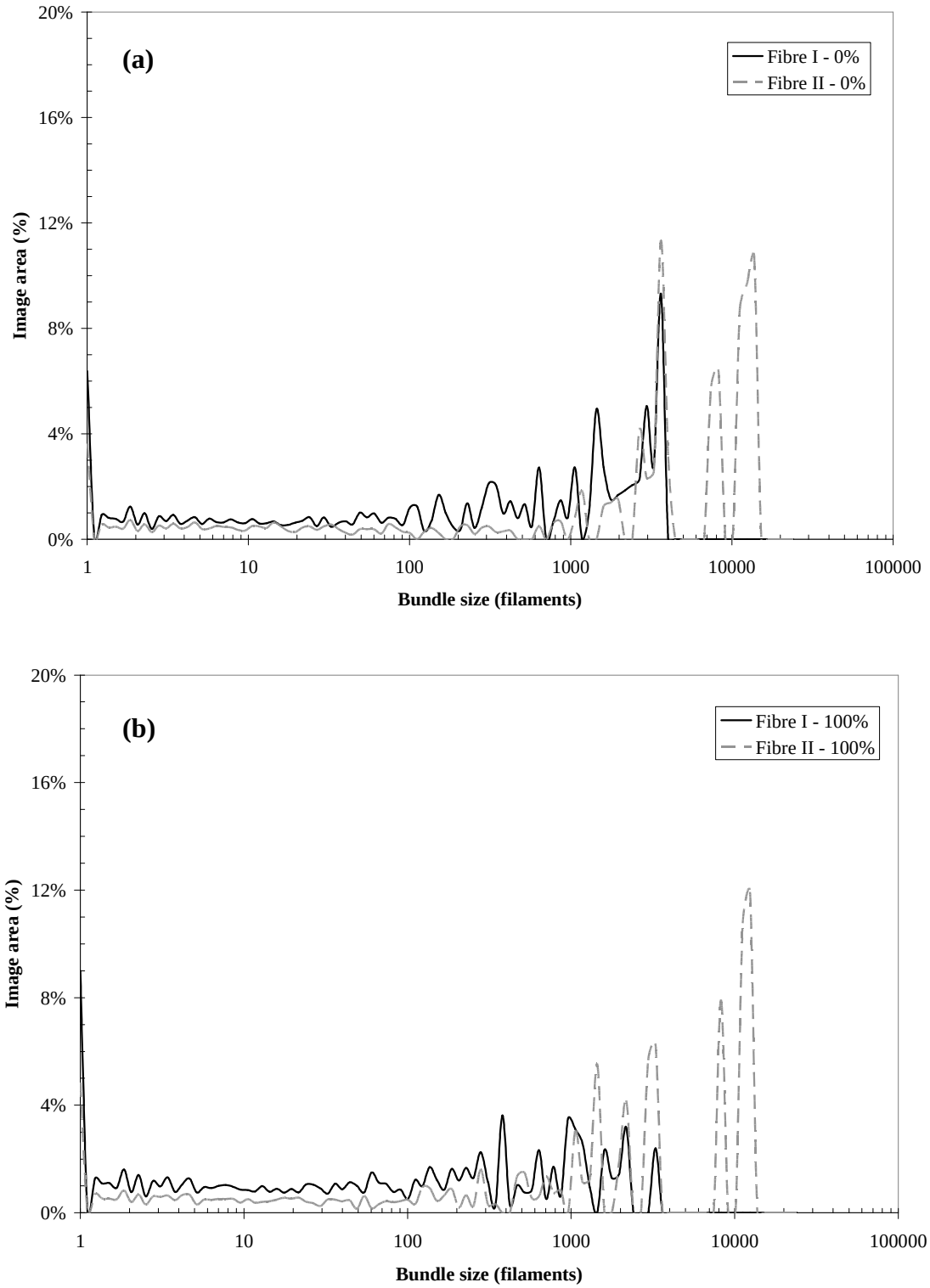


**Figure 4-8 Filament count distributions for (a) 0% induced filamentisation and (b) 100% induced filamentisation for both Fibres I and II**

### *4.3.6.2. Orientation distributions*

In the present case the fibre length is often much longer than micrograph dimensions (approximately 2mm×2mm) and therefore there is insufficient resolution to determine the in-plane distribution experimentally. The in-plane orientation distribution is assumed to be uniformly random, since tensile tests in Chapter 3 confirm that there is no measurable difference in mechanical properties parallel and perpendicular to the direction of robot travel with the present installation at Nottingham.

The out-of-plane fibre orientation distribution was determined experimentally by taking images at the filament level (×50 magnification). Rather than using contiguous images, micrographs were taken at 2mm intervals to ensure that filaments were sampled from different tows. Up to 60,000 individual filaments were sampled for each level of filamentisation. Images were converted to binary and a series of erosion and dilation operators were used to clearly define the boundary of contacting filaments (using a macro written by Fan [184]). A mean best rectangle was then fitted to each object in the image using the Aphelion software and the orientation of the major axes from the horizontal gave a measure of the out-of-plane orientation (see Figure 4-9).

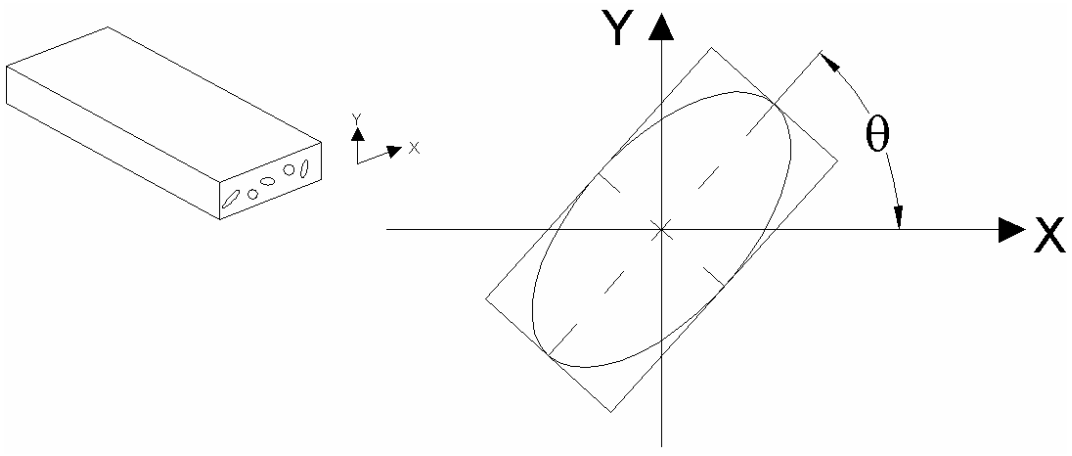


**Figure 4-9 Schematic showing how the out-of-plane fibre orientations were measured. A mean best rectangle was established for each filament and the orientation was measured between the major axis of the ellipse and the x-axis.**

Little variation in out-of-plane distribution was observed for the different fibre architectures. A non-linear regression analysis was performed in each case to

summarise the orientation data. Figure 4-10 shows a trigonometric function fitted to the data in the form of Equation 4-32:

$$\psi(\theta,\phi) = a \sin^{2(b-1)} \theta \qquad \textbf{Equation 4-32}$$

'*a*' is a normalisation constant to ensure the area under the probability distribution function is equal to unity. The parameter, '*b*', controls the shape of the out-of-plane distribution and is approximately 26 for both Fibre I and Fibre II in all cases. To contextualise, when '*b*' is infinity all of the fibres are aligned in the 1-2 plane. When '*b*' is unity the fibres are 3D random in space and when '*b*' is zero all of the fibres are aligned in the 3-direction (i.e. all fibres are out-of-plane). Equation 4-32 can subsequently be used in Equation 4-22 and Equation 4-23 to determine the second and fourth order orientation tensor components.

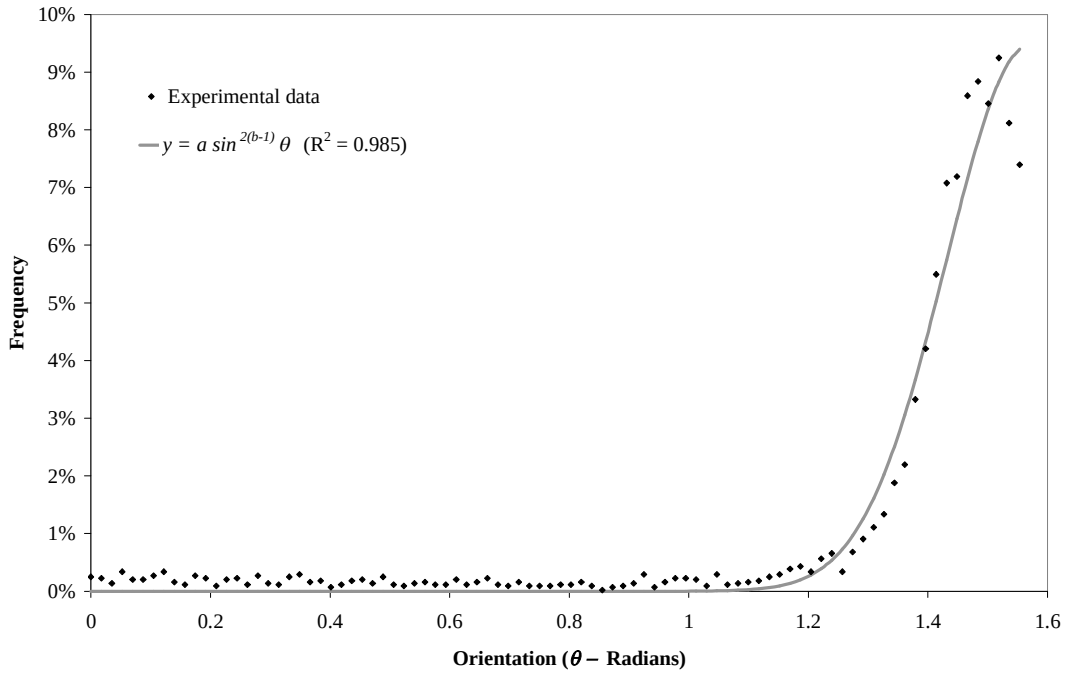


**Figure 4-10 Representative out-of-plane orientation distribution for DCFP laminates, where $\theta$ is measured from the vertical, (see Figure 7-53). (All of the fibres are aligned out of the loading plane when $\theta$ is zero, and are all in-plane when $\theta$ is 1.57 ($\pi$/2)). Experimental data was filtered into 1º classes, which were subsequently converted into radians. Non-linear regression was performed in order to fit a trigonometric function to the data, where *b*~26 for each filamentisation case and *a* is an integration constant dependent on the size of the population. $R^2$ is the Pearson correlation factor.**

| | Shape Parameter *b* | | | | | | | | | | | | | |
|---|---|---|---|---|---|---|---|---|---|---|---|---|---|---|
| | ∞ | 1000 | 300 | 200 | 100 | 50 | 25 | 20 | 15 | 10 | 5 | 3 | 1 | 0 |
| | 2D Random | | | | | | | | | | | | 3D Random | Aligned 3-axis |
| **Tensor** | | | | | | | | | | | | | | |
| $a_{11}$ | 0.5000 | 0.4998 | 0.4992 | 0.4988 | 0.4975 | 0.4950 | 0.4902 | 0.4878 | 0.4839 | 0.4762 | 0.4545 | 0.4286 | 0.3333 | 0.0000 |
| $a_{22}$ | 0.5000 | 0.4998 | 0.4992 | 0.4988 | 0.4975 | 0.4950 | 0.4902 | 0.4878 | 0.4839 | 0.4762 | 0.4545 | 0.4286 | 0.3333 | 0.0000 |
| $a_{33}$ | 0.0000 | 0.0005 | 0.0017 | 0.0025 | 0.0050 | 0.0099 | 0.0196 | 0.0244 | 0.0323 | 0.0476 | 0.0909 | 0.1429 | 0.3333 | 1.0000 |
| $a_{1111}$ | 0.3750 | 0.3746 | 0.3738 | 0.3731 | 0.3713 | 0.3677 | 0.3607 | 0.3573 | 0.3519 | 0.3416 | 0.3147 | 0.2857 | 0.2000 | 0.0000 |
| $a_{2222}$ | 0.3750 | 0.3746 | 0.3738 | 0.3731 | 0.3713 | 0.3677 | 0.3607 | 0.3573 | 0.3519 | 0.3416 | 0.3147 | 0.2857 | 0.2000 | 0.0000 |
| $a_{3333}$ | 0.0000 | 0.0000 | 0.0000 | 0.0000 | 0.0001 | 0.0003 | 0.0011 | 0.0017 | 0.0029 | 0.0062 | 0.0210 | 0.0476 | 0.2000 | 1.0000 |
| $a_{1122}$ | 0.1250 | 0.1249 | 0.1246 | 0.1244 | 0.1238 | 0.1226 | 0.1202 | 0.1191 | 0.1173 | 0.1139 | 0.1049 | 0.0952 | 0.0667 | 0.0000 |
| $a_{1212}$ | 0.1250 | 0.1249 | 0.1246 | 0.1244 | 0.1238 | 0.1226 | 0.1202 | 0.1191 | 0.1173 | 0.1139 | 0.1049 | 0.0952 | 0.0667 | 0.0000 |
| $a_{1133}$ | 0.0000 | 0.0002 | 0.0008 | 0.0012 | 0.0025 | 0.0048 | 0.0092 | 0.0113 | 0.0147 | 0.0207 | 0.0350 | 0.0476 | 0.0667 | 0.0000 |
| $a_{2233}$ | 0.0000 | 0.0002 | 0.0008 | 0.0012 | 0.0025 | 0.0048 | 0.0092 | 0.0113 | 0.0147 | 0.0207 | 0.0350 | 0.0476 | 0.0667 | 0.0000 |
| $a_{1313}$ | 0.0000 | 0.0002 | 0.0008 | 0.0012 | 0.0025 | 0.0048 | 0.0092 | 0.0113 | 0.0147 | 0.0207 | 0.0350 | 0.0476 | 0.0667 | 0.0000 |
| $a_{2323}$ | 0.0000 | 0.0002 | 0.0008 | 0.0012 | 0.0025 | 0.0048 | 0.0092 | 0.0113 | 0.0147 | 0.0207 | 0.0350 | 0.0476 | 0.0667 | 0.0000 |

**Table 4-3** **Tensor components calculated for a range of out-of-plane orientation distribution shape parameters (Equation 4-32).**

## 4.4. Results and discussion

The multi-stage stiffness model developed above is applied here to experimental data from Chapter 3. A sensitivity study is performed to investigate the effect of a number of key parameters, some of which have been assumed during the development of the model. Predictions are then compared with the remaining data in Chapter 3 to investigate the effects of filament count and fibre length.

### 4.4.1. Sensitivity study

The sensitivity of the current model to a number of key parameters is investigated in Figure 4-12 through to Figure 4-16. The input data used for the model is shown in Table 4-4. Figure 4-12 shows the theoretical effect of a mean filament count on the calculated modulus of the composite ($E_1 = E_2$) for a constant laminate volume fraction of 30%. Modulus is approximately constant for tows containing fewer than 100 filaments. For a fixed volume of carbon, homogeneity is optimised when large tows are split into smaller bundles. The graph shows that tows with increasingly larger filament counts display a gradual reduction in modulus, where laminates produced from bundles containing 24,000 filaments have a modulus 42% lower than laminates comprising single filaments.

Two normal distributions have been used to model generic filament count distributions in order to examine the sensitivity of the analytical prediction to various other input parameters (Table 4-5 and Figure 4-11). These distributions have been chosen to represent two extreme levels of induced filamentisation for a 14mm long tow. Figure 4-13 shows the theoretical effect of composite fibre volume fraction on modulus for both distributions. The highly filamentised material responds linearly to volume fraction whereas the lower filament count material displays reduced properties across all observed $V_f$ levels. This can be attributed to the smaller bundle aspect ratio (length/diameter) for the low level case. It has previously been shown that $E_1$ is particularly sensitive to aspect ratio and that tows with aspect ratios exceeding 200 can be considered to be continuous (predictions for $E_1$ within 99% of continuous case in Section 4.2.3). For the current work the average tow aspect ratios are approximately 15

and 500 for the low and high filamentisation cases respectively. The distributions converge at the limiting volume fraction of 0.6 (where composite volume fraction equals tow volume fraction), above which no rational results lie.

| Property | Value | | Designation |
|---|---|---|---|
| Fibre length | 14.375 | mm | $l$ |
| Filament diameter | 0.007 | mm | $Ø_f$ |
| Tow volume fraction | 0.6 | | $V_{tow}$ |
| Plane strain bulk modulus | 20.19 | GPa | $K_i$ ($k_{23}$) |
| Cross modulus | 12.14 | GPa | $L_i$ |
| Axial modulus under axial strain | 234.23 | GPa | $n_i$ |
| Transverse shear modulus | 8.06 | GPa | $m_i$ ($m_{23}$) |
| Axial shear modulus | 10 | GPa | $p_i$ ($m_{12}$) |
| Matrix Poisson's ratio | 0.38 | | $v_o$ |
| Matrix modulus | 3 | GPa | $E_o$ |
| Composite volume fraction | 0.3 | | $V_f$ |
| Out of plane parameter *(see Equation 4-32)* | ∞ | | $b$ |

**Table 4-4 Analytical model input parameters, where subscript i denotes the ith reinforcement phase corresponding with Equation 4-10 and subscript o refers to the matrix phase. The out-of-plane parameter of infinity assumes the fibres are perfectly planar. Data for carbon fibre has been taken from [173] and data for the epoxy matrix has been determined experimentally.**

| Level of induced filamentisation | Mean filament count | Standard deviation |
|---|---|---|
| Low | 12,000 | 1,400 |
| High | 10 | 5 |

**Table 4-5 Two normal distributions used to model generic bundle distributions for extreme levels of induced filamentisation**

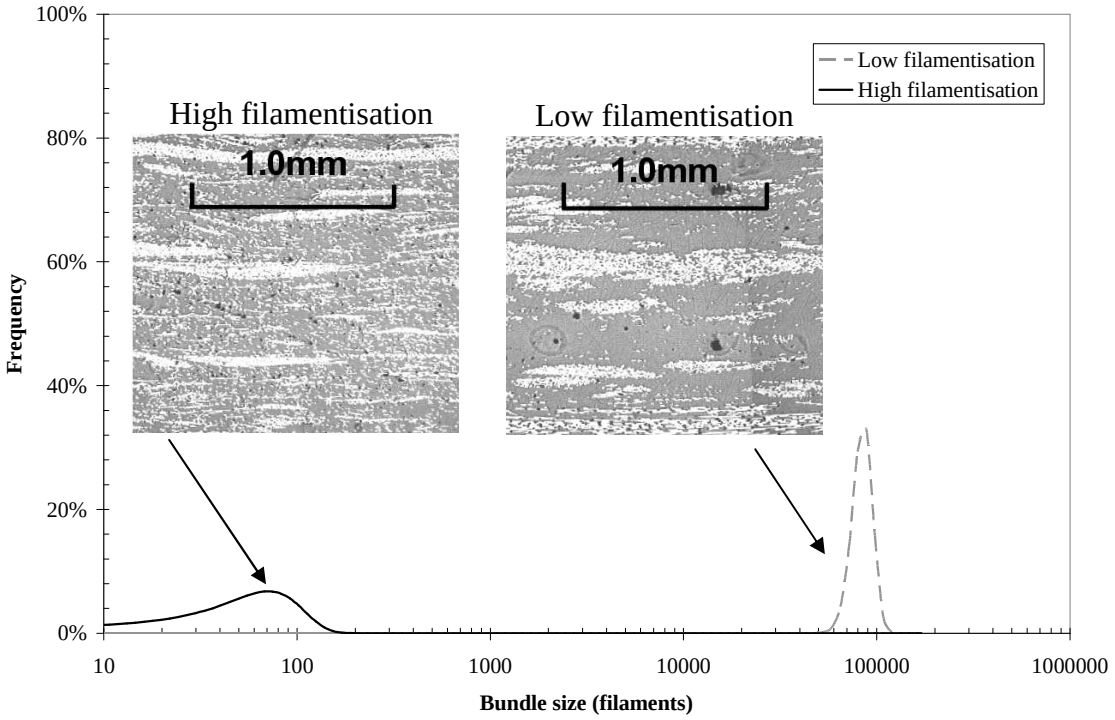


**Figure 4-11 Generic frequency distribution for two fibre types. Micrographs show typical 6mm fibre length meso-structures.**

Figure 4-14 shows the effect of tow volume fraction for the two generic distributions. Tow volume fraction has no effect on the highly filamentised material as the variation in aspect ratio is insignificant, since both filament and bundle levels are over the respective critical values. However, beyond a volume fraction of 30% (lower limit for tow volume fraction in this instance, where $V_{tow} = V_f$), the low filamentised material exhibits a reduction in modulus. Increasing the tow volume fraction effectively reduces the homogeneity of the laminate by creating regions of high fibre concentration surrounded by matrix rich zones. Maximum reduction in properties at a ceiling value of $V_{tow}$ (90.7% assuming hexagonal packing of filaments) is 39%. A representative value of 60% was determined for $V_{tow}$ from micrographs of large fibre bundles and will be used in subsequent analyses.

The effects of matrix modulus can be seen in Figure 4-15 to affect the two generic materials differently. The highly filamentised material retains higher composite modulus at much lower values of matrix modulus compared with the low filamentisation case. This suggests that the laminate properties are much more matrix

dominated for higher filament counts, since there is a large variation in local volume fraction in the laminate as a result of more highly concentrated filament regions and clearer matrix rich regions (see micrographs Figure 4-11). At a baseline matrix modulus of 3GPa the modulus of the low filamentisation material is 31% lower than the highly filamentised case, this disadvantage increases to 41% at $E_0$=2GPa and to 59% at $E_0$=1GPa.

A sensitivity analysis is presented in Figure 4-16 to determine the effect of introducing an increasing proportion of out-of-plane fibres. Component $a_{33}$ is the orientation average of $\langle p_3 p_3 \rangle$ and provides a direct measure of the degree of out-of-plane fibres. The parameter '*b*' (Equation 4-32) is inversely proportional to $a_{33}$ and $a_{3333}$ and therefore a range of values can be used to investigate the generic effect of non-planar fibre orientations on the elastic properties. Figure 4-16 shows the results of a sensitivity analysis to determine the effect of out-of-plane angles on the stiffness of DCFP laminates. Second and fourth order tensor components are listed in Table 4-3 for range of values of *b*. The in-plane modulus is significantly reduced by introducing out-of-plane fibres. There is approximately a 40% reduction in the tensile stiffness when the fibre orientation state changes from 2D random to 3D random for both levels of filamentisation. However, in practice the 14mm fibres are much longer than the 3mm cavity depth, therefore out-of-plane angles ($\theta$) are limited. From Figure 4-10 the maximum out-of-plane angle is 26º (measured from the 1-2 plane, indicated on the graph at $\theta$=*1.117* radians). Using an appropriate value of *b*=26 reduces the laminate modulus by only 5% for each filamentisation case, compared with a planar fibre distribution. Since the current model uses a separate orientation and aggregate averaging approach it enables a different out-of-plane angle distribution to be used for each filament count, which may be more appropriate.

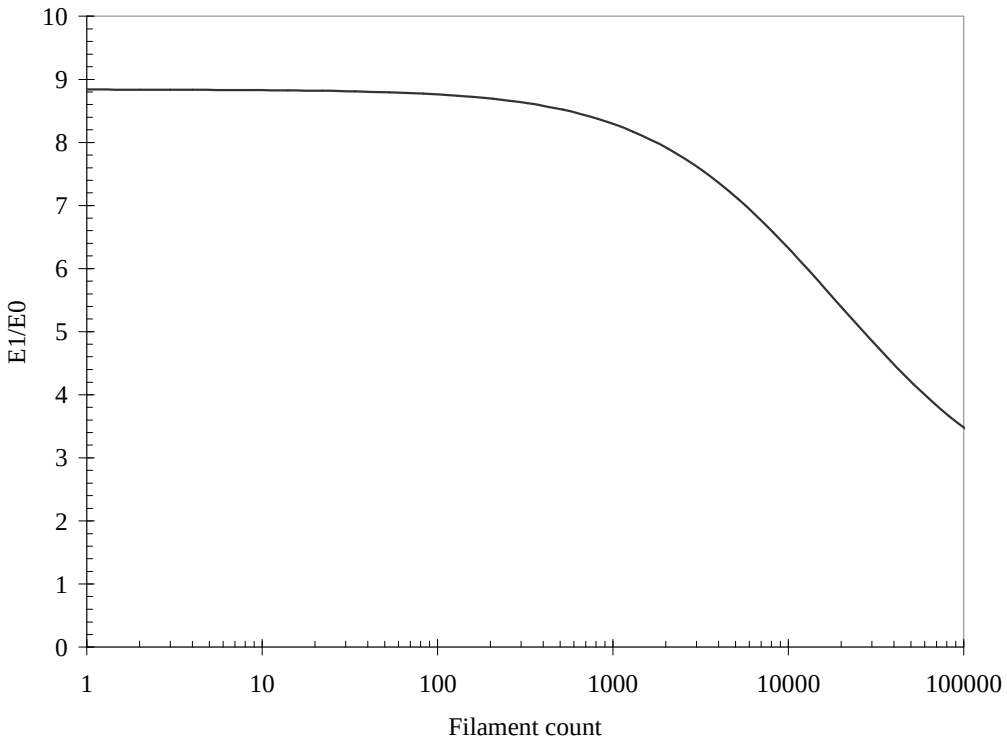


**Figure 4-12 Theoretical effect of filament count upon composite modulus**

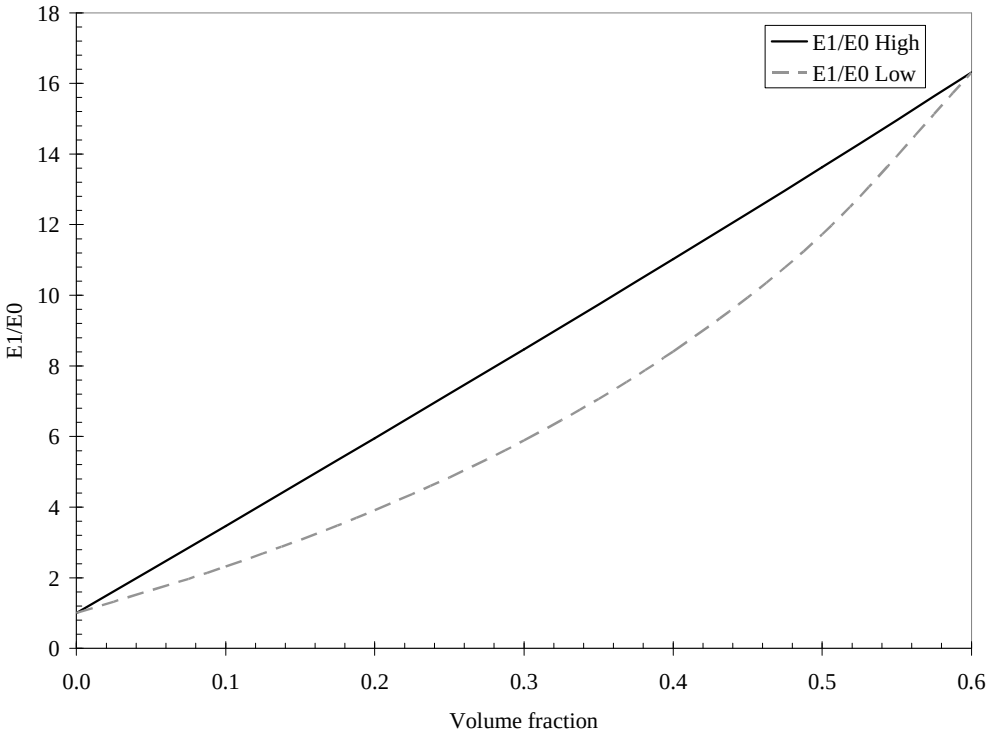


**Figure 4-13 Theoretical effect of laminate volume fraction upon composite modulus for two levels of induced filamentisation (high and low)**

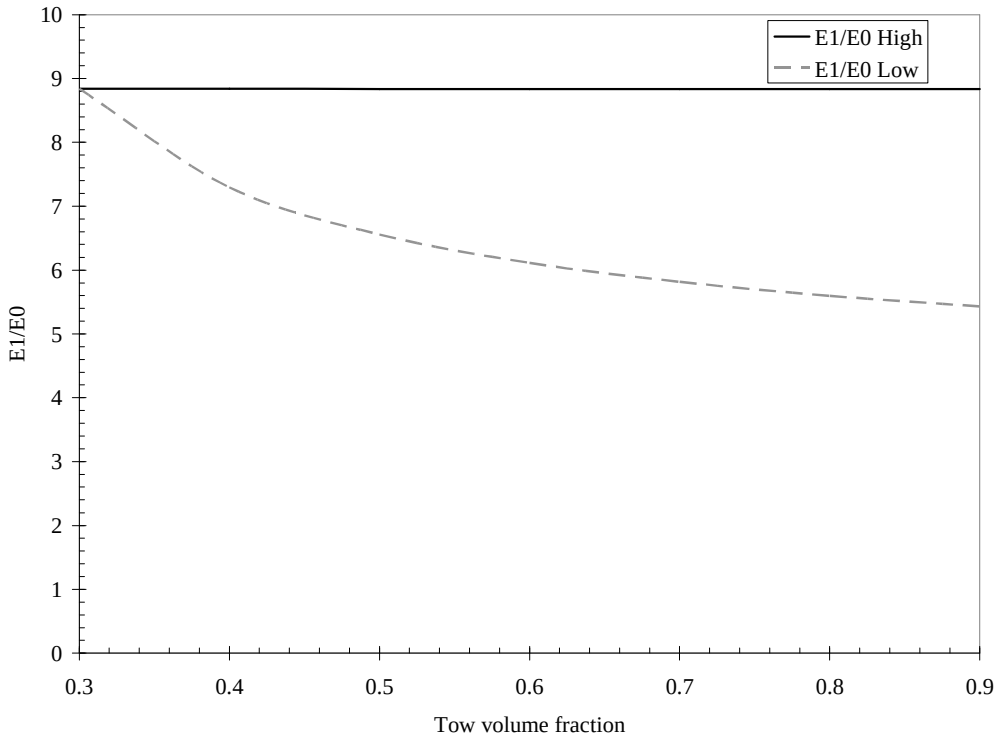


**Figure 4-14 Theoretical effect of tow volume fraction upon composite modulus, ($V_f$=30%) for two levels of filamentisation (high and low).**

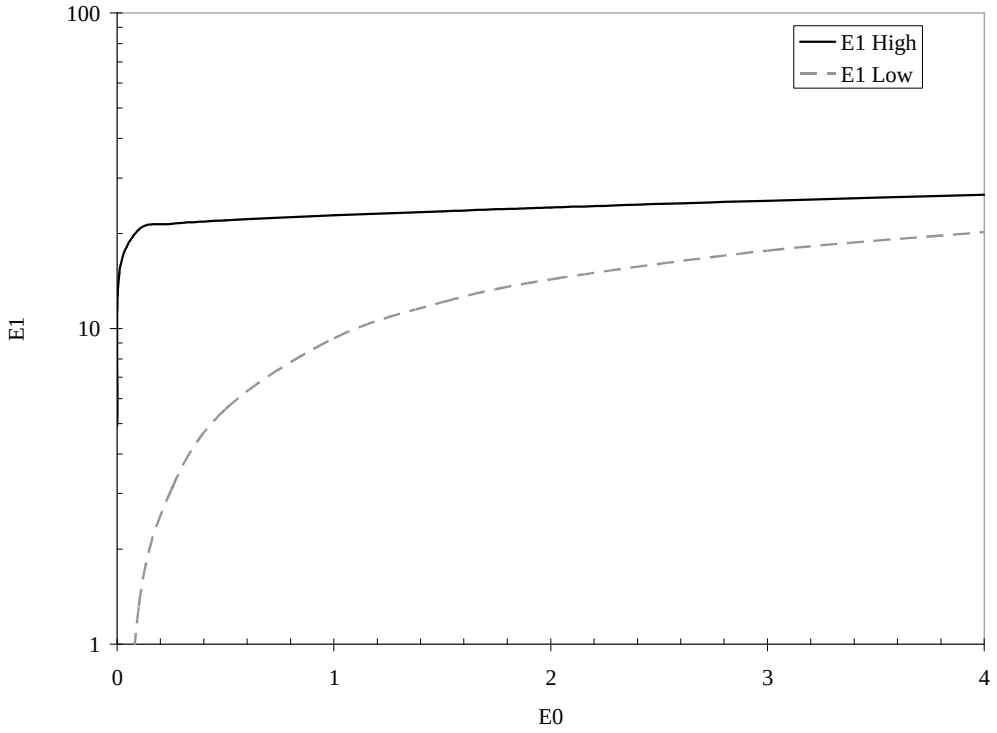


**Figure 4-15 Theoretical effect of matrix modulus upon composite modulus for two levels of filamentisation (high and low)**

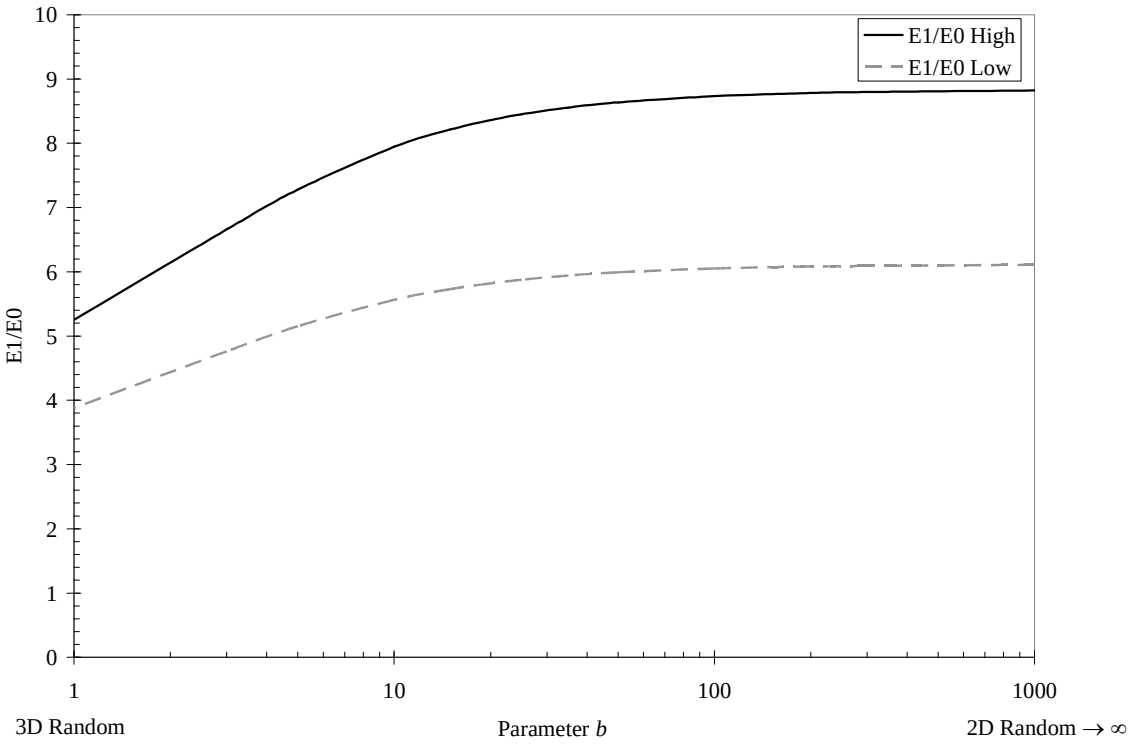


**Figure 4-16 Theoretical effect of out-of-plane angle distribution upon modulus for two levels of filamentisation (high and low). Values of *b*=100 and *b*=1000 are within 98.9% and 99.9% respectively of the exact 2D random case when *b* is infinity.**

### 4.4.2. Constant filament count

A variable filament count is one factor which complicates mechanical property prediction for DCFP laminates over other random fibre materials. The model is applied here to a laminate of a constant filament count, to eliminate one independent variable in order to assess the accuracy of the methodology rather than the quality of the empirical parameters. The final aggregate averaging stage of the model is therefore ignored. A carbon tow supplied by Hexcel was used for this study because it has high bundle integrity [55, 187]. The tow comprises eight 3K bundles grouped together to form one large 24K tow, which splits upon chopping into consistent filament counts. The model input parameters are listed in Table 4-6 for the AS4 carbon and DLS1692 epoxy resin.

Three fibre volume fractions were investigated; 18%, 27% and 48% and a fibre length of 23mm was chosen to ensure that the tows did not fragment. Figure 4-17 shows a comparison between the experimental tensile data and stiffness predictions using the multi-level model. An excellent agreement is demonstrated between the two data sets,

with the relative error being only 5% at each point. This error falls well within the coefficient of variation bands for the experimental values, which range from 9% to 15%.

| Property | Designation | Value | |
|---|---|---|---|
| Tow length (AS4) | $L$ | 23 | mm |
| Filament diameter | $Ø_1$ | 0.007 | mm |
| Tow filament count | $F$ | 3000 | |
| Tow volume fraction | $V_{tow}$ | 0.6 | |
| Plane strain bulk modulus | $k_{tow}$ | 8.97 | GPa |
| Cross modulus | $l_{tow}$ | 5.91 | GPa |
| Axial modulus under axial strain | $n_{tow}$ | 141.24 | GPa |
| Transverse shear modulus | $m_{tow}$ | 2.74 | GPa |
| Axial shear modulus | $p_{tow}$ | 3.11 | GPa |
| Matrix modulus (DLS1692) | $E_o$ | 3.2 | GPa |
| Matrix Poisson's ratio | $v_o$ | 0.35 | |
| Matrix ordinary bulk modulus | $\kappa_0$ | 3.56 | GPa |
| Matrix shear modulus | $\mu_0$ | 1.19 | GPa |

**Table 4-6 Material properties for AS4 carbon tows [188] and DLS1692 epoxy resin.**

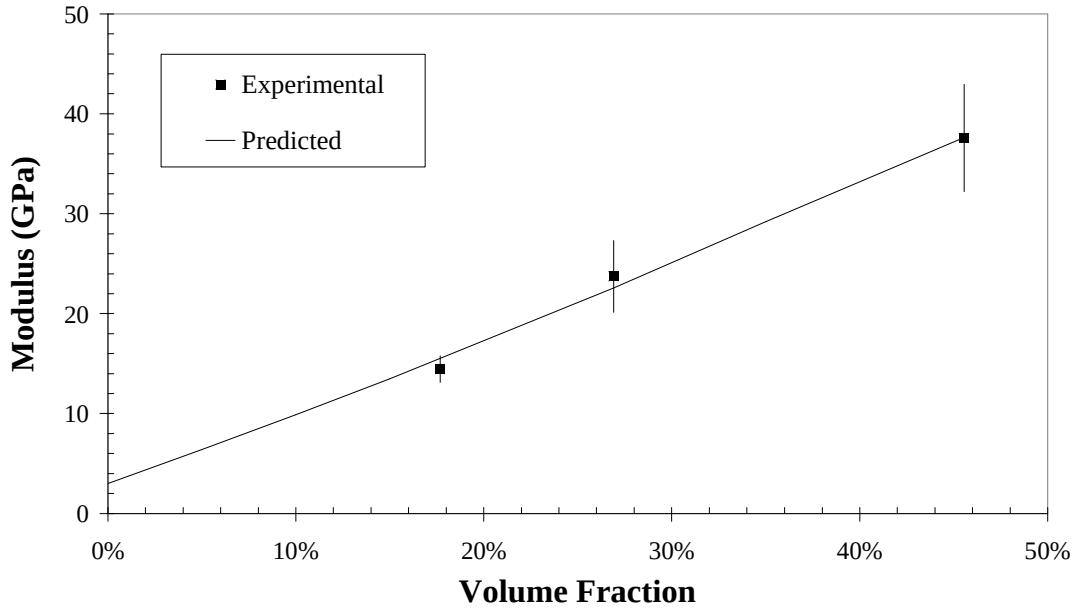


**Figure 4-17 Comparison of multi-level stiffness model and experimental tensile data for a DCFP laminate containing consistent 3K carbon bundles. The model assumes the fibres are planar and therefore no consideration is given for fibre waviness out-of-plane.**

Dahl *et al.* [187] have recently studied the effects of fibre tow size on DCFP laminates using variants of the Hexcel AS4 fibre (0.5, 1, 1.5, 3, 6 and 12K). Preforms were manufactured with 25mm long fibres, using the facilities at the NCC, Dayton, Ohio. Plaques were moulded using an unspecified epoxy resin, 2mm thick with a nominal fibre volume fraction of 35% in each case. The input parameters presented in Table 4-6 are used to predict the effect of filament count on the tensile modulus.

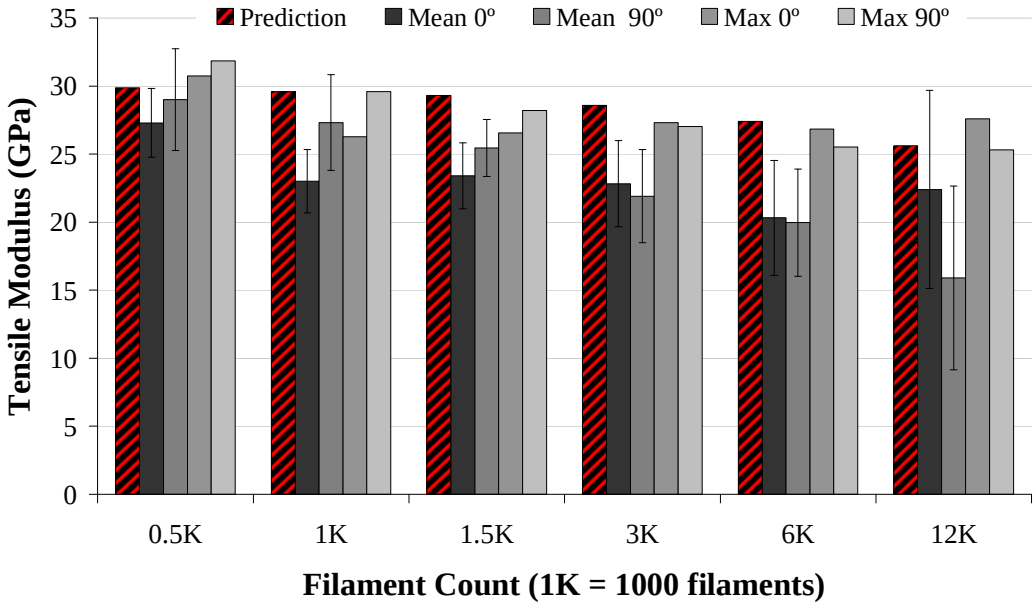


**Figure 4-18 Predicted values vs. experimental values for a range of DCFP laminates containing different carbon filament counts. Preforms were produced on the P4 preformer at the NCC, Dayton, Ohio. Tests were performed at 0º and 90º to check for orientation dependence. The average and maximum values are presented for each orientation as a function of tow size.**

Figure 4-18 summarises the predicted and experimental results. The 0.5K case is over predicted by just 6% when an overall average is calculated from the 'Mean 0º' and 'Mean 90º' experimental data sets. This error approaches 34% for the 12K laminate. There is a clear discrepancy in some instances between the tensile modulus at 0º and 90º. This was previously experienced in Section 3.3 and can be attributed to the preforming machine used at the National Composites Centre, USA.

It is important to note the difference between the mean experimental values for the 3K plaque in Figure 4-18 and the prediction curve in Figure 4-17. The experimental mean values from the current study appear to be ~25% lower than the previous study. This may be partly due to a difference in matrix material, or more likely due to the

difference in specimen thickness (2mm as opposed to 3mm). The model homogenises the properties of the composite over a representative volume element (RVE) of an equivalent continuum. However, no consideration regarding the size of the RVE is given and therefore geometric disorders and irregularities such as unreinforced areas (the influence of which is likely to increase as the laminate becomes thinner and the tow filament count increases) are overlooked [82]. This also explains why the predictions are much closer to the experimental data for the 0.5K tow, but diminish as the tow size increases to 12K.

There are concerns over the number of specimen repeats taken during the study by Dahl et al [187]. Four test repeats at each orientation, for every tow size, do not provide sufficient confidence (see Section 3.2.3). The mean values for the 0.5K case could vary by ±2.5GPa and as much as ±7.0GPa for the 12K case. This is supported by the fact that the maximum modulus in each instance is much closer to the predictions than the mean (within ~10%). As a first approximation the model appears to provide reasonable predictions against the experimental data. The effect of increasing filament count is correctly predicted by the stiffness model, but errors in magnitude can be attributed to the neglected scale effects. The model is most accurate for thicker laminates (>3mm) when larger tow sizes are in use.

### 4.4.3. Variable filament counts

The multi-level model is applied to laminates containing various filament count distributions presented in Figure 4-19, using the data in Table 4-4 for the constituents at Level 1. Predictions are compared against the experimental data from Section 3.5. Two 24K tows were used during this study with different tendencies towards filamentisation. In the present application Fibre I was highly susceptible to fragmentation compared with Fibre II. Induced filamentisation was then imposed upon both fibre types at five levels, between 0% (no air pressure in filamentisation chamber) and 100% (7 bar applied to filamentisation apparatus).

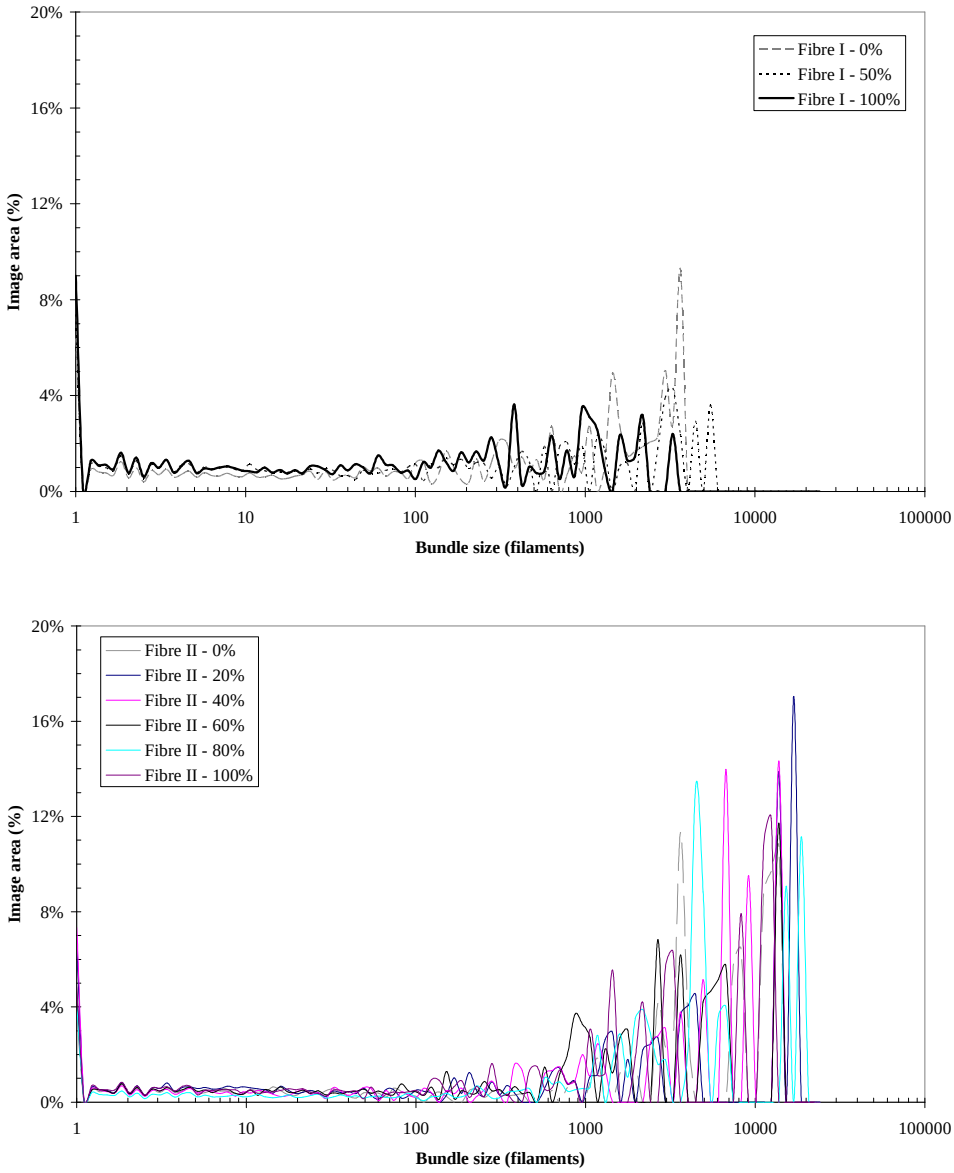


**Figure 4-19 Filament count distributions for a range of laminates with different levels of induced filamentisation. Two fibre types are studied: Fibre I (high natural filamentisation) and Fibre II (low natural filamentisation).**

The results for the analytical stiffness predictions in Figure 4-20 were generated using the input data from Table 4-4. The shape of the data for Fibre II is reflected well in the analytical predictions, which suggests that the image analysis technique can successfully distinguish between small variations in filament count distribution. Modulus is consistently over-predicted, on average by 10% and 8% for fibre types I and II respectively. Predictions are within 15% at the low filamentisation level, but are within 5% for highly filamentised tows (for both fibre types).

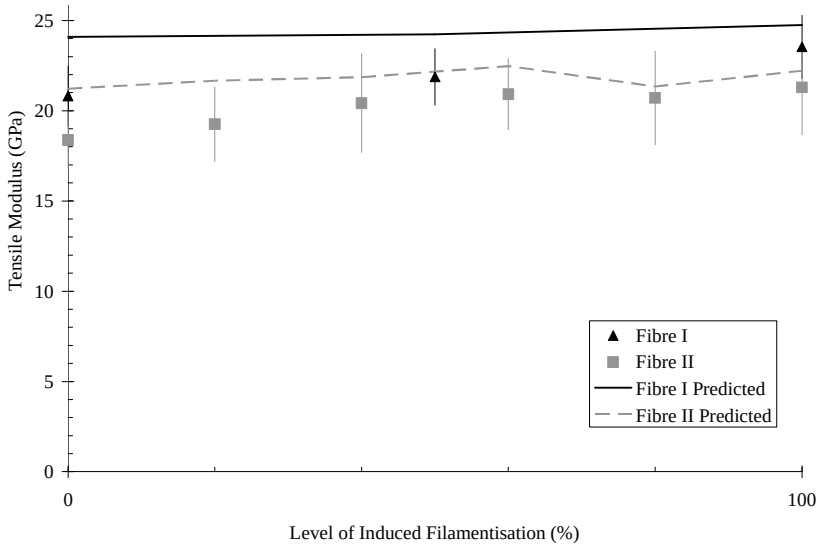


**Figure 4-20 Tensile modulus for fibre types I (high natural filamentisation) and II (low natural filamentisation) for increasing levels of induced filamentisation**

In addition to the neglected scale effects discussed in Section 4.4.2, other possible sources of error can be attributed to the determination of the tow filament counts. It is assumed that the tow volume fraction is constant at 60%. Whilst the moduli of highly filamentised laminates are independent of tow volume fraction, Figure 4-14 shows that laminates produced with non-filamentised fibres are highly sensitive to tow volume fraction. The volume fraction will change locally within the tow due to compaction from neighbouring tows, but may also vary due to different levels of induced filamentisation as the air flows between the individual filaments to separate the tow.

The in-plane orientation correction factor of 0.6366, used to compensate for in-plane orientations when determining the tow filament count, is a conservative value and will yield over-predicted values for stiffness. This value was calculated by determining the average increase in cross sectional area when a filament was rotated between 0º and 90º. As discussed previously, an incomplete range of in-plane filament orientations was observed when determining the tow geometry from optical micrographs. The orientation of bundles with high in-plane angles are indistinguishable using the image acquisition system and were therefore overlooked. Micrographs also fail to give an appreciation for any tow end spreading which may occur due to DCFP processing. This effect was reported in Section 3.4 when high levels of induced filamentisation were employed with long cut lengths. Tow integrity is maintained but the tow ends spread, resulting in lower tow volume fractions at the ends.

### 4.4.4. Effect of fibre length

The stiffness model is applied to the experimental data from Section 3.4 in order to explain the observed performance trends for increasing fibre length. An initial comparison is made between two theoretical levels of filamentisation, as shown in Figure 4-21. Low filamentisation represents a constant filament count of 24,000 and high filamentisation is for a bundle of only 100 filaments. The high filamentisation case increases sharply for low aspect ratios and plateaus at approximately 10mm (99% of the stiffness value at fibre length of 1m). In contrast, the low filamentisation case increases steadily and does not plateau until a length of ~150mm is reached because of the inefficient high filament count. Figure 4-21 will be used to explain the stiffness versus length effects reported in Chapter 3.

At the time of writing filament count distributions were unavailable for the two extreme filamentisation levels at different fibre length. A method is described in Appendix H.6 to estimate the mean bundle size for stiffness prediction purposes. The method is based on observations made during the DCFP process to determine the length at which the tow begins to fragment. The estimated mean bundle sizes are shown in Table 3-2 and have been used to predict the stiffness of the experimental DCFP laminates. (Other constituent properties are taken from Table 4-4).

The bundle size predictions give similar results for filamentised and non-filamentised fibres at a length of 115mm, so there are obvious limitations to this method in terms of agreement with experimental results (Figure 3-15). The anticipated effect of fibre length for a constant filament count in Figure 4-21 is different to the experimental results presented in Figure 3-15, particularly for the low filamentisation case because of the effect of natural filamentisation. A reduction in filament count for decreasing length is reflected in the predictions in Figure 4-22. The model over predicts the experimental data by an average of 8% for both levels of filamentisation, but the correlation is better for low levels of filamentisation, particularly for shorter fibres. For fibre lengths between 6mm and 28mm predictions are within 6.5% of the experimental data.

For fibres lengths beyond 28mm the predicted stiffness tends towards the stiffness of the filamentised fibres because of the assumed bundle sizes. It has been confirmed that

as fibre length increases, the net bundle size converges towards the original filament count (24K in this particular case). However, for lengths of 115mm highly filamentised tows do not split but the ends of the bundles fan out, exhibiting a much lower tow volume fraction than the 60% assumed. A lower tow volume fraction for a constant composite volume fraction means that the filaments are more homogeneously distributed and the number of resin rich areas is likely to reduce.

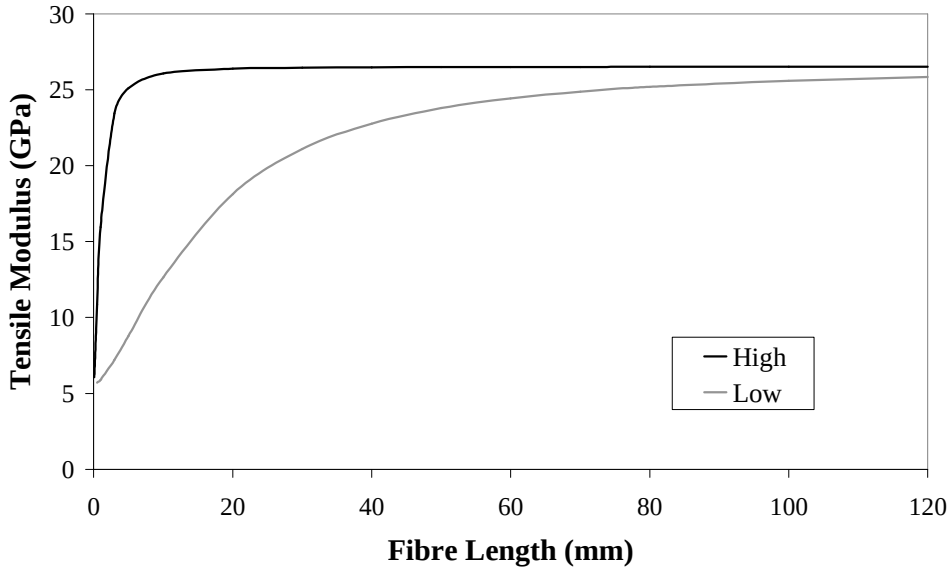


**Figure 4-21 Predicted tensile modulus versus fibre length using the multi-stage stiffness model. Constant filament counts of 100 (high) and 24,000 (low) are assumed and also a constant tow volume fraction of 60%.**

| Fibre length (mm) | Filamentised | Mean bundle size (number of filaments) |
|---|---|---|
| 3 | Yes | 24 |
| 6 | Yes | 109 |
| 14 | Yes | 551 |
| 23 | Yes | 1411 |
| 29 | Yes | 2205 |
| 58 | Yes | 8820 |
| 115 | Yes | 24000 |
| 3 | No | 338 |
| 6 | No | 1527 |
| 14 | No | 7752 |
| 23 | No | 19845 |
| 29 | No | 24000 |
| 115 | No | 24000 |

**Table 4-7 Predicted mean bundle sizes for varying chop length and level of filamentisation. A tow volume fraction of 60% was assumed.**

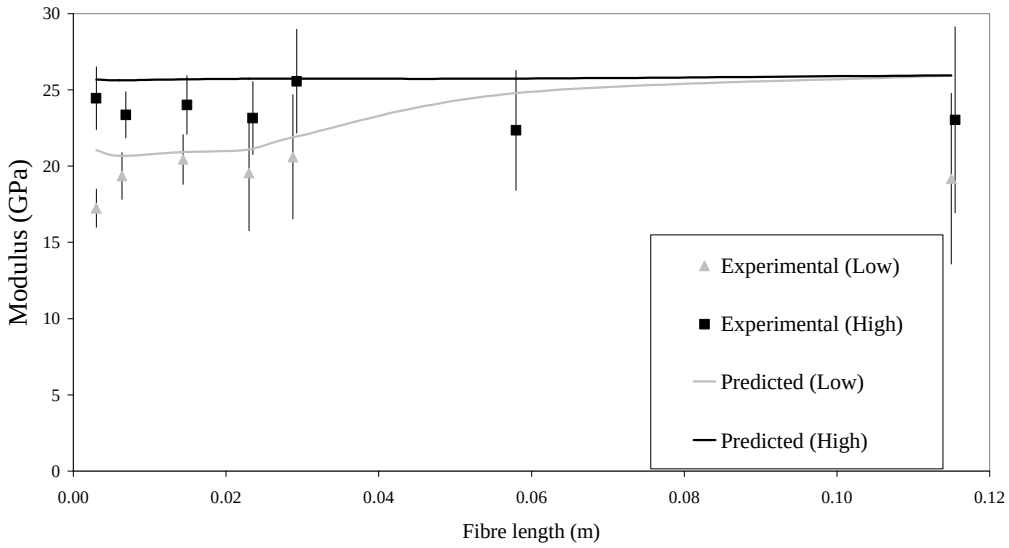


**Figure 4-22 Predicted and experimental modulus results as a function of fibre length and degree of induced filamentisation (Low and high). (Note: experimental points for the high filamentisation case have been offset by 0.005m to improve clarity).**

### 4.4.5. Full material characterisation

Following the developmental work in Chapter 2 and Chapter 3 an optimum set of material parameters were determined for DCFP. Short fibre lengths and maximum levels of filamentisation yield optimum specific properties, when utilising large filament count tows. The experimental results from the full material characterisation study are used to further validate the stiffness model. It is anticipated that the predictions will be much closer to this set of data because heterogeneities caused by stochastic coverage effects are minimised. Filament count distributions are presented in Figure 4-23 and the out-of-plane orientation distribution is assumed to be identical to Figure 4-10. The material properties of the constituents are listed in Table 4-8.

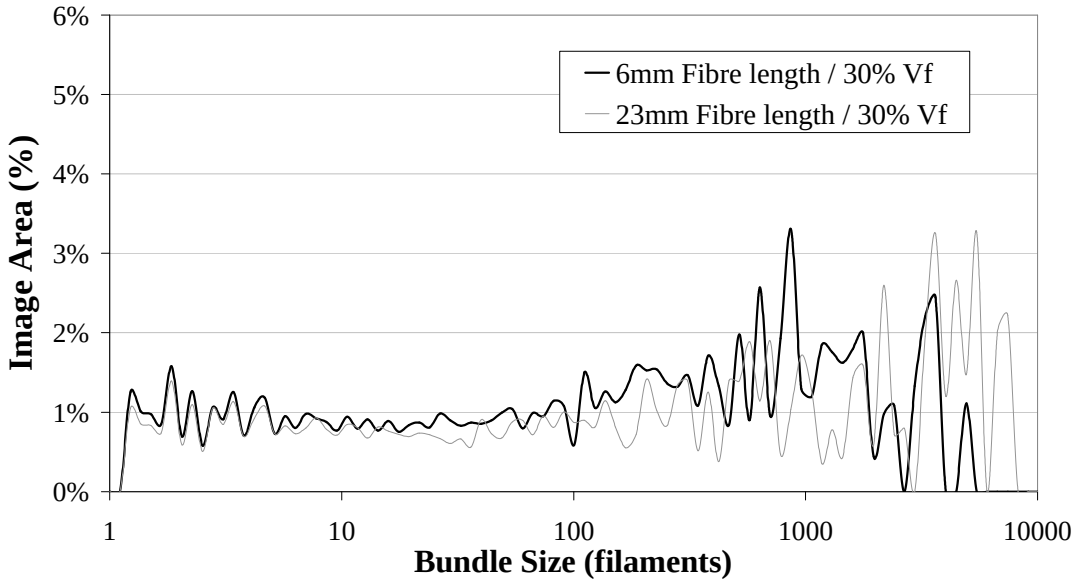


**Figure 4-23 Filament count distributions for the full material characterisation laminates. Both fibre lengths were investigated but the filament count distributions were assumed to be independent of the laminate volume fraction.**

| Property | Value | | Designation |
|---|---|---|---|
| Filament diameter | 0.007 | mm | $Ø_f$ |
| Tow volume fraction | 0.6 | | $V_{tow}$ |
| Plane strain bulk modulus | 20.19 | GPa | $K_i$ ($k_{23}$) |
| Cross modulus | 12.14 | GPa | $L_i$ |
| Axial modulus under axial strain | 234.23 | GPa | $n_i$ |
| Transverse shear modulus | 8.06 | GPa | $m_i$ ($m_{23}$) |
| Axial shear modulus | 10 | GPa | $p_i$ ($m_{12}$) |
| Matrix Poisson's ratio | 0.37 | | $\nu_o$ |
| Matrix modulus | 3.7 | GPa | $E_o$ |
| Composite volume fraction | 0.3 | | $V_f$ |

**Table 4-8 Analytical model input parameters for the full material characterisation study. The carbon type is Tenax STS and the epoxy resin is DW2 supplied by Hexcel.**

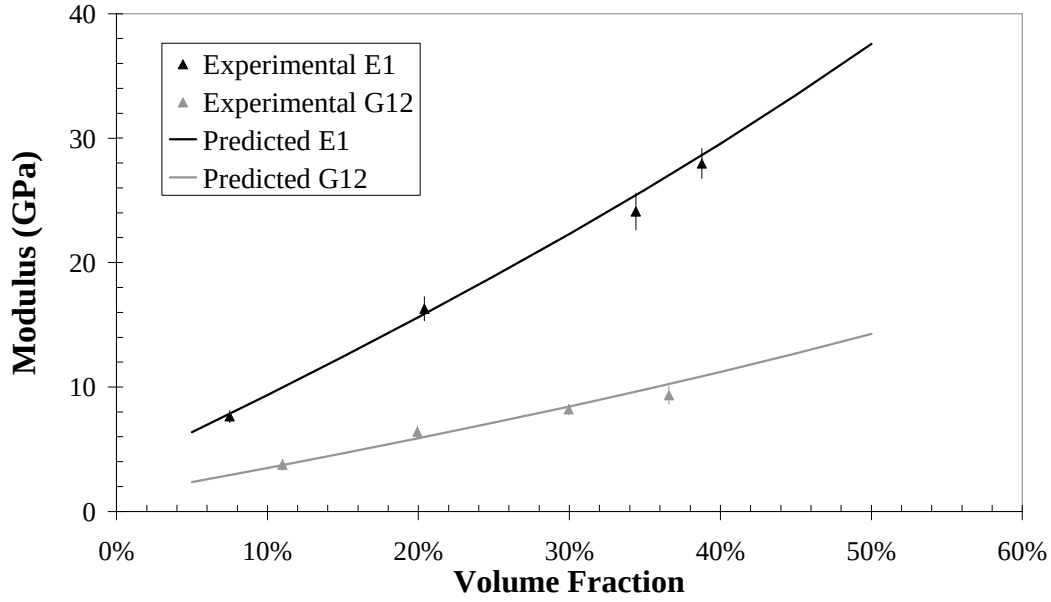


**Figure 4-24 A comparison of predictions vs. experimental data for the in-plane tensile modulus and the in-plane shear modulus. Laminates were manufactured with 6mm long fibres at a range of volume fractions.**

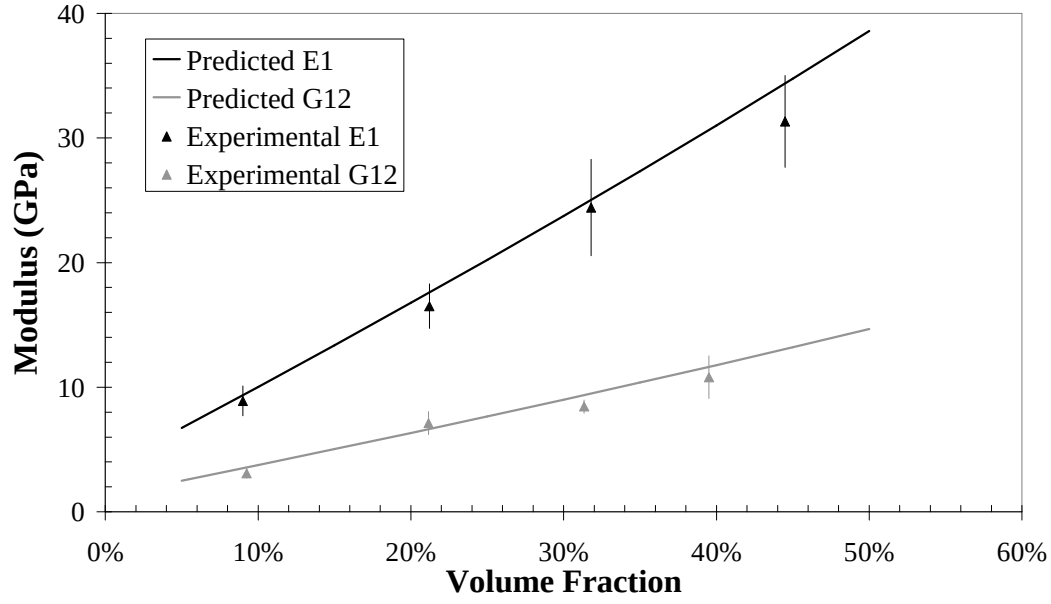


**Figure 4-25 A comparison of predictions vs. experimental data for the in-plane tensile modulus and the in-plane shear modulus. Laminates were manufactured with 23mm long fibres at a range of volume fractions.**

Stiffness predictions are presented in Figure 4-24 and Figure 4-25 for the 6mm and 23mm fibre lengths respectively. A comparison is made between the experimental data and the model for both in-plane tensile modulus and in-plane shear modulus. Generally, there is a very good agreement between experiment and prediction for the two fibre lengths in both tension and shear. For the 6mm fibre case the tensile modulus

predictions are within 3% at 8% $V_f$ and within 5% at 39% $V_f$. The shear modulus is within 0.8% at 11% $V_f$ and within 9% at 37% $V_f$. Clearly, the accuracy of the predictions decreases with increasing fibre volume fraction (however, there is a lower confidence level for the higher volume fraction plaques as indicated by the larger error bars in Figure 4-24 and Figure 4-25). This is an inherent problem with inclusion-based models that stem from the Mori-Tanaka method [156]. Mori and Tanaka generalised the non-dilute fibre case of Eshelby [155], therefore predictions are generally accurate at low volume fractions and at the extreme fibre concentration case, but intermediate concentrations are subjected to a mathematical fit [147]. This problem is irrelevant for most random materials, particularly for short (<5mm) fibres used in injection moulding, because the fibre volume fraction rarely exceeds 20%. However, volume fractions approaching 50% have been achieved for DCFP as shown. The experimental data obeys a strong linear relationship for increasing $V_f$ (correlation coefficients >94% in each case) and therefore the model is seen to diverge from the experimental data at intermediate volume fractions.

The accuracy of the model appears to be stable with increasing fibre length (for the lengths tested). This was previously investigated in Section 4.4.4 but the trends observed were confounded by using assumed bundle sizes. For the 23mm case the error between experiment and prediction for the tensile modulus is just 5% at 9% $V_f$ and 9% at 45% $V_f$. The shear modulus is within 6% at 9% $V_f$ and within 8% at 39% $V_f$.

Predictions in Figure 4-24 and Figure 4-25 incorporate the out-of-plane (OOP) fibre orientation distribution presented in Figure 4-10. Additional predictions in Figure 4-26 show the effect of assuming a perfectly planar orientation distribution. Predicted values are higher without OOP correction. The error for the tensile data set increases from 3% to 12% at 8% $V_f$ and from 5% to 16% at 39% $V_f$. For the shear data the error increases from 0.8% to 9% at 11% $V_f$ and from 9% to 19% at 37% $V_f$.

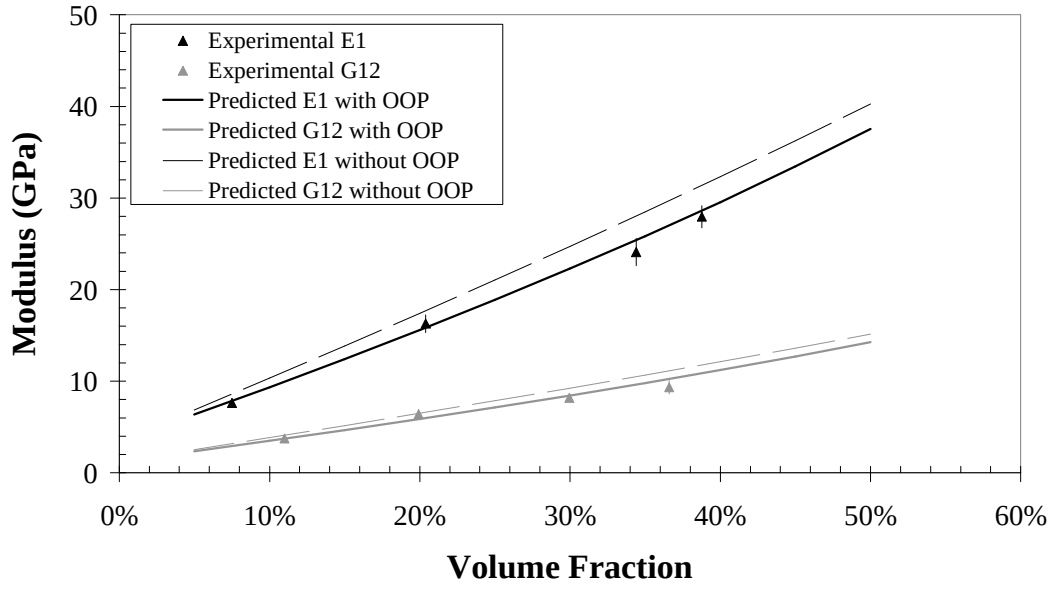


**Figure 4-26 The effect of with or without out-of-plane (OOP) correction to account for fibre waviness. The data set is for the 6mm fibre case previously presented in Figure 4-24.**

## *4.5. Conclusions*

A fundamental consideration for DCFP stiffness prediction is adopting a multi-level modelling approach to account for filament packing in the mesoscopic fibre architecture. A model has been developed using an inclusion-based approach, which is applied at both the filament and tow levels. The model has been validated using experimental data from Chapter 3 and in general there is good agreement, albeit with slight over-prediction by the model in both tension and shear.

A sensitivity analysis has been performed for a selection of key parameters and the most significant result shows that there is negligible difference in tensile stiffness between preforms consisting of single filaments or 100 filament bundles. Therefore in practice, a controlled level of filamentisation is required to create a material of constant filament count to eliminate the occurrence of single filaments that cause fibre packing issues. This material will provide a cost-effective alternative to a commercial split-tow carbon fibre.

The effects of filament count, fibre length and composite volume fraction have all been studied. The model shows the correct trend with increasing fibre length (given the

limitations of employing a mean bundle size and tow volume fraction), but the properties are generally over predicted by 5-10% for lengths between 6mm and 23mm.

Predictions are within 5% of the experimental values for a consistent filament count of 3K. When the filament count increases from 0.5K to 12K the model demonstrates the correct trend (a reduction in stiffness) but again the magnitude of the predictions is too high. This error can be attributed to a low level of statistical confidence in this set of experimental results but also to scale effects. Accuracy of the model reduces as the laminate becomes thinner for a constant areal density of fibre because of the associated coverage effects. Accuracy of the model is also dependent on the fibre volume fraction. Predictions are within 5% for volume fractions of 10% but this error increases to 13% when the volume fraction approaches 40%.

The model has the capability of differentiating between different levels of filamentisation, using empirical data from optical micrographs to establish filament count distributions. The methodology used to determine these distributions does give representative values, but the model currently over predicts the experimental stiffness by approximately 10% at a fibre length of 14mm. Improved property prediction requires more in-depth image analysis techniques to accurately determine the filament count, tow volume fractions and both the in-plane and out-of-plane orientation distributions.

# Chapter 5. Analytical tensile strength prediction

## *5.1. Objectives*

Two models are developed in this chapter to predict the tensile strength of random DCFP laminates. Critical fibre length is a major influencing factor for both models and a modification is made to the conventional slip theory [102] in order to improve the strength predictions for bundled materials. The first model is analytical and utilises the stiffness tensor derived in Chapter 4. The literature highlights the need for independent stiffness and strength models, so a second stochastic model is presented which is based on a critical zone concept. A multi-level approach is adopted in both cases (filament and bundle), which is validated using the experimental data from Chapter 3.

## *5.2. Literature review*

Unlike stiffness, the strength of a discontinuous fibre will never attain that of a continuous fibre because of the stress concentrations introduced at the fibre ends. The length at which a plateau in strength occurs may be up to 5 to 10 times longer than the corresponding critical length for stiffness [65, 152, 189]. The difference between critical aspect ratios for stiffness and strength increases with increasing fibre-matrix adhesion and with increasing fibre/matrix stiffness ratio [65]. The iso-strain condition assumed by the ROM does not hold true for discontinuous fibres because of the introduction of fibre ends. For this reason Kelly and Tyson [102] derived expressions *(slip theory)* to account for the effect of fibre length on strength. The failure mechanism of the composite is governed by the fibre length. Failure is initially dominated by debonding of transverse fibres, followed by matrix cracking [137]. Fibres in the loading direction will eventually debond if the length is below a critical threshold; otherwise final laminate failure occurs due to fibre fracture for longer fibres. Kelly and Tyson introduced the critical length term into the ROM in the form of an efficiency factor. Only 95% of the continuous composite strength is achieved when the fibre length is ten

times longer than the critical value [190]. Therefore it may be important to consider strength independently from stiffness when developing predictive models.

A revised slip [114] model shows that the tensile strength of a carbon tow is reduced by 20% when the number of filaments increases from 50 to 2000. At a critical load the central fibres slip within the tow relative to the perimeter because of a smaller interfacial bond surface per unit area. However, this modified slip theory becomes inappropriate as $E_f/E_m$ increases because total bundle pull-out occurs [80, 81]. The original Kelly-Tyson critical length expression was derived for UD, non-contacting metal fibres. The validity of such transfer models should be questioned for high $V_f$ random composites as the number of fibre-fibre contacts increases. It becomes increasingly difficult to predict the axial fibre stress and the interfacial shear stress for contacting fibres due to the changes in the stress fields caused by fibre interactions, potentially leading to damage development in neighbouring fibres [191].

CLT in conjunction with a suitable micromechanical model provides a good approximation for the elastic constants and also has the flexibility to be used to determine strengths for discontinuous, random fibre composites. The Halpin-Kardos strength reduction factors (SRF) [134] were developed to determine the effective discontinuous ply strengths from equivalent continuous ply data. Comparisons with experimental data [163] show that this approach gives better predicted values than earlier statistical ROM approaches. However, it is assumed that the load is maintained within each failed ply until final laminate failure, representing an upper bound case. It is also noted that predictions are highly sensitive to the SRF values.

Progressive failure models have been combined with the ROM for stiffness to determine the strength of 2D random composites [64, 192]. The initial elastic modulus is calculated by the continuum equivalent of the ROM to determine the orientation dependence of each ply [143]. This method under predicts the tensile modulus by up to 40% (see Nielsen and Chen in Section 4.2.1.1) and consequently yields low predicted strength values for carbon DCFP. Although an excellent correlation against experimental data is reported in [64], a non-predictive fitting parameter is introduced at the validation stage. Developed progressive failure techniques are limited to the

macroscopic level since they are unable to account for the fibre-matrix interface and fibre-fibre contacts at higher volume fractions.

The strength of discontinuous fibre composites beyond the critical aspect ratio is dominated by stochastic length effects. A strength model [97, 193] coupled with Weibull theory [88] accounts for the strength variability in longer fibres due to critical flaws. Weibull effects are significant as the strength of carbon fibre is reduced by almost 40% when the length is increased from 5mm to 80mm [97]. The level of macroscopic homogeneity is much more important for strength, since failure is dominated by the weakest link. The ROM has been modified [194, 195] to consider the effects of variable fibre length and the influence of fibre-fibre interactions. Microcracks are most likely to form at fibre ends, initiating failure in a critical cross-section of the laminate that has been weakened by the accumulation of cracks. Wetherhold [107, 196] considers strength to be proportional to the number of fibres crossing a critical zone, relative to the number of fibres that end within the zone. As fibres cross one another the load is shared, reducing the average fibre load. Local reinforcement is improved as the probability of fibre fracture is reduced, thereby increasing the composite strength. The issue of fibre-fibre contacts is also investigated by Pan [110] to provide a quantitative understanding for determining the mechanical properties of random fibre composites. It is important to understand the inherent stochastic nature of strength; hence a comprehensive model must consider the probabilistic aspects of fibre length and fibre orientation.

## *5.3. Current modelling limitations*

As with stiffness, fibre length effects are evident in two areas; critical length effects and coverage effects. For the first, maximum utilisation of the fibre properties only occurs beyond a critical length, at the transition from fibre pull-out to fibre breakage. A model such as Kelly-Tyson's slip theory is poorly understood for random, bundled materials. The filament aspect ratio in DCFP is irrelevant because it is significantly larger than the critical threshold. The bundle level is therefore the scale of interest but fibre-fibre interactions and inconsistent bundle profiles complicate the prediction of the critical bundle length.

The second length effect is stochastic. Shorter fibres give greater macroscopic homogeneity for a finite area of both areal density and fibre orientation distribution, but also exhibit higher ultimate strengths because of the associated Weibull effects. The level of macroscopic homogeneity is much more important for strength, since failure is dominated by the weakest link. A comprehensive strength model should therefore consider these stochastic influences. Both effects must be considered at the tow level rather than the filament level, as the tow cross-section is on the same scale as the thickness of the laminate.

## *5.4. Critical bundle length model*

### 5.4.1. Introduction

Strength models that rely on slip-theory to predict the effects of varying fibre aspect ratio are highly sensitive to the critical length, since the strength properties of the fibre are essentially reduced by the ratio of fibre ineffective length over effective length. The predicted critical length for a 6K carbon tow ranged from 3.3mm to 129.5mm in [48], subject to the packing geometry used to determine the effective tow diameter. A more reliable expression is required, which will form an integral part of the multi-stage modelling approach outlined later in this section.

The slip theory of Kelly and Tyson can be extended to predict critical tow lengths by regarding a bundle of filaments as a single, large diameter fibre. Reinhart [159] postulates that the critical length for a tow can be calculated in the same way as it is determined for a circular fibre. In the present work, it is proposed that the effective tow diameter for any given tow shape is calculated based on the tow perimeter, rather than the width as previously suggested in [48], as this will provide a more realistic estimate for the embedded tow surface area. For any tow size, the number of filaments '$n$' and the diameter of each filament, $\varnothing_f$ are known. Thus, the tow cross-sectional area can be calculated by determining the average tow volume fraction by microscopy. Assuming the tow volume fraction and hence the tow cross-sectional area remain unchanged, the

tow perimeter can be calculated for any given tow shape. Carbon preforms have been seen to exhibit a distribution of bundle sizes but in the present work, for the purpose of mechanical property prediction, a mean bundle size will be adopted.

### 5.4.2. Methodology

The interfacial shear forces acting on the embedded tow surface area at the tow/matrix interface can be balanced against the ultimate tensile forces applied to the tow:

$$\sigma^*_{tow} A_{tow} = \tau_i P_{tow} l_{ce} \quad \textbf{Equation 5-1}$$

where $l_{ce}$ is the critical embedded length of the tow, $\tau_i$ is the interfacial shear strength between the tow and the matrix and $\sigma^*_{tow}$, $A_{tow}$ and $P_{tow}$ are the fracture strength, cross sectional area and perimeter of the tow respectively. The critical tow length is twice the critical embedded length, as there is an ineffective length at each end of the fibre. When rearranged in terms of critical length, Equation 5-1 becomes:

$$l_c = \frac{2\sigma^*_{tow} A_{tow}}{\tau_i P_{tow}} \quad \textbf{Equation 5-2}$$

The area of a single tow can be calculated from the filament cross sectional area, the filament count '*n*' and the assumed volume fraction within the tow, $V_{tow}$

$$A_{tow} = \frac{\pi \emptyset_f^{\,2} n}{4 V_{tow}} \quad \textbf{Equation 5-3}$$

The following approximation is assumed for the area of an ellipse;

$$A_{tow} = \frac{\pi w t}{4} \quad \textbf{Equation 5-4}$$

Expressions for tow width, *w*, and thickness, *t* can be determined as a function of tow cross-sectional aspect ratio, by equating Equation 5-3 and Equation 5-4.

$$w = \beta\sqrt{\frac{\varnothing_f{}^2 n}{\beta V_{tow}}} \qquad \text{where cross-sectional aspect ratio, } \beta = \frac{w}{t} \qquad \textbf{Equation 5-5}$$

$$t = \sqrt{\frac{\varnothing_f{}^2 n}{\beta V_{tow}}} \qquad \textbf{Equation 5-6}$$

$w$ and $t$ can be obtained from optical micrographs in order to determine $\beta$. The perimeter of the elliptical tow can be approximated using the following;

$$P_{tow} = \pi\sqrt{\frac{\left(w^2 + t^2\right)}{2} - \frac{\left(w-t\right)^2}{8}} \qquad \textbf{Equation 5-7}$$

Equation 5-5 and Equation 5-6 can be substituted into Equation 5-7 to give the perimeter of the tow, $P_{tow}$:

$$P_{tow} = \frac{\pi}{4}\sqrt{\frac{8\beta\varnothing_f{}^2 n}{V_{tow}} + \frac{8\varnothing_f{}^2 n}{\beta V_{tow}} - 2\left(\beta\sqrt{\frac{\varnothing_f{}^2 n}{\beta V_{tow}}} - \sqrt{\frac{\varnothing_f{}^2 n}{\beta V_{tow}}}\right)^2} \qquad \textbf{Equation 5-8}$$

Equation 5-3 and Equation 5-8 can subsequently be substituted into Equation 5-2 for the critical tow length:

$$l_c = \frac{2\sigma^*_{tow}\varnothing_f{}^2 n}{\tau_i V_{tow}\sqrt{8\gamma\left(\beta^2+1\right) - 2\left[\left(\beta-1\right)\sqrt{\gamma}\right]^2}} \qquad \textbf{Equation 5-9}$$

where the constant $\gamma$ is the following;

$$\gamma = \frac{\varnothing_f{}^2 n}{\beta V_{tow}} \qquad \textbf{Equation 5-10}$$

Assuming the tow is analogous to a large single fibre, the strength of the tow, $\sigma^*_{tow}$ can be determined using $V_{tow}$ in a ROM calculation:

$$\sigma^{*}_{tow} = \sigma_f V_{tow} + (1 - V_{tow})\sigma_m$$ **Equation 5-11**

It is assumed that the tow shape is a perfect ellipse, although in practice tow shapes vary greatly depending on the level of compaction, filamentisation and interference from neighbouring tows. Micrographs were taken to establish the tow cross-sectional geometry for a 6K, non-filamentised carbon tow shown in Figure 5-1. Image analysis software was employed to establish the average cross-sectional aspect ratio of 17:1. The critical length becomes less significant as the filament count and hence perimeter of the bundle is reduced. Figure 5-2 shows that the predicted critical tow length for a 6K tow is 4.93mm, which is within the two bounds determined by Rondeau *et al* [48]. This model will provide valuable input parameters for the two strength models proposed below.

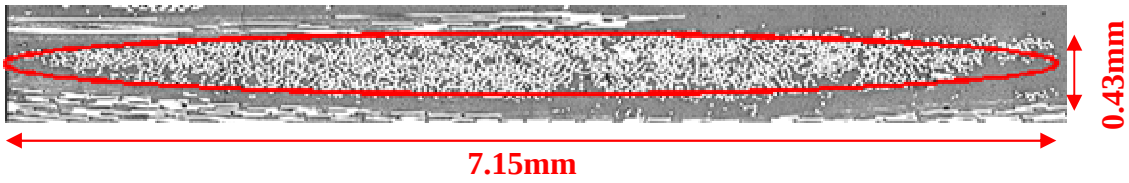


**Figure 5-1 Representative micrograph taken from a plaque consisting of 6K HTA tows embedded in an epoxy matrix. The epoxy sizing agent applied to the surface of the HTA fibre yields low levels of natural filamentisation. An average tow cross-sectional aspect ratio of 17 was determined.**

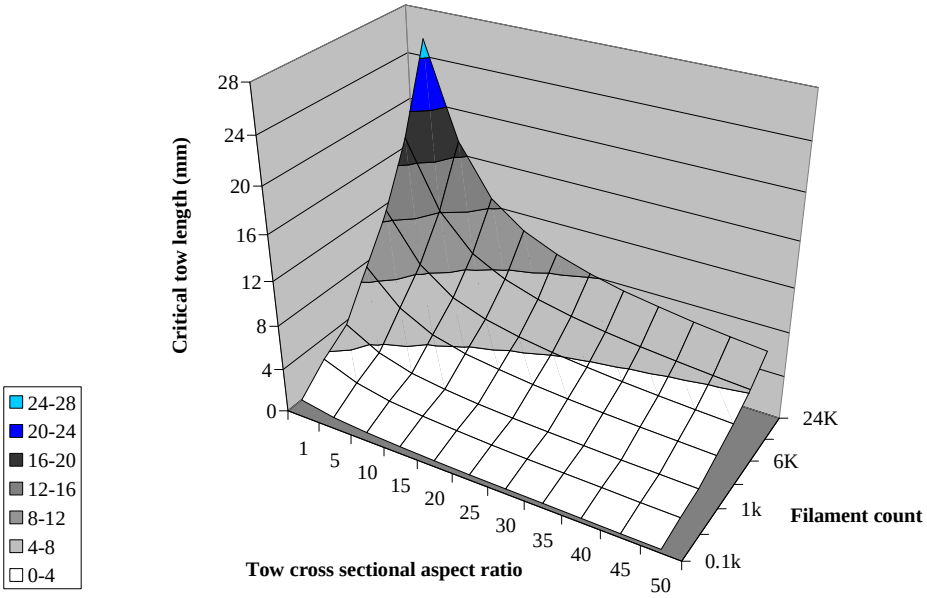


**Figure 5-2 Critical tow length as a function of tow cross-sectional aspect ratio (width/thickness) and filament count for a constant tow volume fraction of 60% (an average value obtained from optical micrographs). The tow failure strength (2424MPa) is calculated using the ROM (see Equation 5-11), assuming a filament failure stress of 4000MPa. The tow failure stress is therefore constant with length, but further work in this chapter will discuss the Weibull effects on the length vs. strength relationship for carbon tows.**

### 5.4.3. Results and discussion

The critical bundle length model has been applied to the experimental data from the fibre length study in Section 3.4. A critical length effect can be observed in Figure 3-16 between 3mm and 6mm for the low filamentisation case. Critical bundle length predictions are used in this section to explain these results.

Table 5-1 shows the predicted critical bundle lengths using the circular profile (Kelly-Tyson method [102]) and the elliptical profile method (Equation 5-9) for the fibre lengths tested in Figure 3-16. The critical bundle lengths from the elliptical method are 61% lower than those obtained from the Kelly-Tyson method. The tested fibre lengths for the low filamentisation case are less than the corresponding Kelly-Tyson critical lengths from 3mm to 29mm. This implies that a transition from fibre pull-out to fibre fracture would occur between 29mm and 115mm. However, Figure 3-16 clearly shows that a reduction in strength occurs below 6mm. Since the fibre length effects are not observed in isolation it cannot be confirmed if a plateau in strength would be observed at 6mm if the effect of natural filamentisation was eliminated. Although the

experimental lengths are greater than the critical length predictions from the elliptical method, the critical lengths associated with bundle sizes of 338 filaments ($l_c$=2.17mm) and 1527 ($l_c$=4.61mm) are more realistic than from the Kelly-Tyson model when considering Figure 3-16. These bundle sizes correspond to experimental lengths of 3mm and 6mm, where it has been confirmed using SEM that pull-out does occur. Further validation work is clearly required using materials with a constant filament count, which can resist fragmentation down to lengths of 1 or 2mm.

| Fibre length (mm) | Filamentised | Mean bundle size (number of filaments) | Bundles per $cm^3$ | COV angle (%) | Critical bundle length (Kelly-Tyson) (mm) | Critical bundle length (Ellipse) (mm) | Fibre-fibre crossovers per unit length |
|---|---|---|---|---|---|---|---|
| 3 | Yes | 24 | 203356 | 7.4 | 1.50 | 0.58 | 8078 |
| 6 | Yes | 109 | 22387 | 8.9 | 3.20 | 1.23 | 3791 |
| 14 | Yes | 551 | 1968 | 30.4 | 7.20 | 2.77 | 1686 |
| 23 | Yes | 1411 | 480 | 59.2 | 11.52 | 4.43 | 1053 |
| 29 | Yes | 2205 | 245 | 87.0 | 14.40 | 5.54 | 843 |
| 58 | Yes | 8820 | 30 | 246.1 | 28.80 | 11.07 | 421 |
| 115 | Yes | 24000 | 5 | 615.6 | 47.50 | 18.26 | 250 |
| 3 | No | 338 | 14439 | 10.8 | 5.64 | 2.17 | 2534 |
| 6 | No | 1527 | 1598 | 33.3 | 11.98 | 4.61 | 1192 |
| 14 | No | 7752 | 139 | 113.8 | 27.00 | 10.38 | 529 |
| 23 | No | 19845 | 34 | 228.9 | 43.19 | 16.61 | 331 |
| 29 | No | 24000 | 22 | 292.5 | 47.50 | 18.26 | 296 |
| 115 | No | 24000 | 5 | 615.6 | 47.50 | 18.26 | 250 |

**Table 5-1 Predicted mean bundle sizes for varying chop length and level of filamentisation, also showing angle distribution variation and predicted critical bundle lengths for both circular and elliptical profiles. All models assume a composite volume fraction of 30% and a tow volume fraction of 60%. The critical fibre lengths quoted are assuming the tow strength is constant at 4000MPa. However, the tow strength is a function of the fibre length therefore the critical tow length is also a function of the fibre length.**

## *5.5. Analytical strength model*

### 5.5.1. Introduction

The micromechanical model of van Hattum and Bernado [97] has been further developed in this chapter to predict the tensile strength of laminates containing a random distribution of transversely isotropic bundles. A multi-stage model is adopted and the approach is split across four levels: single UD fibre strength; UD bundle strength; discontinuous UD ply strength and orientation averaging. The fourth order stiffness tensor ($C_{ijkl}$) for each UD ply (see Section 4.3.3) is subsequently used to calculate the fourth order strength tensor, in order to apply a suitable failure criterion.

### 5.5.2. Level 1 – Single UD fibre strength

Fibres tend to be brittle solids and due to flaws along their lengths, their strengths are stochastic in nature. The mean strength of a fibre ($\bar{\sigma}$) is customarily described using a Weibull distribution [88]:

$$\bar{\sigma} = \sigma_0(l)\Gamma\left(1+\frac{1}{m}\right) \qquad \textbf{Equation 5-12}$$

where $\Gamma$ is the gamma function, $\sigma_0(l)$ is the Weibull scale parameter which is a function of the gauge length and $m$ is the Weibull modulus (a high $m$ indicates a low variability in strength). Equation 5-12 can be expressed in terms of the filament strength as a function of the gauge length as follows:

$$\sigma_f(l) = \sigma_0\Gamma\left(1+\frac{1}{m}\right)l^{-\gamma/m} \qquad \textbf{Equation 5-13}$$

where $\gamma$ is a constant determined experimentally and $\sigma_0$ is the filament strength at $l$=1mm. Van Hattum and Bernado [97] present the required parameters for a Tenax HTA 5131 carbon fibre. Values of $m$=9.7060, $\gamma$=1.5083 and $\sigma_0$ =5199.4MPa are used

for subsequent calculations. The effect of increasing filament length on the tensile strength is demonstrated in Figure 5-3. The tensile strength of the filament is reduced by 37% as the gauge length increases from 5mm to 100mm.

The critical filament length ($l_{c_{filament}}$) of the filament can be calculated using the conventional Kelly-Tyson model [102]:

$$l_{c_{filament}} = \frac{\sigma_f(l)d}{2\tau}$$ **Equation 5-14**

The fibre strength (as a function of the fibre length) is estimated using Equation 5-13. The fibre diameter ($d$) is constant at 7μm and the shear strength can be approximated according to Van Hattum and Bernado [97], assuming a perfect interfacial bond and an isotropic matrix as:

$$\tau = \frac{\sigma_m}{\sqrt{3}}$$ **Equation 5-15**

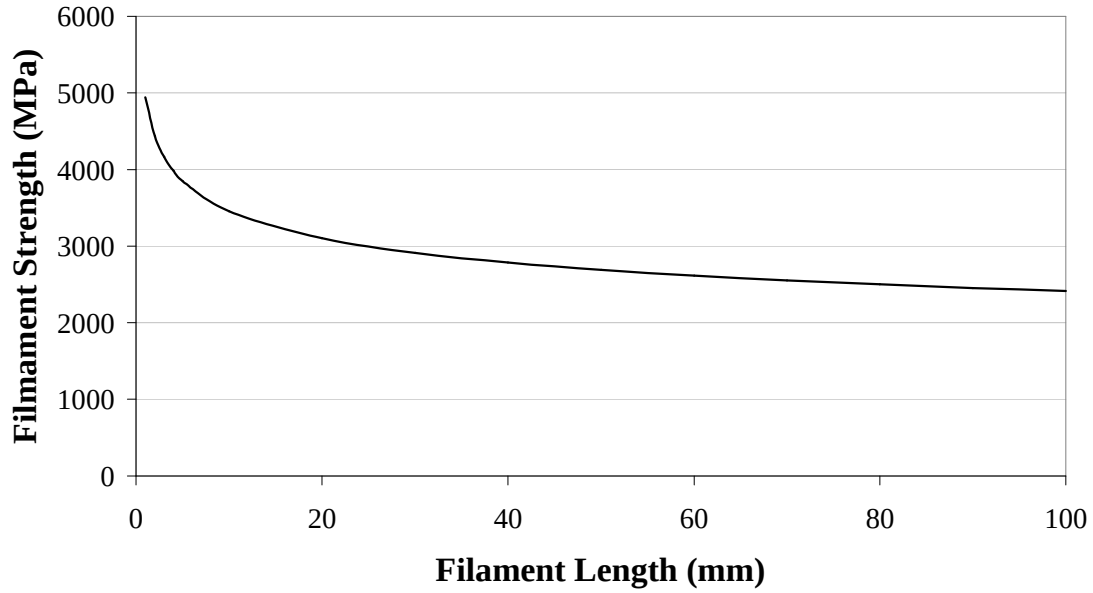


**Figure 5-3 Level 1: The influence of fibre length on the tensile strength of carbon filaments. Weibull parameters and constants are taken from [97] for Tenax carbon fibre. Incidentally, the manufacturer's data sheets for both STS and HTA fibre report a tensile strength of 4300MPa in every case.**

### 5.5.3. Level 2 – UD bundle strength

The longitudinal tensile strength of a unidirectional bundle with length dependent properties can be expressed using a piecewise ROM function [102]:

$$\sigma_{tow}(l) = V_{tow}\frac{\tau l}{d} + \sigma'_m\left(1 - V_{tow}\right) \quad \text{for } l < l_{c_{filament}} \qquad \textbf{Equation 5-16}$$

$$\sigma_{tow}(l) = V_{tow}\sigma_f(l)\left(1 - \frac{l_{c_{filament}}}{2l}\right) + \sigma'_m\left(1 - V_{tow}\right) \quad \text{for } l \geq l_{c_{filament}} \qquad \textbf{Equation 5-17}$$

where $\sigma_{tow}(l)$ is the failure strength of the tow at a given length

$\sigma_f(l)$ is the failure strength of a single filament for a given length

$l_{c_{filament}}$ is the critical filament length

$l$ is the length of the bundle

$V_{tow}$ is the volume fraction of filaments within the tow

$\sigma'_m$ is the ultimate stress of the matrix

Equation 5-13, Equation 5-14 and Equation 5-15 are substituted into either Equation 5-16 or Equation 5-17 depending on the critical length inequality. Tow strength as a function of filament length is plotted in Figure 5-4. The matrix failure strength is taken to be 65MPa (determined experimentally for epoxy DLS1678). Beyond the peak at 2mm there is a distinct reduction in strength with increasing length caused by the associated Weibull effects. Tow strength is reduced by 35% when the gauge length is increased from 5mm to 100mm. The shape of the curve depicts the general trend observed in the experimental DCFP strength data presented in Figure 3-16.

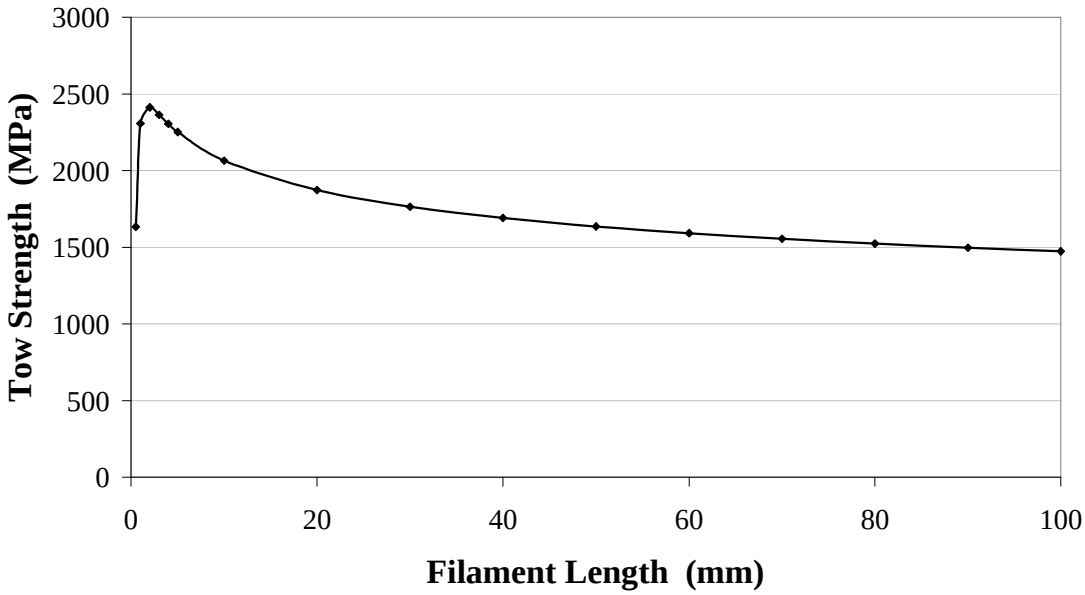


**Figure 5-4 Level 2: Tow strength vs. filament length for a carbon/epoxy tow with a tow volume fraction of 60%. Beyond the critical length a reduction in strength is experienced due to Weibull effects. This forms the second level of a multi-stage model for predicting strength of DCFP laminates. The values presented here are independent of filament count (considered at Level 3).**

### 5.5.4. Level 3 – UD ply strength

The Kelly-Tyson ROM model [102] is re-applied at Level 3 to calculate the strength of UD plies containing transversely isotropic bundles. Potential Weibull effects associated with increasing the filament count within the tow are unknown. However, the effect of increasing tow filament count is manifested in the increased tow diameter, where higher filament counts can reduce the laminate strength due to a smaller interfacial bond surface per unit area of cross section. Equation 5-16 and Equation 5-17 are modified accordingly to predict the longitudinal strength of the ply:

$$\sigma_{ply}(l) = V_{ply}\frac{\tau l}{d_{tow}} + \sigma'_m\left(1 - V_{ply}\right) \qquad \text{for } l < l_{c_{tow}} \qquad \textbf{Equation 5-18}$$

$$\sigma_{ply}(l) = V_{ply}\sigma_{tow}(l)\left(1 - \frac{l_{c_{tow}}}{2l}\right) + \sigma'_m\left(1 - V_{ply}\right) \qquad \text{for } l \geq l_{c_{tow}} \qquad \textbf{Equation 5-19}$$

where $V_{ply}$ compensates for the resin contained within the tow at Level 2:

$$V_{ply} = \frac{V_f}{V_{tow}}$$ **Equation 5-20**

The strength of a tow is calculated using the method outlined in Section 5.5.3 as a function of fibre length and the critical length of the tow ($l_{c_{tow}}$) is calculated using the elliptical method developed in Section 5.4. It is important to note that the critical length of the tow is also a function of the fibre length. From Equation 5-9, the critical tow length is directly proportional to the fibre strength, which is a function of the tow length due to the Weibull effects, shown in Figure 5-4. The effective diameter of the tow ($d_{tow}$) is a function of the tow filament count, filament diameter and the tow volume fraction.

Figure 5-5 shows the strength-length relationship for the UD plies at Level 3. Longer tow lengths are required for larger filament counts before a plateau in strength is observed. The same characteristic shape as Figure 5-4 is observed, but the critical length appears to be dependent on the filament count.

Equation 5-18 or Equation 5-19 is used to calculate the second and fourth order strength tensors for the UD ply. The tensor components for a transversely isotropic laminate (isotropic in the 2-3 plane) are [97]:

$$F_i = \{0\}$$ **Equation 5-21**

$$F_{ij} = \begin{pmatrix} \frac{1}{\sigma_{ply}^{\,2}} & \frac{-1}{2\sigma_{ply}^{\,2}} & \frac{-1}{2\sigma_{ply}^{\,2}} & 0 & 0 & 0 \\ \frac{-1}{2\sigma_{ply}^{\,2}} & \frac{1}{\sigma_{plyT}^{\,2}} & \left(\frac{1}{2\sigma_{ply}^{\,2}} - \frac{1}{\sigma_{plyT}^{\,2}}\right) & 0 & 0 & 0 \\ \frac{-1}{2\sigma_{ply}^{\,2}} & \left(\frac{1}{2\sigma_{ply}^{\,2}} - \frac{1}{\sigma_{plyT}^{\,2}}\right) & \frac{1}{\sigma_{plyT}^{\,2}} & 0 & 0 & 0 \\ 0 & 0 & 0 & \left(\frac{4}{\sigma_{plyT}^{\,2}} - \frac{1}{\sigma_{ply}^{\,2}}\right) & 0 & 0 \\ 0 & 0 & 0 & 0 & \frac{1}{\tau^2} & 0 \\ 0 & 0 & 0 & 0 & 0 & \frac{1}{\tau^2} \end{pmatrix}$$

**Equation 5-22**

The interfacial shear stress of the tow ($\tau$) is assumed to be the same as for the filament level (Equation 5-15) and the transverse ply strength can be calculated as follows:

$$\sigma_{plyT} = \sigma_m \left(1 - V_{ply}\right)$$

**Equation 5-23**

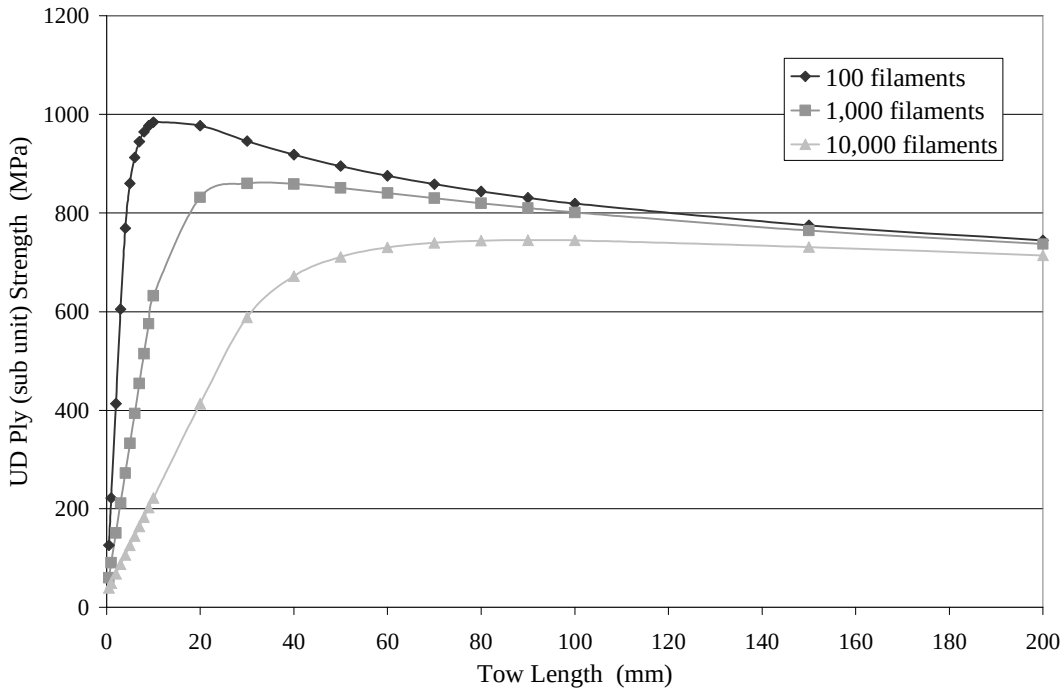


**Figure 5-5 Level 3: Longitudinal ply strength vs. tow length. The UD tows from level 2 are arranged into UD plies at a volume fraction of 50% (to achieve a composite $V_f$ of 30%). The effect of filament count is also shown.**

### 5.5.5. Level 4 – Orientation averaging

An orientation averaging process is utilised to randomise the UD plies containing transversely isotropic bundles. Firstly, the tensors in Equation 5-21 and Equation 5-22 are rewritten in terms of strain, in order to derive the strength tensor of the random laminate by assuming each ply is subjected to a constant strain. The second ($G_i$) and fourth order ($G_{ij}$) strain tensors are as follows (using contracted notation):

$$G_i = F_m C_{mi} \qquad \textbf{Equation 5-24}$$

$$G_{ij} = F_{mn} C_{mi} C_{nj} \qquad \textbf{Equation 5-25}$$

where $C_{mi}$ and $C_{nj}$ are transformations of the fourth order stiffness tensor for the UD ply, previously calculated in Chapter 4 using the Qiu and Weng model [173]. These tensor transformations are explained more clearly in Appendix.J using matrix notation. The unidirectional strain tensors in Equation 5-24 and Equation 5-25 are multiplied by the second and fourth order orientation tensors, as derived by Advani and Tucker [154], in the same way as for the stiffness model in Appendix H.3):

$$\begin{aligned}\left\langle G_{ijkl} \right\rangle = {} & B_1 a_{ijkl} + B_2 \left( a_{ij}\delta_{ij} + a_{kl}\delta_{ij} \right) \\ & + B_3 \left( a_{ik}\delta_{jl} + a_{il}\delta_{jk} + a_{ji}\delta_{ik} + a_{jk}\delta_{il} \right) \\ & + B_4 \left( \delta_{ij}\delta_{kl} \right) + B_5 \left( \delta_{ik}\delta_{jl} + \delta_{il}\delta_{jk} \right)\end{aligned} \qquad \textbf{Equation 5-26}$$

$$\left\langle G_{ij} \right\rangle = A_1 a_{ij} + A_2 \delta_{ij} \qquad \textbf{Equation 5-27}$$

$\left\langle G_{ij} \right\rangle$ and $\left\langle G_{ijkl} \right\rangle$ are converted back into contracted notation (see Appendix.I) and the inverses are calculated so that the orientation average strength tensors can be determined as follows:

$$\left\langle F_{ij} \right\rangle = \left\langle G_{mn} \right\rangle \left\langle C_{mi} \right\rangle^{-1} \left\langle C_{nj} \right\rangle^{-1} \qquad \textbf{Equation 5-28}$$

$$\left\langle F_i \right\rangle = \left\langle G_m \right\rangle \left\langle C_{mi} \right\rangle^{-1} \qquad \textbf{Equation 5-29}$$

Where $\langle C_{ij} \rangle^{-1}$ is the inverse of the orientation averaged stiffness tensor calculated using the Qiu and Weng model [173].

Finally, the Tsai-Wu failure criterion is applied to determine the failure stress of the random laminate since it is widely acknowledged that it is suitable for anisotropic materials [197]. Failure in the random laminate occurs when the following condition is met:

$$\langle F_i \rangle \sigma_i + \langle F_{ij} \rangle \sigma_i \sigma_j = 1 \qquad \textbf{Equation 5-30}$$

### 5.5.6. Results and discussion

The analytical model is validated in this section using experimental data from the literature and Chapter 3. Currently, the model accommodates only a mean filament count rather than the distributions established in Chapter 4. However, comparisons similar to those presented for the stiffness model in Section 4.4.2 can be made. The two independent variables of interest are the fibre length and the filament count. The model is initially compared with the experimental data from Section 3.4.2, which investigates the effect of fibre length at two induced filamentisation levels. The filament counts are unknown since they are a function of both the fibre length and the level of induced filamentisation. An analytical method presented in Appendix H.6 is used to estimate the filament count for each instance (see Table 3-2). The remaining input parameters for this study are presented in Table 5-2.

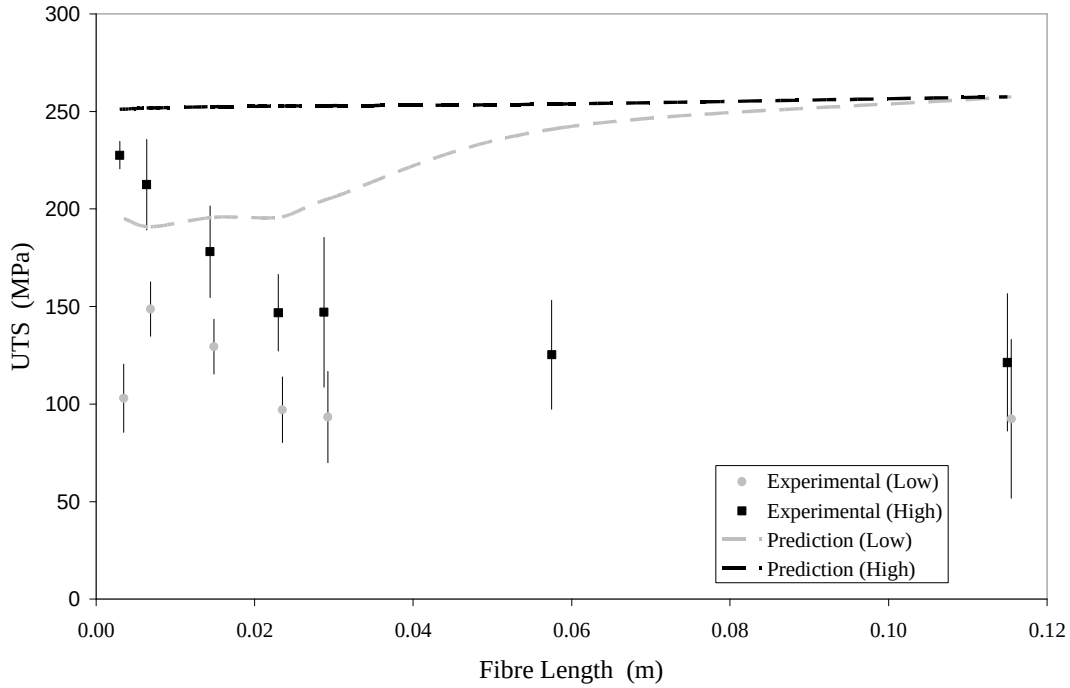


**Figure 5-6 Predicted and experimental ultimate tensile strength results as a function of fibre length and level of induced filamentisation. The level of natural filamentisation is a function of fibre length, which increases with shorter fibres. Low and high refer to the degree of induced filamentisation. (Note: the low filamentisation case has been offset by 0.0005m to improve clarity)**

The analytical strength model can clearly distinguish between different levels of filamentisation at short fibre lengths according to Figure 5-6. Discrepancy between prediction and experiment at longer fibre lengths can be attributed to a change in tow volume fraction. Although the filament count within the tow remains unchanged at lengths >100mm, the tow experiences end splaying which effectively increases the tow diameter and therefore reduces the strength of the laminate according to Equation 5-18.

The model by van Hattum and Bernado was originally developed for short fibres (0.16mm) [97], but has also been employed in a recent paper [193] to predict the length-strength relationship for longer fibres (12.5mm – 50mm). The extended model is used here to predict the tensile strength of laminates containing fibre lengths from 3-115mm. Although the characteristic shape of the curves from Level 1 (Figure 5-3), Level 2 (Figure 5-4) and Level 3 (Figure 5-5) is shared by the experimental data, the final laminate predictions from Level 4 do not reflect the experimental values. The strength results presented in Figure 5-6 show that this model is directly dependent on

the stiffness result from the Qiu and Weng model presented in Figure 4-22. Thus, the strength predictions are also grossly over estimated.

The model is also compared with the experimental DCFP strength data of Dahl *et al.* [187]. Laminates were produced with varying filament counts to investigate the effect of bundle size, using laminates 2mm thick with a nominal fibre volume fraction of 35% and 25mm long fibres. Details of constituent materials are not given in the literature so the input parameters for the model are taken from Table 5-2. However, it is specified that carbon tows have been selected to resist fragmentation therefore a mean filament count should be representative in this case. Figure 5-7 indicates that the general trend of increasing filament count versus decreasing strength is captured by the model. The prediction is within 5% at a filament count of 0.5K but the accuracy of the model reduces severely with increasing tow size, with errors approaching 143% at a filament count of 12K.

The accuracy of the model clearly diminishes as the homogeneity of the preform decreases (increasing both fibre length and filament count in Figure 5-6 and Figure 5-7 respectively). The model is strongly influenced by the volume-averaged stiffness tensor, which does not account for the stochastic effects that dominate the tensile strength of an inhomogeneous laminate.

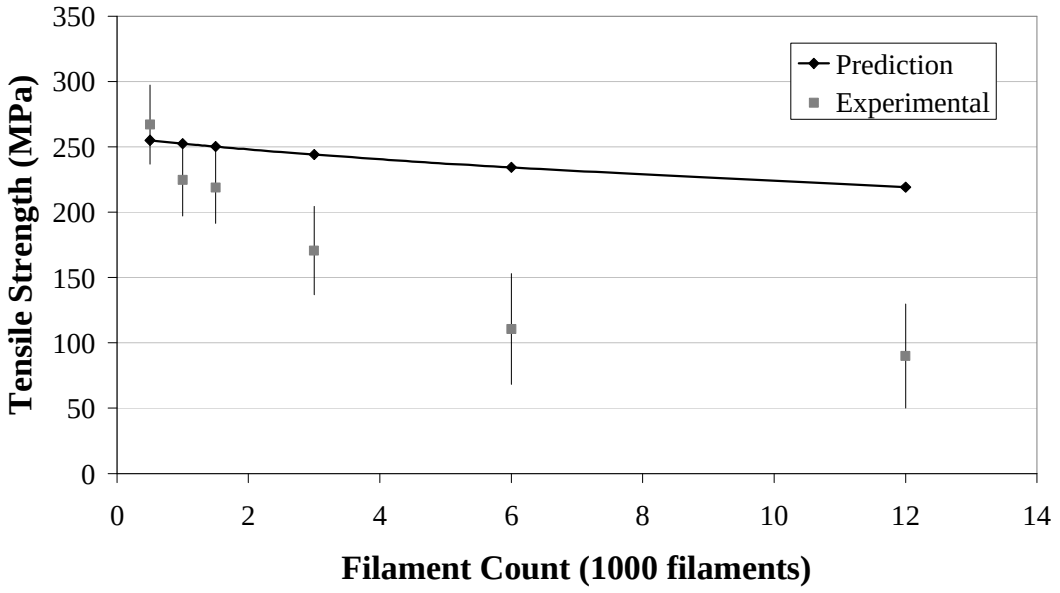


**Figure 5-7 Comparison between analytical strength model and experimental data taken from [187]. Random DCFP laminates contain 25mm tows of increasing filament counts at a nominal fibre volume fraction of 35%.**

| Property | Value | | Designation |
|---|---|---|---|
| Filament diameter | 0.007 | mm | $Ø_f$ |
| Tow volume fraction | 0.6 | | $V_{tow}$ |
| Composite volume fraction | 0.3 | | $V_f$ |
| Out of plane parameter for orientation av. | $\infty$ | | $b$ |
| | | | |
| **Stiffness Parameters** | | | |
| Plane strain bulk modulus | 20.19 | GPa | $K$ ($k_{23}$) |
| Cross modulus | 12.14 | GPa | $L$ |
| Axial modulus under axial strain | 234.23 | GPa | $n$ |
| Transverse shear modulus | 8.06 | GPa | $m$ ($m_{23}$) |
| Axial shear modulus | 10 | GPa | $p$ ($m_{12}$) |
| Matrix Poisson's ratio | 0.38 | | $\nu_o$ |
| Matrix modulus | 3 | GPa | $E_o$ |
| | | | |
| **Strength Parameters** | | | |
| Filament Weibull shape parameter (modulus) | 9.706 | | $m$ |
| Filament Weibull scale parameter | 5199.4 | MPa | $\sigma_o$ |
| Gamma | 1.5083 | | $\gamma$ |
| Matrix strength | 65 | MPa | $\sigma_m$ |

**Table 5-2 Analytical model input parameters used to validate the model against experimental data from Chapter 3 and the literature.**

## *5.6. Stochastic strength model*

### 5.6.1. Introduction

From the discussions in Section 5.5.6 and the literature reviewed in Section 4.2 it is apparent that independent strength and stiffness models should be considered and the stochastic nature of DCFP laminates should be incorporated for more accurate strength prediction. In this section a critical zone model developed by Wetherhold [107, 196, 198] is used in conjunction with the first two levels of the analytical model from Section 5.5 to predict the strength of random DCFP laminates. The model is used to study the effects of increasing both fibre length and tow filament count.

### 5.6.2. Methodology

Fibre crossovers were used in Chapter 2 as a qualitative measure of preform coverage and areal density variation. Results indicated that degree of preform coverage directly influenced the tensile strength of DCFP laminates, since fibre crossovers provide increased local reinforcement through load sharing at the crossover point [107]. Filamentisation, fibre length and laminate thickness are all critical factors in determining the number of crossover points, especially laminate thickness, where thick laminates tend to give full realisation of properties and thinner parts have lower strength and greater variability. Wetherhold [107, 196] provides an appropriate way of incorporating these stochastic effects into a strength prediction model by modifying the critical zone model of Fukuda and Chou [194, 195] for random fibre composites.

As a composite specimen progresses towards final fracture, the role of fibres bridging a microcrack becomes more important. Some of these microcracks may have been formed during composite manufacture, but additional ones form at bundle ends when a load is applied due to stress concentrations. They are expected to grow and coalesce during progressive fracture, resulting in a critical damage zone [107]. Within a critical zone, $\beta l$, the number of bridging fibres versus the number of fibres ending within the zone is evaluated (see Figure 5-8). Microcracking initiates failure at strains below the fibre failure strain. Ending fibres bear no load within the zone and final failure occurs in the critical section due to the accumulation of cracks. The strength of the composite is therefore directly proportional to the ratio of bridging fibres to ending fibres. The critical zone length, $\beta l$ is equivalent to the fibre ineffective length, (half the critical tow length, calculated from Equation 5-9), where $l$ is the average fibre length and $\beta$ is calculated as follows [190]:

$$\beta = \frac{l_c}{2l}$$ **Equation 5-31**

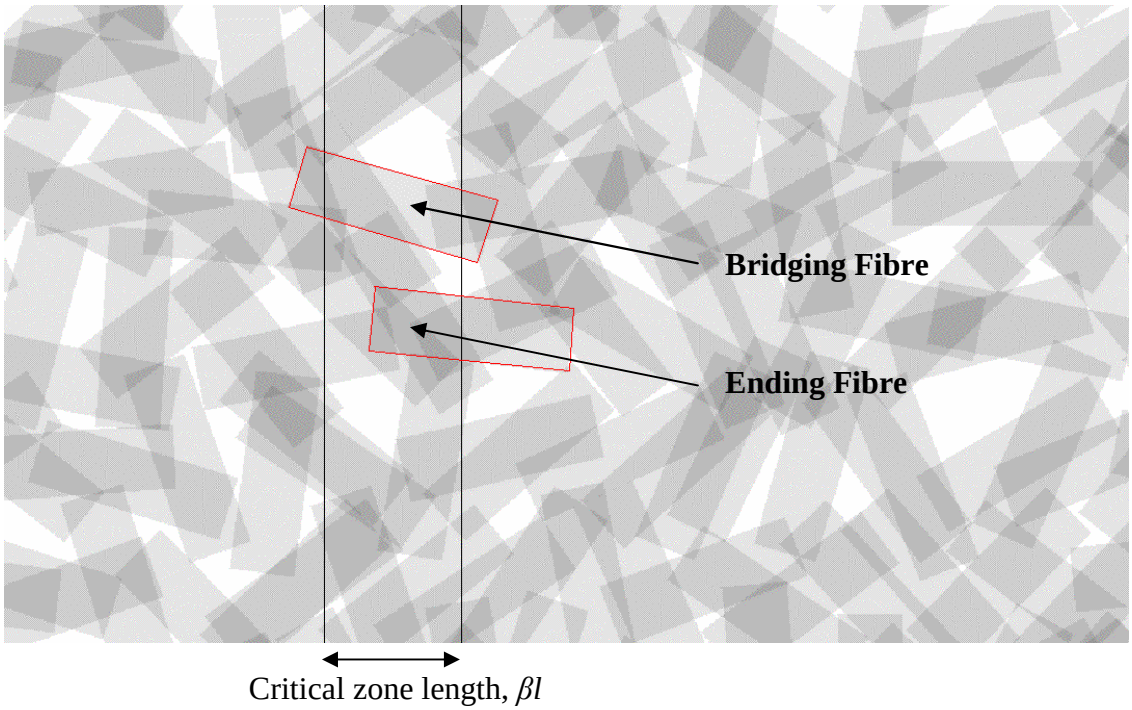


**Figure 5-8** **Schematic diagram of the critical zone concept.**

The onset of fracture occurs when the fibres bridging the critical zone reach their failure load. The load $L$ at the point of failure, carried by fibres at a distribution of angles is as follows:

$$L = \sum_{i}^{n} L_i$$ **Equation 5-32**

where $L_i$ is the component of the load carried by fibres orientated at angles between $\phi_i$ and $\phi_{i-1}$ to the loading direction and $n$ is the number of discrete angle intervals. Wetherhold [107] develops the model to incorporate a continuous orientation distribution, but a Monte-Carlo or similar numerical method is required for implementation. Strength variability is not studied here; therefore a discrete orientation distribution of 20 intervals is used and a uniform random orientation distribution is assumed. The failure stress of the composite is simply calculated using the following:

$$\sigma_c = \frac{L}{bc}$$ **Equation 5-33**

where *bc* is the specimen cross-sectional area.

A piecewise function is established to determine the probability that a fibre will possess an average angular orientation of $\bar{\phi}_i$ and will also bridge the critical gap:

$$p\left(\bar{\phi}_i\right)=\begin{cases}\dfrac{l\cos\bar{\phi}_i-\beta l}{a}P_i & l\cos\bar{\phi}_i \geq \beta l \\ 0 & l\cos\bar{\phi}_i < \beta l\end{cases} \qquad \textbf{Equation 5-34}$$

where *a* is the specimen length and $P_i$ is the proportion of fibres at the discrete angle $\bar{\phi}_i$ (the mid point of the orientation range $\phi_i$ to $\phi_{i-1}$). Equation 5-34 is used to determine the average load $L_i$ carried by the fibres at orientation $\bar{\phi}_i$:

$$L_i = p\left(\bar{\phi}_i\right)NA_{tow}\sigma_{tow}\cos^3\bar{\phi}_i \qquad \textbf{Equation 5-35}$$

$\sigma_{tow}$ is the ultimate strength of the tow and this is calculated directly from Section 5.5.3, using Equation 5-16 or Equation 5-17. The Weibull effects associated with increasing fibre length are therefore manifested in this calculation. *N* is the number of tows contained within the specimen volume. Assuming the specimen is prismatic with length *a*, width *b* and thickness *c*, *N* can be calculated as follows:

$$N=\frac{abcV_f}{A_{tow}l_{tow}} \qquad \textbf{Equation 5-36}$$

$V_f$ is the volume fraction of tows within the laminate; $l_{tow}$ is the average tow length and $A_{tow}$ is the cross-sectional area of the tow which can be calculated from Equation 5-3. To conclude, Equation 5-35 is evaluated for each discrete orientation, the summation is made using Equation 5-32 and finally the failure stress of the laminate is calculated from Equation 5-33.

### 5.6.3. Results and discussion

For the strength predictions shown in Figure 5-9, the parameter$\beta$ is calculated to be approximately 0.1 and 0.3 for the high and low levels of filamentisation respectively. The experimental data is taken from Chapter 3 and it is assumed that all of the fibres are beyond the critical length. This model cannot distinguish between filamentised and non-filamentised materials as such because the increased number of tows obtained with a smaller filament count is directly countered by the reduced area of the bundles, i.e. the volume of carbon remains constant. However, strength variations can be expected with varying levels of filamentisation, as the tow failure strength is calculated from the Weibull-based van Hattum [97] model detailed above. Non-filamentised tows have longer critical lengths and therefore reduced failure stresses compared with those with high filamentisation. The closed-form method developed in [196] is used with a uniform fibre angle distribution of 20 equally spaced intervals from $-\pi/2$ to $\pi/2$. The fibre lengths and filament counts in Table 3-2 were used to give the results shown in Figure 5-9 for critical gap lengths of $\beta l$ as discussed above.

The stochastic strength model shows very good agreement against the highly filamentised experimental data but the magnitude is sensitive to the calculated value of $\beta$. Further analysis shows that the prediction for the filamentised case increases by 6% when $\beta$ is halved to 0.05, but reduces by 13% for each length when $\beta$ is doubled to 0.2. Accuracy of the model is therefore directly dependent on the critical bundle length, which is currently calculated by the unproven elliptical method outlined above. The fit of the model diminishes with decreasing fibre length and errors of up to 18% are seen at 3mm for the curve presented in Figure 5-9. This discrepancy is thought to be a function of the filament count rather than the fibre length. This issue will be discussed in more detail below.

For the non-filamentised case, the stochastic model is unable to capture the reduction in strength at 3mm because it is assumed that all fibres are beyond the critical length. The predicted strength for the low filamentisation case is 9% lower than the experimental value for a length of 29mm but is 45% lower at 6mm. When this curve is compared to those in Figure 5-5 it is clear that the low filamentisation case (10,000 filaments) has

not yet reached a plateau in strength for the longer fibres because of the large inefficient bundles. The shape of the curve is therefore dominated by critical length effects rather than the inherent stochastic effects. In practice, the stochastic effects are considered to be more dominant for the low filamentisation case because the bundle size is on the same scale as the laminate thickness. Sections 3.2.8.1 and 3.2.8.2 demonstrated that greater heterogeneity can be expected for thinner laminates. But since the effects of filamentisation are not truly considered with this model, (the model is sensitive to the volume of carbon fibre, yet insensitive to filament packing) these factors are not reflected in the predictions for the low filamentisation case.

The model has also been validated against the experimental data from [187] and the effect of increasing filament count is presented in Figure 5-10. The overall trend of increasing filament count and decreasing strength is captured by the model, but the predictions are more reliable at lower filament counts. This supports the findings in Figure 3-16, which demonstrated that the accuracy of the model diminishes with increasing filament count. As discussed previously, the model does not distinguish between different filament counts as such, but laminate strength is inversely proportional to the bundle size since the tow failure strength is a function of the tow diameter. Although the Weibull length effects are taken into consideration, currently no data are available for the Weibull effects associated with the tow filament count. Therefore, the inaccuracy of the model at higher filament counts can be attributed to this oversight. The ‘Coleman factor’ [96] indicates that the strength of a large (definition of large unspecified), loose bundle is approximately 70% of the strength of a single filament, for a coefficient of variation of 17%. Assuming in the present case that a 12K tow can be classified as ‘large’, the error between the prediction and experiment in Figure 5-10 is reduced from 54% to just 12% by reducing the current bundle strength by 70%. The Coleman factor is independent of the filament count parameter so a correction cannot be applied at the remaining filament counts.

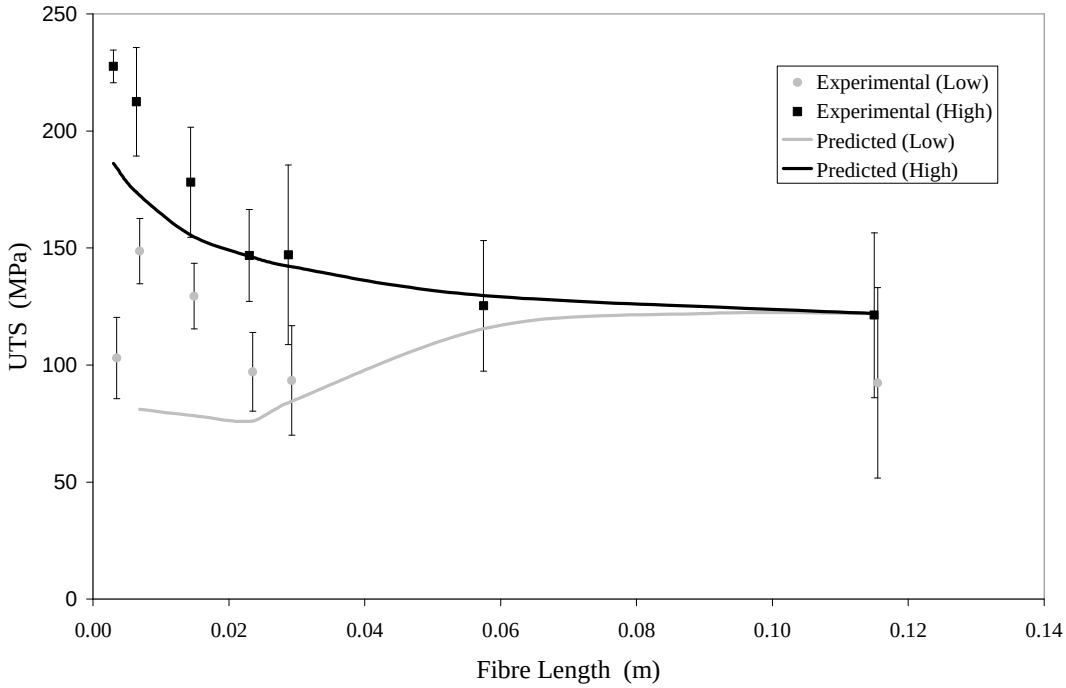


**Figure 5-9 Predicted and experimental ultimate tensile strength results as a function of fibre length and level of induced filamentisation. The level of natural filamentisation is a function of fibre length, which increases with shorter fibres. Low and high refer to the degree of induced filamentisation. (Note: the low filamentisation case has been offset by 0.0005m to improve clarity)**

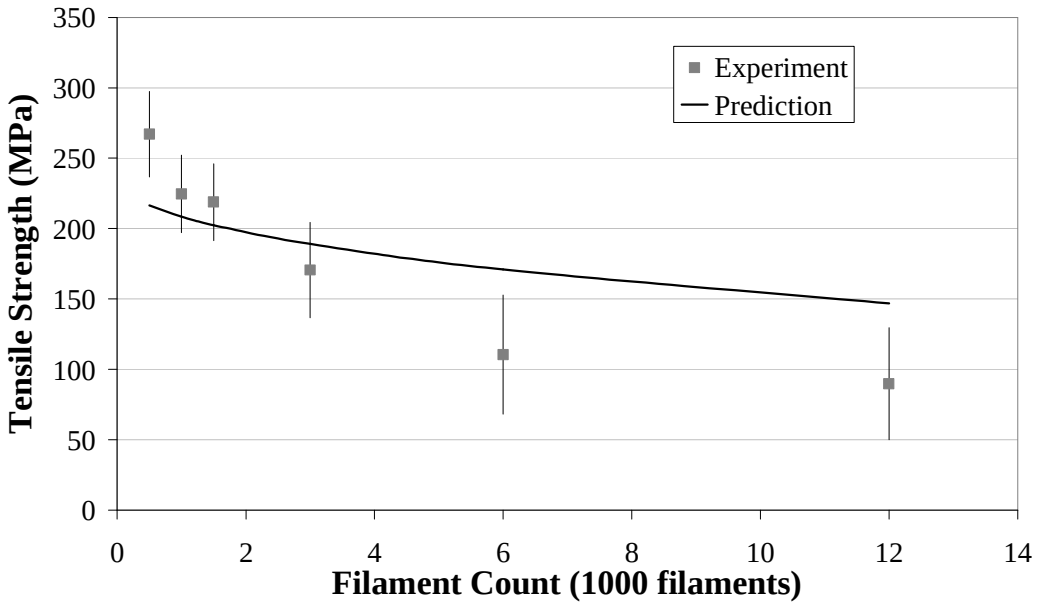


**Figure 5-10 Comparison of stochastic model with experimental data taken from [187]. Tensile strength is studied as a function of increasing tow filament count for a constant tow volume fraction of 60%. Laminate volume fraction is 35%.**

## 5.7. Conclusions

From the review of literature it is clear that the critical length effect for fibre bundles is poorly understood. Most discontinuous fibre strength models depend on a critical length term in order to derive the effective mechanical properties from a corresponding continuous system. The use of an elliptical profile modifies the conventional Kelly-Tyson theory to more accurately account for discontinuous tow properties in this chapter. Critical length predictions using this method show good correlation with the mechanical testing results but cannot be fully validated until accurate information about the bundle size is obtained. In the present work a mean bundle size has been assumed, although it is seen that a distribution of sizes exists in reality. This critical bundle length model forms the foundation of two random DCFP strength models.

An analytical model has been developed using a multi-level approach to account for the complex DCFP fibre architecture. Results show that the model is directly dependent on the stiffness tensor, calculated in order to derive the corresponding strain tensor. Predictions are therefore up to 170% higher than the experimental values for fibre lengths of up to 115mm. The review of literature indicates that independent stiffness and strength models are required for discontinuous fibre composites because of stress concentrations introduced at the fibre ends. Different critical lengths can be expected for stiffness and strength and the discrepancy between these lengths is a function of the fibre-matrix adhesion and the fibre/matrix stiffness ratio.

This work has shown that stochastic variations are very important in a material of this nature. A stochastic strength model has been modified to incorporate Weibull effects and to include variable filament counts for accurate property prediction. A good agreement is observed for highly filamentised fibres at all lengths but the model does not successfully differentiate between different levels of filamentisation. The associated Weibull effects for increasing filament count have been overlooked, hence the strength of the low filamentisation case is grossly under predicted.

# Chapter 6. Comparison of DCFP with commercial body panel systems

## *6.1. Objectives*

The nature of this work has been to optimise the DCFP process for producing thin laminates, typically less than 3mm in thickness. In this chapter the mechanical and physical properties of DCFP/RTM have been compared with a variety of commercial, fabric-based, carbon body panel systems. The main objective was to establish if cost-effective processes and materials are suitable for producing high quality closure panels. Properties including specific bending stiffness, specific in-plane performance, dent resistance and notch sensitivity were studied using automotive strip steel as an overall benchmark. One of the body panel systems and a cosmetic variant of DCFP were taken forward for detailed mechanical performance and cost comparison. A target weight save of 40% was specified for the composite panels over the existing steel production part. An automotive front fender was replicated from the two composite systems and compared to the steel counter part using a generic four-point bending test. Event-driven, technical cost modelling has been used to allow comparison of the chosen processes at a range of production volumes, based on a combination of data accumulated during the production of prototypes and estimates of the industrial process for the benchmark steel fender.

## *6.2. Introduction*

Falling material costs and processing innovations are leading to an increased use of carbon fibre in automotive applications. A wide variety of manufacturing processes are available for the production of body-in-white (BIW) closure panels, but the choice is strongly dependent upon the manufacturing volume. Highly labour-intensive processes such as the emerging low cost prepreg and semi-preg body panel systems can prove cost effective for low production volume [199], niche vehicle applications (e.g. 1000

parts per annum). Increasing levels of automation and the elimination of intermediate materials (e.g. fabrics, pre-impregnation, ply stacking etc.) are essential for higher volume manufacture. A processing route that can be automated and can directly utilise the raw materials is preferred. DCFP is a potential solution for medium volume production levels (10,000-30,000ppa). Sheet moulding compounds (SMCs) are currently in use in some applications, where a cost saving over metal parts can be obtained for a higher range of volumes (50,000-80,000ppa). However, glass fibre based materials are not able to return the weight savings required (>30%). Carbon fibre based moulding compounds, such as Hexcel's HexMC, Menzolit-Fibron's AdvancedSMC and DSM's CF-SMC are more promising for significant weight savings of up to 50% over steel.

Commercial body panel systems have been selected over a range of production volumes in order to validate the DCFP material. Semi-structural BIW components are primarily designed for high specific flexural modulus and dent resistance. This study aims to characterise each system and to establish the potential weight savings available for panels of equivalent flexural stiffness. The lay-up of each composite system has been specified to match the bending stiffness of 0.7mm sheet steel. Systems have been compared for flexural properties, in-plane properties, formability, dent resistance, notch sensitivity and cost.

## *6.3. Material characterisation for semi-structural applications*

### 6.3.1. Material selection

Full details of the materials selected for this study are available in Appendix.B. The lay-up of each system was designed to give a comparable bending stiffness to 0.7mm steel. Manufacturer's guidelines were followed and the shortest cycle time was selected where a choice was available. Brief details of each system are provided in Table 6-1 along with the fibre volume fraction, laminate thickness and the designation used throughout this chapter.

For low part volumes (<500ppa) a range of non-aerospace prepregs have been studied. The 2×2 twill fabrics are woven from high filament count tows (6K and 12K) of low grade carbon fibre, typically a high strength derivative rather than a more expensive high modulus. All prepregs have been consolidated under vacuum-only conditions rather than using a costly autoclave processing route. Final fibre volume fractions were 40%.

Resin film infusion (RFI) has opened up out-of-autoclave processing to higher production volumes (<1500ppa) by significantly reducing processing times and tooling costs. Materials are often supplied in kit form with all of the required fibre and resin in one laminated stack, which significantly reduces the lay-up time and in some cases drape characteristics are superior [199]. Fabric layers sandwich a resin film and are initially dry, improving air removal from the stack and therefore eliminating the requirement for debulking between plies. Two RFI materials have been selected for this study using the same 6K and 12K woven fabrics and similar B-stage cured resin system as the prepregs. The formability of RFI is of interest because the fibres are pre-stacked and the fabrics are typically much heavier than a comparable prepreg.

A low cost, liquid resin system is used to impregnate dry 6K and 12K 2×2 twill fabrics to investigate the effect of processing route. These liquid resin infused (LRI) plaques are directly comparable to the prepreg and RFI materials and will highlight the influence of the impregnation method on the mechanical properties. As shown in the appendix (Figure 7-3), there are considerable cost savings for using a liquid resin system because of the elimination of the pre-impregnation stage over the RFI and prepreg systems.

Due to the increased interest in carbon fibre for automotive closure applications, a number of prepreg manufacturers have developed dedicated body panel systems based on the RFI concept. Three materials are compared in this study: SP Systems' SPRINT; Cytec's Carboform; and ACG's ZPreg. Each system consists of dry woven fabrics sandwiched about a resin film with some form of low density core material to enhance bending stiffness. Achieving a class-A surface finish is paramount for exterior panels, therefore each system is used in conjunction with a surfacing ply (resin rich film with a fine glass weave) to minimise fibre print through and porosity.

For the medium volume level (~30,000ppa) DCFP preforms were made using two 24K Toho Tenax STS-J 5631 (1% PU surface sizing) tows processed simultaneously. The chop length was a hybrid (1× 23mm and 16× 5.75mm cut lengths for each revolution of the cutting roller) to maximise mechanical performance whilst maintaining dry preform stiffness and strength. The target robot speed was $0.4ms^{-1}$ with an approximate distance of 0.05m between successive passes. Initial calculations showed that a thickness of 2mm was required to match the bending stiffness of the 0.7mm steel benchmark. The final lay-up consisted of four layers; 100gsm veil/ 550gsm/550gsm/100gsm veil. The veil layers consisted of highly filamentised carbon tows (Toho Tenax 24K STS 5411) to promote a resin rich layer at the panel surface. This significantly reduces the surface roughness [61] by reducing fibre strike-through and was essential here in order to meet the critical threshold of $R_a$=0.16μm as stipulated in [200]. Flat plaques were moulded via RTM using DLS1692, a low-cost, high-reactivity epoxy resin system developed by Hexcel.

A commercial carbon fibre SMC was selected to represent the high production volume for 50-80,000 ppa. HexMC material is manufactured from chopped uni-directional prepreg, consisting of random bundles of fibre 50mm long by 8mm wide. These plaques were compression moulded using 80% charge coverage at a pressure of 80bar. HexMC is of particular interest because the mechanical performance should be comparable to DCFP.

| | Designation | Product | Fibre Volume Fraction (%) | Laminate Thickness (mm) | Supplier |
|---|---|---|---|---|---|
| 1 | Steel | DC05 53544 | - | 0.70 | Corus |
| 2 | Aluminium | AA-6111-T4 | - | 1.00 | Alcan |
| 3 | Semi-preg 1 | SPRINT CBS | - | 2.13 | SP Systems |
| 4 | Semi-preg 2 | ZPreg | - | 1.48 | ACG |
| 5 | Semi-preg 3 | Carboform | - | 1.42 | Cytec |
| 6 | 6K RFI | 6K 2×2 twill weave | 40 | 1.30 | SP Systems |
| 7 | 12K RFI | 12K 2×2 twill weave | 45 | 1.35 | SP Systems |
| 8 | 6K Prepreg | 6K 2×2 twill weave | 40 | 1.27 | SP Systems |
| 9 | 12K Prepreg | 12K 2×2 twill weave | 40 | | SP Systems |
| 10 | 6K LRI | 6K 2×2 twill weave DLS1554-2 | 51 | 1.17 | SP Systems Hexcel |
| 11 | 12K LRI | 12K 2×2 twill weave DLS1554-2 | 56 | 1.06 | SP Systems Hexcel |
| 12 | ASMC | HexMC | 57 | 1.30 | Hexcel |
| 13 | DCFP | 24K STS 5631 / 5411 DLS1692 | 21 | 1.78 | Toho Tenax Hexcel |

**Table 6-1 Candidate materials studied during DCFP benchmarking against commercial body panel systems. Designations are used throughout this chapter in reference to each respective system.**

### 6.3.2. Flexural properties

Candidate materials were initially assessed for flexural performance using a 3 point bend test (see Appendix D.1.5) to ensure they were comparable to 0.7mm steel (normalised results are presented in Figure 6-1). The flexural modulus generally falls within ±20% of the steel benchmark. Flexural performance of the prepreg, LRI and RFI materials is dominated by the laminate thickness, with the thicker, lower fibre volume fraction parts having higher flexural modulus. The average thickness of the LRI panels was approximately 1.10mm compared with 1.35mm for the RFI materials, which translates to a volume fraction of 56% and 40% respectively. Although the flexural stiffness for the ASMC material is too low, adding more charge material will increase the thickness of the laminate to improve the flexural performance. Figure 6-3 shows that the specific bending stiffness for ASMC is 150% higher than the steel benchmark, with sufficient scope to increase the mass of the ASMC panel whilst still achieving a

40% weight save. This problem is not easily resolved for the LRI because the target weight reduction would not be achieved if additional plies were introduced.

Semi-preg 1 and DCFP were specifically engineered to match the bending stiffness of 0.7mm steel (Semi-preg1 is within 0.7% and DCFP is within 3.7%). Both of these systems have an areal mass of approximately 2.3kg/m$^2$ and therefore both yield a mass reduction of 57% over the equivalent steel panel, as shown by Figure 6-2 .

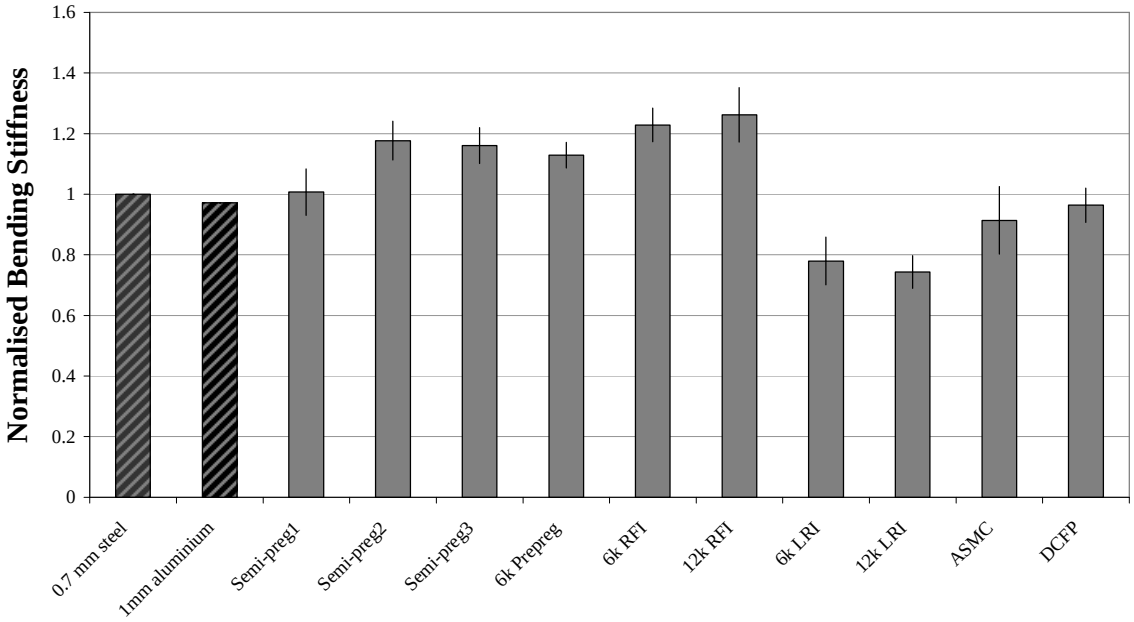


**Figure 6-1 Bending stiffness (EI) results normalised to 0.7mm steel for candidate systems (values for metals taken from supplier data)**

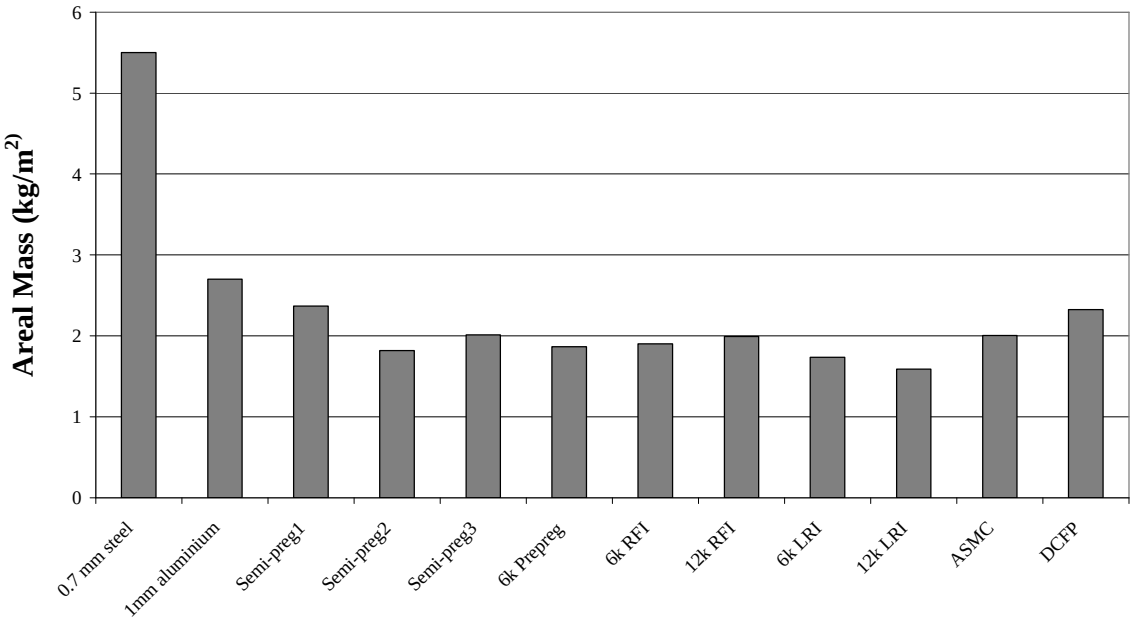


**Figure 6-2 Areal mass of each candidate body panel material**

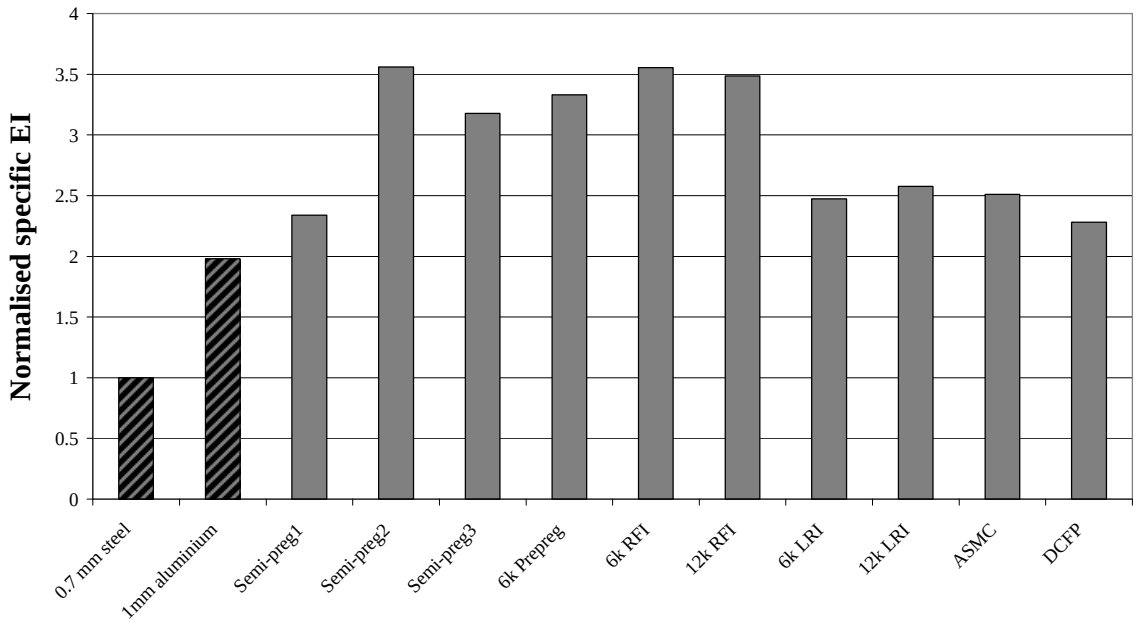


**Figure 6-3 Specific bending stiffness (based on areal mass) normalised to 0.7mm steel for candidate systems.**

### 6.3.3. Fabric formability

Formability during lay-up is one important factor in determining the suitability of a prepreg material for low volume manual production. The shear compliance of the fabric-based materials has been determined using a conventional picture frame test (see Appendix D.1.7 for details), where shear forces are presented as a function of shear angle. Tests were recorded using a digital camera to determine the fibre locking angle – the orientation at which the fabric starts to wrinkle. Prepreg, RFI and LRI were the three main materials of interest for this study because they use different impregnation routes for the same woven fabrics. The RFI material contains twice the areal mass of carbon fibre compared with the other two systems. Therefore, two layers of prepreg and LRI fabric were tested in the rig to enable a direct comparison with the RFI material.

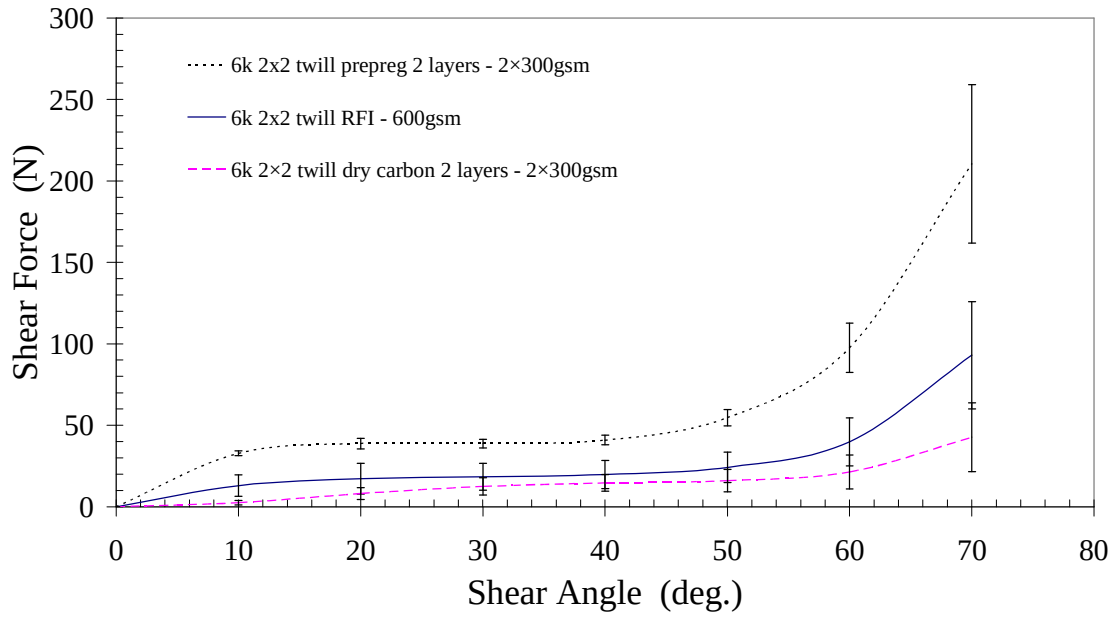


**Figure 6-4 Shear compliance curves for three candidate carbon fibre based systems at room temperature. Each system shares the same 6K 2×2 twill fabric but a different impregnation route.**

The initial resistance to shear of the prepreg is much higher than the RFI and LRI systems. RFI impregnation does not reduce the shear force of the prepreg to the level of the dry fabric (LRI), but does significantly reduce it by ~80% of the difference. Shear angles of 50º were achieved for the RFI material before the fabric started to wrinkle, compared with only 40º for the prepreg system. Single plies of prepreg and dry fabric (LRI) were also tested. The force required to shear a single ply of dry fabric was exactly half the force required for two plies for any given shear angle. An interaction between the tacky prepreg plies caused the shear force profile for two plies to be higher than if it had been derived through superposition. Nesting occurs between the fabric layers which causes the tows to deform and the fabric to shear inhomogeneously. The force required to shear two prepreg plies is therefore more than double the force required to shear a single ply for any given shear angle. Figure 6-5 confirms that the shear performance of RFI is superior to that of prepreg at higher shear angles (>40º), even for twice the fibre content.

The shear behaviour of the bulk plies (excluding the surfacing ply) of the three dedicated semi-preg body panel systems are presented in Figure 6-6. The three materials perform very differently due to their varied impregnation routes. Semi-preg 2 has a much lower shear stiffness than the other two systems and the shear profile is

similar to that of the dry fabric in Figure 6-5. The resin is applied in continuous stripes rather than in film form to enable better air removal at the tool face during consolidation. Whilst the shear stiffness is very low, the fabric does not shear uniformly as Figure 6-7 shows. The degree of shear in the black impregnated stripes is lower than in the white regions during the test, as indicated by the relative widths of the black to white stripes. This would cause local variations in the fibre angle and consequently variations in mechanical performance for the moulded laminate.

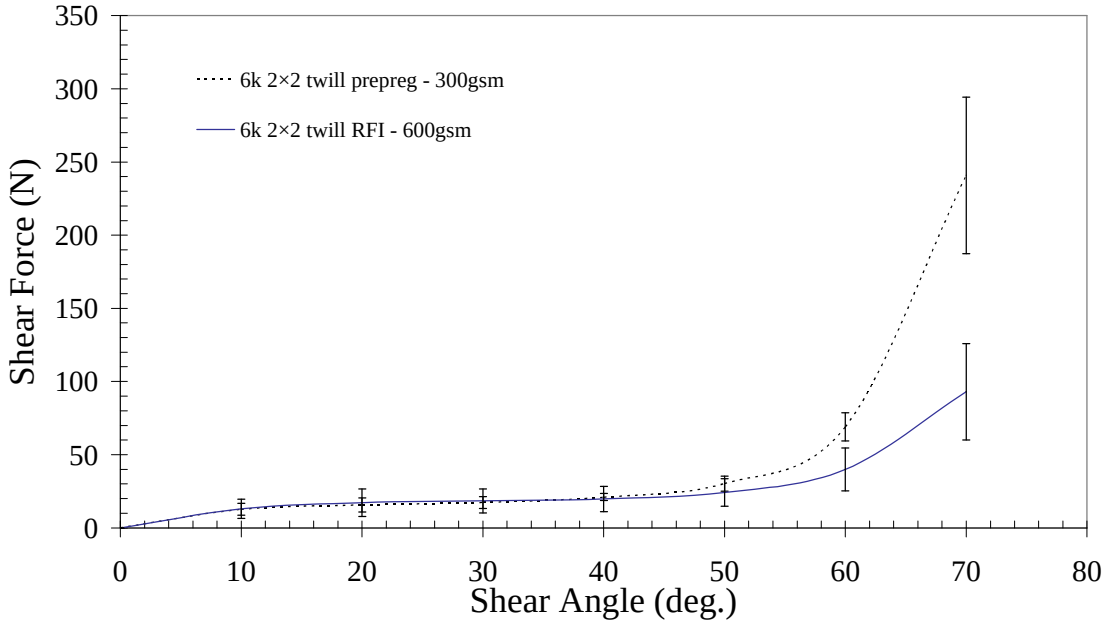


**Figure 6-5 Room temperature shear compliance curves for a single layer of 6K prepreg and a stacked RFI system.**

Semi-preg 1 uses the same matrix film system as the RFI materials tested above, but the resin film contains low density glass microspheres to improve the specific bending properties. This core material increases the shear stiffness over the range of angles tested (at a steady state shear angle of 30º the required shear force increases from 18.4N to 29.6N). The shear stiffness of semi-preg 3 was much higher than any other material tested. This is a three part system (surface ply/core ply/backing ply) whereas the other dedicated body panel systems both have 2. The surface ply of semi-preg 3 was omitted and the shear compliance of the core ply and backing ply was tested together. The core material is a dry polyester felt and this was the mating surface to the backing ply, eliminating any coupling between the two. Although the carbon fibre content is similar for semi-preg 1 and semi-preg 3, the shear characteristics are considerably better for

semi-preg 1. Firstly, the polyester core material does not shear as effectively as the embedded microspheres in the resin film. Secondly, the out life of this material is much greater than the other two systems and consequently the specified viscosity of the matrix is much higher at room temperature. The manufacturer's data sheet suggests that the optimum forming temperature is 40ºC which is a distinct disadvantage over the other two semi-preg systems for manual hand lay-up at room temperature.

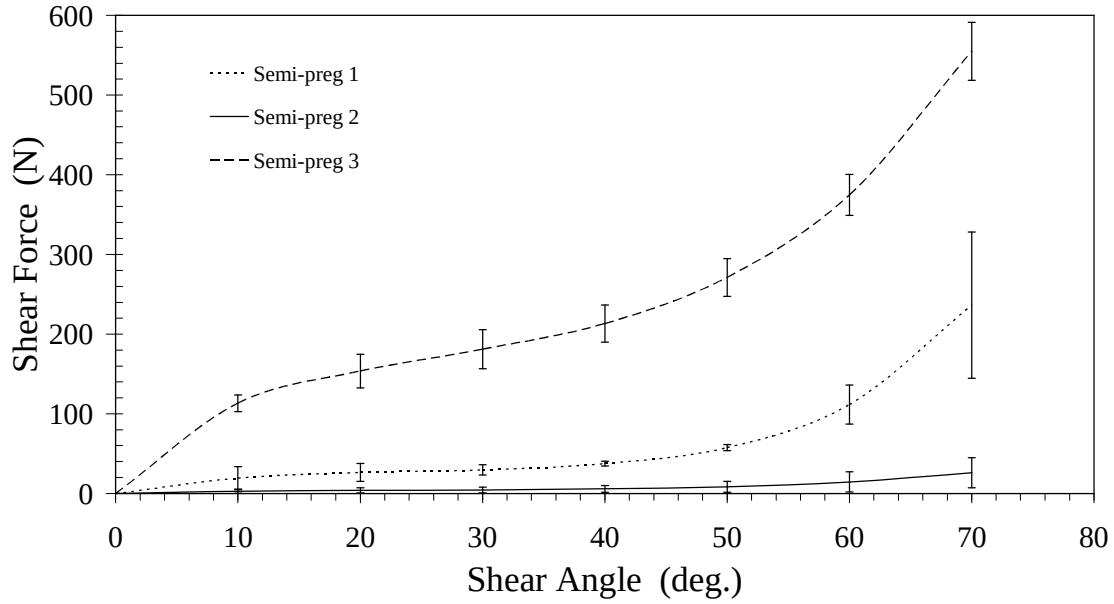


**Figure 6-6 Room temperature shear compliance curves for the three dedicated body panel systems. Only the reinforcement plies are tested.**

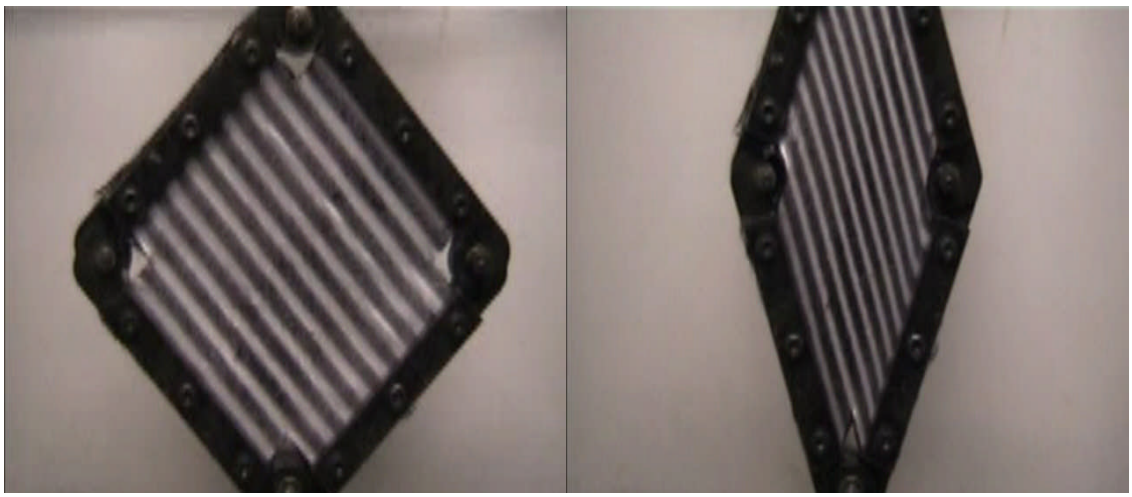

**Figure 6-7 Photographs taken (left) at the beginning and (right) during the picture frame test for ZPreg. The ratio of impregnated (black) to dry (white) fibres at the start of the test is 1:1. The right hand image shows that the impregnated stripes have sheared less than the dry stripes.**

### 6.3.4. Dent resistance

Dent resistance is an important physical parameter of automotive body panels and is defined as the force required to yield a permanent plastic deformation [201]. The magnitude of the denting force or the indentation energy is either measured for a given dent depth [202-204], or at the onset of visible denting [205, 206]. Testing is usually performed quasi-statically to simulate low speed collisions, such as door-door contact in car parks, but dynamic tests are sometimes used to simulate hail stones using falling weights or ballistic methods. Dynamic tests are particularly important for rate sensitive materials like some polymer composites.

Dent resistance is primarily influenced by the yield stress of the material and the panel thickness [202]. Higher yield strengths delay the onset of plasticity and therefore increase the force required to produce a permanent deformation. The yield strength of steel for example, can be increased by work-hardening during stamping, or bake-hardening during the paint process to improve the dent resistance of the panel [203, 204]. The relationship between Young's modulus and dent performance however, is less understood, with various trends being reported for panels of equivalent thickness but differing moduli [203, 207].

Other important variables include component geometry, boundary conditions, radii of curvature and location of dent (relative to panel constraints) [201, 204]. Processing such as stamping and pressing also indirectly affects the dent performance of metallic panels due to the local change in thickness during forming. A greater control over thickness variation can be achieved with polymer-composite moulding processes such as RTM, which have matched tools to provide high dimensional stability.

There are no published standards for dent resistance, which has led researchers to develop their own methods for design and quality control purposes [201, 202]. Most researchers use a hemi-spherical indenter on a double-curved part [201-203] to characterise the dent resistance. Component geometry, especially part curvature, significantly influences the dent results [201], therefore previous dent studies have been component specific which makes cross comparison of results very difficult.

A displacement-controlled denting procedure was used for this study using flat coupons (developed in-house by Weager [205], see Appendix D.1.6), which makes specimen preparation easy and cross-comparison of results more accurate. In general, the carbon composite panels performed 5-6 times better than the steel panel. Figure 6-8 shows that the steel strip reaches the visible dent threshold at 0.5mm of displacement, whereas the composite panels are permanently dented after being subjected to a 2.25-3.25mm displacement. At small displacements (<1.5mm) the dent performance of the DCFP material is around 3 times lower than the semi-preg body panel systems, possibly due to the compliance of the random chopped fibres compared to the continuous woven fabric. At larger displacements (~3mm) the semi-preg body panel system is around 25% better. Performance of the sandwich panel semi-preg 1 degrades rapidly once the core is damaged in compression; this effect is visible after 3.5mm of displacement.

Although each panel has a similar bending stiffness (EI) to 0.7mm steel (Figure 6-1), there is a strong trend ($R^2$=0.8723) between dent performance and specific flexural stiffness, as demonstrated in Figure 6-9. Generally, the fabric based prepregs and semi-pregs exhibit better dent performance compared with the random DCFP and ASMC systems. This effect can be attributed the variation in specimen thickness. The random panels are generally thicker than the fabric-based plaques because of their inherently lower modulus, in order to achieve a comparable bending stiffness. Therefore the thinner woven plaques are more compliant and deflect at low loads, whereas the A surface of the random material is more susceptible to local damage by the indenter at the same loading. There is also a clear relationship between dent performance and material cost as shown by Figure 6-10. Although the dent performance of the prepreg system is ~6 times better than the steel panel, the material cost is 39 times higher. Achieving an acceptable painted surface finish with the woven prepreg is also a major challenge [9] and the dent performance of the painted composite panel is unknown. Minor dents in steel panels can be successfully pushed out from the B surface without damage to the paint, significantly reducing the cost of repairs. However, the painted surface of the composite panel may become broken due to the low strain to failure of the underlying substrate. As the specimen is strained, the underside is put in tension and a shear force develops through the thickness. Possible damage modes include compressive yielding under the indenter, tensile failure of the composite underside or

even delamination. These failure modes severely reduce the possibility of restoring the panel without a respray.

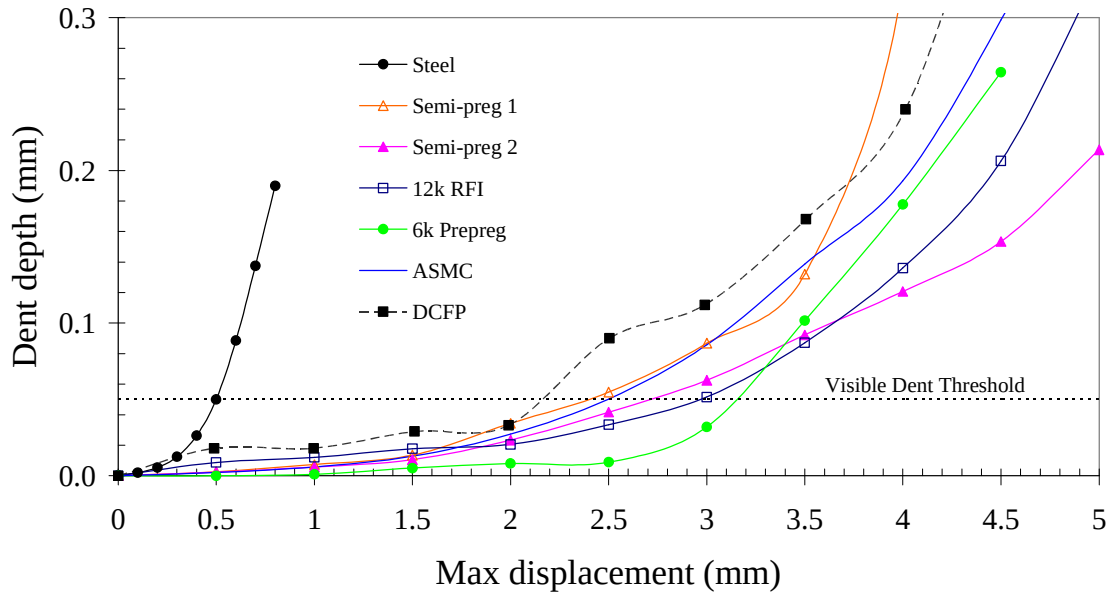


**Figure 6-8 Flat plate dent test results showing visible dent threshold for a selection of the candidate body panel materials**

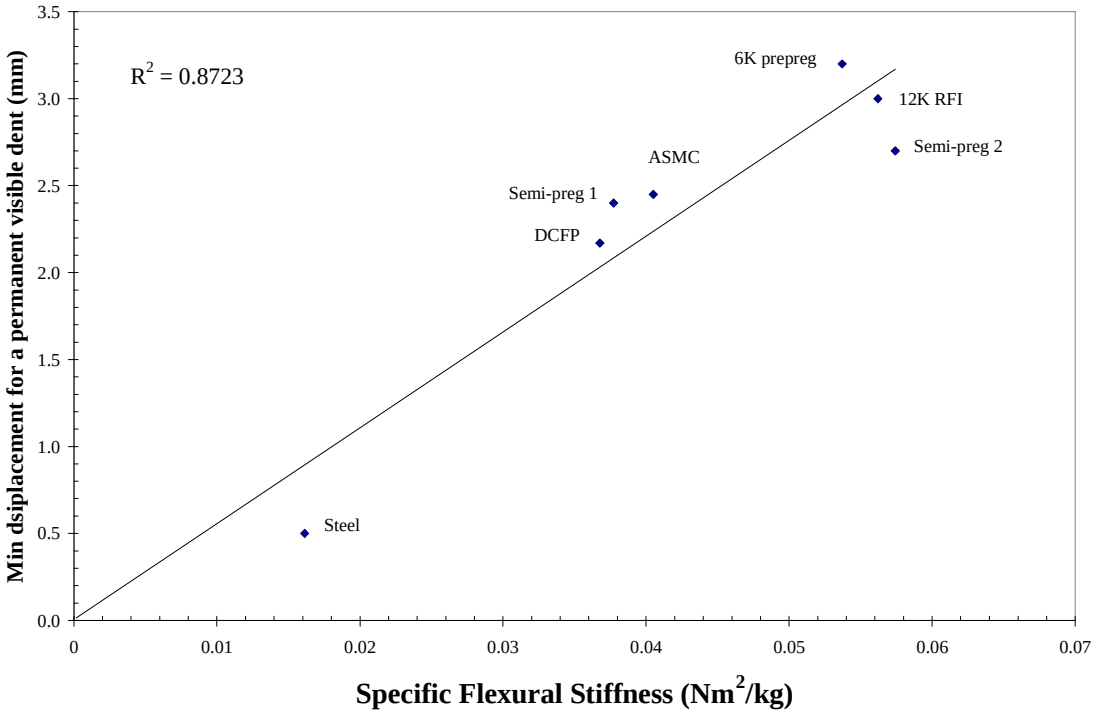


**Figure 6-9 Relationship between dent performance and specific flexural stiffness.**

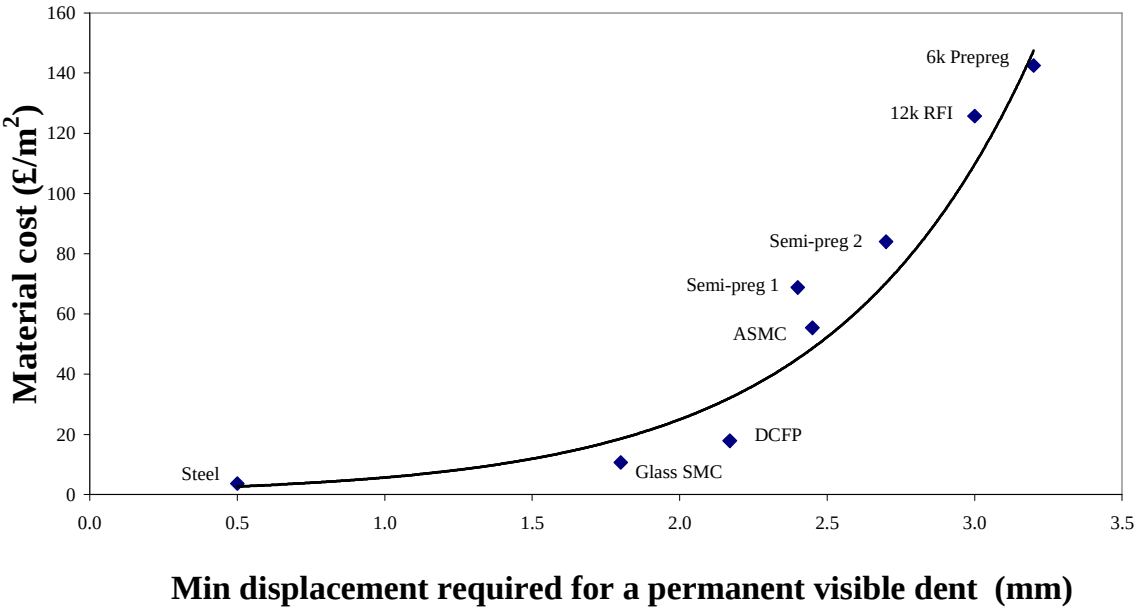


**Figure 6-10 Comparison of raw material cost and the dent performance of a selection of body panel systems. Dent performance is expressed as the minimum displacement required for a permanent visible dent to remain on the specimen surface. A typical automotive glass SMC (22% E-glass by volume/ LPA filled UP) is compared with the carbon systems [205].**

### 6.3.5. In-plane mechanical performance

Quasi-static tensile, compressive and shear tests have been completed in order to characterise the in-plane properties of the candidate body panel systems. Although the flexural stiffness of each panel is similar, the in-plane properties differ depending on the laminate architecture. The fabric-based 0/90º materials had a distinct advantage over the discontinuous, random DCFP and ASMC materials and arguably should have been manufactured using a quasi isotropic $(0º/\pm45º/90º)_s$ arrangement. However, the dedicated semi-preg body panel systems were supplied in a laminated kit and were designed to be used in a 0/90º configuration, therefore the remaining systems were all moulded similarly for comparison.

Figure 6-11 show that the stiffness of the prepreg, RFI and LRI materials are generally 100-150% higher than the semi-preg materials. The absolute values are presented in each case rather than the effective stiffness; therefore the thickness of the core is not discounted in the modulus calculation even though it contributes little stiffness or strength to the laminate. It is also important to note that the semi-preg systems have approximately 50% of the carbon content of the prepreg, RFI and LRI systems. The

flexural stiffness is achieved through the increased second moment of area from the core material, rather than the stiffness of the carbon skins.

The random ASMC material performs very well in comparison to the semi-preg systems, in terms of both stiffness and strength (see Figure 6-12). The random nature of the ASMC would be particularly useful in torsion or shear applications since the shear modulus is approximately 50% of the tensile modulus, compared with ~10% for a continuous, 0/90º woven panel. The shear strength is also approximately the same as the tensile strength for ASMC, something which was previously noted for the DCFP material in Section 3.6.3 and is repeated in Figure 6-12 for the cosmetic variant. The ASMC material forms a useful benchmark against the DCFP material for both stiffness and strength, since it is the closest competitor. Semi-structural DCFP is mechanically competitive with the commercial ASMC material. Although the tensile, compressive and shear moduli are all 50% higher than DCFP, the carbon volume fraction of ASMC is also approximately 50% higher (27% vs. 57%). The fibre fraction of ASMC is fixed and the volume of the charge is used to control the specimen thickness and therefore the flexural properties. The volume fraction of the DCFP material is more freely controlled and can be increased in order to match the moduli of ASMC, whilst still maintaining an appreciable weight save over the steel panel. The tensile strength of DCFP is 30% higher than ASMC when normalised to a volume fraction of 57% because of coverage related issues. High filament count tows remain in bundle form but are sheared by the compression moulding process. There are few tow cross-overs per unit thickness and stress concentrations form at the bundle tips due to the synchronised filament ends. This makes ASMCs unsuitable for very thin components (<2mm) and also highlights the importance of the filamentisation technique used for DCFP processing.

Figure 6-13 and Figure 6-14 shows the effect of impregnation method and fibre tow size on the stiffness and strength for the fabric-based body panel systems. All three systems were vacuum consolidated but the mechanical properties were slightly different in each case due to the molecular weight variation between resin systems. The tensile properties and fracture toughness of the resin system are proportional to the molecular weight [207]. An indication of the variation between the three systems can be established by comparing the initial resin viscosities, where higher molecular

weights result in higher viscosities. The prepreg has a minimum viscosity during processing of 70P, compared with 21P for RFI (both measured at 80ºC) and 2.25P for the LRI system (measured at 25ºC). The stiffness of the 6K prepreg is therefore higher than the 6K RFI, which is higher than the 6K LRI, in tension, compression and shear (Figure 6-13, normalised with respect to volume fraction). This trend is also repeated for the tensile, compressive and shear strengths (Figure 6-14, normalised with respect to volume fraction). The tensile stiffness and strength of the 6K LRI panel are 10% and 8% lower than the 6K prepreg respectively. The raw materials of the liquid infusion route offer a 54% cost saving over the prepreg (see Figure 7-3, Appendix B.3).

Tow filament count also presents a trade-off between mechanical performance and material cost. Filament count was of particular importance for the DCFP materials tested in Chapter 3 because of the stochastic effects associated with the preform coverage and the large stress raisers at the bundle ends. Higher filament counts for the fabric-based materials cause poor fibre nesting between plies and an increase in tow waviness/crimp. Figure 6-13 and Figure 6-14 show the effect of increasing the tow filament count on the in-plane stiffnesses and strengths respectively for the RFI and LRI systems. Figure 6-13 demonstrates that tensile, compressive and shear moduli are lower for the 12K fabric in comparison to the 6K equivalent, for both the RFI and LRI processes. Tensile and shear moduli are approximately 10% lower, but the compressive moduli are up to 30% lower due to a lower onset of fibre buckling caused by the fibre waviness. Trends regarding strengths (Figure 6-14) are inconclusive because of an unforeseen difference in carbon grade between the 6K and 12K fabrics. The 6K fabrics were woven from T300 carbon tows, with a fibre failure strength of 3.5GPa. The 12K fabrics were woven from T700, which has a 40% higher failure strength of 4.9GPa compared with the 6K. Superficially, the tensile strengths of the 12K materials in Figure 6-14 appear to be higher than the 6K because of the difference in carbon fibres. Yet the compressive strengths remain to be lower for the 12K fabric because of the buckling effects. This same trend is anticipated for the tensile strengths if the raw materials were the same.

This section has shown that both filament count and manufacturing process do have an effect on both stiffness and strength. However, significant cost savings can be achieved by opting for a heavier tow and a resin film approach.

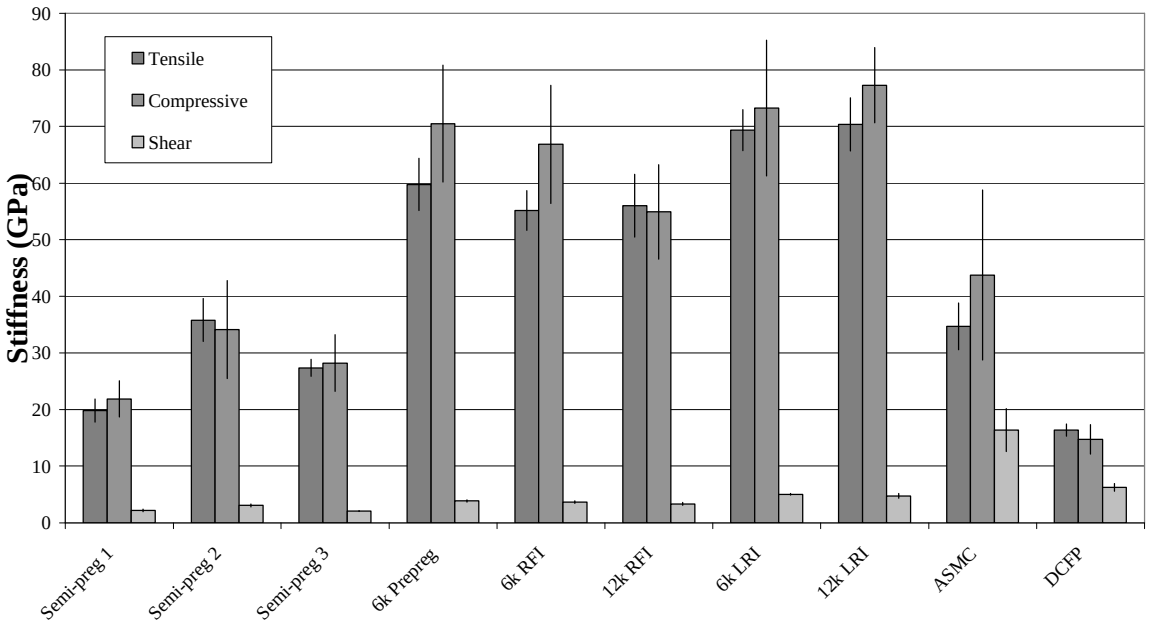


**Figure 6-11 In-plane stiffness results for tension, compression and shear.**

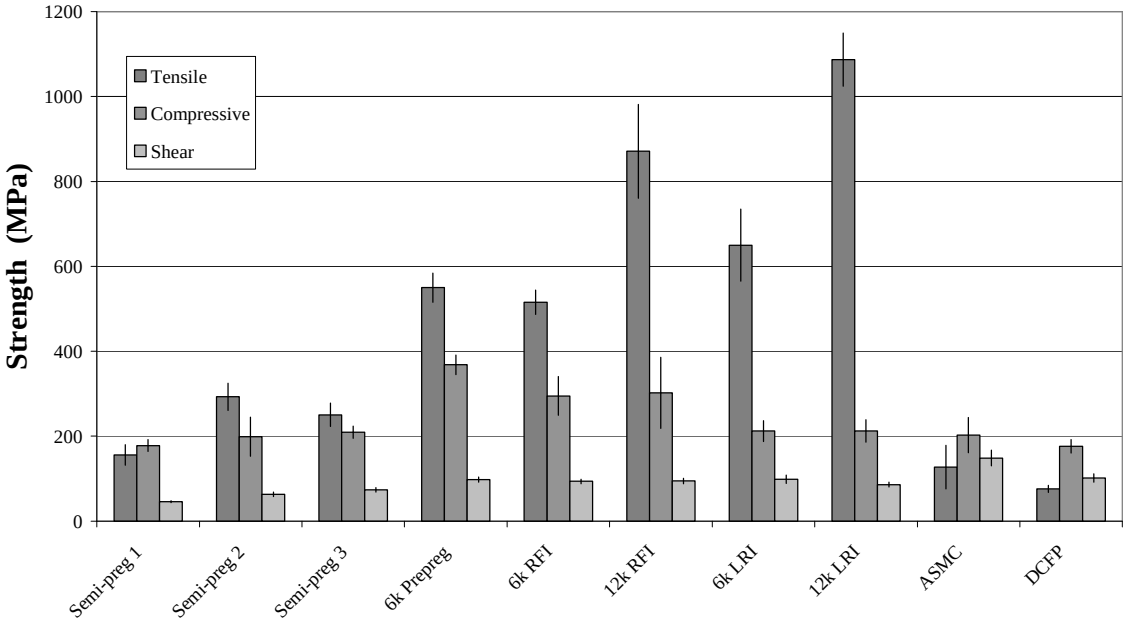


**Figure 6-12 In-plane tensile, compressive and shear strengths for a range of automotive body panel systems**

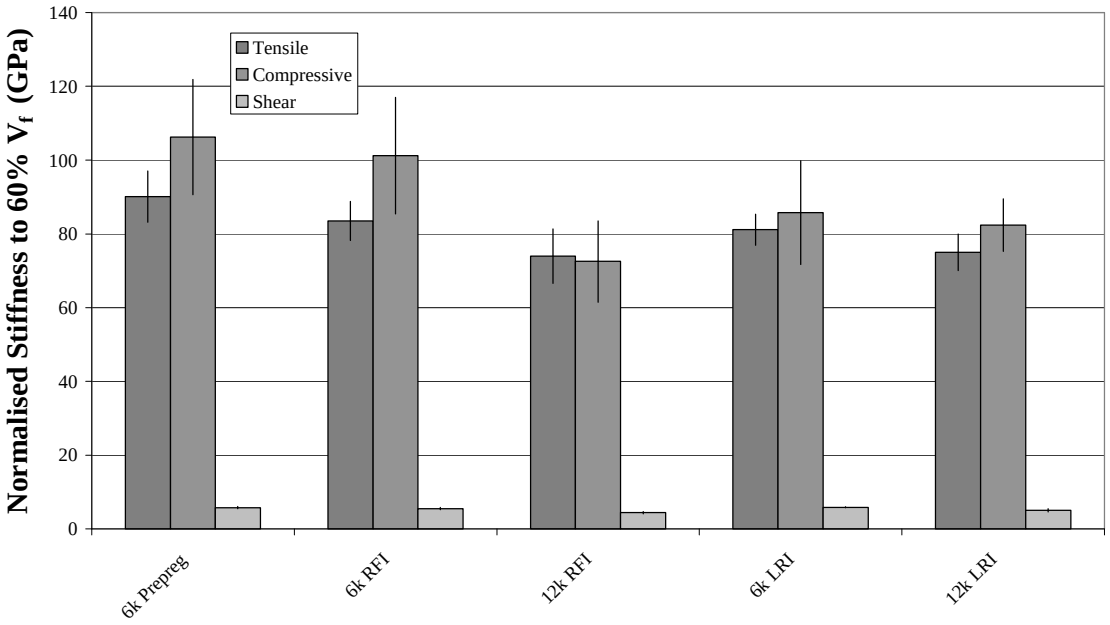


**Figure 6-13 Tensile, compressive and shear stiffness normalised with respect to volume fraction for a selection of fabric-based body panel materials. Stiffness values were all normalised linearly at a fibre volume fraction of 60%.**

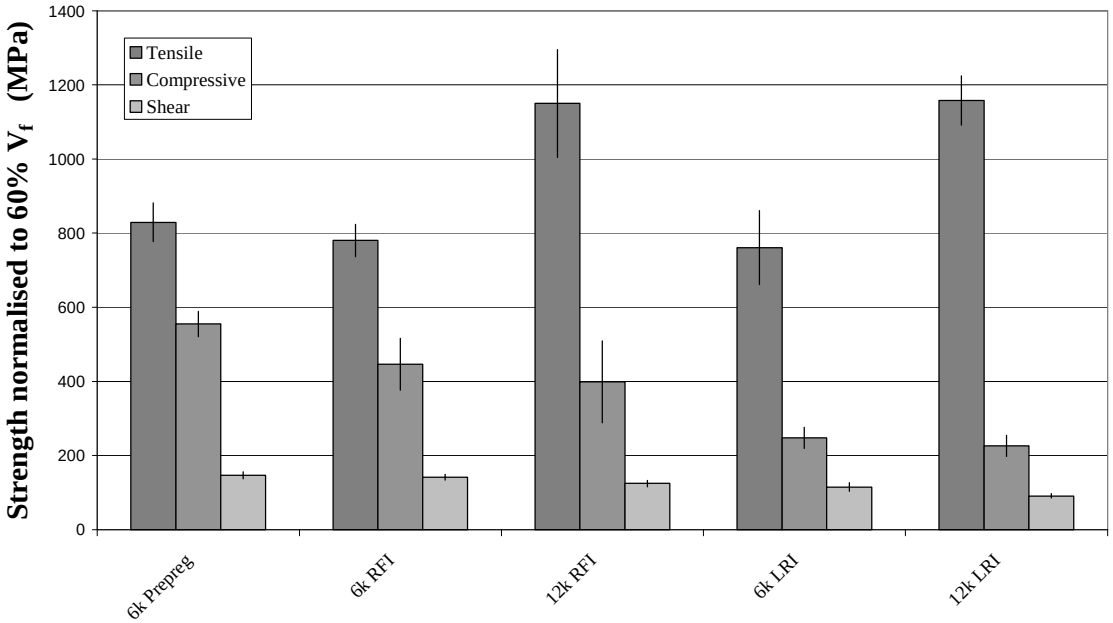


**Figure 6-14 Tensile, compressive and shear strength normalised with respect to volume fraction for a selection of fabric-based body panel materials. Strength values were all normalised linearly at a fibre volume fraction of 60%.**

## 6.3.6. Notch sensitivity

### *6.3.6.1. Introduction*

The concept of fracture toughness implies consideration of a material property and therefore should be independent of geometric crack length. This has been shown to not be the case for short fibre materials [137], so it is preferable to consider the problem of notched strength instead. Experimental data have shown that the presence of a hole in a continuous fibre laminate results in a severe reduction in tensile strength [208]. From the many conflicting arguments in the literature it is clear that the notch sensitivity of random fibre materials is poorly understood. This section of the work seeks to determine the notch sensitivity of DCFP materials, studying the effects of both fibre length and filament count, whilst comparing the results with the continuous fibre semi-preg 1 system. The notch sensitivity is of particular importance for closure panels because they are often fastened to the main BIW using bolts or contain features which act as discontinuities in the panel. Optimum in-plane properties for DCFP laminates are obtained using short, filamentised bundles. This raises concern regarding the notch sensitivity because of poor crack bridging and small damage zone characteristics [137] associated with this type of material in comparison to a long fibre, high filament count variant.

The onset of notch sensitivity is defined to occur when the notched specimen strength falls to 85% of an unnotched reference specimen [209]. Hitchen *et al*. [210] found that the notch sensitivity of random carbon fibre laminates was independent of fibre length (1, 5, 15mm), but dependent on the notch curvature/diameter (Ø1-10mm). Random materials with long (25mm) or continuous (CFRM) fibres exhibited a low sensitivity to notches for notch diameters in the range of 2-15mm [137, 211]. Lindhagen and Berglund [209] used an analytical model to establish the magnitude of the notch required to observe the onset of notch sensitivity. The threshold diameter was found to be much larger than previously tested, in the order of 30-140mm.

### *6.3.6.2. Methodology*

Methodology outlined by Lindhagen and Berglund [209] was followed in order to determine the notch sensitivity of the DCFP and semi-preg materials. Circular notches of Ø9.5mm to Ø30mm were tested in straight-sided tensile specimens, whilst maintaining a constant diameter-to-width ratio of 3:8. A standard tensile specimen was used as a benchmark in each case and notched specimens were cut to the same 250mm gauge length but with increasing widths (25, 46, 60 and 80mm). The notch sensitivity results were assumed to be independent of length since the gauge length was over three times longer than the largest width and ten times longer than the fibre length. Five materials were tested during this work as outlined in Table 6-2.

| | Material | Fibre length | Fibre arrangement |
|---|---|---|---|
| **1** | DCFP 1 | 23mm | Non-filamentised random |
| **2** | DCFP 2 | 6mm | Non-filamentised random |
| **3** | DCFP 3 | 23mm | Filamentised random |
| **4** | DCFP 4 | 6mm | Filamentised random |
| **5** | Semi-preg 1 | Continuous | 0/90º woven |

**Table 6-2 Notch sensitivity testing materials test matrix.**

### *6.3.6.3. Results and discussion*

Figure 6-16 shows the absolute strength values for the five materials tested. The highly filamentised short fibre DCFP 4 exhibited the highest unnotched strength (207MPa) and the non-filamentised DCFP 1 and DCFP 2 exhibited the lowest (~60MPa). The unnotched tensile strength of the semi-preg was closely matched by DCFP 3 at approximately 130MPa. However, the strength of the semi-preg falls to the same level as DCFP 1 once a notch is introduced. Figure 6-15 and Figure 6-16 indicate that the notch sensitivity of the DCFP material is largely dominated by the bundle size rather than the fibre lengths tested.

Relative strength retentions are plotted in Figure 6-17 for increasing notch diameters. All strength values have been normalised with respect to the strength of the unnotched reference specimens. DCFP 1 (non filamentised / long fibre) was seen to be insensitive

to the notch sizes tested. No significant reduction in strength is observed for any of the hole diameters and the small fluctuations about the 100% mark can be attributed to experimental variation, reported in the form of error bars in Figure 6-16. DCFP 3 (filamentised / long fibre) is the second most insensitive material since it crosses the threshold at a notch diameter of 15mm. DCFP 2 crosses the 85% threshold at Ø8.5mm and finally DCFP 4 and the semi-preg are the most notch sensitive systems, both crossing the threshold at approximately Ø3.5mm.

Longer fibres in high filament count tow form exhibit much better fracture toughness properties than short single filaments. This was previously reported in [137] for the notch sensitivity of GMT materials and in [121] for glass-based SMCs. Lindhagen and Berglund [212] identify the damage mechanisms relating to different random fibre architectures, with a specific emphasis on damage zone creation. Micrographs show that damage initiates at transverse bundles/fibres and only later develops around stress concentrations such as the notch [212]. The transverse bundles/fibres debond from the matrix followed by matrix yielding (for ductile resins) and possibly microcracking. Cracks propagate along the transverse or off-axis fibres and eventually coalesce. Final failure is governed by fracture or pull-out of longitudinal fibres in the loading direction. The final failure mechanism is dependent on the fibre critical length, which is governed by the bundle filament count and fibre length.

Figure 6-15 shows the relative size of the damage zones for a bundled material and a filamentised material. Damage initiates in highly stresses regions or at local concentrations. Fibre bundles oriented transversely to the load are the initiation point in the top image. Cracks form and then grow along the length of the fibre, but deviate due to the longitudinal fibres crossing the transverse fibres. This causes a large damage zone which may or may not coincide with the notch. For the short, filamentised material multiple damage zones can initiate at different transverse fibres throughout the material (see the bottom image of Figure 6-15). The presence of the notch concentrates the damage zone and a crack forms near to the notch equator. The crack propagates in a straightforward manner unhindered by crossing fibres, resulting in a much smaller damage zone compared with the bundled material.

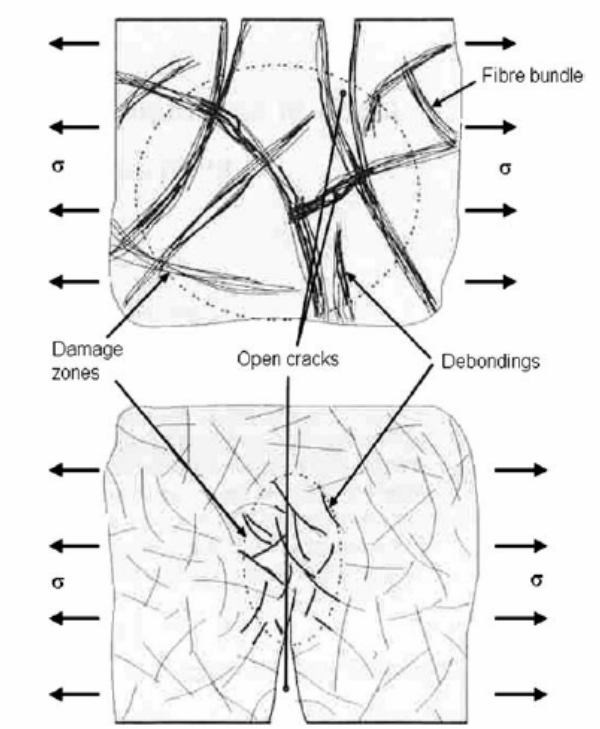


**Figure 6-15 Damage zone creation (shown as dotted rings) for two different fibre architectures. (Top) Non-filamentised bundle material (Bottom) Short fibre filamentised material. Image taken from [137].**

The size of the damage zone is proportional to the amount of energy dissipated, therefore the bundled material exhibits a much higher fracture toughness, hence a lower sensitivity to notches [137]. Although the highly filamentised, short fibre DCFP material (DCFP 4) is more sensitive to circular notches than a bundled material, the notch sensitivity characteristics are still comparable to a woven 0/90º semi-preg, as shown by Figure 6-17. Furthermore, the ultimate strength of DCFP 4 is approximately 50% higher than the semi-preg for each notch size (see Figure 6-16).

The random fibre architecture of DCFP gives this material a distinct advantage over the continuous 0/90º semi-preg material in terms of notch sensitivity. The woven material is macroscopically homogeneous and therefore damage initiates at the stress concentration of the notch tip. The stress raiser at the notch concentrates the damage zone, which remains to be very small in the absence of off-axis fibres. Final failure is catastrophic, as the longitudinal fibres reach their failure strength and fracture at the equator of the notch. Fibre pull out is also negligible so energy dissipation is much lower in comparison to the random material. The fracture toughness of the woven material is generally lower than DCFP.

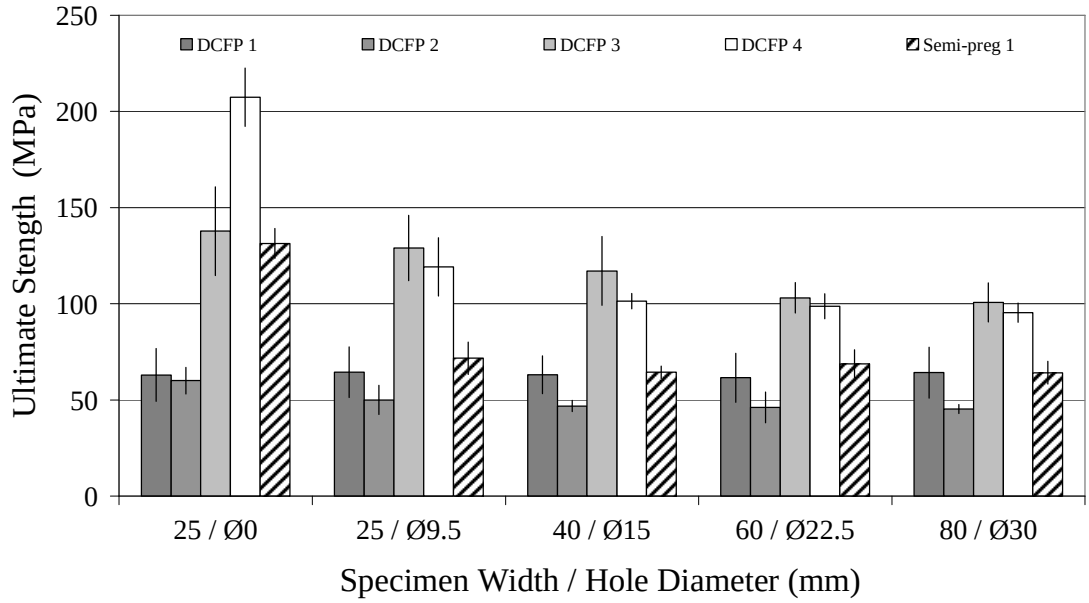


**Figure 6-16 Notch sensitivity results for four DCFP plaques and one semi-preg plaque. The DCFP plaques are distinguished by the fibre length (long (23mm) or short (6mm)) and the level of induced filamentisation (high or low).**

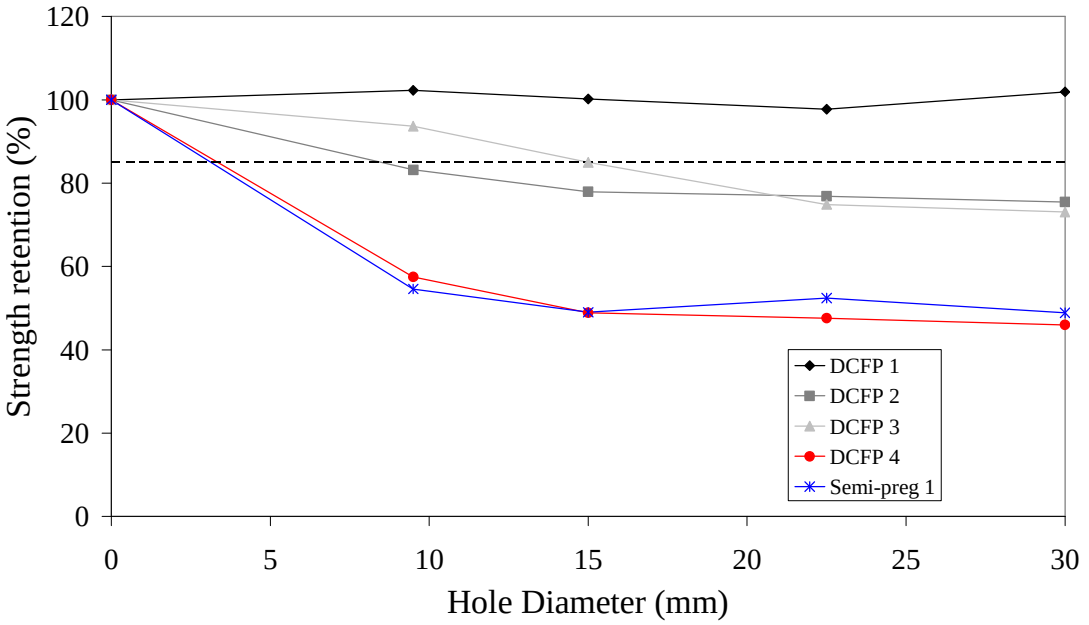


**Figure 6-17 Notched strength normalised with respect to the un-notched strength for four DCFP plaques and one semi-preg plaque. The dotted line denotes the notch sensitivity threshold of 85%.**

### 6.3.7. Material characterisation conclusions

The mechanical and physical properties of DCFP/RTM laminates have been compared with a variety of commercial, fabric-based, carbon body panel systems. The main

objective was to establish if cost-effective processes and materials are suitable for producing high quality closure panels for automotive applications. This study aimed to characterise each system and to determine the potential weight savings available for panels of equivalent flexural stiffness. Whilst the bending stiffness (EI) of each composite panel was equivalent to that of 0.7mm steel, the specific EI was between 100-250%. This equates to a weight saving of at least 57% for each composite system over the metallic benchmark. Although semi-structural closure panels are primarily designed for high specific flexural modulus, dent resistance is an important secondary consideration. Dent resistance of the composite body panel systems was 5-6 times higher than the equivalent steel panel in each case.

A high quality surface finish is required by the automotive industry and therefore porosity and fibre strike through are unacceptable features. Schubel *et al.* [213] show that a veil material or a surface film is essential for achieving an acceptable class-A surface finish. The prepreg, RFI, LRI and ASMC systems do not pass the surface roughness criterion outlined in [200].

In conclusion, in this case the experimental data has shown that all of the low-cost carbon composite solutions meet the fundamental flexural stiffness, mass reduction and dent resistance criteria. Selection of a suitable system for automotive closure applications is governed by production volume, material cost and surface quality. A semi-preg system utilising a high filament count tow would be a suitable choice at low production volumes (<1500). Semi-preg 1 utilises RFI technology, resulting in excellent drape characteristics and a reduction in lay-up times through the utilisation of high density fabrics. Material costs are 30% lower for Semi-preg 1 than other comparable semi-preg systems, weight saving is maximised by using a low density core material and a resin-rich surfacing film produces an acceptable surface finish [213].

At intermediate volume levels (<20,000) high levels of automation make liquid moulding processes such as RTM economically viable. The in-plane mechanical properties of DCFP are comparable with the low volume semi-preg systems and additional surface assessment testing has shown that an acceptable surface finish can be achieved by using highly filamentised fibres at the part surface. The rapid cycle times of advanced SMCs (~5 minutes) are attractive at higher production volumes (>20,000).

The mechanical performance of the carbon ASMC material is satisfactory but it currently suffers from an inadequate surface finish [213] due to porosity caused by entrapped air.

## *6.4. Semi-structural DCFP demonstrator component*

A demonstrator component was selected to showcase the DCFP process by comparing the in-service bending performance against other candidate materials. A front fender from a Ford KA vehicle was chosen as being representative of a typical steel closure panel. The geometry was selected to allow manufacture of similar size preforms in the laboratory-scale DCFP machine. The benchmark steel fender was chosen to represent the high volume production level and composite equivalents were manufactured for the medium and low levels. Results from the preceding characterisation study were used to select suitable materials; the DCFP material was chosen for the medium level and Semi-preg 1 was chosen for the low volume level. Two composite tool sets were constructed for the main study; a 3-part mould tool (see Appendix C.1.4) and upper and lower preforming tools for the laboratory-scale directed-fibre preformer (shown in Figure 6-19). The mould tool was constructed to enable both prepreg processing and liquid resin infusion of DCFP preforms. A demonstrator DCFP fender and preform are shown in Figure 6-18 and Figure 6-19.

A cyclic load-deflection test was developed to characterise the in-service performance of the fenders. Parts were clamped in a rig at four corner locations (shown in Figure 7-38, Appendix D.1.11), which was subsequently fitted to an electro mechanical loading frame. The 4 point loading configuration resulted in a combination of local membrane and bending loads, and therefore the performance of the part was represented by a combination of the flexural rigidity and the in-plane properties seen in Figure 6-1 and Figure 6-11. Crosshead displacement and load were recorded at a constant speed of 10mm/min. The displacement was increased cyclically in 2mm increments until the load reached a maximum. Part stiffness was determined from between 1 and 5mm of displacement on the load-displacement curve. Subsequent tests were used to indicate the onset of permanent deformation and the peak load. A

minimum of three fenders were tested for each material and average values are presented in subsequent figures.

Figure 6-20 shows that the flexural stiffness properties observed for flat coupons in Figure 6-1 are not reflected in the final stiffness values for the fender components. The stiffness of the steel fender was higher than both Semi-preg 1 (46%) and DCFP (18%). The moulding of the DCFP part by vacuum infusion led to inconsistencies in part thickness of ±17%, which would not be encountered in a production RTM part. This effect was seen as a significant contribution to the discrepancy between flat coupon tests and the whole part test. Final part masses were 1.86kg (steel), 1.06kg (Semi-preg 1) and 0.95kg (DCFP). The target weight save was thus achieved (43% Semi-preg 1 and 49% DCFP) and overall the specific stiffness was increased over the steel part by 20% for Semi-preg 1 and 66% for DCFP.

Figure 6-21 shows cyclic load-deflection profiles for steel, Semi-preg 1 and DCFP structures. The steel structure reached a peak load of 109N before plastic buckling limited further load (peak load was reached at 12mm). The Semi-preg 1 panel attained a similar peak load of 107N but at a much larger displacement of 19mm. Reversal of load up to this point resulted in no visible permanent deformation. The DCFP part sustained a peak load of 155N at a displacement of 22mm, after which surface cracks formed. Damage accumulated in the DCFP part with successive loading steps, as seen by a reduction in stiffness, and this damage was greater than that seen in the Semi-preg 1 panel because of the damage mechanism described in Section 6.3.6.3.

This study has demonstrated the potential of the DCFP process for semi-structural closure applications. Although the in-service bending performance was restricted by the single sided tool, it remained competitive against the semi-preg and the steel counterpart. Flat coupon test results in Figure 6-1 show that the bending stiffness of the DCFP component can be matched to that of the steel, in which case a ~40% weight save is achievable. Whilst the cycle time of DCFP/Vacuum Infusion processing cannot compete with steel stampings, this study has shown that cycle times are 89% lower than for pre-impregnated fabrication routes. The total cycle time for the DCFP fender was 49 minutes in total (6 minutes preforming + 43 minutes moulding) compared with 7.5 hours for the semi-preg system (4.25 hour lay-up + 3.25 hours moulding).

**Figure 6-18 Completed DCFP fender (left) with preform (centre) and steel stamping (right). The images show the level of detail which can be captured using the DCFP process.**

**Figure 6-19 (Left) Upper preform tool for 3D front fender suspended above the lower preform tool. (Right) Photograph showing completed preform in lower preform tool. Hybrid fibre length is visible, with large tows providing improved preform cohesion**

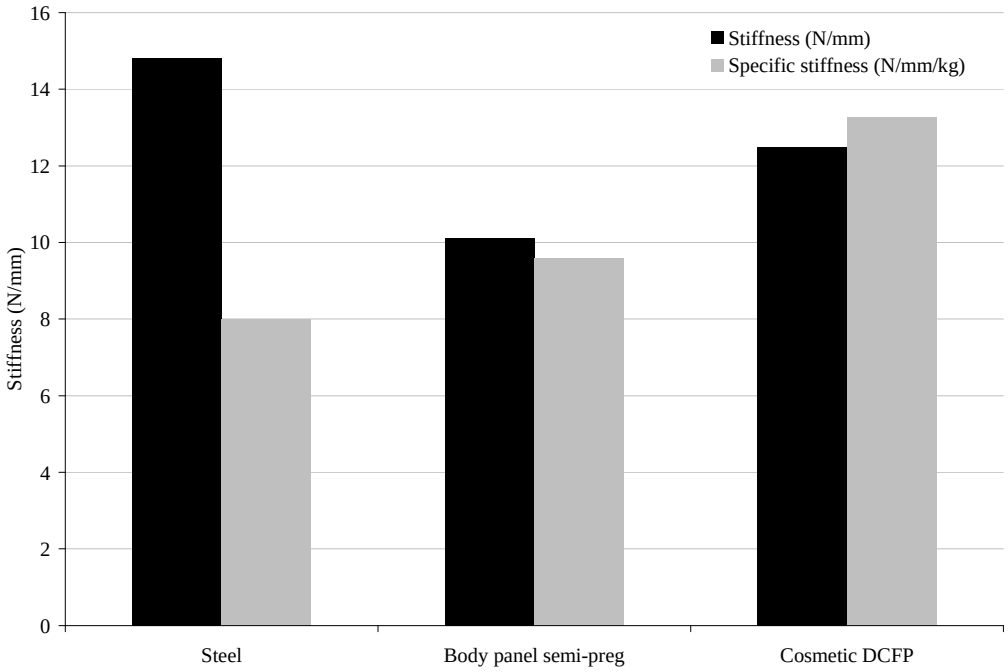


**Figure 6-20 Stiffness results for 4-point bend test on generic fender component**

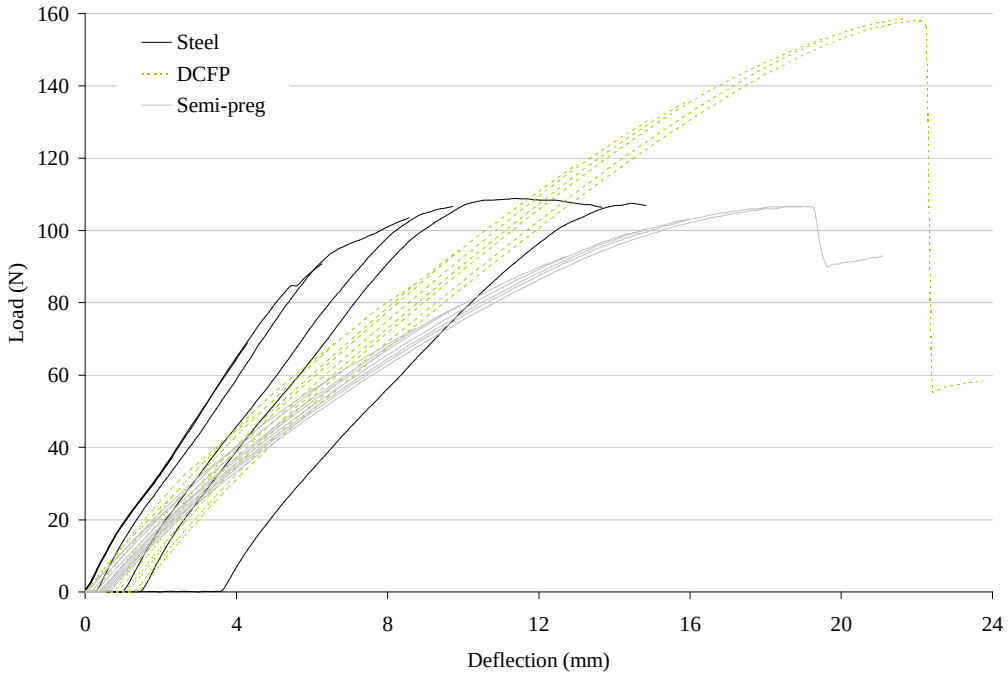


**Figure 6-21 Load-deflection profile for steel fender (2-14mm displacement); semi-preg body panel system fender (2-20mm displacement) and DCFP fender (2-22mm displacement). All in 2mm increments**

## *6.5. Cost analysis*

### 6.5.1. Introduction

The manufacturing processes used for the demonstrator fender are assessed via a detailed technical cost model, based on a combination of data accumulated during the production of the composite prototypes and estimates of the industrial process for the steel fender. Technical cost modelling techniques allow prediction of final part cost by splitting the manufacture of items into a series of tasks, each of which has associated labour content, cycle time, capital equipment, materials and tooling. The approach has been widely discussed in the literature e.g. [214, 215]. Cost modelling of this type is highly sensitive to the accuracy of the input data, but a sensitivity analysis can be performed where uncertainties exist, in order to examine the effect of input parameters.
A generic parametric event-driven technical cost modelling approach has been adopted, as developed by Turner *et al.* [216], which enables the analysis of virtual or current parts for comparison with other materials and processes. Varying levels of automation can also be examined and thus, processes can be cost-optimised at various projected annual production levels. No specific part production volume is assumed, but limits of applicability are obtained for all processes. Details of the methodology can be found in [217, 218].

Simulation results depend on a number of assumptions and the most significant are presented here: Part programme lifetime is assumed to be 5 years, such that tooling costs are amortised over the duration of the programme. Direct labour is charged at £9/hour unskilled and £30/hour for skilled (prepreg laminating). An indirect labour factor of 75% is applied together with a fringe factor of 50%. Interest is set at 7.5% and building cost at £72.90/$m^2$/p.a. Additional assumptions regarding tooling, labour usage and capital equipment can be found in [216].

Estimated materials costs are shown in Table 6-3 and are obtained from a variety of sources. Predictions for the steel part cost are based on finished part mass with the wastage factor shown. Composite part costs are based on the demonstrator parts discussed above (for a part area of ~0.3m). Capital equipment and tooling are shown in

Table 6-4. The events for each process are shown in Table 6-5 and where relevant, a reference is made to capital equipment, tooling and raw materials employed at each step. Cycle times and events have been estimated for the steel part and determined experimentally for DCFP and semi-preg parts. Where necessary, values from the research DCFP machine have been scaled to full production (e.g. cycle time). All processes are automated and employ minimal manual labour.

| Description | Unit cost (£) | | Wastage (%wt) | Part cost (£) |
|---|---|---|---|---|
| Steel 0.7mm | 0.51 | /kg | 15 | 1.09 |
| Semi-preg 1 body panel system + surface film | 49.12 | /$m^2$ | 40 | 20.63 |
| Vac bag & consumables | | | | 0.53 |
| 1300gsm carbon fibre (Tenax STS 24K) | 10.27 | /kg | 3 | 13.76 |
| Epoxy resin (Hexion/RPP 828LVEL / 6514) | 2.50 | /kg | 5 | 3.69 |
| Epoxy binder (Reichhold Pretex 110) | 8.95 | /kg | | 0.58 |
| Primer | | | | 1.26 |
| Release agent | | | | 0.15 |

**Table 6-3 Process cost model material costs**

### 6.5.2. Results

Figure 6-22 shows the overall results for the three processes. Part cost is highly dependent on tooling cost and necessary investment level. The semi-preg route requires low investment and is the lowest cost solution up to around 400 parts per annum, beyond which the cost stabilises. Individual tools only have a prescribed life of 1000 mouldings and therefore due to the long cycle time, multiple parallel tools are required for every additional 200 parts produced per annum.

The cost of the steel part continues to decrease over the entire production range studied, as the influence of tooling costs become less significant, although the rate reduces above 100,000 where the cost per part is only ~£17. The carbon DFP process requires much lower tooling investment (<20%) compared with the steel and is the lowest cost solution between ~400 and ~10,000 parts per annum. Note that this part is relatively simple and does not require any assembly operations, so no advantage is gained with the composite solutions via parts integration.

Cost breakdown at three production levels is shown in Figure 6-23. The steel part is almost entirely dominated by tooling costs whereas the semi-preg part has a more even balance of tooling and labour costs. Note also that raw materials costs are fixed and do not contribute to final part cost as much as perhaps anticipated. This factor is shown in Figure 6-24 where low-cost DCFP (based upon 24K STS fibres) is compared to a 3K carbon fibre with all other factors held constant. The 24K price is between that of 3K carbon and a glass/polyester part based on existing technology.

| Description | Cost (£) | Parts per machine | Floor Area ($m^2$) | Power Usage (kW) | Lifetime (cycles) |
|---|---|---|---|---|---|
| Steel stamping press | 1,000,000 | 1 | 300 | 100 | |
| Large stamping press | 1,500,000 | 1 | 660 | 150 | |
| DCFP system | 1,000,000 | 2 | 288 | 200 | |
| Large RTM / SMC press | 900,000 | 1 | 84 | 50 | |
| RTM injection system | 30,000 | 1 | 24 | 3 | |
| CNC trimmer | 250,000 | 2 | 84 | 30 | |
| Oven | 150,000 | 10 | 120 | 100 | |
| CNC ply cutter | 100,000 | 1 | 120 | 2 | |
| Freezer | 50,000 | 1000 | 98 | 10 | |
| Small single-sided tool (Prepreg) | 50,000 | 1 | | | 1000 |
| Small matched tool low pressure (RTM) | 200,000 | 1 | | | 100,000 |
| Storage Rack | 10,000 | 20 | | | 1,000,000 |
| CNC / Waterjet fixture | 20,000 | 2 | | | 10,000 |
| Inspection fixture | 20,000 | 1 | | | 10,000 |
| Silicone vacuum bag | 1,000 | 1 | | | 500 |
| DCFP preforming tool | 20,000 | 0.5 | | | 100,000 |
| Fender stamping tool main | 800,000 | 1 | | | 1,000,000 |
| Fender stamping tool secondary | 500,000 | 1 | | | 1,000,000 |

**Table 6-4 Process cost model capital equipment & tooling information**

| Process | Description | Cycle time (s) | Labour (persons) | Capital equipment tooling* | Material input |
|---|---|---|---|---|---|
| Steel | Metallic blanking (large press) | 60 | 1 | 2/17 | Steel Sheet |
| | Robotic auto transfer | | | | |
| | Metallic blanking (medium press) | 20 | 1 | 1/18 | |
| | Robotic auto transfer | | | | |
| | Metallic blanking (medium press) | 20 | 1 | 1/18 | |
| | Robotic auto transfer | | | | |
| | Metallic blanking (medium press) | 20 | 1 | 1/18 | |
| | Metal finish | 80 | 2 | | |
| | Paint primer coat | 1170 | 0.1 | 11 | Primer |
| | Inspection | 278 | 1 | 14 | |
| Semi-preg | CNC ply cut | 60 | 1 | 8 | Semi-preg |
| | CNC ply cut | 60 | 1 | 8 | Semi-preg |
| | Semi-preg laminate surface ply | 7200 | 1 | 10 | |
| | Semi-preg laminate backing ply | 7200 | 1 | 10 | |
| | Apply consumables | 900 | 1 | 10/15 | Consumables |
| | Semi-preg cure | 11700 | 0.25 | 7/10 | |
| | Demould | 360 | 1 | 10 | |
| | Prepare mould tool | 600 | 1 | 11 | Release agent |
| | Manual abrade | 900 | 1 | | |
| | Paint primer coat | 1170 | 0.1 | 11 | Primer |
| | Inspection | 278 | 1 | 14 | |
| | Freezer storage | 1450 | 0 | 9 | |
| DCFP | DCFP spray & unload | 360 | 0.5 | 3/16 | Carbon fibres |
| | Prepare mould tool | 600 | 1 | 11 | Release agent |
| | Load preform | 60 | 0.1 | 4/11 | |
| | RTM inject | 120 | 1 | 11/14 | Epoxy resin |
| | RTM in-mould cure | 1800 | 0.1 | 11 | |
| | Freestanding postcure | 3600 | 0 | 7/12 | |
| | CNC rout/trim | 300 | 0.5 | 6/13 | |
| | Manual abrade | 900 | 1 | | |
| | Paint primer coat | 1170 | 0.1 | 11 | Primer |
| | Inspection | 278 | 1 | 14 | |

**Table 6-5 Process cost model events for steel, semi-preg and DCFP respectively. * Capital equipment / tooling refer to the item number in Table 6-4.**

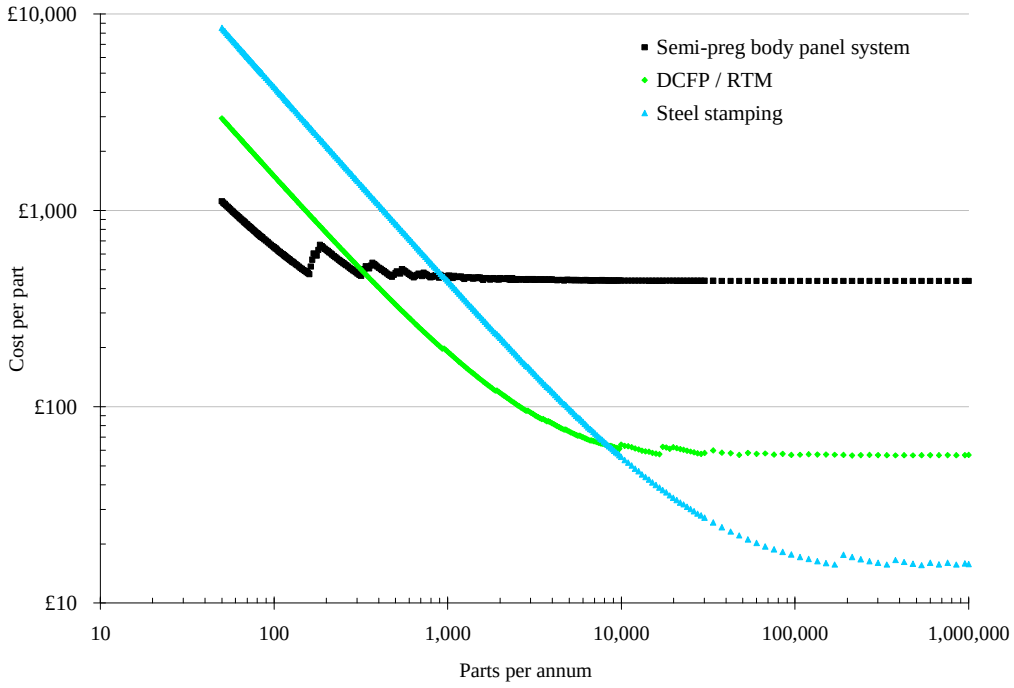


**Figure 6-22 Cost per part against annual production level (note log/log scale)**

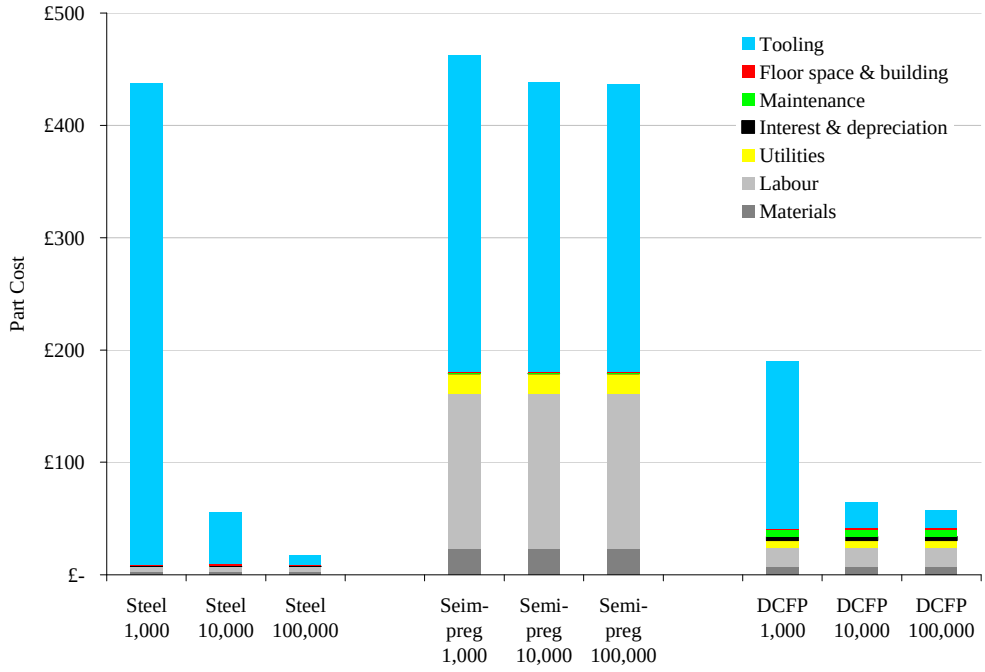


**Figure 6-23 Cost breakdown into major cost areas for 3 processes at volume levels of 1000, 10,000 and 100,000 parts per annum**

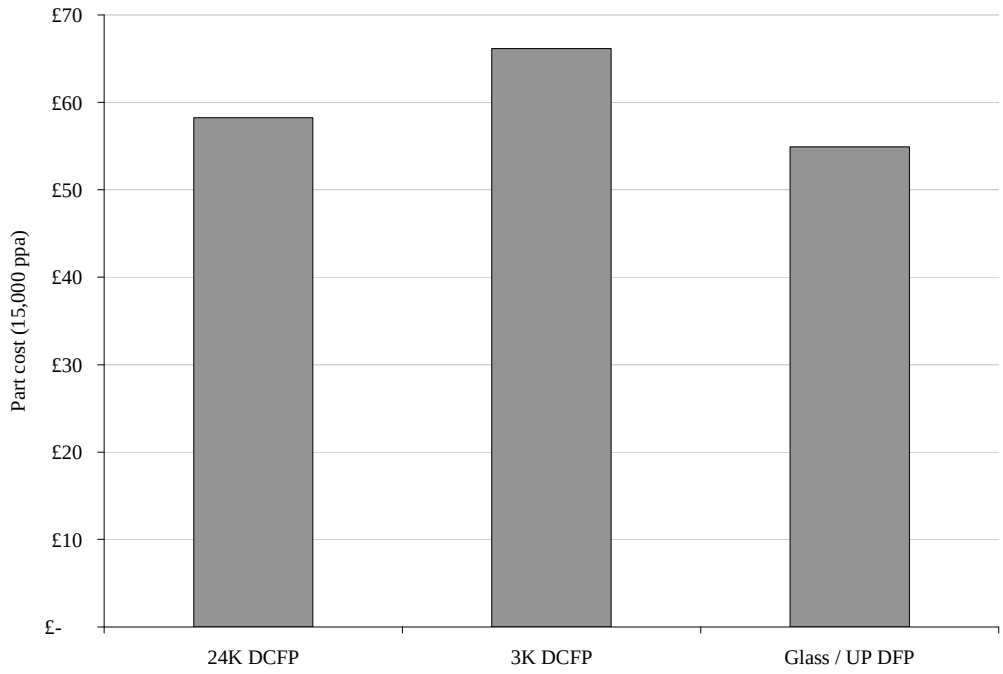


**Figure 6-24 Effect of raw material costs on part cost for 24K carbon (£10/kg), 3K carbon (£30/kg) and glass fibres (£1.5/kg) in a polyester matrix. Glass part is 50% thicker to compensate for reduction in stiffness**

## *6.6. Conclusions*

A variety of candidate carbon fibre based composite manufacturing processes have been examined for automotive body panel applications. Low-cost carbon fibre semi-preg, prepreg and resin film infusion methods have been evaluated, and a candidate semi-preg system and a directed fibre preforming / resin transfer moulding process were taken forward and compared with an existing steel stamping for a front fender. Mechanical testing results demonstrate that the carbon fibre composite solutions can provide 40 to 50% weight saving for an equivalent bending stiffness, and greatly improved dent resistance.

Cost is an important factor but is highly sensitive to required part production level. In this work a commercial semi-preg body panel system was shown to be cost effective up to around 400 parts per annum, whereupon a DCFP system becomes cheaper. For higher production levels (around 10,000 parts per annum and above) steel is the lowest cost option. In reality the two parallel concerns of weight save and cost must be

rationalised and this work does not aim to establish the importance associated with the reduction of mass for any particular application. In addition, the chosen part does not give any opportunity for mass and cost reduction via parts integration.

The predicted flexural performance of the three materials was not reflected in the performance of the 3D fender part in this work. Consideration must therefore be given to maintaining the theoretical advantages of the composite material by careful design of load transfer points etc. It is unlikely that an optimum composite part can be designed as a direct replacement for an existing metallic one. As the requirement for mass reduction in vehicles becomes more pressing and the price of carbon fibre reduces, the need for an effective carbon fibre preforming method becomes more important for low to medium volume production (e.g. in the most profitable sectors of niche vehicles and performance derivatives). Critical to the cost-effective implementation of carbon fibre is the use of low cost, high filament count fibres. Conventional non-crimp fabric processing routes are not cost effective due to the high levels of manual labour and the high cost of intermediate materials.

# Chapter 7. Conclusions

## *7.1. Thesis conclusions*

The aim of this chapter is to present the major conclusions established during this work. This thesis is primarily concerned with understanding the influence of microstructural parameters on the mechanical and physical properties of carbon fibre laminates produced by directed fibre preforming. Significant process developments have enabled carbon fibre preforms to be consistently manufactured using an automated directed fibre process. Extensive experimental studies have been performed to characterise the material in order to study the effect of the preform microstructure and two analytical models have been developed to predict in-plane tensile stiffness and strength. This section is divided according to the content of each chapter and the results are evaluated in terms of improving the quality of DCFP laminates.

### 7.1.1. Process development

Preliminary work indicated that DCFP preforms were inconsistent (inter-preform variation was approximately 15%) when produced using a modified glass-based machine. This was attributed to the mechanical chopping device. A new chopping apparatus was developed to provide independent control of filamentisation level, exhaust pressure and blockage prevention to minimise the disruption of previously deposited fibres. Inter-preform variation was successfully reduced to 5%, providing more confidence in observed trends.

Process optimisation has shown that a high tool-centre-point (300mm) and low robot speed (200mm/s) produces a more uniform coverage of fibre using the present installation, (83% fibre coverage, compared with only 53% for a low TCP (100mm) and a higher robot speed (800mm/s)). A second study investigating the effect of fibre lay-down strategy has shown that spraying two orthogonal layers only marginally (~10%) improves the areal density variation across the plaque. However, processing a

single 24K tow over two separate layers, rather than two tows over a single layer, improves the areal density variation by up to 30%. Preform quality is therefore directly influenced by cycle time.

### 7.1.2. Areal density effects

Non-structural automotive body panels are conventionally produced from 0.7mm steel and composite substitutes are typically designed to have an equivalent flexural stiffness. It is therefore essential that the DCFP process is capable of producing thin (<3mm) laminates with a consistent areal density. Experimental studies have shown that laminate thickness (global areal density) is the most significant variable of all of the independent variables considered during this work. Mechanical properties are reduced in thin parts as a consequence of poor fibre coverage, leading to unreinforced areas. Stiffness was reduced by 7.5% and strength by 18.8% when the areal density was reduced from 2.25kg/m$^2$ to 0.75kg/m$^2$ (4mm laminate to 1.5mm laminate respectively).

A strong correlation exists between local areal density variation and the mechanical performance of DCFP laminates. The following independent variables were subsequently studied in an attempt to compensate for the detrimental effect of reducing the laminate thickness.

### 7.1.3. Filamentisation effects

Industrial, high filament count (>24K) tows are inexpensive compared to aerospace-grade carbon fibres and present the opportunity for aggressive cost reductions. Tow filamentisation enables high filament count tows to be processed successfully, using pneumatic techniques to fragment the tow. Filamentisation effectively reduces the average tow filament count to provide a more homogeneous distribution of fibres within directed fibre preforms.

It has been established that two forms of tow filamentisation exist; natural and induced. Natural filamentisation is influenced by tow-related parameters, such as the level of

surface treatment, sizing chemistry and chop length. Induced filamentisation is generated at the fibre chopping head using high velocity air. When both natural and induced filamentisation levels were maximised, increases in both stiffness (13%) and strength (55%) were noted as the average filament count was reduced to 425 for a 24K tow.

Preform compaction trials showed that an unacceptable level of loft can be generated by excessive filamentisation. Preforms can exceed 120mm in thickness, which limits the maximum volume fraction to less than 30% and presents a real challenge for the production of 3D shapes. However, it is envisaged that filamentisation is only necessary for thin laminates (e.g. exterior body panels), since fibre homogenisation improves as the laminate thickness increases. Therefore volume fractions approaching 50% are achievable when using concentrated bundles, making DCFP suitable for primary structural applications.

### 7.1.4. Length effects

The nature of the directed fibre preforming process produces varying degrees of filamentisation over the range of tow lengths considered as discussed, and consequently length effects are not seen in isolation. However, the net effect of reducing fibre length is clear; shorter fibres (exceeding the critical length) significantly improve composite performance.

Composite modulus is seen to be independent of fibre length beyond the critical value. Conversely, shorter fibres enhance tensile strength due to fewer critical flaws (Weibull effects), improved preform coverage and lower filament counts through natural filamentisation. Strength obeys a characteristic Weibull-shaped relationship (decreasing power law) with increasing length.

From a processing perspective, shorter fibres are able to conform to tight radii for intricate components, but inherently reduce the overall preform integrity because of poor binder adhesion. This causes problems when transferring a large preform to the moulding station and also increases the risk of fibre washing during the injection phase.

A hybrid fibre length (i.e. 6mm and 23mm) has proven to be a suitable compromise between processing and mechanical performance.

### 7.1.5. In-plane study

Tensile testing was used for screening purposes during the development stage of this work. A full range of in-plane tests confirm that tensile testing was indicative of the general trends observed in both compression and shear. The in-plane properties of DCFP follow a strong, linear relationship for increasing fibre volume fractions.

All in-plane moduli appear to be independent of fibre length, beyond the critical value which is a function of the filament count. Shear strength also appears to be independent of fibre length; both tensile and compressive strengths are lower for longer fibre lengths. In tension, the microscopic filament strength is lower for longer fibres and longer bundles are also less susceptible to natural filamentisation. In compression, longer fibres are more likely to fail due to Euler buckling because of increased levels of fibre waviness. Consequently, the compressive strength decreases with increasing fibre length.

### 7.1.6. Stiffness modelling

A fundamental consideration for DCFP stiffness prediction is to adopt a multi-level modelling approach to account for filament packing in the mesoscopic fibre architecture. A model has been developed using an inclusion-based approach, which is applied at both the filament and tow levels. The model has been validated using experimental data and the agreement is generally within 15%.

The most significant prediction is that the tensile stiffness appears to be independent of filament count below a bundle size of 100 filaments. In practice, this implies that a controlled level of filamentisation or tow splitting could be adopted to create a material of constant filament count, in order to minimise the fibre packing issues associated with

single filaments. This material would provide a cost-effective alternative to a commercial split-tow carbon fibre.

The current model incorporates all of the limitations exposed for conventional random fibre models, except for the ability to model process-induced stochastic variation. This effect becomes more influential as the tow size increases and the laminate thickness decreases, as large variations in local areal density occur.

### 7.1.7. Strength modelling

Most discontinuous fibre strength models depend on a critical length term in order to derive the effective mechanical properties from a corresponding continuous system. An elliptical bundle profile has been used to modify the conventional Kelly-Tyson theory to more accurately account for discontinuous tow properties. Critical length predictions using this method show good correlation with the mechanical testing results, but limited bundle size data has prevented extensive validation.

A stochastic strength model has been developed using a multi-level approach to incorporate Weibull effects and to include variable filament counts for accurate property prediction. Predictions are within 20% for highly filamentised fibres at all lengths, but the model does not successfully differentiate between different levels of filamentisation. The associated Weibull effects for increasing filament count have been overlooked; hence the strength of non-filamentised preforms is under predicted by ~45%.

### 7.1.8. DCFP comparison with commercial systems

A fundamental aim of this project was to develop a means for producing composite components with cost parity to aluminium, whilst exploiting the mass reduction potential offered by carbon fibre. Mechanical testing results demonstrate that DCFP components can provide 15% weight saving for an equivalent bending stiffness to 1.0mm aluminium (or 40% to 0.7mm steel) and greatly improved dent resistance.

Intermediate textile conversion and labour content were identified as major cost elements for carbon fibre composites. DCFP is a fully automated preforming solution that uses fibres in the raw and most inexpensive form. (DCFP raw material costs are estimated to be only 16% of carbon prepreg, based on €14.00/kg for STS carbon fibre and €2.11/kg for epoxy). Comparisons with a quasi-isotropic non-crimp fabric have shown that the moduli of random DCFP laminates are within 16% of a continuous fibre material. Compression and shear strengths are also comparable but the tensile strength is only 48% of that of the NCF because of the presence of fibre ends. However, the mechanical performance of DCFP is comparable to carbon-based SMCs, where material costs are 3-4 times greater and capital expenditure in tooling is higher. Further improvements to the mechanical properties can be made, but with the expense of using smaller bundle sizes.

Cost projections by Ford US suggest that resin transfer moulded DCFP components are economical up to intermediate volumes (30,000-50,000ppa). In this work a DCFP component was shown to be cost effective between 400 and 10,000 parts per annum, when compared to a commercial semi-preg body panel system and steel respectively. The chosen demonstrator part was simple and did not give any opportunity for mass and cost reduction via parts integration, therefore these values are considered to be conservative.

# Appendix.A. Publications

The following papers have been produced as a result of this work, some of which are in press at the time of writing.

1. '**Affordable lightweight body structures**',
   N A Warrior, C D Rudd, L T Harper, T A Turner, P J Schubel
   Oral presentation at Lean Weight Vehicles 5 Conference, Warwick, November 2003.

2. '**Affordable Lightweight BOdy Structures (ALBOS)**',
   N A Warrior, L T Harper, T A Turner, P J Schubel, C D Rudd, K N Kendall
   Oral presentation at 2004 JSAE Annual Congress, Pacifico Yokohama, Japan, May 2004.

3. '**Affordable lightweight body structures**',
   N A Warrior, C D Rudd, T A Turner, P J Schubel, L T Harper
   Oral presentation at IOM3 Materials Congress, 2004, London.

4. '**Surface Analysis of "Class A" Polymer Composite Substrates for the Automotive Industry** ',
   P J Schubel, L T Harper, T A Turner, N A Warrior, C D Rudd, K N Kendall
   Oral presentation at the 4th Asian-Australasian Conference on Composite Materials, Sydney, 2004.

5. '**Automated Preform Manufacture for Affordable Lightweight Body Structures**',
   L T Harper, T A Turner, N A Warrior, C D Rudd
   Oral presentation at the 26th SAMPE Europe International Conference, Porte de Versailles, Paris, April 2005.

6. '**Coverage and Mechanical Properties of Spray-Processed Random Carbon Fibre Composites**',
   L T Harper, T A Turner, N A Warrior, C D Rudd
   Oral presentation at the 15th International Conference of Composite Materials, International Convention Centre (ICC), Durban, South Africa, June 2005.

7. **'Spray-processed carbon composites for affordable lightweight body structures'**,
   N A Warrior, L T Harper, T A Turner, P J Schubel, C D Rudd
   Oral presentation at Lean Weight Vehicles 6 Conference, Warwick, December 2005.

8. **'Low Cost Carbon Fibre-based Automotive Body Panel Systems'**,
   L T Harper, T A Turner, N A Warrior, C D Rudd
   Oral presentation at the 27th SAMPE Europe International Conference, Porte de Versailles, Paris, March 2006.

9. **'Characterisation of random carbon fibre composites from a directed fibre preforming process: Analysis of microstructural parameters'**,
   L T Harper, T A Turner, N A Warrior, J S Dahl, C D Rudd
   Composites Part A: Applied Science and Manufacturing, 2006. 37(11): p2136-2147

10. **'Characterisation of random carbon fibre composites from a directed fibre preforming process: The effect of fibre length'**,
    L T Harper, T A Turner, N A Warrior, C D Rudd
    Composites Part A: Applied Science and Manufacturing, 2006. 37(11): p1863-1878

11. **'Characterisation of random carbon fibre composites from a directed fibre preforming process: The effect of tow filamentisation'**,
    L T Harper, T A Turner, N A Warrior, C D Rudd
    Composites Part A: Applied Science and Manufacturing, Article In Press (JCOMA-1947), Accepted 21 September 2006.

12. **'Low cost carbon-fibre based automotive body panel systems – A performance and manufacturing cost comparison'**,
    T A Turner, L T Harper, N A Warrior, C D Rudd
    Submitted to Journal of Automobile Engineering - Proceedings of the Institution of Mechanical Engineers Part D

# Appendix.B. Materials investigated

## *B.1. DFP reinforcement*

Various single-ended formats of carbon tow supplied by Toho Tenax Europe GmbH are summarized in Table 7-1. All derivatives have a fibre modulus of 240GPa ±1GPa and a failure strength of approximately 4000MPa ± 500MPa. The net filament count (the designated value of K represents 000's of filaments per bundle) is the main variation, which represents a major cost element as shown by Figure 7-1. The 24K tow is the most cost-effective variant because of current market usage and therefore the majority of DFP development has been utilising the Toho Tenax 24K STS fibre.

Two variants of the 24K STS fibre are available; (R) and (J). Fundamentally they have identical mechanical properties but different physical characteristics. They are manufactured on different fibre winding apparatus which results in different cross-sectional profile. Fibre R has an elliptical cross-section and is much more susceptible to fragmentation during DFP processing. In contrast, Fibre J is much flatter and tow integrity is maintained.

Unsized carbon fibres were used to create veils for surface critical preforms. Poor tow integrity enabled the tows to fragment to create very light (50-100gsm), lofted layers of fibre at the preform surface.

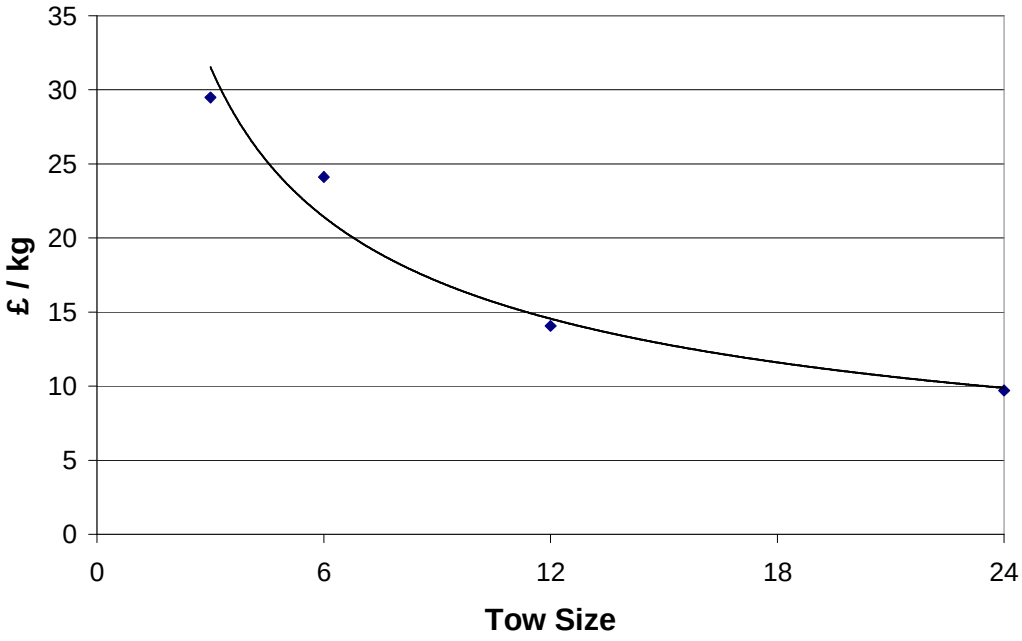


**Figure 7-1 Carbon fibre cost as a function of tow size. Prices supplied by Toho Tenax Europe GmbH for non-aerospace grade carbon (November 2003). Tow sizes 3, 6 and 12K are all type HTA carbon and 24k is STS.**

| Designation | Fibre Modulus (GPa) | Fibre Strength (MPa) | Elongation at break (%) | Filament Diameter (μm) | Linear Mass (tex = g/km) | Sizing Type | Sizing Level (%) |
|---|---|---|---|---|---|---|---|
| 6K (R) HTA 5131 | 238 (1.1) | 3833 (3.9) | 1.5 (3.6) | 7 | 400 | Epoxy resin based on bisphenol-A | 1.27 |
| 12K (R) HTS 5631 | 241 (1.1) | 4501 (4.2) | 1.8 (4.0) | 7 | 800 | Polyurethane with 0.3% epoxy resin | 0.96 |
| 12K (R) HTA 5001 | 238 (1.3) | 3950 (4.0) | 1.6 (%) | 7 | 800 | Unsized | 0 |
| 24K (R) STS 5631 | 238 (1.1) | 4400 (3.5) | 1.7 (3.4) | 7 | 1200 | Polyurethane with 0.3% epoxy resin | 0.97 |
| 24K (J) STS 5631 | 238 (1.1) | 4400 (3.5) | 1.7 (3.4) | 7 | 1200 | Polyurethane with 0.3% epoxy resin | 0.95 |
| PPG 1084/2400 | 84 | - | - | 13 | 2400 | Silane | 0.6 |

**Table 7-1 Summary of DFP reinforcement properties taken from manufacturers' data (values in brackets denote the coefficient of variation (%)). All carbon fibre variants were manufactured with a PAN precursor and were selected from the Tenax Toho non-aerospace product range.**

## B.2. Epoxy resins

Epoxy resins were provided by Hexcel Composites, Duxford during this work. DLS1554-2 is a liquid epoxy suitable for vacuum infusion and is typically used for large wind turbine applications. This resin was initially chosen as a comparison against the epoxies used in prepregs and semi-pregs (see Appendix B.3). However, the low reactivity of this system consequently results in a 4 hour cycle time, which is unacceptable for automotive volume use. A resin development programme with Hexcel resulted in four formulations (outlined in Table 7-2) which were intended for moulding the DFP preforms. DLS1648 was developed directly from DLS1554-2 by accelerating the resin and increasing the functionality. This reduced the cycle time to 30 minutes. Other iterations followed to improve shrinkage, increase glass transition temperature ($T_g$) and reduce cost. These intermediate formulations have been used in parts of this work but the final iteration (DLS1692) was used for surface critical technology demonstrators. Resins designated 'DLS' were two part development liquid systems designed to achieve complete cure within 30 minutes or less (see Table 7-2). Part A was a commercially available liquid Bisphenol A epoxy resin but hardeners (Part Bs) were a complex mixture of aliphatic amines in each case.

DW2 was not developed during this study but is also not commercially available. It shares the same cycloaliphatic amine hardener chemistry as the commercial RTM120 system and was used for a structural demonstrator because of its superior tensile strength (Table 7-3).

A comparison of tensile properties is presented in Figure 7-2 for the four DFP epoxy systems, where preforms were manufactured from Tenax 24K STS (R) fibre with no induced filamentisation. This laminate specification was highly sensitive to the matrix material and provided a more reliable comparison than neat resin testing. However, some neat resin tests were subsequently conducted to provide input properties for analytical modelling (see Table 7-3).

| Epoxy System | Part A : Part B | Cure temp (ºC) | Cure time (min) | Tg (ºC) | Viscosity @ 25ºC (mPas) | Raw material cost (€/kg) |
|---|---|---|---|---|---|---|
| DLS1554-2* | 100 : 15.6 | 80 | 240 | 94 | 225 | 3.00 |
| DLS1648 | 100 : 28.2 | 90 | 30 | 94 | 220 | 4.15 |
| DLS1678 | 100 : 28.2 | 90 | 20 | 107 | 240 | 5.73 |
| DLS1692 | 100 : 16.3 | 100 | 15 | 113 | 110 @ 50ºC | 2.11 |
| DW2 | 100 : 32.5 | 120 | 30 | - | - | - |

**Table 7-2 Moulding details for epoxy resin systems supplied by Hexcel Composites for moulding DFP laminates. * DLS1554-2 was only used to mould engineered fabrics but was the initial iteration in the resin development programme.**

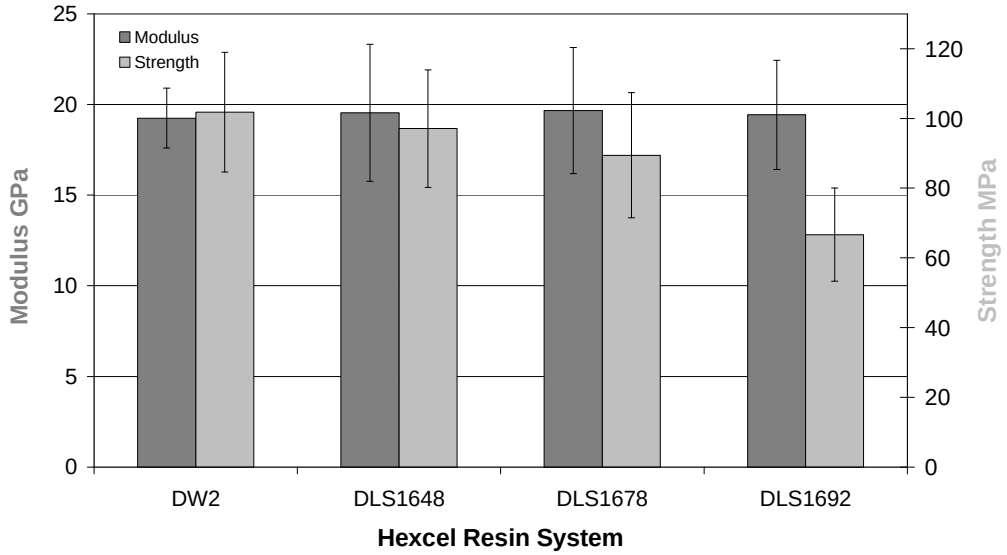


**Figure 7-2 Comparison of tensile properties for four epoxy resin systems using during DFP laminate studies. Preforms were manufactured from Tenax 24K STS (R) fibre. A volume fraction of 30% was used with no induced filamentisation. Mean and standard deviation values are presented based on 20 specimen repeats for each scenario.**

| | Modulus (GPa) | | Tensile Strength (MPa) | |
|---|---|---|---|---|
| **Resin System** | **Av.** | **COV (%)** | **Av.** | **(COV)%** |
| DW2 | 3.712 | 13.57 | 76.02 | 4.46 |
| DLS1648 | 3.012 | 5.85 | 74.49 | 1.93 |
| DLS1678 | 2.804 | 4.92 | 65.25 | 6.93 |

**Table 7-3 Neat resin properties for a selection of epoxy systems. Mean and coefficient of variation (COV) are calculated from 5 repeats for each scenario.**

## *B.3. Commercial automotive body panels*

A range of commercially available body panel systems was selected to evaluate the mechanical and physical performance of carbon DFP (see Table 7-4). Steel and aluminium sheet were used as reference materials because of their obvious association with the automotive industry. Additional materials were all carbon fibre/epoxy composites and were chosen to span the DFP production volume of 30,000ppa. A carbon moulding compound represented the 50,000ppa level and a selection of woven fabrics moulded by different means were used for the low volume level of typically less than 10,000ppa. Each system was selected to provide laminates of equivalent bending stiffness to 0.7mm steel. The material cost of each system is given in Figure 7-3 and detailed descriptions are given below.

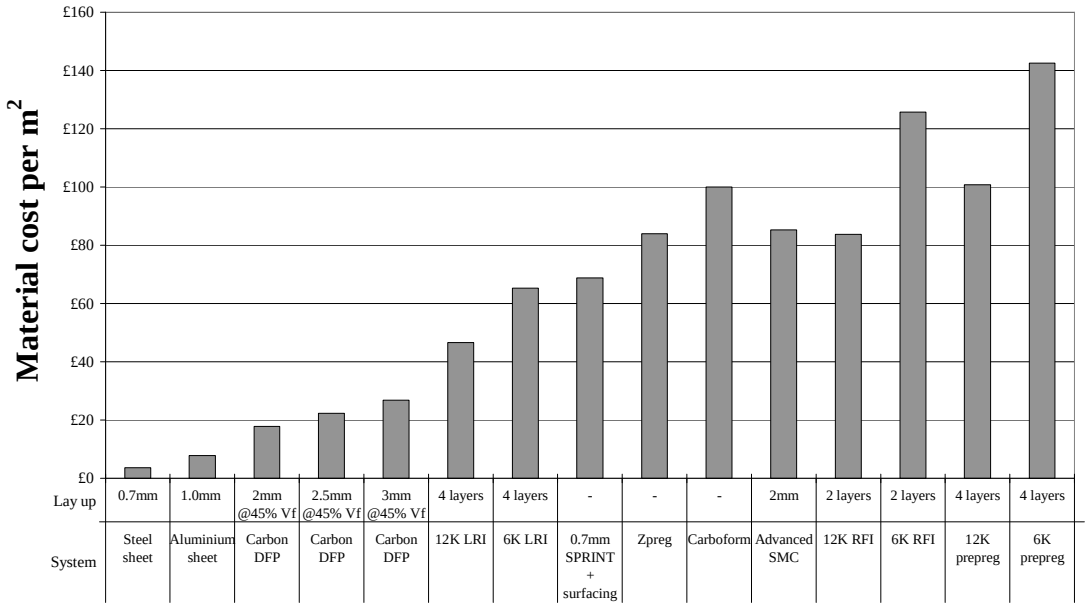


**Figure 7-3 Raw material costs per metre square of all of the systems presented in Chapter 6. Values have been obtained from material suppliers based on volume use.**

| Material / Process | Product | Supplier | Designation | Intended Production Volume (000) |
|---|---|---|---|---|
| Steel | - | Corus | DC05 53544 | 100+ |
| Aluminium | - | Alcan | AA-6111-T4 | 100+ |
| | | | | |
| Advanced SMC | HexMC | Hexcel Composites | HexMC/C/2000/R1A | 50-100 |
| Semi-preg | SPRINT CBS | SP Systems | CBS/ST86/RC2/0.7/RE4/1000/42%. SF95 | <10 |
| Semi-preg | ZPreg | Advanced Composites Group | ZPREG263 VTS263 | <10 |
| Semi-preg | Carboform | Cytec Engineered Materials | 100/SL/280T/SurfaceMaster905 CP/750/1250 100/BL/280T | <10 |
| Resin Film Infusion | 6K 2×2 twill weave | SP Systems | ST85/RC300T/42%/RC300T/1000 | <10 |
| Resin Film Infusion | 12K 2×2 twill weave | SP Systems | ST85/RC303T/42%/RC300T/1000 | <10 |
| Prepreg | 6K 2×2 twill weave | SP Systems | SE84LV/RC300T/1000/42% | <10 |
| Prepreg | 12K 2×2 twill weave | SP Systems | SE84LV/RC303T/1000/42% | <10 |
| Liquid Resin Infusion | 6K 2×2 twill weave | SP Systems Hexcel Composites | RC300T/1000 DLS 1554-2 | <10 |
| Liquid Resin Infusion | 12K 2×2 twill weave | SP Systems Hexcel Composites | RC303P/1000 DLS 1554-2 | <10 |

**Table 7-4 Overview of the commercial body panel systems investigated during this study**

### B.3.1. Steel – DC05 53544

Low alloy automotive strip steel was supplied by Corus, UK at 0.7mm thickness with an untreated surface. It is cold rolled and continuously annealed and has the following elemental composition: C 0.002, Si 0.001, S 0.012, P 0.01 ,Mn 0.163, Ni 0.015, Cu 0.012, Sn 0.002, Cr 0.012, Ti 0.067, As 0.002, Mo 0.002, Nb 0.001, Sal 0.044, N 0.0021. The proof stress (at 0.2%) is between 154 and 165MPa and the ultimate tensile strength is between 306 and 318MPa. This material is suitable for stamping and roofs of high volume, mainstream passenger vehicles are one typical application.

### B.3.2. Aluminium - AA-6111-T4

Aluminium alloy was supplied by Alcan, UK at a thickness of 1.0mm. AA6111 is a heat treatable alloy of aluminium, magnesium and silicon and is commonly used in automotive outer skin applications. Sheets are supplied electrolytically cleaned and then coated with MP404 stamping lubrication to assist forming. All specimens were age hardened prior to testing using a typical paint-baking cycle of 180ºC for 30 minutes. The tensile modulus of this material is 69GPa and the proof stress (at 0.2%) and maximum tensile stress are 146MPa and 282MPa respectively.

### B.3.3. Advanced sheet moulding compound – HexMC®

HexMC is a compression moulding compound manufactured by Hexcel Composites. It enables parts to be made for complex 3D applications that have abrupt changes in thickness. It consists of an epoxy sheet covered with random 50mm × 8mm strips of chopped prepreg tape. Fibres are Fortafil® 503 and the epoxy matrix is formulated with an internal release agent. It is supplied on a roll and layers are cut and stacked to cover 80% of the mould surface. Moulding is typically done at 120°C at 50 to 150 bar pressure, depending on the complexity of the part, and cure times are dependant on part thickness (see Figure 7-4). The areal mass off the roll is 2000g/m$^2$, and the nominal fibre volume fraction is 57%.

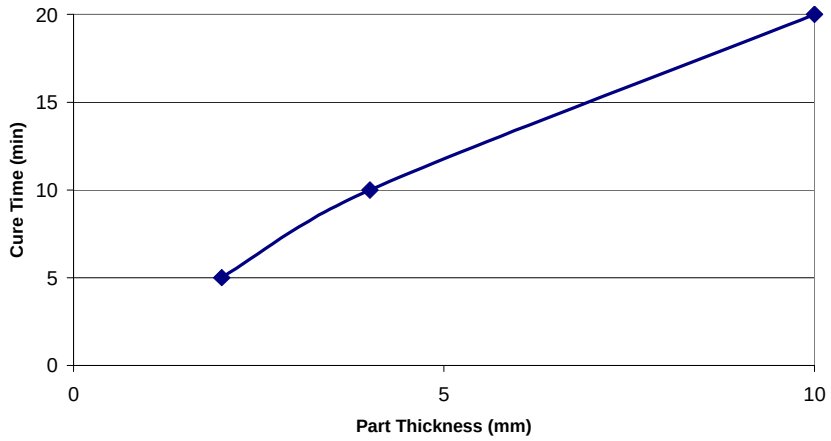


**Figure 7-4 Graph showing cure time versus part thickness for carbon HexMC. Moulding pressures typically range from 50 to 150 bar.**

## B.3.4. Carbon semi-pregs

These dedicated body panel systems are designed to be used in a single layer to replace an equivalent steel panel. Materials were supplied by SP Systems (SPRINT CBS/ST86/RC2/0.7/RE4/1000/42%), Cytec (Carboform CP/750/1250 and 100/BL/280T) and the Advanced Composite Group (ZPREG263). The three systems selected have different architectures but share the common principle of using partially, pre-impregnated fibre skins and a low density core to create a lightweight sandwich panel (see Figure 7-5). Epoxy resin is B-stage cured and applied to the fabric surface in sheet form, or in zebra stripes as in the case of ZPreg. In addition to each of the reinforcing plies, surface enhancement films supplied by the respective manufacturers were used to achieve an acceptable surface finish. Each system was moulded using vacuum only consolidation.

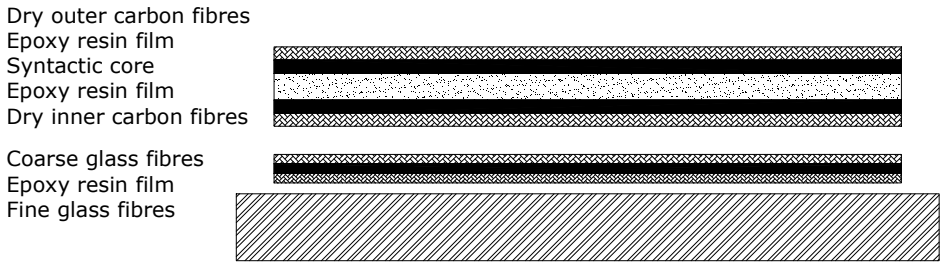


**Figure 7-5 Schematic of a typical semi-preg layup. Each system contains one or two reinforcement plies comprising of dry fibres, resin film and a core material. An additional surface film enhances the finish.**

### *B.3.4.1. SPRINT CBS*

SPRINT CBS is a single layered body panel system designed to replace an equivalent steel panel. The dry fibres and matrix used are identical to those described for the RFI material. The variant used in this testing is the balanced version designated CBS/ST86/RC2/0.7/RE4/1000/42%. The material contains a 0.7mm syntactic core and an optional 'class-A' film was used (designated SF95) to enhance the surface finish. SF95 comprises a thin epoxy film sandwiched between a layer of very fine glass cloth and a layer of coarser glass cloth to aid air removal from the surface of the laminate. Figure 7-6 shows the geometry of the SPRINT CBS material. The 0.7mm syntactic core spaces the two reinforcement layers to improve the bending characteristics.

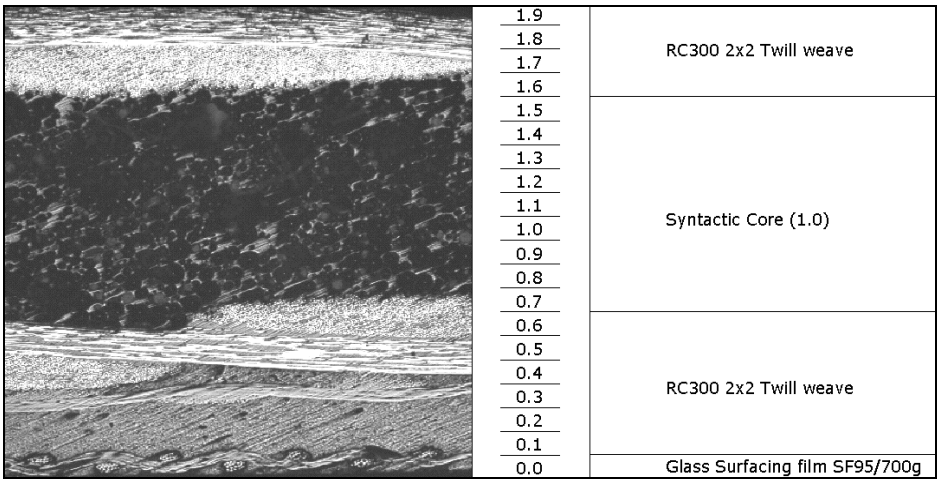


**Figure 7-6 SPRINT CBS is an RFI material containing a syntactic core. Glass microspheres are suspended in the matrix to form a syntactic core. The core and reinforcement layers, denoted by RC300, form a single ply. A separate resin rich glass surfacing film is applied at the A surface.**

The rear surface of the laminated stack was covered with one layer of peel ply and a layer of non-perforated release film overlapped the edge of the laminate by around 50mm. A layer of breather was applied before vacuum bagging the whole arrangement. The average overall cycle time for SPRINT CBS was 3 hours 10 minutes as shown by the profile below.

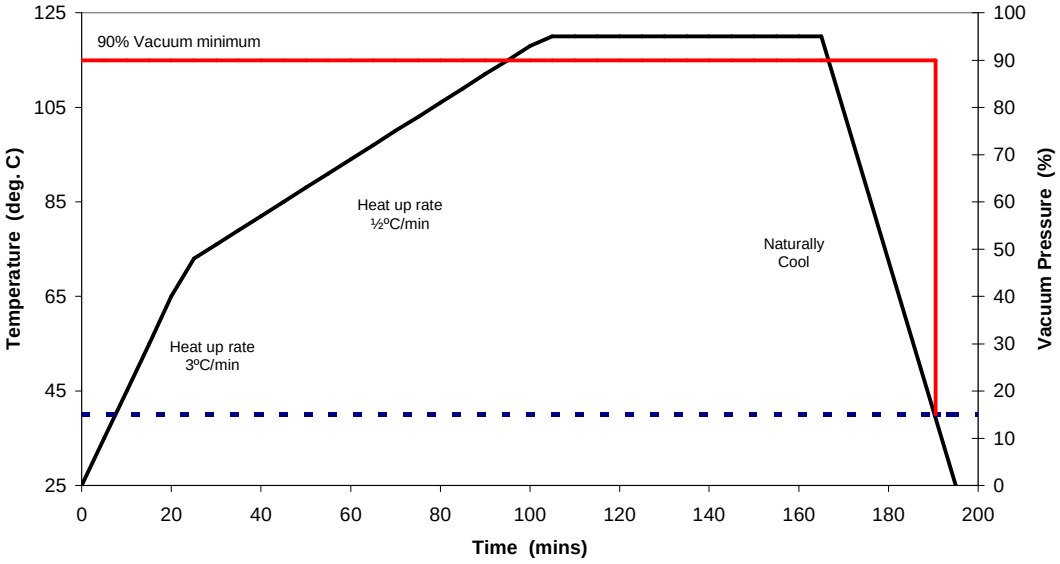


**Figure 7-7 Moulding cycle for SPRINT CBS**

### *B.3.4.2. Carboform*

Carboform is a vacuum-only consolidated body panel systems manufactured by Cytec Industries. It is a three part system consisting of a surfacing layer, core ply and a bulking layer, designated 100/SL/280T/SurfaceMaster905, CP/750/1250 and 100/BL/280T respectively. Both the surface layer and backing layer utilise 3k carbon fibres woven in a 4×4 twill, and are pre-infused with CYCOM 754 epoxy resin. The core layer consists of a non-woven polyester material backed by an epoxy film. The cure envelope ranges from 8 hours at 70˚C, down to 4 hours at 90˚C. All three layers are applied tacky side down enabling the surfacing film to adhere to the tool face. Figure 7-8 shows the lay-up sequence.

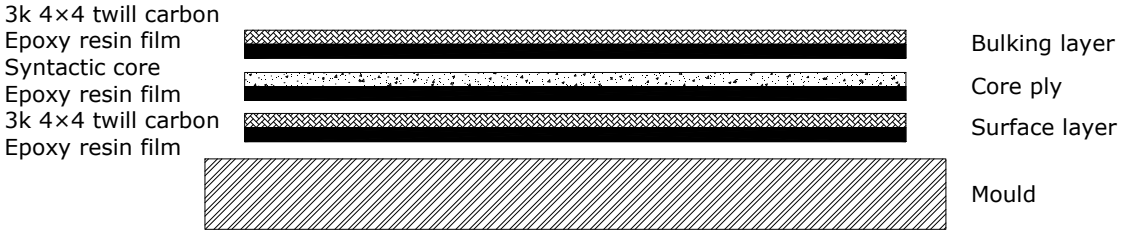


**Figure 7-8 Schematic showing the layup of Carboform. The system consists of three separate laminated layers.**

A layer of 300gsm woven glass fabric was interleaved at the edges of each ply to aid air removal. A layer of non-perforated release film covered the component followed by a

single layer of breather material, ensuring the glass tows made contact with the breather. Average cycle time was 2 hours 40 minutes (Figure 7-9). Full vacuum was maintained throughout and the part was demoulded when the surface temperature had cooled to 40˚C.

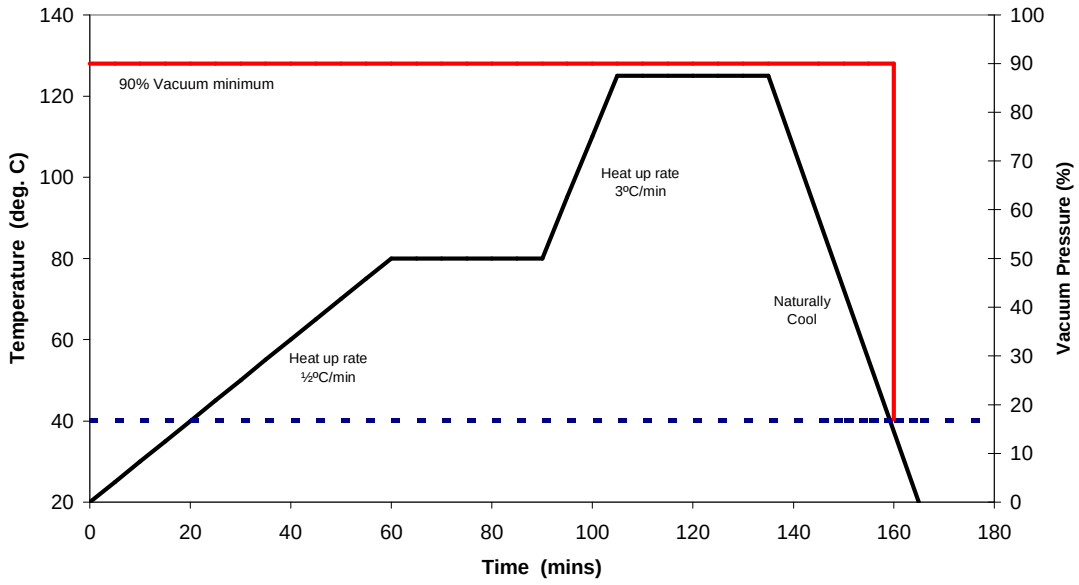


**Figure 7-9 Moulding cycle for Cytec's Carboform**

### *B.3.4.3. ZPreg*

Z-Preg is a dedicated body panel system designed for vacuum only processing, manufactured by the Advanced Composites Group (ACG). It consists of a two-layer surfacing ply (ZPREG263) plus a backing ply (VTS263). Stripes of a black pigmented resin are sandwiched between a dry glass surfacing fabric and a dry 3k 4×4 twill carbon inner fabric. This configuration enhances air removal from the mould surface and improves drape characteristics. The backing ply consists of a 3k 2×2 twill dry fabric attached to a syntactic core material. Typical cure temperatures range from 80˚C to 120˚C.

A single layer of material is used with the surfacing film in contact with the tool face. The surfacing film is laid glass side down, allowing the material to tack to the mould surface and allow a path for any air to escape. The following micrograph shows the geometry of the ZPreg material. The syntactic core is suspended in the epoxy resin of the VTS263 part, but migrates through the dry inner fabric into the ZPreg263.

ZPreg requires very few bagging consumables. A layer of perforated release film was laid over the entire rear surface, extending 25mm over the edges of the stack. A single layer of lightweight breather was then applied, doubling the layers near the vacuum pump and gauge connections. A band of tacky tape was applied around the perimeter of the tool before applying the vacuum membrane. No peel ply was used during the moulding of the ZPreg plaques, which was apparent when trying to ascertain the average thickness of the plaque (see Appendix E.5). Average cycle time was only 1 hour 50 minutes because of hot demoulding, shown by Figure 7-11.

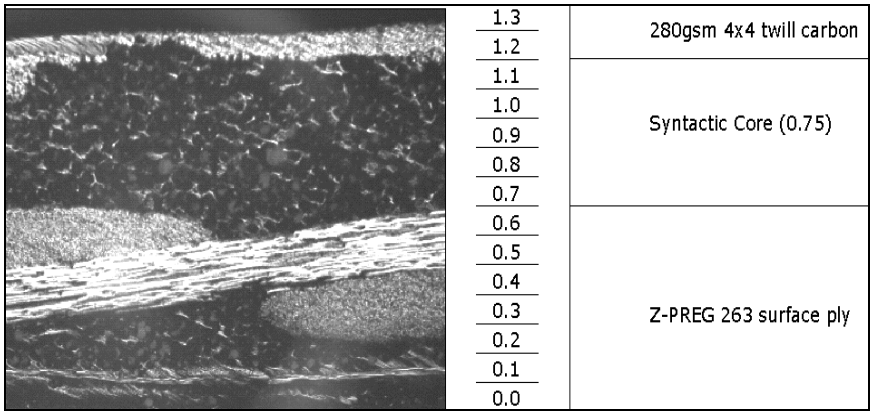


**Figure 7-10 Micrograph of ZPreg. The material is supplied in two parts: The 4×4 twill weave and the syntactic core are supplied as one laminate (ZPreg260) and the surfacing ply is supplied as another (VTS263).**

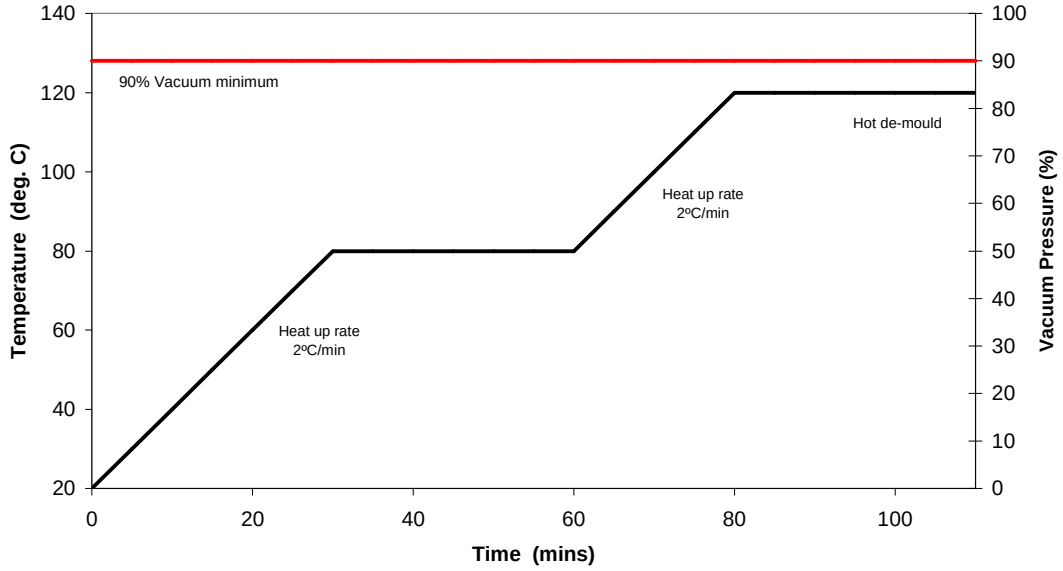


**Figure 7-11 ZPreg moulding cycle. Processing time was significantly reduced by hot demoulding.**

### B.3.5. Resin film infusion (RFI)

Two semi-preg systems (supplied by SP Systems) were selected in order to investigate the effect of the resin film infusion process on the mechanical and physical properties of laminates, compared with conventional prepreg and liquid moulding techniques. Resin film infusion (RFI) is a process whereby a viscous, B-stage cured epoxy film is sandwiched between dry carbon fabrics. Air removal between layers and at the surface is improved because the reinforcement layers are dry, reducing void levels and the need for debulking compared with conventional prepregs. Although the areal mass is typically high, partial resin impregnation makes RFI materials much easier to form than equivalent prepregs. Two derivatives have been studied here, both supplied by SP Systems. The epoxy matrix was SE84 in each case, with 42% resin content by weight at manufacture. Both 6K (RC300) and 12K (RC303) fabrics in 2×2 twill configurations were chosen, with equal fibre weights in the 0º and 90º directions, having a combined areal density of 600gsm. A total of 1200gsm is required to achieve a comparable bending stiffness to 0.7mm steel, (see Figure 7-12). At the time of writing the total cost of two layers of RFI material was £125/$m^2$ and £83/$m^2$ for the 6K and 12K respectively. These materials are named RFI throughout to avoid confusion with the semi-preg systems containing low density cores.

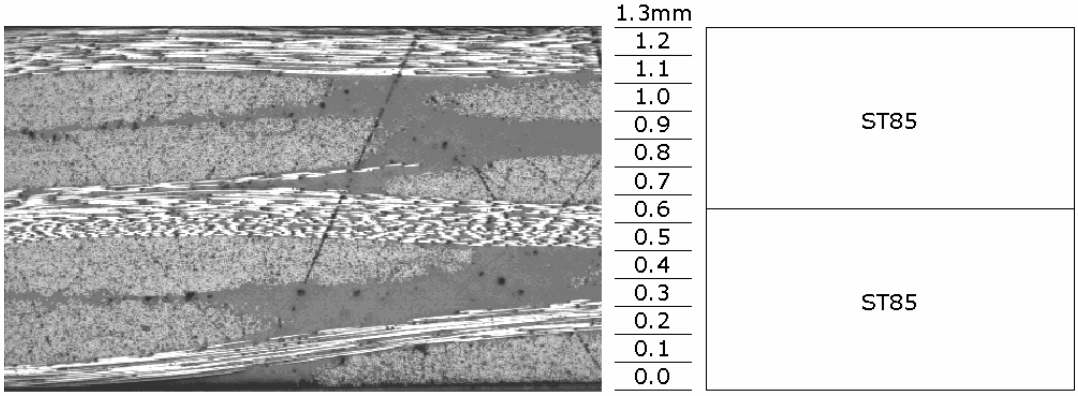


**Figure 7-12 Micrograph showing the through-thickness architecture of a 6K RFI material. Two layers are used to provide an equivalent bending stiffness to 0.7mm steel.**

All RFI plaques were moulded by vacuum-only consolidation on a heated glass plate (Appendix 7.1.8.C.1). During lay-up, glass tows were placed between plies in contact with the breather material to aid air evacuation out of the laminate. A dry nylon peel ply material was applied over the laminate, covered by a non-perforated release film. A single layer of breather was used to cover the release film but was doubled up near the

vacuum connection and gauge. The average overall cycle time for RFI was 2 hours 35 minutes as shown by Figure 7-13. A full vacuum was maintained until the surface temperature had fallen below 40˚C, after which the part was de-moulded.

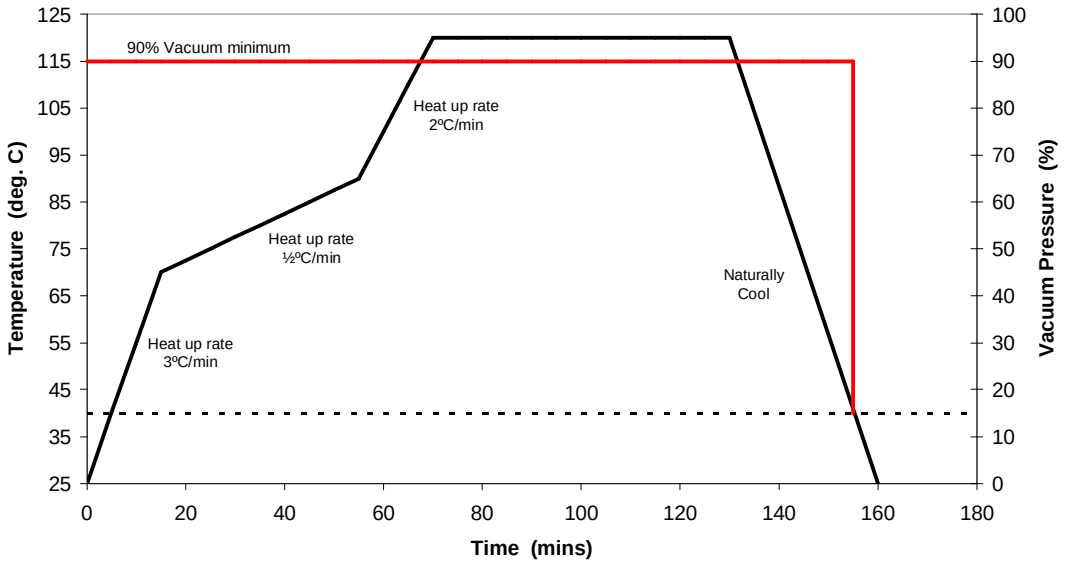


**Figure 7-13 Moulding cycle for RFI materials**

## B.3.6. Prepreg

An out-of-autoclave prepreg with identical fibre architecture and resin chemistry to the RFI material was chosen for comparison. RC300 is a 6k carbon/epoxy prepreg supplied by SP Systems based on 300gsm high strength carbon (230GPa modulus, 3.5GPa UTS). The weave style is a 2x2 twill with 3.7 ends/cm and equal fibre weights in the 0˚ and 90˚ directions of 149.1g/m$^2$. The epoxy matrix is SE84LV with 42% resin content at manufacture. Four layers of material are used, balanced about the mid plane, to produce laminates with equivalent bending stiffness to 0.7mm steel (at a total cost of £142/m$^2$). Voids are clearly evident at the interfaces between the four layers, seen by the black dots in Figure 7-14. Debulking is required if a lower void content is required, which is a disadvantage over the equivalent RFI material.

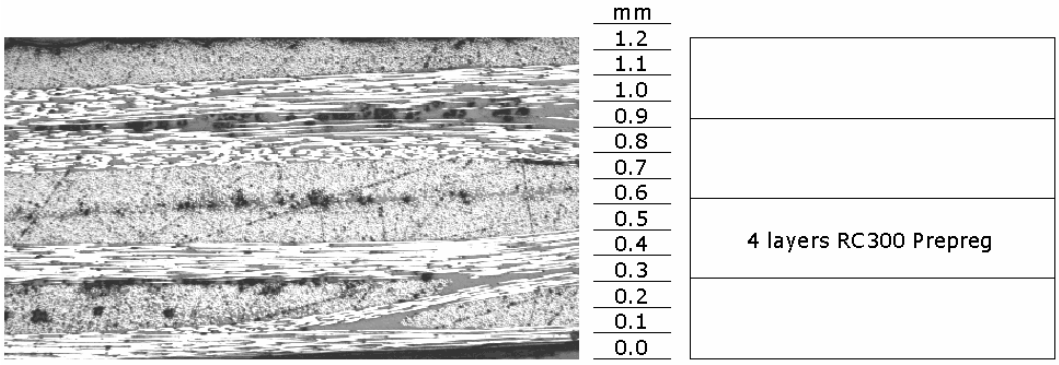


**Figure 7-14 Micrograph of the 6K prepreg system. Voids are visible at the ply interfaces.**

During moulding, a dry nylon peel ply material was applied over the laminate, covered by a perforated release film to bleed out excess resin. A single layer of breather was used to cover the release film but was doubled up near the vacuum connection and gauge. A conventional vacuum bag was then applied over the whole arrangement. The average overall cycle time for this prepreg was 3 hours 15 minutes as shown by Figure 7-15. A full vacuum was maintained until the surface temperature had fallen below 40˚C, whereupon the part was demoulded.

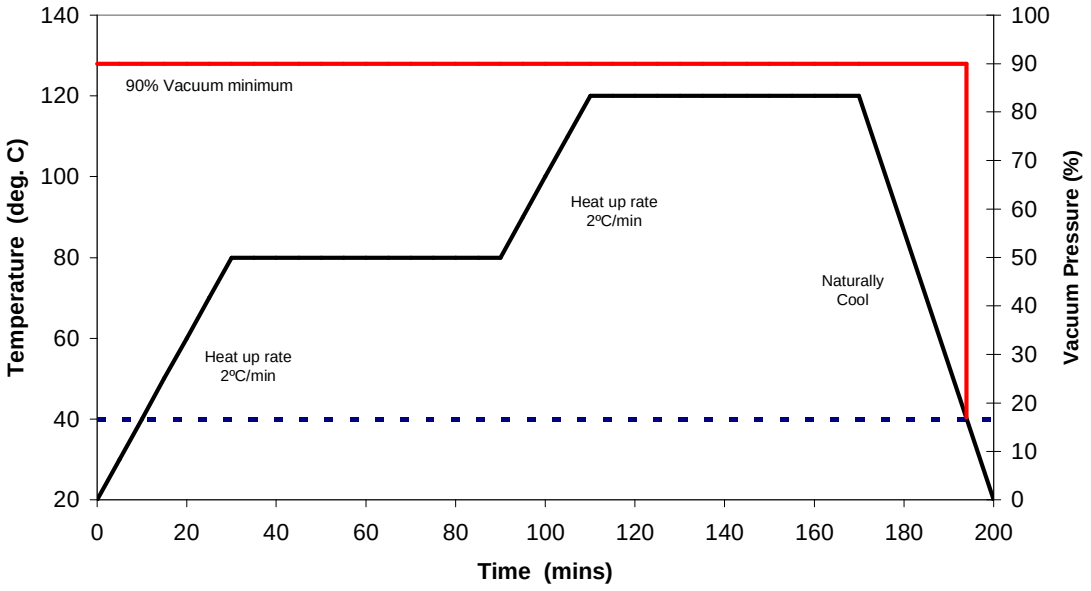


**Figure 7-15 Prepreg moulding cycle**

## B.3.7. Liquid resin infusion (LRI)

The same 6K and 12K reinforcement fabrics from the RFI materials were used in a liquid infusion process. RC300 is the same 300gsm high strength 6K carbon fabric used

in the 6k prepreg above (230GPa modulus, 3.5GPa UTS), but is infused with a liquid form of epoxy resin rather than a film. RC303 is a 2×2 twill, 300gsm, high strength, 12k carbon fabric, with the same modulus as RC300 but a higher tensile strength (230GPa modulus, 4.9GPa UTS). Four layers of fabric, balanced about the mid plane, were infused under vacuum with resin, whilst stacked on a heated glass tool (see Appendix C.1). The epoxy matrix was a trial formulation by Hexcel, named DLS 1554-2 (see Appendix B.2 for details). The cure schedules ranged from the recommended 4 hours at 80˚C down to 1 hour at 100˚C.

Coils were positioned down the leading and trailing edges of the stacked fibres, into which the resin inlet pipe and vent pipe were fed respectively. The springs were used promote a uniform flow front, rather than race tracking to the vacuum connector. A layer of nylon peel ply covered the laminate followed by a layer of infusion mesh. The infusion mesh encouraged the resin to initially flow of the top surface of the laminate stack before sinking through the thickness to ensure full wet-out. This entire arrangement was then vacuum bagged.

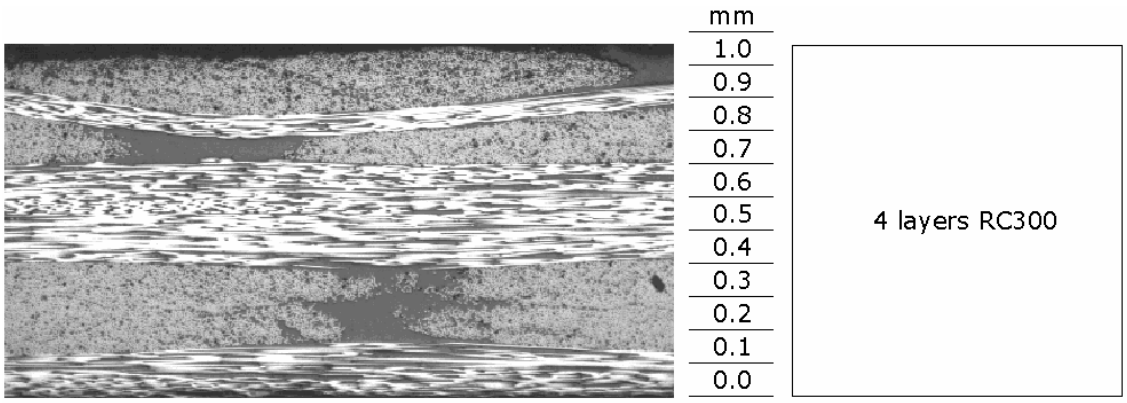


**Figure 7-16 Micrograph of 6K RFI material. Four layers of 300gsm fabric were required to give an equivalent bending stiffness to 0.7mm steel**

The resin mix consisted of 100 parts epoxy resin component (DLS 1554-2 Part A) to 16 parts hardener component (DLS 1554-2 Part B). The inlet pipe was plugged prior to the vacuum pump being switched on to remove all air from the laminate. The glass mould was pre-heated to 40˚C before infusion. The average overall cycle time was 4 hours 45 minutes. Unlike the other systems, the LRI epoxy resin was cured using the recommended cure schedule rather than the fastest.

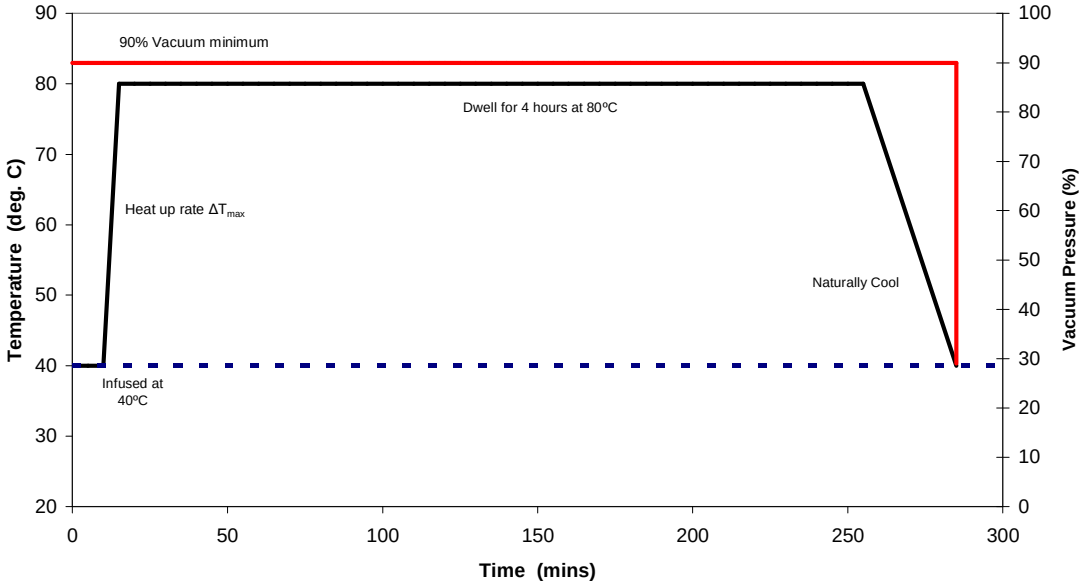


**Figure 7-17 LRI moulding cycle. DLS1554-2 liquid epoxy was used with four layers of 300gsm, 2×2 twill 0º/90º fabric.**

## *B.4. Ancillary materials*

### B.4.1. Release agent

Chem-trend Chemlease PMR-90 was selected as the release agent for all mould tools and DFP preforming tools. It was applied by wiping a thin layer on to all mould surfaces at 40ºC where possible. Solvents were allowed to almost totally evaporate (usually 15-20 seconds at 40ºC) before the tool surface was wiped for a second time with a clean cloth. This process was repeated up to 5 times on each mould surface, with 15 minutes between applications. Since PMR-90 is a semi-permanent release system, up to eight mouldings were possible before the cycle was repeated.

### B.4.2. Binder

During DFP preform manufacture a binder material is deposited with the chopped fibres to provide integrity for handling and to resist fibre washing during impregnation. The following binders have been used:

*DSM Neoxil 940*

A high molecular weight bisphenolic polyester powder with a specific gravity of 1.1g/cm$^3$. This binder has historically been used to produce glass fibre preforms at the University of Nottingham and has a melting point of 120ºC.

*Wacker Vinnex M81*

Vinnex M81 is a cross-linking styrene/acrylic-ester copolymer, suitable for powder spray gun application. The bulk density of this binder is 0.44-0.54g/cm$^3$ and cross-linking is initiated at 150ºC. Up to 58% binder would pass through a U.S standard mesh size of 100 (U.S. #100).

*Reichold Pretex 110*

This binder is the preferred system used in industrial DFP production. Pretex 110 is a powdered epoxy (95% by weight) with a curing agent (Dicyandiamide, 5% by weight) and is insoluble in styrene and other organic solvents. It has a specific density of 1.19g/cm$^3$ and gels at 150ºC after 70 seconds. Only 30% binder would pass through U.S. #100.

### B.4.3. Clear casting resin

High clarity Reichhold Norpol 320-3200 polyester resin was used to mount specimens of material to facilitate polishing and subsequent optical microscopy. Approximately 0.5% NL49P cobalt accelerator and 1.5% Butanox M50 catalyst were used to initiate the curing process. When cured this resin is transparent.

# Appendix.C. Manufacture

This appendix describes the manufacturing processes used to fabricate specimens and components for experimental testing. Resin transfer moulding (RTM) has been used to mould preforms produced by DFP. RTM can support DFP production volumes (30,000ppa-50,000ppa) and is preferred in industry because of its low volatile emissions and excellent repeatability compared with open-mould processes. The majority of the other candidate materials were moulded by vacuum-only consolidation, which is generally suitable for lower production volumes (<10,000ppa). Although consolidation pressure is limited to 100kPa, recent developments in semi-preg technology now mean that it is possible to produce laminates with high specific properties and an acceptable surface quality.

## *C.1. Moulding processes*

### C.1.1. Resin transfer moulding

A hydraulic manipulator [219] was used to mould flat DFP preforms. The lower mould platen was ground and chromium plated to produce a surface roughness (*Ra*) of 0.05μm. The cavity depth between the upper and lower platens was determined by inter-changeable steel picture frames. The mouldable area was 734×500mm and Ø6.2mm extruded silicon o-rings were used to seal the tool faces (see Figure 7-18). The mould was preheated prior to resin injection using a 48kW, two-zone oil heater. Mould temperatures varied from 60º to 120º depending on the epoxy (see Appendix B.2). A network of thermocouples and pressure transducers was located in the upper platen to provide process data.

Preforms were die-cut in a 50tonne press to prevent resin race-tracking from undersized preforms. The mould cavity was evacuated of air using a vacuum pump. Resins were pre-mixed and occasionally pre-heated and then end-injected into an edge gate to promote a linear flow front across the width of the tool. A pressure pot was used for injection and pressures varied between 100kPa and 900kPa depending on the

permeability of the preforms. Cured plates were extracted from the mould at temperature and transferred to an oven for free standing post cure.

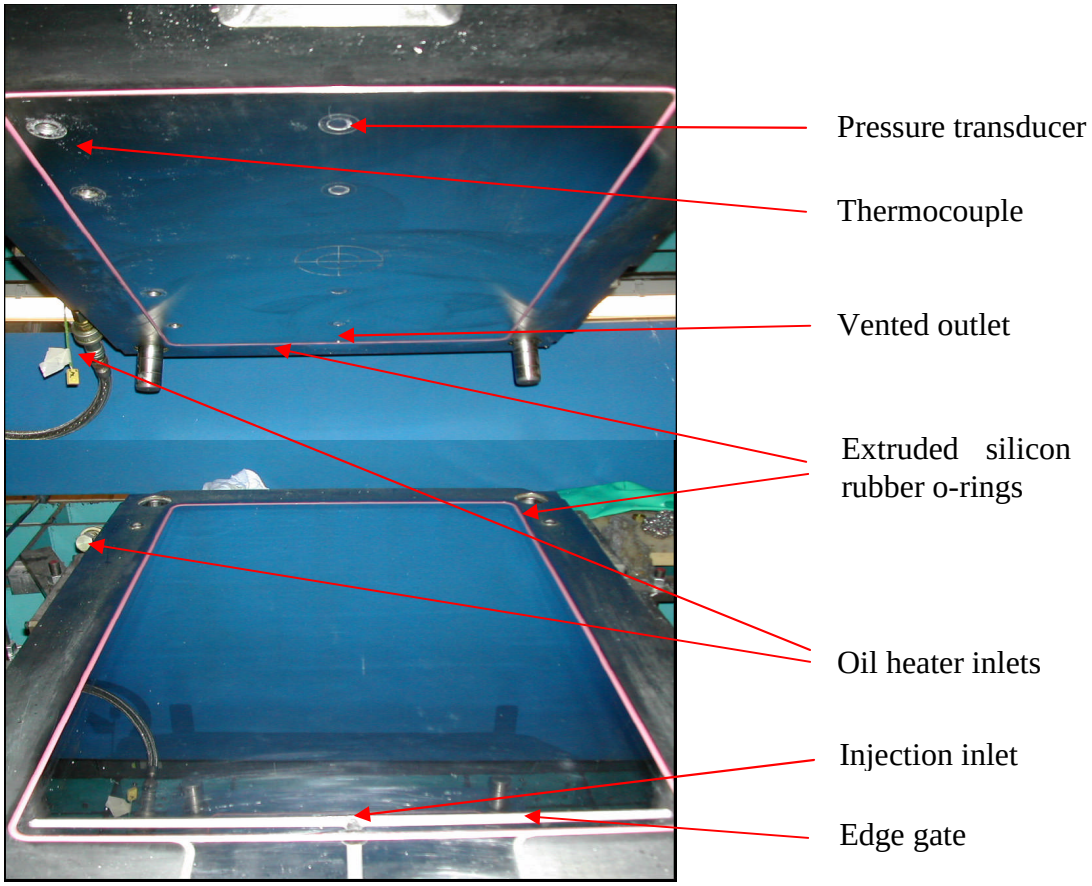


**Figure 7-18 Photographs of the upper and lower mould tools in the RTM manipulator. A rectangular picture frame (not shown) is placed between the two tool surfaces to provide a variable cavity depth.**

### C.1.2. Compression moulding

The advanced SMC was processed by compression moulding in a Bradley & Turton 220ton hydraulic press. The tool consists of two halves fixed to an upper and lower heating platen (see Figure 7-19). The upper tool has a spring-loaded outer frame which makes contact with the lower tool to provide a seal, before the centre platen compresses the charge. The working area of the mould is 265×125mm, with a surface finish of 0.53 μm *Ra* [200]. An 80% charge was placed in the pre-heated press at 120 ºC. The charge was consolidated under 8MPa clamping pressure for 5 minutes and then demoulded to produce a 2 mm laminate.

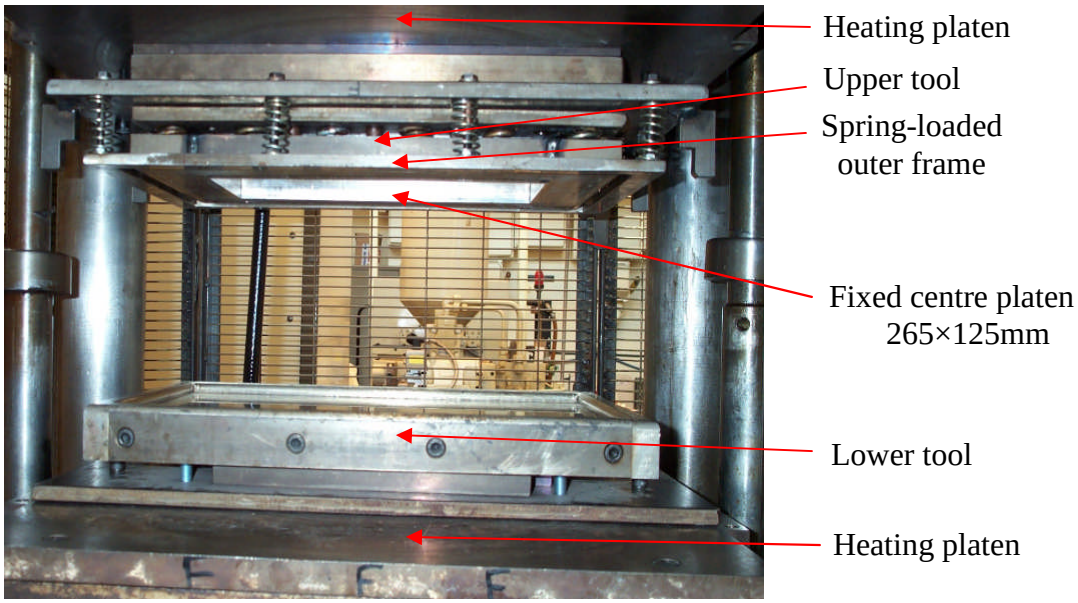


**Figure 7-19 Compression moulding tool mounted in hydraulic press.**

### C.1.3. Vacuum-only consolidation

Prepreg and semi-preg laminates were all vacuum bagged on a tempered glass plate, backed with a silicon rubber heater. Mould temperature was regulated by a closed-loop PID (proportional integral derivative) controller and a central thermocouple. The glass plate measured 500×500×5mm but the maximum working area was 450×450mm due to thermal losses at the edge (see Figure 7-20). Moulding temperature was commonly 120ºC but each material had specific ramp rates because of different matrix viscosity-temperature profiles. The fastest cure schedule was always chosen where multiple options were offered (see Appendix B.3).

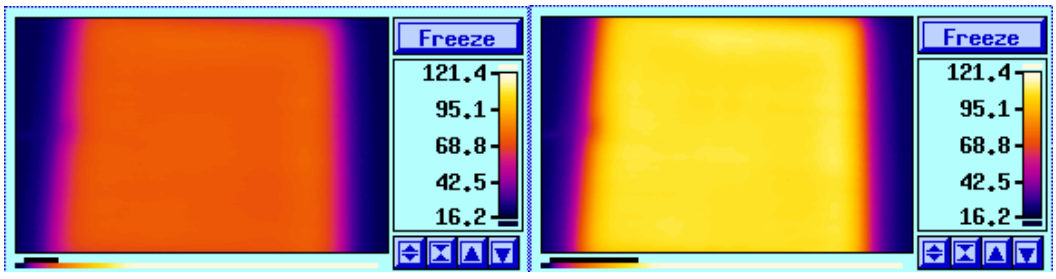


**Figure 7-20 Thermal images of the moulding plate at 80ºC (left) and 120ºC (right). The thermal losses can be seen around the perimeter of the plate but the images confirm that there is no thermal gradient over the 450×450mm moulding area.**

A typical moulding configuration is shown in Figure 7-21. A dry polyamide peel ply material (Tygavac Stitch Ply A) was draped over the laminate, covered by a perforated

release film (Tygavac WL3600 P90) to bleed out excess resin. A single layer of polyester breather (Airtech Ultraweave 606) was used to cover the release film but was doubled up near the vacuum connection and gauge to prevent lock-off. A conventional vacuum bag (Airtech WN1500 bagging film) was then applied over the whole arrangement. A vacuum of >950 mbar was maintained until the surface temperature had fallen below 40°C, whereupon the part was demoulded. All samples were postcured for 2 hours at 90ºC.

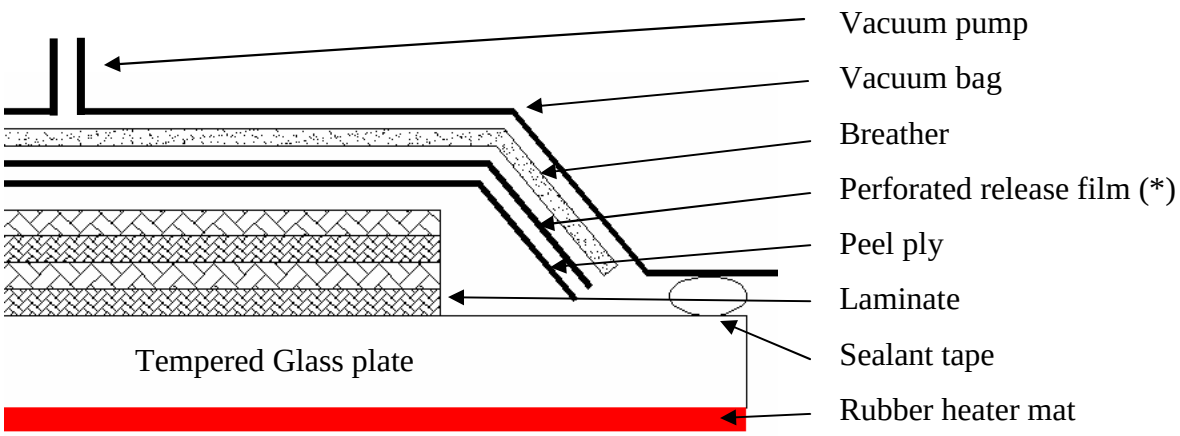


**Figure 7-21 Schematic of a typical prepreg/semi-preg moulding configuration. (* Non-perforated release film (Tygavac WL3600) was used for all semi-preg systems to prevent resin bleeding)**

### C.1.4. Vacuum infusion

The glass moulding plate described above was used to produce flat laminates for the two LRI materials discussed in Appendix B.3. A single-sided tool was also manufactured to produce 3D front fenders for a Ford KA passenger vehicle (see Figure 7-22).

A steel fender was used to create a mould plug and then a three part tool was manufactured using hand lay-up techniques, in order to capture the component under cuts. An epoxy gel coat filled with slate powder provided a durable moulding surface. This tool was manufactured solely for mechanical property characterisation and it was acknowledged that a “Class A” surface would not be achieved with this tool.

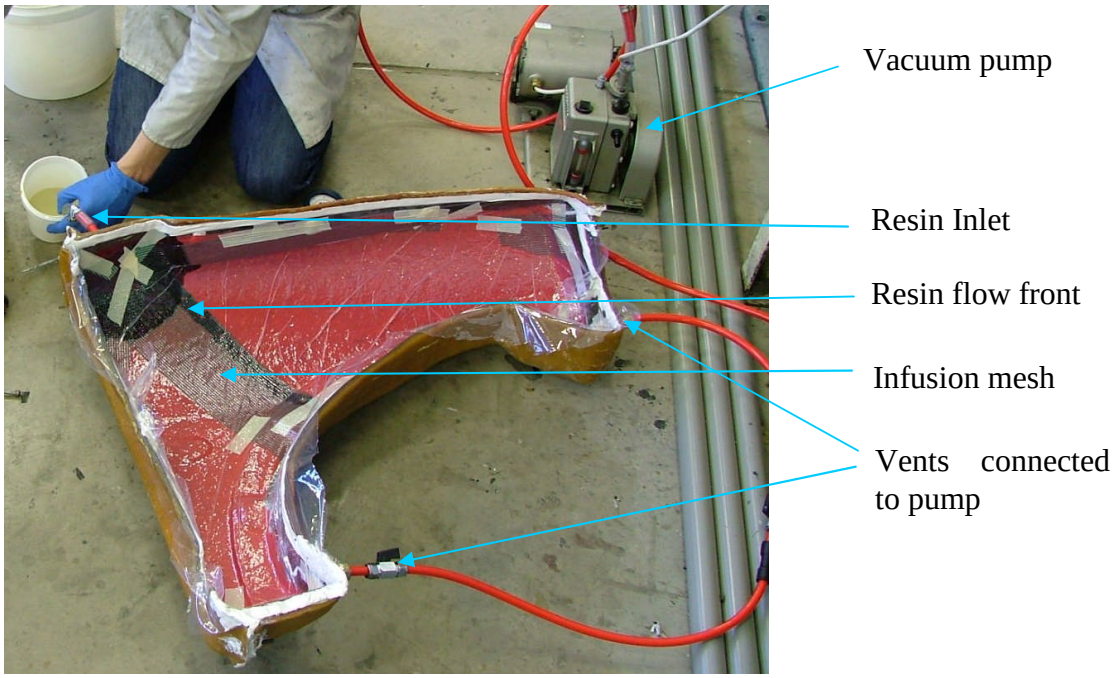


**Figure 7-22 Photograph of the moulding arrangement for a Ford fender**

The tool flanges were sealed with silicon sealant before being bolted together. A single mould inlet and two vents were used during infusion to steer the flow (see Figure 7-22). A schematic of the bagging procedure is shown in Figure 7-23 (this arrangement was also used for the glass moulding plate). An infusion mesh was draped over the laminate to improve resin flow. A vacuum runner inside the bag was connected to the inlet pipe to promote a linear flow front and to prevent race tracking between the inlet and the vacuum pump connection. Resin was infused at temperature and the tool was preheated to 50ºC in a fan-assisted oven. (Cure cycles for the relevant resin systems can be found in Appendix B.2) A vacuum of 950 mbar was maintained until the surface temperature had fallen below 40°C, whereupon the part was demoulded. All samples were post cured for 2 hours at 90ºC in a hot air oven.

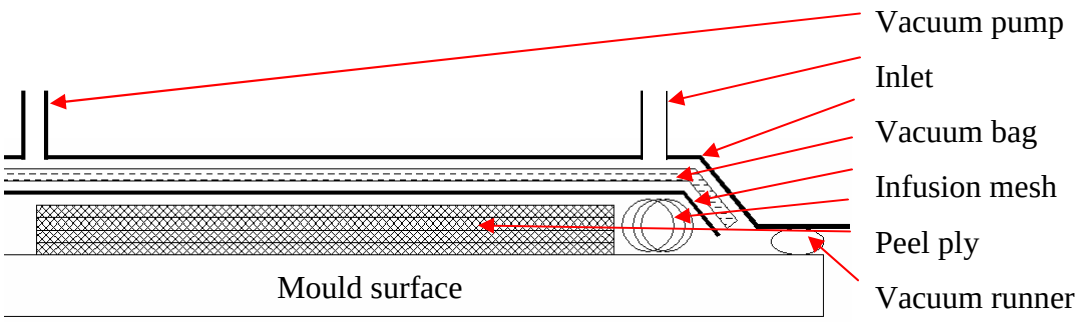


**Figure 7-23 Schematic of a typical liquid resin infusion moulding process. The ancillary materials were the same as those used for the semi-preg materials.**

# Appendix.D. Experimental methods

All testing was performed on an electro-mechanical Instron 1195 testing machine in a temperature controlled laboratory at 20ºC ±1ºC (unless otherwise stated).

## D.1.1. Sample preparation

The majority of test specimens were abrasive waterjet cut at 100mm/min using a CNC controlled machine. This ensured that inter-plaque variations could be studied with confidence. Machined edges were finished with a light sanding of 600 grit abrasive paper.

Notches for Iosipescu specimens were sharpened with a scalpel blade prior to testing. Notches for V-Rail Shear specimens (see Appendix D.1.3) were sharpened using a Strigon pantograph with a Ø2.6mm router tool.

Specimens for fabric formability tests and preform characterisation studies, such as areal mass variation and dry preform strength, were all produced using die cutters in a 50tonne hydraulic press.

## D.1.2. In-plane tensile and compression tests

Tensile tests were executed according to BS 2782-3:Method 326F:1997 at a test speed of 1mm/min [220]. Force was measured by a 50kN load cell and strain was measured by an LVDT extensometer with a 50mm gauge length. At least three repeat tests were conducted in the 0º and 90º orientations. The number of test repeats was increased to up to sixty specimens for plaques with large standard deviations. The number of specimens required was determined by calculating the 95% confidence interval of the mean values according to BS 2846-3:1975 [221]. A standard 25mm specimen width was adopted but the effect of gauge width formed a separate study in Section 3.2.9. Young's modulus was determined from the gradient of the stress-strain curve in the linear region between $0.001 < \varepsilon_1 < 0.003$.

Compressive tests were conducted to BS EN ISO14126:1999 using an IITRI static compression rig [222]. The recommended test speed of 1mm/min was used. Uniaxial strain gauges with a 5mm gauge length (Kyowa KFG-5-120-C1-11L1M2R) were bonded to the specimen surface with cyanoacrylate and connected via an Instrunet 100 data logger to a dedicated PC. The testing rig was assessed for misalignment and bending using a pair of strain gauges. Figure 7-24 shows the strain-time history of two gauges bonded on opposite sides of a 0º/90º prepreg specimen. The average percentage difference between the two gauges up to the point of failure is 1.47%. This is within the acceptable 3% limit of the test standard and therefore no correction for bending was required. The compressive modulus was determined from the gradient of the stress-strain curve in the linear region between $0.001 < \varepsilon_1 < 0.003$.

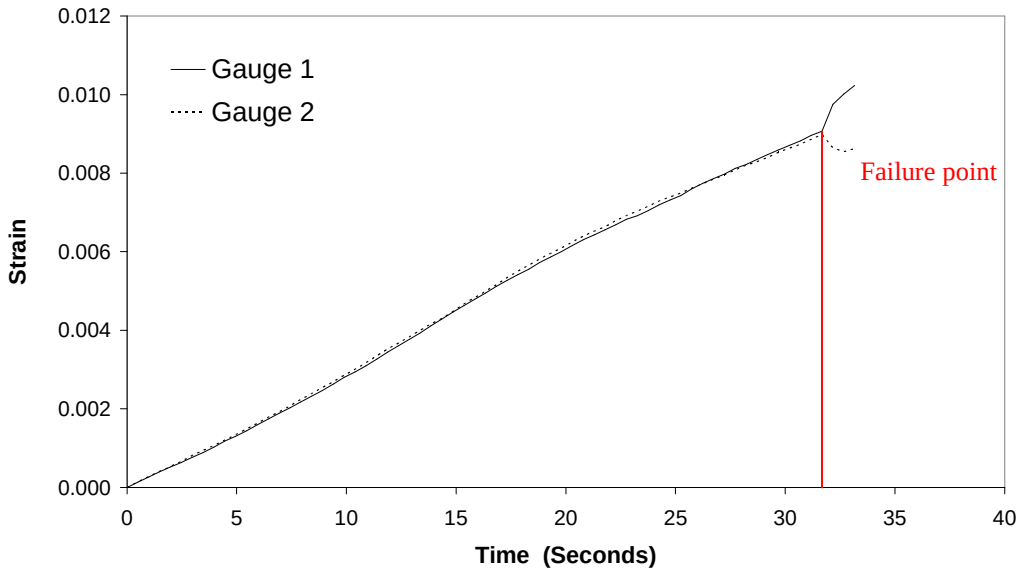


**Figure 7-24 Comparison of two strain gauges, aligned but bonded to opposite faces of a 0º/90º prepreg specimen. Similar strain-time histories confirm that the specimen did not encounter any bending from equipment misalignment.**

## D.1.3. In-plane shear

### *D.1.3.1. Review of methods*

Testing techniques for determining tensile and compressive properties are widely accepted but shear testing is more complex and suitable methods are often debated [223-226]. At least 10 different methods are available for determining the in-plane

shear properties [227] but the Iosipescu, two-rail and short beam shear methods are the most commonly used for random materials. The Iosipescu test is often favoured because it produces a region of pure shear between the notches [225, 228] and specimen preparation is quick in comparison to the two rail shear method. A diagram of the testing fixture is presented in Figure 7-25. However, there are concerns that premature failure occurs due to stress concentrations present at the notch root. Barnes *et al.* [228] used FEA to confirm that complex stress distributions do exist at the notch tips but they depend on the level of orthotropy and fibre orientation and are negligible for isotropic materials. The Iosipescu shear test was used to characterise random SMC materials in [229] rather than the two rail shear test. Higher shear strengths were observed for the Iosipescu method because the two rail shear specimens failed in bending.

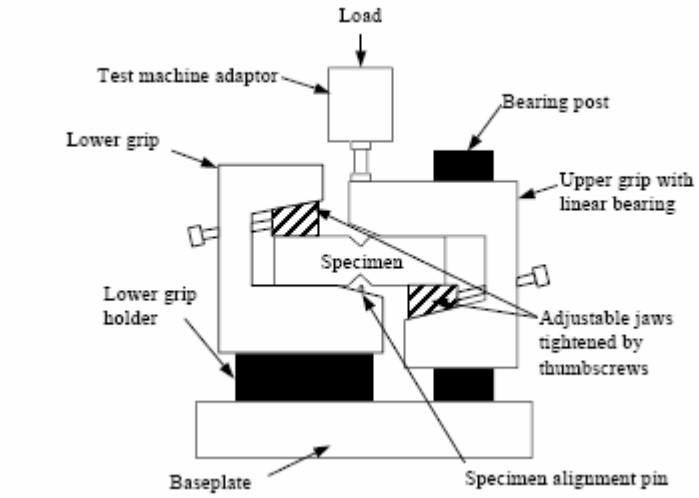


**Figure 7-25 Schematic of the Iosipescu shear testing fixture (Diagram courtesy of Crookston [230])**

A number of authors have studied the effect of specimen geometry on the shear properties. Walrath and Adams [229] showed that the notch depth was insignificant for shear tests on glass SMC and that an acceptable failure was achieved through the centre of the notches for specimens reinforced with fibres in the 1-2 plane [231]. Other studies have concentrated on the effect of the notch angle. The recommended notch opening ($2\theta$) by Neumeister and Melin [232, 233] is determined by a simple rescaling operation based on the ratio of the Young's moduli along the axes of orthotropy ($\lambda$):

$$\tan\theta = \frac{1.43}{\sqrt[4]{\lambda}} \qquad \text{where } \lambda = \frac{E_x}{E_y}$$ **Equation 7-1**

Modification of the notch angle is an attempt to reduce the occurrence of stress concentrations by homogenising the stress field. An optimum angle of 110º is recommended for isotropic materials, but problems occur at greater levels of orthotropy as larger angles shorten the gripping area. Larger gripping forces are then required which cause crushing along the loading faces.

One of the drawbacks of the Iosipescu method is the test preparation time. Hawong *et al.* [234] have simplified the loading mechanism so that specimens are face loaded rather than end loaded. FEA results indicate that although the stress distributions are more symmetrical for the revised test, the magnitude of the shear strengths are the same as the conventional Iosipescu test for both 90º and 110º notch angles. However, an angle of 110º is favoured since the maximum shear stress values are experienced at the centre of the specimen, rather than at the root of the notch as with the 90º specimen.

Adams *et al.* [235] combined the Iosipescu test with the common two-rail shear test in order to characterise the shear properties of high shear strength (>500MPa), quasi-isotropic laminates. Specimen geometry is scaled from the Iosipescu standard with a 90º notch, but the test fixture is based on the two-rail shear arrangement. The V-notched rail shear arrangement is shown in Figure 7-26. Specimens are face loaded to permit greater specimen clamping forces and to eliminate premature failure caused by end loading. Previously the Iosipescu test was restricted to fibre tow sizes smaller than 12K [236] because of the 11mm central gauge width, but the scaled geometry of the V-notched rail shear enables materials with much larger tow sizes to be tested.

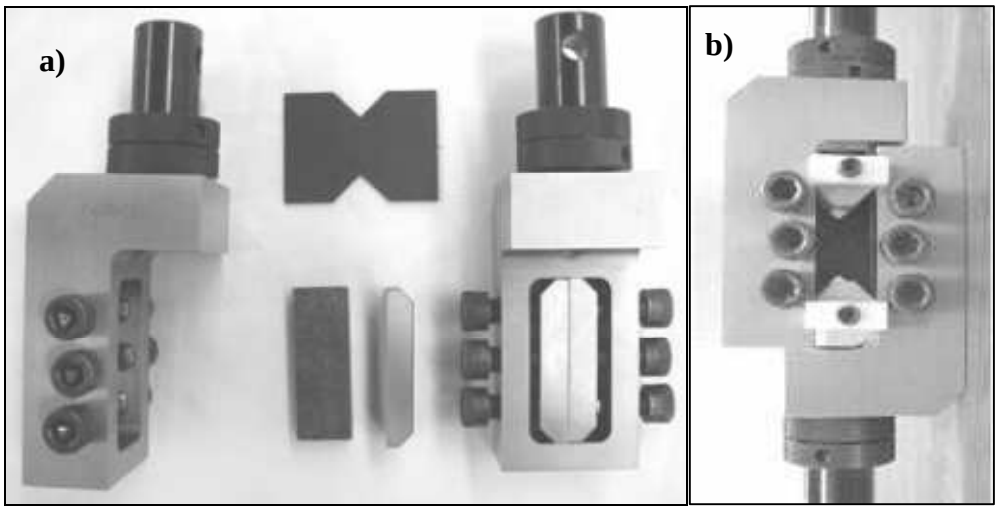


**Figure 7-26 a) V-notched rail shear testing fixture as supplied by Wyoming Test Fixtures Inc. b) Assembled rig with specimen and rig alignment blocks in position. The rig is loaded in tension rather than in compression, unlike the conventional Iosipescu test.**

### *D.1.3.2. Shear testing of random materials*

In this work the shear properties of the optimised random DFP material have been characterised using the V-notched rail shear method, according to ASTM D7078 - 05 [237]. The effect of notch angle was studied before a full experimental programme was undertaken and the method was validated against the conventional Iosipescu test. Figure 7-27 shows that the V-notched rail method yields comparable moduli but higher shear strengths when compared to the Iosipescu test. The shear strengths are 21.5% higher for the V-notch rail shear test when comparing the 90º notch angles. Figure 7-28 clearly shows evidence of crushing at the loading points of the Iosipescu specimen.

The effect of notch angle appears to be insignificant as there is little difference in stiffness or strength for the two angles investigated (Figure 7-28). There was therefore no justifiable reason to deviate from the ASTM standard test geometry outlined in [237].

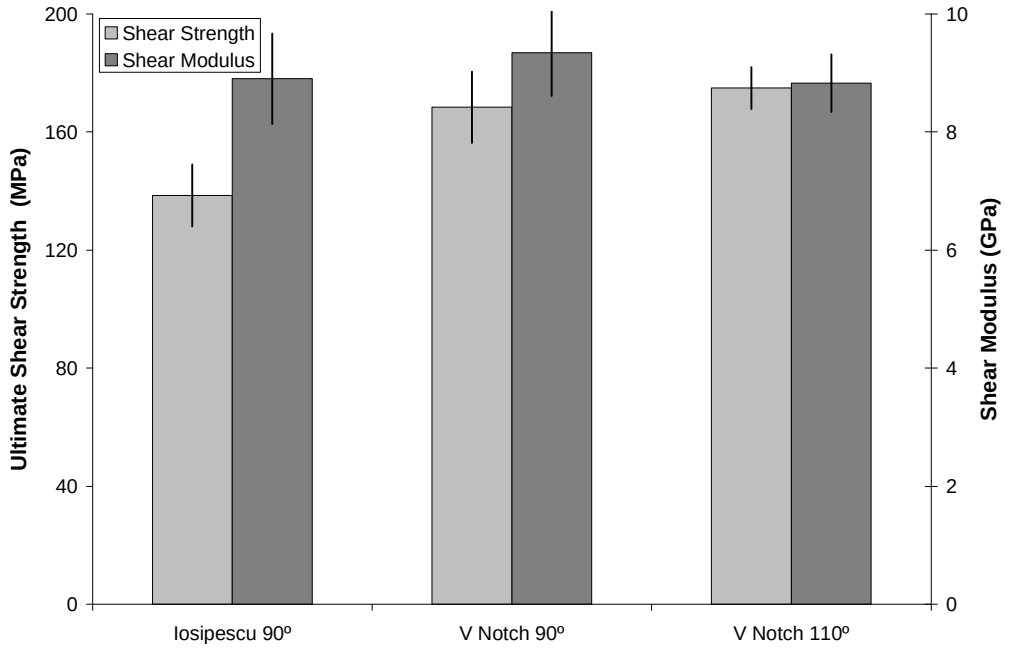


**Figure 7-27 Comparison of the V-notched rail shear test method and the Iosipescu shear method. The effect of notch angle is also presented for the V-notch rail shear method. Specimens were taken from the same plaque, comprising 6mm, 24K bundles at a nominal volume fraction of 30%. This DFP material was chosen because of the relatively low coefficient of variation (6.5%) achieved during tensile testing. The average values and the standard deviation bars are presented for five repeat tests for each scenario.**

### *D.1.3.3. Shear testing of woven materials*

The Iosipescu test has been successfully used to determine the shear properties of multi-directional prepregs [227]. Comparison of the tensile and compressive strains in [238] confirm that a pure shear region can be expected at the centre of the specimen with this type of material. The Iosipescu method was subsequently chosen to determine the shear properties for the woven 0º/90º composites described in Appendix B.3, according to ASTM D5379 - 93 [236].

Specimen geometry for both the Iosipescu test and the V-notched rail test are presented in Figure 7-29. A two-gauge strain rosette (Kyowa KFG-3-120-D16-11L1M2S) was bonded in the centre of the notch roots, orientated at ±45º to the loading direction. Data acquisition for strain and load was at 3Hz and tests were performed at 2mm/min. The engineering strain was calculated by taking the absolute average of the two gauges on each rosette:

$$\varepsilon_{12} = \left|\varepsilon_{+45^\circ}\right| - \left|\varepsilon_{-45^\circ}\right|$$ **Equation 7-2**

Shear modulus calculations assume homogenous stress and strain in the region between the notch roots. The ultimate shear stress is calculated by dividing the ultimate applied force by the cross-sectional area of the specimen between the notches (assuming that the area remains unchanged during the test). The shear modulus is then calculated from the gradient of the stress-strain curve at $0.0005 < \varepsilon_{12} < 0.0025$.

Both testing fixtures were assessed for misalignment and off-axis loading. Two rosettes were used on opposite sides of a specimen for strain comparison. Fernie [239] showed that there was no bending present in the Iosipescu rig and identical strains were measured from each rosette. Similar results in Figure 7-30 confirm that the V-notched rail shear rig is also acceptable, with an average variation 2.04% between gauges.

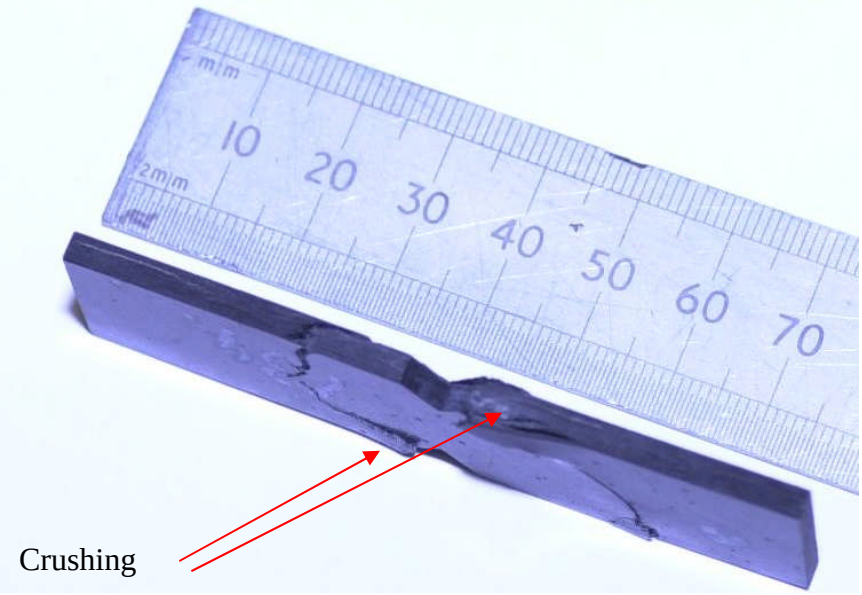


**Figure 7-28 Picture showing crushing which occurred during Iosipescu tests for the random DFP material.**

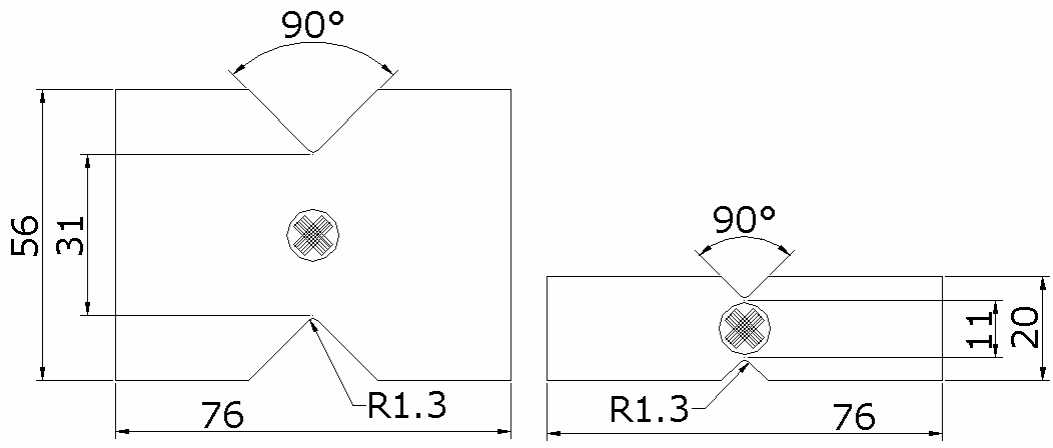


**Figure 7-29 Specimen geometry for a) Iosipescu shear method and b) V-notched rail shear method. (All dimensions in mm)**

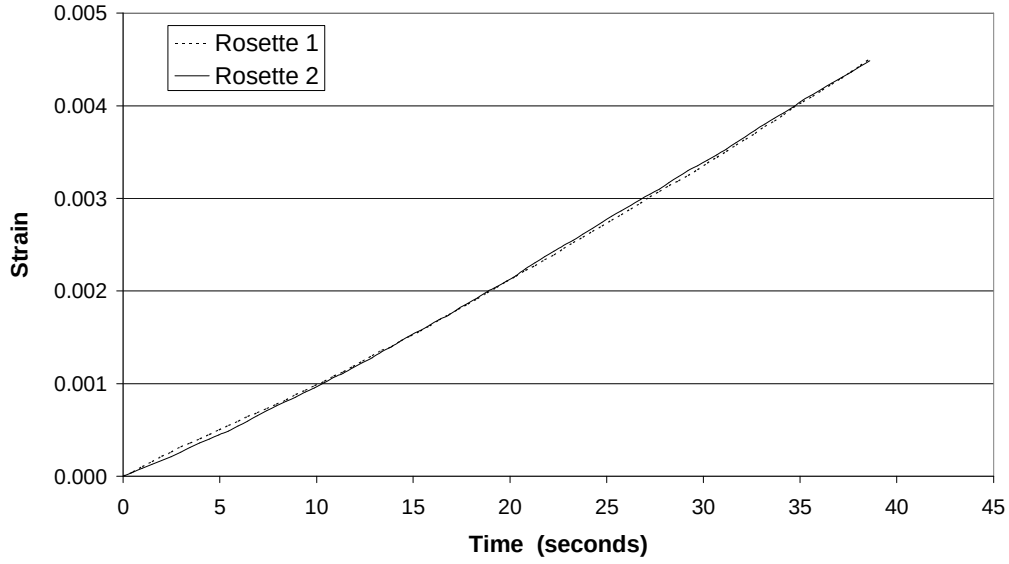


**Figure 7-30 Strain-time history for two ±45º rosettes bonded to opposite sides of a V-notched rail shear specimen. Strain values are up to the point of first-ply failure only and not to the end of the test. Specimen was a 0º/90º prepreg.**

## D.1.4. In-plane notch sensitivity

No published test standard was available for testing the materials sensitivity to notches, so the methodology used by Lindhagen and Berglund [209] was adopted. Previous studies using small notch sizes (Ø5-15mm) failed to establish the onset of notch sensitivity [137], therefore notch sizes from Ø9.5mm to Ø30mm were used. A constant diameter-to-width ratio of 3:8 was maintained for central, circular notches. A standard straight-sided tensile specimen was used as a benchmark and notch specimens had the

same gauge length but increasing widths (25, 46, 60 and 80mm). Tests were performed at 1mm/min and force was measured by a 50kN load cell. Ultimate stress was calculated by taking the peak load and dividing by the central specimen cross section (i.e. specimen width minus notch diameter). Ultimate strength results were normalised with respect to the un-notched specimen properties and the onset of notch sensitivity was defined as an 85% reduction in strength from the un-notched case [209].

### D.1.5. Out-of-plane bending (3 point bend test)

All composite samples were tested using a three point bending regime to determine the flexural modulus and strength according to BS EN 2746:1998 [240]. The flexural testing was performed on a Hounsfield series S testing machine, with a constant span to specimen thickness ratio of 16:1. The loading roller and support rollers were Ø5mm and a 1kN load cell was used to measure the applied force. Flexural modulus was calculated using the displacement of the cross head, which travelled at a rate of 1mm/min.

Width and thickness measurements were taken at ten arbitrary points using digital vernier callipers to an accuracy of ±0.001mm. Specimens produced by vacuum consolidation had severe variations in thickness and were also measured on a coordinate measuring machine (CMM) for comparison (see Appendix E.5). The percentage difference between the two methods is presented in Table 7-5 for a selection of materials. The relative difference is small, with the vernier measurements being ~5% lower than the CMM. However, the bending stiffness (EI) is underestimated by 14% as a consequence. This systematic error must be considered for subsequent calculations.

### D.1.6. Dent resistance

An in-house denting procedure developed by Weager [205] was used to determine the dent resistance of flat coupons. The test was performed quasi-statically using a Ø25mm hemi-spherical indenter attached to a 25kN load cell. Specimens were 125×125mm plates and were located on an anvil using four pins (see Figure 7-31). The specimen was constrained by a clamping ring with four M10 bolts. Dent depth was measured

using both a linear variable differential transformer (LVDT) and the crosshead displacement of the testing machine. Dent depths from both measurement techniques were within 1% of each other for metallic panels but the LVDT underestimated the dent depth for some of the composite panels at low indentation forces (< 2.5kN). The LVDT measured the dent depth from the underside of the panel and not from the indented side and therefore did not account for localised crushing at the indentation site. Consequently, the crosshead displacement was used for composite panels where a disparity was observed between the two measurement techniques.

Denting was performed cyclically to minimise the number of test samples required. Each specimen was indented in increasing 0.5mm steps up to 5mm at a constant rate of 10mm/min. Specimens were loaded, immediately unloaded and then a pause was taken before reloading commenced to allow full viscoelastic recovery of the composite. Weager [205] performed a sensitivity study and found that a 5 minute pause between each cycle was sufficient to allow for 90% of the total recovery for carbon-epoxy components (this equates to an accuracy of 0.01mm). Typical force-displacement curves are presented in Figure 7-32. The onset of a permanent dent occurs when the displacement does not return back to zero after the 5 minute recovery period. The final dent depth after a 5mm indentation is indicated by the arrow along the displacement axis. Three repeat tests were performed for each material and the average dent depth for a given displacement was calculated. Weager [205] established that cyclic testing has no detrimental effect on the dent results for metal specimens, however, cyclic testing was found to be conservative for composite specimens. The force required to form a permanent visible dent in a glass fibre/polypropelene sample was found to be 10% higher for a cyclic test compared with a single indentation.

Previous dent resistance studies compare denting forces at constant dent depths of 0.1mm [201] or 0.2mm [203]. The depth at which a dent becomes permanently visible is the primary interest of the automotive industry for cosmetic applications. Weager [205] performed a subjective analysis on dented steel panels to establish that the visible dent threshold is at 0.05mm for the naked eye. This depth has been used for subsequent comparisons of all the body panel materials in this study to establish their relative dent resistance.

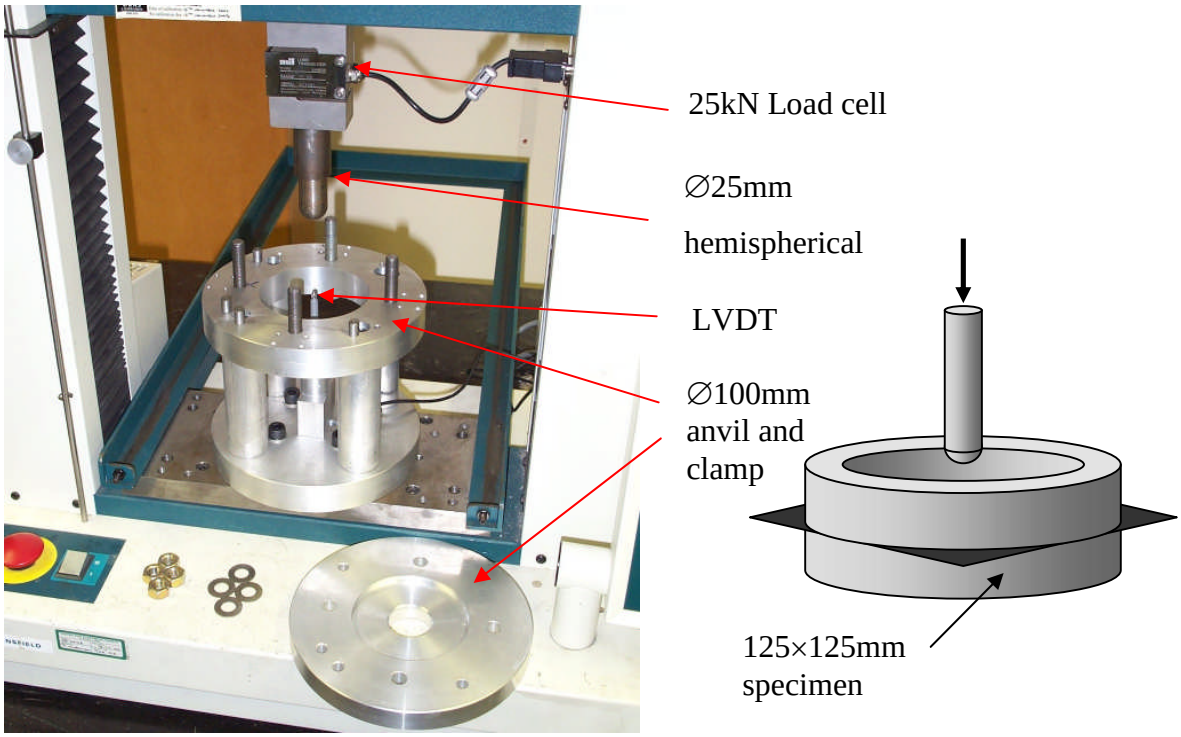


**Figure 7-31 In-house dent test. (Left) Photograph of the fixture located in the Hounsfiled testing machine. (Right) Schematic of a specimen constrained between the anvil and the clamping ring. Reproduced courtesy of Weager [205].**

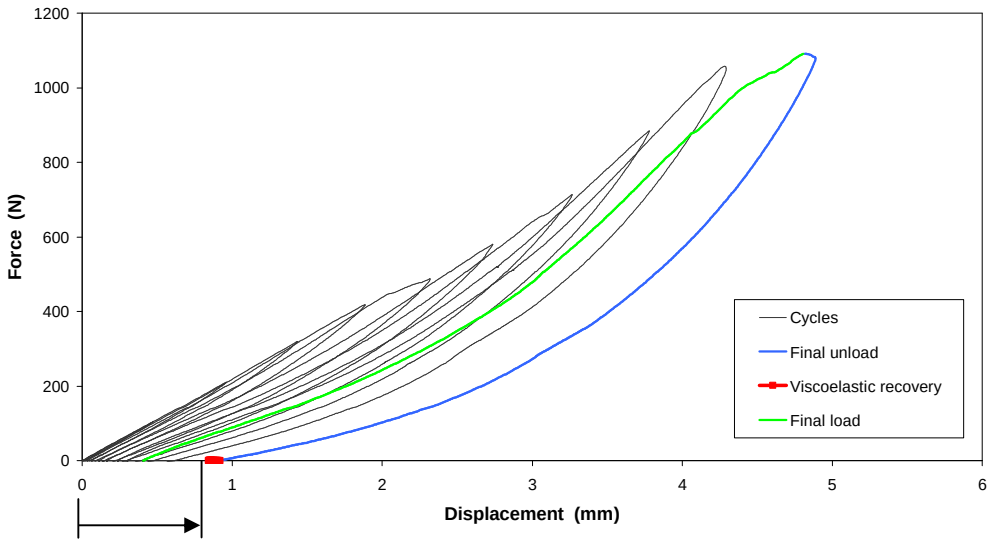


**Figure 7-32 Force-displacement curves for a typical denting cycle. Ten complete load/unload cycles are shown for displacements increasing in 0.5mm steps. The final cycle also shows typical viscoelastic recovery observed during each 5 minute pause between cycles. Arrow along the x-axis denotes the final dent depth after a 5mm displacement.**

### D.1.7. Fabric formability

Shear compliance tests were conducted to determine the formability of the engineered fabrics outlined in Appendix B.3. There are no published test standards for performing shear tests on continuous fibre fabrics, but the two most widely used methods are the picture frame test and the bias extension test. A review by Harrison *et al*. [241] suggests that deformation mechanisms involved in picture frame testing are much closer to those that occur during component forming than those experienced during bias extension. Furthermore, the picture frame test is more repeatable and induces a homogeneous shear deformation throughout the specimen, which simplifies the analysis of results. The only concern with the picture frame test is the boundary conditions imposed on the specimen. Figure 7-33 shows the test arrangement, including the four clamping plates used to constrain the specimen. Loose clamping may fail to induce the required kinematics, whilst over-clamping can cause spurious results if the fibres are even slightly misaligned.

Fabric formability tests for this work were carried out on a Hounsfield testing machine using the picture frame method. (Figure 7-33 shows the geometry of the picture frame rig and a loaded specimen). All tests were carried out in a temperature controlled room at 20˚C. Test samples were cut using a die-cutter from undeformed areas of the roll to ensure that there was no fibre misalignment. Specimens were tightly clamped (20Nm on each bolt) rather than pinned and were tested at a constant speed of 100mm/min. Force and crosshead displacement were recorded during each test and the shear force and shear angles were then calculated from the crosshead data .

The shear force ($F_s$) can be calculated from the measured force ($F_x$) in the direction of extension by Equation 7-3:

$$F_s = \frac{F_x}{2\cos\Phi} \qquad \textbf{Equation 7-3}$$

The frame angle ($\Phi$) can be determined from the crosshead displacement ($D_x$) and the side length ($L$) of the shear frame:

$$\Phi = \cos^{-1}\left[\frac{1}{2^{½}} + \frac{D_x}{2L}\right]$$ **Equation 7-4**

In this case the side length is 145mm, as shown by Figure 7-33. The shear angle is given by Equation 7-5:

$$\theta = \frac{\pi}{2} - 2\Phi$$ **Equation 7-5**

Graphs of shear force against shear angle were then plotted for each material.

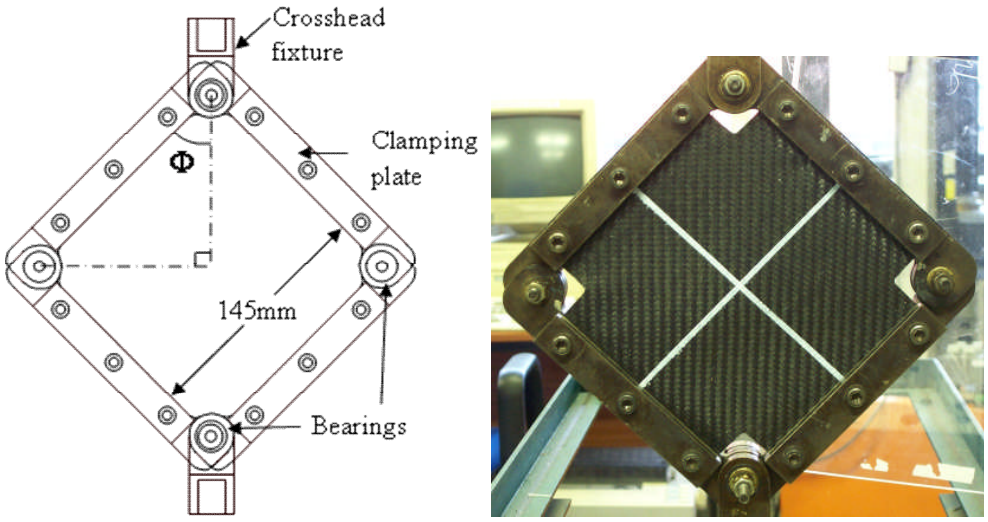


**Figure 7-33 (Left) Schematic of picture frame rig used for shear compliance testing of fabrics. (Right) Prepreg layer loaded into frame. White lines were drawn to aid the detection of fabric wrinkling beyond the locking angle.**

## D.1.8. Fibre directionality characterisation

There are no published testing standards available for determining the degree of orientational bias induced by the DCFP process. An in-house test was developed to establish the level of in-plane orthotropy for DFP laminates rather than conducting a large number of tensile tests at off-axis angles.

The methodology is based on a conventional three point bend test [240], but uses circular disc specimens rather than rectangular beams. The chosen specimen diameter (Ø200mm) was larger than the longest fibre length (115mm) to ensure a representative volume was tested. Each laminate was labelled with a datum line in the biased fibre direction before specimens were water-jet cut. This datum was aligned with a protractor inscribed on the base plate of the testing rig, using the four corner pins to ensure the specimen was central to the loading roller.

Transverse tensile properties were determined before bending tests were performed. Tensile specimens were cut from the same plaques as the bend specimens and transverse failure strains were used to establish a safe working load within the elastic region. A load of 300N was subsequently used for all bending specimens at each orientation and the displacement was recorded from cross head measurements.

Bend specimens were loaded, immediately unloaded, rotated by 18º and loaded again for angles between 0º to 180º inclusive. Three repeat discs were tested for each scenario and the first disc of each set was tested from 0º to 360º to certify that no plastic deformation had occurred. Errors were below 3% for each case and can be attributed to specimen misalignment rather than plastic deformation because no audible matrix cracking was detected.

Figure 7-35 shows a typical force-displacement curve for a bend test and the region used for the stiffness calculation. Stiffness is calculated from the gradient of the line between 2mm and 6mm displacement and is expressed as N/mm because the width of the specimen is variable between the loading point and the supports. The stiffness at each orientation is finally normalised with respect to the stiffness at 0º.

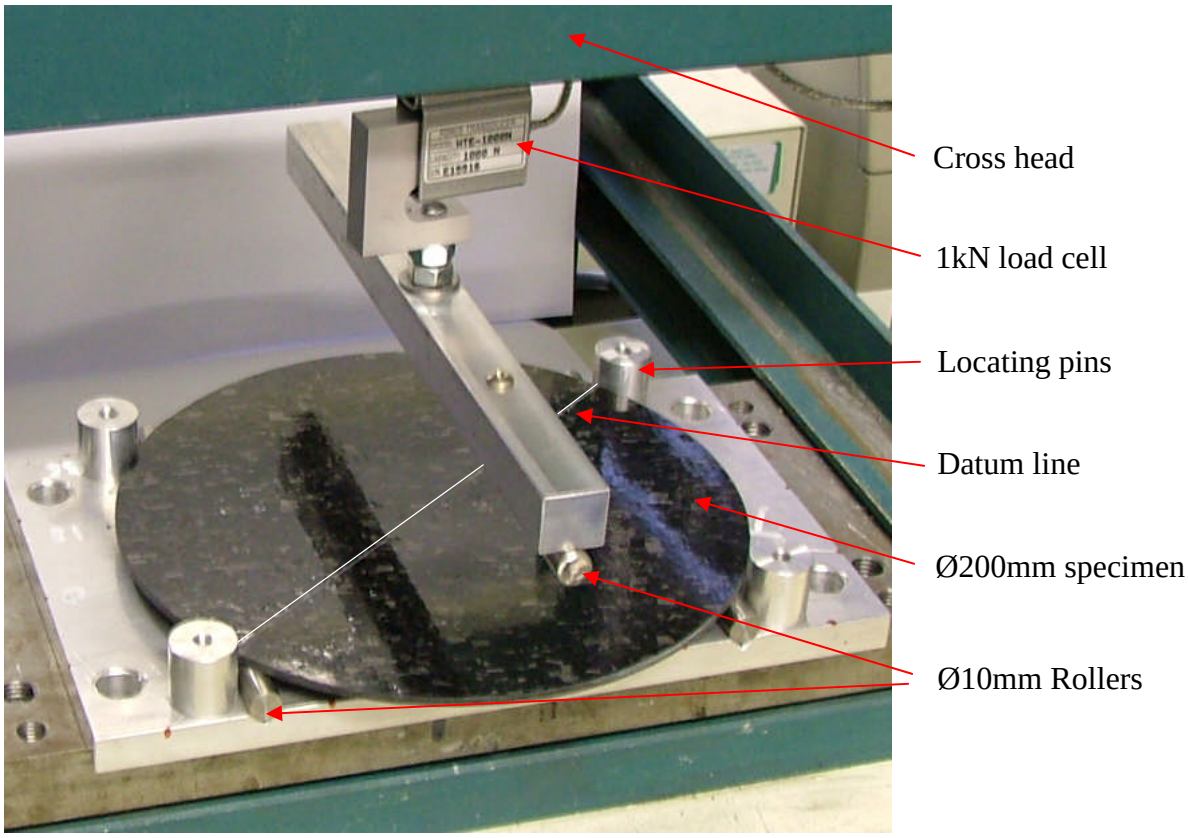


**Figure 7-34 Testing rig for determining the degree of directional bias in the fibre orientation distribution**

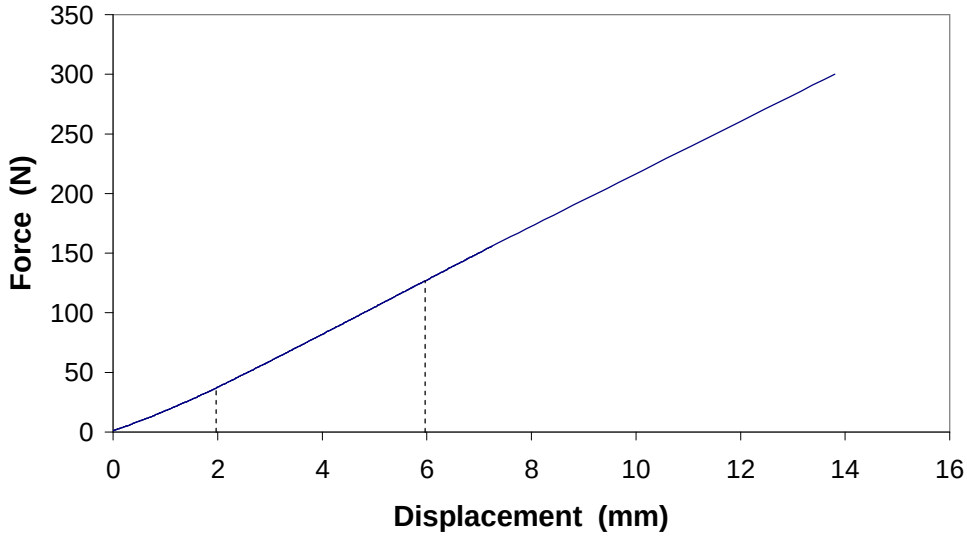


**Figure 7-35 Typical force-displacement curve used to determine the bending stiffness of composite discs at a range of off-axis orientations. The dotted lines show the region which is typically used for the stiffness calculation. The force-displacement curve shown is for a DFP material with 28mm long fibres which have been orientated using a diffuser.**

## D.1.9. Preform compaction characterisation

Preform thickness was measured before consolidation using a rule to provide a quantitative estimate of fibre loft. Additionally, Ø100mm coupons were die-cut from preforms and compaction tested to simulate mould tool closure. An Ø80mm flat platen was lowered at a speed of 100mm/min from a datum towards a flat platen on a Hounsfield testing machine. The applied force was measured using a 1KN load cell and the displacement was measured from the cross-head to an accuracy of 0.0001m. The resulting force-displacement data was converted to pressure-displacement and volume fraction-displacement. Six repeat specimens were tested and each was pre-weighed. The mass was used to normalise the results linearly to the target areal density of 1.5kg/m$^2$ and the data was subsequently summarised according to the following equation [128, 129] (see Section 3.5.4.2):

$$V_f = K + AP^B$$ **Equation 7-6**

where $V_f$ is the expected laminate volume fraction for a given compaction pressure $P$, using fitting parameters $A$ and $B$ (the compaction stiffening index).

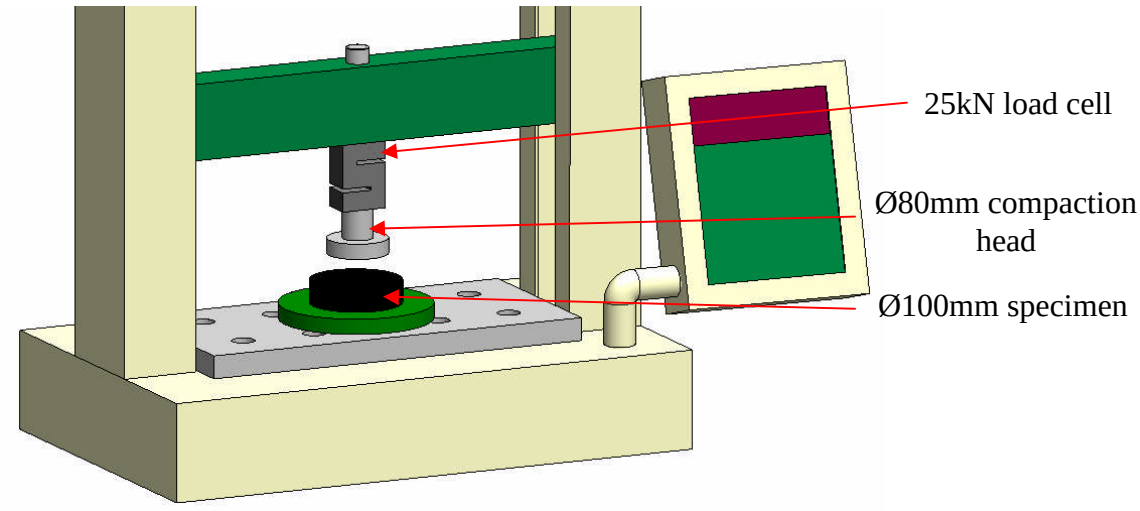


**Figure 7-36 Preform compaction testing configuration. Force was recorded by a 25kN load cell and displacement was monitored from the cross head. The test was to simulate the tool closure during RTM moulding.**

### D.1.10. Preform tear resistance

Preform tear resistance is an important attribute, particularly for handling between the DFP station and the RTM mould tool. Binder type and binder level have been studied in Section 2.3.2 to establish a balance between handleability and final laminate performance. Tensile tests were performed on dry DFP preforms to establish the ultimate tensile load according to ISO3342:1995 [242]. Specimens were stamped 280mm long and 115mm wide and were tested with an initial distance between the grips of 200mm. Grips were custom made with rubber pads on the contact faces to ensure that a constant clamping force was applied across the width of the specimen. Ten repeat tests were performed on a Hounsfield testing machine at a cross head speed of 10mm/min (see Figure 7-37). No specimen slippage or breakage was noted within the vicinity of the clamps (within 10mm) during testing.

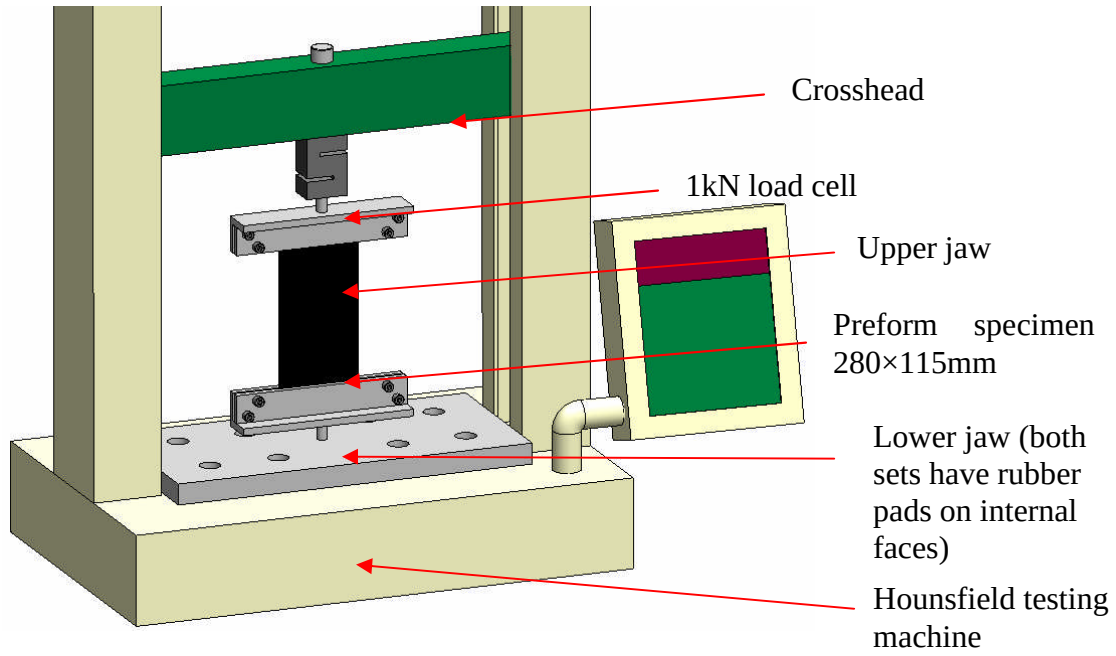


**Figure 7-37 Loading configuration used to determine the preform tear resistance.**

### D.1.11. In-service test for a Ford KA front fender

A front fender from a Ford KA passenger vehicle was selected as a demonstrator component for this thesis. DCFP and semi-preg panels were moulded by vacuum infusion and vacuum consolidation respectively, using the mould tool described in

Appendix C.1. These panels were compared with an off-the-shelf steel counterpart using a four-point bend test to evaluate the relative mechanical performance.

An in-house testing fixture was designed to fit onto an Instron 1195 testing machine. The rig consisted of a flat 10mm aluminium sheet and three support blocks. Figure 7-39 shows how the panel was constrained on the rig relative to the loading arm. Clamping points replicated how the panel would be constrained on the vehicle. A large bend test was performed using a section of aluminium angle to simulate an in-service load (Figure 7-39). The panel was initially loaded to depth of 2mm and then unloaded. A five minute pause was given before the panel was loaded again in increasing 2mm steps. A typical force-displacement history is plotted in Figure 7-40 for one of the steel panels. Displacement was recorded directly from the cross head. In this case, no visible deformation was observed for the 2mm and 4mm cycles since the force-displacement curves both returned to the origin. Panels were compared for peak load and initial stiffness (calculated from the straight line portion of the 2mm cycle curve).

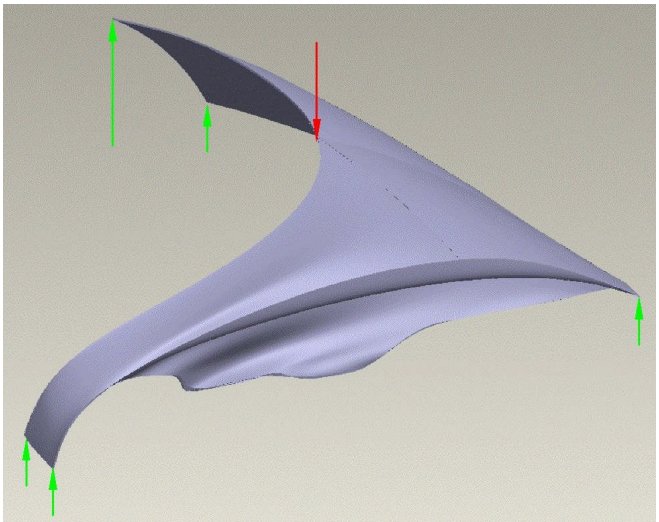

**Figure 7-38 3D CAD geometry of the KA bend test rig. Green arrows show the built-in constraints and the red arrow shows the loading point.**

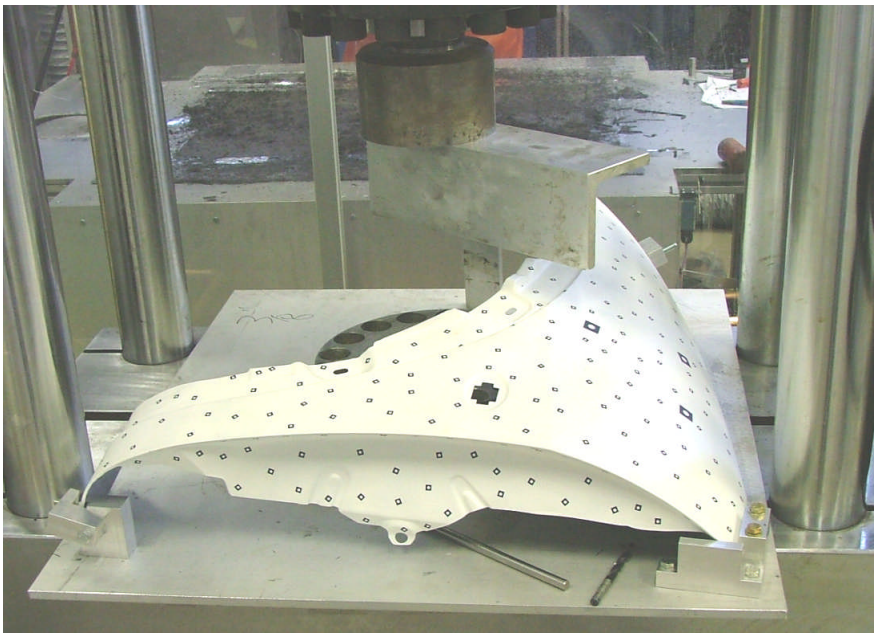

**Figure 7-39 Bend test rig used to evaluate the mechanical performance of candidate body panel materials. The tested panel is from a Ford passenger vehicle and is constrained at three corner points. The rig is centrally positioned on a universal testing machine and bolted into position. Loading is through a section of aluminium angle, 100×100mm in cross section with a 10mm thickness. Force-displacement data is recorded from the cross head for increasing 2mm displacement steps.**

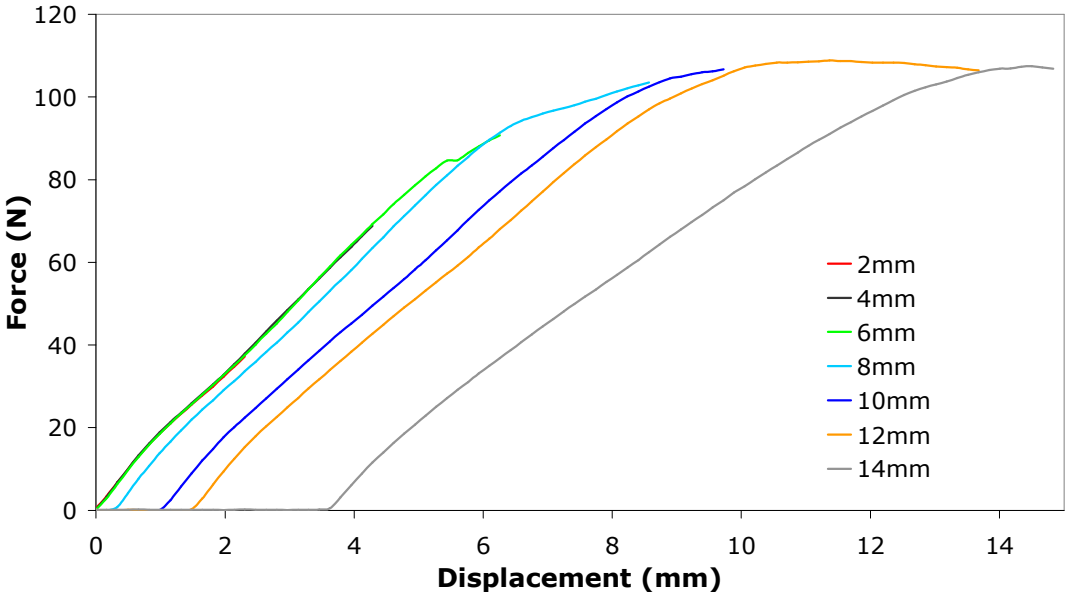


**Figure 7-40 Force-displacement history for a steel fender subjected to a cyclic bend test. No visible deformation was observed for the initial 2mm and 4mm cycles as the curves both returned to the origin.**

# Appendix.E. Characterisation methods

## *E.1. Optical microscopy*

The internal structure of composite laminates was studied using optical microscopy. Specimens (~10mm×25mm×3mm) were cut from areas of interest and end-mounted into Ø40mm diameter casting pots using an epoxy adhesive. Clear casting resin (detailed in Appendix B.3.1) was poured into the pots and cured at room temperature overnight. Once cured, specimens were removed, trimmed to a thickness of 15mm and then ground parallel using a surface grinder. Subsequent polishing was performed on an orbital Struers DAP-7 machine equipped with an automatic holder (Struers Pedemin-S), in a complementary motion at 125rpm. Five grades of abrasive paper (120, 400, 600, 1200 and 4000) were used for five minute periods and the cycle was completed using a flocked wheel with 1μm alumina paste. Specimens were checked under a microscope for scratches and re-polished where necessary. Specimens were examined under a Zeiss® Axiolab optical microscope fitted with a monochrome CCD camera. A PC fitted with a Fast Data Translation Framegrabber (DT3155) was used to convert the XY image field into 512×512 pixels. Image acquisition was automated using a Multicontrol® 2000 stage to ensure image alignment and to capture large fields of interest.

## *E.2. SEM*

Scanning Electron Microscopy (SEM) was used to study the fracture sites of DFP laminates. Specimens (25×10×3mm) were mounted on aluminium stubs using a carbon adhesive pad prior to being sputter coated with gold. Silver or carbon paste was used to ensure good contact along the mounting surfaces. Samples were then analysed using an XL-30 SEM.

## *E.3. Volume fraction determination*

Fibre volume fraction was determined by two different methods, depending on the laminate moulding process. Plaques produced by vacuum-only consolidation, such as prepreg, were characterised using the loss on ignition technique according to ASTM D 2584-94 [243]. Thermo-gravimetric analysis was used to produce a calibration curve to account for carbon loss due to oxidation. After 1 hour at 625ºC a carbon mass loss of 2.3% was recorded for the Toray fibres (used in all of the prepregs/RFI/LRI materials) and the volume fraction figures have been adjusted accordingly. Manufacturers' data was used for the HexMC material because of excessive oxidation.

Loss on ignition requires small 25×25mm samples which are not representative samples for the DFP material, particularly since areal density varied by ±15% at times. For this reason DFP plaques were characterised by the 'density method' according to CRAG method 1000 [244]. Plaques were produced by RTM had good thickness consistency (1% COV) and the volume fraction was calculated using the mass of the preform and the moulded laminate. Details of these determination techniques can be found below.

### E.3.1. Loss on ignition

Loss on ignition, or burn-off testing [243], was conducted to establish the fibre content of plaques produced by vacuum consolidation. Specimens were cut into 25×25mm squares from six random locations of each plaque to provide an indication of the volume fraction variation and also a representative mean value. Ceramic crucibles and composite specimens were pre-dried in a hot air oven at 50ºC. The crucible was weighed with ($m_2$) and without ($m_1$) the specimen to an accuracy of 1.0mg. The arrangement was then loaded into a Carbolite AAF1100 electric muffle furnace for one hour at 625ºC. Finally, the crucible and residue ($m_3$) were weighed and the mass fraction ($M_f$) of the composite was calculated using Equation 7-7:

$$M_f = \frac{m_3 - m_2}{m_1 - m_2} \times 100$$ **Equation 7-7**

The density of carbon fibre ($\rho_f$) and epoxy ($\rho_m$) were assumed to be 1.79g/cm$^3$ and 1.1g/cm$^3$ using manufacturers' data respectively. These values were used in Equation 7-8 to determine the composite volume fraction:

$$V_f = \frac{\left(\frac{m_3 - m_1}{\rho_f}\right)}{\left(\frac{m_3 - m_1}{\rho_f}\right) + \left(\frac{m_2 - m_3}{\rho_m}\right)} \times 100$$ **Equation 7-8**

## E.3.2. Thermo-gravimetric analysis (TGA)

Thermo-gravimetric analysis (TGA) was performed on carbon fibres to determine mass loss due to oxidation. TGA was used to evaporate all available surface compounds for detection using a Perkin Elmer Pyris 1 instrument. Approximately 5mg of sample was heated in air from ambient to 625ºC at a rate of 50ºC/min. The 6K and 12K tow are used in the LRI, RFI and prepreg fabrics described in Appendix B.3. On average there is a 2.3% reduction in carbon fibre mass when subjected to the same isothermal conditions as used for the loss on ignition determination. This can be attributed to both oxidation but also the removal of the fibre surface treatment. This mass reduction can be used to adjust the experimental volume fraction from burn-off tests. The mass loss due to oxidation ($m_o$) can be incorporated into Equation 7-8 as follows:

**Equation 7-9**

$$V_f = \frac{\left(\frac{m_o + m_3 - m_1}{\rho_f}\right)}{\left(\frac{m_o + m_3 - m_1}{\rho_f}\right) + \left(\frac{m_o + m_2 - m_3}{\rho_m}\right)} \times 100$$

The oxidation rate, based on $CO_2$ detection, is much greater for the Fortafil® fibre. There was no residue in the crucible when determining the volume fraction using loss on ignition techniques. Courtaulds Grafil PAN precursor is rich in sodium, which causes lower thermal stability and acts as a catalyst to the oxidation process [245]. The calibration curve for the Fortafil fibre was not used for adjusting experimental volume fractions of the HexMC material. Instead, the manufacturers' figure of 57% was adopted because there was no resin escapement from the tool.

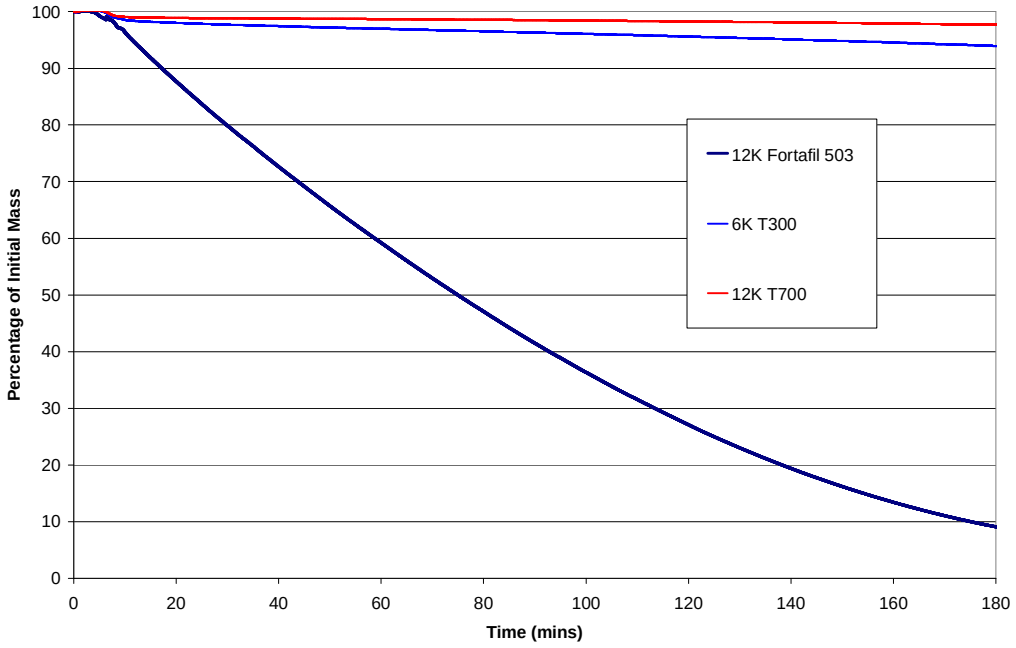


**Figure 7-41 Graph to show the percentage mass loss over time for three types of carbon fibre. All specimens were ramped to 625ºC at 50°C/min and then dwelled for 3 hours. The 6K and 12K tows are used in all of the SP Systems fabrics (RC300 and RC303 respectively). Fortafil® 503 fibres are used in HexMC.**

### E.3.3. Density method

The sample areas used for other $V_f$ determination techniques were considered to be too small for the DFP material, given the degree of areal density variation encountered. Fibre volume fraction for DFP plaques was determined using the mass of the fibre preform ($m_1$) and the mass of the moulded laminate ($m_2$). Preforms were initially over-sized and then die-cut to exact dimensions to ensure the preform area was always consistent. The density of carbon fibre ($\rho_f$) and epoxy ($\rho_m$) were assumed to be

1.79g/cm$^3$ and 1.1g/cm$^3$ using manufacturers' data respectively. The volume fraction was calculated as follows:

$$V_f = \frac{\frac{m_1}{\rho_f}}{\frac{m_1}{\rho_f} + \left( \frac{m_2 - m_1}{\rho_m} \right)}$$

**Equation 7-10**

## *E.4. Preform areal mass analysis*

Initial DFP process optimisation was assessed by stamping contiguous coupons from fibre preforms. This technique was also used to validate the areal density predictions from the DFP process simulation outlined in Section 2.3. Preforms were initially die-cut into 700×500mm rectangles to replicate the area moulded by RTM. A smaller die cutter was used to take 50×50mm samples over the entire mouldable area. Coupons were weighed to an accuracy of ±10μg.

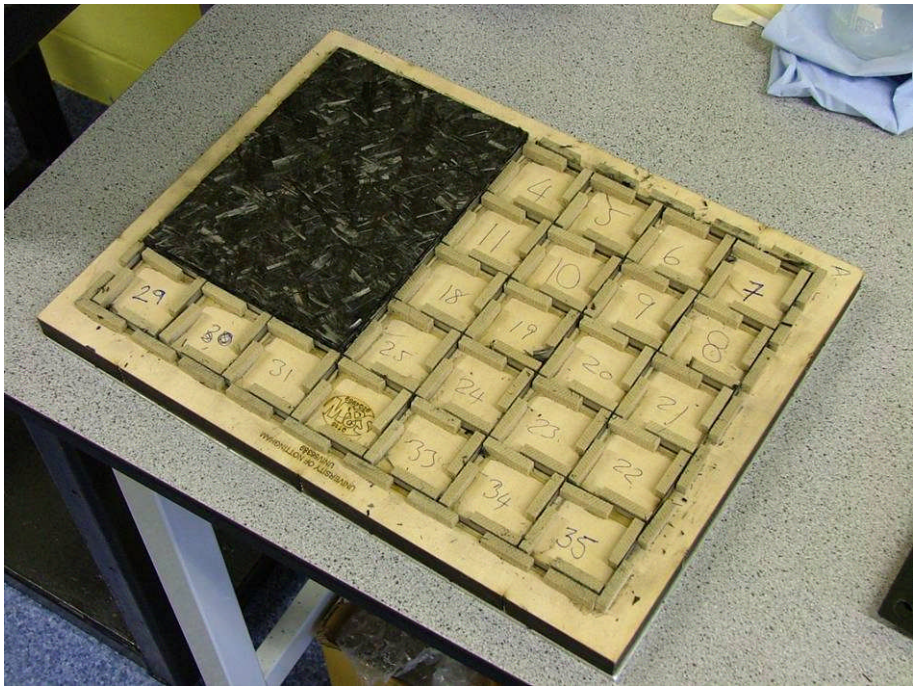

**Figure 7-42 Die cutter used to sample the areal mass of DCFP preforms during process optimisation. The cutter is split into contiguous 50×50mm squares.**

## *E.5. CMM measurements*

Conventionally, material testing requires three measurements of each specimen in each direction to obtain an accurate average value. Plaques produced by vacuum consolidation on a single-sided tool had a rippled B surface due to the underlying fibre architecture. Ten thickness measurements were taken for each three-point-bend specimen using vernier callipers. Sample plaques were also measured by a coordinate measuring machine, over a 20×20mm area at a 1mm pitch. Each plaque was secured on the machine using double-sided adhesive tape. Depth measurements were taken at analysis point from a vertical datum. Figure 7-43 demonstrates the degree of waviness on the rear surface of an LRI plaque. The percentage difference between the two methods is presented in Table 7-5 for a selection of materials. Ten thickness measurements was considered to be representative.

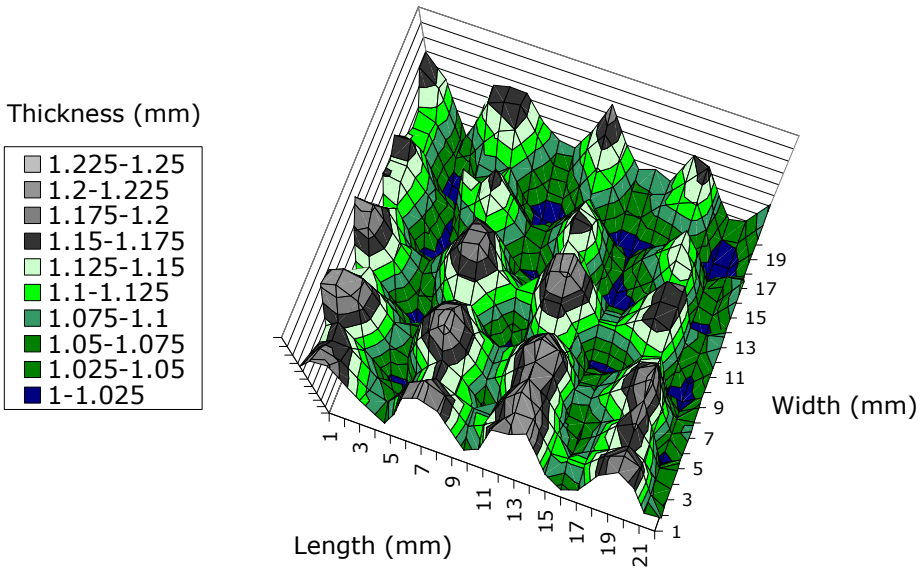


**Figure 7-43 Thickness distribution of a vacuum consolidated moulding measured using a CMM machine. Sample plaque was a 12K LRI material. Measurements were taken over a 20×20mm area using a 1mm grid pitch.**

| | Coordinate Measuring Machine | | Vernier Calipers | | % difference |
|---|---|---|---|---|---|
| | **Av thickness** | **COV (%)** | **Av thickness** | **COV (%)** | |
| ZPreg | 1.50389 | 4.23 | 1.484 | 2.28 | 1.3 |
| 6K LRI | 1.24687 | 2.97 | 1.1685 | 5.53 | 6.3 |
| 12 LRI | 1.10274 | 5.33 | 1.059 | 3.91 | 3.9 |
| 6K RFI | 1.37185 | 2.66 | 1.299 | 1.00 | 5.3 |
| 12K RFI | 1.42212 | 1.23 | 1.345 | 3.35 | 5.4 |

**Table 7-5 Comparison of thickness measurements taken from a selection of laminates produced under vacuum consolidation. Ten measurements were taken using a digital vernier calliper for six specimens and 440 measurements were taken using a coordinate measuring machine on a 1mm square pitch from the same laminate. Percentage difference between the two methods is presented.**

# Appendix.F. DCFP process simulation methodology

This section gives details of the process simulation methodology and lists any assumptions used. The user is presented with a graphical interface for entering the input parameters (see Figure 7-44). The simulation tool has been designed to account for both fibre and machine related parameters on the quality of DCFP preforms.

A robot spray path is defined from the specified tool geometry and spray path offset. The number of east/west sweeps required is calculated from the width of the preform and the spray path offset

$$Number\ of\ \ sweeps = \frac{Preform\ width}{Robot\ \ path\ offset} \qquad \textbf{Equation 7-11}$$

The mass of fibre required to fulfil the areal density requirements is calculated for each sweep as follows:

$$Mass\ of\ \ fibre\ \ per\ sweep = \frac{Target\ areal\ density \times Preform\ area}{Number\ of\ \ sweeps} \qquad \textbf{Equation 7-12}$$

Therefore the linear length of fibre required per sweep can be determined from the linear density (a function of the filament count) of the chosen roving:

$$Length\ of\ \ fibre\ \ per\ sweep = \frac{Mass\ of\ \ fibre\ \ per\ sweep}{Linear\ tow\ density} \qquad \textbf{Equation 7-13}$$

The time it takes for the robot to complete one linear sweep is calculated by

$$Time\ \ for\ one\ sweep = \frac{Preform\ length}{Robot\ speed} \qquad \textbf{Equation 7-14}$$

Therefore using Equation 7-13 and Equation 7-14 the linear speed at which the fibres leave the chopping apparatus can be calculated:

$$Linear\ \ fibre\ speed = \frac{Length\ of\ \ fibre\ \ per\ sweep}{Time\ \ for\ one\ sweep}$$ **Equation 7-15**

The linear fibre speed is subsequently used to calculate the number of tow segments leaving the gun per second:

$$Tow\ segments\ \ per\ second = \frac{Linear\ \ fibre\ speed}{Chopped\ \ fibre\ length}$$ **Equation 7-16**

The robot position is incremented along the spray path by a time step, generated from the robot speed and areal density of the preform. The time step is calculated as follows:

$$Robot\ time\ step = \left(Tow\ segments\ \ per\ second\right)^{-1}$$ **Equation 7-17**

The robot spray path is divided up by the robot time step to give discrete locations for the chopper gun to deposit fibres. At each robot time step a virtual circle is drawn to depict the base of the spray cone. The diameter of the circle is a function of the TCP height and robot speed, as discussed in Section 2.3.1.1. The number of tows deposited within each circle depends on the number of tows being processed simultaneously by the gun. The polar coordinates of the centroid of each deposited tow are determined by the generation of two random numbers. $\theta_{ij}$ is a random angle between 0 and $2\pi$ radians and the radius $R_{ij}$ is based on a random number returned from a normal distribution, with mean 0 and standard deviation 0.5. This equates to a 95% probability that the fibre segment will fall within the prescribed virtual circle. This is assumed to be representative of the spray deposition process as shown by Figure 2-21. Finally, the tow orientation $\phi_{ij}$ about its geometric centre is determined by a third random number between 0 and $\pi$ radians.

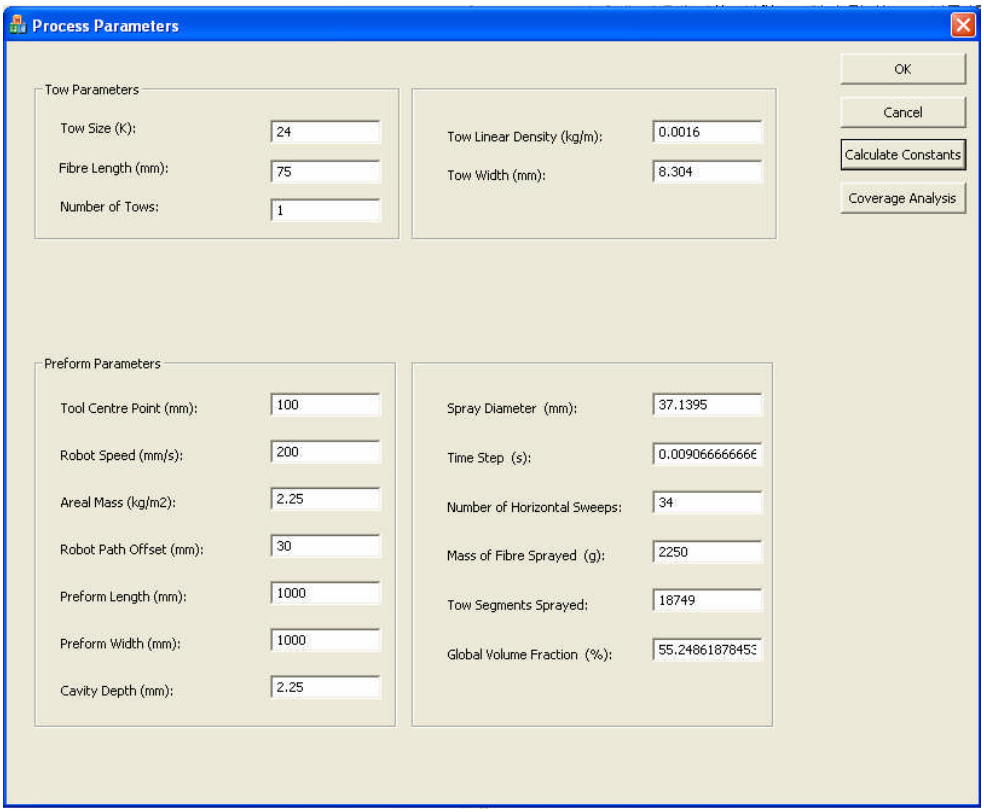


**Figure 7-44 Graphical user interface for entering input parameters for the process simulation. Inputs are all shown on the left hand side of the screen and outputs are calculated on the right. The input parameters are split into two categories; fibre parameters and machine related parameters.**

Once the spray deposition process is complete the program is used to determine the number of fibre crossovers at discrete grid locations. The user defines the pitch of an analysis grid (see Figure 7-45), which is over laid on top of the preform. At each grid point the program cycles through all of the tows in order to determine which segments coincide with the grid point. This can be visualised in Figure 7-46. The number of tow crossovers are stored in a two dimensional array, indexed by the coordinates of each grid point. This information is used in a number of subsequent calculations. The program stores the number of times zero fibres are detected at each grid point and this is used to calculate the percentage coverage value as follows:

$$Percentage\ coverage\ value = \frac{Number\ of\ \ zero\ \ fibre\ occurences}{Total\ number\ of\ \ grid\ \ points} \qquad \textbf{Equation 7-18}$$

This information is only significant if the target areal mass is low, as previously experienced in Section 2.3.1.1. Areal mass variation is a far more useful parameter for determining the quality of DCFP preforms. The coverage analysis grid is sub-divided

into 50×50mm squares to represent the coupons used for the areal mass investigation in Section 2.3.1.2. A summation is made of the total number of tow crossovers for all of the grid points within each square. The coefficient of variation of all of the squares is calculated to represent the areal mass variation of the preform.

Finally, an orientation distribution is compiled for the fibres within the area of interest (Figure 7-45). As the program determines the percentage coverage value and the areal mass variation, the orientation of each fibre is stored within an array and is plotted in the form of a radial histogram. This provides the user with a quick and useful visualisation of the level of macroscopic homogenisation.

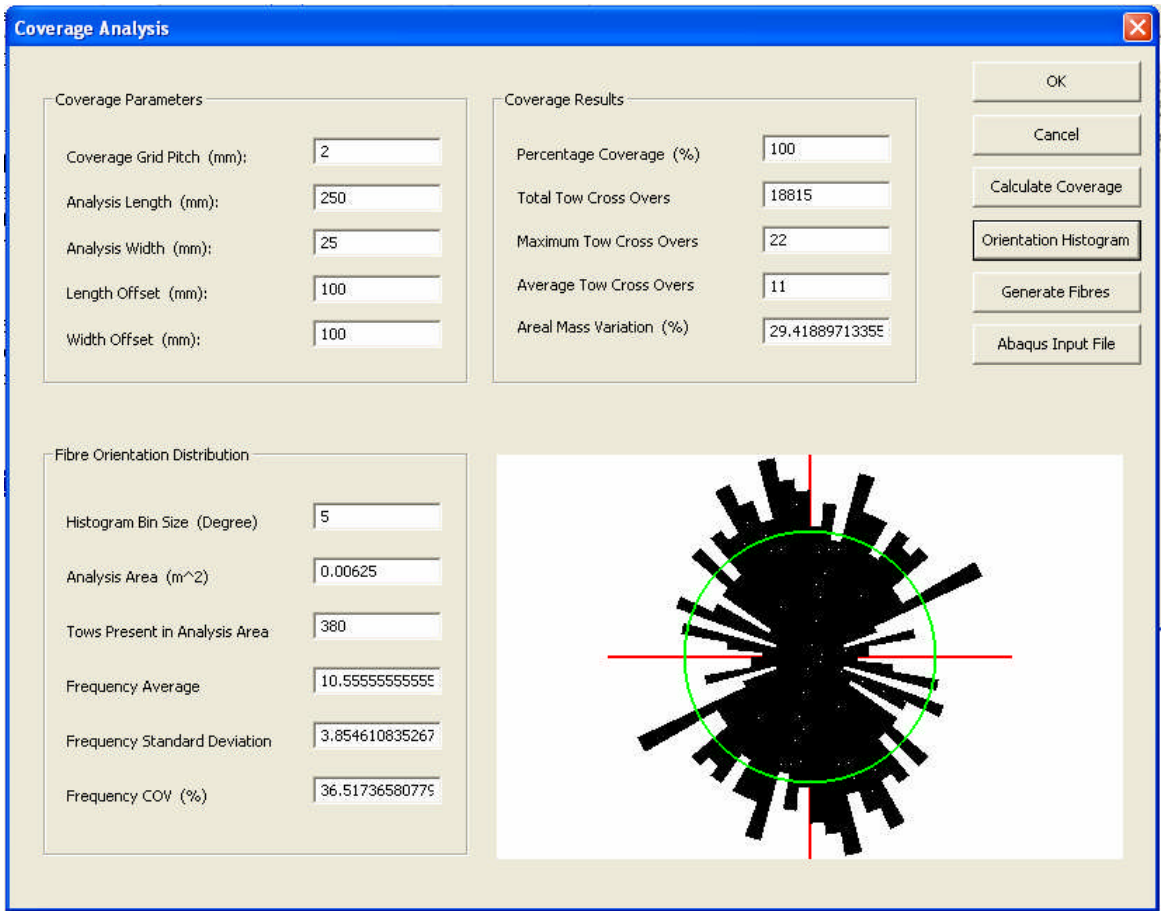


**Figure 7-45 Graphical user interface for determining the percentage coverage value, the areal mass variation and the orientation distribution of the simulated preform.**

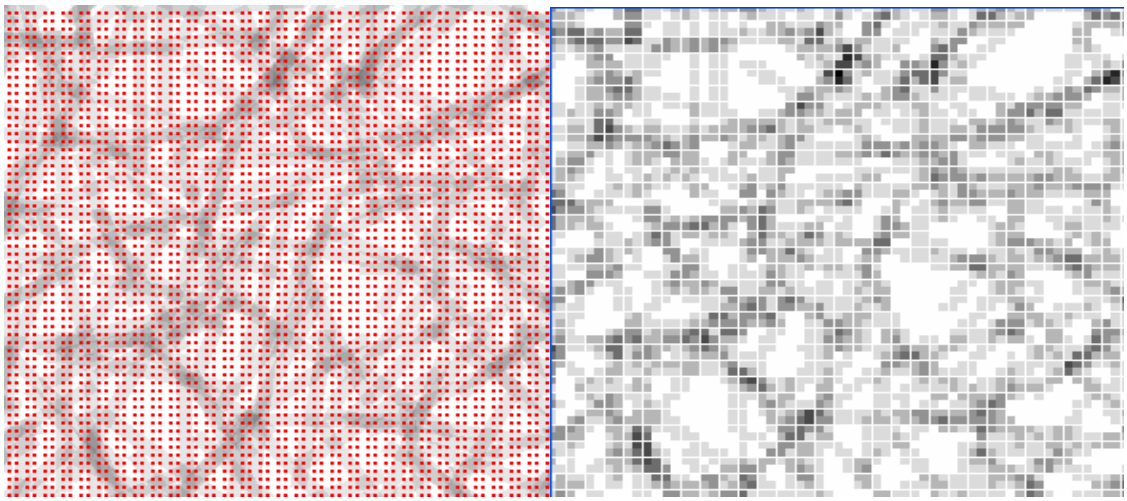

**Figure 7-46 (Left) A square array grid overlaid on top of the deposited fibres. The number of tows present at each grid point is determined from the coordinates of each fibre. (Right) A greyscale image showing the number of tow crossovers at each grid point. A value of 255 (white) indicates no fibres are present and a value of 0 (black) represents the maximum number of tow crossovers within the preform, (7 tows in this case). A linear scale is used for all greyscale values in between.**

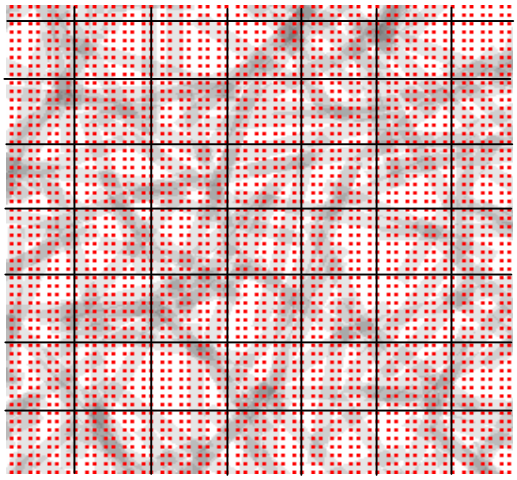

**Figure 7-47 The coverage grid which is overlaid on top of the fibres is subdivided into 50×50mm squares to determine the areal mass variation. The number of tow crossovers at each grid point are summed within each corresponding square and the coefficient of variation is calculated to represent the areal mass variation of the preform.**

# Appendix.G. Experimental Results

| Tow size (K) | Fibre length (mm) | Areal density (kg/m$^2$) | Volume fraction (%) | Modulus (GPa) | COV (%) | Rel. Error (%) | UTS (MPa) | COV (%) | Rel. Error (%) |
|---|---|---|---|---|---|---|---|---|---|
| 6 | 25 | 0.75 | 27.6 | 22.2 | 10.8 | 6.8 | 164.5 | 13.4 | 8.5 |
| 6 | 25 | 1.5 | 27.6 | 21.5 | 12.2 | 7.7 | 182.1 | 11.9 | 7.5 |
| 6 | 25 | 2.25 | 31.1 | 25.9 | 7.3 | 4.6 | 207.0 | 10.2 | 6.5 |
| 6 | 50 | 0.75 | 27.6 | 21.7 | 11.7 | 7.4 | 155.1 | 11.8 | 7.5 |
| 6 | 50 | 1.5 | 27.6 | 22.2 | 13.1 | 8.3 | 169.2 | 11.2 | 7.1 |
| 6 | 50 | 2.25 | 31.1 | 24.5 | 13.4 | 8.5 | 221.0 | 8.9 | 5.6 |
| 6 | 75 | 0.75 | 27.6 | 20.0 | 16.3 | 10.3 | 130.1 | 25.8 | 16.3 |
| 6 | 75 | 1.5 | 27.6 | 21.1 | 21.0 | 13.3 | 161.2 | 18.6 | 11.8 |
| 6 | 75 | 2.25 | 31.1 | 24.9 | 13.4 | 8.5 | 189.7 | 14.2 | 9.0 |
| 12 | 25 | 0.75 | 27.6 | 22.0 | 6.8 | 4.3 | 176.8 | 1.8 | 1.1 |
| 12 | 25 | 1.5 | 27.6 | 23.2 | 10.6 | 6.7 | 203.0 | 9.3 | 5.9 |
| 12 | 25 | 2.25 | 31.1 | 25.5 | 15.5 | 9.8 | 208.0 | 14.3 | 9.0 |
| 12 | 50 | 0.75 | 27.6 | 21.1 | 12.8 | 8.1 | 158.3 | 19.1 | 12.1 |
| 12 | 50 | 1.5 | 27.6 | 24.6 | 14.4 | 9.1 | 189.9 | 16.8 | 10.6 |
| 12 | 50 | 2.25 | 31.1 | 26.8 | 12.6 | 8.0 | 215.5 | 15.4 | 9.7 |
| 12 | 75 | 0.75 | 27.6 | 20.0 | 11.0 | 7.0 | 130.7 | 24.7 | 15.6 |
| 12 | 75 | 1.5 | 27.6 | 22.2 | 25.8 | 16.3 | 181.9 | 20.2 | 12.8 |
| 12 | 75 | 2.25 | 31.1 | 24.5 | 9.8 | 6.2 | 206.6 | 16.5 | 10.4 |
| 24 | 25 | 0.75 | 27.6 | 23.3 | 13.2 | 8.3 | 141.0 | 26.2 | 16.6 |
| 24 | 25 | 1.5 | 27.6 | 24.3 | 12.1 | 7.7 | 214.2 | 12.4 | 7.8 |
| 24 | 25 | 2.25 | 31.1 | 23.3 | 11.8 | 7.5 | 174.7 | 26.2 | 16.6 |
| 24 | 50 | 0.75 | 27.6 | 19.2 | 16.0 | 10.1 | 145.1 | 22.5 | 14.2 |
| 24 | 50 | 1.5 | 27.6 | 21.6 | 10.0 | 6.3 | 183.7 | 11.5 | 7.3 |
| 24 | 50 | 2.25 | 31.1 | 26.3 | 11.7 | 7.4 | 214.3 | 15.0 | 5.9 |
| 24 | 75 | 0.75 | 27.6 | 20.8 | 14.7 | 9.3 | 79.3 | 24.1 | 15.2 |
| 24 | 75 | 1.5 | 27.6 | 20.5 | 16.3 | 10.3 | 150.9 | 18.5 | 11.7 |
| 24 | 75 | 2.25 | 31.1 | 24.5 | 12.7 | 8.0 | 184.3 | 17.7 | 11.2 |

**Table 7-6 Overall experimental tensile results for 27 carbon plaques used to study the effect of fibre coverage on the tensile properties of DCFP. Presented values are averages of specimens cut at both 0º and 90º orientations. Slight variations in volume fraction were encountered due to the limited choice of moulding frames. Relative error values are calculated from Equation 3-1.**

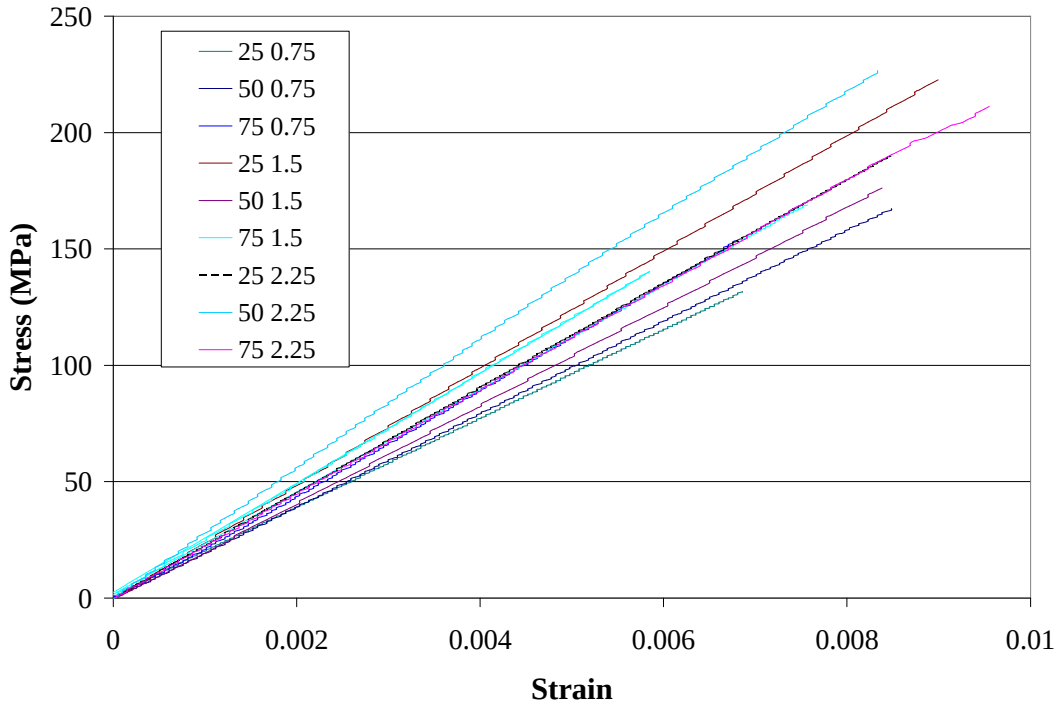


**Figure 7-48 Stress/strain response for a selection of DCFP plaques produced at the NCC in Dayton, Ohio. Plaques were all produced using 24K tows. Legend shows the fibre length (25, 50 or 75mm) and the target areal mass of the preform (0.75, 1.5 or 2.25kg/m$^2$).**

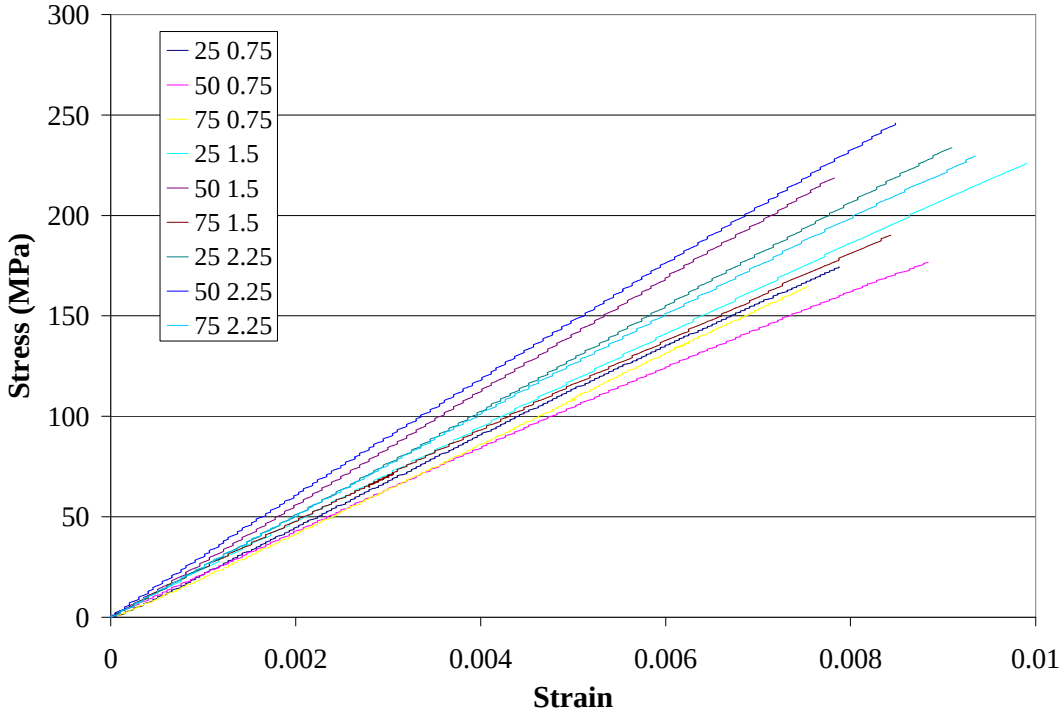


**Figure 7-49 Stress/strain response for a selection of DCFP plaques produced at the NCC in Dayton, Ohio. Plaques were all produced using 12K tows. Legend shows the fibre length (25, 50 or 75mm) and the target areal mass of the preform (0.75, 1.5 or 2.25kg/m$^2$).**

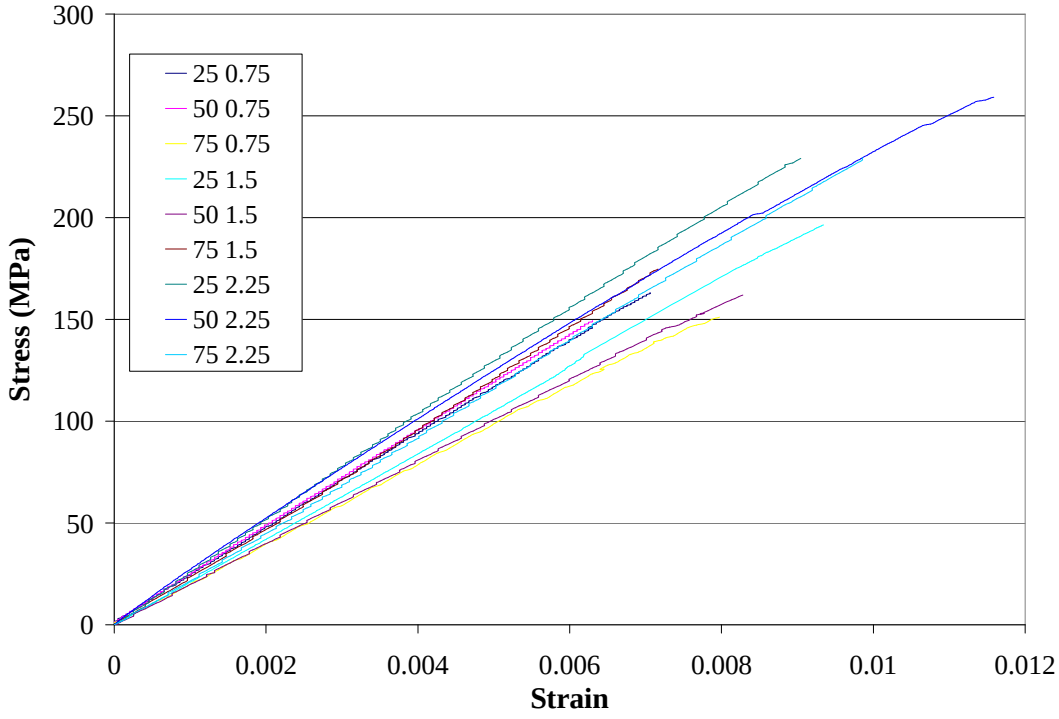


**Figure 7-50 Stress/strain response for a selection of DCFP plaques produced at the NCC in Dayton, Ohio. Plaques were all produced using 6K tows. Legend shows the fibre length (25, 50 or 75mm) and the target areal mass of the preform (0.75, 1.5 or 2.25kg/m$^2$).**

| Fibre length (mm) | Filamentised | Modulus (GPa) | St Dev (GPa) | COV (%) | Relative error (%) | UTS (MPa) | St Dev (MPa) | COV (%) | Relative error (%) |
|---|---|---|---|---|---|---|---|---|---|
| 3 | No | 17.4 | 1.24 | 7.2 | 8.2 | 103.0 | 17.4 | 16.9 | 4.4 |
| 6 | No | 19.4 | 1.54 | 7.9 | 6.5 | 148.7 | 13.9 | 9.3 | 2.4 |
| 14 | No | 20.4 | 1.62 | 7.9 | 4.2 | 129.4 | 14.0 | 10.8 | 2.8 |
| 23 | No | 19.5 | 3.77 | 19.3 | 8.1 | 97.1 | 16.8 | 17.3 | 4.5 |
| 28 | No | 20.6 | 4.07 | 19.8 | 7.5 | 93.4 | 23.4 | 25.0 | 6.5 |
| 115 | No | 19.2 | 5.59 | 29.2 | 5.4 | 92.4 | 34.5 | 37.3 | 9.6 |
| 3 | Yes | 24.4 | 2.05 | 8.4 | 9.7 | 227.6 | 7.0 | 3.1 | 0.8 |
| 6 | Yes | 23.3 | 1.40 | 6.0 | 4.9 | 212.5 | 23.2 | 10.9 | 2.8 |
| 14 | Yes | 24.7 | 1.72 | 7.0 | 3.7 | 178.1 | 23.5 | 13.2 | 3.4 |
| 23 | Yes | 23.1 | 2.40 | 10.4 | 4.3 | 146.8 | 19.6 | 13.3 | 3.4 |
| 29 | Yes | 25.0 | 5.05 | 20.2 | 7.5 | 147.1 | 38.4 | 21.5 | 6.7 |
| 58 | Yes | 22.4 | 3.94 | 17.6 | 4.6 | 125.3 | 27.9 | 22.3 | 5.7 |
| 115 | Yes | 21.8 | 5.79 | 26.5 | 5.0 | 121.3 | 35.2 | 29.0 | 6.5 |

**Table 7-7 Experimental tensile results for the fibre length study (Section 3.4). A total of 60 specimens were tested per fibre length for each level of filamentisation. A 24K tow was used to manufacture each plaque at a nominal fibre volume fraction of 30%. The two levels Relative error values are calculated from Equation 3-1.**

| Fibre Type | Level of Filamentisation (%) | Modulus (GPa) | St Dev (GPa) | Relative Error (%) | UTS (MPa) | St Dev (MPa) | Relative Error (%) |
|---|---|---|---|---|---|---|---|
| I | 0 | 20.8 | 1.7 | 3.6 | 96.4 | 8.9 | 4.1 |
| I | 50 | 21.9 | 1.6 | 3.2 | 133.6 | 17.5 | 5.9 |
| I | 100 | 23.5 | 1.7 | 3.3 | 149.7 | 19.8 | 5.9 |
| II | 0 | 18.4 | 1.6 | 3.8 | 58.7 | 4.8 | 3.7 |
| II | 20 | 19.3 | 2.1 | 4.8 | 79.8 | 13.9 | 7.8 |
| II | 40 | 20.4 | 2.7 | 6.0 | 75.1 | 8.9 | 5.3 |
| II | 60 | 20.9 | 2.0 | 4.2 | 96.9 | 11.7 | 5.4 |
| II | 80 | 20.7 | 2.6 | 5.6 | 75.8 | 12.1 | 7.1 |
| II | 100 | 21.3 | 2.6 | 5.5 | 84.5 | 10.9 | 5.8 |

**Table 7-8 Experimental tensile results for the filamentisation study presented in Section 3.5. Filamentisation level is expressed as a percentage of the air pressure applied in the filamentisation cavity (from 0 to 7 bar). Fibre lengths were 14mm in all cases and the relative error for both modulus and UTS are calculated from Equation 3-1.**

| Fibre Length (mm) | Volume Fraction ($V_f$) | Stiffness (GPa) | Standard Deviation (GPa) | Relative Error (%) | Strength (MPa) | Standard Deviation (MPa) | Relative Error (%) |
|---|---|---|---|---|---|---|---|
| 6 | 7.5 | 7.6 | 0.5 | 2.9 | 41.8 | 3.2 | 3.5 |
| 6 | 20.4 | 16.3 | 1.0 | 2.6 | 120.7 | 11.7 | 4.3 |
| 6 | 34.4 | 24.1 | 1.5 | 2.8 | 184.8 | 24.3 | 5.9 |
| 6 | 38.8 | 28.0 | 1.2 | 1.9 | 217.0 | 26.0 | 5.4 |
| 23 | 9.0 | 8.9 | 1.2 | 6.0 | 35.7 | 3.9 | 4.9 |
| 23 | 21.2 | 16.5 | 1.8 | 4.8 | 92.0 | 14.3 | 6.9 |
| 23 | 31.8 | 24.4 | 3.9 | 7.1 | 130.6 | 23.0 | 7.9 |
| 23 | 44.5 | 31.3 | 3.7 | 5.3 | 208.5 | 27.8 | 6.0 |

**Table 7-9** **Tensile properties from the full in-plane material characterisation study presented in Section 3.6.**

| Fibre Length (mm) | Volume Fraction ($V_f$) | Stiffness (GPa) | Standard Deviation (GPa) | Relative Error (%) | Strength (MPa) | Standard Deviation (MPa) | Relative Error (%) |
|---|---|---|---|---|---|---|---|
| 6 | 11.0 | 8.5 | 0.5 | 2.4 | 149.5 | 6.0 | 1.8 |
| 6 | 19.9 | 14.7 | 0.9 | 2.6 | 230.1 | 6.8 | 1.3 |
| 6 | 30.0 | 19.9 | 1.0 | 2.2 | 252.1 | 8.8 | 1.6 |
| 6 | 36.6 | 25.5 | 1.1 | 2.0 | 318.6 | 10.9 | 1.5 |
| 23 | 9.2 | 6.9 | 0.8 | 5.3 | 128.1 | 15.1 | 5.3 |
| 23 | 21.2 | 13.0 | 1.5 | 5.3 | 170.1 | 8.4 | 2.2 |
| 23 | 31.4 | 21.1 | 1.1 | 2.4 | 242.8 | 13.8 | 2.5 |
| 23 | 39.5 | 27.2 | 3.8 | 6.2 | 268.5 | 20.5 | 3.4 |

**Table 7-10 Compression properties from the full in-plane material characterisation study presented in Section 3.6.**

| Fibre Length (mm) | Volume Fraction ($V_f$) | Stiffness (GPa) | Standard Deviation (GPa) | Relative Error (%) | Strength (MPa) | Standard Deviation (MPa) | Relative Error (%) |
|---|---|---|---|---|---|---|---|
| 6 | 11.0 | 3.8 | 0.4 | 5.3 | 67.6 | 4.7 | 3.1 |
| 6 | 19.9 | 6.4 | 0.5 | 3.6 | 116.5 | 7.6 | 2.9 |
| 6 | 30.0 | 8.2 | 0.4 | 2.3 | 161.8 | 9.3 | 2.6 |
| 6 | 36.6 | 9.3 | 0.7 | 3.5 | 168.4 | 12.1 | 3.2 |
| 23 | 9.2 | 3.1 | 0.4 | 5.6 | 57.4 | 4.6 | 3.6 |
| 23 | 21.2 | 7.1 | 0.9 | 5.8 | 115.6 | 22.6 | 8.8 |
| 23 | 31.4 | 8.4 | 0.5 | 2.8 | 154.6 | 18.0 | 5.2 |
| 23 | 39.5 | 10.8 | 1.7 | 7.1 | 196.8 | 24.6 | 5.6 |

**Table 7-11 Shear properties from the full in-plane material characterisation study presented in Section 3.6**

# Appendix.H. Multi-level analytical stiffness model

Analytical modelling has been split across four levels in order to determine the stiffness of DCFP laminates (as discussed in Section 4.3). This strategy supports the complexities associated with the mesoscale architecture and the random fibre orientations.

## *H.1. Elastic constants of a transversely isotropic bundle*

The first level seeks to determine the elastic constants of a transversely isotropic bundle containing carbon filaments. Weng [172] reformulated Mori-Tanaka's theory [156] to investigate the behaviour of composite materials containing anisotropic constituents. Following the notation used by Hill [181], the stress-strain relationship for a transversely isotropic arrangement of fibres is as follows:

$$\sigma = L_{tow}\varepsilon \qquad \textbf{Equation 7-19}$$

The bold-faced letters represent second order tensors and the ordinary capital letter a fourth order tensor. $L_{tow}$ is the elastic moduli tensor and when expanded can be written as:

$$\tfrac{1}{2}\left(\sigma_{22}+\sigma_{33}\right)=k\left(\varepsilon_{22}+\varepsilon_{33}\right)+l'\varepsilon_{11} \qquad \textbf{Equation 7-20}$$

$$\sigma_{11}=l\left(\varepsilon_{22}+\varepsilon_{33}\right)+n\varepsilon_{11} \qquad \textbf{Equation 7-21}$$

$$\sigma_{22}-\sigma_{33}=2m\left(\varepsilon_{22}-\varepsilon_{33}\right) \qquad \textbf{Equation 7-22}$$

$$\sigma_{23}=2m\varepsilon_{23} \qquad \textbf{Equation 7-23}$$

$$\sigma_{12}=2p\varepsilon_{12} \qquad \textbf{Equation 7-24}$$

$$\sigma_{13}=2p\varepsilon_{13} \qquad \textbf{Equation 7-25}$$

Therefore from Equation 7-20 through to Equation 7-25 the elastic moduli tensor, $L_{tow}$ can be summarised as follows:

$$L_{tow} = \left(2k, l, l^{'}, n, 2m, 2p\right)$$ **Equation 7-26**

When $L_{tow}$ possesses diagonal symmetry (i.e. $L_{ijkl} = L_{klij}$) it is common to express Equation 7-26 in terms of only five components (since $l = l'$):

$$L_{tow} = \left(2k, l, n, 2m, 2p\right)$$ **Equation 7-27**

*k, l, n, m, p* are therefore the plane-strain bulk modulus, cross modulus, axial modulus under axial strain, and the transverse and axial shear moduli respectively. According to Christensen [246], the elastic constants of the bundle can be determined from Equation 7-27:

$$E_{11} = n - \frac{l^2}{k}$$ **Equation 7-28**

$$\nu_{12} = \frac{l}{2k}$$ **Equation 7-29**

$$\mu_{23} = m$$ **Equation 7-30**

$$\mu_{12} = p$$ **Equation 7-31**

$$k_{23} = k$$ **Equation 7-32**

$$E_{22} = \frac{4\left(kn - l^2\right)m}{n\left(m + k\right) - l^2}$$ **Equation 7-33**

From here it is necessary to calculate the components of the elastic moduli tensor in order to determine the elastic constants in Equation 7-28 to Equation 7-33. Using Weng's [172] reformulated version of the Mori-Tanaka theory, the effective moduli for the composite under a prescribed displacement is:

$$L_{tow} = \left(\sum_{r=0}^{1} c_r L_r A_r\right)\left(\sum_{r=0}^{1} c_r A_r\right)^{-1}$$ **Equation 7-34**

Subscript $r$ refers to the phase, where 0 is the matrix phase and 1 the reinforcement phase. $c_r$ is the volume fraction and $L_r$ is the elastic moduli tensor of the $r^{th}$ phase respectively. $A_r$ is the average strain-concentration tensor when a single $r^{th}$ phase inclusion is embedded in the infinite matrix. This can be calculated as follows:

$$A_r = \left[I + S_0 L_0^{-1}\left(L_r - L_0\right)\right]^{-1}$$ **Equation 7-35**

where $I = [1,0,0,1,1,1]$ and $S_0$ is the Eshelby $S$-tensor for the matrix phase [155]. $A_0$ is equivalent to $I$ for the matrix phase:

$$A_0 = I = [1,0,0,1,1,1]$$ **Equation 7-36**

To evaluate Equation 7-34 for the fibre phase it is necessary to calculate six components:

$$A_r = \left[\frac{d^{(r)}}{l^{(r)}}, -\frac{g^{(r)}}{l^{(r)}}, -\frac{h^{(r)}}{l^{(r)}}, \frac{c^{(r)}}{l^{(r)}}, \frac{1}{e^{(r)}}, \frac{1}{f^{(r)}}\right]$$ **Equation 7-37**

These six components are directly calculated using the Eshelby S-tensor:

$$c^{(r)} = 1 + \frac{2\left(k_r - k_0\right)}{E_0}\left[(1-\nu_0)\left(S_{2222} + S_{2233}\right) - 2\nu_0 S_{2211}\right] + \frac{2\left(l_r - l_0\right)}{E_0}\left[(1-\nu_0)S_{1122} - \nu_0 S_{1111}\right]$$ **Equation 7-38**

$$d^{(r)} = 1 + \frac{\left(n_r - n_0\right)}{E_0}\left[S_{1111} - 2\nu_0 S_{1122}\right] + \frac{2\left(l_r - l_0\right)}{E_0}\left[(1-\nu_0)S_{1122} - \nu_0 S_{1111}\right]$$ **Equation 7-39**

$$e^{(r)} = 1 + \frac{2\left(m_r - m_0\right)}{m_0} S_{2323}$$ **Equation 7-40**

$$f^{(r)} = 1 + \frac{2\left(p_r - p_0\right)}{p_0} S_{1212}$$ **Equation 7-41**

$$g^{(r)} = \frac{2\left(k_r - k_0\right)}{E_0}\left[(1-\nu_0)S_{1122} - \nu_0 S_{1111}\right] + \frac{l_r - l_0}{E_0}\left[S_{1111} - 2\nu_0 S_{1122}\right]$$ **Equation 7-42**

$$h^{(r)} = \frac{n_r - n_0}{E_0}\left[S_{2211} - \nu_0\left(S_{2222} + S_{2233}\right)\right] + \frac{l_r - l_0}{E_0}\left[\left(1-\nu_0\right)\left(S_{2222} + S_{2233}\right) - 2\nu_0 S_{2211}\right]$$

**Equation 7-43**

$$l^{(r)} = c^{(r)}d^{(r)} - 2g^{(r)}h^{(r)}$$

**Equation 7-44**

Parameters *k, l, n, n* and *p* have the same definitions as in Equation 7-27 (subscripts denote the corresponding phase) and $E_0$ and $\nu_0$ are the elastic modulus and Poisson's ratio of the matrix respectively. The remaining matrix phase components can be expressed in terms of the ordinary bulk modulus ($\kappa_0$) and the shear modulus of the resin ($\mu_0$):

$$l_0 = \kappa_0 - \tfrac{2}{3}\mu_0$$

**Equation 7-45**

$$n_0 = \kappa_0 + \tfrac{4}{3}\mu_0$$

**Equation 7-46**

$$m_0 = p_0 = \mu_0$$

**Equation 7-47**

$$k_0 = \kappa_0 + \tfrac{1}{3}\mu_0$$

**Equation 7-48**

For a spheroidal inclusion, fourth order components of Eshelby's S-tensor, $S_{ijkl}$ [155] can be calculated as functions of the matrix Poisson's ratio ($\nu_0$), the fibre aspect ratio ($\alpha$) and the fibre shape factor ($g$) as follows [125]:

$$S_{1111} = \frac{1}{2\left(1-\nu_0\right)}\left\{1 - 2\nu_0 + \frac{3\alpha^2 - 1}{\alpha^2 - 1} - \left[1 - 2\nu_0 + \frac{3\alpha^2}{\alpha^2 - 1}\right]g\right\}$$

**Equation 7-49**

$$S_{2222} = S_{3333} = \frac{3}{8\left(1-\nu_0\right)}\frac{\alpha^2}{\alpha^2 - 1} + \frac{1}{4\left(1-\nu_0\right)}\left[1 - 2\nu_0 + \frac{3\alpha^2}{4\left(\alpha^2 - 1\right)}\right]g$$

**Equation 7-50**

$$S_{2233} = S_{3322} = \frac{1}{4\left(1-\nu_0\right)}\left\{\frac{\alpha^2}{2\left(\alpha^2 - 1\right)} - \left[1 - 2\nu_0 + \frac{3}{4\left(\alpha^2 - 1\right)}\right]g\right\}$$

**Equation 7-51**

$$S_{2211} = S_{3311} = \frac{1}{2\left(1-\nu_0\right)}\frac{\alpha^2}{\alpha^2 - 1} + \frac{1}{4\left(1-\nu_0\right)}\left\{\frac{3\alpha^2}{\alpha^2 - 1} - \left(1 - 2\nu_0\right)\right\}g$$

**Equation 7-52**

$$S_{1122} = S_{1133} = -\frac{1}{2\left(1-\nu_0\right)}\left[1 - 2\nu_0 + \frac{1}{\alpha^2 - 1}\right] + \frac{1}{2\left(1-\nu_0\right)}\left[1 - 2\nu_0 + \frac{3}{2\left(\alpha^2 - 1\right)}\right]g$$

**Equation 7-53**

$$S_{2323} = \frac{1}{4(1-\nu_0)}\left\{\frac{\alpha^2}{2(\alpha^2-1)} + \left[1-2\nu_0 + \frac{3}{4(\alpha^2-1)}\right]g\right\}$$ **Equation 7-54**

$$S_{1212} = S_{1313} = \frac{1}{4(1-\nu_0)}\left\{1-2\nu_0 - \frac{\alpha^2+1}{\alpha^2-1} - \frac{1}{2}\left[1-2\nu_0 - \frac{3(\alpha^2+1)}{\alpha^2-1}\right]g\right\}$$ **Equation 7-55**

Where the shape factor of the fibre can be calculated….

…for a prolate shape (α > 1) as $g = \frac{\alpha}{(\alpha^2-1)^{3/2}}\left\{\alpha(\alpha^2-1)^{1/2} - \cosh^{-1}\alpha\right\}$ **Equation 7-56**

…for an oblate shape (α < 1) as $g = \frac{\alpha}{(1-\alpha^2)^{3/2}}\left\{\cos^{-1}\alpha - \alpha(1-\alpha^2)^{1/2}\right\}$ **Equation 7-57**

The aspect ratio dependence of the elastic moduli tensor $L_{tow}$ is manifested through the S-tensor using the shape parameter $g$. It is now possible to calculate all of the components of $A_r$ in Equation 7-37, using Equation 7-38 through to Equation 7-44. Returning to Equation 7-34, it is logical to split this calculation into two components:

$$\sum c_r L_r A_r = \left(c^{CLA}, g^{CLA}, h^{CLA}, d^{CLA}, e^{CLA}, f^{CLA}\right)$$ **Equation 7-58**

$$\left(\sum c_r A_r\right)^{-1} = \left(c^{CAI}, g^{CAI}, h^{CAI}, d^{CAI}, e^{CAI}, f^{CAI}\right)$$ **Equation 7-59**

The right hand side components of Equation 7-58 are as follows:

$$c^{CLA} = \sum 2c_r\left(k_r d^{(r)} - l_r g^{(r)}\right)/l^{(r)}$$ **Equation 7-60**

$$d^{CLA} = \sum c_r\left(n_r c^{(r)} - 2l_r h^{(r)}\right)/l^{(r)}$$ **Equation 7-61**

$$e^{CLA} = \sum 2c_r m_r / e^{(r)}$$ **Equation 7-62**

$$f^{CLA} = \sum 2c_r p_r / f^{(r)}$$ **Equation 7-63**

$$g^{CLA} = \sum c_r\left(l_r d^{(r)} - n_r g^{(r)}\right)/l^{(r)}$$ **Equation 7-64**

$$d^{CLA} = \sum c_r\left(l_r c^{(r)} - 2k_r h^{(r)}\right)/l^{(r)}$$ **Equation 7-65**

The right hand side components of Equation 7-59 are as follows:

$$c^{CAI} = \left(\sum c_r c^{(r)} / l^{(r)}\right) / l^{CAI} \quad \textbf{Equation 7-66}$$

$$d^{CAI} = \left(\sum c_r d^{(r)} / l^{(r)}\right) / l^{CAI} \quad \textbf{Equation 7-67}$$

$$e^{CAI} = \left(\sum c_r / e^{(r)}\right)^{-1} \quad \textbf{Equation 7-68}$$

$$f^{CAI} = \left(\sum c_r / f^{(r)}\right)^{-1} \quad \textbf{Equation 7-69}$$

$$g^{CAI} = \left(\sum c_r g^{(r)} / l^{(r)}\right) / l^{CAI} \quad \textbf{Equation 7-70}$$

$$h^{CAI} = \left(\sum c_r h^{(r)} / l^{(r)}\right) / l^{CAI} \quad \textbf{Equation 7-71}$$

$$l^{CAI} = \left(\sum \frac{c_r d^{(r)}}{l^{(r)}}\right)\left(\sum \frac{c_r c^{(r)}}{l^{(r)}}\right) - 2\left(\sum \frac{c_r g^{(r)}}{l^{(r)}}\right)\left(\sum \frac{c_r h^{(r)}}{l^{(r)}}\right) \quad \textbf{Equation 7-72}$$

The product of Equation 7-58 and Equation 7-59 results in Equation 7-34. The elastic moduli tensor can thus be expressed in the form of Equation 7-26:

$$2k = c^{CLA} c^{CAI} + 2h^{CLA} g^{CAI} \quad \textbf{Equation 7-73}$$

$$l = g^{CLA} c^{CAI} + d^{CLA} g^{CAI} \quad \textbf{Equation 7-74}$$

$$l' = h^{CLA} d^{CAI} + c^{CLA} h^{CAI} \quad \textbf{Equation 7-75}$$

$$n = d^{CLA} d^{CAI} + 2g^{CLA} h^{CAI} \quad \textbf{Equation 7-76}$$

$$2m = e^{CLA} e^{CAI} \quad \textbf{Equation 7-77}$$

$$2p = f^{CLA} f^{CAI} \quad \textbf{Equation 7-78}$$

The parameters from Equation 7-73 through to Equation 7-78 can be used to establish the elastic properties in Equation 7-28 through to Equation 7-33. Input parameters presented in Table 7-12 have been used to determine the effect of tow volume fraction on the elastic properties of the bundle (Figure 7-51). Whilst filament length is an input at this stage, it is generally accepted that the filaments are infinitely long because the fibre aspect ratio is over 800 for even the smallest DCFP chop length.

| Property | Designation | Value | |
|---|---|---|---|
| Filament length | $L$ | 23 | mm |
| Filament diameter | $Ø_1$ | 0.007 | mm |
| Aspect ratio ($L$ / $Ø_1$) | α | 2054 | |
| | | | |
| Fibre plane strain bulk modulus | $k_1$ | 20.19 | GPa |
| Fibre cross modulus | $l_1$ | 12.14 | GPa |
| Fibre axial modulus under axial strain | $n_1$ | 234.23 | GPa |
| Fibre transverse shear modulus | $m_1$ | 8.06 | GPa |
| Fibre axial shear modulus | $p_1$ | 10 | GPa |
| | | | |
| Matrix Poisson's ratio | $v_o$ | 0.38 | |
| Matrix modulus | $E_o$ | 3 | GPa |
| Matrix ordinary bulk modulus | $\kappa_0$ | 4.16 | GPa |
| Matrix shear modulus | $\mu_0$ | 1.09 | GPa |

**Table 7-12 Input parameters required to calculate the elastic constants of a transversely isotropic carbon fibre tow. Subscript *1* refers to the carbon filament phase and subscript *0* refers to the matrix. Values for fibre properties have been taken directly from [173] and matrix values are experimental.**

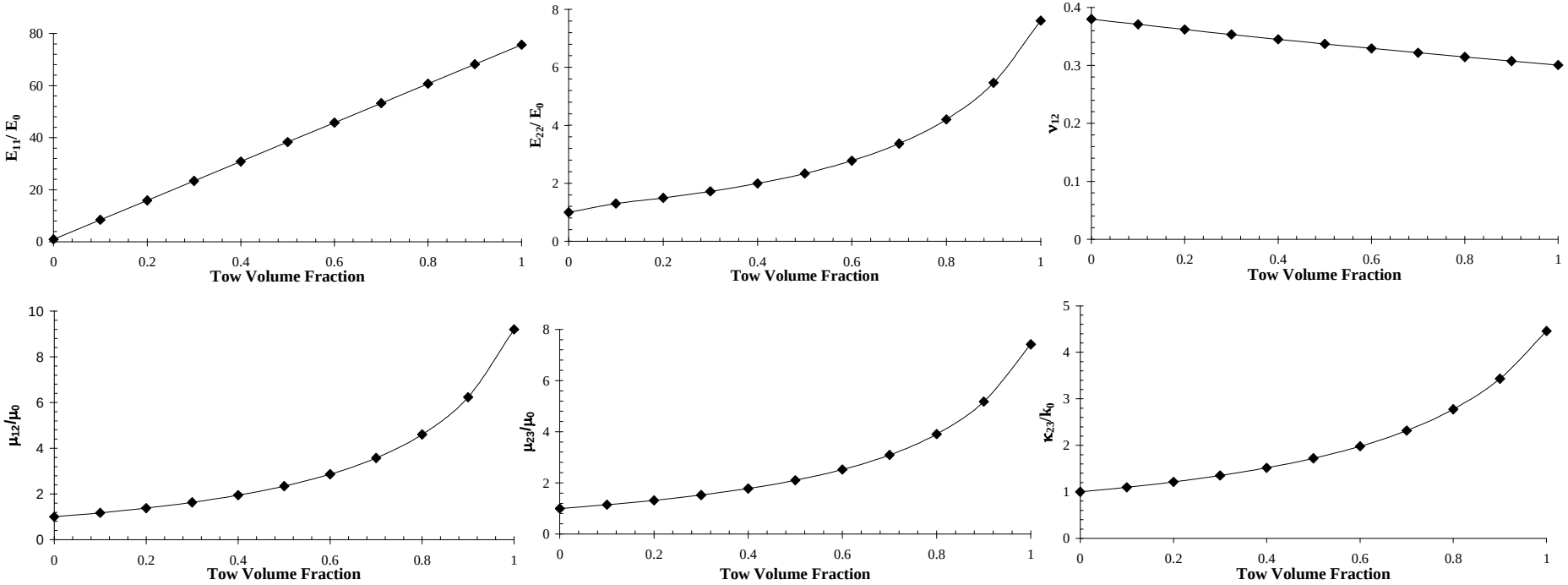


**Figure 7-51 Graphs showing the effect of increasing tow volume fraction on a 23mm long, transversely isotropic bundle. (Top row, left to right) Longitudinal modulus; transverse modulus, Poisson's ratio. (Bottom row, left to right) Shear modulus in the 1-2 plane, shear modulus in the 2-3 plane and the ordinary bulk modulus in the 2-3 plane.**

## *H.2. Elastic constants of a UD sub-unit (ply level)*

The properties determined for the UD bundle in Appendix H.1 are used here to calculate the effective properties of a UD ply containing discontinuous bundles. The bundle is the reinforcing phase, where the components of the elastic moduli tensor for the tow (determined in Equation 7-73 through to Equation 7-78) are used as input parameters in Equation 7-38 through to Equation 7-44.

The effective bundle diameter is directly proportional to the filament count ($F$) and filament diameter ($Ø_f$) and inversely proportional to the tow volume fraction ($c_{tow}$):

$$Ø_{tow} = \frac{F Ø_f}{c_{tow}} \qquad \textbf{Equation 7-79}$$

The tow aspect ratio $\alpha_{tow}$ can subsequently be calculated using Equation 7-79 and the fibre length $L$.

$$\alpha_{tow} = \frac{L}{Ø_{tow}} \qquad \textbf{Equation 7-80}$$

The reinforcement length significantly affects the elastic response of the laminate at this level. At level 1 the filament lengths were considered to be continuous since the aspect ratio approached infinity. At level 2 however, the aspect ratios are orders of magnitude smaller because of the large bundle diameter. For example, the aspect ratio of a 15mm long, 24K tow is approximately 10 compared with an aspect ratio of 2140 for the same length filament. Equation 7-80 is therefore used in Equation 7-56 or Equation 7-57 depending on the shape function of the bundle.

The same procedure as used for the tow is now followed to determine the elastic moduli tensor of the UD ply. An adjustment is made to the reinforcement volume fraction at this level, as it is necessary to account for the volume of resin contained within each of the bundles from level 1. Therefore the volume fraction at the ply level is:

$$c_{ply} = \frac{c_f}{c_{tow}}$$ **Equation 7-81**

where $c_f$ is the volume fraction of the final laminate.

The outputs from level 1 for a carbon bundle are summarised in Table 7-13, with the additional parameters required to calculate the UD ply properties at level 2 (composite volume fraction, tow filament count and tow volume fraction). The resultant properties for a ply containing UD, discontinuous 23mm fibres are presented in Figure 7-52.

| Property | Designation | Value | |
|---|---|---|---|
| Tow length | $L$ | 23 | mm |
| Filament diameter | $Ø_1$ | 0.007 | mm |
| Tow filament count | $F$ | 3000 | |
| Tow volume fraction | $c_{tow}$ | 0.6 | |
| Random composite volume fraction | $V_f$ | 0.3 | |
| | | | |
| Plane strain bulk modulus | $k_{tow}$ | 8.97 | GPa |
| Cross modulus | $l_{tow}$ | 5.91 | GPa |
| Axial modulus under axial strain | $n_{tow}$ | 141.24 | GPa |
| Transverse shear modulus | $m_{tow}$ | 2.74 | GPa |
| Axial shear modulus | $p_{tow}$ | 3.11 | GPa |
| | | | |
| Matrix Poisson's ratio | $v_o$ | 0.38 | |
| Matrix modulus | $E_o$ | 3 | GPa |
| Matrix ordinary bulk modulus | $\kappa_0$ | 4.16 | GPa |
| Matrix shear modulus | $\mu_0$ | 1.09 | GPa |

**Table 7-13 Input parameters required to calculate the elastic constants of a UD ply containing discontinuous, transversely isotropic bundles. A constant filament count has been selected, with a bundle volume fraction of 60%. Subscript *tow* refers to the reinforcement phase and is analogous to subscript *1* in Equation 7-34. Subscript *0* refers to the matrix and values for the matrix have been determined experimentally.**

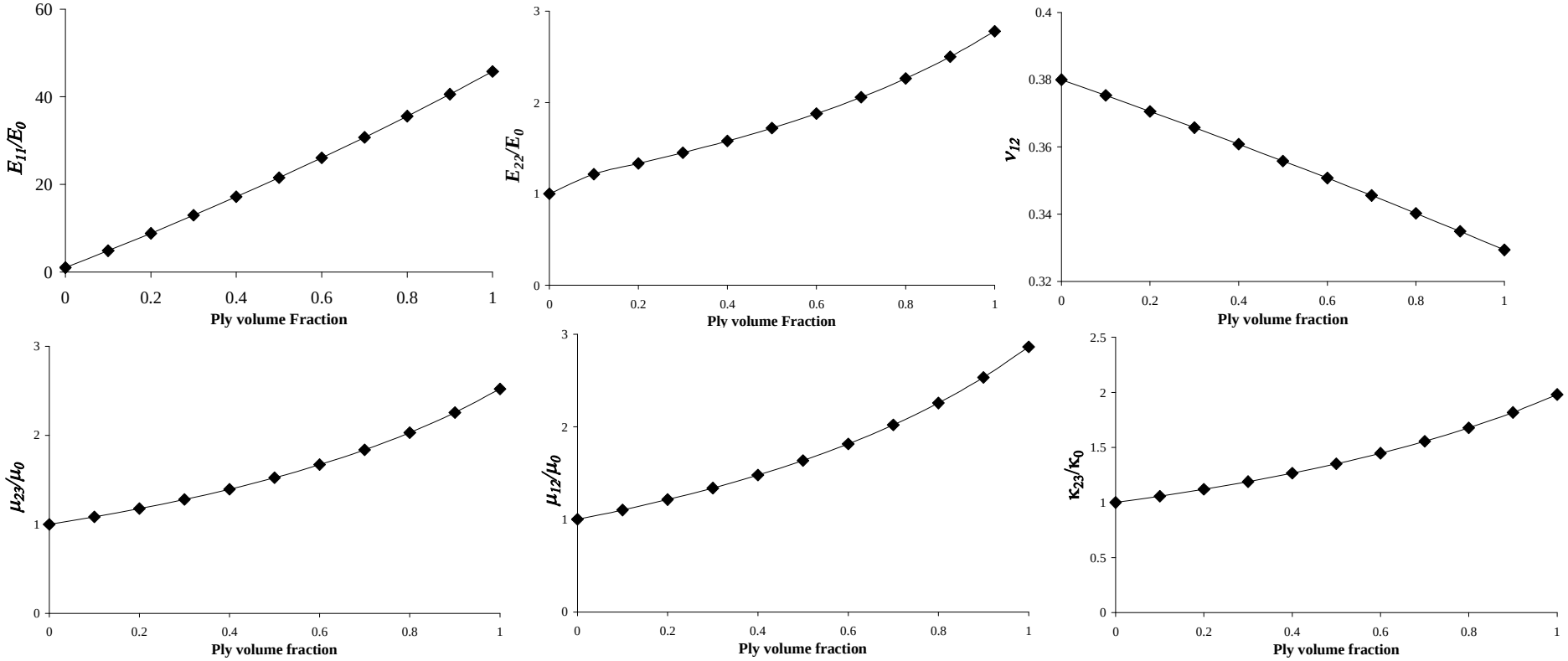


**Figure 7-52 Graphs showing the effect of increasing volume fraction for a ply containing 23mm long, transversely isotropic bundles (3000 filaments). (Top row, left to right) Longitudinal modulus; transverse modulus, Poisson's ratio. (Bottom row, left to right) Shear modulus in the 1-2 plane, shear modulus in the 2-3 plane and the ordinary bulk modulus in the 2-3 plane.**

## *H.3. Orientation Averaging*

So far, the effective elastic constants have been calculated for a UD ply containing discontinuous bundles. This level seeks to orientate multiple plies in order to simulate a random fibre material. A tensorial approach developed by Advani and Tucker [154] is used to enable 3D fibre orientation distributions to be studied. Orientation tensors are used to summarise the influence of the orientation state on the stress tensor by replacing the complete probability distribution function with a more compact description. Three dimensional fibre orientation envelopes can be described by just twelve tensor components, which are used to perform a volume-weighted average on the stiffness tensor to determine the influence of the fibre orientation distribution.

### H.3.1. Calculating second and fourth order orientation tensor components

The spatial orientation of a single fibre can be described by the Cartesian components ($p_1$, $p_2$, $p_3$) of a unit vector ***p***, as shown in Figure 7-53 [154]. A representative element of the present random material contains many fibres of a constant length but different orientations, which can be described generally by a 3D probability density function $\psi(\theta,\phi)$. Although the probability density function is a complete description of the orientation state, it is longwinded - particularly for 3D fibre distributions. Orientation tensors are therefore used because they are more compact and are formed by calculating the dyadic product of the vector ***p*** and integrating with the distribution function over all possible directions. Only the even order tensors are of interest, since the odd orders are all zero. The second and fourth order orientation tensors are evaluated as:

$$a_{ij} = \left\langle p_i p_j \right\rangle \equiv \int_0^{2\pi}\int_0^{\pi} p_i p_j \psi(\theta,\phi) \sin\theta \, d\theta \, d\phi \qquad \textbf{Equation 7-82}$$

$$a_{ijkl} = \left\langle p_i p_j p_k p_l \right\rangle \equiv \int_0^{2\pi}\int_0^{\pi} p_i p_j p_k p_l \psi(\theta,\phi) \sin\theta \, d\theta \, d\phi \qquad \textbf{Equation 7-83}$$

where $\langle \ \rangle$ denotes post orientation averaging.

An explanation is provided below for determining the second and fourth order tensor components using Equation 7-82 and Equation 7-83 respectively.

The orientation probability density function $\psi(\theta,\phi)$ can be derived experimentally by measuring the in-plane ($\phi$) and out-of-plane ($\theta$) orientations from optical micrographs. A closure approximation is then used to represent the data set. Advani and Tucker [154] show that the accuracy of the closure approximation governs the precision of predictions when using tensors rather than a complete probability density function. Figure 7-54 is a typical in-plane orientation distribution for a DCFP laminate and Figure 7-55 is the corresponding out-of-plane fibre orientation. Clearly, the closure approximation for the in-plane distribution is a constant (e.g. $c$), whilst a sinusoidal function provides a good correlation for the out-of-plane distribution (determined in this instance using a non-linear regression program called NLREG v.6.3). Thus, the two closure approximations can be incorporated into Equation 7-82 and Equation 7-83 as follows:

$$a_{ij} = \left\langle p_i p_j \right\rangle \equiv \int_0^{2\pi}\int_0^{\pi} p_i p_j \left(ac \sin^{2(b-1)}\theta\right) \sin\theta \, d\theta \, d\phi \qquad \textbf{Equation 7-84}$$

$$a_{ijkl} = \left\langle p_i p_j p_k p_l \right\rangle \equiv \int_0^{2\pi}\int_0^{\pi} p_i p_j p_k p_l \left(ac \sin^{2(b-1)}\theta\right) \sin\theta \, d\theta \, d\phi \qquad \textbf{Equation 7-85}$$

The product of the two constants $a$ and $c$ can be replaced by a single value $k$, which is commonly known as the normalisation constant. This is essentially used to ensure that the volume within the 3D orientation envelope does not exceed unity and is calculated in the following way:

$$\int_0^{2\pi}\int_0^{\pi} k\sin^{2(b-1)}\theta\ sin\theta\ d\theta\ d\phi = 1 \qquad \textbf{Equation 7-86}$$

Once $k$ has been established it is possible to calculate the second and fourth order tensor components. The three components of the unit vector $\boldsymbol{p}$ (see Figure 7-53) are:

$$p_1 = \sin\theta\cos\phi \qquad \textbf{Equation 7-87}$$

$$p_2 = \sin\theta\sin\phi \qquad \textbf{Equation 7-88}$$

$$p_3 = \cos\theta \qquad \textbf{Equation 7-89}$$

These components are substituted into either Equation 7-84 or Equation 7-85. For example, the following calculation would be performed to calculate $a_{11}$:

$$a_{11} = \int_0^{2\pi}\int_0^{\pi} \sin^2\theta\cos^2\phi\left(k\sin^{2(b-1)}\theta\right) sin\theta\ d\theta\ d\phi \qquad \textbf{Equation 7-90}$$

and likewise to calculate $a_{2233}$:

$$a_{2233} = \int_0^{2\pi}\int_0^{\pi} \sin^2\theta\sin^2\phi\cos^2\theta\left(ac\sin^{2(b-1)}\theta\right) sin\theta\ d\theta\ d\phi \qquad \textbf{Equation 7-91}$$

The tensor components for a value of $b$=26 are presented in Table 7-14, along with the tensor components sets for 2D random and 3D random fibre orientation distributions.

| | 2D Random | *b*=26 | 3D Random | Aligned 3-axis |
|---|---|---|---|---|
| **Tensor** | | | | |
| $a_{11}$ | 0.5000 | 0.4902 | 0.3333 | 0.0000 |
| $a_{22}$ | 0.5000 | 0.4902 | 0.3333 | 0.0000 |
| $a_{33}$ | 0.0000 | 0.0196 | 0.3333 | 1.0000 |
| $a_{1111}$ | 0.3750 | 0.3607 | 0.2000 | 0.0000 |
| $a_{2222}$ | 0.3750 | 0.3607 | 0.2000 | 0.0000 |
| $a_{3333}$ | 0.0000 | 0.0011 | 0.2000 | 1.0000 |
| $a_{1122}$ | 0.1250 | 0.1202 | 0.0667 | 0.0000 |
| $a_{1212}$ | 0.1250 | 0.1202 | 0.0667 | 0.0000 |
| $a_{1133}$ | 0.0000 | 0.0092 | 0.0667 | 0.0000 |
| $a_{2233}$ | 0.0000 | 0.0092 | 0.0667 | 0.0000 |
| $a_{1313}$ | 0.0000 | 0.0092 | 0.0667 | 0.0000 |
| $a_{2323}$ | 0.0000 | 0.0092 | 0.0667 | 0.0000 |

**Table 7-14 Second and fourth order tensor components for a range of orientation distributions. The case when *b*=26 refers to a sinusoidal closure approximation described in Figure 7-55.**

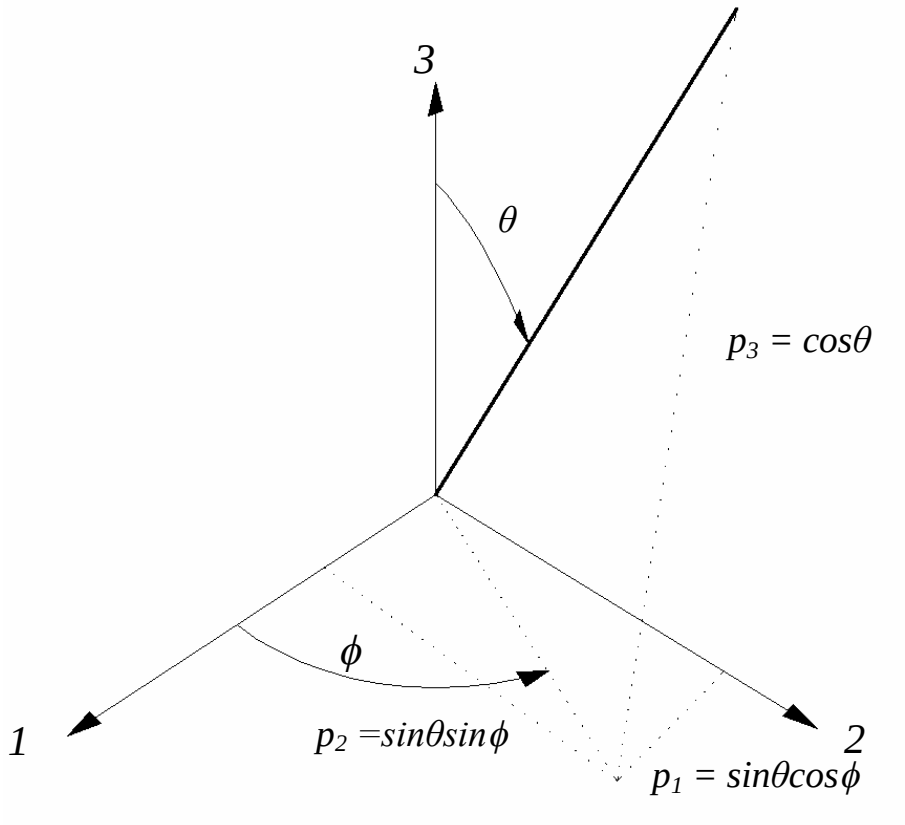


**Figure 7-53 Coordinate system used to define the unit vector *p***

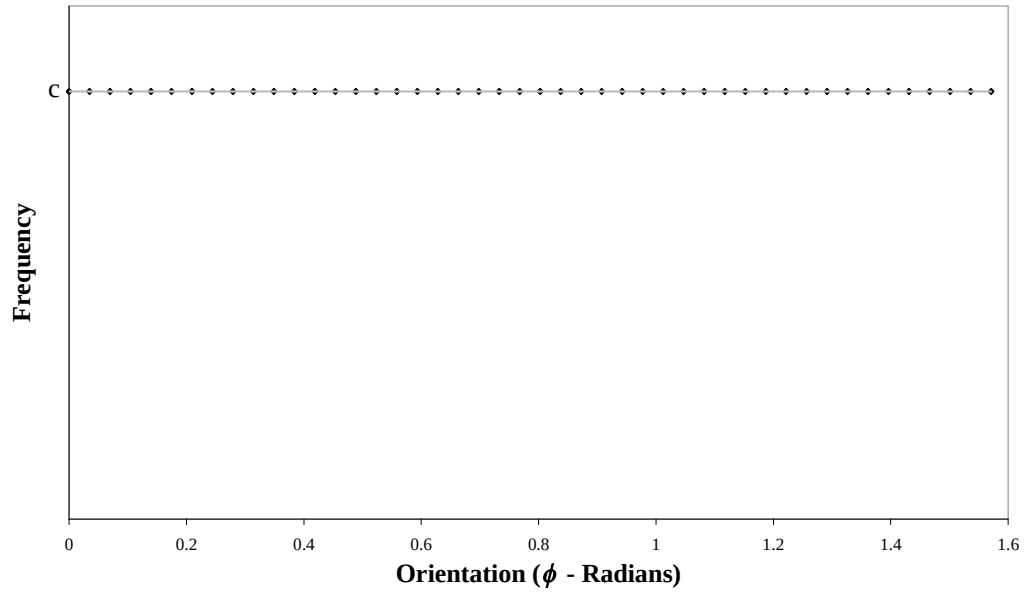


**Figure 7-54 Assumed in-plane orientation distribution for DCFP laminates.**

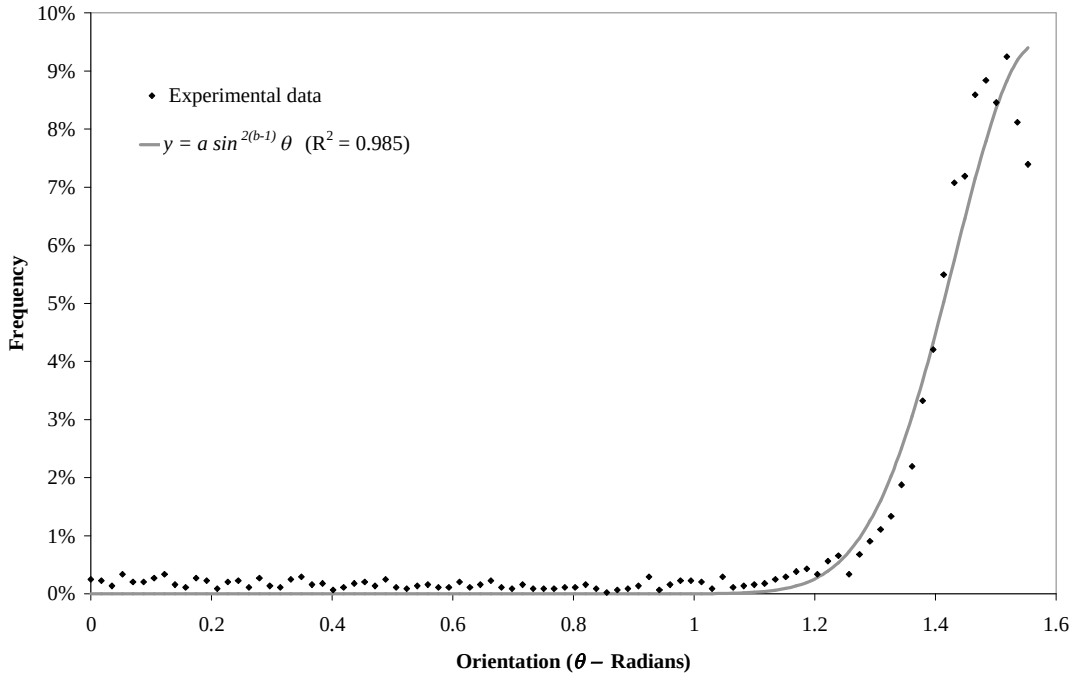


**Figure 7-55 Representative out-of-plane orientation distribution for DCFP laminates where $\theta$ is measured from the vertical, (see Figure 7-53). Non-linear regression was performed in order to fit a trigonometric function to the data, where b~26 for each filamentisation**

## H.3.2. Calculating the stiffness tensor

The orientation tensor components calculated in Appendix H.3.1 are now be used to determine the orientation dependence of the elastic stiffness matrix for the final

laminate. Following the methodology of Camacho et al. [182], it is possible to compute the orientation averages directly from the orientation tensors and the fourth order stiffness matrix $C_{ijkl}$. The elastic moduli tensor for the UD ply at level 2 is output in the form of Equation 7-27. This can be expressed in terms of $C_{ijkl}$ as follows (in contracted notation (see Appendix.I)):

$$C_{11} = n \quad \textbf{Equation 7-92}$$

$$C_{22} = m + k \quad \textbf{Equation 7-93}$$

$$C_{12} = l \quad \textbf{Equation 7-94}$$

$$C_{66} = p \quad \textbf{Equation 7-95}$$

$$C_{23} = k - m \quad \textbf{Equation 7-96}$$

The invariants of $C_{ijkl}$ can be expressed in contracted form:

$$B_1 = C_{11} + C_{22} - 2C_{12} - 4C_{66} = n + m + k - 2l - 4p \quad \textbf{Equation 7-97}$$

$$B_2 = C_{12} - C_{23} = l - (k - m) \quad \textbf{Equation 7-98}$$

$$B_3 = C_{66} + \tfrac{1}{2}(C_{23} - C_{22}) = p - m \quad \textbf{Equation 7-99}$$

$$B_4 = C_{23} = k - m \quad \textbf{Equation 7-100}$$

$$B_5 = \tfrac{1}{2}(C_{22} - C_{23}) = 2m \quad \textbf{Equation 7-101}$$

The final orientation average of the stiffness tensor $C_{ijkl}$ is calculated using Equation 7-97 through to Equation 7-101 as follows:

$$\begin{aligned}\langle C_{ijkl} \rangle = {} & B_1 a_{ijkl} + B_2 (a_{ij}\delta_{ij} + a_{kl}\delta_{ij}) \\ & + B_3 (a_{ik}\delta_{jl} + a_{il}\delta_{jk} + a_{ji}\delta_{ik} + a_{jk}\delta_{il}) \\ & + B_4 (\delta_{ij}\delta_{kl}) + B_5 (\delta_{ik}\delta_{jl} + \delta_{il}\delta_{jk})\end{aligned} \quad \textbf{Equation 7-102}$$

where $a_{ijkl}$ and $a_{ij}$ are the components from the second and fourth order orientation tensor and $\delta_{ij}$ is Kronecker delta function. The compliance matrix ($S_{ijkl}$) is calculated from the inverse of the stiffness matrix ($C_{ijkl}$). Assuming the UD plies are all orthotropic [247]:

$$\left\langle S_{ijkl} \right\rangle = \left\langle C_{ijkl} \right\rangle^{-1} = \left\langle \begin{matrix} C_{11} & C_{12} & C_{13} & 0 & 0 & 0 \\ C_{12} & C_{22} & C_{23} & 0 & 0 & 0 \\ C_{13} & C_{23} & C_{33} & 0 & 0 & 0 \\ 0 & 0 & 0 & C_{44} & 0 & 0 \\ 0 & 0 & 0 & 0 & C_{45} & 0 \\ 0 & 0 & 0 & 0 & 0 & C_{66} \end{matrix} \right\rangle^{-1}$$

**Equation 7-103**

$$\left\langle S_{ijkl} \right\rangle = \left\langle \begin{matrix} 1/E_{11} & -\upsilon_{21}/E_{22} & -\upsilon_{31}/E_{33} & 0 & 0 & 0 \\ -\upsilon_{12}/E_{11} & 1/E_{22} & -\upsilon_{32}/E_{33} & 0 & 0 & 0 \\ -\upsilon_{13}/E_{11} & -\upsilon_{23}/E_{22} & 1/E_{33} & 0 & 0 & 0 \\ 0 & 0 & 0 & 1/G_{23} & 0 & 0 \\ 0 & 0 & 0 & 0 & 1/G_{13} & 0 \\ 0 & 0 & 0 & 0 & 0 & 1/G_{12} \end{matrix} \right\rangle$$

**Equation 7-104**

where $\left\langle \ \right\rangle$ denotes post orientation averaging.

The elastic constants for a laminate containing bundles of 3000 filaments are presented in Figure 7-56. Input parameters for the model have been taken from Table 7-13 and it is assumed that the fibres are planar, with random in-plane orientations (tensor components have been taken from Table 7-14). The volume fraction is restricted to 60% because the composite volume fraction cannot exceed the tow volume fraction.

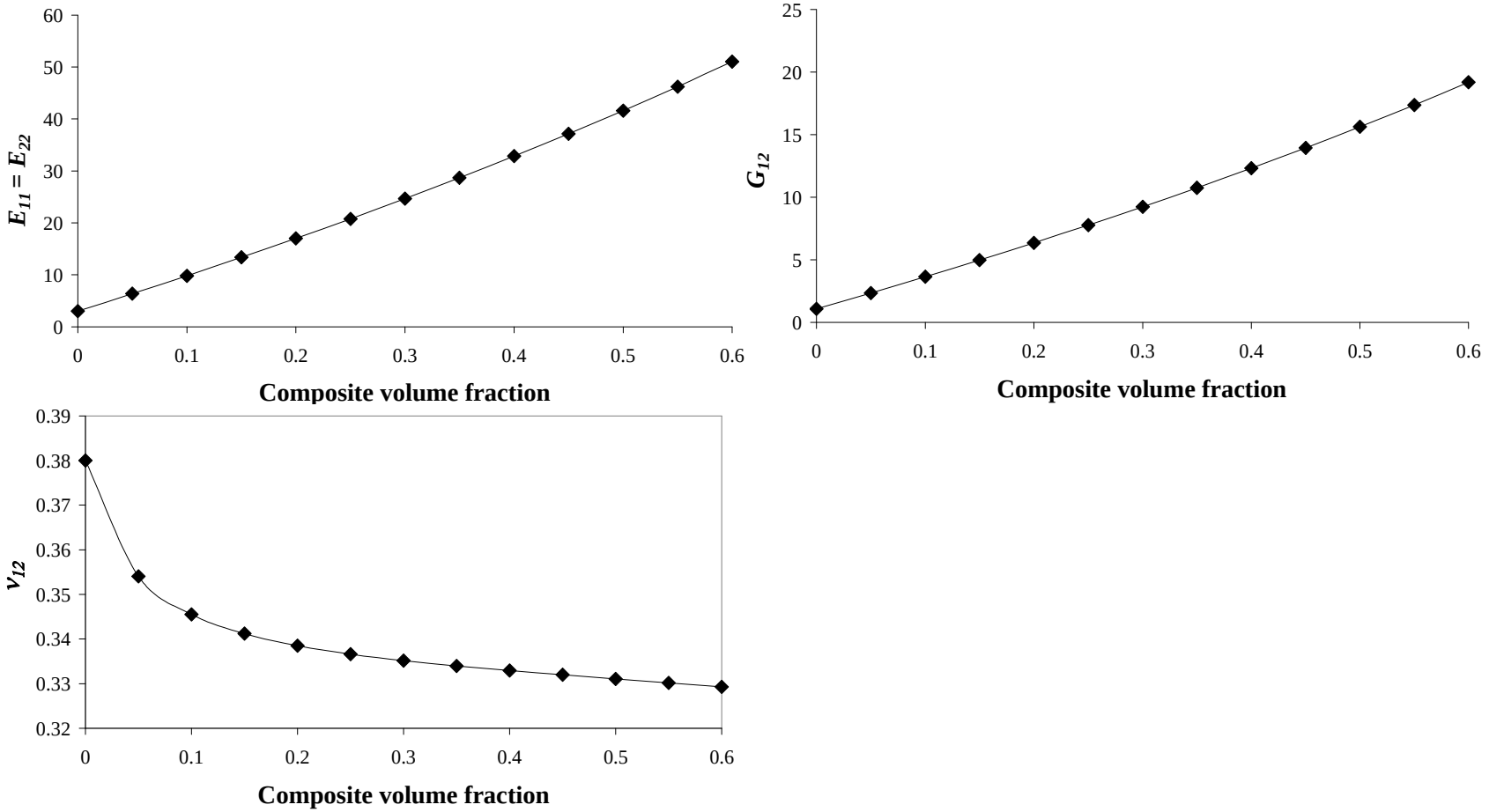


**Figure 7-56 Predictions for the in-plane tensile modulus, shear modulus and Poisson's ratio of a random laminate containing 3K bundles.**

## H.4. Aggregate Averaging

Bundle fragmentation is induced during fibre chopping to yield much smaller bundles, but there is insufficient control over the pneumatic technique to produce constant filament counts. Mechanical performance is sensitive to bundle size (as shown in Chapter 3), therefore it is essential that the stiffness model can accept a distribution of filament counts. So far, Levels 1 to 3 have been used to predict the elastic constants of a random DCFP material with a constant bundle size, but an aggregate averaging process is used at level 4 to model filament count distributions.

Following the work of Camacho *et al.* [182], a random laminate comprising tows of various filament counts is assumed to be a hybrid, containing multiple two-phase composites. Each two-phase composite is associated with a different mean filament count and the corresponding stiffness matrix $\langle C_{ijkl} \rangle$ is determined using levels 1 to 3. Filament count distributions have been determined by optical microscopy methods as described in Appendix E.1. Results are expressed in terms of number of filaments, enabling an effective circular bundle diameter to be calculated for the constituent tows in each composite (assuming a constant tow volume fraction in each). The stiffness matrix of the overall random laminate is determined by averaging the stiffness matrices of all the two-phase composites, assuming a constant strain is applied to each:

$$\{C\} = \sum_{i=1}^{n} \alpha_i \left\langle C^i \right\rangle \qquad \textbf{Equation 7-105}$$

where $\langle C^i \rangle$ is the stiffness tensor of the $i^{th}$ two-phase composite (post orientational averaging) and $\alpha_i$ is the proportion of tows of this particular filament count. According to Camacho *et al.* [182] this aggregate averaging procedure takes the same form as the orientational averaging of Advani and Tucker [154] however, at the present level the weighting fraction is the volume of material assigned to each two-phase composite rather than the orientation.

## H.5. Image analysis

Optical micrographs were used to determine the tow filament count distributions within each laminate. An automated stage enabled contiguous images to be taken of the through thickness (2-3 direction) architecture, using an optical microscope. Images were assembled in AutoCAD, as shown in Figure 7-57, using the origin coordinates (bottom left corner of each image) stored during image acquisition. The greyscale of each image was inverted (white to black) using Paint Shop Pro v.6.0 before being analysed with UTHSCSA ImageTool v.4.0 (see Figure 7-58).

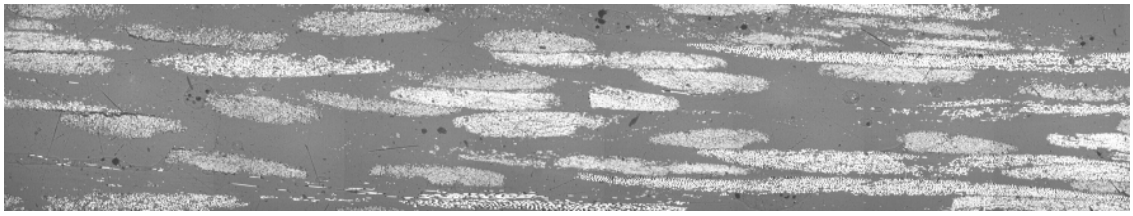

**Figure 7-57 A montage of five optical micrographs 2.12mm × 10.58mm (512 × 2560 pixels)**

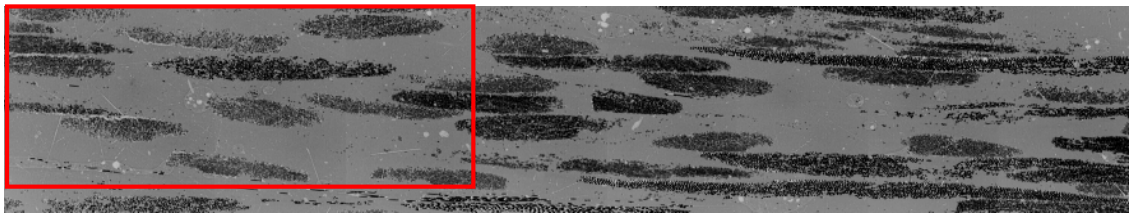

**Figure 7-58 Inverted greyscale image from Figure 7-57. Rectangle highlights a magnified area of interest shown in Figure 7-59.**

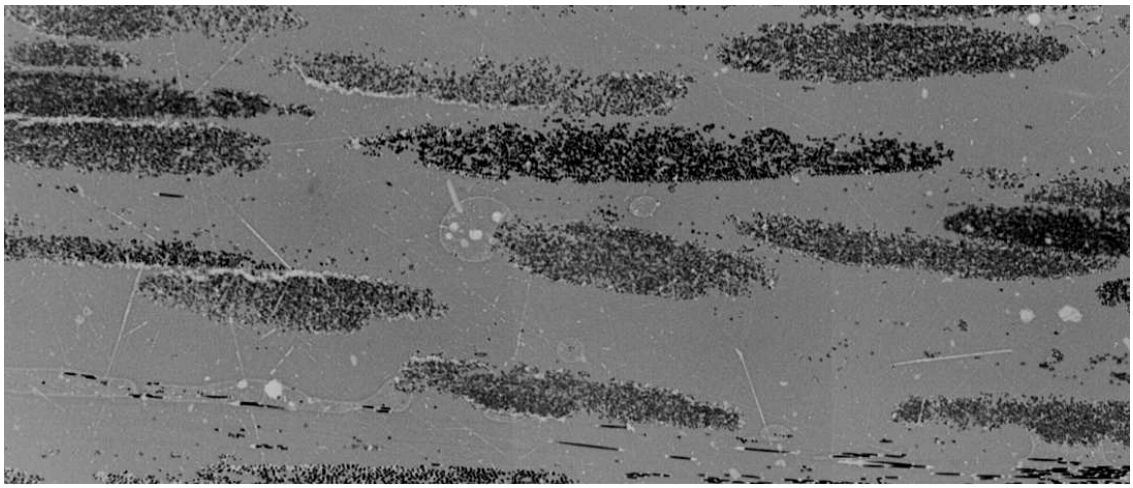

**Figure 7-59 Area of interest taken from Figure 7-58. This image will be used to explain the processing required to determine the tow filament counts.**

The magnified region shown in Figure 7-59 illustrates the process used to obtain the tow filament count distribution for each laminate. The grey pixel levels in the images are used to discriminate between objects using a process called thresholding, which separates objects on the basis of their grey level or brightness and creates a resulting binary image. The major difficulty in microscope image analysis is determining a suitable grey scale threshold. Figure 7-60 demonstrates (a) the correct threshold value, (b) the effect of the value being too high and (c) too low. Pixels with a greyscale value of 101 are set to 255 (white) in Figure 7-60(a) and the remaining pixel values are all converted to 0 (black) to create a binary image (see Figure 7-61 for a binary image of the full specimen). The threshold value was consistently taken to the left of the peak on the greyscale frequency plot, which resulted in a value of 100±2 in each case.

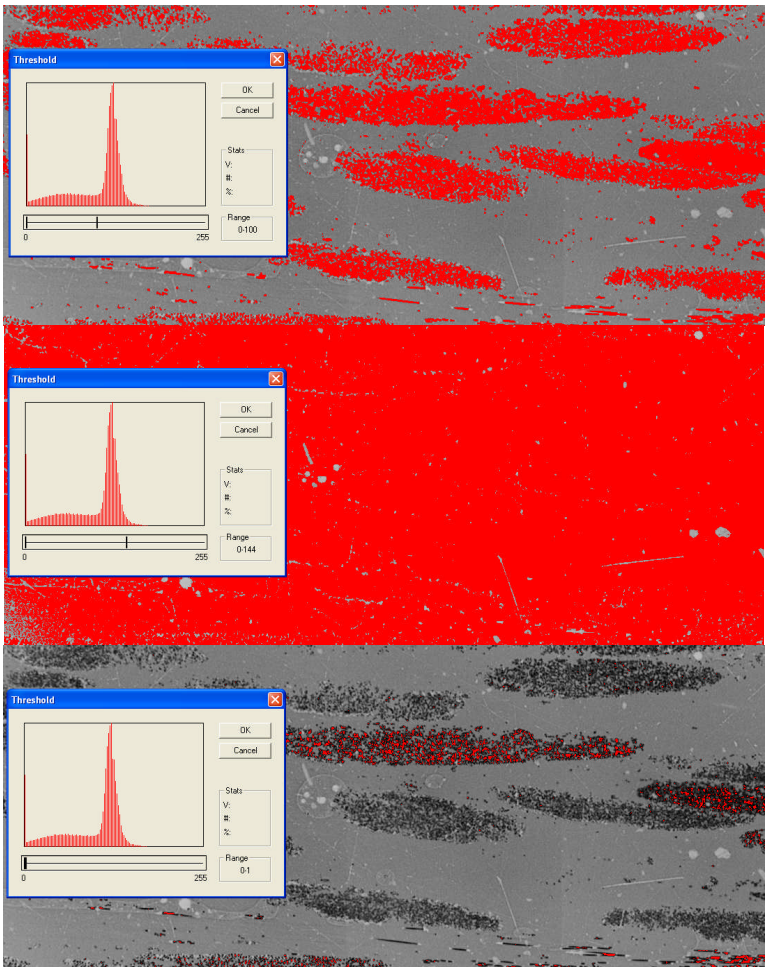


**Figure 7-60 A photomicrograph subjected to various greyscale thresholds (a) 100 (b) 144 (c) 1**

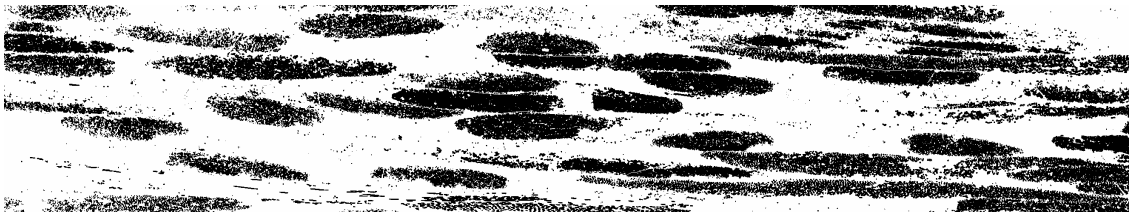

**Figure 7-61 Binary image of the montage of micrographs presented in Figure 7-57**

Incomplete fibre bundles crossing the image boundary were eliminated using the edge detection feature in ImageTool, prior to analysing the filament count distribution. The resulting effect can be observed by comparing Figure 7-63 with Figure 7-61. The number of discrete black objects within the image is detected using the 'Find Object' feature in image tool as shown by Figure 7-62. Each object is then categorised according to the number of pixels it contains. Using a graticule, it was established that 242 pixels are equivalent to one linear millimetre at ×5 magnification. Each filament is therefore constructed from approximately 7 pixels in the binary image. Table 7-15 demonstrates that approximately 1400 objects were detected which had a pixel count of less than 7. These objects were discarded and the discrepancy was attributed to image aberrations. The data in Table 7-15 was subsequently converted into filament count data using the 7 pixels / filament conversion factor.

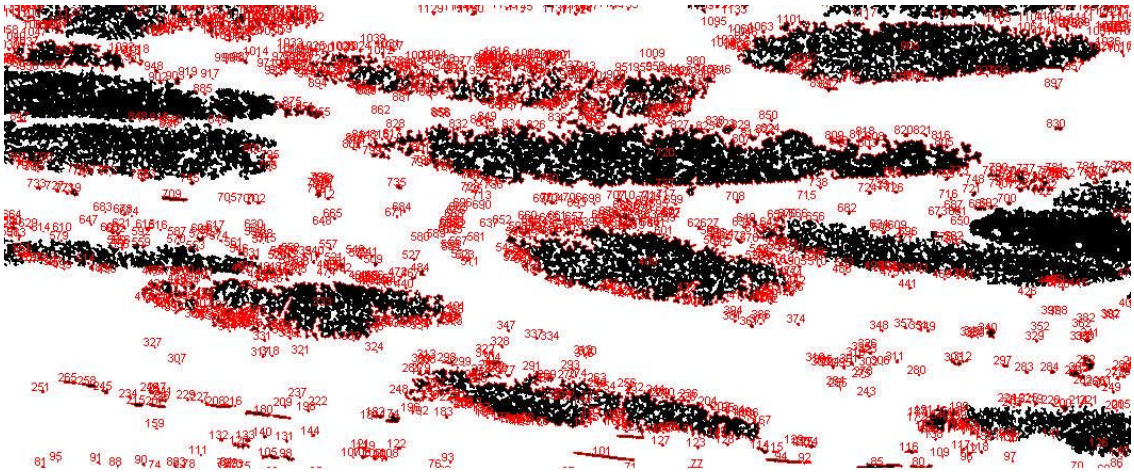

**Figure 7-62 Binary image showing the effect of the 'Find Objects' feature in image tool. Each discrete black object is detected and assigned an integer.**

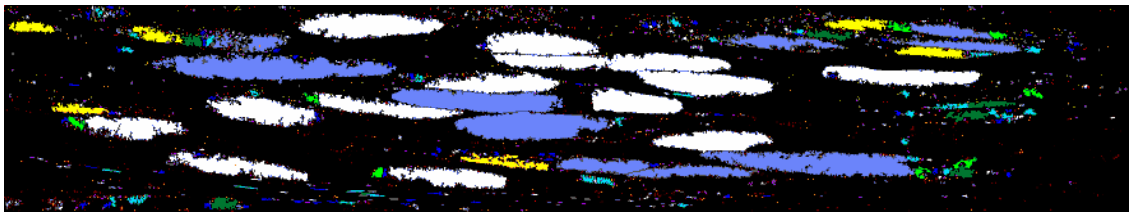

**Figure 7-63 Micrograph montage after object analysis has been performed. Objects detected within the image are categorised according to number of pixels. Also note that objects crossing the image boundary have been removed for improved accuracy.**

| | Pixel Count | Count | Mean Value | Std. Dev |
|---|---|---|---|---|
| Mean | | 203.43 | 2649.65 | 405.33 |
| Std. Dev. | | 418.19 | 5247.32 | 726.38 |
| | <7 | 1484 | 3.6 | 2.07 |
| | 7 - 14 | 683 | 10.25 | 1.94 |
| | 14 - 35 | 398 | 22.12 | 5.88 |
| | 35 - 70 | 143 | 48.13 | 9.49 |
| | 70 - 140 | 60 | 98.27 | 20.84 |
| | 140 - 350 | 36 | 209.56 | 52.58 |
| | 350 - 700 | 8 | 491.88 | 89.5 |
| | 700 - 1400 | 6 | 1126.33 | 224.4 |
| | 1400 - 3500 | 6 | 2304.83 | 429.96 |
| | 3500 - 7000 | 6 | 4821.67 | 780.87 |
| | 7000 -14000 | 14 | 9779.64 | 1837.4 |
| | 14000 -35000 | 4 | 18178.75 | 2219.66 |
| | 35000 -70000 | 0 | 0 | 0 |
| | >70000 | 0 | 0 | 0 |

**Table 7-15 Summary of bundle sizes classified according to the number of pixels within each object**

## *H.6. Bundle size estimate for increasing fibre length*

In order to apply the developed analytical models, some knowledge of filament count is required. The filament count within the tow is non-constant and is dependent on the original size of the tow (i.e. 24000 filaments), the cut length, fibre parameters (i.e. surface treatment) and processing parameters (air pressure). In the present work, bundle size is estimated using the following method: It is assumed that the fibre volume fraction within the tow is constant at 60% and that the tow cross-sectional aspect ratio, $\beta$ (2-3 direction) is constant at 17:1. It is also assumed that down to a threshold tow aspect ratio, $\lambda$ (1-3 direction) the tow will be transported to the tool face without fragmenting. Values for $\lambda$ have been estimated from image analysis by comparing mean bundle sizes. Aspect ratios of 15 and 4 have been selected to represent the high

filamentisation and low filamentisation cases respectively. Therefore, for any given fibre length the filament count after fragmentation ($n_f$) has been calculated as follows:

$$n_f = \frac{4A_{tow}V_{tow}}{\pi Ø_f{}^2}$$ **Equation 7-106**

The following approximation is assumed for the area of an elliptical tow;

$$A_{tow} \approx \frac{\pi wt}{4}$$ **Equation 7-107**

where $t$ is the tow thickness and $w$ the width, calculated by:

$$w = \frac{l_f}{\lambda}$$ **Equation 7-108**

$$t = \sqrt{\frac{Ø_f{}^2 n}{\beta V_{tow}}}$$ **Equation 7-109**

Substituting Equation 7-107, Equation 7-108 and Equation 7-109 into Equation 7-106 gives $n_f$ in terms of the cross-sectional aspect ratio and the threshold tow aspect ratio:

$$n_f = \begin{cases} \dfrac{l_f{}^2 V_{tow}}{\lambda^2 \beta Ø_f{}^2} & n_f < n \\ n & \textit{for all other values} \end{cases}$$ **Equation 7-110**

A piecewise function is adopted to prevent $n_f$ from exceeding the original tow filament count $n$ (24K in this case) when lengths exceed the threshold aspect ratio. Figure 7-64 shows the predicted mean bundle sizes for the aspect ratios given above (values are also summarised in Table 3-2 for fibre lengths of interest).

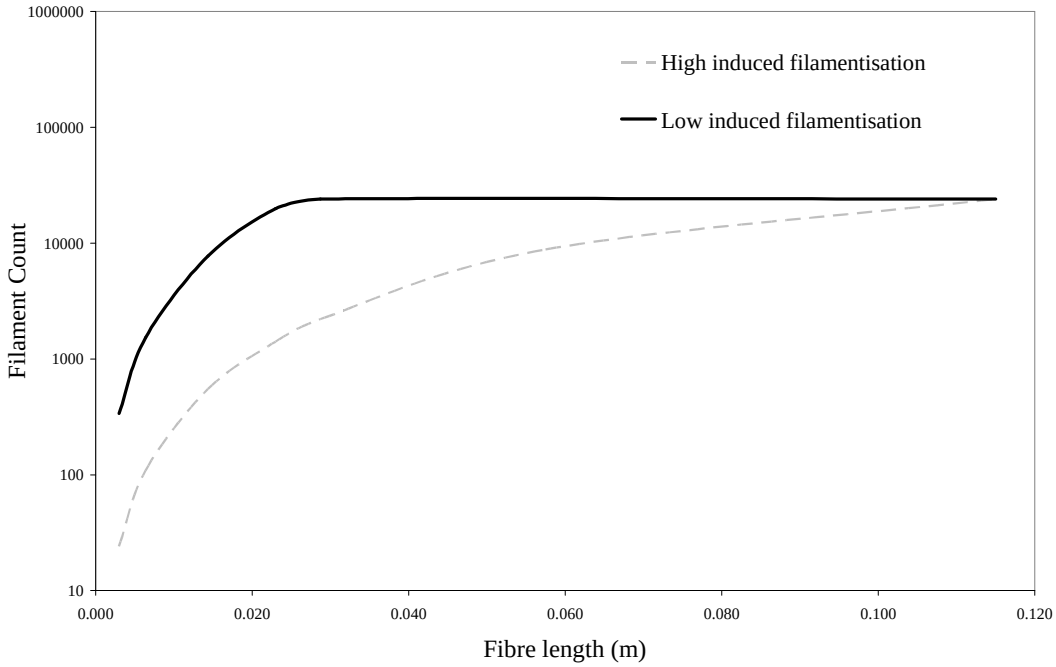


**Figure 7-64 Assumed mean bundle sizes for two levels of induced filamentisation. Values are summarised in Table 2 and have subsequently been used for mechanical property prediction.**

# Appendix.I. Contracted tensor notation

Tensors are used in a number of scientific fields, such as geology, mechanical engineering, and astronomy. They can be thought of as generalisations of vectors and matrices, but the key feature is that they transform on the rotation of coordinates. Tensor indices are part of *index notation* and the number of subscripts denotes the order of the tensor, for example $C_{ijkl}$ is a fourth order tensor. Contracted notation is a rearrangement of terms such that the number of indices is reduced. The number of free indices for a fourth order tensor is reduced from 4 to 2. The contracted indices notation is shown below for a symmetric tensor:

$11 \rightarrow 1$
$22 \rightarrow 2$
$33 \rightarrow 3$
$23\, or\, 32 \rightarrow 4$
$13\, or\, 31 \rightarrow 5$
$12\, or\, 21 \rightarrow 6$

For example components of a fourth order stiffness tensor are rearranged in contracted notation as follows:

$$C_{1122} \rightarrow C_{12}$$

and

$$C_{2323} \rightarrow C_{44}$$

# Appendix.J. Tensor transformations

The tensor notation used in Section 5.5.5 is re-written here in matrix notation form. Second and fourth order strain tensors of UD plies are calculated from the respective strength tensors and the fourth order stiffness tensor.

The fourth order strain tensor is calculated as follows:

$$G_{ij} = F_{mn} C_{mi} C_{nj}$$ **Equation 7-111**

where $F$ is the strength tensor and $C$ is the stiffness tensor. Using conventional matrix notation this can be written as follows:

$$G = \left(\left[F^T\right]\left[C\right]\right)^T (C)$$ **Equation 7-112**

Superscript T denotes the transpose of the matrix. The second order strain tensor is calculated by:

$$G_i = F_m C_{mi}$$ **Equation 7-113**

Using conventional matrix notation this can be written as follows:

$$G = \left[C^T\right]\left[F\right]$$ **Equation 7-114**

# References


1. Venkatakrishnan, K., *Climate change policies and global automotive industry*, in *http://www.frost.com/prod/servlet/cif-econ-insight.pag?docid=49415398*. 2005.
2. Jambor, A. and M. Beyer, *New cars - new materials.* Materials and Design, 1997. 18(4): p. 203-209.
3. Stieg, J., L.H. Bax, and M.F.R. Rijn. *Introduction to TECABS: Technologies for carbon fibre reinforced automotive body structures*. in *5th International Conference on Materials for Lean Weight Vehicles*. 2003. Warwick.
4. Ellis, M. and A. Tautscher. *Aluminium material and process selection within the Jaguar XJ BIW*. in *5th International Conference on Materials for Lean Weight Vehicles*. 2003. Warwick.
5. Adam, H., *Carbon fibre in automotive applications.* Materials and Design, 1997. 18(4/6): p. 349-355.
6. Carle, D. and G. Blount, *The suitability of aluminium as an alternative material for car bodies.* Materials and Design, 1999. 20: p. 267-272.
7. Cole, G.S. and A.M. Sherman, *Lightweight materials for automotive applications.* Materials Characterization, 1995. 35: p. 3-9.
8. Das, S., *The cost of automotive polymer composites: A review and assessment of DOE's lightweight materials composite research*. 2001, Energy Division - Oak Ridge National Laboratory: Oak Ridge, Tennessee.
9. Manson, J.-A.E., M.D. Wakeman, and N. Bernet, *2.16 Composite Processing and Manufacturing - An Overview*, in *Comprehensive Composite Materials*, A. KELLY and C. ZWEBEN, Editors. 2000, PERGAMON. p. 577-607.
10. Marsh, G., *Europe gets tough on end-of-life composites.* Reinforced Plastics, 2003(September): p. 34-39.
11. Pickering, S.J., R.M. Kelly, J.R. Kennerley, C.D. Rudd, and N.J. Fenwick, *A fluidised-bed process for the recovery of glass fibres from scrap thermoset composites.* Composites Science and Technology, 1999. 60: p. 509-523.
12. Pallett, R.J. and R.J. Lark, *The use of tailored blanks in the manufacture of construction components.* Materials Processing Technology, 2001. 117: p. 249-254.
13. Miller, W.S., L. Zhuang, A.J. Witterbrood, P.D. Smet, A. Haszler, and A. Vieregge, *Recent development in aluminium alloys for the automotive industry.* Materials Science and Technology: A, 2000. 280: p. 37-49.
14. Taylor, K.C. and A. Sanchdev, *Energy and Transportation: Challenges for the Chemical Sciences in the 21st Century*. 2003, Washington: The National Academy Press. 56-61.
15. Friedrich, H. and S. Schumann, *Research for a "new age magnesium" in the automotive industry.* Journal of Materials Processing Technology, 2001. 117: p. 276-281.
16. Marsh, G., *Composites on the road to the big time?* Reinforced Plastics, 2003. Automotive supplement(February): p. 33-47.
17. Jacob, A., *Driving forces.* Reinforced Plastics, 2003. Automotive supplement(February): p. 23-25.

18. Brandt, M.R. and S.R. Reeve. *Directed fibre preform case studies*. in *Composites 2001 Convention and Trade Show*. 2001. Tampa FL USA: Composite Fabricators Association.
19. Stanley, L., *Unlocking mainstream markets for composite products.* Reinforced Plastics, 2002(November): p. 28-30.
20. Chavka, N.G. and J.S. Dahl. *P4 preforming technology development utilizing E-glass and carbon fibers*. in *SAMPE International Symposium*. 1999. Detroit, Michigan.
21. Stewart, R., *New developments help composites compete.* Reinforced Plastics, 2003. Automotive supplement(February): p. 27-31.
22. Eisenstein, P., *Celebrity Special - The SLR supercar*, in *Professional Engineer*. 2003. p. 29.
23. Akovali, G., *Handbook of composite fabrication*. 2001, Shawbury, Shropshire: Rapra Technology Ltd.
24. Palmen, N., *Bumber Beams - TowFlex fabric products provide performance and manufacturing benefits for BMW M3 Bumper Beams.*, in *Automotive Industries*. 2005.
25. Weilgat, A., *Composites use up in auto industry - Supplier technology - Brief article*, in *Automotive Industries*. 2002.
26. http://www.smc-alliance.com/the_alliance/the_alliance.html, *The European Alliance for SMC*. May 2006.
27. Campbell, F.C., *Manufacturing processes for advanced composites*. 2004: Elsvier Ltd.
28. Feraboli, P. and A. Masini, *Development of carbon/epoxy structural components for a high performance vehicle.* Composites Part B: engineering, 2003(35): p. 323-330.
29. Croizat, H. and B. Boursier. *New possibilities with HexMC, a high performance molding compound*. in *Sixth International Seminar on Experimental Techniques and Design in Composite Materials*. 2003. Vicenza, Italy.
30. Bruderick, M., D. Denton, M. Shinedling, and M. Kiesel, *Carbon fiber composite body structures for the 2003 Dodge Viper.*
31. *Silver Arrow has lightweight SMC parts.* Reinforced Plastics, 2005. February: p. 8.
32. Dahl, J.S., M. Debolt, and D. Steenkamer. *Processing and performance of chopped glass fiber reinforced RTM composites*. in *14th International Conference on Composite Materials*. 2003. San Diego, California: ASC.
33. Rudd, C.D., A.C. Long, K.N. Kendall, and C.G.E. Mangin, *Liquid Moulding Technologies*. 1997: Woodhead Publishing Ltd.
34. Mapleston, P., *Improved preform technology boosts prospects for high speed RTM, SRIM*, in *Modern Plastics International*. 1989. p. 48-53.
35. Verpoest, I., *Composite Preforming Techniques*, in *Comprehensive Composite Materials*, A. KELLY and C. ZWEBEN, Editors. 2001, Pergamon. p. 623-669.
36. Weimer, C., T. Preller, P. Mitschang, and K. Drechsler, *Approach to net-shape preforming using textile technologies. Part I: edges.* Composites: Part A, 2000. 31: p. 1261-1268.
37. Evans, K.E. and M.D. Ferrar, *The packing of thick fibres.* Journal of Physics D: Applied Physics, 1989. 22: p. 354-360.
38. Evans, K.E. and A.G. Gibson, *Prediction of the maximum packing fraction achievable in randomly.* Composites Science and Technology, 1986. 25: p. 149-162.

39. Owen, M.J., C.D. Rudd, V. Middleton, K.N. Kendall, and I.D. Revill, *Resin transfer moulding (RTM) for automotive components.* Composite Materials Technology, 1991. 37: p. 177-183.
40. Tanoglu, M. and A. Tugrul Seyhan, *Investigating the effects of a polyester preforming binder on the mechanical and ballistic performance of E-glass fiber reinforced polyester composites.* International Journal of Adhesion & Adhesives, 2002. 23: p. 1-8.
41. Rudd, C.D., M.R. Turner, A.C. Long, and V. Middleton, *Tow placement studies for liquid composite moulding.* Composites: Part A, 1999. 30: p. 1105-1121.
42. Dockum, J.F. and P.L. Schell. *Fiber directed preform reinforcement: Factors that may influence mechanical properties in liquid composite molding*. in *6th Annual ASM/ESD Advanced Composites Conference*. 1990. Detroit, Michigan: ASM International.
43. Corum, J.M., R.L. Battiste, M.B. Ruggles, and W. Ren, *Durability-based design criteria for a chopped-glass-fiber automotive structural composite.* Composites Science and Technology, 2001. 61: p. 1083-1095.
44. Brooke, L., *Making composites cost-effective. (Automotive Composites Consortium's P4 Process)*, in *Automotive Industries*. 1998.
45. Chavka, N.G., J.S. Dahl, and E.D. Kleven. *F3P fiber preforming for the Aston Martin Vanquish*. in *SAMPE Europe International Conference*. 2001. Paris.
46. Carpenter, J. and D. Warren, *First commercial application of DOE-funded automotive composites R&D (Programmable Powdered Preform Process, P4).* http://www.ott.doe.gov/success.html, 2001.
47. Warrior, N.A., L.T. Harper, T.A. Turner, P.J. Schubel, C.D. Rudd, and K.N. Kendall. *Affordable Lightweight Body Structures (ALBOS)*. in *JSAE Annual Congress*. 2004. Pacifico, Yokohama.
48. Rondeau, R., S.R. Reeve, and G. Bond. *The effect of tows and filament groups on the properties of discontinuous fiber composites*. in *44th International SAMPE Symposium & Exhibition*. 1999. Long Beach, CA, USA.
49. Reeve, S.R., R. Rondeau, G. Bond, and F. Tervet. *Mechanical property translation in oriented, discontinuous carbon fiber composites*. in *SAMPE International Symposium*. 2000.
50. Griffin, D.A. and T.D. Ashwill. *Alternative composite materials for megawatt-scale wind turbine blades: Design considerations and recommended testing*. in *2003 ASME Wind Energy Symposium*. 2003: American Institute of Aeronautics and Astronautics.
51. Griffin, D.A., *Blade system design studies Volume 1: Composite technologies for large wind turbine blades*. 2002, Global Energy Concepts: Kirkland, Washington.
52. Cordell, T., T. Benson Tolle, and R. Rondeau. *The programmable powdered preform process for aerospace: Affordable performance through composites*. in *SAMPE International Symposium*. 2000.
53. Chavka, N.G., C.D. Warren, J.A. Carpenter, and P.S. Sklad, *Automotive lightweighting materials program annual progress report - P4 carbon fibre preform development*. 2000, U.S. Department of Energy. p. 89-96.
54. Chavka, N.G., C.D. Warren, J.A. Carpenter, and P.S. Sklad, *Automotive lightweighting materials program annual progress report - Development of manufacturing methods for fiber preforms*. 2001, U.S. Department of Energy. p. 93-95.

55. Dahl, J.S., T. Hoseck, C.D. Warren, J.A. Carpenter, and P.S. Sklad, *Automotive lightweighting materials program annual progress report - Development of manufacturing methods for fiber preforms*. 2002, U.S. Department of Energy. p. 93-97.
56. Dahl, J.S., T. Hoseck, C.D. Warren, J.A. Carpenter, and P.S. Sklad, *Automotive lightweighting materials program annual progress report - Development of manufacturing methods for fiber preforms*. 2003, U.S. Department of Energy. p. 93-99.
57. Devries, J.E., N.G. Chavka, and J.S. Dahl. *Recent advances in glass fiber preforming: Implementation of the Ford Programmable Preform Process (F3P)*. in *International Conference for Manufacturing of Advanced Composites*. 2001. Belfast.
58. Das, S. *Cost assessment of carbon-reinforced composite automotive part*. in *14th International Conference on Composite Materials*. 2003. San Diego, Calafornia: ASC.
59. *SRIM pick-up box competitive with steel*, in *Reinforced Plastics*. 2001. p. 18.
60. Carley, E.P., J.F. Dockum, and P.L. Schell. *Preforming for Liquid Composite Molding*. in *Polymer Composites for Structural Automotive Applications*. 1990. Detroit, Michigan.
61. Jander, M. *Industrial RTM - New developments in molding and preforming technologies*. in *Advanced Composite Materials: New Developments and Applications*. 1991. Detroit, Michigan.
62. Sand, K., *Device for feeding out fibres at production of thermosettable fibre reinforced products*, in *United States Patent*. 1998, Aplicator System AB: Sweden. p. 25 claims, 2 drawing sheets.
63. Chavka, N.G. and J.S. Dahl. *P4: Glass fiber preforming technology for automotive applications*. in *44th International SAMPE Symposium*. 1999. Long Beach, CA.
64. Giurgiutiu, V. and K.L. Reifsnider, *Development of strength theories for random fiber composites.* Journal of Composites Technology and Research, 1994. 16(2): p. 103-114.
65. Brady, D.G. and J.L. Kardos. *Short-fiber reinforced thermoplastics*. in *Thermoplastic Composite Materials*. 1991. Amsterdam: Elsevier Science.
66. Turner, T.A., N.A. Warrior, F. Robitaille, and C.D. Rudd, *The influence of processing variables on the energy absorption of composite tubes.* Composites: Part A, 2005. 36: p. 1291-1299.
67. Tanoglu, M. and A.T. Seyhan, *Compressive mechanical behaviour of E-glass/polyester composite laminates tailored with a thermoplastic binder.* Materials Science and Engineering, 2003. A363: p. 335-344.
68. *Textile glass. Mats. Determination of tensile breaking force*, in *International Standard*. BS ISO 3342:1995.
69. Dahl, J.S. and T. Hoseck. *Investigation into the light transmission characteristics of random chopped carbon fiber preforms*. in *48th International SAMPE Symposium*. 2003. Long Beach, CA.
70. Hitchon, J.W. and D.C. Phillips, *The effect of specimen size on the strength of CFRP*. Composites, 1978(April): p. 119-124.
71. Wisnom, M.R., *Size effects in the testing of fibre-composite materials.* Composites Science and Technology, 1999. 59: p. 1937-1957.

72. Sutherland, L.S., R.A. Shenoi, and S.M. Lewis, *Size and scale effects in composites: I. Literature review.* Composites Science and Technology, 1999. 59(2): p. 209-220.
73. Zweben, C., *Is there a size effect in composites?* Composites, 1994. 25(6): p. 451-453.
74. Mulligan, D.R., S.L. Ogin, P.A. Smith, G.M. Wells, and C.M. Worrall, *Fibre-bundling in a short-fibre composite: 1. Review of literature and development of a method for controlling the degree of bundling.* Composites Science and Technology, 2003. 63: p. 715-725.
75. Yurgartis, S.W., *Techniques for the quantification of composite mesostructures.* Composites Science and Technology, 1995. 53: p. 145-154.
76. Piggott, M.R., *Mesostructures and their mechanics in fibre composites.* Advanced Composite Materials, 1996. 6: p. 75-81.
77. Worrall, C.M. and G.M. Wells. *Fibre distribution in discontinuous fibre reinforced plastics: Characterisation and effect on material performance*. in *ECCM 7*. 1996. London.
78. Mulligan, D.R., S.L. Ogin, P.A. Smith, G.M. Wells, and C.M. Worrall. *The effect of fibre-bundling on the mechanical properties of a short-fibre composite*. in *ICCM-11*. 1997. Australia.
79. Mei, T. and M.R. Piggot, *Mesostructure development during molding of sheet molding compounds.* Polymer Composites, 1996. 17(4): p. 548-555.
80. Ericson, M.L. and L.A. Berglund, *Deformation and fracture of glass mat reinforced polypropylene.* Composites Science and Technology, 1992. 43: p. 269-281.
81. Kacir, L., M. Narkis, and O. Ishai, *Oriented short glass fiber composites. III. Structure and mechanical properties of molded sheets.* Polymer Engineering and Science, 1977. 17(4): p. 234-241.
82. Ostaja-Starzewski, M., *Scale effects in materials with random distributions of needles and cracks.* Mechanics of Materials, 1999. 31: p. 883-893.
83. Pecullan, S., L.V. Gibiansky, and S. Torquato, *Scale effects on the elastic behaviour of periodic and hierarchical two-dimensional composites.* Journal of the Mechanics and Physics of Solids, 1999. 47: p. 1509-1542.
84. Hill, R., *Elastic properties of reinforced solids: some theoretical principles.* Journal of the Mechanics and Physics of Solids, 1963. 11: p. 357.
85. Kanit, T., S. Forest, I. Galliet, V. Mounoury, and D. Jeulin, *Determination of the size of the representative volume element for random composites: statistical and numerical approach.* International Journal of Solids and Structures, 2003. 40: p. 3647-3679.
86. Weitsman, Y.J. and A. Ionita. *Aspects of the mechanical response of randomly reinforced, chopped fiber strand, polymeric composites*. in *21st International Congress of Theoretical and Applied Mechanics*. 2004. Warsaw, Poland.
87. Ionita, A. and Y.J. Weitsman, *Randomly reinforced composites: properties, failure and aspects of material design.* Probabilistic Engineering Mechanics, 2006. 21: p. 64-72.
88. Weibull, W., *A statistical theory of strength of materials.* Ingeniorsvetenscapsakademien Handlingar, 1939. 151: p. 1-29.
89. Harlow, D.G. and S.L. Phoenix, *The chain of bundles probability model for the strength of fibrous materials II: A numerical study of convergence.* Journal of Composite Materials, 1978. 12: p. 314-334.

90. Odom, E.M. and D.A. Adams, *Specimen size effect during tensile testing of an unreinforced polymer.* Journal of Materials Science, 1992. 27: p. 1767-1771.
91. Pan, N., H.C. Chen, J. Thompson, M.K. Inglesby, and S.H. Zeronian, *Investigation on the strength-size relationship in fibrous structures including composites.* Journal of Materials Science, 1998. 33: p. 2667-2672.
92. Beyerlein, I.J. and S.L. Phoenix, *Statistics for the strength and size effects of microcomposites with four carbon fibers in epoxy resin.* Composites Science and Technology, 1996. 56: p. 75-92.
93. Pan, N., S. Zhao, and T. Hua, *Relationship between scale effect and structure levels in fibrous structures.* Polymer Composites, 2000. 21(2): p. 187-195.
94. Hull, D., *An introduction to composite materials*. First ed. 1981: Cambridge University Press. 246.
95. Moreton, *The effect of gauge length on the tensile strength of R.A.E. carbon fibres.* Fibre Science and Technology, 1969. 1(4): p. 273-282.
96. Coleman, B.D., *On the strength of classical fibers and fiber bundles.* Journal of Mechanics and Physics of Solids, 1958. 7: p. 60-70.
97. Van Hattum, F.W.J. and C.A. Bernado, *A model to predict the strength of short fibre composites.* Polymer Composites, 1999. 20(4): p. 524-533.
98. Hwang, T.-K., C.-S. Hong, and C.-C. Kim, *Size effect on the fiber strength of composite pressure vessels.* Composite Structures, 2003. 59: p. 489-498.
99. Bullock, R.E., *Strength ratios of composite materials in flexure and in tension.* 1974: p. 200-205.
100. Bader, M.G. and A.M. Priest. *Statistical aspects of fibre and bundle strength in hybrid composites*. in *4th International Conference on Composite Materials (ICCM-IV)*. 1982. Tokyo, Japan.
101. Zweben, C. and B.W. Rosen, *A statistical theory of material strength with application to composite materials.* Journal of the Mechanics and Physics of Solids, 1970. 18: p. 189-206.
102. Kelly, A. and W.R. Tyson, *Tensile properties of fibre-reinforced metals: Copper/Tungsten and Copper/Molybdenum.* Journal of the Mechanics and Physics of Solids, 1965. 13: p. 329-350.
103. Harlow, D.G. and S.L. Phoenix, *Approximations for the strength distribution and size effect in an idealized lattice model of material breakdown.* Journal of Mechanics and Physics of Solids, 1991. 39(2): p. 173-200.
104. Crowther, M.F. and M.S. Starkey, *Use of Weibull statistics to quantify specimen size effects in fatigue of GRP*. Composites Science and Technology, 1988. 31(2): p. 87-95.
105. Marissen, R. and J. Linsen, *Variability of the flexural strength of sheet moulding compounds.* Composites Science and Technology, 1999. 59: p. 2093-2100.
106. Holmberg, J.A., *Application of Weibull Theory to random-fibre composites.* Composites Science and Technology, 1995. 54: p. 75-85.
107. Wetherhold, R.C., *Probabilistic aspects of strength of short-fibre composites with planar fibre distribution.* Journal of Materials Science, 1987. 22: p. 663-669.
108. Gates, D.J. and M. Westcott, *Predicting fiber contact in a three-dimensional model of paper.* Journal of Statistical Physics, 1999. 94(1/2): p. 31-52.
109. Mcgarry, F.J. and M. Fujiwara, *Resin-fibre load transfer in reinforced plastics.* Modern Plastics, 1968. July: p. 143.

110. Pan, N., *A modified analysis of the microstructural characteristics of general fiber assemblies.* Textile Research Journal, 1993. 63(6): p. 336-345.
111. Komori, T. and K. Makishima, *Estimation of fiber-to-fiber contacts in general fiber assemblies.* Textile Research Journal, 1977. 47(13).
112. Eason, T. and O. Ochoa, *Material behaviour of Structural Reaction Injection Molded composites under thermomechanical loading.* Journal of Composite Materials, 2000. 34(5): p. 411-432.
113. Katayama, T., T. Omiya, I. Amano, T. Tanaka, and K. Kuroda, *A study on the characterisation of glass fibre reinforced thermoplastics by transfer moulding.* Composite Structures, 1995. 32: p. 531-539.
114. Trapeznikov, D.A., A.I. Toropov, and O.D. Loskutov, *Modelling approach to optimisation of mechanical properties of discontinuous fibre-reinforced C/C composites.* Composites, 1992. 23(3): p. 174-182.
115. Shih, C. and L. James Lee, *Effect of fiber architecture on permeability in liquid composite molding.* Polymer Composites, 1998. 19(5): p. 626-639.
116. Summerscales, J., *A model for the effect of fibre clustering on the flow rate in resin transfer moulding.* Composites Manufacturing, 1993. 4(1): p. 27-31.
117. Kalaprasad, G., B. Francis, S. Thomas, C.R. Kumar, C. Pavithran, G. Groeninckx, and S. Thomas, *Effect of fibre length and chemical modifications on the tensile properties of intimately mixed short sisal/glass hybrid fibre reinforced low density polyethylene composites.* Polymer International, 2004. 53: p. 1624-1638.
118. Nazhad, M.M., E.M. Harris, T.J. Dodson, and R.J. Kerekes, *The influence of formation on the tensile strength of paper made from mechanical pulps.* Tappi Journal, 2000(December).
119. Meraghni, F. and M.L. Benzeggagh, *Micromechanical modelling of matrix degradation in randomly oriented discontinuous-fibre composites.* Composites Science and Technology, 1995. 55: p. 171-186.
120. Ericson, M.L. and L.A. Berglund, *The effect of microstructure on the elastic modulus and strength of preformed and commercial GMTs.* Polymer Composites, 1993. 14(1): p. 35-41.
121. Kim, J.-K. and Y.-W. Mai, *Fracture of CFRP containing impregnated fibre bundles.* Composites Science and Technology, 1993. 49: p. 51-60.
122. Brandenburg, K.L., *Critical process variables in the white water system that affect glass fiber dispersion.* Tappi Journal, 1993. 76(7): p. 145-148.
123. Wong, K.H., G.Z. Jiang, S.J. Pickering, and C.D. Rudd. *Effect of fibre length and loading on electromagnetic shielding of thermoset composite reinforcement with virgin or recovered carbon fibres*. in *ICCM 15*. 2005. Durban, South Africa.
124. Kerekes, R.J. and C.J. Schell, *Effect of fibre length and coarseness on pulp flocculation.* Tappi Journal, 1995. 78(2): p. 133.
125. Papathanasiou, T.D. and D.C. Guell, *Flow induced alignment in composite materials*. First ed. 1997, Cambridge England: Woodhead Publishing Limited.
126. Eduljee, R.F., R.L. Mccullough, and J.W. Gillespie, *The influence of aggregated and dispersed textures on the elastic properties of discontinuous-fiber composites.* Composites Science and Technology, 1994. 50: p. 381-391.
127. Richards, T., D. Short, and J. Summerscales. *An aircomb technique to produce thin layers of continuous unidirectional mixed fibre reinforcements.* in *14th British Plastics Federation Reinforced Plastics Congress.* 1984. Brighton, UK.

128. Robitaille, F. and R. Gauvin, *Compaction of textile reinforcements for composites manufacturing. I: Review of experimental results.* Polymer Composites, 1998. 19(2): p. 198-216.
129. Quinn, J.A. and J.E. Randall. *Compliance of composite reinforcement materials*. in *Proceedings of the 4th International Conference on Fibre Reinforced Composites*. 1990. Liverpool, UK: IMeche.
130. Verry, J., M.D. Wakeman, V. Michaud, and J.-A.E. Manson, *Manufacturing cost comparison of thermoplastic and thermoset RTM for an automotive floor plan.* Composites: Part A, 2006. 37: p. 9-22.
131. Halpin, J.C., *Stiffness and expansion estimates for oriented short fiber composites.* Journal of Composite Materials, 1969. 3: p. 732-734.
132. Halpin, J.C., *Primer on Composite Materials: Analysis*. 1984: Technomic Publishing Co.
133. Halpin, J.C., K. Jerine, and J.M. Whitney, *The laminate analogy for 2 and 3 dimensional composite materials.* Journal of Composite Materials, 1971. 5: p. 36.
134. Halpin, J.C. and J.L. Kardos, *Strength of discontinuous reinforced composites: 1. Fiber reinforced composites.* Polymer Engineering and Science, 1978. 18(6): p. 496-504.
135. Halpin, J.C. and N.J. Pagano, *The laminate approximation for randomly oriented fibre composites.* Journal of Composite Materials, 1969. 3: p. 720-724.
136. Jacob, G.C., J.M. Starbuck, J.F. Fellers, and S. Simunovic, *Effect of fiber volume fraction, fiber length and fiber tow size on the energy absorption of chopped fiber-polymer composites.* Polymer Composites, 2005. 26(3): p. 293-305.
137. Lindhagen, J.E. and L.A. Berglund, *Notch sensitivity and damage mechanisms of glass mat reinforced polypropylene.* Polymer Composites, 1997. 18(1): p. 40-47.
138. Cox, H.L., *The elasticity and strength of paper and other fibrous materials.* British Journal of Applied Physics, 1952. 3: p. 72-79.
139. Pan, N. *On the elastic property prediction of randomly oriented fiber composites*. in *Mechanics of Plastics and Plastic Composites*. 1995. San Francisco: AMD.
140. Kalaprasad, G., K. Joseph, S. Thomas, and C. Pavithran, *Theoretical modelling of tensile properties of short sisal fibre-reinforced low-density polyethylene composites.* Journal of Materials Science, 1997. 32(16): p. 4261-4267.
141. Blumentrit, B.F., B.T. Vu, and S.L. Cooper, *Mechanical properties of discontinuous fiber reinforced thermoplastics. II. Random-in-plane fibre orientation.* Polymer Engineering and Science, 1975. 15(6): p. 428-436.
142. Christensen, R.M. and F.M. Waals, *Effective stiffness of randomly oriented fibre composites.* Journal of Composite Materials, 1972. 6: p. 518-532.
143. Nielsen, L.E. and P.E. Chen, *Young's modulus of composites filled with randomly oriented fibers.* Journal of Materials, 1968. 3(2): p. 352-358.
144. Krenchel, H., *Fibre Reinforcement.* Copenhagen: Akademisk Forlag, 1964.
145. Pan, N., *The elastic constants of randomly oriented fiber composites: A new approach to prediction.* Science and Engineering of composite materials, 1996. 5(2): p. 63-72.
146. Hashin, Z. and B.W. Rosen, *The elastic moduli of fiber-reinforced materials.* Journal of Applied Mechanics, 1964. 31: p. 223-232.

147. Brooks, R., *Chapter 8 - Materials property modelling and design of short fibre composites*, in *Flow Induced alignment in composite materials*, T.D. PAPATHANASIOU and D.C. GUELL, Editors. 1997, Woodhead Publishing Ltd: Cambridge, England. p. 293-323.
148. Takao, T.W. Chou, and M. Taya, *Effective longitudinal Young's modulus of misoriented short fiber composites.* Journal of Applied Mechanics, 1982. 49: p. 536.
149. Chou, T.W. and S. Nomura, *Fibre orientation effects on the thermoelastic properties of short-fibre composites.* Fibre Science and Technology, 1981. 14: p. 279-291.
150. Fu, S.Y. and B. Lauke, *The elastic modulus of misaligned short-fiber-reinforced polymers.* Composites Science and Technology, 1998. 58(3-4): p. 389-400.
151. Lauke, B. and S.Y. Fu, *Strength anisotropy of misaligned short-fibre-reinforced polymers.* Composites Science and Technology, 1999. 59: p. 699-708.
152. Fu, S.Y. and B. Lauke, *Effects of fibre length and fibre orientation distributions on the tensile strength of short-fiber-reinforced polymers.* Composites Science and Technology, 1996. 56: p. 1179-1190.
153. Siegmund, T., T. Cipra, J. Liakus, and B. Wang. *Processing-microstructure-strength predictions for short fiber reinforced composite structures based on a spray deposition process*. in *2003 ASME International Mechanical Engineering Congress*. 2003. Washington, D.C.
154. Advani, S.G. and C.L. Tucker Iii, *The use of tensors to describe and predict fiber orientation in short fiber composites.* Journal of Rheology, 1987. 31(8): p. 751-784.
155. Eshelby, J.D., *The determination of the elastic field of an ellipsoidal inclusion, and related problems.* Proceedings of the Royal Society of London, 1957. A241: p. 376-96.
156. Mori, T. and K. Tanaka, *Average stress in matrix and elastic energy of materials with misfitting inclusions.* Acta Metallurgica, 1973. 21: p. 571-574.
157. Manera, M., *Elastic properties of randomly oriented short fiber-glass composites.* Journal of Composite Materials, 1977. 11: p. 235-247.
158. Tsai, S.W. and N.J. Pagano, *Invariant properties of composite materials*. Composite Materials Workshop, ed. S.W. TSAI, J.C. HALPIN, and N.J. PAGANO. 1968, Stamford: Technomic Publishing Company. 233-253.
159. Reinhart, T.J. *The potential of oriented, discontinuous carbon fiber preforms for low cost high performance aerospace structures*. in *SAMPE*. 1999. Detroit, Michigan.
160. Brandstetter, J., K. Kromp, H. Peterlik, and R. Weiss, *Measurement of shear lag parameter B for a fibre bundle pull-out geometry.* Composites Science and Technology, 2003. 64: p. 65-70.
161. Galiotis, C., R.J. Young, P.H.J. Yeung, and D.N. Batchelder, *The study of model polydiacetylene/epoxy composites.* Journal of Materials Science, 1984. 19: p. 3640-3648.
162. Fukuda, H. and T.W. Chou, *An advanced shear-lag model applicable to discontinuous fiber composites.* Journal of Composite Materials, 1981. 15: p. 79-91.
163. Kardos, J.L., *Structure property relations for short-fibre reinforced plastics*. 1975, Divisional Technical Meeting, Engineering Properties and Structure Division, SPE: Akron, Ohio. p. 30-53.

164. Halpin, J.C. and J.L. Kardos, *The Halpin-Tsai Equations: A review.* Polymer Engineering and Science, 1976. 16(5): p. 344-352.
165. Nielsen, L.E., *Generalized equation for the elastic moduli of composite materials.* Journal of Applied Physics, 1970. 41(11): p. 4626-4627.
166. Mcgee, S. and R.L. Mccullough, *Combining rules for predicting the thermoelastic properties of particulate filled polymers, polymers, polyblends, and foams.* Polymer Composites, 1981. 2(4): p. 149-161.
167. Tandon, G.P. and G.J. Weng, *The effect of aspect ratio of inclusions on the elastic properties of unidirectionally aligned composites.* Polymer Composites, 1984. 5(4): p. 327-333.
168. Benveniste, Y., *A new approach to the application of Mori-Tanaka's theory in composite materials.* Mechanics of Materials, 1987. 6: p. 147-157.
169. Christensen, R.M., *A critical evaluation for a class of micro-mechanics models.* Journal of Mechanics and Physics of Solids, 1990. 38(3): p. 379-404.
170. Tucker Iii, C.L. and E. Liang, *Stiffness predictions for unidirectional short-fiber composites: Review and evaluation.* Composites Science and Technology, 1999. 59(5): p. 655-671.
171. Hine, P.J., H.R. Lusti, and A.A. Gusev, *Numerical simulation of the effects of volume fraction, aspect ratio and fibre length distribution on the elastic and thermoelastic properties of short fibre composites.* Composites Science and Technology, 2002. 62: p. 1445-1453.
172. Weng, G.J., *The theoretical connection between Mori-Tanaka's theory and the Hashin-Shtrikman-Walpole bounds.* International Journal of Engineering Science, 1990. 28(11): p. 1111-1120.
173. Qiu, Y.P. and G.J. Weng, *On the application of Mori-Tanaka's theory involving transversely isotropic spheroidal inclusions.* International Journal of Engineering Science, 1990. 28(11): p. 1121-1137.
174. Takao, Y. and M. Taya, *The effect of variable fiber aspect ratio on the stiffness and thermal expansion coefficients of a short fiber composite.* Journal of Composite Materials, 1987. 21: p. 140-156.
175. Nielsen, L.E. and R.F. Landel, *Mechanical properties of polymers and composites*. 2nd ed, ed. L.L. FAULKNER. 1994, New York: Marcel Dekker, Inc. 557.
176. Kataoka, Y., M. Taya, and M. Saito. *Effect of fibre clustering on the stiffness and strength of a short fiber composite*. in *Japan-U.S. CCM-VII*. 1995. Kyoto.
177. Summerscales, J., F.J. Guild, N.R.L. Pearce, and P.M. Russels, *Voronoi cells, fractal dimensions and fibre composites.* Journal of Microscopy, 2001. 201(2): p. 153-162.
178. Katayama, T., K. Tanaka, and Y. Miura. *The evaluation of fibre filamentisation in the LFRTP moulding*. in *8th Japan-US conference on composite materials*. 1998.
179. Liakus, J., B. Wang, T. Cipra, and T. Siegmund, *Processing-microstructure-property predictions for short fiber reinforced composite structures based on spray deposition process.* Composite Structures, 2003. 61(4): p. 363-374.
180. Nguyen, B.N. and M.A. Khaleel, *A mechanistic approach to damage in short-fiber composites based on micromechanical and continuum damage mechanics descriptions.* Composites Science and Technology, 2004. 64: p. 607-617.
181. Hill, R., *Continuum micro-mechanics of elastoplastic polycrystals.* Journal of Mechanics and Physics of Solids, 1965. 3(2): p. 89-101.

182. Camacho, C.W. and C.L. Tucker Iii, *Stiffness and thermal expansion predictions for hybrid short fiber composites.* Polymer Composites, 1990. 11(4): p. 229-239.
183. Benveniste, Y., G.J. Dvorak, and T. Chen, *On diagonal and elastic symmetry of the approximate effective stiffness tensor of heterogeneous media.* Journal of Mechanics and Physics of Solids, 1991. 39(7): p. 927-946.
184. Fan, Y.-H., *Fibre orientation and stiffness prediction in short fibre-reinforced thermoplastics*, in *Polymer Composites Group*. 1997, The University of Nottingham: Nottingham. p. 194.
185. Turner, T.A., *The effects of processing variables on the energy absorption of composite crash structures*, in *Mechanical Engineering, School M3*. 2004, The University of Nottingham: Nottingham.
186. Bay, R.S. and C.L. Tucker Iii, *Stereological measurement and error estimates for three-dimensional fiber orientation.* Polymer Engineering and Science, 1992. 32(4): p. 240-253.
187. Dahl, J.S., C.D. Warren, J.A. Carpenter, and P.S. Sklad, *Automotive lightweighting materials program annual progress report - Development of manufacturing methods for fiber preforms*. 2004, U.S. Department of Energy. p. 95-101.
188. *Magnamite AS4 Carbon Fibre Product Data.* http://www.hexcel.com/NR/rdonlyres/5659C134-6C31-463F-B86B-4B62DA0930EB/0/Magnamite_AS4.pdf.
189. Hancock, P. and R.C. Cuthbertson, *Effect of fibre length and interfacial bond in glass fibre-epoxy resin composites.* Journal of Materials Science, 1974. 5: p. 762-768.
190. Chou, T.W., *Microstructural design of fiber composites*. 1992, Cambridge: Cambridge University Press. 569.
191. Mehan, M.L. and L.S. Schadler, *Micromechanical behavior of short-fiber polymer composites.* Composites Science and Technology, 2000. 60: p. 1013-1026.
192. Hahn, H.T., *On approximations for strength of random fiber composites.* Journal of Composite Materials, 1975. 9: p. 316-325.
193. Van Hattum, F.W.J., J.P. Nunes, and C.A. Bernardo, *A theoretical and experimental study of towpreg-based long fibre thermoplastic composites.* Composites: Part A, 2005. 36: p. 25-32.
194. Fukuda, H. and T.W. Chou, *A probabilistic theory for the strength of short fibre composites.* Journal of Materials Science, 1981. 16: p. 1088-1096.
195. Fukuda, H. and T.W. Chou, *A probabilistic theory of the strength of short-fibre composites with variable fibre length and orientation.* Journal of Materials Science, 1982. 17: p. 1003-1011.
196. Wetherhold, R.C., *Probabilistic aspects of the strength of fiber-dominated short-fiber composites II: Biased fiber distribution.* Materials Science and Engineering, 1987. 91: p. 13-18.
197. Tsai, S.W. and E.M. Wu, *A general theory of strength for anisotropic materials.* Journal of Composite Materials, 1971. 5: p. 58-80.
198. Wetherhold, R.C., *Probabilistic aspects of the strength of fiber-dominated short-fibre composites I: Aligned fibers.* Materials Science and Engineering, 1987. 91: p. 7-12.

199. Frost, M., D. Solanki, and A. Mills. *Resin film infusion processing of carbon fibre composite automotive body panels*. in *24th International SAMPE Europe Conference*. 2003. Porte de Versaille, Paris.
200. Schubel, P.J., *Characterisation of 'Class A' polymer composites for the automotive industry*, in *Department of Mechanical Engineering*. 2005, The University of Nottingham: Nottingham.
201. Ekstrand, G. and N. Asnafi, *On testing of the stiffness and the dent resistance of autobody panels.* Materials and Design, 1998. 19: p. 145-156.
202. Asnafi, N., *On strength, stiffness and dent resistance of car body panels.* Journal of Materials Processing Technology, 1995. 49: p. 13-31.
203. Holmberg, S. and P. Thilderkvist, *Influence of material properties and stamping conditions on the stiffness and static dent resistance of automotive panels.* Materials and Design, 2002. 23: p. 681-691.
204. Holmberg, S. and B. Nejabat, *Numerical assessment of stiffness and dent properties of automotive exterior panels.* Materials and Design, 2004. 25: p. 361-368.
205. Weager, B.M., *Composite-metal laminates for automotive applications*, in *Department of Mechanical Engineering*. 2004, The University of Nottingham: Nottingham.
206. Gunnarsson, L. and E. Schedin, *Improving the properties of exterior body panels in automobiles using variable blank holder forces.* Journal of Materials Processing Technology, 2001. 114: p. 168-173.
207. Carter, J.T., G.T. Emmerson, C. Lo Faro, P.T. Mcgrail, and D.R. Moore, *The development of a low temperature cure modified epoxy resin system for aerospace composites.* Composites Part A, 2003. 80: p. 83-91.
208. Whitney, J.M. and R.J. Nuismer, *Stress fracture criteria for laminated composites containing stress concentrations.* Journal of Composite Materials, 1974. 8: p. 253-265.
209. Lindhagen, J.E. and L.A. Berglund, *Application of bridging-law concepts to short-fibre composites. Part 2: Notch sensitivity.* Composites Science and Technology, 2000. 60: p. 885-893.
210. Hitchen, S.A., S.L. Ogin, P.A. Smith, and C. Soutis, *The effect of fibre length on fracture toughness and notched strength of short carbon fibre/epoxy composites.* Composites, 1994. 25(6).
211. Mallick, P.K., *Effects of hole stress concentration and its mitigation on the tensile strength of sheet moulding compound (SMC-R50) composites.* Composites, 1988. 19(4): p. 283-287.
212. Lindhagen, J.E. and L.A. Berglund, *Microscopical Damage Mechanisms in Glass Fiber Reinforced Polypropylene.* Journal of Applied Polymer Science, 1998. 69(7): p. 1319-1327.
213. Schubel, P.J., N.A. Warrior, K.N. Kendall, and C.D. Rudd, *Characterisation of thermoset laminates for cosmetic automotive applications: Part 1 - Surface Characterisation.* Composites Part A, 2006. In press.
214. Kendall, K.N., C.G.E. Mangin, and E. Ortiz, *Discrete event simulation and cost analysis for manufacturing optimisation of an automotive LCM component.* Composites Part A, 1998. 29: p. 711-720.
215. Akermo, M. and B.T. Astrom, *Modelling component cost in compression moulding of thermoplastic composite and sandwich components.* Composites Part A, 2000. 31: p. 319-333.

216. Turner, T.A., L.T. Harper, N.A. Warrior, and C.D. Rudd, *Low cost carbon-fibre based automotive body panel systems - a performance and manufacturing cost comparison.* Submitted to Journal of Automobile Engineering - Proceedings of the Institution of Mechanical Engineers Part D, 2006.
217. Wakeman, M.D. and J.-A.E. Manson, *Cost analysis*, in *Design and manufacture of textile composites*, A.C. Long, Editor. 2005, Woodhead Publishing Ltd.
218. Gutowski, T., D. Hoult, G. Dillon, E.T. Neoh, S. Muter, E. Kim, and M. Tse, *Development of a theoretical cost model for advanced composite fabrication.* composite Manufacturing, 1994. 5(4): p. 231-239.
219. Kendall, K.N., *Mould design for high volume resin transfer moulding*, in *Department of Mechanical Engineering*. 1991, University of Nottingham: Nottingham.
220. *Plastics - Determination of tensile properties*, in *British Standard*. BS 2782-3:Method 326F:1997.
221. *Guide to statistical interpretation of data*, in *British Standard*. BS 2846-3:1975 ISO 3207:1975.
222. *Fibre-reinforced plastics - Determination of compressive properties in the in-plane direction*, in *British Standard*. BS EN ISO 14126:1999.
223. Chiao, C.C. and R.L. Moore, *Measurement of shear properties of fibre composites.* Composites, 1977. 8: p. 161-170.
224. Lee, S. and M. Munro, *Evaluation of in-plane shear test methods for advanced composite materials by the decision analysis technique.* Composites, 1986. 17: p. 13-22.
225. Walrath, D.E. and D.A. Adams, *The Iosipescu shear test as applied to composite materials.* Experimental Mechanics, 1983. March: p. 93-110.
226. Xavier, J.C., N.M. Garrido, M. Oliveira, J.L. Morais, P.P. Camanho, and F. Pierron, *A comparison between the Iosipescu and off-axis shear test methods for the characterisation of Pinus Pinaster Ait.* Composites: Part A, 2004. 35: p. 827-840.
227. Han, L. and M.R. Piggot, *Tension-compression and Iosipescu tests on laminates.* Composites: Part A, 2002. 33: p. 35-42.
228. Barnes, J.A., M. Kumosa, and D. Hull, *Theoretical and experimental evaluation of the Iosipescu shear test.* Composites Science and Technology, 1987. 48: p. 251-268.
229. Walrath, D.E. and D.F. Adams, *Shear strength and modulus of SMC-R50 and XMC-3 composite materials*. 1980, Mechanical Engineering Department, University of Wyoming, Laramie: Wyoming, USA.
230. Crookston, J., *Prediction of elastic behaviour and initial failure of textile composites*, in *Mechanical Engineering*. 2004, The University of Nottingham.
231. Walrath, D.E. and D.F. Adams, *Static and dynamic shear testing of SMC composite materials*. 1980, Mechanical Engineering Department, University of Wyoming, Laramie: Wyoming, USA.
232. Neumeister, J.M. and N.L. Melin. *A modified Iosipescu test for anisotropic composite panels*. in *ICCM 14*. 2003. San Diego, CA.
233. Melin, N.L. and J.M. Neumeister. *Measuring constitutive shear behaviour of orthotropic composites and evaluation of the modified Iosipescu test*. in *ICCM15*. 2005. Durban, South Africa.
234. Hawong, J.-S., D.-C. Shin, and U.-C. Baek, *Validation of pure shear test device using finite element method and experimental methods.* Engineering Fracture Mechanics, 2004. 71: p. 233-243.

235. Adams, D.O., J.M. Moriarty, A.M. Gallegos, and D.F. Adams, *The V-Notched rail shear test.* Journal of Composite Materials, 2005. Submitted.
236. *Standard test method for shear properties of composite materials by the V-notched beam method*, in *The American Society for Testing and Materials*. ASTM D5379 / D5379M - 93.
237. *Standard test method for shear properties of composite materials by V-notched rail shear method*, in *The American Society for Testing and Materials*. D7078/D7078M - 05.
238. Zhou, G., E.R. Green, and C. Morrison, *In-plane and interlaminar shear properties of carbon/epoxy laminates.* Composites Science and Technology, 1995. 55: p. 187-193.
239. Fernie, R., *Loading rate effects on the energy absorption of lightweight tubular crush structures*, in *Department of Mechanical Engineering*. 2002, The university of Nottingham: Nottingham.
240. *Glass fibre reinforced plastics — Flexural test — Three point bend method*. BS EN 2746:1998: British Standard.
241. Harrison, P., M.J. Clifford, and A.C. Long, *Shear characterisation of viscous woven textile composites: a comparison between picture frame and bias extension experiments.* Composites Science and Technology, 2004. 64: p. 1453-1465.
242. *Textile glass. Mats. Determination of tensile breaking force*, in *International Standard*. ISO3342:1995.
243. *Test Method for Ignition Loss of Cured Reinforced Resins*, in *The American Society for Testing and Materials*. ASTM D 2584-94.
244. Curtis, P.T., *CRAG test methods for the measurement of the engineering properties of fibre reinforced plastics*. 1988, Royal Aerospace Establishment, Ministry of Defence, Farnborough, Hants: Technical Report 88012. p. 101.
245. Yin, Y., G.P. Binner, and T.E. Cross, *The oxidation behaviour of carbon fibres.* Journal of Materials Science, 1994. 29: p. 2250-2254.
246. Christensen, R.M., *Mechanics of Composite Materials*. 1979: John Wiley and Sons, Inc.
247. Jones, R.M., *Mechanics of composite materials*. 2nd ed. 1998, Washington D.C.: Taylor and Francis. 519.